Miniature antibodies hit the big time *p. 594*

How long do neutrons really live? *pp. 605 & 627*

Post-snowball Earth sea level rise *p. 649*

Science

$15
11 MAY 2018
sciencemag.org

AAAS

ORIGINS OF A CHYTRID

Amphibian disease spread from Asia by trade *pp. 604 & 621*

CONTENTS

11 MAY 2018 • VOLUME 360 • ISSUE 6389

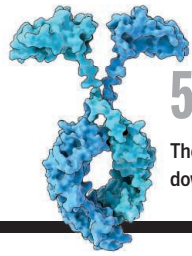

NEWS

IN BRIEF

IN DEPTH

FEATURES

INSIGHTS

PERSPECTIVES

POLICY FORUM

BOOKS *ET AL.*

Published by AAAS

CONTENTS

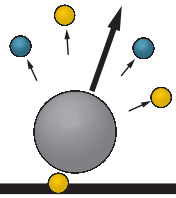

605 & 627
Neutron lifetimes

11 MAY 2018 • VOLUME 360 • ISSUE 6389

LETTERS

RESEARCH

IN BRIEF

RESEARCH ARTICLES

REPORTS

DEPARTMENTS

ON THE COVER

Fire-bellied toads, *Bombina orientalis*, originate from the Korean peninsula. This species entered the expanding pet trade in the 20th century, carrying with it the fungal pathogen *Batrachochytrium dendrobatidis*. Whole-genome sequencing reveals that East Asia is a hotspot of genetic diversity for this chytrid fungus. Subsequently, hypervirulent lineages of the fungus have emerged and caused mass decline in wild amphibian species the world over. See pages 604 and 621. *Photo: Emma Healey/Alamy Stock Photo*

SCIENCE (ISSN 0036-8075) is published weekly on Friday, except last week in December, by the American Association for the Advancement of Science, 1200 New York Avenue, NW, Washington, DC 20005. Periodicals mail postage (publication No. 484460) paid at Washington, DC, and additional mailing offices. The title SCIENCE is a registered trademark of the AAAS. Domestic individual membership, including subscription (12 months): $165 ($74 allocated to subscription). Domestic institutional subscription (51 issues): $1808; Foreign postage extra: Mexico, Caribbean (surface mail) $55; other countries (air assist delivery): $89. First class, airmail, student, and emeritus rates on request. Canadian rates with GST available upon request, GST #125488122. Publications Mail Agreement Number 1069624. **Printed in the U.S.A.**
Change of address: Allow 4 weeks, giving old and new addresses and 8-digit account number. **Postmaster:** Send change of address to AAAS, P.O. Box 96178, Washington, DC 20090–6178. **Single-copy sales:** $15 each plus shipping and handling; bulk rate on request. **Authorization to reproduce** material for internal or personal use under circumstances not falling within the fair use provisions of the Copyright Act is granted by AAAS to libraries and others who use Copyright Clearance Center (CCC) Pay-Per-Use services provided that $35.00 per article is paid directly to CCC, 222 Rosewood Drive, Danvers, MA 01923. The identification code for *Science* is 0036-8075. *Science* is indexed in the *Reader's Guide to Periodical Literature* and in several specialized indexes.

Science
AAAS
1200 New York Avenue, NW, Washington, DC 20005
Clarendon House, Clarendon Road, Cambridge, UK CB2 8FH

SUBSCRIPTION SERVICES For change of address, missing issues, new orders and renewals, and payment questions: 866-434-AAAS (2227) or 202-326-6417, FAX 202-842-1065. Mailing addresses: AAAS, P.O. Box 96178, Washington, DC 20090-6178 or AAAS Member Services, 1200 New York Avenue, NW, Washington, DC 20005

INSTITUTIONAL SITE LICENSES 202-326-6730 **REPRINTS:** Author Inquiries 800-635-7181 **COMMERCIAL INQUIRIES** 803-359-4578 **PERMISSIONS** 202-326-6765, permissions@aaas.org **AAAS Member Central Support** 866-434-2227 www.aaas.org/membercentral.

INFORMATION FOR AUTHORS See www.sciencemag.org/authors/science-information-authors

Published by AAAS

EDITORIAL

Backing up nuclear disarmament

Lassina Zerbo is the executive secretary of the Comprehensive Nuclear-Test-Ban Treaty Organization, Vienna, Austria. info@ctbto.org

Who could have imagined the possibility of an inter-Korean Summit this year, let alone one between the United States and North Korea? Recent news that North Korea may suspend nuclear tests and dismantle its test site is a startling about-face, given the country's multitude of missile and nuclear weapons tests over the past decade. Those incidents increased tensions at a time when questions were being raised about the instruments, approaches, and mechanisms that nations collectively strive to use to rid the world of weapons of mass destruction. At the end of this month, the Comprehensive Nuclear-Test-Ban Treaty Organization (CTBTO) will convene a symposium in Vienna to emphasize what brings real security to the world—negotiated agreements that are effectively verifiable and credibly enforceable. These include the Treaty on the Non-Proliferation of Nuclear Weapons (NPT) and the Comprehensive Nuclear-Test-Ban Treaty (CTBT). The issue is not whether such current institutions and instruments are failing, but rather, preserving their integrity and building further trust in and around them.

"Diplomacy, backed up by... science-based verification tools, remains the key to...security."

It goes without saying that the global political landscape is changing. That is precisely why an immovable global disarmament and nonproliferation architecture, based on instruments including the NPT and the CTBT, constitutes a firm foundation for a future of peace and security.

The NPT entered into force in 1970 to prevent the spread of nuclear weapons and promote peaceful uses of nuclear energy. Some say it is under strain, with North Korea's recent testing activities and events in the Middle East adding to the tensions. If this is so, it is not because of a fatal flaw in the instrument itself, but because not enough has been done to maintain and secure its entire chain of responsibilities—of which the entry into force of the CTBT is an essential part.

The CTBT, a legally binding global ban on nuclear explosive testing by anyone, anywhere, was opened for signature in 1996. It is not in force only because a provision in the treaty requires ratification by a list of 44 states before this occurs. Eight nations have yet to ratify: the United States, China, Iran, Israel, and Egypt—all of which have at least signed, and contribute to the buildup of the CTBT verification regime—along with India, Pakistan, and North Korea.

The CTBT is a fine example of science and technology in action for global peace and security. The treaty establishes a global international monitoring system with hundreds of facilities that are already gathering and transmitting data to a control center at CTBTO headquarters in Vienna, meaning that no nuclear explosion goes undetected. This monitoring system is crucial to future denuclearization in North Korea. The CTBTO's confirmation of a nuclear test by North Korea on 3 September 2017 once again showed how the treaty's verification regime is already working for the benefit of the international community. But the only way to secure this benefit for all time is to bring the treaty into force. Adherence to the treaty by all parties concerned is the only way to overcome the trust deficit that is a real impediment to progress on denuclearization of the Korean Peninsula and to building trust and confidence in the Middle East.

Hard-won treaties like the CTBT and NPT, with their intricate webs of responsibilities, cannot be easily replaced. Let's put these instruments back on track. Diplomacy, backed up by rigorous science-based verification tools, remains the key to unlocking real security. Let's not rethink that.

–Lassina Zerbo

10.1126/science.aau0693

PHOTOS: (INSET) KOREA SUMMIT PRESS POOL/AP PHOTO; (TOP RIGHT) CTBTO

> “Archaeologists from around the world were deprived of a symposium filled with valuable information.”
>
> **Susan Chandler of the Society for American Archaeology**, in *The Washington Post*, about the U.S. Bureau of Land Management blocking staffers from presenting at the society’s annual meeting.

IN BRIEF

Edited by **Jeffrey Brainard**

ASTRONOMY

Greenland scope joins black hole quest

The Greenland Telescope is the northernmost in a global network.

A radio telescope that will help image the shadows of giant black holes in the centers of galaxies opened for business last week in the high Arctic. Erected in December 2017 at Thule Air Base in northern Greenland, the Greenland Telescope is the northernmost component of the Event Horizon Telescope (EHT), a network of radio telescopes that observes these shadows (*Science*, 3 March 2017, p. 893). During testing last month, the Greenland Telescope helped observe one in a nearby galaxy, M87. To resolve such a small and distant object, the EHT combines simultaneous observations from telescopes spread across the globe—the wider the spread, the sharper the image. The Greenland Telescope’s far northern position widens that distribution—although it doesn’t provide a view of the black hole at the center of our own galaxy. The telescope was a U.S.-built prototype for the Atacama Large Millimeter/submillimeter Array, a 64-dish array in Chile, but researchers at Taiwan’s Academia Sinica Institute of Astronomy and Astrophysics led an effort to convert it to work as a stand-alone instrument in Arctic conditions. Eventually, it will be moved to the National Science Foundation’s Summit Station at an elevation of 3200 meters on the ice sheet of central Greenland, where drier air will improve its observations.

A limit on neuroscience grants

SCIENCE POLICY | The U.S. National Institute of Neurological Disorders and Stroke (NINDS) plans to pare back the number of researchers it supports who have $1 million or more per year in grants to free up funds for other labs. Starting next January, the institute will tighten requirements on investigators whose proposed grant would push them over a total of $1 million in National Institutes of Health (NIH) support. To win funding, the proposal will have to receive a peer-review score in the upper half of the overall NINDS percentile cutoff for funding. For example, if the cutoff was the 15th percentile, only those in the seventh percentile and above would be funded. The policy could free up $15 million a year for early career investigators and researchers at risk of losing their only grant. NINDS’s move follows a controversial NIH-wide plan last year to cap an investigator’s total number of grants, which officials quickly withdrew after receiving criticism.

Lander to study Mars’s interior

PLANETARY SCIENCE | NASA’s $814 million InSight lander, launched on 5 May from Vandenberg Air Force Base in California, is starting a half-year journey to Mars, where it will study the planet’s internal structure. Unlike missions that have chased signs of ancient habitability, the lander will listen for marsquakes for clues to the dimensions and composition of the planet’s core, mantle, and crust. InSight is joined for the ride by Mars Cube One, a pair of small satellites that will test miniature radios to relay messages from InSight during its descent.

New editor takes helm at *Nature*

PUBLISHING | Magdalena Skipper, a geneticist who got her Ph.D. from the University of Cambridge in the United Kingdom and who has extensive experience in scientific publishing, will become the first female editor-in-chief of *Nature*, the 149-year-old science journal. Its publisher, Springer Nature, made the announcement on 2 May. Skipper, 49, will also be the first life scientist in the top job at *Nature* when

Detection dogs Will (front) and Ahu (back) helped determine that the eradication project was successful.

CONSERVATION

A rat-free island

The island of South Georgia in the southern Atlantic Ocean is free of rats and mice after the world's largest rodent eradication effort to date, the South Georgia Heritage Trust announced this week. The pests were introduced to the 375,000-hectare British territory by ships during the 18th century and threatened endemic birds such as the South Georgia pipit. From 2011 to 2015, the island trust periodically dropped poisoned bait by air. Starting last year, a team measured the results by monitoring the island for 6 months using camera traps, chewsticks, and other tools; they also walked more than 1600 kilometers accompanied by three terriers trained to detect the scent of any remaining rodents (while ignoring smells of nearby seals).

she moves there on 1 July from her current position as editor-in-chief of the open-access *Nature Communications*. As well as continuing to publish "the most interesting and ground-breaking discoveries," Skipper said in a statement, "I look forward to … providing a voice on important issues such as promoting transparency and diversity in science."

Looted Iraqi artifacts return home

ARCHAEOLOGY | U.S. Immigration and Customs Enforcement last week returned thousands of ancient artifacts to Iraq in a repatriation ceremony. Hobby Lobby, a national arts and crafts retail chain, agreed to pay a $3 million settlement and forfeit the relics, which it bought for $1.6 million from an unnamed dealer in 2010, despite warnings from experts that the artifacts were possibly looted from archaeological sites. The items were originally shipped to the United States in packages falsely labeled as tile samples. The 3800 items, which include bilingual religious texts from the Neo-Babylonian period and several cuneiform tablets that were likely administrative documents from the city of Irisagrig in Mesopotamia, will now go to the National Museum of Iraq in Baghdad.

Australia plans space agency

SPACE EXPLORATION | Australia is creating a space agency with AU$26 million in seed money. The effort, announced 8 May, emphasizes commercial uses of space, but the agency may support some basic research. The new agency could help researchers develop satellites for Earth observation and space science while expanding participation in international missions. It's a "landmark for Australian industry and science," says Peter Quinn, an astronomer at the International Centre for Radio Astronomy Research in Perth, Australia.

PNAS editor resigns under cloud

WORKPLACE | Inder Verma, the prominent cancer scientist and geneticist who was recently accused of sexual harassment, resigned on 1 May as editor-in-chief of the *Proceedings of the National Academy of Sciences*, the prestigious academic journal published by the U.S. National Academy of Sciences (NAS). His resignation came 5 days after *Science* published an article in which eight women alleged that Verma sexually harassed them in incidents from 1976 to 2016 (*Science*, 4 May, p. 480). Verma has denied the allegations. The NAS Council put Verma on temporary leave from the editorship last December, after he was accused, in gender discrimination lawsuits filed last July, of impeding women's careers at the Salk Institute for Biological Studies in San Diego, California. Salk suspended Verma on 20 April, 2 days after receiving questions from *Science* about certain women's sexual harassment allegations.

EU science budget may rise 50%

RESEARCH FUNDING | The European Commission last week proposed spending €100 billion on its next, 7-year science funding program, which the commission says would represent an increase of up to 50% over the current one. But analysts predict that the final amount for Horizon Europe, to begin in 2021, will be lower after lengthy negotiations with the European Parliament and cost-conscious member states. Some lobby groups had called for doubling the budget; this opening bid is "the bare minimum," says Kurt Deketelaere, secretary general of the League of European Research Universities.

SCIENCEMAG.ORG/NEWS
Read more news from *Science* online.

BY THE NUMBERS

$5,300,000

Cost, per case, of using RNA testing to detect eight blood samples infected with Zika virus among 4 million blood donations, *The New England Journal of Medicine* reports. The U.S. government requires all donations to be tested for the virus.

1000

Number of members of the U.S. National Academy of Sciences who signed a statement criticizing President Donald Trump's administration for its plan to withdraw the United States from the Paris climate agreement and for "dismissal of scientific evidence in policy formulation."

PHOTO: OLI PRINCE

PHOTO: AP PHOTO/DARKO VOJINOVIC

HIGHER EDUCATION

Hungarian science troubled by nationalism

Government standoff with Central European University is coming to a head

By **Kata Karáth**

In early April, several days after Viktor Orbán secured his third consecutive term—and fourth overall—as Hungarian prime minister with a landslide victory for his conservative party, the pro-government paper *Figyelő* published a list of more than 200 people it called "mercenaries" of George Soros, the American-Hungarian billionaire philanthropist. The list included investigative journalists and human rights advocates—and 30 academics from the Soros-founded, Budapest-based Central European University (CEU). Diána Ürge-Vorsatz was stunned to find herself accused.

"I have no idea why I am on this list," says the CEU environmental physicist, who was a member of the Intergovernmental Panel on Climate Change when it won the Nobel Peace Prize in 2007. "I have had a very good working relationship with the Hungarian government for decades, and I want to maintain this."

Ürge-Vorsatz is one of many Hungarian academics unnerved by their government's aggressive nationalist agenda, and the intensifying political pressures it is imposing on science. CEU, which attracts top students from Europe and elsewhere for its English-language graduate classes and has 17 research centers focusing on social sciences, business, environment, math, and other topics, has become a prime target, subject to tightening restrictions that some fear could force it out of Hungary. The main grant-funding body for Hungarian science, praised for its independence and transparency in a recent European review, has been replaced by an agency that scientists worry is more susceptible to political influence. And some researchers suggest that the government is increasingly wasting scarce funds on scholarship that promotes a particular agenda or controversial theories of national origin.

Many scientists fear reprisals if they complain publicly—Ürge-Vorsatz had participated in a large pro-CEU protest before she was accused. But Hungary's academic community has not been silent. "Search for truth, freedom of research, civic activism and support for those in need are crucial social values," more 500 Hungarian academics declared in a recent petition. And the Hungarian Academy of Sciences quickly challenged the newspaper's naming of CEU academics. "We find the issue of such harmful listings unacceptable, especially given their bitter resemblance to similar practices in Hungarian history," it said in a statement.

Government spokespeople declined to answer specific questions about CEU, but did address another flash point: the country's growing embrace of traditional Chinese medicine (TCM). On 16 April, Hungary's University of Szeged signed an agreement with the Shaanxi University of Chinese Medicine in Xianyang, China, to bring TCM researchers, medical experts, and lecturers to teach in the region. The University of Pécs in Hungary has had a similar arrangement since 2015.

Last year, the Hungarian government also announced plans to allocate about €4.5 million ($5.3 million) to build a new institute with a whole floor dedicated to TCM at Semmelweis University, one of the most prestigious medical schools in Hungary. The government says it wants to bridge the gap between Western medicine and Eastern alternatives to improve Hungarian health care, and also strengthen the economic, political, and cultural ties between Hungary and China.

At the end of April, however, Zsolt Boldogkői, head of the Department of Medical Biology at the University of Szeged, lamented TCM's growing influence in the country in an open letter to the president of the Hungarian Academy of Sciences. "Acupuncture is based on pseudoscience and a

Hungarian Prime Minister Viktor Orbán, recently re-elected, has overseen budget boosts for science, but many researchers distrust his government's intentions.

technique unsuitable for medical purposes … teaching it on a university level is seriously damaging the reputation of science and fact-based medical treatments," he wrote.

The government has also been channeling significant funds to research institutes seen as backing its nationalist agenda. For example, the Migration Research Institute opened in Budapest in 2015, when an influx of immigrants caused a crisis in Hungary. Since then, it has published many analyses documenting the downside of immigration and the efficacy of the barbed wire fence along the southern borders of Hungary, and questioning the legitimacy of a 2017 European Court of Human Rights decision that said Hungary had wrongfully deported Bangladeshi asylum seekers.

Academics are also wary of the recently announced László Gyula Institute, named after a historian who studied Hungarian national origins. The research institute hasn't opened yet—no site has been chosen nor staff hired—but it reportedly will be managed by the National Institute for Culture, which is run by a private foundation established by Sándor Lezsák, deputy speaker

In May 2017, protesters in downtown Budapest rallied against government actions threatening Central European University.

PHOTO: AP PHOTO/BALAZS MOHAI

of the Hungarian Parliament. Lezsák is an outspoken nationalist who has supported ideas on the roots of Hungarians opposed by most historians, including the theory that they are related to the Huns, Asiatic nomads who were a feared enemy of the Roman Empire.

Hungarian archaeologists complain that the new institute will compete with the efforts of a research unit, run by the Hungarian Academy of Sciences, that already focuses on the same period. "Little is revealed about this [new] institute just yet, but naming it after a publicly well-known archaeologist sounds like a publicity stunt," says one Hungarian university archaeologist, who requested anonymity.

For now, the scientific community mostly trusts the independence of its major national funder, the National Research, Development and Innovation Office (NRDI) in Budapest, which has a budget of about €260 million ($310 million) for research and innovation this year. In 2015, the previous body, the politically independent Hungarian Scientific Research Fund, merged with the much bigger NRDI, and many researchers at the time feared that the decision would open the way to political influence over funding decisions. The president of NRDI has substantial decision-making power over NRDI's funds—by law, 3% can be directed to anything they want, for example—and personally appoints the members of peer-review committees that approve grants.

The current head of NRDI, physicist József Pálinkás, has proved to be a strong advocate for science. Since he took over in 2015, NRDI has created regular grants to encourage basic science research, reward excellence, and support young scientists. Hungary still heavily relies on EU funds to develop its research infrastructure, but Pálinkás next year plans to request a doubling of the national research and innovation budget to more than €520 million. His term ends in 2020, however, and some scientists express concern, in private, that the government will replace him with someone more political.

By then, CEU may have started to pull up stakes. In April 2017, the government amended the nation's higher education law to require, among other things, that CEU have a second campus in New York, its home state, and obtain a bilateral agreement of support between the Hungarian and U.S. governments. In response, CEU rushed to set up classes at Bard College, in Annandale-on-Hudson, New York. In the next few weeks, Orbán's government is due to decide whether CEU has complied with the law and can enroll new students. The university believes it has but is nonetheless making backup plans to move its classes to Vienna, CEU Provost Liviu Matei said last month at the Scholars at Risk Network Global Congress in Berlin. (CEU hopes to retain its research centers in Budapest.) "It will be a very traumatic event," he added. ■

Kata Karáth is a science journalist in Budapest. With reporting by Hinnerk Feldwisch-Drentrup, a journalist in Berlin.

ANIMAL WELFARE

Animal tests surge under new U.S. chemical law

2016 measure urged EPA to reduce animal use, but numbers are rising instead

By **Vanessa Zainzinger**

Two years ago, when the U.S. Congress approved a major rewrite of the nation's chemical safety law, lawmakers ordered federal regulators to take steps to reduce the number of animals that companies use to test compounds for safety. But a recent analysis by two animal welfare groups found that the number of animal tests requested or required by the Environmental Protection Agency (EPA) jumped dramatically last year, from just a few dozen tests involving fewer than 7000 animals in 2016, to more than 300 tests involving some 75,000 rats, rabbits, and other vertebrates.

The cause of the increase isn't clear. But the new law imposes stricter requirements on a broader array of chemicals than its predecessor, including both new products and ones already on the market, and experts say EPA staff may be trying to comply by gathering more test data from companies. Both industry and animal welfare groups are alarmed by the trend, and are asking agency officials to clarify why they are requesting the tests—and how they plan to reduce the number in the future.

In a 27 March letter to EPA officials, the two Washington, D.C.–based groups that produced the analysis—People for the Ethical Treatment of Animals (PETA) and the Physicians Committee for Responsible Medicine (PCRM)—wrote that the "appalling" number of animals being used in tests "indicates EPA is failing to balance" its responsibility to evaluate chemicals' risks against its obligation to pursue alternatives to animal testing.

In 2016, many animal welfare activists applauded lawmakers for including a provision in a major rewrite of the 1976 Toxic Substances Control Act (TSCA) requiring EPA to develop a plan to "reduce, refine or replace" the use of vertebrate ani-

mals in testing. Lawmakers suggested the agency could save time and money by harnessing advances in computer modeling, biochemistry, and cell-based testing methods to replace test animals. They ordered EPA to finalize a long-term strategy for increasing the use of such alternatives by this year.

EPA released a draft of that strategy for public comment in March. In preparing a response, PETA and PCRM used a government database to tally the agency's TSCA-related animal tests over the past 3 years. In 2015, EPA required or requested 21 tests involving 8881 animals, the groups found; in 2016, it asked for 37 tests involving 6539 animals. In 2017, the first full year that the new law was in force, the numbers jumped to 331 tests and 76,523 animals. Some tests involve rats inhaling substances, whereas others call for placing chemicals into the eyes of rabbits.

76,523

Estimated number of animals needed for the 331 chemical safety tests that the Environmental Protection Agency requested in 2017, compared with 6539 in 2016.

The two groups argue that the agency hasn't adequately explained why it can't obtain the needed data from nonanimal tests. A major chemical industry advocacy group, the Washington, D.C.–based American Chemistry Council (ACC), echoes that concern. EPA sometimes appears "unwilling" to rely on data from computational modeling, for example, "even when it is generated from agency-recommended programs," says Jon Corley, an ACC spokesperson.

EPA did not respond to a request for comment on the surge in testing or what might be driving it. One factor might be that EPA staff are not yet fully aware of proven alternatives to animal tests, says Kristie Sullivan, PCRM's vice president of research policy. They might need more training and funding "to stay abreast of new developments in toxicology, so that they can quickly incorporate new methods and kinds of data into their decision-making process," she says.

EPA's views on the matter could become clearer soon. The comment period on its draft strategy for reducing animal tests closes this week, and the agency is required to issue a final plan by 22 June. ■

Vanessa Zainzinger is a science journalist based in the United Kingdom.

CLIMATE CHANGE

NASA cancels carbon monitoring research program

Move undermines efforts to use satellite and aircraft observations to verify greenhouse gas reduction treaties

By **Paul Voosen**

You can't manage what you don't measure. The adage is especially relevant for climate-warming greenhouse gases, which are crucial to manage—and challenging to measure. In recent years, though, satellite and aircraft instruments have begun monitoring carbon dioxide and methane remotely, and NASA's Carbon Monitoring System (CMS), a $10-million-a-year research line, has helped stitch together observations of sources and sinks into high-resolution models of the planet's flows of carbon. Now, President Donald Trump's administration has quietly killed the CMS, *Science* has learned.

The move jeopardizes plans to verify the national emission cuts agreed to in the Paris climate accords, says Kelly Sims Gallagher, director of Tufts University's Center for International Environment and Resource Policy in Medford, Massachusetts. "If you cannot measure emissions reductions, you cannot be confident that countries are adhering to the agreement," she says. Canceling the CMS "is a grave mistake," she adds.

The White House has mounted a broad attack on climate science, repeatedly proposing cuts to NASA's earth science budget, including the CMS, and cancellations of climate missions such as the Orbiting Carbon Observatory 3 (OCO-3). Although Congress fended off the budget and mission cuts, a spending deal signed in March made no mention of the CMS. That allowed the administration's move to take effect, says Steve Cole, a NASA spokesperson in Washington, D.C. Cole says existing grants will be allowed to finish up, but no new research will be supported.

The agency declined to provide a reason for the cancellation beyond "budget constraints and higher priorities within the science budget." But the CMS is an obvious target for the Trump administration because of its association with climate treaties and its work to help foreign nations understand their emissions, says Phil Duffy, president of the Woods Hole Research Center in Falmouth, Massachusetts. And, unlike the satellites that provide the data, the research line had no private contractor to lobby for it.

Many of the 65 projects supported by the CMS since 2010 focused on understanding the carbon locked up in forests. For example, the U.S. Forest Service has long operated the premier land-based global assessment of forest carbon, but the labor-intensive inventories of soil and timber did not extend to the remote interior of Alaska. With CMS financing, NASA scientists worked with the Forest Service to develop an aircraft-based

The Carbon Monitoring System assessed deforestation, such as burning rainforest to clear lands for grazing.

PHOTO: © JACQUES JANGOUX/SCIENCE SOURCE

laser imager to tally up forest carbon stocks. "They've now completed an inventory of forest carbon in Alaska at a fraction of the cost," says George Hurtt, a carbon cycle researcher at the University of Maryland in College Park, who leads the CMS science team.

The program has also supported research to improve tropical forest carbon inventories. Many developing nations have been paid to prevent deforestation through mechanisms like the United Nations's REDD+ program, which is focused on reducing emissions from deforestation and forest degradation. But the limited data and tools for monitoring tropical forest change often meant that claimed reductions were difficult to trust. Stephen Hagen, a senior scientist at Applied GeoSolutions in Newmarket, New Hampshire, was part of a team that with the Indonesian National Institute of Aeronautics and Space developed laser-mapping tools to automatically detect new roads and gaps in tropical forests, monitoring that helped the Indonesian government apply for REDD+ funding. The end of the CMS is disappointing and "means we're going to be less capable of tracking changes in carbon," Hagen says.

The CMS improved other carbon monitoring as well. It supported efforts by the city of Providence to combine multiple data sources into a picture of its greenhouse gas emissions, and identify ways to reduce them. It has tracked the dissolved carbon in the Mississippi River as it flows out into the ocean. And it has paid for researchers led by Daniel Jacob, an atmospheric chemist at Harvard University, to refine their satellite-based observations of methane.

It's an ironic time to kill the program, Jacob says. NASA is planning several space-based carbon observatories, including the OCO-3, which is set to be mounted on the International Space Station later this year, and the Geostationary Carbon Cycle Observatory, due for launch early next decade. The CMS would help knit all these observations together. "It would be a total shame to wind [it] down," Jacob says.

This type of research is likely to continue, Duffy adds, but leadership will pass to Europe, which already operates one carbon-monitoring satellite, with more on the way. "We really shoot ourselves in the foot if we let other people develop the technology," he says, given how important the techniques will be in managing low-carbon economies in the future. Hurtt, meanwhile, holds out hope that NASA will restore the program. After all, he says, the problem isn't going away. "The topic of climate mitigation and carbon monitoring is maybe not the highest priority now in the United States," he says. "But it is almost everywhere else." ■

PHOTO: NIOBE THOMPSON

A documentary reconstruction shows Botai riders, who may have galloped across Kazakhstan about 3500 B.C.E.

ANCIENT DNA

Finding the first horse tamers

Genes suggest that Central Asian hunter-gatherers, not famed Yamnaya herders, first domesticated horses

By **Michael Price**

Taming horses opened a new world, allowing prehistoric people to travel farther and faster than ever before, and revolutionizing military strategy. But who first domesticated horses—and the genetic and cultural impact of the early riders—has long been a puzzle.

The "steppe hypothesis" suggested that Bronze Age pastoralists known as the Yamnaya, or their close relatives, first domesticated the horse. Aided by its fleet transport, they migrated out from the Eurasian steppe and spread their genes, as well as precursors of today's Indo-European languages, across much of Eurasia. But a new study of ancient genomes, published online in *Science* this week, suggests that the Yamnaya's effect on Asia was limited, and that another culture domesticated the horse first. "This is a really exciting paper," says Priya Moorjani, a geneticist at the University of California, Berkeley.

The first signs of horse domestication—pottery containing traces of mares' milk and horse teeth with telltale wear from a riding bit—come from Botai hunter-gatherers, who lived in modern Kazakhstan from about 3700 B.C.E. to 3100 B.C.E. Yet some researchers thought the Botai were unlikely to have invented horse husbandry because they lingered as hunter-gatherers long after their neighbors had adopted farming and herding. These researchers assumed the Botai learned to handle horses from nearby cultures on the steppe, perhaps even the Yamnaya, who were already herding sheep and goats.

Genetic data suggest the Yamnaya migrated both east and west during the Bronze Age, and mixed with locals. Some researchers hypothesize that they also spread early branches of a Proto-Indo-European (PIE) language, which later diversified into today's many Indo-European languages, including English, Italian, Hindi, Russian, and Persian.

To explore the Yamnaya's legacy in Asia, a team led by Eske Willerslev of the University of Copenhagen and the University of Cambridge in the United Kingdom sequenced the whole genomes of 74 ancient Eurasians, most of whom lived between 3500 B.C.E. and 1500 B.C.E. The researchers devised a rough family tree and timeline for these samples and those from later civilizations and modern people.

The team found no Yamnaya DNA in the three Botai individuals, suggesting the two groups hadn't mixed. That implies the Botai domesticated horses on their own, says Willerslev, first hunting the animals, then managing herds for food, and finally using them for other purposes. "It's an extremely important achievement from a group of people we all think of as being pretty simple," he says.

The new work fits with the archaeological evidence and a recent study of DNA from ancient horses themselves (*Science*, 6 April, p. 111), says zooarchaeologist Sandra Olsen at the University of Kansas in Lawrence, a co-author on that study. That work showed that Botai horses were not related to modern horses, hinting at separate domestications by the Botai and other steppe dwellers.

The Yamnaya used horses to migrate far and wide. Yet Willerslev's team found little Yamnaya DNA in Central and South Asia. They saw no trace of it in ancient people from Anatolia in modern Turkey, where Hittite, an early branch of PIE, was likely spoken. That suggests Hittite likely didn't evolve from a language brought by the Yamnaya. "What we see does not support a classical way of looking at the steppe hypothesis," Willerslev says.

He argues for a more nuanced history in which steppe pastoralists weren't the original horse-whisperers or first introducers of PIE to Anatolia. But by seeping into Europe and Asia in multiple migrations, he says, they still rode their steeds to a big role in prehistory. ■

Michael Price is a journalist in California.

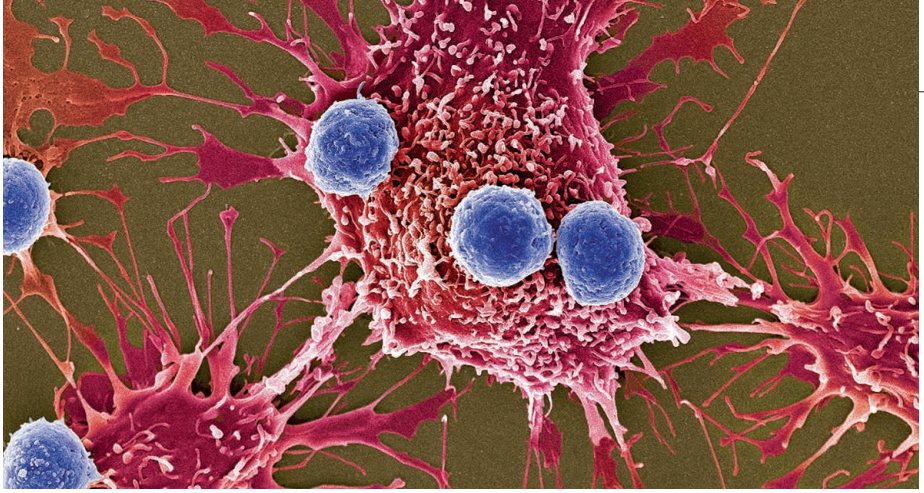

A class of drugs meant to help unleash T cells (blue) on cancer cells (red) stumbled in a recent trial.

PHOTO: STEVE GSCHMEISSNER/SCIENCE SOURCE

BIOMEDICINE

A new cancer immunotherapy suffers a setback

An exciting drug failed in a large trial, triggering a retreat and raising questions about the field's frantic pace

By **Ken Garber**

The surprising failure last month of a large clinical trial of a promising cancer immunotherapy drug from the biotech company Incyte has quickly reverberated across the pharmaceutical industry. Three companies have canceled, suspended, or downsized 12 other phase III trials of the compound, epacadostat, or two similar drugs, together slated to enroll more than 5000 patients with a variety of advanced cancers.

The companies say they aren't dropping the potential drugs, designed to unleash the immune system on cancer cells by blocking an enzyme called indoleamine (2,3)-dioxygenase (IDO). But the retrenching suggests that the frenzy to combine novel drugs with the wildly successful immunotherapies known as checkpoint inhibitors is outpacing the science (*Science*, 23 March, p. 1346). The IDO strategy, says neuroimmunologist Michael Platten of the University of Heidelberg in Germany, "has been moved to randomized clinical trials too fast, and now we realize [the enzyme is] still a black box."

A year ago, the future of IDO inhibitors looked bright. At the June 2017 meeting of the American Society of Clinical Oncology, doctors reported that epacadostat, given with the approved checkpoint inhibitor Opdivo, shrank tumors in 25 of 40 of melanoma patients—roughly double the historical response rate of Opdivo alone. A second epacadostat trial of 63 additional melanoma patients was also impressive, and the drug seemed to work well in other tumor types.

The results from smaller, phase II trials don't always predict how a cancer drug will do in a randomized phase III trial. But the epacadostat data "were pretty compelling," says Yale University immuno-oncologist Mario Sznol, who expected to see some benefit to patients. (Sznol was not involved in any of the trials.) Compared with a checkpoint inhibitor alone, however, epacadostat made no difference for the roughly 350 patients receiving both drugs in Incyte's phase III trial. "The results are disappointing and clear," Incyte Chief Medical Officer Steven Stein in Wilmington, Delaware, said on a conference call announcing an early end to the trial. "The drug didn't perform."

Researchers at the company and elsewhere are baffled. Is IDO simply a bad target? Is Incyte's particular chemical compound flawed? Or were the wrong tumor types or patients treated? "You could go through the whole list of reasons," Sznol says.

The field still generally agrees that IDO makes sense to target, in combination with checkpoint inhibitors. Those drugs release a molecular brake on tumor-killing immune T cells. But the unleashed cells then stimulate the production of IDO, which, in a negative feedback loop, shuts them down again. IDO does this mainly by indirectly activating a protein inside immune cells called the aryl hydrocarbon receptor (AHR). Suppressing IDO should therefore make checkpoint inhibitors work better.

But much about IDO remains unknown, Platten says. Exactly how IDO stifles the immune system is unresolved, nor is it clear which immune cells are most involved, he says. Even the idea that IDO blunts the antitumor effects of checkpoint inhibitors is suspect. "The evidence that this is really happening in the clinical situation … is very slim," Platten says.

The drug, not the target, might be the problem. Some IDO inhibitors bind the AHR and thus could suppress the immune system, the opposite of the drug's intent. NewLink Genetics reports that its drug does activate the AHR, but in a way that it still believes promotes a strong immune response against tumors. Both Incyte and Eli Lilly and Company say their drugs do not affect the AHR.

Levi Garraway, Eli Lilly's senior vice president of oncology global development and medical affairs in Indianapolis, says that going forward the company will try to select patients who are most likely to respond to IDO inhibitors, using unspecified biomarkers. At a recent cancer meeting, immuno-oncologist Tom Gajewski of the University of Chicago in Illinois noted that biomarker analysis in the IDO trials has been "lagging." The epacadostat trial failure, he added, is "a good wake-up call to make sure all the boxes are checked" for new combination therapies. But companies may still be tempted to press ahead with limited data. "There can be a sense of, 'I'd better act now,'" Garraway says.

Sznol agrees that companies probably moved IDO inhibitors into phase III trials too aggressively. But he cautions against making too much of the epacadostat trial failure. "Sure, the field needs a little bit of cold water—no question," he says. "But it shouldn't reduce the enthusiasm that much. … One negative trial doesn't wipe out all the positive results we've seen up to this point." ■

Ken Garber is a science journalist in Ann Arbor, Michigan.

Mass exodus

Three companies have suddenly suspended, canceled, or downsized 13 trials of indoleamine (2,3)-dioxygenase inhibitors (in combination with drugs called checkpoint inhibitors).

COMPANY	DRUG	CANCER
Incyte (nine trials)	epacadostat (INCB24360)	Melanoma, lung, head and neck, urothelial, kidney
Bristol-Myers Squibb (three trials)	BMS-986205	Melanoma, lung, head and neck
NewLink Genetics (one trial)	indoximod (NLG8189)	Melanoma

ASTRONOMY

Fast stars point to supernovae, black holes

Speediest Milky Way stars in Gaia data release include invaders from other galaxies

By **Joshua Sokol**

Ken Shen was so excited that he woke up before his alarm. At noon on 25 April in Europe—3 a.m. for Shen, an astrophysicist at the University of California, Berkeley—the collaboration behind the European Space Agency's Gaia satellite released a data set containing the motions, and much more, for 1.3 billion stars (*Science*, 27 April, p. 363). Shen wanted to sift the data set for the fastest moving stars in the sky, which astronomers prize as forensic tools: When rewound, their trajectories point back to the violent events that launched them. Shen knew his team had to move fast to beat the competition. "I'm a theorist," he says. "Nothing I've ever done has mattered on this timescale."

His eagerness was rewarded. Last week, his team reported the discovery of three white dwarfs—the dying embers of sunlike stars—hurtling through the galaxy at thousands of kilometers per second, perhaps flung out from supernovae explosions. Other groups were also quick off the mark. One reported more than two dozen fast-moving stars, some apparently kicked out by our galaxy's central black hole; another confirmed that a star blazing through the outskirts of the Milky Way actually hails from another galaxy altogether, the Large Magellanic Cloud (LMC). The flood of discoveries has sent astronomers racing to their telescopes to check and classify the swift objects, says Harvard University astronomer James Guillochon. "It's hard to know which stars to look at first."

Astronomers can easily clock a star's velocity toward or away from Earth by observing the Doppler shift of its light. But measuring sideways motion across the sky, necessary for understanding a star's actual speed and where it's headed, was slow and painstaking—until Gaia launched in 2013 and began to measure tiny shifts in the stars' apparent positions. The new release offers measurements of that sideways motion for all 1.3 billion stars, plus radial velocities for 7 million of the brightest ones.

Shen hoped fast stars could help test a particular theory about type Ia supernovae, the explosions of white dwarf stars. The thermonuclear detonations are triggered when a white dwarf sucks material from a companion star until it is heavy enough to fuse carbon nuclei in its core. But the companion's identity is hazy. In one scenario, the white dwarf steals material from an ordinary star. In Shen's favored scenario, a pair of white dwarfs pirouette together, gathering speed until, just before merging, one of them acquires enough material to explode and the other is released into space like a ball in an Olympic hammer throw.

To look for these survivors, Shen's team picked through the Gaia survey for stars with the highest sideways motion. Then they checked these candidates with ground-based telescopes in California, the Canary Islands, and South Africa to classify their stellar types and get their missing radial velocities. Within 24 hours, Shen's team found three white dwarfs that might fit the bill. One moves at 2400 kilometers per second, putting it among the fastest objects in the galaxy, the team reported on 30 April in a paper posted to the preprint repository arXiv.

The team also rewound the paths of these stars 100,000 years in time. One traces back to a nearby supernova remnant, the debris cloud from a previous explosion, deepening the link. "This is a great result, observationally," says astrophysicist Kris Stanek at The Ohio State University in Columbus. Theorists still need more time to consider Shen's scenario, he says, but the white dwarf "probably is a part of a supernova explosion."

Another team led by Tommaso Marchetti at Leiden University in the Netherlands searched Gaia data for fast-moving stars that testify to another kind of galactic violence. On 27 April, they reported on arXiv that they had found 28 of them, some speeding away from the galactic center, where a giant black hole lurks. In theory, the powerful gravity of this black hole can disrupt binary star systems that stray too close, sending one star rocketing away at about 1000 kilometers per second, fast enough to escape the galaxy's own gravitational pull.

Two of Marchetti's stars, however, trace back to outside the galaxy, perhaps to the LMC. Another star, called HVS3, provides an even clearer case. It was discovered in 2005, suspiciously close to the LMC, in the halo of the Milky Way. Gaia data show that HVS3 hails from the heart of the LMC, argues a team led by astronomer Denis Erkal at the University of Surrey in the United Kingdom in a 26 April arXiv paper. It's traveling so fast that it, too, may have gotten its kick from a central black hole—a previously undetected one belonging to the LMC.

"That's big," says Douglas Boubert, a Ph.D. student at the University of Cambridge in the United Kingdom who helped hunt down Gaia's high-speed stars for Erkal, Shen, and Guillochon. Astronomers know that all large galaxies host big black holes, but it isn't clear how many small galaxies like the LMC do. Finding more objects ejected from the LMC would help weigh that black hole, and perhaps confirm Boubert's driving suspicion: that a sizable fraction of the Milky Way's speedsters "are coming from a different galaxy entirely," he says. "Who knows if I'm right." ■

Joshua Sokol is a journalist in Boston.

Stellar speedsters

Astronomers have discovered dozens of stars that move so fast they are not bound by the Milky Way's gravity. Some are likely to hail from other galaxies. One, a white dwarf, can be traced back to a supernova explosion.

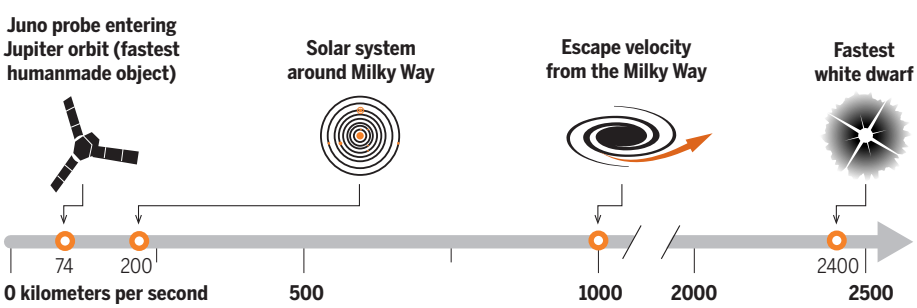

CREDITS: (GRAPHIC) V. ALTOUNIAN AND A. CUADRA/*SCIENCE*; (DATA) NASA; INSTITUTE OF PHYSICS; J. G. HILLS, *NATURE*, VOL. 331, 687 (1998); K. J. SHEN *ET AL.*, ARXIV, 1804.11163 (2018)

FEATURES

A DIFFERENT ANIMAL

One gene separates spring- and fall-run Chinook salmon. Is that enough to justify an endangered species listing?

By **Katie Langin**; *Photography by* **David McLain**

For 40 years, Leaf Hillman, a ceremonial leader of California's Karuk Tribe, has danced on the banks of the Klamath River. Following the tradition of his ancestors, he implores the salmon that have long sustained his tribe to return from the sea.

Chinook, or king, salmon (*Oncorhynchus tshawytscha*) arrive in two waves, in spring and fall, to spawn in freshwater. But the Karuk hold the spring arrivals in "special esteem," Hillman says. The fish leave saltwater in March, having packed enough fat onto their meter-long bodies to sustain them for months, until they mature and spawn far up the river. Fall Chinook spawn lower down in the watershed and mature in the ocean before heading upstream, so they don't carry as much fat.

The spring runs were historically larger, but dams built on the Klamath between 1912 and 1964 denied these so-called springers access to hundreds of kilometers of spawning habitat in the uppermost tributaries. And other changes, such as water diversions for farming, have affected the spring Chinook

Members of California's Karuk Tribe net a Chinook salmon from the Klamath River, where spring runs of the fish are in decline.

more than the fall fish, because springers spend more time in the river. As a result, fewer and fewer spring salmon answer Hillman's appeal these days.

In 2011, conservationists petitioned federal officials to protect the Klamath's spring Chinook runs under the Endangered Species Act of 1973 (ESA). The listing was justified, they argued, under an ESA provision that allows the government to protect a "distinct population segment" of vertebrate as though it were a full-fledged species. But officials at the National Oceanic and Atmospheric Administration (NOAA), which oversees salmon and other anadromous fish that spend part of their lives in the ocean, denied the petition. One reason: Researchers had concluded that the Klamath's spring-run Chinook are genetically similar to fall-run Chinook.

New research findings, however, are forcing scientists and federal officials to revisit that decision. In 2017, researchers announced that they'd identified a single gene that appears to control whether Chinook salmon, as well as steelhead, a closely related species of rainbow trout, migrate upriver before or after reaching sexual maturity. They concluded that the genetic change that produced spring-run Chinook occurred only once in the species's history. And new data published on 29 April on bioRxiv show that in rivers where spring runs disappeared decades ago, less than 1% of the remaining fish carry a copy of the early migration version of the gene. The scarcity of the gene makes it very unlikely a spring run will reappear once lost.

The findings have prompted the Karuk Tribe to submit a new ESA petition to designate the Klamath's spring Chinook as threatened or endangered. The research has also sparked a fierce debate among conservation biologists and even the researchers who made the discovery. At its heart is the question of whether a difference in a single gene should be enough to qualify a population for ESA protection.

"We think that the biological reality is that these fish meet the criteria—the legal criteria—for listing," says Craig Tucker, a biologist in Orleans, California, who works for the Karuk Tribe. But Fred Allendorf, a conservation geneticist at the University of Montana in Missoula, believes "you shouldn't be describing units of conservation, or any taxonomic group, on the basis of a single gene." Instead, he favors taking a broader look at the species's entire genome.

The debate could extend well beyond salmon. The Klamath petition, experts say, could be the leading edge of a new wave of ESA petitions based on detailed genomic analyses that can pinpoint DNA mutations that produced major changes in the biology of an organism.

"It's not just this one decision," predicts Michael Miller, a geneticist at the University of California, Davis, who led the latest salmon studies. It could take decades, he says, for scientists and regulators to figure out "how to deal with this."

THE KLAMATH PETITION is only the latest twist in a long quest to protect the six species of salmon that spawn in U.S. rivers along the Pacific coast. Salmon return to their birth river to spawn and die, so salmon in different rivers often vary in, for example, size, run timing, and genetics. The first ESA petition to protect a distinct, river-specific population came in 1985, and it was followed by a spate of similar requests for salmon in other rivers.

But NOAA faced a big problem in deciding how to respond, recalls Robin Waples, a conservation geneticist at NOAA's Northwest Fisheries Science Center in Seattle, Washington. "Nobody knew what a distinct population segment of salmon was," he says. The ESA didn't specify how distinct a population needed to be to win protection, so Waples was tasked with drafting a policy.

In 1991, he published a definition that holds legal weight to this day: A salmon population is distinct enough to qualify for listing if its members rarely mate with fish from other populations. It also should represent an important piece of the species's evolutionary legacy—a piece that, if it were lost, could not be found elsewhere. Nine U.S. populations of Chinook currently meet those criteria and are listed as threatened or endangered.

But in rivers where spring- and fall-run fish aren't genetically distinct, petitions to list spring Chinook separately haven't gotten far. A key sticking point is that genetic study after genetic study found the same pattern: Spring Chinook generally look like fall Chinook in the same river—and not like spring Chinook in other rivers. That pattern led scientists to conclude that up and down the west coast, each river had evolved its own spring run. And it supported an assumption that if the springers became extinct, they could re-evolve from fall-run fish.

Still, some researchers were curious about which genes were responsible for determining when a salmon leaves the ocean. Miller decided to figure it out. A native of rural western Oregon, he grew up fishing for spring-run salmon. "It's a big part of what my culture is," he says. "I've always been tremendously fascinated by salmon."

He and his colleagues scanned a huge swath of the genomes of spring and fall Chinook taken from rivers in Washington, Oregon, and California. "In 99.99% of the genes, it showed the same old pattern" of spring fish looking like fall fish, says Waples, who wasn't involved in the research. But when Miller's team looked more closely, they detected a handful of spots where the genomes of spring and fall fish differed. Still, the researchers didn't know how many genes were involved because their method—which entailed chopping the genome into tiny pieces and looking at a subset—couldn't pinpoint where the DNA changes were located on various chromosomes. "We were working blind," Miller says.

A breakthrough came when they got their hands on a genome of the rainbow trout, a Chinook relative. To their surprise, when they matched the intriguing snippets of Chinook DNA to the full rainbow trout genome, they saw that all the DNA changes associated with run timing lined up in the same region: in and around a gene called *GREB1L*. The gene doesn't have a known function in salmon, but may interact with a sex hor-

Copco I is one of four Klamath River dams that led to steep spring salmon declines. In a bid to help stocks recover, engineers are set to start removing the dams in 2020.

PHOTO: DAVID MCLAIN

mone to influence the expression of other genes. And its apparent importance to run timing was surprising, because researchers had assumed that migration would be governed by many genes, not just one. "Once we started to get things pieced together, I realized, 'Wow, this is a single [spot in the genome],'" Miller says. "This is the premature migration gene!"

That conclusion—published in 2017 in *Science Advances*—was supported by another finding: Miller's team and a second group found that *GREB1L* is also linked to run timing in steelhead, an anadromous form of rainbow trout that has summer and winter runs. After comparing DNA changes in *GREB1L* in different populations of Chinook and steelhead, the researchers also concluded that the genetic change that created seasonal runs occurred just once in Chinook and just once in steelhead, sometime in the 10 million to 15 million years since the two species split from a common ancestor. That challenged the conventional wisdom that the evolution of spring-run fish had occurred many times within each species.

The findings are rewriting the evolutionary history of early run salmon, scientists say. But they came as little surprise to the Karuk Tribe, Hillman says. "This is what we've always known, that the spring Chinook is not the same animal as the fall Chinook."

NOW, THE QUESTION IS whether NOAA will agree. Officials have started to sort through public comments on the Karuk Tribe's petition, but it could be a year or more before the agency announces its decision. If NOAA decides to list spring Chinook, the ruling could trigger changes to water regulations on the Klamath, such as curtailing diversions for irrigation.

The issue has led to some feisty disagreements among researchers—including those directly involved in the Chinook studies. Five scientists collaborating with Miller, for instance, dropped off the 2017 *Science Advances* paper after a preprint was posted online, but before the paper was published. "One group really wanted to push ahead with more of a conservation emphasis for the paper; the other group thought the results were exciting in and of themselves without pushing that kind of angle," says Andrew Kinziger, a conservation geneticist at Humboldt State University in Arcata, California, and one of the scientists whose name was removed. He believes the data are too "hot off the presses," and that more work is needed before they should be used to influence listing decisions.

Allendorf worries that if NOAA approves the petition, it could open the door to splitting species into ever-finer groups, each with a genetic claim to legal protection. It's a slippery slope, he says, and could become bureaucratically impractical. "What happens if we find another gene that's really important?" he asks. "Does that mean we have to split [a population] even further?"

Waples, a veteran of endangered species debates, agrees that single-gene differences shouldn't become a routine justification for protecting a population. But he thinks it might make sense if the gene codes for a trait that's vital to the ecology and evolution of a species. "Is run timing important enough for salmon that it would justify making a big exception? … I'd like to see more debate on that."

Nina Overgaard Therkildsen, a fish geneticist at Cornell University, believes that "early migrators should receive special protection." They're a unique part of the evolutionary legacy of the species, she says—a part we'd ignore if we overlooked what that single gene tells us about the evolutionary history of Chinook.

Hillman hopes such thinking carries the day at NOAA. An ESA listing could provide the Klamath's spring Chinook with "a little bit of interim relief" before engineers begin to dismantle the Klamath's four dams in 2020. That project—the largest dam removal project ever attempted—will reopen vast stretches of spawning grounds.

In the meantime, Hillman will continue to dance on the banks of the Klamath—hoping that his generation hasn't seen the last of spring-run salmon. ■

SMALL BUT MIGHTY

Miniature antibodies discovered in sharks and camels are a boon for research and perhaps medicine

By **Mitch Leslie**; *Photography by* **Matt Roth**

Helen Dooley admits that she often gets puzzled responses when she describes her work. "People say, 'You bleed sharks for a living?'"

That's an overstatement, but every couple of weeks she and a helper drop by several large fiberglass tanks at the Institute of Marine and Environmental Technology on the Inner Harbor in Baltimore, Maryland. They net a cat shark or nurse shark and wrestle it into a small pool of water that contains a mild sedative. The drug calms the shark so they can lift it from the water and puncture a vein in its tail. Drawing a few milliliters of blood "doesn't take more than a few seconds," Dooley says, after which they return the animal to its aquarium to recover. "They're usually swimming about perfectly normally, and looking for food, after only a minute or so."

Dooley, an immunologist at the University of Maryland (UMD) School of Medicine in Baltimore, has been tapping shark blood for 2 decades for the same reason that other researchers have been draining the veins of llamas, camels, and their relatives. All those animals pump out unusual, diminutive antibodies that are only about half the size of the conventional versions.

Researchers have known about those tiny proteins since the late 1980s, when scientists at the Free University of Brussels (VUB) stumbled across them. But, "Since 2012, the field has really taken off," says biochemist Hidde Ploegh of Boston Children's Hospital. Compared with conventional antibodies, the molecules and even tinier fragments of them, often called nanobodies, are easier for researchers to make, more durable, and more soluble. Small antibodies can work inside cells, and their size allows them to wend deep into tissues, which regular antibodies have a hard time penetrating.

Those qualities have established the molecules as valuable research tools. "As a biochemist, I find them exceedingly useful," Ploegh says. He and his colleagues have deployed them for tasks as diverse as tracking a key immune protein in the body, neutral-

Corrected 11 May 2018. See full text.

Published by AAAS

Blood drawn from a shark provides the immune proteins known as small antibodies.

izing plant viruses, and labeling cancer cells. But the antibodies' most illuminating research role may be binding to and stabilizing wobbly proteins so that researchers can probe their architecture. "What they've been fantastic for is determining crystal structures," says evolutionary immunologist Martin Flajnik, also of UMD's School of Medicine. Indeed, a llama nanobody was key to structure work that won a recent Nobel Prize.

Miniature antibodies are also starting to prove their worth in patients. Later this year, the first nanobody treatment—derived from a llama small antibody—is expected to receive approval in some countries for use in people with a rare clotting disease. More than 40 similar therapies are in the works for diseases as varied as lupus, lung infections, and cancer. Conventional antibodies are mainstays of diagnosis and staple therapies for a host of diseases, but molecular biologist Nick Devoogdt, also of VUB, predicts that their petite cousins will take over in uses "where conventional antibodies are less optimal."

SMALL ANTIBODIES FIRST came to light by accident, when students at VUB objected to analyzing human blood for a lab exam because they worried about the possibility of contracting a disease. They also refused to kill a mouse to obtain its blood, recalls Serge Muyldermans, a molecular biologist at the university. Some rummaging around, Muyldermans says, turned up an alternative: a stash of frozen dromedary camel serum collected to study the animals' parasites.

But another apparent problem cropped up when the students finished analyzing the blood. Along with normal antibodies, they had sifted out what appeared to be an undersize version of the molecules. "We thought that they had done something wrong," Muyldermans says. So he and other scientists at the university investigated further. An analysis of blood from zoo animals in the same evolutionary family, including a Bactrian camel and a llama, revealed that all had the same diminutive antibodies.

The researchers unveiled their discovery in a 1993 *Nature* paper and pointed out a key difference between the small antibodies and their full-size counterparts. A conventional antibody consists of four protein strands—two heavy chains that form the backbone of the Y-shaped molecule and two light chains that cling to the outside of the prongs. The mini-antibodies retain roughly the same shape but are missing the light chains (see graphic, above). How the unusual molecules might benefit the animals wasn't clear, but when Dooley learned about them a few years later, she was fascinated. For her Ph.D. research at the University of Aberdeen in the United Kingdom, she set out to investigate those immune oddities.

She asked VUB researchers for help obtaining samples, and they arranged for colleagues in Morocco to immunize a few camels and send her some blood. After the first shipment arrived, however, the animals mysteriously disappeared, possibly because they were stolen, she says. "I was a year into my Ph.D., and I had no Ph.D. project." But she soon found an alternative to camels. In 1995, Flajnik and colleagues fished an unconventional antibody out of blood from a nurse shark. Like the camel versions, the shark antibody was smaller than the regular variety and lacked light chains. Dooley contacted Flajnik and finished her Ph.D. research on the shark molecules. Then she continued the work as a postdoc in his lab. "That's when we started to dig into the nitty-gritty of shark antibodies," she says.

Humans and mice occasionally churn out antibodies that contain only heavy chains, but researchers think they are duds produced by malfunctioning B cells, the immune factories for such proteins. In contrast, the undersize antibodies of sharks and the camel family are not half-finished rejects. Even though they lack the light chains that help regular antibodies recognize and grab antigens, they can bind tightly to their targets with great specificity, and they appear to be a key part of the animals' response to pathogens. When Dooley and Flajnik injected immune-stimulating antigens into nurse sharks, they discovered that within a few months—the shark immune system is slower to react than ours—the animals were churning out a variety of small antibodies that targeted the foreign molecules. "It's the major antibody used in the nurse shark," Flajnik says.

He and other researchers speculate that the minute antibodies enable immune systems to counteract a broader range of pathogens. Conventional antibodies excel at sticking to

Downsizing antibodies

Human blood teems with conventional antibodies—bulky, Y-shaped proteins that home in on bacteria and viruses. The small antibodies produced by sharks and the camel family differ from those immune molecules not only in size, but also in their structure and binding ability.

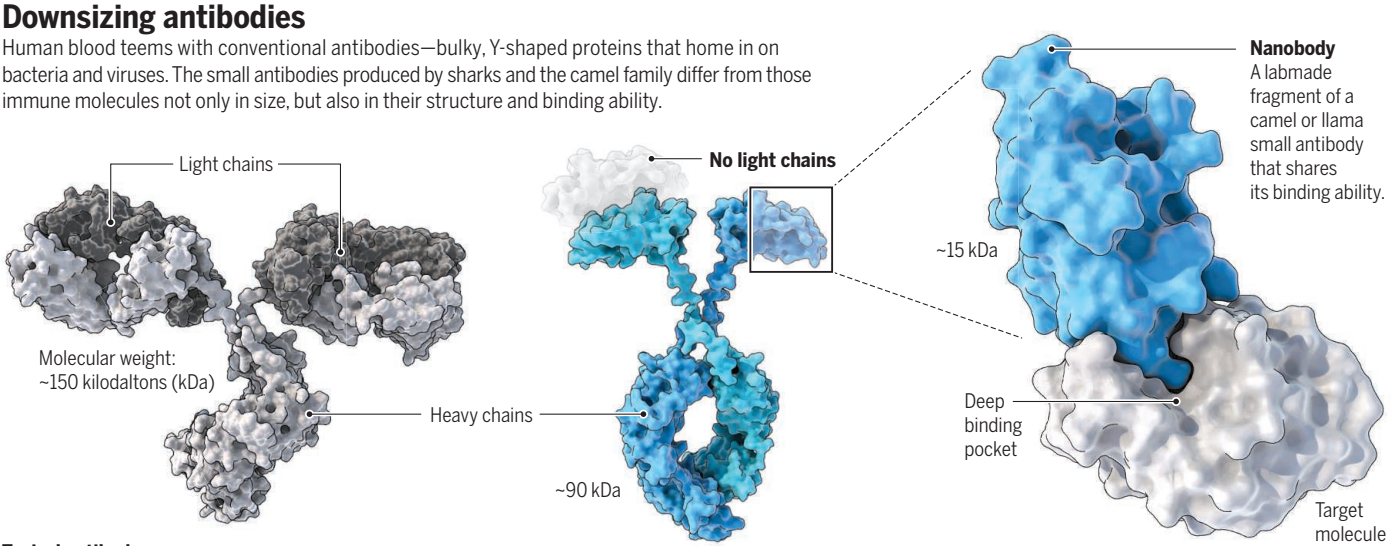

Typical antibody
Two light and two heavy chains intertwine to make a protein that can identify and affix to bits of pathogens or other molecules.

Small antibody
This slimmed-down variety lacks light chains but can still bind to its targets.

Nanobody binding
Because of its binding style, a nanobody can fit into crevices on molecules.

GRAPHIC: C. BICKEL/*SCIENCE*

Corrected 11 May 2018. See full text.

PHOTO: MATT ROTH

flat surfaces on viral and bacterial molecules. Heavy-chain–only antibodies "are skinny and might be able to penetrate canyons and crevices that regular antibodies couldn't get into," says structural immunologist K. Christopher Garcia of the Stanford University School of Medicine in Palo Alto, California.

Small antibodies must have an important role, Muyldermans notes, because they emerged independently in as many as three different lineages: sharks, camels, and probably another group of sharklike fishes. But just what advantage they confer on those animals is a mystery. Scientists know little about shark pathogens, for example, and aren't even sure how to tell when sharks are sick, Dooley says. "They don't just curl up in the corner." Even in camels and their kin, whose diseases are better understood, researchers haven't identified which pathogens the small antibodies combat. At the moment, Muyldermans says, "We have no clue" why the molecules evolved.

THAT HASN'T STOPPED scientists from putting them to work. For most medical and research applications, they prune the small antibodies, leaving only the antigen-binding tip. Nanobodies, as they're called if they come from camels and their relatives, have several handy attributes, Ploegh says. For one, the well-studied bacterium *Escherichia coli* can make them. "You can express them in *E. coli* in exceptionally high yield, and they are easy to purify," he says. In contrast, producing working full-size antibodies in *E. coli* has proved to be difficult, so researchers typically generate them from more expensive cultures of mammalian cells.

Nanobodies also remain functional within cells, whereas conventional antibodies typically fall apart in the cytoplasm. "Suddenly we can do smart things [inside cells] with antibodies," says developmental biologist Markus Affolter of the University of Basel in Switzerland. One clever use, he says, is "a completely new way to manipulate proteins."

He and his colleagues, for example, harnessed nanobodies to eliminate specific proteins from cells. The team started by engineering the cells to produce a nanobody that, on its nonbinding end, carried molecules that direct proteins to the cell's garbage disposal. The other end of the nanobody recognized and attached to a specific protein. Stimulating a cell to manufacture the nanobody caused the protein target to disappear in as little as 3 hours, the researchers reported in 2012.

Depleting a protein by inducing mutations in its gene, a standard approach in basic research, banishes it for good. In contrast, the nanobody technique allows scientists to delete and then restore the molecule, probing its role in more detail. In 2015, for example, a team led by researchers at Baylor College of Medicine in Houston, Texas, engineered fruit flies to generate a nanobody that grabs the protein Dunce—which is essential for insects' ability to learn and remember—and promotes its destruction. The researchers then trained the flies to avoid a certain odor. When the team spurred the flies to start making the nanobody against Dunce, levels of the protein plummeted and the insects became dumber—they had a harder time learning to avoid the odor. When the team shut off production of the antibody, Dunce's abundance bounced back, and the flies became smart again.

Because nanobodies reach deep into the nooks and crannies of molecules they bind to, the fragments have also become favorites for researchers trying to stabilize floppy molecules so they can be crystallized, a first step in determining their structure. In perhaps their most impressive performance, nanobodies enabled Brian Kobilka of Stanford's School of Medicine and his colleagues to capture the first structure of an activated G protein–coupled receptor (GPCR). Those cell membrane proteins relay a multitude of signals into the cell: The adrenaline that makes your heart race, the morphine that eases a patient's pain after surgery, the bitter flavor in a cup of coffee—all act through GPCRs, which also are the targets of about one-third of drugs. Researchers had tried for about 20 years to get crystal structures of typical, switched-on GPCRs, but the molecules were too shifty.

Then Kobilka met structural biologist Jan Steyaert of VUB at a conference, and the two decided to try nanobodies. The researchers and their colleagues injected a llama with the human β2-adrenergic receptor, which responds to adrenaline, and from the animal's blood prepared a set of nanobodies that clamped onto the receptor. In a 2011 *Nature* paper, the scientists revealed that one nanobody locked the GPCR into an active shape, allowing them to determine its crystal structure. "That was a devastatingly effective use" of the molecules, Garcia says, as evidenced by the fact that in 2012, Kobilka shared the Nobel Prize in Chemistry.

Corrected 11 May 2018. See full text.

Helen Dooley periodically captures sharks in research aquaria to obtain small antibodies.

Like Kobilka and Steyaert, researchers who need a supply of small antibodies or nanobodies often start with llamas, camels, or sharks that have been immunized with particular antigens. In response, the animals' immune cells begin to make small antibodies that recognize and fasten onto the antigen. Blood cells isolated from the animals allow scientists to obtain the genes for those antibodies, which they can then insert into bacteria or other microorganisms to synthesize large quantities of the immune molecules. But the animals can take a month or more to respond to the antigen and spawn new small antibodies, and llamas and their relatives won't manufacture versions that target some human proteins that are very similar to their own, notes structural biologist Andrew Kruse of Harvard Medical School in Boston.

Earlier this year, he and his colleagues unveiled a synthetic nanobody library that they say overcomes those limitations. Instead of relying on animals as the source of antibody genes, the researchers synthesized DNA sequences to craft their own. Using the published structures and corresponding amino acid sequences of known nanobodies as a guide, they created more than 100 million custom nanobody genes. They slipped the genes into yeast cells, which served as factories for the molecules. Testing showed that "the fully synthetic library is performing at least as well as animal immunization," Kruse says. He and his colleagues will send it to any academic researchers who pay the shipping costs. Kruse says they are dispatching about 10 to 15 packages a week.

Muyldermans and Steyaert, however, contend that animal-derived nanobodies bind to their targets better than entirely labmade alternatives, so they're sticking with the old-fashioned method. "You never change a winning team, and these llamas are on my team," Steyaert says.

LLAMAS—ALONG WITH SHARKS and camels—may soon be aiding patients. The Ghent, Belgium–based company Ablynx, a spinoff from the original group that discovered the unorthodox antibodies, has already completed a phase III effectiveness trial of one such protein, caplacizumab, for the rare disease acquired thrombotic thrombocytopenic purpura, in which many blood clots can trigger strokes, organ failure, or death. The llama-derived molecule works by latching onto and inactivating a blood protein named von Willebrand factor that promotes clotting—and it's much more clingy than traditional antibodies, notes Edwin Moses, Ablynx's CEO. The company, which presented the positive results of the trial in December 2017 at the American Society of Hematology conference in Atlanta, has applied for approval to sell the drug in Europe and plans to do the same in the United States later this year.

At least seven other small antibody–derived treatments have reached clinical trials—targeting diseases such as rheumatoid arthritis, psoriasis, and lupus—and more than 30 other treatments are under development. Most of those molecules are derived from the antibodies of camels and their relatives, but the first shark-based drug, produced by the Melbourne, Australia–based firm AdAlta, should enter clinical trials later this year, says Mick Foley, the company's chief scientific officer. The drug is meant to alleviate lung fibrosis, a stiffening of the organs caused by the buildup of scar tissue.

Researchers also hope the unique properties of small antibodies will enable them to pry open the blood-brain barrier, an obstacle to treating many brain diseases because it rebuffs most large molecules, including standard antibodies and many other drugs. Ossianix, a Philadelphia, Pennsylvania–based biotech, has crafted a shard of a shark small antibody that binds to a receptor controlling access across the barrier. By stimulating the receptor, the fragment might open the way for drugs such as rituximab, a cancer-killing conventional antibody, to cross into the brain, says Ossianix CEO Frank Walsh.

Other applications beckon. Researchers can equip small antibodies with therapeutic cargoes, such as other drugs or cancer-killing radioactive compounds, without making them so massive that they can't infiltrate tissues or tumors. In addition, the kidneys rapidly filter the molecules out of the blood for excretion—a benefit when the cargo is radioactive. Diminutive antibodies can also be fused to radioactive or fluorescent tracers to illuminate tumors or even guide surgery. To visualize a tumor, for example, "you need small molecules that bind tightly" to the cancer, Devoogdt says. Rapid clearance of a tracer is a plus, as well, because it reduces background noise that can leave the tumor harder to discern. He and his colleagues, along with several other groups, have performed safety trials on nanobodies as tumor-visualizing agents, and they hope to start testing the molecules' therapeutic usefulness in patients next year.

Small antibodies do have some drawbacks for medicine, researchers caution. The rapid excretion of the molecules can be a downside if they leave the body before patients receive their full benefit. Another shortcoming, notes biochemist Jan Gettemans of Ghent University, is that unlike many important drugs, including statins and the anti-HIV drug azidothymidine, the antibodies can't enter cells on their own. Researchers can get them into the cytoplasm by genetically altering cells to produce them, but that's not feasible for most treatments. And although brief studies suggest small antibodies are safe for patients, "there is no clear experience in humans … for a long period of time," Gettemans says. But he and other researchers think the small antibodies' advantages outweigh their shortcomings and are confident that they "will be part of the armamentarium," as Walsh puts it.

Nanobodies targeting an inflammatory molecule light up joints in the paw of an arthritic mouse.

Meanwhile, the mysteries they pose continue to entrance Dooley. She did a stint in drug development—4 years working on a pharmaceutical company's small-antibody project—but these days when she takes a tube of shark blood back to her lab, she's usually trying to answer basic questions such as how the animals switch on their antibody-manufacturing cells. She has become fond of the sharks, too. "They are beautiful animals to work with." If someone did steal the camels she was originally planning to study, she says, "they really did me a favor." ■

PHOTOS: (TOP TO BOTTOM) MATT ROTH; S. PUT *ET AL. THE JOURNAL OF NUCLEAR MEDICINE* **54**, 807 (2013)

Corrected 11 May 2018. See full text.

PERSPECTIVES

GEOPHYSICS

How earthquakes are induced

Conditions within Earth's crust determine whether human subsurface activities lead to earthquakes

By **Thibault Candela,[1] Brecht Wassing,[1] Jan ter Heege,[1] Loes Buijze[1,2]**

Since 2009, the midwestern United States has seen a dramatic rise in earthquakes induced by human activities. Most of these events were caused by massive reinjection of wastewater produced during oil and gas extraction (*1*, *2*). In February 2016, regulators in Oklahoma called for an injection rate reduction after several major events up to moment magnitude 5.8 (M_w 5.8) occurred. On the other side of the Atlantic, an unprecedented number of earthquakes has followed gas extraction from the Groningen field in the Netherlands (*3*). The Dutch government imposed production cuts after a M_w 3.6 event in August 2012 caused structural damage to houses. Intensive research of these two instances of induced seismicity points to contrasting mechanisms, but in both cases, the natural conditions prior to subsurface activities play a dominant part.

Fifty years ago, Healy *et al.* determined that fluid injection at depth causes the pore pressure to rise in a preexisting fault, reducing its strength and potentially leading to its failure (*4*). In contrast, fluid extraction at depth reduces the pore pressure, leading to compaction of the rock mass; the increased

[1]*Applied Geosciences, TNO, Princetonlaan 6, 3584 CB Utrecht, Netherlands.* [2]*HPT Laboratory, Faculty of Geosciences, Utrecht University, Budapestlaan 4, 3584 CB Utrecht, Netherlands. Email: thibault.candela@tno.nl*

PHOTO: HUISMAN MEDIA/ANP/NEWSCOM

An evacuated house shows damage by depletion-induced earthquakes in Bedum near Groningen.

rock stress can drive a preexisting fault to failure. In both settings, the two factors that control induced earthquakes are operational parameters, such as the volume that is injected or produced, and natural conditions, such as the presence of preexisting faults and their ambient stress level. Operational parameters are often assumed to dominate, but that notion may reflect limited knowledge of the locations of preexisting faults and their ambient stress level. For regulatory measures to be effective in mitigating induced seismicity, it is crucial to understand the role of the natural conditions that existed before human activities.

Recent studies have started to collect measurements that help to validate hydromechanical modeling results of changes in pore pressure and stresses after fluid injection or production. For example, time-lapse shear-wave anisotropy analysis has provided direct evidence linking earthquake occurrences to pore pressure increase in the midwestern United States (*5*). Measurements of surface deformation derived from InSAR (Interferometric Synthetic Aperture Radar) have linked swarms of induced events 10 to 30 kilometers from the injection well to pore pressure increases of only ~0.1 MPa, even though pore pressure increases are predicted to be higher close to the well (*2*).

These data point to a mechanism through which wastewater injection induces seismicity (see the figure). During wastewater injection, the pore pressure front diffuses away from the injection wells along highly permeable channels in the disposal aquifers. Once the pressure front reaches large faults that intersect the basement below the reservoir and that are close to their point of tectonic reactivation, even a small pressure increase can trigger earthquakes. In support of this conceptual model, statistical assessment has shown that seismic activity is more highly correlated with the distance between the injection point and the basement than with the net injected volume (*6*). For mitigation of induced earthquakes, knowledge about the presence of faults and their ambient stress level is thus crucial.

At the Groningen gas field, subsidence measurements are now routinely used to calibrate modeled reservoir compaction (*3*). Subsidence measurements show that the observed seismicity is concentrated in areas of high compaction and subsidence, confirming the causal relationship between compaction and seismicity (*3*, *7*). However, besides reservoir compaction, an optimal match between model predictions and observations can only be achieved if faults are included (*3*, *7*). Whereas earthquake-prone faults in the midwestern United States are often unmapped before injection activities, detailed subsurface information is available for the Groningen gas field, which includes more than 600 preexisting faults.

These studies suggest that gas production at the Groningen field induces seismicity through the following mechanism (see the figure). During gas production, the reservoir compacts, resulting in stress buildup along faults. Due to their preexisting offsets, reservoir compartments with different compaction levels are in contact along the faults. This differential compaction can magnify the amount of fault stress that builds up, speeding up the occurrence of earthquakes.

Induced events in the Groningen area have been recorded only after a reduction of the reservoir pore pressure by ~10 MPa, which results in a rock stress increase of similar magnitude. This is generally taken as evidence that before production, most Groningen faults were far from tectonic reactivation (*3*, *7*, *8*). This observation is in contrast with the situation in Oklahoma, where pressure perturbations of ~0.1 MPa can trigger earthquakes. This suggests that the crust there is critically stressed, that is, it contains a subset of faults that are close to failure and that can be reactivated by a slight stress perturbation (*9*).

Comparison of the two cases leads to the conclusion that the timing and location of induced earthquakes are controlled by the spatial distribution and geometry of preexisting faults and ambient stress conditions before subsurface activities. But what about the size of these induced events? A working assumption is that induced ruptures remain confined to the rock volume affected by fluid pressure or stress changes (*10*). Recent studies challenge this assumption and reveal that induced earthquakes might potentially rupture outside of the affected volume (*11*–*14*). In this case, the maximum size of induced earthquakes might be controlled by natural preexisting fluctuations of the stress along the fault, in the same way as natural events.

Mechanisms of induced seismicity

Both wastewater injection and gas extraction can cause induced earthquakes. Detailed observations from the midwestern United States and Groningen, Netherlands, show that in both cases, preexisting conditions in Earth's crust are of central importance.

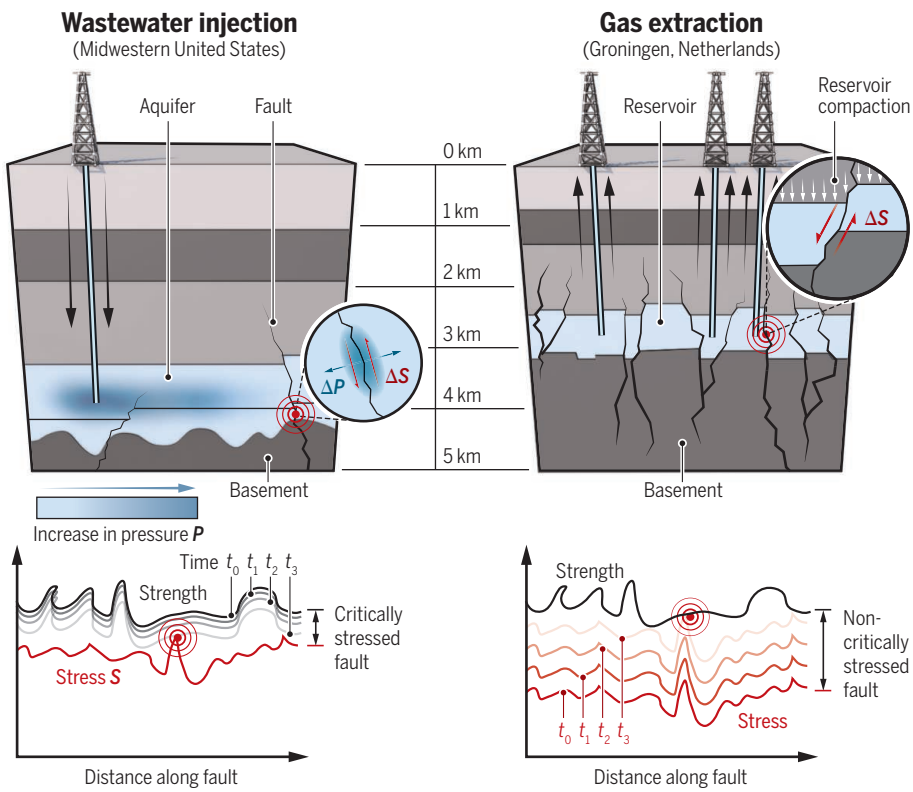

Injection of wastewater leads to a nonuniform pressure front. When the pressure front hits a critically stressed fault, an earthquake is triggered. Only a small strength decrease is needed to trigger an event.

Gas extraction leads to rock compaction, causing a buildup of stress. Sufficient shear stress is necessary to cause the initially noncritically stressed fault to fail, causing an earthquake.

GRAPHIC: C. BICKEL/*SCIENCE*

Published by AAAS

Both for fluid injection in the midwestern United States and for gas extraction at the Groningen field, a spectrum of evidence underscores the central role of preexisting faults and their stress level before subsurface human activities. Mitigation strategies to limit induced earthquakes that solely rely on operational parameters, such as the injected or produced volume, can be used as a first approximation, but much added value lies in subsurface characterization of fault populations and ambient stress. In the case of poor prior knowledge of the subsurface, continuous monitoring of seismicity can help illuminate unmapped faults. For this exercise, recent advances in artificial intelligence should be key to optimize real-time earthquake detection and location during operations (*15*). The state of stress along these preexisting faults can be defined by hydromechanical modeling, calibrated by measurements that are independent of operational parameters, as, for example, surface deformation derived from InSAR.

"...a spectrum of evidence underscores the central role of preexisting faults and their stress level before subsurface human activities."

Instead of considering the subsurface as a uniform tank that undergoes changes controlled by well operations, a continuous data-informed and physics-based modeling approach should incorporate properties of the affected rock volume, including that of the reservoir and faults. Only then can mitigation strategies for induced seismicity, such as targeted injection or production reduction at identified high-risk sites, be optimized. ■

REFERENCES

1. K. Keranen *et al.*, *Science* **345**, 448 (2014).
2. M. Shirzaei *et al.*, *Science* **353**, 1416 (2016).
3. L. van Geuns, K. van Thienen-Visser, *Netherlands J. Geosci.* **96-5**, s1 (2017).
4. J. H. Healy *et al.*, *Science* **161**, 1301 (1968).
5. K. A. Nolte *et al.*, *Sci. Adv.* **3**, e1700443 (2017).
6. T. Hincks *et al.*, *Science* **359**, 1251 (2018).
7. S. J. Bourne, S. J. Oates, *J. Geophys. Res.* **122**, 10299 (2017).
8. D. Dempsey, J. Suckale, *Geophys. Res. Lett.* **44**, 7773 (2017).
9. J. Townend, M. D. Zoback, *Geology* **28**, 399 (2000).
10. A. McGarr, *J. Geophys. Res.* **119**, 1008 (2014).
11. N. J. van der Elst *et al.*, *J. Geophys. Res.* **121**, 4575 (2016).
12. M. Galis *et al.*, *Sci. Adv.* **3**, eaap7528 (2017).
13. F. Grigoli *et al.*, *Science* 10.1126/science.aat2010 (2018).
14. K.-H. Kim *et al.*, *Science* 10.1126/science.aat6081 (2018).
15. T. Perol *et al.*, *Sci. Adv.* **4**, e1700578 (2018).

10.1126/science.aat2776

STRUCTURAL BIOLOGY

Energy powerhouses of cells come into focus

High-resolution structures reveal core design features of rotary ATP synthases and ATPases

By **Patricia M. Kane**

In every kingdom of life, rotary adenosine triphosphate (ATP) synthases and adenosine triphosphatases (ATPases) play key roles in cellular energy generation and release processes. In mitochondria, chloroplasts, and bacteria, F-type (F_1F_o) ATP synthases synthesize ATP using energy from a proton gradient. They are also able to perform the reverse process, generating proton gradients by ATP hydrolysis. The related V-type (V_1V_o) ATPases have similar structures and serve as proton pumps. Two articles in this issue report structures of membrane-embedded ATP synthases from yeast mitochondria [Srivastava *et al.*, page 619, (*1*)] and spinach chloroplasts [Hahn *et al.*, page 620, (*2*)]. Together with other recent structures, these articles define core design principles of rotary ATP synthases and ATPases but also highlight organism-specific differences.

Rotary ATP synthases require the tightly coupled activities of two different motors: a membrane motor that uses energy from the proton gradient to drive rotation of a central rotor and a peripheral motor that uses rotation-driven conformational changes to support ATP synthesis. The peripheral motor (designated F_1 or V_1) contains the ATP binding sites. In the binding-change mechanism proposed by Boyer (*3*), three equivalent catalytic sites alternately bind adenosine diphosphate (ADP) and phosphate, synthesize ATP, and release the ATP produced, driven by conformational changes in the central rotor connected to the membrane motor. In 1994, the first high-resolution structure of F_1 captured the catalytic sites in three different conformations (*4*). More recently, structures of intact vacuolar H^+–ATPases (V-ATPases) (*5*, *6*) and ATP synthases (*7*), including the spinach chloroplast enzyme reported by Hahn *et al.*, have shown the central rotor at multiple distinct rotational positions. These structures support the universality of the binding-change mechanism and provide additional insights into mechanisms of rotational coupling.

Department of Biochemistry and Molecular Biology, State University of New York (SUNY) Upstate Medical University, Syracuse, NY 13210, USA. Email: kanepm@upstate.edu

The membrane motor (F_o or V_o) includes a ring of proteolipid c subunits (the c-ring) bound to the central rotor (see the figure). The c-ring rotates against a membrane-bound stator complex that extends peripherally along the F_1 or V_1 domain and prevents unproductive rotation. Structures of the membrane motor were slower to emerge for a number of reasons, including the inherent dynamics of rotary motors and the loss of structural features or resolution with detergent solubilization. In the absence of high-resolution structural data, biochemical and genetic experiments provided insights into the structure and mechanism of the membrane motors. Extensive mutagenesis of F_o and V_o subunits in model organisms identified conserved charged and polar amino acids in the membrane-embedded a and c subunits (see the figure) that are required for function (*8*, *9*). These residues provide a path for proton transport through the membrane at the interface of the single a subunit and the c-ring.

Recent cryo–electron microscopy structures are clarifying the membrane motor structure and its coupling mechanisms and revealing both common and organism-specific structural features. Allegretti *et al.* (*10*) first visualized two long transmembrane helices that are almost horizontal in the membrane, oriented in parallel with the membrane surface, in the a subunit of F_o from the green alga *Polytomella*; this has proven to be a notably conserved feature of membrane motors (*1*, *2*). Amino acids of the a subunit that are involved in proton transport align along one face of these horizontal helices, which make close contact with the c-ring. This contact separates aqueous pores that come from either side of the membrane. Taken together, previous data (*6*, *7*, *10*, *11*) and current structures (*1*, *2*) invoke an ATP synthesis mechanism in which each essential c-ring carboxylate of the c-ring is protonated at one side of the membrane, travels through the membrane on the outside of the c-ring until it encounters the a subunit, and is deprotonated, releasing the proton at the opposite side of the membrane (*11*).

The amino acid side chains at the a-c subunit interface are critical for the protonation-deprotonation cycle (see the figure). Recent

structures have overcome barriers of low or anisotropic resolution to envision this interface (*11*–*13*). Previous work had identified an absolutely conserved arginine in the a subunit as essential for proton transport (*14*). This arginine has been proposed to promote rotation by electrostatic attraction of the newly deprotonated c subunit as well as to separate the aqueous channels approaching from each side of the membrane. The recent structures vary in the position of the conserved arginine relative to the closest c-ring carboxylate. Autoinhibited yeast V_o structures show a salt bridge between these residues (*12*, *13*). In the spinach chloroplast ATP synthase, the conserved arginine is ~4.5 Å from the nearest c-ring glutamate, whereas in the yeast ATP synthase, the corresponding carboxylate more closely approaches the arginine, suggesting an interaction during rotation. On the basis of oligomycin-binding results, Srivastava *et al.* suggest that the c-ring may be plastic, with conformational changes at the a-c interface propagating across the c-ring. One caveat is that all of the complexes visualized at high resolution are inhibited in some way. For example, rotation in the yeast F_1F_o structure is blocked by fusion of rotor and stator subunits; the spinach chloroplast enzyme is in the dark state, with rotation suppressed by the formation of an inhibitory disulfide bond.

The structures reported in (*1*, *2*) will drive exploration of a number of long-standing questions. All rotary ATPases have three catalytic sites in the peripheral motor, but the number of proteolipids in the membrane motor's c-ring varies from 8 to 15 and is not divisible by three in most organisms. Furthermore, in V_o c-rings, each proteolipid is twice as large as those in F_o c-rings but still carries a single proton-bearing carboxylate (*12*, *13*). Membrane motors must be able to accommodate both different ratios of protons released per ATP synthesized or hydrolyzed and different rotational step sizes.

On the basis of the three rotational states seen for the spinach chloroplast enzyme, Hahn *et al.* propose that elasticity in the peripheral stator helps to determine the step size of rotation in the membrane motor (*2*), although others have suggested that the rotor may be more elastic than the stator (*15*). Consistent with step size being mandated in part by peripheral stator structure, stators show considerably more variation between organisms than the core subunits of the peripheral or membrane motors. As their variable and conserved structural features come into focus, the underlying mechanistic principles, organism-specific differences, and regulation of these versatile and important enzymes will also emerge. ■

REFERENCES

1. A. P. Srivastava *et al.*, *Science* **360**, eaas9699 (2018).
2. A. Hahn *et al.*, *Science* **360**, eaat4318 (2018).
3. P. D. Boyer, R. L. Cross, W. Momsen, *Proc. Natl. Acad. Sci. U.S.A.* **70**, 2837 (1973).
4. J. P. Abrahams, A. G. Leslie, R. Lutter, J. E. Walker, *Nature* **370**, 621 (1994).
5. J. Zhao, S. Benlekbir, J. L. Rubinstein, *Nature* **521**, 241 (2015).
6. A. Nakanishi, J. I. Kishikawa, M. Tamakoshi, K. Mitsuoka, K. Yokoyama, *Nat. Commun.* **9**, 89 (2018).
7. A. Zhou *et al.*, *eLife* **4**, e10180 (2015).
8. S. B. Vik *et al.*, *Biochim. Biophys. Acta* **1458**, 457 (2000).
9. M. Toei, S. Toei, M. Forgac, *J. Biol. Chem.* **286**, 35176 (2011).
10. M. Allegretti *et al.*, *Nature* **521**, 237 (2015).
11. N. Klusch, B. J. Murphy, D. J. Mills, O. Yildiz, W. Kühlbrandt, *eLife* **6**, e33274 (2017).
12. M. T. Mazhab-Jafari *et al.*, *Nature* **539**, 118 (2016).
13. S. H. Roh *et al.*, *Mol. Cell* **69**, 993 (2018).
14. B. D. Cain, R. D. Simoni, *J. Biol. Chem.* **264**, 3292 (1989).
15. A. Wachter *et al.*, *Proc. Natl. Acad. Sci. U.S.A.* **108**, 3924 (2011).

10.1126/science.aat6275

Rotary ATPases and ATP synthases

Recent structures, including two described in this issue (*1*, *2*), elucidate the mechanism by which ATPases and ATP synthases generate and release energy.

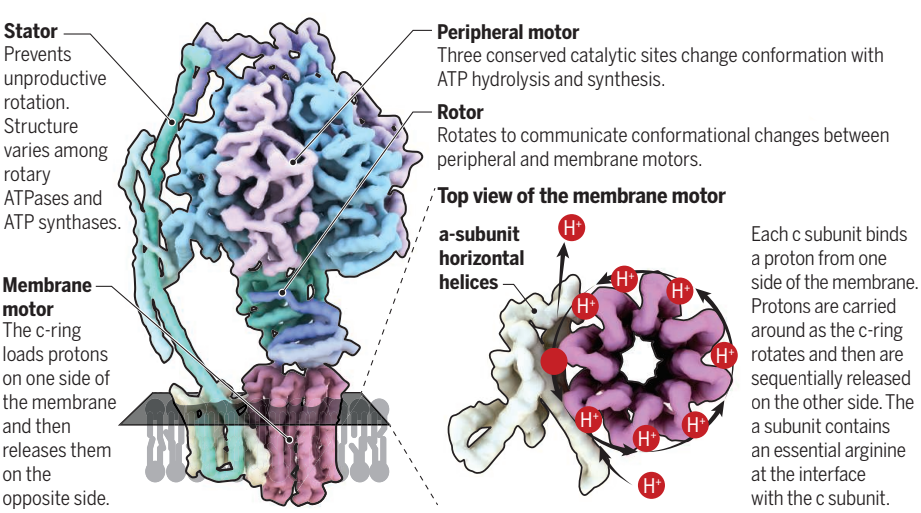

CREDIT: (GRAPHIC) N. DESAI/*SCIENCE*; (3D MODEL) EMDB ID: EMD-3164

DEVELOPMENT

How does temperature determine sex?

Temperature-responsive epigenetic regulation clarifies a 50-year-old mystery in reptiles

By **Arthur Georges**[1] *and* **Clare E. Holleley**[2]

Sex determination in reptiles is a complex affair, because incubation temperature and genes interact in many species to regulate sexual development and decide sexual fate, male or female (*1*–*4*). A central question that has remained unanswered is, what molecular mechanism allows temperature to so profoundly influence the developmental pathways that determine sex? The means to identify a master sex-determining gene in species with genetic sex determination is well established—identify genes on the sex chromosomes, demonstrate which of these are differentially expressed in male and female embryos early in development, and manipulate their expression to demonstrate reversal of sex (*5*–*7*). Not so with identifying the mechanisms of temperature-dependent sex determination (TSD). Temperature could exert its effect on any of the many autosomal genes involved in sexual differentiation, even those peripherally involved, provided their altered expression is capable of reversing sex. Little wonder that, in the 50 years since TSD was discovered in reptiles (*8*), we have not advanced far in our understanding of the mechanisms of TSD. This is about to change. On page 645 of this issue, Ge *et al.* (*9*) report that transcription of the chromatin modifier gene *Kdm6b* (lysine-specific demethylase 6B) responds to temperature in the red-eared slider turtle *Trachemys scripta elegans*, and confers temperature sensitivity to a key sex-determining gene, *Dmrt1* (doublesex- and mab-3–related transcription factor 1).

Ge *et al.* previously showed that *Dmrt1* is differentially expressed early in embryonic development before the gonads differentiate structurally (*10*). Additionally, *Dmrt1* expression is high at male-producing tem-

[1]*University of Canberra, ACT 2601, Australia.*
[2]*Commonwealth Scientific and Industrial Research Organisation, GPO Box 1700, Canberra, ACT 2601, Australia.*
Email: georges@aerg.canberra.edu.au; clare.holleley@csiro.au

perature (MPT) and low at female-producing temperature (FPT). As such, *Dmrt1* is a strong candidate for the male sex-determining gene in this TSD species of turtle, consistent with the master sex-determining role of other DM domain–containing genes in some fish, amphibians, and birds (*7, 11, 12*). Depending on the species, these DM domain genes initiate and maintain the male sexual trajectory, and suppress genes important for female development during the critical stages of embryogenesis.

What Ge *et al*. have now discovered (*9*) is that experimental down-regulation of *Kdm6b* at 26°C (normally an MPT) shifts embryos from a male to a female developmental trajectory. This occurs because the protein KDM6B is a lysine-specific demethylase with a central role in epigenetic regulation of gene expression. Suppressing *Kdm6b* expression reduces demethylation of its target, trimethylated lysine 27 on histone 3 (H3K27), a histone modification that would otherwise repress *Dmrt1* promoter activity. Thus, high amounts of KDM6B at MPT activate *Dmrt1* gene expression and determine male sex, whereas reduced amounts of KDM6B repress *Dmrt1* expression. Trimethylated H3K27 was not found on the promoters of any other sex genes that were differentially expressed early in development. Maintaining the trimethylation of H3K27 by experimentally down-regulating *Kdm6b* suppresses expression of *Dmrt1* and leads to female development at MPT. This is convincing evidence of a role in TSD for highly conserved epigenetic modifiers including, but not necessarily limited to, KDM6B (see the figure).

Kdm6b is a member of the Jumonji gene family that is implicated in reptile and mammalian sex determination. For example, in mice, another Jumonji family member, *Kdm3a*, encodes a protein that catalyzes H3K9 demethylation of the mammalian sex-determining gene *Sry* (sex-determining region Y) to enable its expression above the required threshold for male development (*13*). In reptiles, the role of Jumonji family members appears to be more complex. Depending on the temperature, an intron is alternatively retained or excised during transcription of *Kdm6b* [and at least one other family member, *Jarid2* (Jumonji and AT-rich interaction domain containing 2)] in the red-eared slider turtle, American alligator, and the bearded dragon lizard (*14*). In red-eared slider turtles, the intron is retained in *Kdm6b* transcripts of embryos incubated at the lower MPT (26°C), but not those incubated at the higher FPT (32°C). The transcribed intron, when brought into frame, is riddled with premature stop codons, which presumably leads to altered or disrupted KDM6B function in embryos incubated at 26°C. Up-regulation of *Kdm6b* coincident with intron retention and potentially compromised function may at first seem contradictory. However, alternative splicing of Jumonji genes has the potential to alter the targets of gene silencing, gene activation, and the recruitment of chromatin remodeling complexes [for example, PRC2 (Polycomb repressive complex 2)] in ways that are not yet fully understood. Intron retention presumably interacts with the regulatory processes outlined by Ge *et al*. (*9*) to determine sex.

Questions remain as to whether Jumonji genes such as *Kdm6b* are responding directly to temperature or, alternatively, are regulated by upstream temperature-sensitive elements yet to be discovered. One such candidate to recently emerge (*4, 14*) is the gene *Cirbp* (cold-inducible RNA binding protein), which encodes a temperature-inducible RNA binding protein with broad imputed function in messenger RNA stabilization and translational regulation (*15*). *Cirbp* is expressed early in gonadal development in the common snapping turtle *Chelydra serpentina*, and its expression influences sex determination of embryos incubated under a regime in which temperature is equivocal in its influence (*4*). Remarkably, a single point mutation in this gene is sufficient to eliminate temperature sensitivity.

These recent findings (*4, 9, 14*) have dramatically shifted the focus of inquiry from direct thermosensitivity of candidate sex-determining genes to higher-order thermosensitive epigenetic processes that differentially release influential sex genes for expression. We are on the cusp of finally understanding the mechanisms by which temperature exerts its influence on sexual fate. A central role for these highly conserved and fundamental processes of chromatin modification leaves open the possibility that different sex genes can become enlisted to function as temperature-sensitive sex-determining genes, thus explaining the astonishing diversity of sex determination in reptiles (*12*). ■

REFERENCES

1. A. E. Quinn *et al.*, *Science* **316**, 411 (2007).
2. C. E. Holleley *et al.*, *Nature* **523**, 79 (2015).
3. L. Mork, M. Czerwinski, B. Capel, *Dev. Biol.* **386**, 264 (2014).
4. A. L. Schroeder *et al.*, *Genetics* **203**, 557 (2016).
5. A. H. Sinclair *et al.*, *Nature* **346**, 240 (1990).
6. Z. Cui *et al.*, *Sci. Rep.* **7**, 42213 (2017).
7. C. A. Smith *et al.*, *Nature* **461**, 267 (2009).
8. M. Charnier, *CR Séances Soc. Biol. L'Ouest Afr.* **160**, 620 (1966).
9. C. Ge *et al.*, *Science* **360**, 645 (2018).
10. C. Ge *et al.*, *Development* **144**, 2222 (2017).
11. C. Shao *et al.*, *Genome Res.* **24**, 604 (2014).
12. I. Miura, *Sex. Dev.* **11**, 298 (2017).
13. S. Kuroki *et al.*, *Science* **341**, 1106 (2013).
14. I. W. Deveson *et al.*, *Sci. Adv.* **3**, e1700731 (2017).
15. X. Zhu, C. Bührer, S. Wellmann, *Cell. Mol. Life Sci.* **73**, 3839 (2016).

10.1126/science.aat5993

Proposed temperature-dependent epigenetic regulation

At MPT, *Kdm6b* expression is up-regulated directly or by an upstream temperature-sensitive regulator such as *Cirbp*. KDM6B then demethylates the *Dmrt1* promoter, leading to up-regulation of its expression and male development. Additionally, at MPT, transcription of *Kdm6b* and *Jarid2* with a retained intron (IR) is up-regulated; their function is unknown. At FPT, *Kdm6b* and *Jarid2* expression is down-regulated and they are transcribed without the retained intron. Presumably, *Jarid2* is sufficiently expressed to enable PRC2 to trimethylate H3K27 on the *Dmrt1* promoter and suppress its expression, leading to female development.

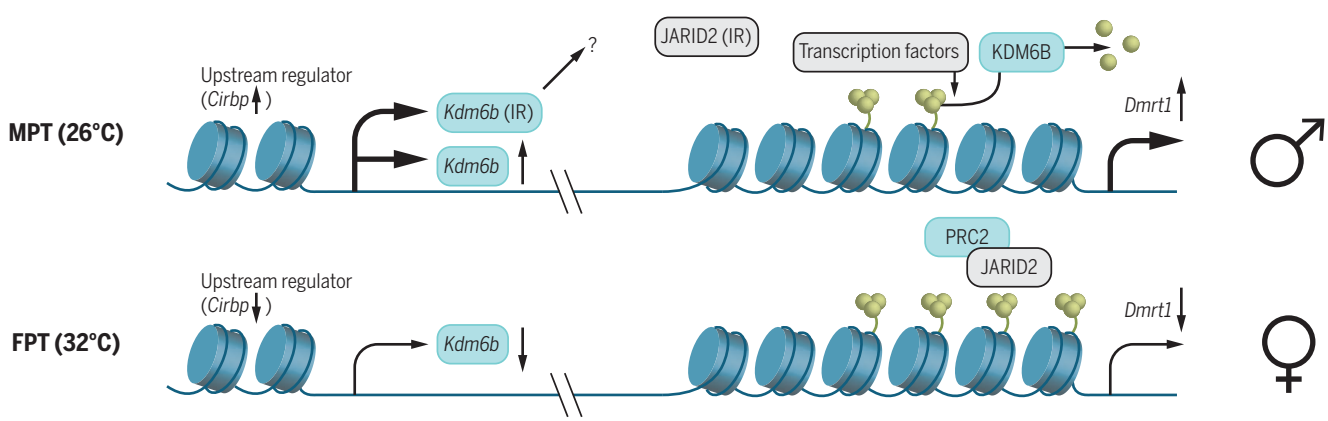

GRAPHIC: N. DESAI/*SCIENCE*

METABOLISM

Metabolite regulates differentiation

Compartmentalized NAD⁺ metabolism regulates transcription to control adipogenesis

By **Sophie Trefely**[1,2] *and* **Kathryn E. Wellen**[1]

Cellular differentiation involves dynamic epigenetic, transcriptional, and metabolic remodeling as cells transition to a new identity. Evidence is mounting that metabolism and gene regulation are intimately linked, with changes in metabolite availability modulating or even triggering gene transcription. One way that metabolites regulate gene expression is as substrates of enzymes that carry out post-translational modification of transcription factors and histones. Such metabolites likely have distinct biological roles in different compartments of the cell, and in particular within the nucleus (*1*, *2*). Yet, the extent to which the nucleus is a separate metabolic compartment from the cytosol and the mechanisms by which nuclear metabolite levels affect expression of specific genes have remained largely unknown. On page 618 of this issue, Ryu *et al.* (*3*) demonstrate that compartmentalized synthesis of the metabolite oxidized nicotinamide adenine dinucleotide (NAD⁺), regulates adipocyte differentiation, a process that is essential for metabolic health, through transcriptional control.

NAD⁺ is crucial for metabolic redox reactions and is also a substrate for sirtuin deacetylates and poly[adenosine diphosphate (ADP)–ribose (PAR)] polymerase (PARP) enzymes. PARP-1 is best known for its involvement in DNA repair, which underlies the sensitivity of BRCA1 and BRCA2 mutant cancers to PARP inhibition (*4*). But PARP family members also participate in diverse cellular processes, including transcriptional regulation and RNA biology (*4*). NAD⁺ is consumed in the sirtuin and PARP reactions and must be resynthesized by nicotinamide mononucleotide (NMN) adenylyl transferase (NMNAT) enzymes, which generate NAD⁺ from NMN and adenosine triphosphate (ATP). There are three mammalian NMNAT isoforms with distinct subcellular localization: NMNAT-1 (nuclear), NMNAT-2 (cytosolic), and NMNAT-3 (mitochondrial), suggesting that NAD⁺ synthesis could be distinctly regulated in each compartment.

Previously, PARP-1 was found to restrain adipocyte differentiation through PARylation of the adipogenic transcription factor C/EBPβ (CCAAT/enhancer binding protein β) (*5*), which inhibits its transcriptional activity. Reduced nuclear PARylation occurred in the first 48 hours of differentiation, facilitating C/EBPβ activation and adipogenesis. Because PARP-1 expression was not regulated during early adipogenesis, Ryu *et al.* asked whether the availability of NAD⁺ might control PARP-1 activity.

The authors found that silencing nuclear NMNAT-1 before induction of adipocyte differentiation reduced PARylation and promoted differentiation, mirroring the response to PARP-1 knockdown. The enhancement of differentiation mostly occurred through C/EBPβ, suggesting that C/EBPβ function is suppressed by PARP-1 in an NMNAT-1–dependent manner. Upon induction of differentiation, PARylation decreases, allowing C/EBPβ to bind gene promoters, including those encoding peroxisome proliferator–activated receptor–γ (PPARγ) and C/EBPα that direct terminal adipocyte differentiation (see the figure).

Is reduced PARylation a consequence of reduced NAD⁺ concentrations? A striking increase in expression of the cytosolic enzyme NMNAT-2 occurred within 4 hours of induced differentiation. This raised the intriguing possibility that cytosolic and nuclear NAD⁺ may be differentially regulated. They measured NAD⁺ concentrations at subcellular resolution in live cells using a fluorescent biosensor (*6*) and observed a decrease in nuclear NAD⁺ levels accompanied by increased cytosolic NAD⁺ within hours of induction. Importantly, owing to the affinity of PARP-1 for NAD⁺ (*7*), the drop in nuclear NAD⁺ concentration should be sufficient to limit the PARP-1 reaction rate. Thus, by competing for NMN, NMNAT-2 up-regulation drives nuclear NAD⁺ depletion, enabling C/EBPβ activation and adipogenesis. Intriguingly, NMNAT-2 up-regulation was glucose-dependent, indicating that only when glucose is abundant will nuclear NAD⁺ levels decline to permit differentiation. Compartmentalized NAD⁺ metabolism thus represents a mechanism to couple adipogenesis with nutrient availability.

That metabolism is compartmentalized within membrane-bound organelles such as mitochondria or lysosomes is well established (*8*). By contrast, large nuclear pores permit small molecules such as NAD⁺ to passively diffuse between the nucleus and cytosol, suggesting that metabolites are at equilibrium between these compartments. However, Ryu *et al.* provide strong evidence that at least in some conditions, these compartments are largely distinct. Although the mechanism by which the nuclear and cytosolic NAD⁺ are segregated remains unknown, the authors propose that restriction of diffusion by macromolecular crowding or the formation of complexes between proteins that produce and consume NAD⁺ may result

Nuclear NAD⁺ controls adipocyte differentiation

Compartmentalized synthesis of NAD⁺ regulates gene transcription.GAPDH, glyceraldehyde-3-phosphate dehydrogenase.

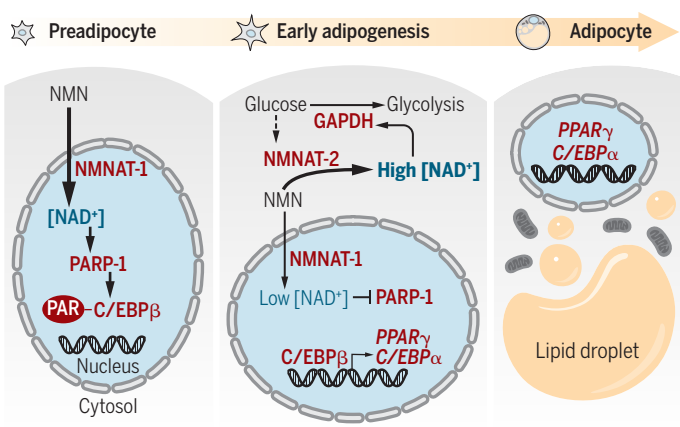

Nuclear NAD⁺ concentration is high, and C/EBPβ activity is restrained by PARP-1–dependent PARylation.

Cytosolic NMNAT-2 expression is induced in a glucose-dependent manner, depleting the supply of NMN for nuclear NAD⁺ synthesis, reducing PARylation, and allowing C/EBPβ activation.

C/EBPβ transcriptional targets include *PPARγ* and *C/EBPα*, which direct terminal adipocyte differentiation.

GRAPHIC: A. KITTERMAN/*SCIENCE*

[1]*Department of Cancer Biology, Abramson Family Cancer Research Institute, Perelman School of Medicine, University of Pennsylvania, Philadelphia, PA 19104, USA.* [2]*A.J. Drexel Autism Institute, Drexel University, Philadelphia, PA 19104, USA. Email: wellenk@upenn.edu*

in the functional separation of metabolism. Importantly, the demonstration of divergent NAD^+ metabolism in the nucleus and cytosol during adipocyte differentiation shows not only that the two pools are distinct but that their separation represents a point of regulation in control of a physiological process.

Analogous regulation likely applies to other metabolites such as acetyl–coenzyme A (CoA) and *S*-adenosylmethionine (SAM), which are needed in the nucleus for histone acetylation and histone and DNA methylation, respectively. Both acetyl-CoA and SAM are thought to be present in the cell at levels that can limit acetyltransferase and methyltransferase activity (*9*); yet, definitive measurements of these metabolites specifically within the nucleus are lacking. Nevertheless, enzymes that produce acetyl-CoA and SAM are present and distinctly regulated within the nucleus (*1*, *2*), and recent metabolic evidence also supports the notion of functional separation between nuclear and cytosolic pools of acetyl-CoA (*10*, *11*).

In addition to prompting further investigation into the nuclear and cytosolic compartmentalization of metabolism, the Ryu *et al.* study raises a number of intriguing questions about NAD^+ metabolism in adipocytes and other cell types. NAD^+ rises with calorie restriction and exercise and is proposed as a mediator of their beneficial effects through regulation of sirtuin activity (*12*). SIRT1 in particular could be affected by variations in nuclear NAD^+ levels, raising questions about the potential role of NAD^+ compartmentalization in regulating the myriad processes controlled by SIRT1 (*13*). Furthermore, how might compartmentalized NAD^+ metabolism integrate with other stimuli that affect NAD^+ levels, such as aging, caloric restriction, and circadian oscillations (*13*)? How does nuclear NAD^+ affect other cellular differentiation processes or responses to stimuli that are regulated by PARPs or sirtuins, and how might dysregulation of compartmentalized NAD^+ production contribute to disease states or present therapeutic opportunities? Notably, *NMNAT-1* is deleted in some cancers (*14*). The findings of Ryu *et al.* will surely prompt numerous important avenues of investigation. ■

REFERENCES

1. S. Sivanand *et al.*, *Trends Biochem. Sci.* **43**, 61 (2018).
2. A. Kinnaird *et al.*, *Nat. Rev. Cancer* **16**, 694 (2016).
3. K. W. Ryu *et al.*, *Science* **360**, eaan5780 (2018).
4. R. Gupte *et al.*, *Genes Dev.* **31**, 101 (2017).
5. X. Luo *et al.*, *Mol. Cell.* **65**, 260 (2017).
6. X. A. Cambronne *et al.*, *Science* **352**, 1474 (2016).
7. M.-F. Langelier *et al.*, *J. Biol. Chem.* **285**, 18877 (2010).
8. A. S. H. Costa *et al.*, *Int. Rev. Cell Mol. Biol.* **332**, 213 (2017).
9. M. A. Reid *et al.*, *Nat. Cell Biol.* **19**, 1298 (2017).
10. S. Zhao *et al.*, *Cell Rep.* **17**, 1037 (2016).
11. V. Bulusu *et al.*, *Cell Rep.* **18**, 647 (2017).
12. S. Imai *et al.*, *Trends Cell Biol.* **24**, 464 (2014).
13. C. Cantó *et al.*, *Cell Metab.* **22**, 31 (2015).
14. F. L. Muller *et al.*, *Nature* **488**, 337 (2012).

10.1126/science.aat6663

CONSERVATION

The hidden biodiversity of amphibian pathogens

Discovery of additional amphibian chytrid pathogens increases conservation concerns

By **Karen Lips**

Since the discovery of the salamander chytrid pathogen [*Batrachochytrium salamandrivorans* (*Bsal*)] (*1*), the world has been preoccupied with determining where it does and does not occur (*2*) so that policies can be implemented to prevent introduction into unaffected areas (*3*). Pathogenic chytrids cause chytridiomycosis, a disease of the skin that can cause mortality and die-offs, including population declines and species extinctions. In the United States—the world's biodiversity hot spot for salamanders and currently free of *Bsal*—a multinational scientific task force has been created to test the susceptibility of native species and to prepare an emergency response should *Bsal* be detected (*4*). Meanwhile, attention to *Bsal*'s better-known cousin *B. dendrobatidis* (*Bd*), another chytrid pathogen that has decimated amphibian populations around the world, has faded, in part because of perceptions that once *Bd* is present, conservation actions and policy options are limited. On page 621 of this issue, O'Hanlon *et al.* (*5*) remind us that *Bd* remains a serious threat to global amphibian biodiversity and clarify where and when *Bd* came from and how it spread.

The Brazilian pumpkin toadlet (*Brachycephalus pitanga*) is host to *Bd*Brazil.

PHOTO: ALBERTO LOPEZ TORRES

O'Hanlon *et al.* use whole-genome sequencing of 234 *Bd* cultures taken from around the globe to identify East Asia as the site of origin of *Bd*, including the Global Panzootic Lineage (*Bd*GPL), the invasive, hypervirulent form of chytrid that has been implicated in losses of amphibians from six regions (*5*, *6*). The authors date the emergence of *Bd*GPL to the second half of the 20th century, consistent with the period of high commercial trade in amphibians. The authors describe phylogenetic patterns of *Bd* as clustering into five main lineages—four of which were previously identified (*6*) and one entirely new, genetically distinct, hyperdiverse lineage from the Korean peninsula. The high genetic diversity of this new Asian lineage differs from that of the other four lineages, all of which exhibit a pattern of genetic diversity typical of population fluctuations and/or natural selection and consistent with increases in spatial distribution or in the number of host species. This suggests that East Asia is the most likely source of origin for amphibian chytrid pathogens. O'Hanlon *et al.* also identify two new kinds of hybrid lineages, raising the possibility that introductions of new lineages might produce more hybrid chytrids. Finally, the authors show that all *Bd* variants are present in the commercial trade of amphibians (including food, pets, and scientific specimens), demonstrating contemporary intercontinental transmission and the failure of international biosecurity measures to control the spread of this pathogen.

Department of Biology, University of Maryland, College Park, MD 20742, USA. Email: klips@umd.edu

The implications of these new findings are wide ranging. For example, although *Bd*GPL is globally distributed, other lineages are geographically restricted. This identifies areas that might be susceptible to new invasions by these endemic lineages and may explain variation in species responses to infection (*7*, *8*). Despite decades of research, quantitative studies of the impacts of chytridiomycosis on amphibian populations are lacking from most areas, especially Asia (*8*). Demographic analyses are critical in providing robust estimates of demographic parameters such as species or population-specific survival and mortality rates and population growth rates. In addition, mark-recapture studies that follow the fate of infected individuals are needed to identify mechanisms underlying the causes of population decline, persistence, or recovery and to identify effective conservation measures.

To control emerging infectious diseases (EIDs), we also need a better understanding of the relative contributions of global change (for example, changes in climate, land use, and trade) on the emergence and spread of pathogens. Knowing that all chytrid lineages are circulating in trade routes, but not all are globally distributed (*5*), highlights the need for coinfection experiments to predict responses to future invasions. Knowledge of how the trade ecosystem might amplify disease by promoting hybridization events among lineages or by facilitating the spread of lineages into naïve populations could be useful to mitigate and manage disease within the live-animal trade.

Many areas of the world lack chytrid cultures, disease surveillance programs, or amphibian population studies necessary to study or conserve amphibian biodiversity. Developing collaborative partnerships between investigators from these regions and established research groups could increase the global capacity to understand the emergence of *Bd* and responses of amphibian populations. Even more important is the need to expand veterinary capacity for wildlife diseases. Many national veterinary authorities lack sufficient resources, staff, or bandwidth to respond effectively to the rapidly increasing numbers of wildlife pathogens that threaten global biodiversity.

Proactive measures to address EIDs will be possible when we can predict future outbreaks, species susceptibility, and disease spread, perhaps through analyses to model disease outbreaks from genomics, Google search histories, or social media data (*9*, *10*). Advanced detection technologies would improve the ability to address new introductions. Alternatively, coordination of citizen science programs might serve as an early warning system in some regions.

Successful mitigation of the impacts of chytridiomycosis is also lacking. No effective treatments exist for wild populations, and policies restricting imports are only as strong as enforcement efforts (*7*). One of the most important advances in the global response to *Bsal* was the development of an emergency response plan (*11*, *12*), including the establishment of a *Bsal* task force (*4*); such a coordinated effort is lacking for *Bd* and could speed discovery and identify effective interventions.

Both *Bd* and *Bsal* are notifiable diseases under the World Organisation for Animal Health (OIE) standards, but, despite global support, this agreement has lacked strong, consistent enforcement. Strengthening application of the OIE standards should be a first step. In the United States, new laws are needed to improve the ability of the U.S. Fish and Wildlife Service to monitor and control invasive species and diseases (*13*). New policies developed in collaboration with trade organizations, lobbyists, and national and international organizations to implement quarantine measures, testing procedures, and clean-trade programs could minimize the risk of pathogen introductions. The European Union has recently approved such a law (*14*).

The work of O'Hanlon *et al.* serves as a case study for studying and addressing EIDs. With accelerating global change in a more connected world, we can expect to see more EIDs, so international collaborations such as this one will be increasingly necessary to address global pathogens of wildlife, agriculture, and humans. ■

REFERENCES

1. A. Martel *et al.*, *Science* **346**, 630 (2014).
2. T. A. Yap *et al.*, *Science* **349**, 481 (2015).
3. U.S. Department of the Interior, Fish and Wildlife Service, "50 CFR Part 16, Injurious wildlife species: Listing salamanders due to risk of salamander chytrid fungus," *Fed. Reg.* **81**, 1534 (2016).
4. M. J. Gray *et al.*, *PLOS Pathog.* **11**, e1005251 (2015).
5. S. J. O'Hanlon *et al.*, *Science* **360**, 621 (2018).
6. R. A. Farrer *et al.*, *Proc. Natl. Acad. Sci. U.S.A.* **108**, 18732 (2011).
7. T. W. J. Garner *et al.*, *Phil. Trans. R. Soc. B* **371**, 20160207 (2016).
8. K. R. Lips, *Phil. Trans. R. Soc. B* **371**, 20150465 (2016).
9. B. A. Han *et al.*, *Proc. Natl. Acad. Sci. U.S.A.* **112**, 7039 (2015).
10. F. T. Burbrink *et al.*, *Sci. Adv.* **3**, e1701387 (2017).
11. E. H. C. Grant *et al.*, *U.S. Geological Survey Open-File Report 2015–1233* (2015); http://dx.doi.org/10.3133/ofr20151233.
12. E. H. C. Grant *et al.*, *Front. Ecol. Environ.* **15**, 214 (2017).
13. U.S. Government Accountability Office (GAO), "Live Animal Imports: Agencies Need Better Collaboration to Reduce the Risk of Animal-Related Diseases" (Report GAO-11-9, GAO, 2010).
14. European Commission (2018); http://eur-lex.europa.eu/eli/dec_impl/2018/320/oj .

10.1126/science.aat6411

NUCLEAR PHYSICS

Resolving the neutron lifetime puzzle

A measurement of trapped neutrons dramatically improves control of systematic uncertainties

By **Pieter Mumm**

Free electrons and protons are stable, but outside atomic nuclei, free neutrons decay into a proton, electron, and antineutrino through the weak interaction, with a lifetime of ~880 s (see the figure). The most precise measurements have stated uncertainties below 1 s (0.1%), but different techniques, although internally consistent, disagree by 4 standard deviations given the quoted uncertainties. Resolving this "neutron lifetime puzzle" has spawned much experimental effort as well as exotic theoretical mechanisms, thus far without a clear explanation. On page 627 of this issue, Pattie *et al.* (*1*) present the most precise measurement of the neutron lifetime to date. A new method of measuring trapped neutrons in situ allows a more detailed exploration of one of the more pernicious systematic effects in neutron traps, neutron phase-space evolution (the changing orbits of neutrons in the trap), than do previous methods. The precision achieved, combined with a very different set of systematic uncertainties, gives hope that experiments such as this one can help resolve the current situation with the neutron lifetime.

"Researchers have primarily used two techniques to measure the neutron lifetime, typically referred to as 'beam' and 'bottle' measurements."

National Institute of Standards and Technology, 100 Bureau Drive MS-8461, Gaithersburg, MD 20899, USA. Email: pieter@nist.gov

The semileptonic decay of neutrons is the simplest example of nuclear β-decay and plays a key role in validating our understanding of weak processes. In the early universe, the neutron lifetime ultimately determined the ratio of neutrons to protons during primordial light-element nucleosynthesis. The neutron decay is also closely connected to processes relevant in solar physics and in the detection of reactor antineutrinos (*2*, *3*). In combination with other neutron decay parameters, it affords the potential of a sensitive test of the unitarity of the quark-mixing matrix competitive with, and independent of, other methods (*4*). For these reasons, determining the free neutron lifetime has been the focus of extensive experimental effort (*5*) since the first measurement in 1948 (*6*).

Researchers have primarily used two techniques to measure the neutron lifetime, typically referred to as "beam" and "bottle" measurements. In the beam measurement, a very well-characterized beam of cold neutrons (neutrons with energies of a few milli–electron volts) passes through an arrangement of magnetic and electric fields that forms a pseudo-Penning proton trap. Every so often, the trap is emptied, and the decay protons are counted. By comparing the proton detection rate with the number of neutrons traveling through the trap, the neutron lifetime can be readily extracted. Although conceptually simple, this approach depends on accurate proton counting and the absolute determination of the neutron flux at or below the 0.1% level, both of which are extremely challenging. With the lifetime puzzle in mind, an updated measurement based on this technique, with an expected uncertainty of below 1 s, is currently under way (*7*).

An alternative approach that avoids some of the difficulties of the beam method is to trap neutrons for times that are large compared with the lifetime. Neutrons can be cooled from milli– to nano–electron volt energies through nonequilibrium inelastic scattering processes (*8*). These "ultracold" neutrons (UCNs) are of such low energies that they travel only a few meters per second. A useful accident of nature is that for UCNs, gravitational, magnetic, and nuclear interaction energies are roughly similar, so UCNs are easily manipulated (for example, spin-polarized to very high levels). In particular, UCNs below a few hundred nano–electron volts can be trapped in vessels made of appropriately chosen material.

Neutron traps have become the most common method used in neutron lifetime measurements (*9*–*12*). In these experiments, neutrons are loaded into a trap, stored for a variable length of time, and then drained into a detector, where they are counted. By comparing surviving neutrons over multiple storage times, the neutron lifetime can be extracted independently of the absolute number of neutrons loaded into the trap. For this approach to work, neutron losses from the trap during storage must be both minimized and well understood, but neutrons interact strongly with matter. For example, neutrons can be absorbed or scattered by imperfections in the trap. Because UCNs are not in thermal equilibrium with their surroundings, any scattering process will tend to increase their energy and eject them from the trap.

As a result, all material bottle experiments must make corrections for these effects. Such effects can be reduced by using magnetic traps, and there are several examples of this approach (*13*, *14*). More difficult, however, are effects caused by UCN phase-space evolution either during storage or during the unloading of the trap. It is generally the case that some fraction of UCNs in a trap have total energies above the trap depth because some of the energy is in orbital motion. Orbits can evolve slowly, on time scales of hundreds of seconds, and eventually, the UCNs are lost. Similarly, some orbits may take long times to drain and be detected, requiring additional corrections.

The work of Pattie *et al.* combines several clever advances to address these systematic difficulties. Like most other modern experiments, their study uses a magnetic trap. However, in their case, the trap is a semitoroidal magneto-gravitational trap formed from a magnetic Halbach array and gravity. The trap is asymmetric, leading to quasi-chaotic orbits, which creates an efficient and rapid mixing of phase space. This process allows the use of a "cleaner," a neutron absorber placed just below the maximum trap depth. All neutrons that could eventually escape from the trap are quickly removed before the storage period begins. Most importantly, however, Pattie *et al.* developed an in situ detector, consisting of a neutron-absorbing layer deposited on a scintillating material coupled to optical detectors (*14*). Neutron absorption produces light that is detected with high efficiency. This detector can be lowered in stages so that a neutron energy spectrum can be mapped at various storage times and prove that any phase-space evolution is minimized.

The results are remarkable. Once cleaned, the storage time in their trap is >3 weeks, and perhaps most importantly, the unloading sequence is identical at long and short holding times. Thus, not only do Pattie *et al.* report the most precise measurement of the neutron lifetime but also the first modern measurement in which the systematic corrections are below the stated uncertainty. Assuming that the discrepancy with the beam measurements will be understood, a precision of 0.2 s appears quite plausible in the near future. In addition to the impacts discussed above, at this level of precision, comparison with other techniques will allow new precision tests of the Standard Model (*15*). ■

Neutron decay

Free neutrons (n) undergo β-decay through the weak interaction after ~880 s. A new trapping measurement by Pattie *et al.* provides a way to better determine this value.

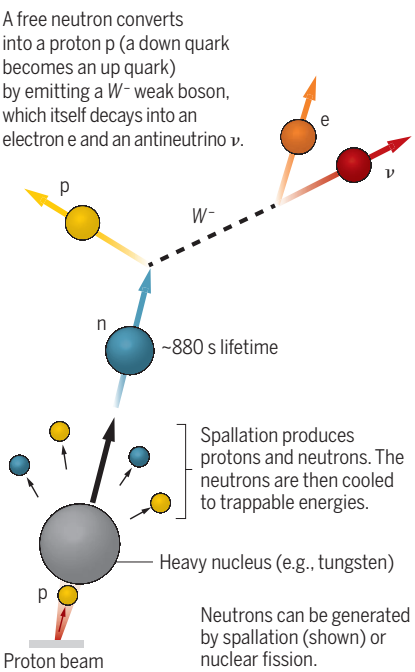

GRAPHIC: N. CARY/*SCIENCE*

REFERENCES

1. R. W. Pattie Jr. *et al.*, *Science* **360**, 627 (2018).
2. R. E. Lopez, M. S. Turner, *Phys. Rev. D* **59**, 103502 (1999).
3. G. Mention *et al.*, *Phys. Rev. D* **83**, 073006 (2011).
4. C. Patrignani *et al.* (Particle Data Group), *Chin. Phys. C* **40**, 100001 (2016).
5. F. E. Wietfeldt, G. L. Greene, *Rev. Mod. Phys.* **83**, 1173 (2011).
6. A. H. Snell, L. Miller, *Phys. Rev.* **74**, 1217 (1948).
7. A. T. Yue *et al.*, *Phys. Rev. Lett.* **111**, 222501 (2013).
8. R. Golub, J. M. Pendlebury, *Phys. Lett. A* **53**, 133 (1975).
9. A. P. Serebrov *et al.*, *Phys. Rev. C* **78**, 035505 (2008).
10. A. Pichlmaier *et al.*, *Phys. Lett. B* **693**, 221 (2010).
11. S. Arzumanov *et al.*, *Phys. Lett. B* **483**, 15 (2000).
12. A. W. Mampe *et al.*, *J. Exp. Theor. Phys. Lett.* **57**, 82 (1993).
13. V. F. Ezhov *et al.*, *Nucl. Instrum. Meth. A* **611**, 167 (2009).
14. C. M. O'Shaughnessy *et al.*, *Nucl. Instrum. Meth. A* **611**, 171 (2009).
15. V. Cirigliano *et al.*, *Prog. Part. Nucl. Phys.* **71**, 93 (2013).

10.1126/science.aat7140

POLICY FORUM

PHOTO: LAYNE KENNEDY/GETTY IMAGES

Amounts of methylmercury in some Great Lakes fish are influenced by the long-range atmospheric transport of mercury from far-away sources.

ENVIRONMENT AND HEALTH

A proposed global metric to aid mercury pollution policy

The Minamata Convention needs policy-relevant insight

By **Noelle E. Selin**

The Minamata Convention on Mercury entered into force in August 2017, committing its currently 92 parties to take action to protect human health and the environment from anthropogenic emissions and releases of mercury. But how can we tell whether the convention is achieving its objective? Although the convention requires periodic effectiveness evaluation (*1*), scientific uncertainties challenge our ability to trace how mercury policies translate into reduced human and wildlife exposure and impacts. Mercury emissions to air and releases to land and water follow a complex path through the environment before accumulating as methylmercury in fish, mammals, and birds. As these environmental processes are both uncertain and variable, analyzing existing data alone does not currently provide a clear signal of whether policies are effective. A global-scale metric to assess the impact of mercury emissions policies would help parties assess progress toward the convention's goal. Here, I build on the example of the Montreal Protocol on Substances that Deplete the Ozone Layer to identify criteria for a mercury metric. I then summarize why existing mercury data are insufficient and present and discuss a proposed new metric based on mercury emissions to air. Finally, I identify key scientific uncertainties that challenge future effectiveness evaluation.

Institute for Data, Systems, and Society and Department of Earth, Atmospheric, and Planetary Sciences, Massachusetts Institute of Technology, Cambridge, MA, USA. Email: selin@mit.edu

METRIC LESSONS, DATA LIMITATIONS

The Montreal Protocol is widely considered an environmental success story. Since its 1987 adoption, amendments and adjustments to accelerate the phaseout of ozone-depleting substances have led to a slowing of emissions and then a decline in the amount of such substances in the stratosphere. Scientists developed the concept of equivalent effective stratospheric chlorine (EESC) (*2*) to address policy-targeted questions about how the stratosphere responds to global actions and applied it in periodic assessment reports to the Montreal Protocol. EESC is calculated with a straightforward equation that connects emissions to effective amounts of halogens in the stratosphere without using a complex model (*2*). Parson (*3*) argued that this metric allowed negotiators to make progress because it conveyed the implications of the problem, while avoiding much of the complexity, uncertainty, and controversy then associated with ozone loss processes. EESC was used by policy-makers to examine relative benefits of different control options and to help evaluate progress of the agreement over time.

A similar type of metric would be useful for mercury under the Minamata Convention. Following the EESC example, such a metric would have several characteristics. It would be global in scale: Although mercury poses local, regional, and global challenges (*4*), global treaties address environmental issues for which national and regional action is insufficient. The metric should convey information about changes in global mercury damages from anthropogenic sources, be straightforward to calculate, and allow policy-makers to compare implications of different proposals. It should also acknowledge scientific uncertainty and be able to accommodate changes in knowledge over time.

The global scientific community has mobilized and organized much information in support of international efforts to address mercury pollution. Emission inventories [e.g., (*5*)] include sources of mercury from the burning of fossil fuels, artisanal and small-scale gold mining, and the use of mercury in industrial processes. Recent efforts have quantified releases to land and water (*6*). Mercury in products is now recognized to contribute substantially to environmental levels and trends (*7*). A growing database of environmental and biota concentrations contributes to greater understanding of the distribution and impacts of mercury worldwide (*8*).

Two major challenges make existing data insufficient for evaluating the Minamata Convention. First, data on mercury flows, such as emissions to air, do not account for the long environmental lifetime of mercury. Mercury deposited from the atmosphere to water and land can revolatilize and continue to cycle (*4*). Current estimates suggest that

the present-day mercury cycle is enriched by a factor of >7 relative to its state before human influence (*9*). A substantial fraction of present-day concentrations is due to legacy mercury from past human actions. Thus, recovery from mercury pollution on a global scale could take decades to centuries, as today's emissions and releases will become tomorrow's legacy mercury (*10*).

Second, measurements in the environment and biota are variable: They are influenced by multiple factors and need substantial interpretation to link back to emissions changes. For example, food web alterations due to climate change can influence bioaccumulation and thus methylmercury concentrations in predator species (*11*). These dynamics are not well understood. Although data are available in industrialized regions, measurements are lacking elsewhere, challenging our ability to set a global baseline. Where processes are uncertain and mechanistic models are unavailable, it is difficult to conceptually connect how policy choices affect concentrations downstream.

Tracking newly released and legacy mercury through this environmental pathway requires complex, coupled models that encompass ocean, atmosphere, and land reservoirs, and decadal-scale simulations, which are rarely used for policy analysis and are extremely computationally intensive. Two different types of models are commonly used separately by scientists examining these processes: (i) Atmospheric chemical models provide important information on sources and receptors, but most do not represent the decadal-scale implications of anthropogenic emissions, as they have limited representation of land and ocean dynamics. (ii) Biogeochemical cycle models capture this cycling, but need advanced software to run, and their standard output does not allow policy-makers to easily visualize the relative impact of different policy choices. A simpler approach could help policy-makers better understand mercury cycling and the implications of policy options.

A PROPOSED METRIC

The total amount of anthropogenic mercury depositing from the atmosphere to ecosystems provides a useful proxy for the marginal impacts of anthropogenic mercury emissions. The amount of mercury deposition in a given year tracks the amount of atmospheric emission—what goes up must come down. A time-integrated function of anthropogenic emissions can thus approximate the human contribution to deposition both now and in the future, forming a basis for a global-scale mercury metric. Such a metric is intended to be applied in contexts where policy-makers are evaluating different options. Equation 1 summarizes a proposed metric, effective anthropogenic mercury deposition (EAMD):

$$\mathrm{EAMD}(t) = \varepsilon_0[\lambda_1 e^{-\beta_1 t} + \lambda_2(1 - e^{-\beta_2 t}) \quad (1)$$

Given a primary annual atmospheric emission (ε_0) in units of mass, Eq. 1 calculates EAMD (in the same mass units) in year t. Initially, the emission enters the atmosphere and deposits according to its effective atmospheric lifetime following the first part of the equation, with λ_1 representing this initial deposition process and β_1 the associated decay time scale. Subsequently, this mercury is reemitted from land and water and deposits again, with the parameter λ_2 capturing the reemission process and β_2 its behavior with time. The parameters are designed to be calibrated to more detailed models of biogeochemical cycling and could be varied to account for uncertainty. Although a recent analysis suggested that the global mercury biogeochemical system has seven characteristic time scales (*9*), over a policy-relevant (50- to 100-year) time frame, Eq. 1 captures its behavior. The two-term simplification parallels that used in accounting for the carbon cycle in calculating global warming potential (*12*). Parameters calibrated by a nonlinear least-squares fit to a biogeochemical model run for a pulse emission to the atmosphere (*10*) correlate strongly (r^2 = 0.99) with the behavior of the more complex model (see supplementary materials).

Applying the EAMD metric to future emissions projections provides policy-makers with a clear signal about long-term implications of policy choices. Typical analyses of policy impacts using atmospheric chemical models, by contrast, do not account for the influence of current policy choices on future legacy mercury. For example, a recent paper using an atmospheric chemical model to address how Minamata Convention policies could affect mercury deposition in Asia by 2050 estimated, based on an additional analysis using a biogeochemical cycle model, that policy-driven changes in legacy mercury could alter calculated benefits by 30% (*13*).

The figure shows results of the EAMD metric applied to a constant emissions scenario to 2050. The EAMD metric clearly shows that a constant emission level will result in increasing future legacy emissions. Most atmospheric chemical models do not account for this effect and would project constant deposition. By contrast, output from a biogeochemical model analysis projects the declining influence of past legacy emissions together with present emissions that turn into future legacy emissions: Sensitivity runs are needed to derive the new versus historical components shown in the figure. By contrast, EAMD readily calculates the change in expected deposition due to present and future anthropogenic emission. EAMD is simple enough to be implemented in a spreadsheet (see supplementary materials) or online. EAMD allows for transparency of assumptions, straightforward uncertainty analysis by altering parameters, and the ability to account for changes in scientific understanding by recalculating those parameters when biogeochemical models improve. EAMD also avoids the need for policy-makers to debate and reach consensus on underlying scientific processes.

Building on how EESC was used to evaluate policy options, we can examine how EAMD, integrated over time, responds to policy choices. The table shows how integrated EAMD can illuminate the time scales of mercury pollution and show costs

Change in deposition projected by existing models versus EAMD

The atmospheric chemistry transport model is estimated at a constant level. The six-box biogeochemical model includes the offsetting influence of decaying historical emissions plus new emissions. EAMD is calculated for the same continuous emission. See supplementary materials for details.

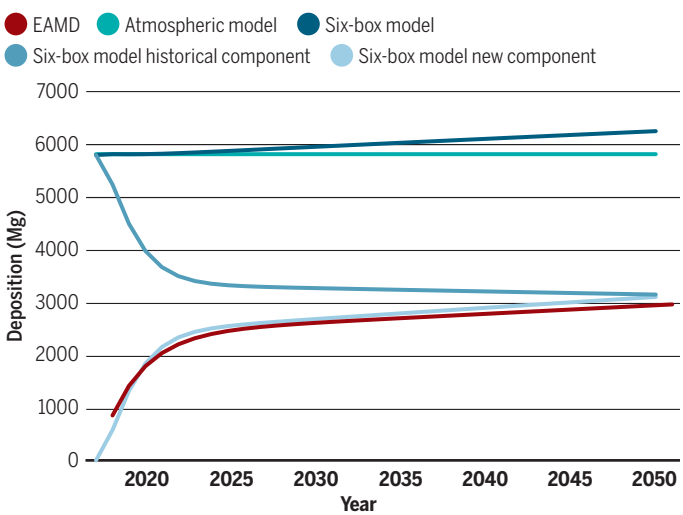

GRAPHIC: J. YOU/SCIENCE

of delayed action. Considering a "maximum feasible reduction" scenario by 2035 (*5*), a >80% cut in emission, reduces integrated EAMD (to 2050) by only 58% relative to a constant emissions scenario. Delaying this reduction trajectory by 15 years reduces the integrated impact to 39%.

LIMITATIONS

The EAMD metric as proposed here has some key limitations. It does not distinguish between emission of different forms of mercury: Whereas elemental mercury has a long atmospheric lifetime, oxidized forms deposit regionally. This can be accounted for in the biogeochemical model calibration *(9)*, however, and could be adjusted to capture future changes in emission speciation that may occur as a result of changes in control technologies *(13)*.

Mercury emissions from products, and releases of mercury to land and water, are not explicitly covered by this metric, which focuses instead on emissions to air. Ideally, projections of future air emissions trajectories should account for potential emissions from products at the end of their useful lives, if not appropriately recycled. Although the primary global transport medium for mercury is the atmosphere, releases to land and water are also addressed by the convention, and these, too, can enter the global biogeochemical cycle (*6*). However, the expected atmospheric emission from anthropogenic land and water releases can be estimated and included in ε_0. An additional term could be developed to account for releases to land and water that reach the global oceans, without first entering the atmosphere. Some estimates suggest that this source can be large (*14*), but at present it is impossible to distinguish between new and legacy mercury entering the global pool via this pathway.

Legacy emissions and releases prior to the defined beginning time are also not captured by the EAMD metric. Although emission reduction policies have little effect on legacy mercury already released, better quantification of its time scales is important for policy analysis going forward. Such knowledge will also be important for interpreting environmental trends in the future, and more measurements are necessary to constrain these processes. Assessment efforts may choose to use a range or distribution of parameters for EAMD obtained by calibrating different biogeochemical models (*9, 15*) and alter them when knowledge improves.

Another potential critique of an emissions-based metric for mercury is that it does not capture real-world fluctuations in climate, land-use change, and other aspects that can change human and wildlife exposure to mercury. Additionally, it does not account for variability: Some ecosystems or people may be more vulnerable to mercury's impacts. Research is clearly still needed to better understand these impacts in particular places. In this way, the parallel to EESC provides a useful example of how a metric can be used in the context of ongoing scientific developments. Effective chlorine content alone does not account for all changes in stratospheric ozone—for example, temperature changes as a result of climate change can affect ozone destruction. Nevertheless, EESC remains useful as a policy-relevant metric, in combination with other analyses of ozone loss and recovery, and has been used to inform analyses of avoided health damages. Similarly, EAMD could be used as a scaling factor to estimate how downstream mercury impacts could change, with all else held constant, as a result of global action. Further applications could also build upon the EAMD formulation to address regional mercury impacts; calibrating the initial term using atmospheric models could account for the fraction of mercury deposited locally.

One reason EESC was effective is that policy-makers agreed upon an ultimate goal: returning stratospheric chlorine concentrations to pre-1980 levels. As chlorine concentrations and resulting ozone depletion in the stratosphere exhibit thresholdlike behavior in their chemical processing, such a goal is feasible. For mercury, no similar policy-relevant thresholds are apparent from science or agreed upon by policy. However, early establishment of a metric could facilitate policy discussion about both desired and feasible levels of environmental recovery.

EAMD for emission reduction scenarios

Integrated EAMD (to 2050 and 2100) is calculated for mercury emission reduction scenarios [following (*5*)], starting in 2017 at a present-day level of 1960 Mg year^{-1} and relative to a baseline in which emission is constant.

POLICY SCENARIO	CHANGE IN EMISSIONS	CHANGE IN INTEGRATED EAMD TO 2050	CHANGE IN INTEGRATED EAMD TO 2100
Linear reduction of atmospheric emissions to 1020 Mg year^{-1} by 2035	-47%	-33%	-41%
Linear reduction of atmospheric emissions to 1020 Mg year^{-1} by 2050	-47%	-22%	-37%
Linear reduction of atmospheric emissions to 300 Mg year^{-1} by 2035	-84%	-58%	-73%
Linear reduction of atmospheric emissions to 300 Mg year^{-1} by 2050	-84%	-39%	-64%

SCIENCE TO SUPPORT GOVERNANCE

New scientific advances are needed both to fully evaluate the impacts of the Minamata Convention and to inform its implementation going forward. Because the Minamata Convention does not include quantitative reduction targets for mercury emissions (*1*), implementation choices such as defining technological options and advancing phaseout dates could have substantial implications for mercury pollution. Periodic effectiveness evaluations should also identify whether further action is needed to meet the Minamata Convention's objective.

A metric such as EAMD could help illustrate the potential implications of these and other future policy choices in a simple and easy-to-use framework. However, other information is also critically needed to monitor, evaluate, and track mercury's progress through the global environment and to better understand its local impacts. New research can help set global baselines and better quantify the processes and dynamics of mercury in the environment and biota. Collecting and assessing these data are critical to our ability to ultimately measure the environmental impact of today's actions on tomorrow's environment. However, while science progresses, a relatively simple proxy can support decision-making moving forward. ■

REFERENCES AND NOTES

1. H. Selin, *Glob. Environ. Polit.* **14**, 1 (2014).
2. J. S. Daniel, S. Solomon, D. L. Albritton, *J. Geophys. Res.* **100**, 1271 (1995).
3. E. A. Parson, *Protecting the Ozone Layer: Science and Strategy* (Oxford Univ. Press, 2003).
4. N. E. Selin, *Annu. Rev. Environ. Resour.* **34**, 43 (2009).
5. J. M. Pacyna *et al.*, *Atmos. Chem. Phys.* **16**, 12495 (2016).
6. D. G. Streets *et al.*, *Environ. Sci. Technol.* **51**, 5969 (2017).
7. H. M. Horowitz, D. J. Jacob, H. M. Amos, D. G. Streets, E. M. Sunderland, *Environ. Sci. Technol.* **48**, 10242 (2014).
8. D. C. Evers, S. E. Keane, N. Basu, D. Buck, *Sci. Total Environ.* **569-570**, 888 (2016).
9. H. M. Amos, D. J. Jacob, D. G. Streets, E. M. Sunderland, *Global Biogeochem. Cycles* **27**, 410 (2013).
10. N. E. Selin, *Environ. Toxicol. Chem.* **33**, 1202 (2014).
11. G. A. Stern *et al.*, *Sci. Total Environ.* **414**, 22 (2012).
12. E. Maier-Reimer, K. Hasselmann, *Clim. Dyn.* **2**, 63 (1987).
13. A. Giang, L. C. Stokes, D. G. Streets, E. S. Corbitt, N. E. Selin, *Environ. Sci. Technol.* **49**, 5326 (2015).
14. H. M. Amos *et al.*, *Environ. Sci. Technol.* **48**, 9514 (2014).
15. A. Qureshi, M. MacLeod, K. Hungerbühler, *Global Biogeochem. Cycles* **25**, GB4012 (2011).

ACKNOWLEDGMENTS

I thank S. Solomon for helpful comments.

SUPPLEMENTARY MATERIALS

www.sciencemag.org/content/360/6389/607/suppl/DC1

10.1126/science.aar8256

BOOKS *et al.*

NEUROSCIENCE

Open minds

A revival in the scientific study of psychedelics prompts a journalist to take a trip

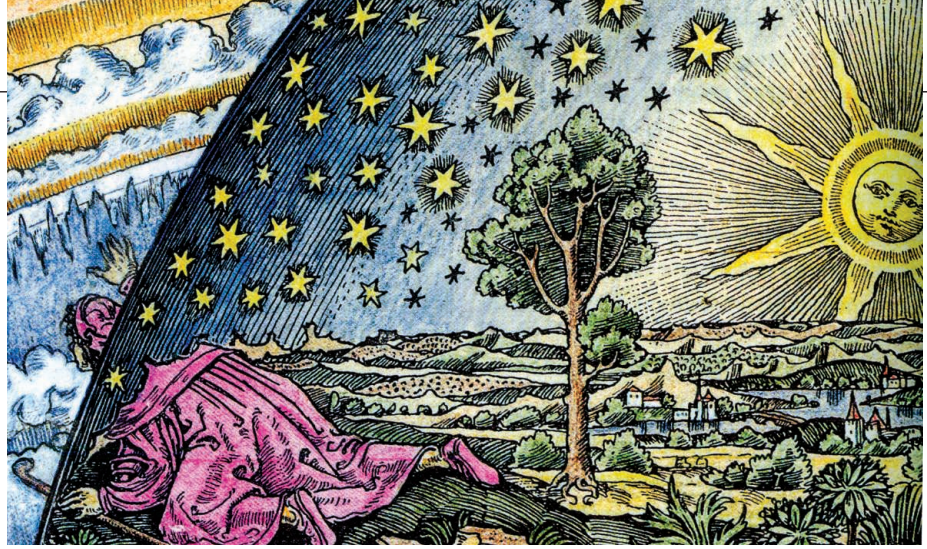

Challenges and opportunities abound in the scientific study of the metaphysical, discovers Pollan.

By **Nicola Pohl**

Known for his writing on plants and food, Michael Pollan, in his latest book, *How to Change Your Mind*, brings all the curiosity and skepticism for which he is well known to a decidedly different topic: the psychedelic drugs D-lysergic acid diethylamide (LSD) and psilocybin. In addition to being a balanced piece of journalistic science writing, this work is also part memoir, as Pollan searches for meaning in life as he enters his early 60s.

Originally hailed as miracle drugs by psychiatrists, LSD, synthesized by the chemist Albert Hofmann in the Sandoz Laboratories in 1938, and psilocybin, a naturally occurring prodrug produced by a variety of mushroom species, became linked to the American counterculture movements in the 1960s. This association would ultimately sour public perception, ending the scientific studies of these compounds for decades.

Advances in brain-imaging tools and other techniques have recently enabled more quantitative studies of consciousness, reinvigorating interest in psychedelic drugs as possible treatments for depression, posttraumatic stress disorder, and other afflictions. *How to Change Your Mind* beautifully updates and synthesizes the science of psychedelics, with a highly personalized touch.

Pollan captures the dilemma of attempting to use the scientific method to interrogate psychedelic drugs, describing the importance of having the right "set and setting" (e.g., social context) for psychedelics to be therapeutically useful. "Western science and modern drug testing depend on the ability to isolate a single variable," he explains. "[B]ut it isn't clear that the effects of a psychedelic drug can *ever* be isolated, whether from the context in which it is administered, the presence of the therapists involved, or the volunteer's expectations."

The idea of conducting a double-blind study is likewise complicated. Recounting a 1962 study in which 20 divinity students were dosed with either psilocybin or a placebo, Pollan notes that telling the subjects apart was not difficult: "[T]hose on the placebo sat sedately in their pews while the others lay down or wandered around the chapel, muttering things like 'God is everywhere' and 'Oh, the Glory!'"

Pollan's narrative is peppered with interesting anecdotes that chart the ways in which psychedelics have influenced recent human history. He writes, for example, about how LSD may have catalyzed the Silicon Valley tech boom. "'It gave us permission to try weird shit in cahoots with other people,'" Stewart Brand, editor of the *Whole Earth Catalog*, tells Pollan at one point.

How to Change Your Mind
Michael Pollan
Penguin Press, 2018. 479 pp.

Brand further credits an LSD experience with having provided the impetus for a campaign he began in 1966 to get the U.S. National Aeronautics and Space Administration to photograph the entire planet. "It occurred to him [while on LSD] that when we think of Earth as flat, as we usually do, we assume it is infinite, and we treat its resources that way," writes Pollan. A picture of a round Earth, Brand reasoned, would convey the finite nature of the planet and compel people to be better stewards of its precious resources.

The book also contains interesting accounts of scientists who had their own experiences with the mystical. Roland Griffiths, for example, was a successful researcher studying caffeine addiction at Johns Hopkins University when a friend introduced him to Siddha yoga at age 50. An experience that occurred during his subsequent meditation practice introduced him to "something way, way beyond a material worldview," he reveals to Pollan. Griffiths ended up switching his research program to the scientific study of psilocybin and went on to publish a landmark double-blind clinical study of the psychological effects of the compound in 2006 (*1*).

Pollan crosses that barrier of objectivity when he decides to take three psychedelics—LSD, psilocybin, and a smoked toad venom containing 5-methoxy-*N*,*N*-dimethyltryptamine (DMT), sometimes known as "the spirit molecule"—himself. The raw travelogue, as he calls it, reveals his struggle with experiences of the spiritual, if not supernatural, as induced by exogenous chemicals. "A phrase like 'boundless being,' which once I might have skated past as overly abstract and hyperbolic, now communicated something specific and even familiar," he writes, reflecting on the profundity of his collective "journeys."

Throughout the book, Pollan makes it clear that he does not advocate illegal drug use. He cites other ways that humans have reached transcendent mental states, including through techniques such as breathing work and meditation. Citations to original sources are provided throughout the book, but they don't break up the flow of chapters, and a separate section of notes and references allows the reader to easily check the works that underpin Pollan's arguments.

Pollan ultimately concludes that psychedelic compounds appear to allow people to relax their brains' inhibitions and abstracting powers—to let go of their egos—so as to see the world afresh. Such experiences can allow a person to achieve balance between too much rigidity and too little structure in their thinking, he argues, which many believe to be the cornerstone of productive creativity. ■

The reviewer is at the Radcliffe Institute for Advanced Study, Harvard University, Cambridge, MA, 02138, and the Department of Chemistry, Indiana University, Bloomington, IN 47405, USA. Email: npohl@indiana.edu

REFERENCE

1. R. R. Griffiths *et al.*, *Psychopharmacology* **187**, 268 (2006).

10.1126/science.aat4324

PALEONTOLOGY

Results roll in from the dinosaur renaissance

An enjoyable round-the-world narrative synthesizes recent paleontological discoveries

By **Victoria Arbour**

The Rise and Fall of the Dinosaurs
A New History of a Lost World
Steve Brusatte
Morrow, 2018. 416 pp.

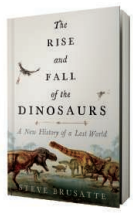

Paleontological research has accelerated in exciting ways over the past two decades, as kids who grew up on *Jurassic Park* and the dinomania of the 1980s and 1990s have joined the ranks of legendary paleontologists leading the "dinosaur renaissance." Steve Brusatte's *The Rise and Fall of the Dinosaurs* takes readers on a tour of the new fossils and discoveries that are shedding light on the dinosaurs' evolutionary story.

The dawn of the dinosaurs, the Triassic period, is still one of the most poorly understood periods in dinosaur history, but it's also where some of the information gaps are being filled most rapidly and most surprisingly. Whereas the end of the age of dinosaurs was abruptly cut short by a meteor, their ascent was complex and drawn-out. New finds from Poland, New Mexico, and Argentina show that dinosaurs were uncommon and relatively unspecialized for the first 30 million years of their existence, and they lived alongside relatives of today's crocodiles that looked much like dinosaurs themselves.

Elsewhere in the Mesozoic era, we meet a variety of newly discovered dinosaurs alongside old favorites. As the giant supercontinent Pangaea split apart during the Jurassic and Cretaceous periods, dinosaurs on newly drifting continents were isolated from each other and began to evolve their own characteristic features. South America was home to the snub-snouted, tiny-armed abelisaurs, Africa to the shark-toothed carcharodontosaurs, and in Transylvania, a bizarre set of dinosaurs includes relatives of *Velociraptor* with not one but two sets of killer sickle claws on their feet.

A chapter of Brusatte's book is dedicated to the evolution of birds from their non-avian dinosaur relatives, one of the most intensively studied aspects of dinosaur evolution over the past 20 years. The veritable flood of fluffy and feathery fossils from China has revealed an amazing diversity of winged dinosaurs. These specimens indicate that feathers evolved long before flight but also suggest that powered, flapping flight may have evolved multiple times in dinosaurs. (We need look no further than the totally weird bat-winged *Yi qi* to see that dinosaurs experimented with many ways to get airborne.)

Unlike all other known dinosaurs, the *Yi qi* appears to have relied on a membranous gliding plane, similar to a bat's, to take flight.

For those who love *Tyrannosaurus rex*—and I suspect that most people are at least a little curious about the most famous of the dinosaurs—two of the book's nine chapters are dedicated to new research on the Tyrant Lizard King and its tyrannosauroid cousins. Tyrannosaurs weren't all giant bone-crunchers with tiny arms: the earliest members of the group started out as small, lightly built, long-armed predators with fancy crests on their heads. Many were feathered, as evidenced by those found in China, where the right kind of conditions preserved soft tissues such as skin.

Unfortunately, the diversity of plant-eating ornithischian dinosaurs gets relatively short shrift in *The Rise and Fall of the Dinosaurs*. Brusatte only briefly covers new research on this group, one of the three major lineages of dinosaurs that has contributed greatly in recent years to our understanding of the big picture of dinosaur evolution and paleobiology. Recent advances in understanding dinosaur growth, biogeography, extinction dynamics, and fine-scale evolutionary changes through time, for example, have only been possible because of the comparatively abundant fossil record of duck-billed hadrosaurs and horned ceratopsians.

Brusatte's personal stories of his work behind the scenes in museum collections and at dinosaur dig sites are full of adventures and humor. Abundant photographs and illustrations help bring these stories to life.

Throughout the book, we're introduced to a cast of paleontologists from around the globe, including Ricardo Martínez, an Argentinian paleontologist who discovered one of the oldest dinosaurs (*Eoraptor*); Lü Junchang, a Chinese paleontologist who named the "Pinocchio rex" tyrannosaur *Qianzhousaurus*; and Grzegorz Niedźwiedzki, a Polish paleontologist who has found thousands of ancient footprints, including trackways made by the ancestors of the dinosaurs. Brusatte highlights the international and multidisciplinary nature of modern-day paleontological research, as well as important historical figures and events.

The contributions of female paleontologists were a bit rarer to find, however. Although the book doesn't set out to provide an exhaustive list of notable researchers, focusing mostly on Brusatte's own collaborations over the years, this was nonetheless surprising, given the fact that at least a third of the current membership of our flagship professional organization, the Society of Vertebrate Paleontology, are women.

Ultimately, however, readers will come away from this book with a greater appreciation for the great strides dinosaur paleontologists have made in the past few decades. I'm hopeful that many will likewise be excited for the work that remains to be done. ■

The reviewer is at the Department of Natural History, Royal Ontario Museum, Toronto, Ontario M5S 2C6, Canada. Email: victoria.arbour@gmail.com

10.1126/science.aat0451

LETTERS

Andean condors (*Vultur gryphus*)

Edited by **Jennifer Sills**

Pesticides thwart condor conservation

Despite global conservation crises, widespread and poorly regulated toxic pesticides still cause preventable tragedies. Carbofuran, a carbamate pesticide, is the most implicated globally (*1*). In January, the latest and most shocking known poisoning incident in South America took place in Argentina, where a single Carbofuran-baited sheep carcass set out by ranchers to combat mammalian predators killed 34 Andean condors (*Vultur gryphus*) (*2*), a threatened, emblematic species of the Andes. This incident raised the number of Andean Condors poisoned in Argentina to at least 66 in the past 13 months (*2*). We must take urgent action to prevent future poisoning incidents.

The effect of pesticide poisoning on Andean condor populations is devastating. The global breeding population is estimated at 6700 mature individuals (*3*), including about 300 individuals in northwestern Patagonia (*4*), close to where the latest incident occurred. Barring an immediate stop to the slaughter, this slow-reproducing, long-lived species (*5*) is likely to be doomed to the same fate as the nine critically endangered condors and vultures worldwide (*6*).

Carbofuran should be banned in the developing world just as it is in Canada, the United States, and the European Union (*1*). Other pesticides should be tightly regulated under a comprehensive and binding international treaty such as that recently published by the United Nations (*7*). Such regulation should ensure monitoring of the pesticide's manufacturing process and its use by consumers, leading to a more responsible, less environmentally harmful use of agrochemicals. This would end the double standards whereby developing countries with weaker regulatory enforcement bear the brunt of mass poisonings, putting both wildlife and human health at risk (*1*, *8*). Legislation and enforcement must go hand in hand with a national commitment to mitigate the underlying causes of poisoning. We recommend strengthening research, environmental education, and collaboration among researchers, managers, and farmers to reduce carnivore-scavenger-livestock conflicts and promote sustainable coexistence among productive human activities and wildlife conservation.

Pablo A. E. Alarcón and Sergio A. Lambertucci*
Grupo de Investigaciones en Biología de la Conservación, INIBIOMA (Universidad Nacional del Comahue-CONICET), Quintral 1250 (R8400FRF), Bariloche, Argentina.
*Corresponding author.
Email: slambertucci@comahue-conicet.gob.ar

REFERENCES

1. N. Richards, *Carbofuran and wildlife poisoning: Global perspectives and forensic approaches* (John Wiley & Sons, 2011).
2. Birldlife International, "34 Andean Condors found dead in Argentina—the poisoning needs to stop" (2018); www.birdlife.org/worldwide/news/34-andean-condors-found-dead-argentina-poisoning-needs-stop.
3. BirdLife International, "IUCN Red List for birds. Species factsheet: *Vultur gryphus*" (2018); http://datazone.birdlife.org/species/factsheet/22697641.
4. S. A. Lambertucci, *Oryx* **44**, 441 (2010).
5. J. Ferguson-Lees, D. A. Christie, *Raptors of the World* (Christopher Helm, 2001).
6. D. L. Ogada *et al.*, *Ann. N. Y. Acad. Sci.* **1249**, 57 (2012).
7. United Nations (UN) Human Rights Council, "Report of the Special Rapporteur on the right to food" (UN General Assembly Report A/HRC/34/48, 2017).
8. M. Eddleston *et al.*, *The Lancet* **360**, 1163 (2002).

10.1126/science.aat6039

Europe's uneven laws threaten scavengers

In 2000, the European Union put sanitary policies into effect to prevent outbreaks of bovine spongiform encephalopathy (*1*, *2*). These policies dictated the removal of carcasses, which in turn threatened the conservation of carrion-eating birds such as vultures, eagles, and kites, as well as carnivorous mammals such as wolves and bears (*1*, *3*). After a long process, biodiversity conservation and public health initiatives have been integrated into a new policy that considers the natural foraging patterns of scavengers when allowing farmers to leave livestock carcasses in the field (*2*, *4*). However, the conservation objectives of this legislation now face a new threat: the lack of consistent criteria to designate scavenger feeding zones (SFZs), where fallen livestock can be left uncollected (*4*).

According to EU legislation, competent authorities can designate SFZs in areas with extensive farming—provided they meet certain sanitary requirements (*4*). However, SFZ policy in EU Member States varies. Bulgaria and Portugal have no SFZs (*5*, *6*), and France has only a few (*7*), whereas Spain has designated large areas and added additional criteria through national and subnational laws (*8*). Consequently, criteria for designating SFZs vary across Spanish autonomous regions. For instance, in Comunidad Valenciana, only Natura 2000 protected areas were selected for SFZ designation (*9*), whereas in La Rioja, scavenger foraging areas in mountain ranges are also considered (*10*). Inconsistent criteria will likely lead to carrion food shortages in some areas. This may alter scavenger foraging behaviors, with detrimental socioeconomic and ecological consequences (*11*).

To successfully integrate environmental concerns into the policies across Europe, the European Union should prioritize uniform criteria for SFZs. We recommend designating SFZs that encompass the large foraging ranges of vultures, which would also include the smaller ranges of other scavengers, such as territorial raptors and large carnivores. EU sanitary regulations have been amended seven times in 10 years, and two Spanish autonomous regions have already expanded initially designated SFZs (*9*, *10*). Establishing large, effective areas for all scavengers (while observing sanitary restrictions) will prevent the need for subsequent legal amendments. Europe's "better regulation" agenda encourages the constant assessment and improvement of EU legislation (*12*), and this goal cannot be met without enforcing a uniform designation of SFZs.

Patricia Mateo-Tomás,[1,2,3]* Pedro P. Olea,[4] José Vicente López-Bao[3]
[1]Centre for Functional Ecology, Department of Life Sciences, University of Coimbra, Calçada Martim de Freitas, 3000-456 Coimbra, Portugal. [2]Institute for Game and Wildlife Research (IREC), UCLM-CSIC-JCCM, 13005 Ciudad Real, Spain. [3]Research Unit of Biodiversity (UO/CSIC/PA), Oviedo University, 33600 Mieres, Spain. [4]Terrestrial Ecology Group (TEG), Departamento de Ecología, Universidad Autónoma de Madrid, 28049 Madrid, Spain.
*Corresponding author.
Email: rktespejos@gmail.com

REFERENCES

1. J. L. Tella, *Nature* **410**, 408 (2001).
2. A. Margalida, M. Carrete, J. A. Sánchez-Zapata, J. A. Donázar, *Science* **335**, 284 (2012).
3. P. Mateo-Tomás *et al.*, *Divers. Distrib.* **21**, 913 (2015).
4. Commission Regulation (EU) No. 142/2011 (2011); https://eur-lex.europa.eu/legal-content/EN/TXT/?uri=uriserv:OJ.L_.2011.054.01.0001.01.ENG&toc=OJ:L:2011:054:TOC.
5. J. Andevski, D. Dobrev, "International workshop on vulture supplementary feeding strategies and practices and integration of the national veterinary and sanitary legislation" (2017); www.4vultures.org/app/download/9314908985/Vulture+feeding+Workshop_ReVultures_E12_final.pdf.
6. E. Arrondo *et al.*, *Biol. Conserv.* **219**, 46 (2018).
7. Ligue pour la Protection des Oiseaux, Fondation Nature & Découvertes, "Technical report on natural carcass disposal" (2013); https://issuu.com/latomatebleue/docs/ctequ_complet [in French].
8. Royal Decree 1632/2011, BOE 284, 125535 (2011); www.boe.es/aeboe/consultas/bases_datos/doc.php?id=BOE-A-2011-18536 [in Spanish].
9. Resolution of 28 November, *Diari Oficial de la Comunitat Valenciana* 7436, 156 (2015); www.dogv.gva.es/datos/2015/01/05/pdf/2014_11741.pdf [in Spanish].
10. Decree 25/2014, Diario Oficial de La Rioja 75 (2014); www.larioja.org/normativa-autonomica/es?modelo=NA&norma=01974 [in Spanish].
11. A. Margalida, D. Campión, J. A. Donázar, *Nature* **480**, 457 (2011).
12. "Communication from the Commission to the European Parliament, the Council, the European and Social Committee and the Committee of the Regions" (2015); http://ec.europa.eu/smart-regulation/better_regulation/documents/com_2015_215_en.pdf.

10.1126/science.aat8492


Kayaks in Alaska's Glacier Bay

PHOTO: SARAH BISBING

LIFE IN SCIENCE

The hidden value of paper records

We are wandering on foot in the forests of Glacier Bay, Alaska, in a steady rain, searching for a tree that is visible in a decades-old photograph. The willows form a green wall as we push through, soaking wet despite our full rubber raingear. We are attempting to rediscover the exact location of what would be—if found—the longest running data set of its kind in the world, established a century ago.

In 1916, Dr. William Cooper began collecting data about individual plant establishment, growth, and death in a specific location, and he returned every 5 to 10 years to the exact spot to create a longitudinal record. The data set is unique given its age and continuity, and it has provided incredible insights to the fields of biology and ecology. However, the plot location was lost and the observation chain broken after Cooper and later his student, Lawrence, died.

The prospect of finding the plot was bleak; the landscape is difficult to navigate, requiring kayaking and scrambling out of radio contact while dealing with thick vegetation, bears, wolves, and the famously bad weather of southeast Alaska. But we had stumbled upon a clue: a faded old photograph taken 50 years ago. Noted on it was a tree we could match up with our 2016 view. The original researchers likely hadn't realized the photograph's future value. It had never been published or intentionally preserved. A similar study conducted in 2018, with the use of iPhone photographs and email, would likely leave future researchers with no such artifacts.

After days of searching, we finally arrive with elation at the tree. With a metal detector, we search the area for the iron rods, now buried, that mark each plot. To our amazement, we relocate every one of the original plots. Our seemingly quixotic journey has ended in success. One casually snapped photo has helped reestablish a long-lost source of invaluable data. Our experience has made us realize the potential value of physical records. When researchers tramp through Glacier Bay in 2118, keeping the plots alive, I hope they can use our photos and notes for something new, something we can't anticipate. I just hope they get better weather.

Brian Buma
University of Colorado, Denver, CO 80204, USA. Email: brian.buma@ucdenver.edu

10.1126/science.aat5382

ERRATA

Erratum for the Report "Translocation of a gut pathobiont drives autoimmunity in mice and humans" by S. Manfredo Vieira *et al.*, *Science* **360**, eaat9922 (2018). Published online 4 May 2018; 10.1126/science.aat9922

Erratum for the Report "A precise measurement of the magnetic field in the corona of the black hole binary V404 Cygni" by Y. Dallilar *et al.*, *Science* **360**, eaat9270 (2018). Published online 20 April 2018; 10.1126/science.aat9270

Erratum for the Report "Predicting reaction performance in C–N cross-coupling using machine learning" by D. T. Ahneman *et al.*, *Science* **360**, eaat7648 (2018). Published online 13 April 2018; 10.1126/science.aat7648

RESEARCH

Structure of yeast ATP synthase

Srivastava et al., *p. 619*

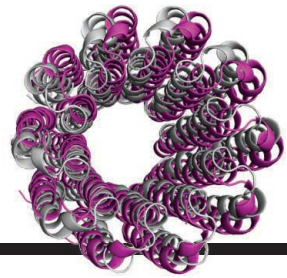

IN *SCIENCE* JOURNALS

Edited by **Caroline Ash**

SNOWBALL EARTH

A fast-melting snowball

The Marinoan "snowball Earth" glaciation covered most of the planet in ice. The surface melted only when enough carbon dioxide had accumulated in the atmosphere to trap the Sun's warmth. Melting must have occurred rapidly, but just how fast has been a topic of conjecture. Myrow *et al.* analyzed the wave ripples preserved in tidally deposited siltstones of the Elatina Formation, South Australia, to determine that sea level must have risen at the astounding rate of nearly 30 centimeters per year during the melting epoch, or roughly 100 times the rate that it is rising today. —HJS

Science, this issue p. 649

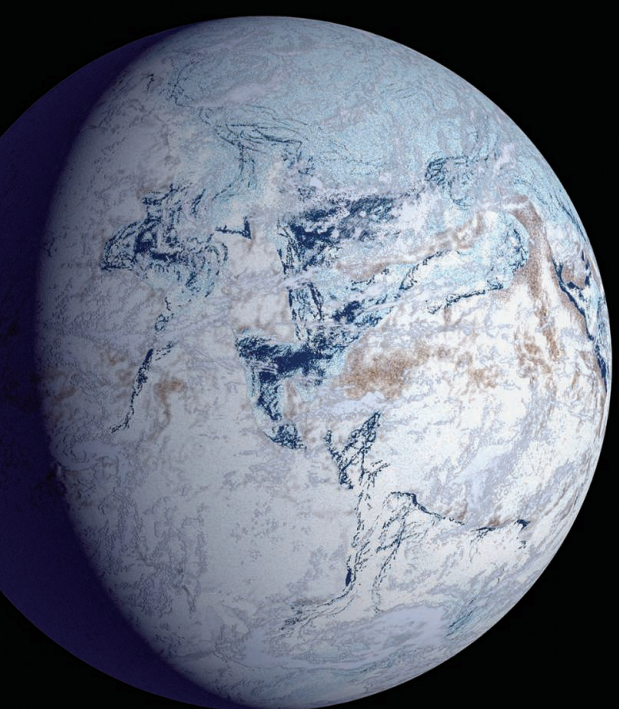

Artist's rendering of the Neoproterozoic snowball Earth

STRUCTURAL BIOLOGY

Toxic hijack of a cell signaling pathway

The pathogen *Clostridium difficile* colonizes the human colon when the normal microbiota is disrupted, often after antibiotic treatment. It is a leading cause of hospital-acquired diarrhea, especially among elderly patients. Chen *et al*. describe a 2.5-Å-resolution crystal structure that shows how a major virulence factor in *C. difficile*, toxin B (TcdB), binds to the G protein–coupled receptor Frizzled (FZD). This receptor activates the Wnt signaling pathway, which regulates homeostasis of the colonic epithelium. Surprisingly, TcdB uses a lipid cofactor to recognize FZD. This cofactor replaces a lipid normally associated with the Wnt ligand that binds FZD to activate signaling. Inhibiting the Wnt pathway likely plays a role in *C. difficile* pathology. —VV

Science, this issue p. 664

CANCER

Anatomically correct tumor genomics

Glioblastoma is the most lethal form of human brain cancer. The genomic alterations and gene expression profiles characterizing this tumor type have been widely studied. Puchalski *et al.* created the Ivy Glioblastoma Atlas, a freely available online resource for the research community. The atlas, a collaborative effort between bioinformaticians and pathologists, maps molecular features of glioblastomas, such as transcriptional signatures, to histologically defined anatomical regions of the tumors. The relationships identified in this atlas, in conjunction with associated databases of clinical and genomic information, could provide new insights into the pathogenesis, diagnosis, and treatment of glioblastoma. —PAK

Science, this issue p. 660

CELL BIOLOGY

Tasting with ATP and mitochondria

The savory taste of umami, the sweetness of sugar, and the bitterness of quinine are transduced by type II taste cells. Unlike most other receptor cells, type II taste cells release their neurotransmitter, adenosine triphosphate (ATP), through voltage-gated CALHM1 channels, instead of in vesicles. Romanov *et al.* found that ATP came from unusually large mitochondria that were adjacent to clusters of CALHM1 channels within the plasma membrane. This anatomy enables neurotransmission that does not rely on vesicles. —WW

Sci. Signal. **11**, eaao1815 (2018).

INTERSTELLAR MEDIUM

A vibrating molecular cloud in three dimensions

Molecular clouds are relatively dense assemblies of interstellar dust and gas (mostly molecular hydrogen) from which stars form. Determining the three-dimensional (3D) morphology of these clouds is difficult because we only see a 2D projection of them onto the sky. While examining far-infrared observations of the nearby Musca cloud, Tritsis and Tassis discovered that the cloud is vibrating with magnetohydrodynamic waves. The pattern of vibrations reveals the 3D structure and shows that Musca is a sheet seen edge-on, not a filament as previously assumed. —KTS

Science, this issue p. 635

CREDITS: (FROM TOP) A. P. SRIVASTAVA *ET AL.*; CHRIS BUTLER/SCIENCE SOURCE

Published by AAAS

EVOLUTIONARY GENOMICS

Selection, recombination, and hybrid evolution

Hybridization is an important force in evolution. The effects of hybridization across the whole genome are not understood. Using a fine-scale genetic map, Schumer *et al*. examined local ancestry in replicate natural hybrid populations of swordtail fish. Each parental species contributes different proportions of genetic material to the genomes of their descendants. Genes from the "minor" (less well-represented) parent occur in regions of the genome that are subject to higher recombination rates and where there are fewer potentially deleterious genes. Neanderthal ancestry in human genomes shows similar patterns. —LMZ

Science, this issue p. 656

FISHERIES

Big mamas matter for fish

The theoretical relationship between reproduction and body size has assumed that total mass relates directly to fecundity, regardless of the number of individuals involved. This assumption leads to fisheries management practices that suggest that one large female fish can be replaced by several smaller females. However, this assumption is incorrect. Barneche *et al*. show that larger females are far more productive than the same weight's worth of smaller females. Management practices that ignore the value of large females could contribute to unexplained declines seen in some fish stocks. —SNV

Science, this issue p. 642

NEUROENGINEERING

Decoding brain-computer interfaces

Brain-computer interfaces (BCIs) can help humans with compromised motor function by using their brain activity to externally control movements. Existing methods, however, require extensive user training and effort. Ganesh *et al*. developed a BCI technique for decoding sensorimotor prediction errors that requires less user energy. It subliminally stimulates the user to think about an activity and then, instead of decoding what movement a user intends, decodes whether the movement that the user wants matches the sensory feedback that the stimulator induced. In 12 healthy individuals performing a wheelchair-turning task, this interface represented movements speedily (within 96 milliseconds) and without any training. —PJB

Sci. Adv. 10.1126/sciadv.aaq0183 (2018).

ORGANIC CHEMISTRY

H-bond to deliver fluoride

Simple fluoride salts are theoretically convenient reagents for carbon-fluorine bond formation. In practice, they are often insoluble in the solvents that dissolve their reaction partners. Pupo *et al*. developed urea-based catalysts that make fluoride soluble through hydrogen bonding. Moreover, their chiral substituents bias the reaction toward one of two mirror image products of C–F bond formation. This strategy should be applicable to the asymmetric addition of other salts, too. —JSY

Science, this issue p. 638

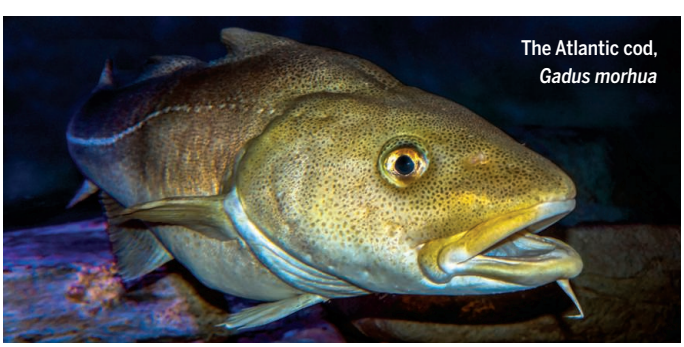

The Atlantic cod, *Gadus morhua*

IN OTHER JOURNALS

Edited by **Sacha Vignieri** *and* **Jesse Smith**

MOLECULAR BIOLOGY

Stress granule transcription

When translation initiation is stalled under stress, nontranslating messenger ribonucleoproteins form insoluble assemblies called stress granules (SGs) in the cytosol. Namkoong *et al*. sequenced all transcripts from purified SGs. They found that although translation of most transcripts is inhibited, only a subset of transcripts form SGs. The length and abundance of the AU-rich elements are key features determining SG-targeting specificity, agreeing with a recent report by Van Treeck *et al*. showing that RNA self-assembly drives SG formation. SGs have been implicated in cancer and neurodegenerative diseases; understanding the specificity of their RNA components and the principles of their formation offers insights into their pathological contribution. —SYM

Mol Cell. 10.1016/j.molcel.2018.02.025; *Proc. Natl. Acad. Sci. U.S.A.* 10.1073/pnas.1800038115 (2018).

ACADEMIC POLICIES

Stop the clock: Tenure, gender, and children

Allowing both male and female faculty to stop their tenure clock when having a child can increase tenure rates for the former and reduce them for the latter. Antecol *et al*. analyzed data on all assistant-professor hires at top-50 economics departments from 1980 to 2005; 44% of women and 47% of men had a child within 5 years of completing their Ph.D., before typical tenure deadlines. Differential effects of clock policies on tenure are driven by the fact that men publish more in top-tier journals after policies take effect, whereas women do not. Policies may not compensate for the specific productivity challenges that women face after childbirth. Despite this early setback, and the subsequent career churn, clock policies do not hurt women's chances of ultimately gaining tenure in the profession. —BW

Amer. Econ. Rev. 10.1257/aer.20160613 (2018).

PHOTO: MIROSLAV HALAMA/SHUTTERSTOCK.COM

ILLUSTRATION: ALICE TURNER/STOCKTREK IMAGES/SCIENCE SOURCE

PALEOECOLOGY

Top-down or bottom-up?

Primary producers and animal consumers interact to determine the structure and function of ecosystems, but how do their relative influences change over time? Jeffers *et al.* used the fossil record of the late Quaternary in Britain and Ireland to study whether the extinction of two-thirds of the native megaherbivores (including mammoths, giant deer, moose, and others) led to the observed expansion of woody plants at the end of the last glacial period. Instead, they found that more influential factors were a warming climate and reduction in fire, with an even more pronounced role for increasing shrub encroachment (followed by trees) in determining ecosystem structure. Plants and plant-soil feedbacks may have been more important than trophic interactions in driving the changes as northern ecosystems moved into the postglacial period. —AMS

Ecol. Lett. 10.1111/ele.12944 (2018).

Was climate warming more important than megafaunal loss for shaping postglacial landscapes in Britain?

CHEMISTRY

Early warning about emerging contaminants

Contamination of environmental samples with harmful chemicals can be detected with high-resolution mass spectrometry (HRMS). This method can provide accurate mass data for the complex mixtures, thus allowing retrospective analysis to look for newly identified contaminants. Alygizakis *et al.* report on a pilot study involving eight reference laboratories in Europe and Australia to investigate whether retrospective screening of HRMS data can be used to establish the extent of a newly identified contaminant's presence in the environment. On the basis of archived data from 48 diverse environmental samples from 14 countries, the study documents widespread occurrence of several chemicals not commonly included in monitoring of environmental samples. Expanding the pilot to a full early-warning system for global emerging contaminants will require a virtual data repository with agreed-upon data standards. —JFU

Environ. Sci. Technol. 10.1021/acs.est.8b00365 (2018).

VASCULAR BIOLOGY

Sensing the stress

When blood flow in arteries increases, surrounding smooth muscle relaxes to allow blood vessel dilation. Using a high-throughput screen for mechanoreceptors that are sensitive to blood flow (shear stress), Xu *et al*. identified a type of sensor expressed by vascular endothelial cells called G protein–coupled receptor 68 (GPR68). Its activation triggers a cell signaling pathway that increases intracellular calcium concentration, an event that is associated with vasodilation. The authors discovered that GPR68 is expressed in mammalian small-diameter blood vessels and that loss of GPR68 expression in mice disrupts the vasodilatory response to increased blood flow. Moreover, a compound that activates GPR68 activity increased vasodilation, indicating that drugs targeting this stress sensor could potentially treat cardiovascular disease. —LC

Cell **173**, 762 (2018).

STRUCTURAL BIOLOGY

Dynamic fibrils drive protein assembly

A low-complexity domain of the protein FUS plays a role in forming RNA granules. Luo *et al.* identify and structurally characterize two reversible amyloid cores (RACs) in this domain. In stable amyloid fibrils, β-strands stack to form β-sheets that pack tightly and exclude water. In contrast, RAC1 forms a kinked coil that stacks along the fibril axis; two such layers interact through tyrosine ring stacking. RAC2 forms β-sheets, but with water molecules between mating sheets. It is already established that the LARK (low-complexity amyloid-like kinked segment) may be broadly involved in membraneless assemblies. The RAC2 structure suggests that reversible fibril formation may occur without kinking. —VV

Nat. Struct. Mol. Biol. **25**, 341 (2018).

COOLING TEXTILES

Scaling up textiles that cool down

Decreasing energy consumption by reducing the need for air conditioning helps combat CO_2 emissions and promotes sustainability. Peng *et al.* present a remarkable scale-up of nanoporous polyethylene microfibers for use in cooling fabrics. These fabrics allow heat to radiate through them while reflecting visible light and can be engineered for wearability. The ability to scale up production is important for making this material cost-effective relative to cotton and other mass-produced textiles. Incorporating cooling fabrics into everyday wardrobes presents an opportunity to decrease indoor cooling. —BG

Nat. Sustain. 10.1038/s41893-018-0023-2 (2018).

ALSO IN *SCIENCE* JOURNALS

Edited by **Caroline Ash**

ADIPOGENIC REGULATION

Integrating glucose and fat

Consuming too much glucose makes you fat, but it is unclear how this conversion is mediated by the body. Glycolysis links to gene transcription via the essential coenzyme nicotinamide adenine dinucleotide in its oxidized state (NAD^+). Ryu *et al*. found that compartmentalized NAD^+ synthesis and consumption integrate glucose metabolism and adipogenic (fat-promoting) transcription during adipocyte differentiation (see the Perspective by Trefely and Wellen). Competition between the NAD^+ precursors—nuclear NMNAT-1 and cytosolic NMNAT-2—for their common substrate, nicotinamide mononucleotide, regulates the balance between nuclear NAD^+ synthesis for adipogenic gene regulation and cytosolic NAD^+ synthesis used in metabolism. —BAP

Science, this issue p. 618; see also p. 603

MOLECULAR MOTORS

Protons find a path

Adenosine triphosphate (ATP) synthases are dynamos that interconvert rotational and chemical energy. Capturing the complete structure of these multisubunit membrane-bound complexes has been hindered by their inherent ability to adopt multiple conformations. Srivastava *et al*. used protein engineering to freeze mitochondrial ATP synthase from yeast in a single conformation and obtained a structure with the inhibitor oligomycin, which binds to the rotating c-ring within the membrane. Hahn *et al*. show that chloroplast ATP synthase contains a built-in inhibitor triggered by oxidizing conditions in the dark chloroplast. The mechanisms by which these machines are powered are remarkably similar: Protons are shuttled through a channel to the membrane-embedded c-ring, where they drive nearly a full rotation of the rotor before exiting through another channel on the opposite side of the membrane (see the Perspective by Kane). —VV and MAF

Science, this issue p. 619, p. 620; see also p. 600

AMPHIBIAN DECLINE

Panzootic chytrid fungus out of Asia

Species in the fungal genus *Batrachochytrium* are responsible for severe declines in the populations of amphibians globally. The sources of these pathogens have been uncertain. O'Hanlon *et al*. used genomics on a panel of more than 200 isolates to trace the source of the frog pathogen *B. dendrobatidis* to a hyperdiverse hotspot in the Korean peninsula (see the Perspective by Lips). Over the past century, the trade in amphibian species has accelerated, and now all lineages of *B. dendrobatidis* occur in traded amphibians; the fungus has become ubiquitous and is diversifying rapidly. —CA

Science, this issue p. 621; see also p. 604

NUCLEAR PHYSICS

How long does a neutron live?

Unlike the proton, whose lifetime is longer than the age of the universe, a free neutron decays with a lifetime of about 15 minutes. Measuring the exact lifetime of neutrons is surprisingly tricky; putting them in a container and monitoring their decay can lead to errors because some neutrons will be lost owing to interactions with the container walls. To overcome this problem, Pattie *et al*. measured the lifetime in a trap where ultracold polarized neutrons were levitated by magnetic fields, precluding interactions with the trap walls (see the Perspective by Mumm). This more precise determination of the neutron lifetime will aid our understanding of how the first nuclei formed after the Big Bang. —JS

Science, this issue p. 627; see also p. 605

METAMATERIALS

Giving a hand to metamaterials

Auxetic materials expand in an unusual way: perpendicular to the direction in which they are stretched. Lipton *et al*. engineered a type of auxetic material that also has handedness. When this material is sheared, it twists either to the right or the left. By tiling the underlying patterns onto spheres and cylinders, rigid or compliant structures can be made. Linear and 4-degree-of-freedom actuators can thus be made from hollow tubes, which could be valuable for a variety of engineering and medical applications. —BG

Science, this issue p. 632

SEX DETERMINATION

Making males and back again

Temperature-dependent sex determination occurs in many reptilian species. An epigenetic mechanism is presumed to be at work, but thus far it has not been identified. Ge *et al*. show that in the red-eared slider turtle, an epigenetic modifier, the histone demethylase KDM6B, binds to the promoter of the dominant male gene to activate male development (see the Perspective by Georges and Holleley). Knock down the expression of KDM6B, and embryos destined to be male turn into females. —SNV

Science, this issue p. 645; see also p. 601

COGNITIVE PSYCHOLOGY

Balancing costs and performance

Deciding whether a novel object is another instance of something already known or an example of something different is an easily solved problem. Empirical mapping of human performance across a wide range of domains has established an exponential relationship between the generalization gradient and interstimuli distance. Sims now shows that this relationship can be derived from a consideration of the costs of optimal information coding. —AMS and GJC

Science, this issue p. 652

GEOPHYSICS

Knowing how to prevent induced earthquakes

Increasing evidence from around the world shows that human activities below Earth's surface, such as gas extraction and wastewater injection, can cause earthquakes. In a Perspective, Candela *et al*. explain some of the underlying mechanisms. Wastewater injection in Oklahoma, USA, and gas extraction in Groningen, the Netherlands, have notoriously caused earthquakes. Although the detailed mechanisms differ in the two situations, preexisting conditions within Earth's crust, such as faults and stresses, play a key role in whether an induced earthquake will occur. Knowledge of subsurface conditions is thus crucial to avoid sites that are vulnerable to induced earthquakes. —JFU

Science, this issue p. 598

T CELLS

Micromanaging NOD1 in T cells

MicroRNAs constitute an additional layer of regulation between gene transcription and translation of mRNA. Schmolka

et al. show that the microRNA miR-146a is highly expressed in a subset of γδ T cells called CD27$^-$ γδ T cells. These cells coexpress the cytokines interleukin-17 and interferon-γ (IFN-γ). miR-146a represses IFN-γ expression in CD27$^-$ γδ T cells by targeting a pattern recognition receptor (PRR) called NOD1, which recognizes bacterial peptidoglycan. Deletion of NOD1 impaired production of IFN-γ in the CD27$^-$ γδ T cells by an as-yet unknown mechanism. The study adds to the increasing appreciation of the noncanonical functions of PRRs. —AB

Sci. Immunol. **3**, eaao1392 (2018).

SPINAL CORD INJURY

Spinal cord stem cell grafts in pigs

Neuronal precursor cells (NPCs) hold promise for treating spinal cord injury. Testing viability and engraftment properties of NPC transplants in large animal models is essential for understanding the clinical potential of this approach. Strnadel *et al.* transplanted syngeneic and allogeneic induced pluripotent stem cell–derived NPCs (iPSC-NPCs) into the spinal cords of naïve pigs and pigs with spinal cord injury. The transplanted cells showed a good safety profile, long-term survival, and differentiation into mature neurons and glial cells. Successful engraftment of allogeneic iPSC-NPCs required only temporary immunosuppression, an important consideration for the future clinical evaluation of iPSC-NPCs for treating spinal injuries. —MM

Sci. Transl. Med. **10**, eaam6651 (2018).

RESEARCH ARTICLE SUMMARY

ADIPOGENIC REGULATION

Metabolic regulation of transcription through compartmentalized NAD^+ biosynthesis

Keun Woo Ryu, Tulip Nandu, Jiyeon Kim, Sridevi Challa, Ralph J. DeBerardinis, W. Lee Kraus*

INTRODUCTION: Nicotinamide adenine dinucleotide (NAD) is an essential small molecule that is involved in a variety of physiological and pathological processes. The oxidized form, NAD^+, serves as a cofactor in metabolic pathways, as well as a substrate for various enzymes that consume it, such as the poly[adenosine diphosphate (ADP)–ribose] polymerases (PARPs) and sirtuins (SIRTs). PARPs and SIRTs cleave NAD^+ into nicotinamide and ADP-ribose, resulting in the irreversible breakdown of NAD^+. Therefore, the resynthesis of NAD^+ is necessary for maintaining normal cellular functions. Increasing evidence has revealed that (i) reduced NAD^+ levels result in altered metabolism and increased disease susceptibility and (ii) restoration of NAD^+ levels can prevent disease progression. Thus, understanding NAD^+ synthesis and catabolism is important for understanding physiological and pathological processes.

RATIONALE: NAD^+ is synthesized by a family of enzymes known as nicotinamide mononucleotide adenylyl transferases (NMNATs). In mammalian cells, NMNATs exhibit distinct subcellular localizations (NMNAT-1 in the nucleus, NMNAT-2 in the cytoplasm and Golgi, and NMNAT-3 in the mitochondria), suggesting that NAD^+ biosynthesis is compartmentalized within the cell. Despite the biological importance of NAD^+, the physiological role of compartmentalized NAD^+ biosynthesis in cells is largely unexplored. Given the dual role of NAD^+ as a metabolic cofactor and a substrate for enzymes involved in gene regulation, we hypothesized that compartmentalized synthesis of NAD^+ might connect cellular metabolism and gene regulation.

RESULTS: Here we show that compartment-specific NAD^+ biosynthesis acts as a key mediator of PARP-1–regulated transcription during adipocyte differentiation, integrating cellular metabolism and the adipogenic transcription program. During adipogenesis, nuclear NAD^+ levels drop concomitantly with a rapid induction of NMNAT-2, the cytoplasmic NAD^+ synthase. Increased NMNAT-2 levels limit the availability of nuclear NMN, a common substrate of NMNATs, thereby leading to a precipitous reduction in nuclear NAD^+ synthesis by NMNAT-1. This reduction of nuclear NAD^+ results in decreased PARP-1 catalytic activity, which in turn reduces inhibitory ADP-ribosylation of the adipogenic transcription factor C/EBPβ. Reduced ADP-ribosylation of C/EBPβ allows it to bind its target genes and drive a proadipogenic transcriptional program that promotes the differentiation of preadipocytes into adipocytes.

ON OUR WEBSITE

Read the full article at http://dx.doi.org/10.1126/science.aan5780

Experimentally, we found that decreasing nuclear NAD^+ synthesis by NMNAT-1 depletion significantly reduced PARP-1 enzymatic activity and enhanced adipogenesis, whereas NMNAT-2 depletion inhibited the drop in nuclear NAD^+ levels and significantly reduced adipocyte differentiation. Moreover, providing exogenous NMN to preadipocytes in culture "short-circuited" the competition between NMNAT-1 and NMNAT-2 for NMN, leading to increased nuclear NAD^+ synthesis during differentiation. This, in turn, increased PARP-1 activity and inhibited adipocyte differentiation.

Adipogenic signaling pathways and increased glucose metabolism were required for the rapid induction of NMNAT-2, and inhibition of glucose metabolism completely abolished the induction of NMNAT-2 during adipogenesis. Preventing NMNAT-2 induction by glucose deprivation restored PARP-1 activity and inhibited C/EBPβ-dependent gene expression. Collectively, these results suggest that NMNAT-1 and NMNAT-2 function as sensors to integrate cellular metabolism and the adipogenic transcription program.

CONCLUSION: We have elucidated a pathway leading from glucose uptake and metabolism, to competition between nuclear and cytoplasmic NMNATs for the NAD^+ biosynthesis precursor NMN, and ultimately to alterations in the activity of PARP-1 and its catalytic target C/EBPβ, a transcription factor that promotes adipogenic gene expression and initiates the process of adipocyte differentiation. Such mechanisms are also likely to play a key role in other biological systems that exhibit dramatic changes in nuclear PARylation as differentiation proceeds or have a high metabolic load. ■

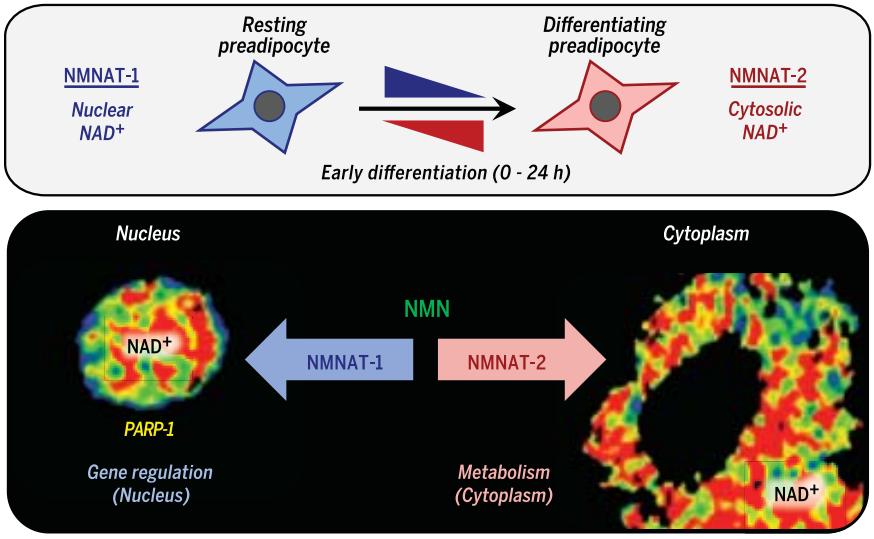

Compartmentalized NAD^+ biosynthesis by NMNATs regulates adipogenesis through PARP-1. NMNATs synthesize NAD^+ from nicotinamide mononucleotide (NMN) and adenosine triphosphate. Nuclear NMNAT-1 provides NAD^+ for nuclear ADP-ribosylation and gene regulation by PARP-1, whereas cytoplasmic NMNAT-2 provides NAD^+ for cytosolic ADP-ribosylation and cellular metabolism. Competition between NMNAT-1 and NMNAT-2 for their common substrate, NMN, promotes compartmentalized regulation of NAD^+ levels, allowing for discrete nuclear and cytoplasmic events. The fluorescent images of NAD^+ in the bottom panel were generated using a NAD^+ sensor localized to the nucleus (left) or the cytoplasm (right).

The list of author affiliations is available in the full article online.
*Corresponding author. Email: lee.kraus@utsouthwestern.edu
Cite this article as K. W. Ryu *et al.*, *Science* **360**, eaan5780 (2018). DOI: 10.1126/science.aan5780

RESEARCH ARTICLE

ADIPOGENIC REGULATION

Metabolic regulation of transcription through compartmentalized NAD$^+$ biosynthesis

Keun Woo Ryu,[1,2,3] Tulip Nandu,[1,2] Jiyeon Kim,[4] Sridevi Challa,[1,2] Ralph J. DeBerardinis,[4,5,6] W. Lee Kraus[1,2,3]*

NAD$^+$ (nicotinamide adenine dinucleotide in its oxidized state) is an essential molecule for a variety of physiological processes. It is synthesized in distinct subcellular compartments by three different synthases (NMNAT-1, -2, and -3). We found that compartmentalized NAD$^+$ synthesis by NMNATs integrates glucose metabolism and adipogenic transcription during adipocyte differentiation. Adipogenic signaling rapidly induces cytoplasmic NMNAT-2, which competes with nuclear NMNAT-1 for the common substrate, nicotinamide mononucleotide, leading to a precipitous reduction in nuclear NAD$^+$ levels. This inhibits the catalytic activity of poly[adenosine diphosphate (ADP)–ribose] polymerase–1 (PARP-1), a NAD$^+$-dependent enzyme that represses adipogenic transcription by ADP-ribosylating the adipogenic transcription factor C/EBPβ. Reversal of PARP-1–mediated repression by NMNAT-2–mediated nuclear NAD$^+$ depletion in response to adipogenic signals drives adipogenesis. Thus, compartmentalized NAD$^+$ synthesis functions as an integrator of cellular metabolism and signal-dependent transcriptional programs.

Extracellular signaling and nutrient availability are major factors determining cell fate decisions (*1*). Biologically appropriate responses to extracellular information require alterations in cellular metabolism and the gene expression programs that control cellular outcomes (*2*). Many enzymes involved in gene regulation require substrates or cofactors that are products of intermediate cellular metabolism, providing a direct link between metabolism and transcription (*1*, *3*). How cells integrate extracellular signals (e.g., hormones) and cellular metabolism to coordinate transcriptional outcomes, however, is poorly understood. Recent findings suggest that fluctuations in nuclear metabolite levels, perhaps controlled by metabolic enzymes in the nucleus, underlie the coordination of these responses (*1*, *3*).

NAD$^+$, the oxidized form of nicotinamide adenine dinucleotide, is an essential small-molecule cofactor in metabolic redox reactions, as well as a substrate for NAD$^+$-dependent enzymes, such as the poly[adenosine diphosphate (ADP)–ribose] polymerases (PARPs) and sirtuins (SIRTs), which play important roles in gene regulation (*4*–*7*). Unlike metabolic redox reactions, which reversibly oxidize or reduce NAD$^+$, PARPs and SIRTs cleave NAD$^+$ into nicotinamide and ADP-ribose, resulting in the irreversible consumption of NAD$^+$. Thus, the resynthesis of NAD$^+$ is crucial for preserving cellular functions. In mammalian cells, NAD$^+$ is synthesized from nicotinamide mononucleotide (NMN) and adenosine triphosphate (ATP) by a family of enzymes known as NMN adenylyl transferases (NMNATs) (*4*, *6*). NMNATs exhibit distinct and mutually exclusive subcellular localizations: NMNAT-1 localizes to the nucleus, NMNAT-2 to the cytoplasm and Golgi, and NMNAT-3 to the mitochondria (Fig. 1A), suggesting compartment-specific regulation of NAD$^+$ biosynthesis within the cell. Given the dual role of NAD$^+$ as a metabolic cofactor and a substrate for enzymes involved in gene regulation, we hypothesized that the compartmentalized synthesis of NAD$^+$ might connect cellular metabolism and gene regulation.

[1]Laboratory of Signaling and Gene Regulation, Cecil H. and Ida Green Center for Reproductive Biology Sciences, University of Texas Southwestern Medical Center, Dallas, TX 75390, USA. [2]Division of Basic Research, Department of Obstetrics and Gynecology, University of Texas Southwestern Medical Center, Dallas, TX 75390, USA. [3]Program in Genetics, Development, and Disease, Graduate School of Biomedical Sciences, University of Texas Southwestern Medical Center, Dallas, TX 75390, USA. [4]Children's Medical Center Research Institute, University of Texas Southwestern Medical Center, Dallas, TX 75390, USA. [5]Department of Pediatrics, University of Texas Southwestern Medical Center, Dallas, TX 75390, USA. [6]McDermott Center for Human Growth and Development, University of Texas Southwestern Medical Center, Dallas, TX 75390, USA.
*Corresponding author. Email: lee.kraus@utsouthwestern.edu

Nuclear NAD$^+$ synthesis regulates PARP-1 activity and adipogenesis

To test this hypothesis, we selected a biological system that requires both dynamic transcriptional regulation and active cellular metabolism, namely, adipogenesis. Adipose tissue is an important regulator of energy balance and glucose homeostasis (*8*). The formation of functional adipocytes is achieved by the differentiation of preadipocytes into mature adipocytes (i.e., adipogenesis), which is tightly controlled by the sequential expression of key adipogenic transcription factors (*9*, *10*), as well as a diverse range of metabolic pathways (*1*, *11*). Chemical inhibition (with FK866) or depletion [with short hairpin RNA (shRNA)–mediated knockdown] of nicotinamide phosphoribosyltransferase (NAMPT), a key enzyme in NAD$^+$ biosynthesis that produces NMN (*12*), has been previously shown to promote adipogenesis in mesenchymal stem cells (*13*), suggesting a potential role of NAD$^+$ biosynthesis in adipocyte differentiation.

To explore the role of compartmentalized NAD$^+$ synthesis during adipogenesis, we first assayed the expression of NMNAT mRNAs in adipose tissue and preadipocytes. We found that NMNAT-1 and NMNAT-2 are expressed in adipose tissue and preadipocytes (fig. S1, A and B), whereas NMNAT-3 is expressed at very low to undetectable levels in preadipocytes (fig. S1B), suggesting potential cross-talk between the nuclear and cytoplasmic NAD$^+$ biosynthesis pathways during adipogenesis. We recently reported on the dynamic regulation of PARP-1 enzymatic activity during adipogenesis (*14*) (figs. S2A, S3A, and S3B), suggesting a role for nuclear NAD$^+$ during adipocyte differentiation.

To determine the effects of nuclear NAD$^+$ biosynthesis on adipogenesis, we used shRNA-mediated knockdown of *Nmnat1* in 3T3-L1 preadipocytes (*15*), a versatile and well-characterized cell line. Depletion of NMNAT-1 dramatically reduced PARP-1 enzymatic activity, as determined by blotting for poly(ADP-ribose) (PAR), which continued to decrease during the early phase (the first 24 hours) of differentiation (Fig. 1B and fig. S2A). PARP-1 activity in NMNAT-1–depleted cells was restored by re-expression of catalytically active, but not inactive, NMNAT-1, suggesting that nuclear NAD$^+$ synthesis is required for PARP-1 activity (fig. S2B). Depletion of NMNAT-1 had a much greater effect on the activity of PARP-1 than on that of SIRT1, a nuclear NAD$^+$-dependent protein deacetylase (fig. S3, C to F), likely owing to the abundant expression of PARP-1 in preadipocytes (fig. S3G). Previously, we showed that inhibition of PARP-1 enzymatic activity during the early phase of adipogenesis in 3T3-L1 cells enhances differentiation (*14*). Depletion of NMNAT-1 phenocopies depletion of PARP-1; it increases lipid accumulation (Fig. 1, C and D), induces the expression of adipocyte marker genes (e.g., *Fabp4* and *Adipoq*), and induces the expression of transcription factors that promote terminal differentiation and maintain adipocyte function (e.g., PPARγ and C/EBPα) (Fig. 2A and fig. S4A). Similar effects on bulk PARP-1–mediated PARylation and the expression of adipocyte marker genes were observed in response to *Nmnat1* knockdown in NIH 3T3 cells (fig. S4, B and C), as well as in response to *Nmnat1* knockout in primary preadipocytes from the stromal-vascular fraction (SVF) of adipose tissue collected from mice (*16*, *17*) (fig. S4, D to F). Together, these results link the proadipogenic phenotype observed upon NMNAT-1 depletion to decreased PARP-1 activity in three different models of adipogenesis.

NMNAT-1 and PARP-1 control adipogenic gene expression through C/EBPβ

In follow-up experiments, we performed RNA sequencing (RNA-seq) using *Nmnat1* or *Parp1* knockdown in 3T3-L1 cells to confirm that enhanced differentiation in response to reduced nuclear NAD^+ synthesis occurs through PARP-1. At 2 days postdifferentiation, we observed significant overlap between the genes whose expression was altered upon *Nmnat1* or *Parp1* knockdown (Fig. 2B), further supporting the conclusion that NMNAT-1 regulates differentiation through PARP-1. To elucidate potential mechanisms underlying NMNAT-1– and PARP-1–dependent transcriptional regulation during adipogenesis, we determined which adipogenic transcription factor binding sites (presumed enhancers) interact with the promoters of NMNAT-1 and PARP-1–co-regulated genes in 3T3-L1 cells by integrating promoter capture Hi-C (PCHI-C) data with transcription factor chromatin immunoprecipitation (ChIP)–seq data (*18*, *19*). Greater than 70% of the promoters of the co-regulated genes looped to binding sites for C/EBPβ, a key adipogenic transcription factor during the early phase of adipocyte differentiation (*9*, *10*) (Fig. 2C and fig. S5, A to C). Together, these results implicate C/EBPβ in the expression of adipogenic genes upon NMNAT-1 and PARP-1 depletion, leading to enhanced adipocyte differentiation. Importantly, C/EBPβ expression was not altered upon *Nmnat1* knockdown in 3T3-L1 cells, either at the mRNA or protein level (Fig. 2, D and E), suggesting that enhanced differentiation was not due to increased expression of C/EBPβ. We have recently shown that PARP-1 PARylates C/EBPβ during the early phase of adipogenesis, thereby inhibiting its DNA-binding ability (*14*). Indeed, depletion of NMNAT-1 significantly increased C/EBPβ binding to target gene promoters, as assessed by ChIP–quantitative real-time polymerase chain reaction (qPCR) (Fig. 2F). In addition, the genes whose promoters interact with known C/EBPβ binding sites were significantly induced upon depletion of NMNAT-1 or PARP-1 (Fig. 2G and fig. S5D). These results demonstrate that nuclear NAD^+ synthesis by NMNAT-1 regulates PARP-1 enzymatic activity, which in turn modulates the adipogenic transcription program by regulating the binding of C/EBPβ to its target genes.

Increases in cytoplasmic NAD^+ synthesis by NMNAT-2 reduces nuclear NAD^+ levels

Because PAR levels rapidly decrease during differentiation (Fig. 3A and fig. S2A) and nuclear NAD^+ synthesis is required for PARP-1 enzymatic activity, we hypothesized that NAD^+ levels may decrease during the early phase of adipogenesis. Unexpectedly, however, the total intracellular NAD^+ levels did not change during differentiation (Fig. 3A). We then postulated that nuclear NAD^+ could be regulated differently from total intracellular NAD^+. To test this hypothesis, we used NAD^+ biosensors that contain a bipartite NAD^+-binding domain from a bacterial NAD^+-dependent DNA ligase fused to cpVenus fluorescent protein, with either nuclear or cytoplasmic localization signals (*20*) (Fig. 3B, top). These nuclear and cytoplasmic NAD^+ sensors exhibited reduced fluorescence upon the binding of NAD^+ (fig. S6, A to C). We expressed either the nuclear or cytoplasmic sensor and a corresponding cpVenus-only control in 3T3-L1 cells. We then generated a dose-response curve by normalizing the external NAD^+ concentration and permeabilizing the cells with digitonin (*20*). As previously reported, NAD^+ decreased the fluorescent signal from the sensors in a dose-dependent manner but had no effect on the cpVenus-only control (*20*) (fig. S6, D and E). When treated with FK866, an inhibitor of NAMPT that depletes intracellular NAD^+ in all subcellular compartments, both the nuclear and cytoplasmic NAD^+ sensors exhibited a strong increase in NAD^+ sensor fluorescence owing to loss of NAD^+ binding (fig. S6, F to J). Thus, these sensors are capable of measuring changes in subcellular NAD^+ levels. Using the dose-response curve generated by NAD^+ permeabilization (fig. S6E), we estimated subcellular NAD^+ concentrations to be ~100 μM in both the nucleus and the cytoplasm, consistent with previous observations in human embryonic kidney 293T and HeLa cells (*20*).

Using 3T3-L1 cells expressing the nuclear NAD^+ sensor, we observed an increase in the sensor signal during the early phase of differentiation, indicating a decrease in nuclear NAD^+ levels (Fig. 3, B and C, left, and fig. S7A). This decrease in nuclear NAD^+ levels occurred concurrently with a decrease in PARP-1 enzymatic activity (Fig. 3A and figs. S2A and S3A). At 8 hours postdifferentiation, the estimated nuclear NAD^+ concentration was near 40 μM—well below PARP-1's Michaelis constant (K_m) for NAD^+ [~85 to 110 μM (*21*)]—indicating that decreases in nuclear NAD^+ levels have the potential to regulate PARP-1 enzymatic activity during differentiation.

Given the observed decrease in nuclear NAD^+ levels without a change in total intracellular NAD^+ levels, we hypothesized that NAD^+ levels in another subcellular compartment might be altered differently from those in the nuclear compartment. In this regard, we observed that the levels of mRNA and protein for the cytosolic NAD^+ synthase, NMNAT-2, were rapidly induced within 8 hours of differentiation (Fig. 3A and figs. S8, S9A, and S9B). These changes in NMNAT-2 mRNA and protein were accompanied by increased levels of cytoplasmic NAD^+

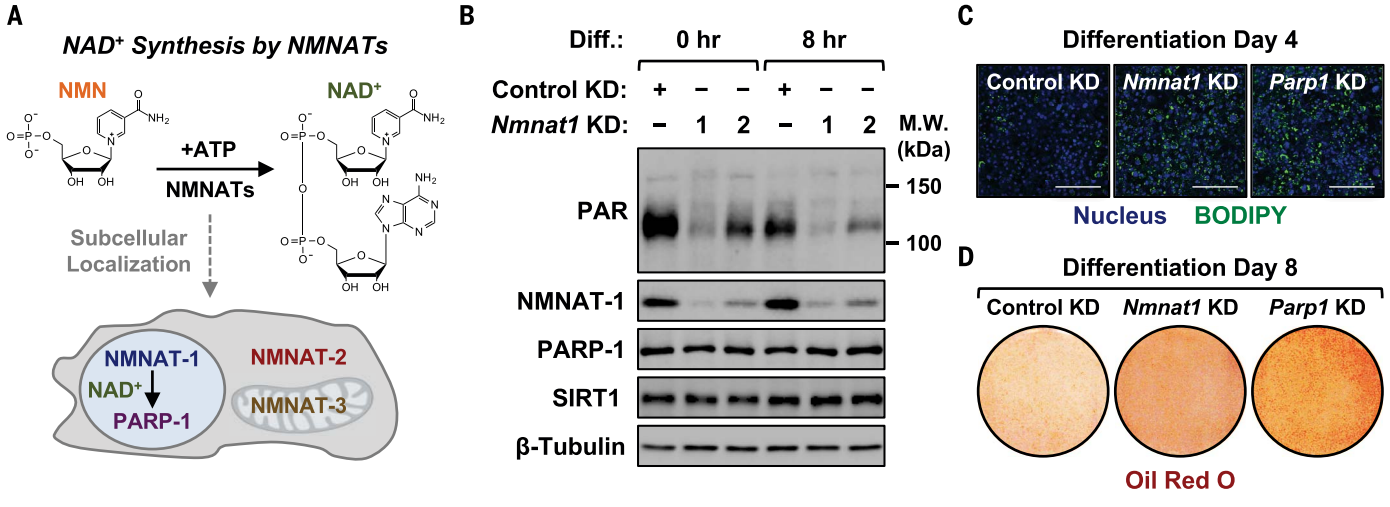

Fig. 1. NMNAT-1 regulates PARP-1 activity and adipocyte differentiation. (**A**) Schematic representation of NAD^+ biosynthesis by NMNATs and their subcellular localization. (**B**) Western blot showing the levels of PAR upon shRNA-mediated knockdown (KD) of *Nmnat1* during the early phase of adipogenesis in 3T3-L1 cells. PAR levels (primarily automodification of PARP-1) represent the enzymatic activity of PARP-1. Blots of NMNAT-1, PARP-1, and SIRT1 are shown for comparison (β-tubulin was used as a control). M.W., molecular weight. (**C** and **D**) Accumulation of lipid droplets at 4 days (C) and 8 days (D) of differentiation after knockdown of *Nmnat1* or *Parp1* in 3T3-L1 cells. Lipids were stained using BODIPY 493/503 [green, (C)] or Oil Red O [red, (D)], and nuclei were stained using TO-PRO-3 [blue, (C)]. Scale bars in (C), 150 μm.

during differentiation (Fig. 3, B and C), suggesting that a rapid induction of cytoplasmic NAD^+ synthesis may lead to compartmentalized regulation of NAD^+. To determine whether the rapid induction of NMNAT-2 might be responsible for the concomitant reduction in nuclear NAD^+ levels, we measured nuclear NAD^+ levels upon *Nmnat2* knockdown. Unexpectedly, depletion of NMNAT-2 (fig. S9, A and B) blocked the reduction in nuclear NAD^+ levels during differentiation (Fig. 3, D and E, and fig. S7B), suggesting that increased cytoplasmic NAD^+ synthesis may control nuclear NAD^+ levels. Moreover, depletion of NMNAT-2 increased nuclear PARP-1 enzymatic activity (fig. S9B) and inhibited adipogenesis, as determined by the expression of adipogenic marker genes (Fig. 3F), without altering the total intracellular NAD^+ levels (fig. S9C). We further tested whether NMNAT-2 induction was sufficient to regulate PARP-1 activity by using 3T3-L1 cells expressing doxycycline (Dox)–inducible NMNAT-2. Nuclear PARP-1–mediated PARylation was significantly decreased in cells expressing wild-type NMNAT-2 but not in cells expressing a catalytically dead NMNAT-2 mutant (fig. S9D). Collectively, these data indicate that NMNAT-2–mediated cytoplasmic NAD^+ synthesis inhibits the enzymatic activity of PARP-1.

Competition for NMN regulates nuclear NAD^+ levels during adipocyte differentiation

How might the induction of cytoplasmic NAD^+ synthesis inhibit nuclear NAD^+ synthesis and other nuclear events? One explanation is that NMNAT-2 competes with NMNAT-1 for their common substrates, NMN or ATP, thereby limiting substrate availability in the nucleus for NMNAT-1. In cells, the concentration of NMN is considerably lower than that of ATP (*22*), and the NMNATs have K_m values for ATP that are significantly lower than the intracellular ATP concentration (*12*). Moreover, NMN is thought to be the rate-limiting factor for NAD^+ biosynthesis (*4*, *12*). Therefore, we hypothesized that a rapid induction of NMNAT-2 would deplete NMN from the nucleus and decrease the nuclear NAD^+ concentration during differentiation (Fig. 4A). To test this hypothesis, we provided an exogenous source of NMN to 3T3-L1 cells in the culture medium. Consistent with a previous report (*23*), NMN supplementation

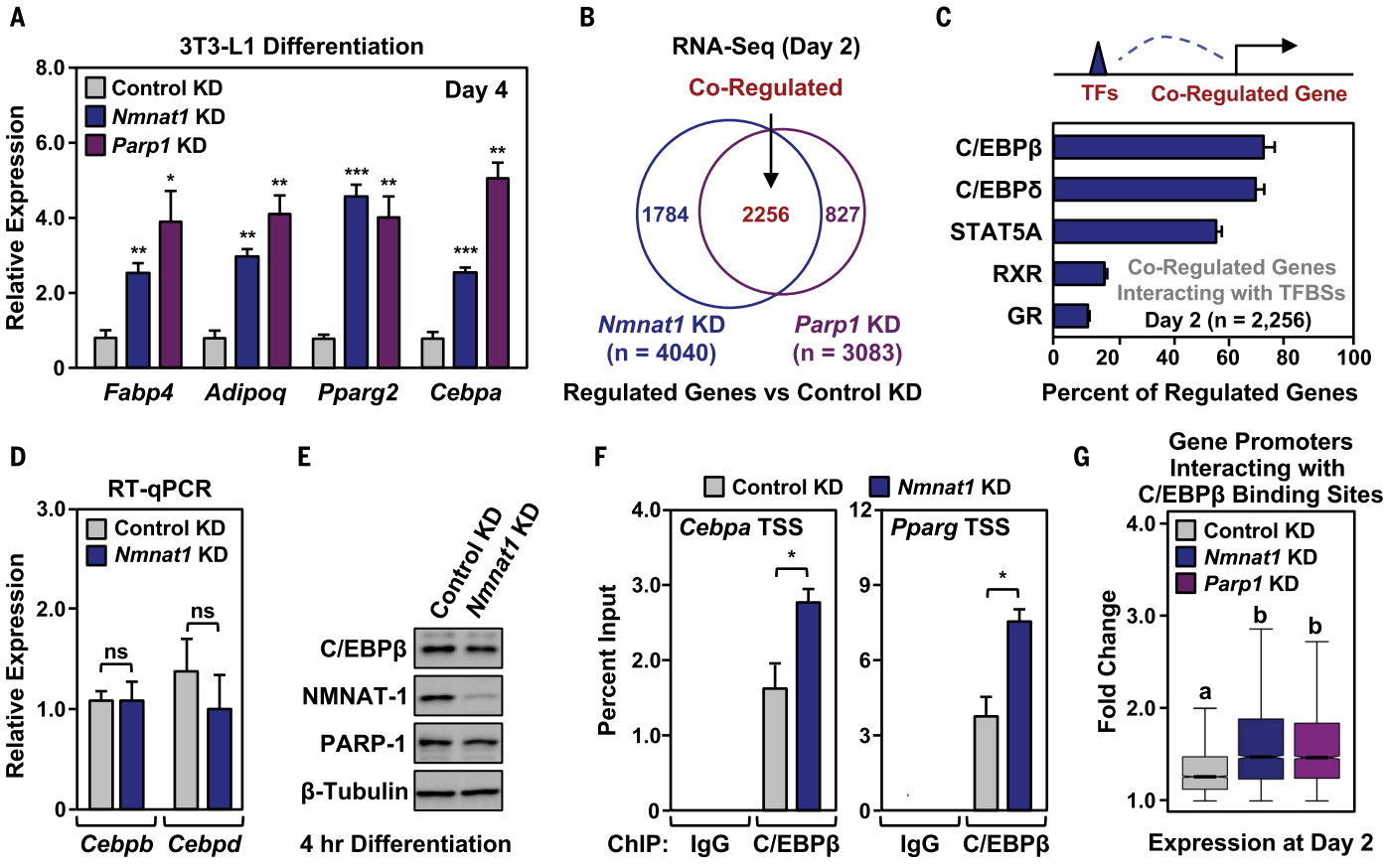

Fig. 2. NMNAT-1 and PARP-1 regulate the adipogenic transcriptional program through C/EBPβ. (**A**) Expression of adipocyte marker genes in 3T3-L1 cells at 4 days of differentiation, as determined by RT-qPCR. Each bar represents the mean + SEM ($n = 3$). Asterisks indicate significant differences from the corresponding control (Student's *t* test; $^*P < 0.05$, $^{**}P < 0.01$, $^{***}P < 0.001$). (**B**) RNA-seq assay of genes regulated upon *Nmnat1* or *Parp1* knockdown in 3T3-L1 cells compared with control knockdown after 2 days of differentiation. The overlapping region of the Venn diagram indicates co-regulated genes. (**C**) Percent of promoters of NMNAT-1 and PARP-1–co-regulated genes [from (B)] that interact with binding sites for adipogenic transcription factors (TFs). The interaction between the promoter regions of the co-regulated genes and the transcription factor binding sites (TFBSs) were determined by integrating published PCHi-C data [National Center for Biotechnology Information (NCBI) Gene Expression Omnibus (GEO) data set GSE95533] and ChIP-seq data (NCBI GEO data set GSE27826). Bars show means + SEM. (**D** and **E**) Levels of *Cebpb* mRNA assessed by RT-qPCR (D) and C/EBPβ protein assessed by Western blotting (E) in 3T3-L1 cells after knockdown of *Nmnat1*. Each bar represents the mean + SEM ($n = 3$). ns, not significant (Student's *t* test; $P > 0.05$). (**F**) C/EBPβ binding at the *Cebpa* and *Pparg* gene promoters in 3T3-L1 cells after 4 hours of differentiation, as determined by ChIP-qPCR assays. Each bar represents the mean + SEM ($n = 3$). Bars marked with asterisks are significantly different from the control (Student's *t* test; $^*P < 0.05$). (**G**) Expression of genes whose promoters interact with C/EBPβ binding sites upon knockdown of *Nmnat1* or *Parp1*. Significant C/EBPβ ChIP-seq peaks at 4 hours postdifferentiation were compared with PCHi-C–determined looping events to define the interactions. The expression level of those genes after 2 days of differentiation was compared with the expression level in control knockdown cells at day 0 to determine the fold change. Up-regulated genes (fold change > 1) were used in the analysis. Bars marked with different letters are significantly different from each other (Wilcoxon rank sum test; $P < 0.0001$).

increased the total intracellular NAD^+ levels (Fig. 4B). NMN supplementation blocked the depletion of nuclear NAD^+ during differentiation (Fig. 4, C and D, and fig. S7C), which resulted in increased PARP-1 enzymatic activity (Fig. 4E). Supplementation with NMN also inhibited the reduction of PARP-1 activity upon ectopic expression of NMNAT-2 (fig. S9E). These results suggest that NMN availability in the nucleus dictates the extent of nuclear NAD^+ biosynthesis. Furthermore, promoting elevated nuclear NAD^+ levels with NMN supplementation inhibits adipogenesis in both 3T3-L1 cells and primary SVF preadipocytes, as determined by the expression of adipogenic marker genes (Fig. 4F). Thus, high nuclear NAD^+ levels act as an inhibitory signal for adipocyte differentiation by regulating PARP-1 activity. The inhibitory effect of NMN supplementation on adipocyte differentiation was abolished upon knockdown of either *Nmnat1* or *Parp1* (Fig. 4G), and induction of NMNAT-2 expression did not restore PARP-1 enzymatic activity after *Nmnat1* knockdown (fig. S10), further supporting our conclusion that nuclear NAD^+ synthesis regulates adipocyte differentiation.

NMNAT-2 induction is associated with enhanced glucose metabolism

To understand why cells would require increased cytoplasmic NAD^+ synthesis to regulate nuclear events during differentiation, we considered the role of NAD^+ as a metabolic cofactor (Fig. 5A). During differentiation, we observed a rapid induction of key genes involved in glucose metabolism within 8 hours of differentiation, indicating increased glucose metabolism during the early phase of adipogenesis (fig. S11A). To confirm these results, we differentiated 3T3-L1 cells in medium containing D[U-^{13}C]glucose (U, uniformly labeled) and measured ^{13}C enrichment in intracellular metabolites by mass spectrometry (fig. S11B). We observed a rapid (within 8 hours) increase in glycolytic intermediate metabolites containing glucose-derived ^{13}C, as well as citrate m+2 (citrate containing two additional mass units from ^{13}C) upon differentiation (fig. S11, C and D), indicating an increase in glucose flux into glycolysis and the tricarboxylic acid (TCA) cycle during the early phase of adipogenesis. Depletion of NMNAT-2, however, did not affect the expression of genes involved in glucose metabolism (Fig. 5B and fig. S12A). We hypothesized that elevated NMNAT-2 levels might support increased glucose metabolism during differentiation by providing a supply of cytoplasmic NAD^+. Changes in cytoplasmic NAD^+ concentrations could potentially affect the kinetics of the enzymes involved in glucose metabolism (fig. S12B). Indeed, *Nmnat2* knockdown decreased cytoplasmic NAD^+ levels (fig. S12, C and D), as well as lactate secretion (fig. S12E) and the levels of glucose-derived citrate m+2

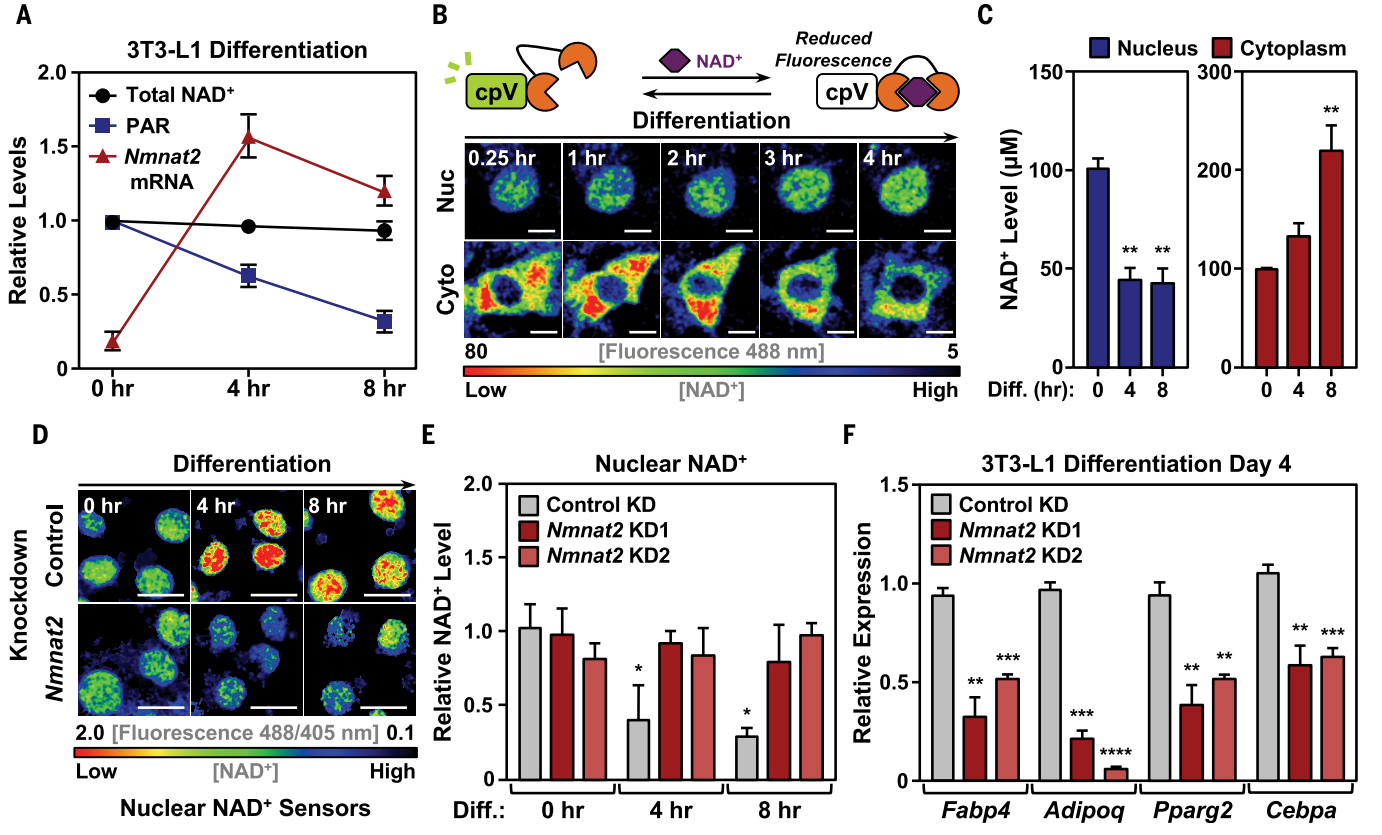

Fig. 3. Nuclear NAD^+ levels are regulated through compartmentalized biosynthesis. (**A**) The levels of total intracellular NAD^+ (enzyme-linked NAD^+ assay), PAR (Western blot), and *Nmnat2* mRNA (RT-qPCR) were determined at the indicated differentiation time points in 3T3-L1 cells (means ± SEM). (**B**) Detection of nuclear (Nuc) and cytoplasmic (Cyto) NAD^+ levels in 3T3-L1 cells by using a cpVenus-based NAD^+ biosensor. Representative images of NAD^+ sensor fluorescence during the early phase of differentiation are shown. (**C**) Changes in subcellular NAD^+ levels during the early phase of differentiation of 3T3-L1 cells. NAD^+ levels were calculated from sensor$_{(488/405\ nm)}$/control$_{(488/405\ nm)}$ fluorescence ratios determined by flow cytometry using a standard curve. Each bar represents the mean + SEM (n = 7). Bars marked with asterisks are significantly different from the undifferentiated (0 hours) control [analysis of variance (ANOVA); $^{**}P < 0.01$]. (**D**) Representative images of nuclear NAD^+ sensor fluorescence (488/405 nm) during differentiation upon *Nmnat2* knockdown. (**E**) Effect of *Nmnat2* knockdown on nuclear NAD^+ levels in 3T3-L1 cells. Relative nuclear NAD^+ levels were determined from the sensor$_{(488/405\ nm)}$/control$_{(488/405\ nm)}$ fluorescence ratio using flow cytometry. Each bar represents the mean + SEM (n = 3). Asterisks indicate significant differences from the control knockdown at the 0-hour time point (ANOVA; $^{*}P < 0.05$). (**F**) Effect of *Nmnat2* knockdown on the differentiation of 3T3-L1 cells. Differentiation was assessed by the expression of adipocyte marker genes. Each bar represents the mean + SEM (n = 3). Asterisks indicate significant differences from the control (Student's t test; $^{**}P < 0.01$, $^{***}P < 0.001$; $^{****}P < 0.0001$). Scale bars, 10 μm in (B) and 20 μm in (D).

(Fig. 5C and fig. S12F). However, *Nmnat2* knockdown did not reduce the glucose flux back to basal levels (Fig. 5C and fig. S12, E and F), suggesting that induction of NMNAT-2 is not solely driving the enhanced glucose metabolism during differentiation, but rather supports glucose metabolism by supplying cytoplasmic NAD^+.

We explored further whether the elevated levels of NMNAT-2 are dependent on changes in glucose flux by altering glucose levels in the differentiation medium. Unexpectedly, the induction of NMNAT-2 was abolished when 3T3-L1 cells were differentiated in medium containing low levels of glucose (Fig. 5D). PAR levels remained high during differentiation with glucose deprivation (Fig. 5D), suggesting that the absence of NMNAT-2 induction leads to sustained levels of nuclear NAD^+ and PARP-1 enzymatic activity. Similar results were observed when the cells were differentiated in the presence of glycolysis inhibitor 2-deoxyglucose, supporting the

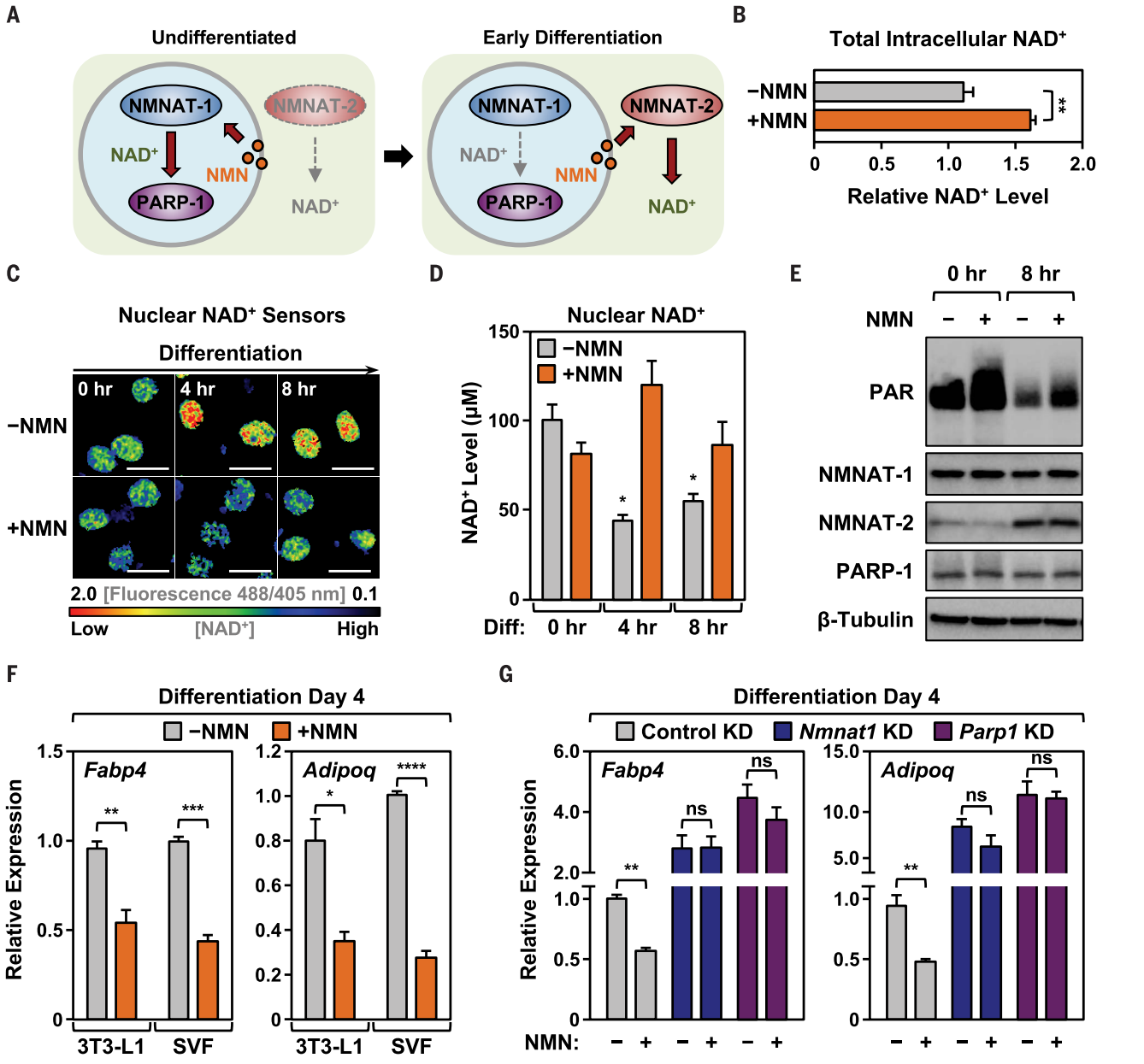

Fig. 4. Substrate competition between NMNAT-1 and NMNAT-2 regulates nuclear NAD^+ levels during differentiation. (**A**) Schematic representation of substrate competition between NMNAT-1 and NMNAT-2. (**B** to **D**) Supplementation with exogenous NMN disrupts NMNAT-1 and NMNAT-2 substrate competition. Effects on total intracellular NAD^+ (B) and nuclear NAD^+ levels [(C) and (D)] upon supplementation with 1 mM NMN are shown. Bar graphs [(B) and (D)] represent means + SEM ($n = 7$). Asterisks indicate significant differences from the undifferentiated (0 hours) control (ANOVA; $^*P < 0.05$; $^{**}P < 0.01$). Representative images (C) show changes in nuclear NAD^+ sensor fluorescence ratios during differentiation. Scale bars, 20 μm. Nuclear NAD^+ levels (D) were, determined by the sensor$_{(488/405\ nm)}$/control$_{(488/405\ nm)}$ fluorescence ratios using flow cytometry. (**E**) Western blots showing the rescue of PARP-1 enzymatic activity during early differentiation upon supplementation with 5 mM NMN. PAR levels indicate PARP-1 enzymatic activity. (**F** and **G**) Supplementation with exogenous NMN (5 mM) inhibits the differentiation of control 3T3-L1 and SVF cells (F), but not NMNAT-1– and PARP-1–depleted cells (G). The expression of adipocyte marker genes determined by RT-qPCR was used to assess the extent of differentiation. Each bar represents the mean + SEM ($n = 3$). Asterisks indicate significant differences versus the corresponding control (Student's t test; $^*P < 0.05$, $^{**}P < 0.01$, $^{***}P < 0.001$, $^{****}P < 0.0001$); ns, not significant (Student's t test; $P > 0.05$).

conclusion that NMNAT-2 induction depends on glucose metabolism (Fig. 5E). However, the increase in *Nmnat2* mRNA was not affected by glucose levels or inhibition of glycolysis (fig. S13A), and the inhibition of proteasome-mediated protein degradation prevented NMNAT-2 degradation upon glucose deprivation (fig. S13B), suggesting that the glucose-dependent modulation of NMNAT-2 levels occurs through posttranslational regulation.

Because PARP-1 PARylates C/EBPβ and inhibits its DNA binding (*14*), we hypothesized that a loss of NMNAT-2 induction upon glucose deprivation might alter C/EBPβ DNA binding. The expression of C/EBPβ was not affected by glucose metabolism, either at the mRNA or protein level (fig. S14, A and B). However, the binding of C/EBPβ to target gene promoters was dramatically reduced when glycolysis was inhibited during differentiation (Fig. 5F), and adipogenesis was significantly reduced when glucose was deprived from the medium (fig. S15, A and B), suggesting that adipogenic transcription is regulated by glucose metabolism. The inhibitory effect of glucose deprivation on adipogenesis was abolished upon knockdown of *Nmnat1* and *Parp1* (fig. S15B), supporting the conclusion that metabolic regulation of adipogenic transcription is mediated by nuclear NAD^+ synthesis and PARP-1.

A similar pathway for compartmentalized NAD^+ biosynthesis exists in cancer cells

We further tested whether similar mechanisms play a key role in a completely different biological system. We focused on the SH-SY5Y human neuroblastoma cell line, which expresses a high level of *NMNAT2* (fig. S16, A and B). Consistent with our observations in preadipocytes, knockdown of *NMNAT2* in SH-SY5Y cells significantly increased PARP-1 enzymatic activity (fig. S16C). In addition, *NMNAT2* knockdown inhibited the growth of the cells, suggesting that NMNAT-2 is important for cancer cell growth (fig. S16D). Moreover, glucose deprivation in SH-SY5Y cells also decreased the levels of NMNAT-2 protein and increased the enzymatic activity of PARP-1 (fig. S16, E and F). Collectively, these data suggest that compartmentalized NAD^+ biosynthesis is not only important in adipogenesis, but can also play a key role in other biological processes, such as a cancer cell growth.

Discussion

Our studies have elucidated the pathway leading from enhanced glucose metabolism to the adipogenic

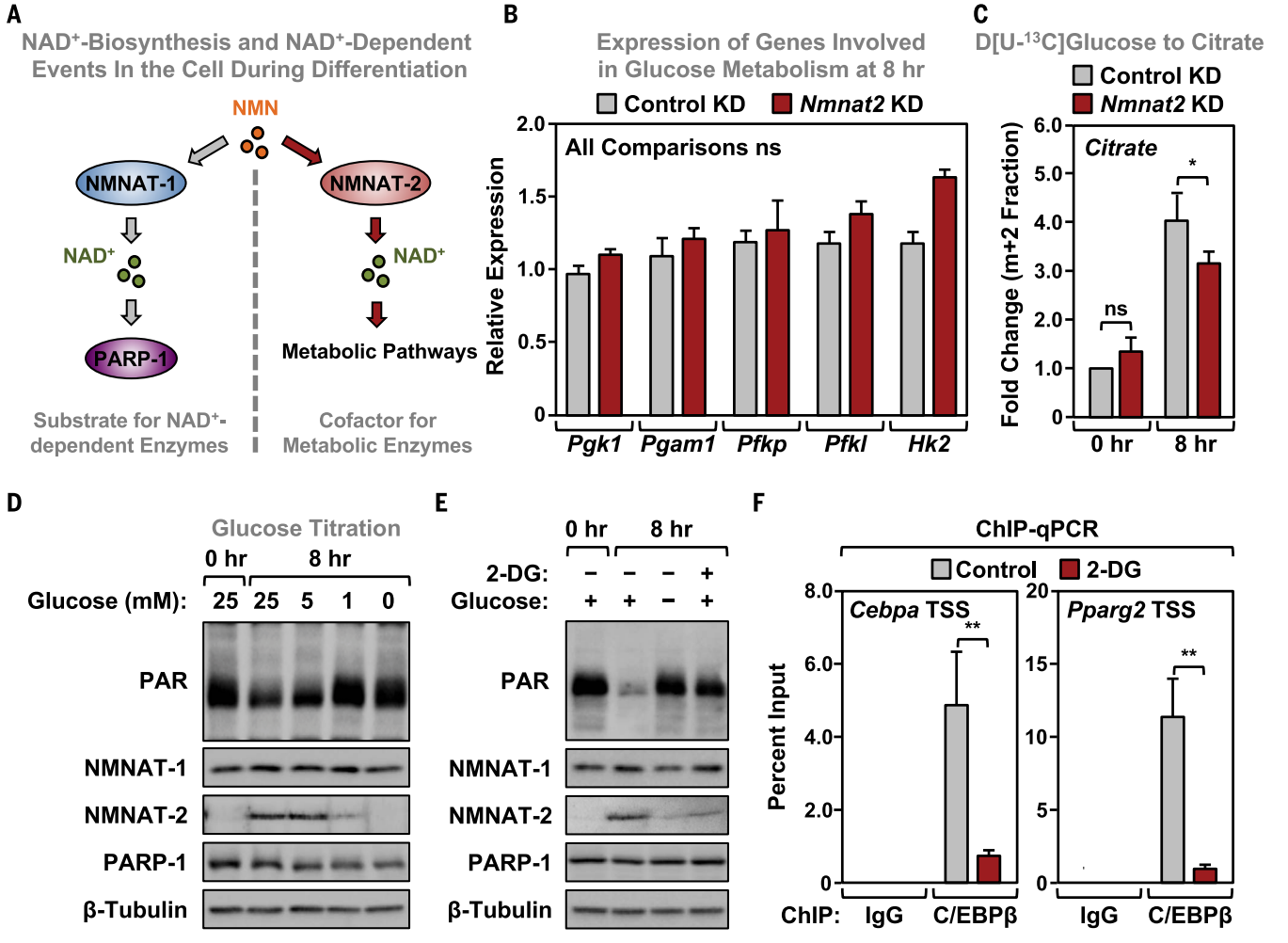

Fig. 5. NMNAT-2 induction is associated with enhanced glucose metabolism during the early phase of adipogenesis. (**A**) Schematic representation of the potential role of NMNAT-1 and NMNAT-2 during adipocyte differentiation. (**B**) *Nmnat2* knockdown does not affect the expression of genes involved in glucose metabolism after 8 hours of differentiation, as determined by RT-qPCR. None of the minor differences are significant (Student's *t* test; $P > 0.05$). (**C**) *Nmnat2* knockdown alters glucose flux during the differentiation of 3T3-L1 cells. Mass isotopomer analysis of citrate m+2 in cells with or without *Nmnat2* knockdown. Asterisks indicate significant differences from the corresponding control (Student's *t* test; $*P < 0.05$); ns, not significant (Student's *t* test; $P > 0.05$). (**D** and **E**) Expression of NMNAT-2 in 3T3-L1 cells differentiated in the presence of various extracellular glucose levels (D) or the glycolysis inhibitor 2-deoxyglucose (2-DG) (E) by Western blotting. (**F**) Regulation of C/EBPβ binding to target gene promoters in 3T3-L1 cells by ChIP-qPCR upon inhibition of glycolysis with 2-DG. The assays were done 8 hours postdifferentiation. Asterisks indicate significant differences from the corresponding control (Student's *t* test; $**P < 0.01$). TSS, transcription start site. Throughout, bars represents means + SEM.

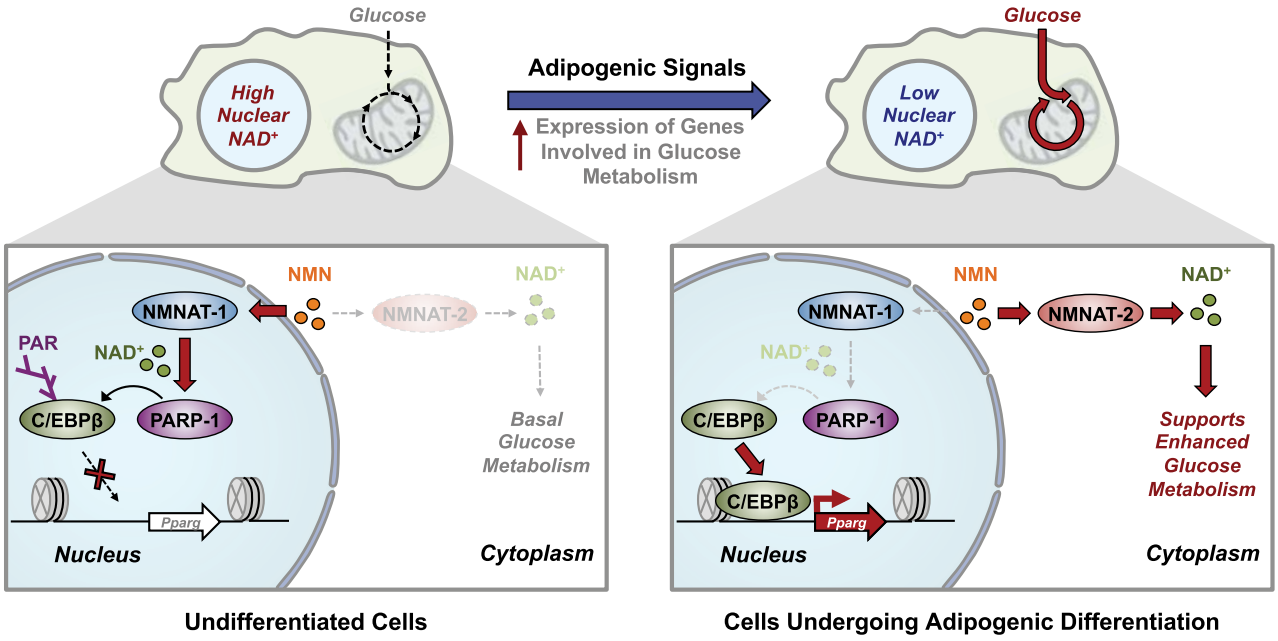

Fig. 6. Model for the coordination of transcription and glucose metabolism during adipocyte differentiation through compartmentalized NAD$^+$ biosynthesis. In undifferentiated 3T3-L1 cells, NMN is used mostly by NMNAT-1 to synthesize nuclear NAD$^+$, which supports PARP-1 activity. Active PARP-1 ADP-ribosylates the adipogenic transcription factor C/EBPβ, which inhibits its chromatin binding and transcriptional activities, preventing differentiation in the absence of an adipogenic signal. During differentiation, the expression of genes involved in glucose metabolism increases, leading to a rapid induction of glucose flux in 3T3-L1 cells. Concurrently, NMNAT-2 is rapidly induced to support the high local NAD$^+$ demands caused by enhanced glucose metabolism, thereby limiting NMN availability in the nucleus for NMNAT-1 to synthesize nuclear NAD$^+$. Reduced nuclear NAD$^+$ concentrations lead to reduced PARP-1 activity, allowing C/EBPβ to initiate the adipogenic transcription program. Competition for the NAD$^+$ precursor, NMN, between the nuclear and cytoplasmic NMNATs results in changes in nuclear NAD$^+$ levels, allowing cells to coordinate glucose metabolism and transcription.

gene expression program that drives the differentiation of adipocytes. Briefly, we have shown that compartmentalized NAD$^+$ biosynthesis is a crucial component of transcriptional regulation during adipocyte differentiation. Proper regulation of nuclear NAD$^+$ levels is achieved by the rapid induction of the cytosolic NAD$^+$-synthesizing enzyme, NMNAT-2, which consumes NMN in the cytoplasm, thereby limiting NMN availability in the nucleus. Reduced nuclear NMN levels lead to reduced nuclear NAD$^+$ synthesis, ultimately reducing PARP-1 enzymatic activity and C/EBPβ PARylation and enhancing C/EBPβ binding to target genes to drive the adipogenic transcription program (Fig. 6). Consistent with this model, decreasing nuclear NAD$^+$ synthesis by *Nmnat1* knockdown rapidly enhances differentiation, whereas increasing nuclear NAD$^+$ by NMN supplementation or *Nmnat2* knockdown inhibits adipogenesis. Compartmentalized NAD$^+$ biosynthesis is tightly linked to glucose metabolism, and increased glucose metabolism is required for the rapid induction of NMNAT-2, thus integrating cellular metabolism and the adipogenic transcription program. Collectively, our studies demonstrate that compartmentalized NAD$^+$ biosynthesis plays a key role in orchestrating intracellular metabolism and signal-regulated transcription. Such mechanisms likely play an important part in other biological systems that exhibit dramatic changes in nuclear PARylation as differentiation proceeds [e.g., embryonic stem cells (*24*)] or have a high glucose demand [e.g., cancer cells (*25*)].

Intracellular NAD$^+$ concentrations, compartmentalization, and biological outcomes

During differentiation, the free nuclear NAD$^+$ concentration, as measured by a nuclear NAD$^+$ sensor, drops from above PARP-1's K_m for NAD$^+$ (~100 μM) to below its K_m for NAD$^+$ (~40 μM) (Fig. 3C). This suggests that fluctuations in free nuclear NAD$^+$ have the ability to regulate the activity of PARP-1 and, perhaps, other nuclear NAD$^+$-dependent enzymes with suitable K_m values for NAD$^+$. The previously reported total intracellular NAD$^+$ concentration in cultured mammalian cells [~300 to 500 μM (*26*)] exceeds the estimated free NAD$^+$ concentration in the distinct subcellular compartments (Fig. 3C) (*20*). The disparity between total and free NAD$^+$ suggests that a portion of intracellular NAD$^+$ may be bound to protein, consistent with previous results (*26*). Therefore, cellular events that facilitate the release of protein-bound NAD$^+$ or, alternatively, promote the binding of NAD$^+$ to proteins could potentially alter the amount of free NAD$^+$ and consequently the enzymatic activity of NAD$^+$-consuming enzymes. Given that the free NAD$^+$ concentration is a key regulator of NAD$^+$-dependent enzymes, understanding the factors that regulate free versus bound NAD$^+$ could point to a previously unrecognized regulatory mechanism for NAD$^+$-dependent enzymes.

Our data show that nuclear NAD$^+$ biosynthesis is necessary for PARP-1–dependent regulatory events during the differentiation of preadipocytes. Such compartmentalization of metabolites, small molecules, and ions within the cell is not unprecedented. For example, cyclic adenosine monophosphate (cAMP) (*27*), Ca^{2+} (*28*), ATP (*29*), and acetyl–coenzyme A (CoA) (*30*) have also been reported to be compartmentalized and exhibit compartment-specific fluctuations in their concentrations. As with NAD$^+$, the precise mechanisms governing the compartmentalization and regulation of cAMP, Ca^{2+}, ATP, and acetyl-CoA are also unclear. In the case of nuclear versus cytoplasmic NAD$^+$, the diameter of the nuclear pore would not be expected to impose any physical barrier to the diffusion of NAD$^+$ between these two compartments (*31*). So how might compartmentalization occur?

One possibility is that cellular NAD$^+$ synthesis may be restricted to the site of consumption to support local demands, similar to cAMP, which is produced in distinct microdomains to increase local concentrations (*27*). This effect could be mediated by colocalization of metabolite producers and consumers, so that the consumers use the free metabolites as substrates before the metabolites can diffuse an appreciable distance away from their sources (*32*), perhaps through a

substrate-channeling mechanism (*33*). In this regard, NMNAT-1 binds to, colocalizes with, and regulates the enzymatic activity of PARP-1 and other chromatin-bound NAD^+-dependent enzymes at target gene promoters (*34*, *35*), which is consistent with a substrate-channeling mechanism.

Another possibility is that the nucleus and cytoplasm share a contiguous NAD^+ pool that can be altered independently and transiently in a temporal manner. Although the diffusion of small molecules should be extremely fast, reaching equilibrium rapidly when in free solution, diffusion rates can be inhibited considerably by molecular crowding inside the cell (*36*), which may allow cells to regulate metabolite pools in a compartment-specific manner. In this case, rapid and robust local changes in metabolite synthesis or consumption may cause local changes within a compartment that are not distributed across the entire pool. Indeed, we observed rapid induction of NMNAT-2 and glucose metabolism during differentiation (Fig. 3A and figs. S8, S9A, S9B, S11C, and S11D), suggesting that enhanced synthesis and consumption of NAD^+ in the cytoplasm under these conditions may restrict the diffusion of newly synthesized NAD^+. Further studies will be required to determine whether these or other mechanisms govern the compartmentalization and regulation of intracellular NAD^+.

Nuclear NAD^+ concentration and the activity of nuclear NAD^+-dependent enzymes

Although PARP-1 is considered to be the major NAD^+-consuming enzyme in the nucleus, other NAD^+-dependent enzymes, such as PARP-2, PARP-3, and SIRTs, are also present in the nucleus. Among these, SIRT1 has been reported to be a key regulator of various metabolic processes, with a catalytic activity that depends on intracellular NAD^+ concentrations (*7*). Thus, it is reasonable to speculate that fluctuations in nuclear NAD^+ levels may also regulate SIRT1 enzymatic activity. The reported K_m of SIRT1 for NAD^+ varies between 2.2 and ~300 μM, depending on the substrate and the study reporting the effect (*26*, *37*). If the K_m of SIRT1 for NAD^+ is below ~40 μM (*37*), then the changes that we observed in nuclear NAD^+ concentrations during the early phase of differentiation would not be sufficient to effect SIRT1 catalytic activity. In contrast, if the K_m of SIRT1 for NAD^+ is well above ~100 μM (*26*), then the changes that we observed in nuclear NAD^+ concentrations might possibly affect SIRT1 catalytic activity—but likely not nearly to the same extent as that of PARP-1, whose K_m is near the basal predifferentiation concentrations of NAD^+ in the preadipocytes (~100 μM was the highest nuclear NAD^+ concentration that we measured; Fig. 3C). Our results in 3T3-L1 cells favor the former possibility, because we observed a moderate effect of differentiation or *Nmnat1* knockdown on SIRT1 activity with acetylated H4K16 (histone H4 lysine 16) or acetylated p53 (fig. S3, C to F).

Although fluctuations in nuclear NAD^+ concentrations have little effect on SIRT1 enzymatic activity in 3T3-L1 cells, other regulatory mechanisms, such as allosteric regulatory interactions with NMNAT-1 at target gene promoters (*35*) or functional interactions with DBC-1 (*38*), may play an important role. These additional mechanisms, which could provide distinct approaches for the cell to regulate SIRT1 versus PARP-1, may be key to understanding the cell type– or tissue-specific regulation of NAD^+-dependent enzymes. *Nmnat1* knockdown significantly increased p53 acetylation levels in differentiated adipocytes (fig. S3, E and F), suggesting that SIRT1 activity is more sensitive to nuclear NAD^+ synthesis in mature adipocytes. This result supports previous reports that SIRT1 plays a critical role in adipocyte metabolism through $PPAR_\gamma$ regulation (*39*, *40*). Thus, NMNAT-1 and SIRT1 may play critical roles in fully differentiated adipocytes, but not the early stages of adipogenesis. In fact, the expression of *Sirt1* in preadipocytes is significantly lower than that of *Parp1* (fig. S3G) and increases during differentiation (*39*). These observations suggest that nuclear NAD^+ may regulate gene expression through distinct NAD^+-dependent enzymes in different biological processes, such as early adipogenesis versus mature adipocyte biology. Efforts to understand the biological importance of NMNATs have been largely limited to their function in neurodegeneration. However, given the role of NAD^+ as a universal metabolic cofactor and a substrate for enzymes that are known to regulate metabolic processes in a variety of tissues and cell types (*6*, *7*, *26*), we should expand our thinking about these NAD^+ biosynthetic enzymes. In particular, further exploration of their roles in compartment-specific NAD^+ synthesis and the regulation of metabolism in vivo is needed. The use of tissue-specific depletion of NMNATs, PARPs, and SIRTs will undoubtedly be required to resolve such questions in the future.

Materials and methods

Generation of *Nmnat1* conditional knockout mice

Frozen $Nmnat1^{tm1a(EUCOMM)Wtsi}$ embryos on a C57BL/6N background were obtained from the International Mouse Phenotyping Consortium (IMPC; MGI ID 1913704) and were recovered at UT Southwestern's Transgenic Core Facility. All mice were housed and maintained at UT Southwestern's Animal Resource Center. The reporter cassette was removed by crossing $Nmnat1^{tm1a/tm1a}$ mice with FLP recombinase-expressing B6.129S4-$Gt(ROSA)26Sor^{tm2(FLP*)Sor}$/J mice (The Jackson Laboratory, stock no. 012930). After removing the reporter cassette, the resulting $Nmnat1^{loxP/+}$ mice were self-crossed to generate homozygous $Nmnat1^{loxP/loxP}$ progeny. To produce mice with a Tamoxifen-inducible conditional allele of *Nmnat1* ($Nmnat1^{loxP/loxP}$; *CAG-cre/ERT2*), $Nmnat1^{loxP/loxP}$ mice were crossed with transgenic mice containing a *CAG-cre/ERT2* cassette [B6.Cg-Tg(*CAG-cre/Esr1**)5Amc/J; The Jackson Laboratory, stock no. 004682]. All of the mouse genotypes were confirmed by short-range PCR, using PCR primers listed in the supplementary materials.

All of the studies with mice were performed according to IACUC guidelines under a protocol approved by UT Southwestern's Animal Use Committee.

Isolation of SVF cells from white adipose tissue

SVF cells were isolated as described previously (*41*). Briefly, 4- to 6-week-old male mice (2 mice per condition) were sacrificed and the inguinal white adipose tissue (WAT) was collected. The WAT was washed, pooled, minced, and digested for 2 hours at 37°C in 10 ml of digestion solution [100 mM HEPES pH 7.4, 120 mM NaCl, 50 mM KCl, 5 mM glucose, 1 mM $CaCl_2$, 1 mg/ml collagenase D (Roche, 11088858001), and 1.5% BSA]. The digested WAT tissue was filtered through a 100-μm cell strainer to remove undigested tissue, and 30 ml of SVF cell culture medium [10% FBS, 1% penicillin/streptomycin in DMEM/F12, GlutaMAX (Life Technologies, 10565-018)] was added to dilute the digestion buffer. The flow-through was centrifuged for 5 min at 600*g* to collect the SVF cells. The cell pellet was resuspended in 10 ml of SVF culture medium, and passed through a 40-μm cell strainer to remove clumps of cells and large adipocytes. The cells were collected again by centrifugation at 600*g* for 5 min, resuspended in SVF culture medium (5 ml per 2 mouse equivalents), and plated in a 6-cm-diameter collagen-coated culture dish until well attached.

Cell culture and differentiation

SVF cells (*16*, *17*) were grown in SVF culture medium until confluent and were then cultured for 2 more days under contact inhibition. The cells were then treated for 2 days with an adipogenic cocktail (MDI), including 0.5 mM IBMX (3-isobutyl-1-methylxanthine; Calbiochem, 410957), 1 μM dexamethasone (Sigma, D4902), and 5 μg/ml insulin (Sigma, I-5500). Subsequently, the cells were cultured in medium containing 5 μg/ml insulin for the indicated times before collection.

3T3-L1 cells (*15*) and NIH/3T3 cells were obtained from the American Type Cell Culture (ATCC, CL-173 and CRL-1658, respectively) and were mycoplasma-free. They were maintained in DMEM (Cellgro, 10-017-CM) supplemented with 10% fetal bovine serum (Atlanta Biologicals, S11550) and 1% penicillin/streptomycin. For the glucose titration experiments, the 3T3-L1 cells were grown in DMEM without glucose (Life Technologies, 11966-025). For the induction of adipogenesis, the 3T3-L1 cells were grown to confluence and then cultured for 2 more days under contact inhibition. The cells were then treated for 2 days with an MDI adipogenic cocktail containing 0.25 mM IBMX, 1 μM dexamethasone, and 10 μg/ml insulin. Subsequently, the cells were cultured in medium containing 10 μg/ml insulin for the indicated times before collection. For the induction of adipogenesis in NIH/3T3 cells, 1 μM Rosiglitazone (Sigma, R2408) was added to promote the differentiation process.

293T cells were obtained from the ATCC (CRL-3216) and were mycoplasma-free. They were maintained in DMEM (Cellgro, 10-017-CM) supplemented with 10% fetal bovine serum and 1% penicillin/streptomycin.

MCF-7 cells, kindly provided by Benita Katzenellenbogen (University of Illinois, Urbana-Champaign), were cultured in minimal essential medium (MEM; Sigma, M1018) supplemented with 5% calf serum (Sigma, C8056), 1% penicillin/streptomycin (Gibco, 15140122), and 25 μg/ml gentamicin (Gibco, 15710064).

MCF10A (CRL-10317), MDA-MB-231 (HTB-26), and SH-SY5Y (CRL-2266) cells were obtained from ATCC. MCF10A cells were cultured in mammary epithelial cell culture kit (Lonza, CC-2551B) and MDA-MB-231 cells were cultured in RPMI 1640 (Sigma, R8758) supplemented with 10% fetal bovine serum and 1% penicillin/streptomycin. SH-SY5Y cells were cultured in DMEM (Cellgro, 10-017-CM) supplemented with 20% fetal bovine serum and 1% penicillin/streptomycin.

Cell treatments

3T3-L1 or SVF were exposed to various treatments and culture conditions for the experiments described herein. For treatment with NMN (1 mM or 5 mM; Sigma, N3501), MG-132 (10 μM, Sigma, M7449), or 2-deoxy-D-glucose (5 mM; Sigma, D8375), the cells were grown until confluent and then pretreated with either compound for 2 hours prior to the addition of the MDI cocktail. The cells were then differentiated in medium with MDI in the presence of NMN or 2-deoxy-D-glucose for the indicated times before collection. For differentiation longer than 2 days, the compounds were added to the medium with MDI for 2 days, then removed when changing culture medium. For SIRT1 inhibition, the cells were treated with 10 μM Sirtinol (Calbiochem, 566320) for 48 hours before collection. For the Dox-inducible system, we treated the cells with 1 μg/ml (for NAD^+ sensors and Dox-inducible knockdown) or 250 ng/ml (for NMNAT-2 overexpression) Dox for 48 hours. For NAMPT inhibition, we treated the cells with 50 nM FK866 (Sigma, F8557) for 48 hours. For Tamoxifen-inducible, Cre-mediated *Nmnat1* deletion, $Nmnat1^{loxP/loxP}$; *CAG-CreERT2* SVF cells were cultured until confluent and were then treated with 1 μM 4-hydroxytamoxifen (4-OHT; Sigma, H7904) for 2 days before the induction of adipogenesis, as described above.

Antibodies

The custom rabbit polyclonal antiserum against PARP-1 used for Western blotting and ChIP assays was generated by using a purified recombinant antigen comprising the amino-terminal half of PARP-1 (*42*) (now available from Active Motif; cat. no. 39559). The custom rabbit polyclonal antiserum against NMNAT-1 was raised against purified recombinant human and mouse NMNAT-1 (Pocono Rabbit Farm and Laboratory). The custom recombinant antibody-like anti-poly-ADP-ribose binding reagent (anti-PAR) was generated and purified in-house (now available from EMD Millipore, MABE1031). The other antibodies used were as follows: C/EBPβ (Santa Cruz, sc-150X), NMNAT-2 (Abcam, ab56980), β-Tubulin (Abcam, ab6046), SIRT1 [custom rabbit polyclonal antiserum raised against mouse SIRT1 (*35*)], acetyl-p53 K379 (Cell signaling, #2570), p53 (Cell signaling, #2524), H4K16Ac (Millipore, 07-329), Histone H4 (Millipore, 07-108), rabbit IgG (Invitrogen, 10500C), goat anti-rabbit HRP-conjugated IgG (Pierce, 31460), and goat anti-mouse HRP-conjugated IgG (Pierce, 31430).

Molecular cloning to generate expression and knockdown vectors

shRNAs targeting Nmnat1, Parp1, and NMNAT2

shRNA constructs targeting mouse *Nmnat1* mRNA (TRCN0000111435, TRCN0000335596) and control shRNA (SHC002) were purchased from Sigma. We generated an shRNA construct targeting mouse *Parp1* mRNA by cloning a double-stranded oligonucleotide (5′-GGGCAAGCACAGTGTCAAA-3′) into the pLKO.1 vector (SHC001), which confers puromycin resistance. Dox-inducible shRNA sequences targeting human *NMNAT2* mRNA were purchased from Dharmacon (V3THS400729, V3THS400730, V3THS_400733) and were cloned individually, along with a corresponding control shRNA targeting luciferase, into the pTRIPZ vector using a double-stranded oligonucleotide (5′-AGATATGGGCTGAATACAAATC-3′).

RNAi-resistant Nmnat1 expression constructs

cDNA was prepared by extracting total RNA from 3T3-L1 cells using Trizol (Invitrogen, 15596026), followed by reverse transcription using superscript III reverse transcriptase (Invitrogen, 18080051) and an oligo(dT) primer according to manufacturer's instructions. *Nmnat1* cDNA was then amplified from the cDNA library and cloned into the pBabe-neo (Addgene, 1767) retroviral expression vector using the primers listed in the supplementary materials. cDNAs for an RNAi-resistant mutant and a catalytically inactive mutant (W170A) were generated by site-directed mutagenesis using Pfu Turbo DNA polymerase (Agilent, 600250) with the primers listed in the supplementary materials.

Quantitative cpVenus-based NAD^+ sensor constructs

Expression vectors for cpVenus-based nuclear and cytoplasmic NAD^+ sensors and their corresponding cpVenus-only controls (*20*) were kindly provided by M. Cohen and R. Goodman. DNA coding for the sensors or controls was amplified from the expression vectors provided using the primers listed in the supplementary materials and then cloned into the pINDUCER20 lentiviral Dox-inducible expression vector (Addgene, plasmid no. 44012) (*43*) using Gibson assembly (NEB, E2621).

Dox-inducible Nmnat2 expression constructs

cDNA was prepared as described above. *Nmnat2* cDNA was then amplified from the cDNA library and cloned into pINDUCER20 lentiviral Dox-inducible expression vector using the primers listed in the supplementary materials. A catalytically inactive *Nmnat2* mutant (H24D) was generated by site-directed mutagenesis using Pfu Turbo DNA polymerase using the primers listed in the supplementary materials.

Generation of cell lines with stable knockdown or ectopic expression

Cells were transduced with either lentiviruses or retroviruses for stable knockdown or ectopic expression. We generated lentiviruses by transfection of the pLKO.1 constructs described above, together with: (i) an expression vector for the VSV-G envelope protein (pCMV-VSV-G, Addgene plasmid no. 8454), (ii) an expression vector for GAG-Pol-Rev (psPAX2, Addgene plasmid no. 12260), and (iii) a vector to aid with translation initiation (pAdVAntage, Promega) into 293T cells using GeneJuice transfection reagent (Novagen, 70967) according to the manufacturer's protocol. The resulting viruses were collected in the culture medium, concentrated by using a Lenti-X concentrator (Clontech, 631231), and used to infect cells.

Retroviruses were generated by transfection of the pMSCV constructs described above, together with an expression vector for the VSV-G envelope protein (pCMV-VSV-G), into Phoenix Ampho cells using GeneJuice transfection reagent (Novagen, 70967) according to the manufacturer's protocol. The resulting viruses were used to infect.

Stably transduced cells were selected with puromycin (Sigma, P9620; 2 μg/ml) or G418 sulfate (Sigma, A1720; 1 mg/ml).

Knockdown of *Nmnat2* using siRNAs

Commercially available siRNA oligos targeting *Nmnat2* (Sigma, SASI_Mm01_00083355, SASI_Mm01_00083356, and SASI_Mm01_00083357) were transfected at a final concentration of 20 nM using Lipofectamine RNAiMAX reagent (Invitrogen, 13778150) according to the manufacturer's instructions. All experiments were performed 48 hours after siRNA transfection.

Preparation of cell lysates and Western blotting

3T3-L1 and SVF cells were cultured and differentiated as describe above. The cells were then washed twice with ice-cold PBS and lysed with Lysis Buffer (20 mM Tris-HCl pH 7.5, 150 mM NaCl, 1 mM EDTA, 1 mM EGTA, 1% NP-40, 1% sodium deoxycholate, 0.1% SDS) containing 1 mM DTT, 250 nM ADP-HPD (Sigma, A0627; a PARG inhibitor to prevent PAR chain cleavage during extraction), 10 μM PJ34 (a PARP inhibitor to prevent PAR synthesis during extraction), and 1x complete protease inhibitor cocktail (Roche, 11697498001). For measuring SIRT1 activity, 10 mM sodium butyrate (a class I/II HDAC inhibitor) and 10 μM Sirtinol (a sirtuin inhibitor) were added to the lysate to prevent deacetylation during extraction. For the chromatin fractions, lysed cells were sonicated in Lysis Buffer to solubilize the chromatin. For the nuclear and cytoplasmic fractions, the cells were first resuspended in Isotonic Buffer (10 mM Tris-HCl pH 7.5, 2 mM $MgCl_2$, 3 mM $CaCl_2$, 0.3 M sucrose, 1 mM DTT, and 1x complete protease inhibitor cocktail), incubated on ice for 15 min, and lysed by the addition of 0.6% IGEPAL

CA-630 detergent with gentle vortexing. The nuclei from the lysed cells were pelleted by centrifugation, and the supernatant was collected as the cytoplasmic fraction. The pelleted nuclei were resuspended in Nuclear Extraction Buffer (50 mM Tris-HCl pH 7.4, 500 mM NaCl, 1 mM EDTA, 1% IGEPAL CA-630, 1 mM DTT, and 1x complete protease inhibitor cocktail) to produce the nuclear lysate. All lysates were incubated on ice for 30 min for extraction and then centrifuged to clarify. The supernatants were collected, run on a 6% polyacrylamide-SDS gel (for PARP-1 and PAR analyses) or a 10% polyacrylamide-SDS gel (for NMNAT-1, C/EBPβ, NMNAT-2, β-tubulin), and transferred to a nitrocellulose membrane. The membranes were blocked with 5% nonfat milk in TBST and incubated with the primary antibodies described above in 1% nonfat milk in TBST, followed by anti-rabbit HRP-conjugated IgG (1:5000) or anti-mouse HRP-conjugated IgG (1:3000). Western blot signals were detected using an ECL detection reagent (Thermo Fisher, 34077, 34095).

GTEx tissue expression analyses

The expression profiles of *NMNAT1* and *NMNAT2* in different human tissues was determined based on RPKM values using GTEx (*44*) (www.gtexportal.org/home/) with dbGaP Study Accession phs000424.v6.p1 (www.ncbi.nlm.nih.gov/projects/gap/cgi-bin/study.cgi?study_id=phs000424.v6.p1).

RNA isolation and RT-qPCR

3T3-L1 cells or SVF cells were seeded at ~2×10^5 cells per well in 6-well plates and treated as described above. For tissue RNA isolations, 6- to 8-week-old C57BL/6 male mice were used. The cells and tissues were collected and total RNA was isolated using Trizol Reagent (Invitrogen) according to the manufacturer's protocols. Total RNA was reverse transcribed using oligo (dT) primers and MMLV reverse transcriptase (Promega) to generate cDNA. The cDNA samples were subjected to qPCR using gene-specific primers, as described below. For the reverse transcription quantitative real-time PCR (RT-qPCR) analyses, "relative expression" was determined in comparison to a value from the first biological replicate of the control sample. Target gene expression was normalized to the expression of *Tbp* mRNA (mouse) or *RPL19* mRNA (human). The normalized value from the first biological replicate of the control sample was set to 1 and all the rest of the values, including the values from other biological replicate of controls, were plotted against it. All experiments were performed a minimum of three times with independent biological replicates to ensure reproducibility and a statistical significance of at least $P < 0.05$. Statistical differences between control and experimental samples were determined using the Student's *t* test. All experimental groups that were compared had similar variance as determined by the standard deviation of the biological replicates within each group.

ChIP-qPCR

3T3-L1 cells were cultured, differentiated, and treated as described above in 15-cm-diameter plates. ChIP was performed as described previously (*45*, *46*), with slight modifications. Briefly, the cells were cross-linked with 1% formaldehyde in PBS for 10 min at 37°C and quenched in 125 mM glycine in PBS for 5 min at 4°C. Cross-linked cells were then collected by centrifugation and lysed in Farnham Lysis Buffer (5 mM PIPES pH 8.0, 85 mM KCl, 0.5% NP-40, 1 mM DTT, and 1x complete protease inhibitor cocktail). A crude nuclear pellet was collected by centrifugation, resuspended in Sonication Buffer (50 mM Tris-HCl pH 7.9, 1% SDS, 10 mM EDTA, 1 mM DTT, and 1x complete protease inhibitor cocktail), and sonicated to generate chromatin fragments of ~300 bp in length. The soluble chromatin was clarified by centrifugation, diluted 1:10 with Dilution Buffer (20 mM Tris-HCl pH 7.9, 0.5% Triton X-100, 2 mM EDTA, 150 mM NaCl, 1 mM DTT, and 1x complete protease inhibitor cocktail) and pre-cleared with protein A agarose beads.

The pre-cleared samples were used in immunoprecipitation reactions with antibodies against C/EBPβ or with rabbit IgG (as a control) with incubation overnight at 4°C. The samples were washed with Low Salt Wash Buffer (20 mM Tris-HCl pH 7.9, 2 mM EDTA, 125 mM NaCl, 0.05% SDS, 1% Triton X-100, 1 μM aprotinin, and 1 μM leupeptin), High Salt Wash Buffer (20 mM Tris-HCl pH 7.9, 2 mM EDTA, 500 mM NaCl, 0.05% SDS, 1% Triton X-100, 1 μM aprotinin, and 1 μM leupeptin), LiCl Wash Buffer (10 mM Tris-HCl, pH 7.9, 1 mM EDTA, 250 mM LiCl, 1% NP-40, 1% sodium deoxycholate, 1 μM aprotinin, and 1 μM leupeptin), and 1x Tris-EDTA (TE). The immunoprecipitated genomic DNA was eluted in Elution Buffer (100 mM $NaHCO_3$, 1% SDS), digested with proteinase K and RNase H to remove protein and RNA, respectively, and then extracted with phenol: chloroform:isoamyl alcohol. The ChIPed genomic DNA was subjected to qPCR using gene-specific primers, as described below. The immunoprecipitation of genomic DNA was normalized to the input. All experiments were performed a minimum of three times with independent biological replicates to ensure reproducibility and a statistical significance of at least $P < 0.05$. Statistical differences between control and experimental samples were determined using the Student's *t* test. All experimental groups that were compared had similar variance as determined by the standard deviation of the biological replicates within each group.

qPCR

qPCR was performed as described previously (*47*). Briefly, cDNA or ChIPed DNA samples were mixed with 1x SYBR Green PCR master mix and primers (forward and reverse, 250 nM), and were then subjected to 45 cycles of amplification (95°C for 10 s, 60°C for 10 s, 72°C for 1 s) following an initial 5 min incubation at 95°C using a Roche LightCycler 480 384-well detection system. Melting curve analyses were performed to ensure that only the targeted amplicon was amplified. All qPCR-based experiments were performed a minimum of three times with independent biological replicates to ensure reproducibility and a statistical significance of at least $P < 0.05$. Statistical differences between control and experimental samples were determined using the Student's *t* test. All experimental groups that were compared had similar variance as determined by the standard deviation of the biological replicates within each group. The sequences of the primers are listed in the supplementary materials.

RNA-seq

Generation of RNA-seq libraries

Two biological replicates of control, *Nmnat1*, and *Parp1* knockdown 3T3-L1 cells were differentiated as described above. Total RNA was isolated using the RNeasy kit (Qiagen) according to the manufacturer's instructions. The total RNA was then enriched for polyA+ RNA using Dynabeads Oligo(dT)25 (Invitrogen). The polyA+ RNA was then used to generate strand-specific RNA-seq libraries as described previously (*48*). The RNA-seq libraries were subjected to QC analyses (i.e., number of PCR cycles required to amplify each library, the final library yield, and the size distribution of final library DNA fragments) and sequenced using an Illumina HiSeq 2000.

Analysis of RNA-seq data

The raw data were subjected to QC analyses using the FastQC tool (*49*). The reads were then mapped to mouse genome (mm10) using the spliced reader aligner TopHat version 2.0.13 (*50*). Transcriptome assembly was performed using cufflinks v.2.2.1 (*51*) with default parameters. The transcripts were merged into two distinct, nonoverlapping sets using cuffmerge, followed by cuffdiff to call the differentially regulated transcripts. The significantly ($P < 0.05$) regulated genes upon *Nmnat1* or *Parp1* knockdown compared to control knockdown at the indicated time points were used to find the commonly regulated gene set. Similar analyses were performed with published RNA-seq data sets (GSE57415, GSE29899).

Linking transcription factors to gene regulation using PCHi-C data

In order to determine the transcription factors that bind upstream of the NMNAT-1 and PARP-1 commonly regulated genes, we queried publicly available ChIP-seq data sets for C/EBPβ, STAT5A, RXRα, C/EBPδ, and GR (NCBI GEO accession number GSE27826) (*19*) and the called peaks from these data sets were lifted over to mm10. To determine which transcription factors interact with the promoters of PARP-1 and NMNAT-1 co-regulated genes, raw sequence reads from published PCHi-C data (GSE95533) (*18*) were processed using the HiCUP pipeline (*52*), which maps the positions of di-tags against the mouse genome (mm10), filters out experimental artifacts (e.g., circularized reads and re-ligation products), and removes all duplicate reads. Hicpipe (*53*), version 0.9 was used to correct the PCHi-C contact maps using the restriction enzyme site HindIII and the mapped paired reads. A custom script (available from W.L.K. upon request) was used to define all the interactions between the promoters and the transcription factor binding sites. The genomic loci interacting with the promoters of genes

co-regulated by *Nmnat1* and *Parp1* knockdown were compared to the individual transcription factor ChIP-seq peaks to identify the promoter-transcription factor binding site interactions. The number of NMNAT-1 and PARP-1 regulated genes containing significant ChIP-seq peaks of the specified transcription factors at their interacting genomic loci were divided by the total number of NMNAT-1/PARP-1 co-regulated genes to determine the percent of co-regulated gene promoters interacting with each transcription factor.

To determine the expression levels of the genes whose promoters interact with C/EBPβ binding sites, we first identified C/EBPβ binding sites using ChIP-seq data (GSE27826) and then determined all the promoters interacting with these binding sites using PCHI-C (GSE95533). Among these gene promoters, we took only the genes expressed in 3T3-L1 cells (FPKM > 1) during differentiation. The expression level of these genes (determined by RNA-seq) in control, *Nmnat1* and *Parp1* knockdown 3T3-L1 cells at day 2 or 4 was compared to the control knockdown at day 0 to calculate the fold change for each gene. Up-regulated genes were defined as fold change greater than 1. All custom scripts are available by request from W.L.K.

Genomic data sets

The new RNA-seq generated for this study can be accessed from the NCBI's Gene Expression Omnibus (GEO) repository (www.ncbi.nlm.nih.gov/geo/) using the accession number GSE96764.

Intracellular lipid staining

BODIPY staining

3T3-L1 cells were seeded on sterile cover slips in 24-well plates and differentiated as described above. The cells were rinsed twice with 1x PBS and fixed with 4% paraformaldehyde. The fixed cells were washed twice with 1x PBS and stained with 1 μg/ml of BODIPY 493/503 (Life Technologies, D3922) for 10 min. The cells were then washed three times with 1x PBS and counter-stained with 1 μM TO-PRO-3 (Life Technologies, T3605) for 2 min. The cover slips were then mounted onto glass slides with VECTASHIELD Mounting Medium (Vector Laboratories, H-1000). Confocal images were acquired using a Leica SP2 confocal microscope.

Oil Red O staining

3T3-L1 cells were cultured in 6-well plates and differentiated as described above. After 8 days of differentiation, the cells were rinsed twice with 1x PBS and fixed with 4% paraformaldehyde. The fixed cells were washed with water and incubated in 60% isopropanol for 5 min. After incubation, the isopropanol was removed and replaced with 0.3% Oil-red-O working solution for 5 min. The Oil Red O working solution was prepared by diluting a stock solution (0.5% in isopropanol; Sigma, O1391) with water (3:2).

Measurement of total intracellular NAD^+ levels

3T3-L1 cells were cultured and differentiated as described above. For NAD^+ measurements, the cells were harvested with 0.5 M perchloric acid and neutralized with and equal volume of 0.55 M of K_2CO_3. The samples were then centrifuged and the supernatants were collected for metabolite measurement. Total intracellular NAD^+ or NADH levels were measured using a NAD^+/NADH colorimetric assay kit (Cyclex, CY-1253) following the manufacturer's instructions. For the NAD^+ measurement, "relative level" was determined in comparison to a value from the first biological replicate of the control sample. A value from the first biological replicate of the control sample was set to 1 and all the rest of the values were plotted relative to that.

Determination of nuclear and cytoplasmic NAD^+ levels using cpVenus-based sensors

3T3-L1 cells expressing nuclear or cytoplasmic NAD^+ sensors and their corresponding cpVenus-only controls were used to measure changes in subcellular NAD^+ levels. The cells were treated with 1 μg/ml Dox to induce expression of the sensors for 48 hours prior to the experiment. The NAD^+ sensor experiments were performed as described previously (*20*), with details provided below.

Purification of sensor proteins

Expression vectors for the sensors and their corresponding cpVenus-only controls (described above) were transfected into 293T cells using lipofectamine 3000 (Thermo Fisher, L3000015) following the manufacturer's protocol. After 48 hours, the cells were washed twice with ice-cold PBS and collected via centrifugation. Whole cell extracts were prepared from the cells expressing the cytoplasmic sensor or the corresponding cytoplasmic control by resuspending the cells in Lysis Buffer [50 mM Tris-HCl pH 7.4, 150 mM NaCl, 1 mM EDTA, 0.5% IGEPAL CA-630, 1 mM DTT, and 1x complete protease inhibitor cocktail (Roche)], incubating them for 30 min at 4°C, and then clarifying the lysate by centrifugation. Extracts were prepared from the cells expressing the nuclear sensor or the corresponding nuclear control, by resuspending the cells in Isotonic Buffer (10 mM Tris-HCl pH 7.5, 2 mM $MgCl_2$, 3 mM $CaCl_2$, 0.3 M sucrose, 1 mM DTT, and 1x complete protease inhibitor cocktail), incubating them on ice for 15 min, and lysing them by the addition of 0.6% IGEPAL CA-630 detergent with gentle vortexing. The nuclei from the lysed cells were collected by centrifugation, resuspended in Nuclear Extraction buffer (50 mM Tris-HCl pH 7.4, 150 mM NaCl, 1 mM EDTA, 1% IGEPAL CA-630, 1 mM DTT, and 1x complete protease inhibitor cocktail), and incubated for 30 min at 4°C. The resulting nuclear extract was clarified by centrifugation. Both the whole cell and nuclear extracts were incubated with anti-FLAG M2 affinity gel (Sigma, A2220) at 4°C for 4 hours to allow binding of the FLAG-tagged sensors and controls. The resin was washed five times in either the Lysis Buffer or the Nuclear Extraction Buffer, respectively, for 10 min at 4°C with constant mixing. The proteins were eluted with 500 μg/ml of 3x FLAG peptide (Sigma, F4799) made in wash buffer. The eluates were dialyzed in Dialysis Buffer (100 mM Tris-HCl pH 7.4, 150 mM NaCl, 1 mM EDTA, 0.5 mM DTT, 100 μM PMSF, and 20% glycerol). The concentrations of the protein solutions were measured using Bradford assays. The purity of the sensor and control proteins was confirmed by SDS-PAGE with subsequent silver staining using a Pierce silver staining kit (Thermo Fisher, 24600) following the manufacturer's protocol.

Measurement of in vitro fluorescence changes using spectroscopy

Purified sensor and control proteins (250 nM) were incubated with the indicated amount of NAD^+ in total reaction volume of 75 μl. The samples were incubated at RT for 15 min and the fluorescence was measured using a Spark 20M plate reader (Tecan). Excitation and emission spectra were 488 nm and 530 nm, respectively, with slit widths of 5 nm band pass for the excitation and 10 nm band pass for the emission. A standard curve was generated using the ratio of fluorescence values (sensor fluorescence/cpVenus fluorescence), which were fitted to a sigmoidal regression model using GraphPad Prism 7.

Imaging

3T3-L1 cells were seeded on chambered cover slips (Thermo Fisher, 155411) and cultured in FluoroBrite media (Thermo Fisher, A1896701) supplemented with 10% FBS (TET tested; Atlanta Biologicals, S103050) and 1% penicillin/streptomycin. Images were acquired using an inverted Zeiss LSM 780 confocal microscope affixed with a 37°C, 5% CO2 incubator. To measure NAD^+-dependent fluorescence changes, both the sensor and its corresponding cpVenus-only control were imaged with excitation at 488 nm and emission at 525 nm. The signal levels from the sensors and the controls were measured with excitation at 405 nm and emission at 525 nm.

Image analysis

We used Image J software to subtract background, set thresholds, select the regions of interest (ROIs), and quantify fluorescence intensity. Ratiometric analyses (488/405 nm) of the sensor versus control were used to normalize sensor expression levels and to analyze the changes in subcellular NAD^+ levels. To generate a pixel-by-pixel ratiometric images, we used a custom MATLAB program (available by request from W.L.K.). Average ratiometric values for the undifferentiated 3T3-L1 cells were defined as 1, and the rest of the data were normalized accordingly.

Flow cytometry

3T3-L1 cells were cultured and differentiated as described above. For flow cytometry analysis, the cells were trypsinized and triturated with FluoroBrite media containing 10% FBS and 1% penicillin/streptomycin. The data were collected on a BD Biosciences LSR II flow cytometer. The cells were gated using forward scatter (FSC) and side scatter (SSC) for the live cells and then further gated on both SSC and FSC width to ensure that individual cells were analyzed. FITC (excitation

488 nm, emission 530/30 nm) and BV510 (excitation 405 nm, emission 525/50 nm) were used for the sensor and control fluorescence. For the nuclear control, cytoplasmic sensor, and cytoplasmic control, we analyzed 1×10^4 cells. For the nuclear sensor, we analyzed 5×10^4 cells due to lower expression levels of the sensor. 3T3-L1 cells without fluorescent protein were used as a negative control to set a threshold for the analysis. The data were analyzed with FlowJo software and sensor/control ratiometric analyses were performed using a derived function on the software. Cells with high levels of sensor or control signals (about 5×10^3 cells per condition in each biological replicates) were subjected to ratiometric analysis (488/405 nm) to obtain the values for each cell. Geometric mean fluorescence intensity of the ratio was determined for each condition, and the values for sensor were divided by the values for the corresponding cpVenus-only control to account for any pH effects [sensor (488/405)/cpVenus (488/405)] (*20*). Changes in subcellular NAD^+ levels were analyzed by normalizing the values relative to undifferentiated or vehicle treated 3T3-L1 cells. All experiments were performed a minimum of three times with independent biological replicates to ensure reproducibility and a statistical significance of at least $P < 0.05$. Statistical differences between control and experimental samples were determined using ANOVA or Student's *t* test. All experimental groups that were compared had similar variance as determined by the standard deviation of the biological replicates within each group.

Permeabilization of cells to NAD^+

3T3-L1 cells expressing a sensor and the corresponding cpVenus-only control were cultured as described above. To generate NAD^+ dose-response curves for the sensors, the cells were trypsinized and suspended with FluoroBrite media containing 10% FBS and 1% penicillin/streptomycin. The cells were then permeabilized with 0.001% digitonin while exposed to the indicated amounts of NAD^+ with incubation at RT for 15 min. The samples were subjected to flow cytometry and analyzed as described above. All of the values were plotted relative to the values obtained using 10 μM NAD^+ from 8 replicates. For image analysis, the cells were cultured in chambered cover slips as described above. After acquiring images for untreated conditions, 0.001% digitonin and the indicated amount of NAD^+ were added to the media, equilibrated for 15 min to obtain NAD^+-dependent changes in signal. The images were analyzed as described above.

Quantification of intracellular NAD^+ levels

To determine the intracellular NAD^+ levels, the standard curve generated from the NAD^+ permeabilization assays described above were fitted to a sigmoidal regression model using GraphPad Prism 7 $\left\{y = \min + \left[\frac{\max - \min}{1+10^{((\log IC50 - x)\ x\ \text{Hillslope})}}\right]\right\}$. The ratiometric values relative to 10 μM NAD^+ were entered into the equation as a y value to calculate the intracellular (nuclear or cytoplasmic) NAD^+ levels. An average of 32 replicates from 11 independent experiments were interpolated to obtain values for *x*. To measure the changes in NAD^+ levels under different experimental conditions, the fluorescence ratio was measured using flow cytometry, as described above, and normalized to the control conditions (e.g., undifferentiated 3T3-L1). The NAD^+ concentrations were then determined from the standard curve using ratiometric values in comparison to the values from undifferentiated 3T3-L1. For the estimation of cytoplasmic NAD^+ levels at 8 hours postdifferentiation upon *Nmnat2* knockdown, the fluorescence ratio was measured using flow cytometry as described above, and the relative NAD^+ level compared to the control knockdown was determined. The estimated NAD^+ concentration was calculated based on the assumption that the cytoplasmic NAD^+ concentration at 8 hours postdifferentiation in control knockdown cells were similar to the measured cytoplasmic NAD^+ levels in 3T3-L1 cells at 8 hours of differentiation.

Analysis of metabolic flux

3T3-L1 cells were grown to confluence, and then grown for another 2 days under contact inhibition. Induction of adipogenesis was achieved as described above until indicated time points. To quantify different mass isotopomers of intracellular citrate by GC/MS (*54*), the cells were washed with PBS and incubated in medium containing an isotopically enriched nutrient (i.e., D[U-^{13}C] glucose and unlabeled glutamine for measuring glucose flux) for 1 min or 5 min. Labeled cells were then rinsed with ice-cold 0.9% saline and lysed with three freeze-thaw cycles in cold 50% methanol/50% water. The lysates were centrifuged to remove precipitated proteins and a standard (50 nmol of sodium 2-oxobutyrate) was added. The samples were then evaporated and derivatized using tertbutyldimethylsilyl (TBDMS, Sigma) (*55*). One microliter of the derivatized sample was injected into an Agilent 6970 gas chromatograph equipped with a fused silica capillary GC column and networked to an Agilent 5973 mass selective detector. Retention times of citrate were validated using pure standards. The abundance of the citrate ions was monitored at *m/z* 459, pyruvate at *m/z* 174-177, and lactate at *m/z* 261-264. The measured distribution of mass isotopomers was corrected for the natural abundance of ^{13}C. M+2 indicates the percent enrichment of citrate, two carbons of which were ^{13}C-labeled, providing a measure of glucose flux through the TCA cycle.

Analysis of lactate secretion

3T3-L1 cells were cultured in 6-well plates as described above. siRNAs were transfected 48 hours prior to the experiments and the cells were differentiated as described above for the indicated times. The media was collected and the assay was performed using a glycolysis cell-based assay kit (Cayman Chemical, 600450) following the manufacturer's instructions.

NMNAT2 expression in cancer cells

The expression profiles of *NMNAT2* in different cancer cells was determined based on TPM values from the Cancer Cell Line Encyclopedia (CCLE). CCLE data was downloaded from the web-based omics platform OASIS (http://www.oasis-genomics.org/).

Cell proliferation assays

SH-SY5Y cells expressing Dox-inducible shRNAs targeting luciferase or *NMNAT2* were plated at a density of 1×10^5 cells per well in 6-well plates and were induced using 1 μg/ml doxycycline added to the medium (Day 0). After 24 hours, the medium was removed and replaced with fresh medium containing 1 μg/ml of doxycycline. The cells were grown until the indicated time points, with replacement of the medium every 48 hours. The cells were then fixed with 10% formaldehyde and stained with 0.1% crystal violet in 75 mM phosphoric acid. After washing with a copious amount of water, the crystal violet was extracted from the cells using 10% acetic acid and measured as absorbance at 562 nm.

REFERENCES AND NOTES

1. C. Lu, C. B. Thompson, Metabolic regulation of epigenetics. *Cell Metab.* **16**, 9–17 (2012). doi: 10.1016/j.cmet.2012.06.001; pmid: 22768835
2. A. E. Boukouris, S. D. Zervopoulos, E. D. Michelakis, Metabolic enzymes moonlighting in the nucleus: Metabolic regulation of gene transcription. *Trends Biochem. Sci.* **41**, 712–730 (2016). doi: 10.1016/j.tibs.2016.05.013; pmid: 27345518
3. J. A. van der Knaap, C. P. Verrijzer, Undercover: Gene control by metabolites and metabolic enzymes. *Genes Dev.* **30**, 2345–2369 (2016). doi: 10.1101/gad.289140.116; pmid: 27881599
4. A. Chiarugi, C. Dölle, R. Felici, M. Ziegler, The NAD metabolome—a key determinant of cancer cell biology. *Nat. Rev. Cancer* **12**, 741–752 (2012). doi: 10.1038/nrc3340; pmid: 23018234
5. B. A. Gibson, W. L. Kraus, New insights into the molecular and cellular functions of poly(ADP-ribose) and PARPs. *Nat. Rev. Mol. Cell Biol.* **13**, 411–424 (2012). doi: 10.1038/nrm3376; pmid: 22713970
6. K. W. Ryu, D. S. Kim, W. L. Kraus, New facets in the regulation of gene expression by ADP-ribosylation and poly(ADP-ribose) polymerases. *Chem. Rev.* **115**, 2453–2481 (2015). doi: 10.1021/cr5004248; pmid: 25575290
7. R. H. Houtkooper, E. Pirinen, J. Auwerx, Sirtuins as regulators of metabolism and healthspan. *Nat. Rev. Mol. Cell Biol.* **13**, 225–238 (2012). doi: 10.1038/nrm3293; pmid: 22395773
8. A. G. Cristancho, M. A. Lazar, Forming functional fat: A growing understanding of adipocyte differentiation. *Nat. Rev. Mol. Cell Biol.* **12**, 722–734 (2011). doi: 10.1038/nrm3198; pmid: 21952300
9. R. Siersbæk, R. Nielsen, S. Mandrup, Transcriptional networks and chromatin remodeling controlling adipogenesis. *Trends Endocrinol. Metab.* **23**, 56–64 (2012). doi: 10.1016/j.tem.2011.10.001; pmid: 22079269
10. E. D. Rosen, O. A. MacDougald, Adipocyte differentiation from the inside out. *Nat. Rev. Mol. Cell Biol.* **7**, 885–896 (2006). doi: 10.1038/nrm2066; pmid: 17139329
11. K. E. Wellen *et al.*, ATP-citrate lyase links cellular metabolism to histone acetylation. *Science* **324**, 1076–1080 (2009). doi: 10.1126/science.1164097; pmid: 19461003
12. J. R. Revollo, A. A. Grimm, S. Imai, The NAD biosynthesis pathway mediated by nicotinamide phosphoribosyltransferase regulates Sir2 activity in mammalian cells. *J. Biol. Chem.* **279**, 50754–50763 (2004). doi: 10.1074/jbc.M408388200; pmid: 15381699
13. Y. Li *et al.*, Nicotinamide phosphoribosyltransferase (Nampt) affects the lineage fate determination of mesenchymal stem cells: A possible cause for reduced osteogenesis and increased adipogenesis in older individuals. *J. Bone Miner. Res.* **26**, 2656–2664 (2011). doi: 10.1002/jbmr.480; pmid: 21812028
14. X. Luo *et al.*, PARP-1 controls the adipogenic transcriptional program by PARylating C/EBPβ and modulating its transcriptional activity. *Mol. Cell* **65**, 260–271 (2017). doi: 10.1016/j.molcel.2016.11.015; pmid: 28107648
15. H. Green, O. Kehinde, An established preadipose cell line and its differentiation in culture. II. Factors affecting the adipose

conversion. *Cell* **5**, 19–27 (1975). doi: 10.1016/0092-8674(75)90087-2; pmid: 165899
16. M. S. Rodeheffer, K. Birsoy, J. M. Friedman, Identification of white adipocyte progenitor cells in vivo. *Cell* **135**, 240–249 (2008). doi: 10.1016/j.cell.2008.09.036; pmid: 18835024
17. R. L. Van, C. E. Bayliss, D. A. Roncari, Cytological and enzymological characterization of adult human adipocyte precursors in culture. *J. Clin. Invest.* **58**, 699–704 (1976). doi: 10.1172/JCI108516; pmid: 956396
18. R. Siersbæk *et al*., Dynamic rewiring of promoter-anchored chromatin loops during adipocyte differentiation. *Mol. Cell* **66**, 420–435.e5 (2017). doi: 10.1016/j.molcel.2017.04.010; pmid: 28475875
19. R. Siersbæk *et al*., Extensive chromatin remodelling and establishment of transcription factor 'hotspots' during early adipogenesis. *EMBO J.* **30**, 1459–1472 (2011). doi: 10.1038/emboj.2011.65; pmid: 21427703
20. X. A. Cambronne *et al*., Biosensor reveals multiple sources for mitochondrial NAD^+. *Science* **352**, 1474–1477 (2016). doi: 10.1126/science.aad5168; pmid: 27313049
21. M. F. Langelier, D. D. Ruhl, J. L. Planck, W. L. Kraus, J. M. Pascal, The Zn3 domain of human poly(ADP-ribose) polymerase-1 (PARP-1) functions in both DNA-dependent poly (ADP-ribose) synthesis activity and chromatin compaction. *J. Biol. Chem.* **285**, 18877–18887 (2010). doi: 10.1074/jbc.M110.105668; pmid: 20388712
22. Y. Sasaki, T. Nakagawa, X. Mao, A. DiAntonio, J. Milbrandt, NMNAT1 inhibits axon degeneration via blockade of SARM1-mediated NAD^+ depletion. *eLife* **5**, e19749 (2016). doi: 10.7554/eLife.19749; pmid: 27735788
23. J. Yoshino, K. F. Mills, M. J. Yoon, S. Imai, Nicotinamide mononucleotide, a key NAD(+) intermediate, treats the pathophysiology of diet- and age-induced diabetes in mice. *Cell Metab.* **14**, 528–536 (2011). doi: 10.1016/j.cmet.2011.08.014; pmid: 21982712
24. Z. Liu, W. L. Kraus, Catalytic-independent functions of PARP-1 determine Sox2 pioneer activity at intractable genomic loci. *Mol. Cell* **65**, 589–603.e9 (2017). doi: 10.1016/j.molcel.2017.01.017; pmid: 28212747
25. M. V. Liberti, J. W. Locasale, The Warburg effect: How does it benefit cancer cells? *Trends Biochem. Sci.* **41**, 211–218 (2016). doi: 10.1016/j.tibs.2015.12.001; pmid: 26778478
26. R. H. Houtkooper, C. Cantó, R. J. Wanders, J. Auwerx, The secret life of NAD+: An old metabolite controlling new metabolic signaling pathways. *Endocr. Rev.* **31**, 194–223 (2010). doi: 10.1210/er.2009-0026; pmid: 20007326
27. M. Zaccolo, T. Pozzan, Discrete microdomains with high concentration of cAMP in stimulated rat neonatal cardiac myocytes. *Science* **295**, 1711–1715 (2002). doi: 10.1126/science.1069982; pmid: 11872839
28. M. F. Leite *et al*., Nuclear and cytosolic calcium are regulated independently. *Proc. Natl. Acad. Sci. U.S.A.* **100**, 2975–2980 (2003). doi: 10.1073/pnas.0536590100; pmid: 12606721
29. R. H. Wright *et al*., ADP-ribose-derived nuclear ATP synthesis by NUDIX5 is required for chromatin remodeling. *Science* **352**, 1221–1225 (2016). doi: 10.1126/science.aad9335; pmid: 27257257
30. V. Bulusu *et al*., Acetate Recapturing by Nuclear Acetyl-CoA Synthetase 2 Prevents Loss of Histone Acetylation during Oxygen and Serum Limitation. *Cell Rep.* **18**, 647–658 (2017). doi: 10.1016/j.celrep.2016.12.055; pmid: 28099844
31. K. E. Knockenhauer, T. U. Schwartz, The Nuclear Pore Complex as a Flexible and Dynamic Gate. *Cell* **164**, 1162–1171 (2016). doi: 10.1016/j.cell.2016.01.034; pmid: 26967283
32. H. Lee, W. C. DeLoache, J. E. Dueber, Spatial organization of enzymes for metabolic engineering. *Metab. Eng.* **14**, 242–251 (2012). doi: 10.1016/j.ymben.2011.09.003; pmid: 21946160
33. J. Ovádi, V. Saks, On the origin of intracellular compartmentation and organized metabolic systems. *Mol. Cell. Biochem.* **256**, 5–12 (2004). doi: 10.1023/B:MCBI.0000009855.14648.2c; pmid: 14977166
34. T. Zhang *et al*., Regulation of poly(ADP-ribose) polymerase-1-dependent gene expression through promoter-directed recruitment of a nuclear NAD+ synthase. *J. Biol. Chem.* **287**, 12405–12416 (2012). doi: 10.1074/jbc.M111.304469; pmid: 22334709
35. T. Zhang *et al*., Enzymes in the NAD+ salvage pathway regulate SIRT1 activity at target gene promoters. *J. Biol. Chem.* **284**, 20408–20417 (2009). doi: 10.1074/jbc.M109.016469; pmid: 19478080
36. P. M. Kekenes-Huskey, C. E. Scott, S. Atalay, Quantifying the Influence of the Crowded Cytoplasm on Small Molecule Diffusion. *J. Phys. Chem. B* **120**, 8696–8706 (2016). doi: 10.1021/acs.jpcb.6b03887; pmid: 27327486
37. J. L. Feldman *et al*., Kinetic and Structural Basis for Acyl-Group Selectivity and NAD(+) Dependence in Sirtuin-Catalyzed Deacylation. *Biochemistry* **54**, 3037–3050 (2015). doi: 10.1021/acs.biochem.5b00150; pmid: 25897714
38. J. E. Kim, J. Chen, Z. Lou, DBC1 is a negative regulator of SIRT1. *Nature* **451**, 583–586 (2008). doi: 10.1038/nature06500; pmid: 18235501
39. F. Picard *et al*., Sirt1 promotes fat mobilization in white adipocytes by repressing PPAR-gamma. *Nature* **429**, 771–776 (2004). doi: 10.1038/nature02583; pmid: 15175761
40. R. Mayoral *et al*., Adipocyte SIRT1 knockout promotes PPARγ activity, adipogenesis and insulin sensitivity in chronic-HFD and obesity. *Mol. Metab.* **4**, 378–391 (2015). doi: 10.1016/j.molmet.2015.02.007; pmid: 25973386
41. R. K. Gupta *et al*., Zfp423 expression identifies committed preadipocytes and localizes to adipose endothelial and perivascular cells. *Cell Metab.* **15**, 230–239 (2012). doi: 10.1016/j.cmet.2012.01.010; pmid: 22326224
42. M. Y. Kim, S. Mauro, N. Gévry, J. T. Lis, W. L. Kraus, NAD+-dependent modulation of chromatin structure and transcription by nucleosome binding properties of PARP-1. *Cell* **119**, 803–814 (2004). doi: 10.1016/j.cell.2004.11.002; pmid: 15607977
43. K. L. Meerbrey *et al*., The pINDUCER lentiviral toolkit for inducible RNA interference in vitro and in vivo. *Proc. Natl. Acad. Sci. U.S.A.* **108**, 3665–3670 (2011). doi: 10.1073/pnas.1019736108; pmid: 21307310
44. GTEx Consortium, The Genotype-Tissue Expression (GTEx) pilot analysis: Multitissue gene regulation in humans. *Science* **348**, 648–660 (2015). doi: 10.1126/science.1262110; pmid: 25954001
45. M. Kininis *et al*., Genomic analyses of transcription factor binding, histone acetylation, and gene expression reveal mechanistically distinct classes of estrogen-regulated promoters. *Mol. Cell. Biol.* **27**, 5090–5104 (2007). doi: 10.1128/MCB.00083-07; pmid: 17515612
46. R. Krishnakumar *et al*., Reciprocal binding of PARP-1 and histone H1 at promoters specifies transcriptional outcomes. *Science* **319**, 819–821 (2008). doi: 10.1126/science.1149250; pmid: 18258916
47. X. Luo, M. Chae, R. Krishnakumar, C. G. Danko, W. L. Kraus, Dynamic reorganization of the AC16 cardiomyocyte transcriptome in response to TNFα signaling revealed by integrated genomic analyses. *BMC Genomics* **15**, 155 (2014). doi: 10.1186/1471-2164-15-155; pmid: 24564208
48. S. Zhong *et al*., High-throughput illumina strand-specific RNA sequencing library preparation. *Cold Spring Harb. Protoc.* 10.1101/pdb.prot5652 (2011). doi: 10.1101/pdb.prot5652; pmid: 21807852
49. S. Andrews, FastQC (2015); www.bioinformatics.babraham.ac.uk/projects/fastqc.
50. D. Kim *et al*., TopHat2: Accurate alignment of transcriptomes in the presence of insertions, deletions and gene fusions. *Genome Biol.* **14**, R36 (2013). doi: 10.1186/gb-2013-14-4-r36; pmid: 23618408
51. C. Trapnell *et al*., Transcript assembly and quantification by RNA-Seq reveals unannotated transcripts and isoform switching during cell differentiation. *Nat. Biotechnol.* **28**, 511–515 (2010). doi: 10.1038/nbt.1621; pmid: 20436464
52. S. Wingett *et al*., HiCUP: Pipeline for mapping and processing Hi-C data. *F1000Res* **4**, 1310 (2015). pmid: 26835000
53. E. Yaffe, A. Tanay, Probabilistic modeling of Hi-C contact maps eliminates systematic biases to characterize global chromosomal architecture. *Nat. Genet.* **43**, 1059–1065 (2011). doi: 10.1038/ng.947; pmid: 22001755
54. A. R. Mullen *et al*., Reductive carboxylation supports growth in tumour cells with defective mitochondria. *Nature* **481**, 385–388 (2011). doi: 10.1038/nature10642; pmid: 22101431
55. T. Cheng *et al*., Pyruvate carboxylase is required for glutamine-independent growth of tumor cells. *Proc. Natl. Acad. Sci. U.S.A.* **108**, 8674–8679 (2011). doi: 10.1073/pnas.1016627108; pmid: 21555572

ACKNOWLEDGMENTS

We thank B. Gibson and A. Lee for intellectual input and critical comments on this manuscript. We also thank X. Cambronne and M. Cohen for the cpVenus-based NAD^+ sensors and R. Gupta for help with the isolation of SVF cells and the experiments conducted with them. **Funding:** This work was supported by a grant from the NIH/NIDDK (R01 DK058110) and funds from the Cecil H. and Ida Green Center for Reproductive Biology Sciences Endowment to W.L.K., as well as grants from the NIH/NCI (R35 CA22044901) and the Howard Hughes Medical Institute Faculty Scholars Program to R.J.D. **Author contributions:** K.W.R. and W.L.K. conceived this project and developed it with input from R.J.D. K.W.R. and W.L.K. designed the experiments and oversaw their execution. K.W.R. performed most of the experiments and analyzed the data, with assistance as follows: T.N. analyzed the RNA-seq data, R.J.D. and J.K. performed the glucose flux experiments and helped analyze the results, and S.C. performed replicates of some of the experiments to confirm the results. K.W.R. prepared the initial drafts of the figures and text, which were edited and finalized by W.L.K. with input from the other authors. W.L.K secured funding to support this project and provided intellectual support for all aspects of the work. **Competing interests:** W.L.K. is a founder of and consultant for Ribon Therapeutics. W.L.K. is an inventor on U.S. patent 9,599,606 held by UT Southwestern Medical Center that covers the ADP-ribose detection reagents. **Data and materials availability:** The new genomic data sets generated for these studies are available from the NCBI's GEO database under accession number GSE96764. The *Nmnat1* floxed mice are available from the European Conditional Mouse Mutagenesis Program (EUCOMM) under a material transfer agreement with the European Conditional Mouse Mutagenesis Program (EMMA). The ADP-ribose detection reagents, which are licensed to and sold by Millipore, are available from W.L.K. under a material transfer agreement with UT Southwestern Medical Center. The fluorescent NAD^+ biosensors are available from M. Cohen under a material transfer agreement with the Oregon Health & Science University.

SUPPLEMENTARY MATERIALS

www.sciencemag.org/content/360/6389/eaan5780/suppl/DC1
Figs. S1 to S17
List of Primers
References (*56*–*58*)

3 May 2017; resubmitted 14 December 2017
Accepted 16 March 2018
10.1126/science.aan5780

RESEARCH ARTICLE SUMMARY

MOLECULAR MOTORS

High-resolution cryo-EM analysis of the yeast ATP synthase in a lipid membrane

Anurag P. Srivastava,* Min Luo,* Wenchang Zhou, Jindrich Symersky, Dongyang Bai, Melissa G. Chambers, José D. Faraldo-Gómez, Maofu Liao,† David M. Mueller†

INTRODUCTION: The mitochondrial adenosine triphosphate (ATP) synthase is the enzyme responsible for the synthesis of more than 90% of the ATP produced by mammalian cells under aerobic conditions. The chemiosmotic mechanism, proposed by Peter Mitchell, states that the enzyme transduces the energy of a proton gradient, generated by the electron transport chain, into the major energy currency of the cell, ATP. The enzyme is a large (about 600,000 Da, in the monomer state) multisubunit complex, with a water soluble complex (F_1) that contains three active sites and a membrane complex (F_o) that contains the proton translocation pathway, principally comprised of the a subunit and a ring of 10 c subunits, the c_{10}-ring (10 in yeast, 8 in mammals). F_1 has a central rotor that, at one end, is within the core of F_1 and, at the other end, is connected to the c_{10}-ring of F_o. During ATP synthesis, the c_{10}-ring rotates, driven by the movement of protons from the cytosol to the mitochondrion, and in turn, the rotor rotates within F_1 in steps of 120°. The rotation of the rotor causes conformational changes in the catalytic sites, which provides the energy for the phosphorylation of adenosine diphosphate (ADP), as first proposed in the binding-change hypothesis by Paul Boyer. The peripheral stalk acts as a stator connecting F_1 with F_o and prevents the futile rotation of F_1 as the rotor spins within it.

RATIONALE: Structural studies of the ATP synthase have made steady progress since the structure of the F_1 complex was described in pioneering work by John Walker. However, obtaining a high-resolution structure of the intact ATP synthase is challenging because it is inherently dynamic. To overcome this conformational heterogeneity, we locked the yeast mitochondrial rotor in a single conformation by fusing a subunit of the stator with a subunit of the rotor, also called the central stalk. The engineered ATP synthase was expressed in yeast and reconstituted into nanodiscs. This facilitated structure determination by cryo–electron microscopy (cryo-EM) under near native conditions.

RESULTS: Single-particle cryo-EM enabled us to determine the structures of the membrane-embedded monomeric yeast ATP synthase in the presence and absence of the inhibitor oligomycin at 3.8- and 3.6-Å resolution, respectively. The fusion between the rotor and stator caused a twisting of the rotor and a 9° rotation of the c_{10}-ring, in the direction of ATP synthesis, relative to the putative resting state. This twisted conformation likely represents an intermediate state in the ATP synthesis reaction cycle. The structure also shows two proton half-channels formed largely by the a subunit that abut the c_{10}-ring and suggests a mechanism that couples transmembrane proton movement to c_{10}-ring rotation. The cryo-EM density map indicates that oligomycin is bound to at least four sites on the surface of the F_o c_{10}-ring that is exposed to the lipid bilayer; this is supported by binding free-energy molecular dynamics calculations. The sites of oligomycin-resistant mutations in the a subunit suggest that changes in the side-chain configuration of the c subunits at the a-c subunit interface are transmitted through the entire c_{10}-ring.

ON OUR WEBSITE

Read the full article at http://dx.doi.org/10.1126/science.aas9699

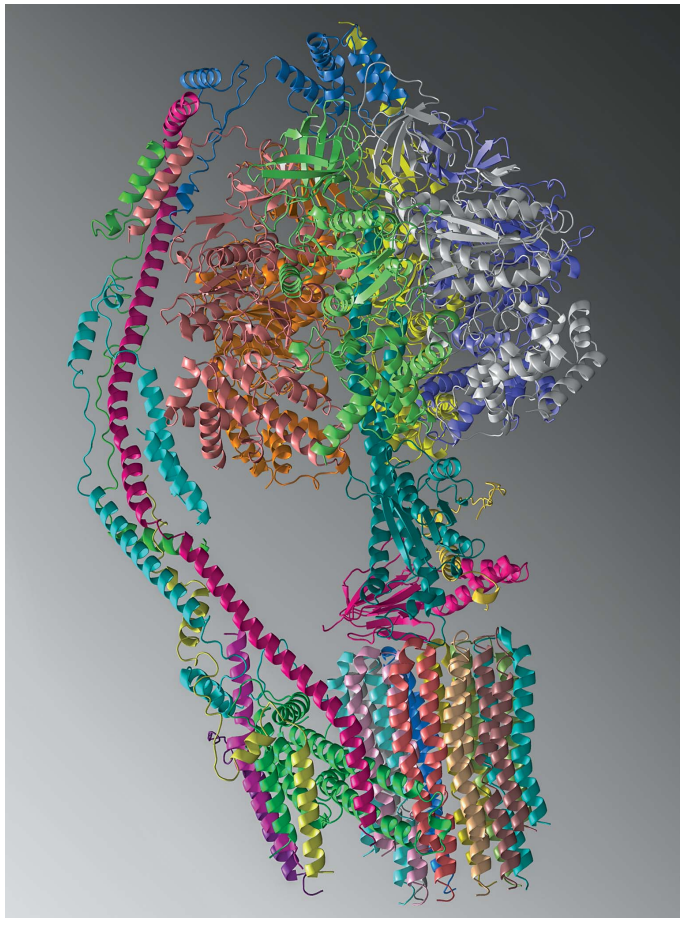

Structure of the monomeric yeast ATP synthase, as determined by cryo-EM, shown as a ribbon diagram. The subunits are shown in different colors. The F_1 complex is located at the top center and is composed of six subunits forming a nearly spherical structure and three subunits comprising the central stalk, or rotor. The F_o complex is located at the bottom, with the identity of the c_{10}-ring clearly seen. The peripheral stalk, or stator, is on the left, and the rotor is in the center of the molecule, extending into F_1.

CONCLUSION: Our results provide a high-resolution structure of the complete monomeric form of the mitochondrial ATP synthase. The structure provides an understanding of the mechanism of inhibition by oligomycin and suggests how extragenic mutations can cause resistance to this inhibitor. The approach presented in this study paves the way for structural characterization of other functional states of the ATP synthase, which is essential for understanding its functions in physiology and disease. ■

The list of author affiliations is available in the full article online.
*These authors contributed equally to this work.
†Corresponding author. Email: david.mueller@rosalindfranklin.edu (D.M.M.); maofu_liao@hms.harvard.edu (M.Li.)
Cite this article as A. P. Srivastava *et al.*, *Science*, **360**, eaas9699 (2018).
DOI: 10.1126/science.aas9699

RESEARCH ARTICLE

MOLECULAR MOTORS

High-resolution cryo-EM analysis of the yeast ATP synthase in a lipid membrane

Anurag P. Srivastava,[1]* Min Luo,[2]* Wenchang Zhou,[3] Jindrich Symersky,[1] Dongyang Bai,[1] Melissa G. Chambers,[2] José D. Faraldo-Gómez,[3] Maofu Liao,[2]† David M. Mueller[1]†

Mitochondrial adenosine triphosphate (ATP) synthase comprises a membrane embedded F_o motor that rotates to drive ATP synthesis in the F_1 subunit. We used single-particle cryo–electron microscopy (cryo-EM) to obtain structures of the full complex in a lipid bilayer in the absence or presence of the inhibitor oligomycin at 3.6- and 3.8-angstrom resolution, respectively. To limit conformational heterogeneity, we locked the rotor in a single conformation by fusing the F6 subunit of the stator with the δ subunit of the rotor. Assembly of the enzyme with the F6-δ fusion caused a twisting of the rotor and a 9° rotation of the F_o c_{10}-ring in the direction of ATP synthesis, relative to the structure of isolated F_o. Our cryo-EM structures show how F_1 and F_o are coupled, give insight into the proton translocation pathway, and show how oligomycin blocks ATP synthesis.

The mitochondrial adenosine triphosphate (ATP) synthase is composed of two distinct molecular motors, F_1 and F_o (Fig. 1 and Movie 1). F_1 includes three catalytic subunits around a central rotor that rotates to effect ATP synthesis. F_o is a transmembrane proton turbine that includes the c_{10}-ring, a ring of 10 c subunits, which rotates in steps of 36° as it moves protons from the cytosol to the matrix space, down an electrochemical gradient (*1*). The c_{10}-ring in F_o is physically coupled to the rotor in F_1, and therefore, proton translocation drives the synthesis of ATP. F_1 is held in place by a peripheral stator that prevents the rotation of the body of F_1 and restricts the wobbling of its central rotor relative to the c_{10}-ring. Relative to the stator, the F_1 rotor can be in three distinct positions (rotomers), whereas a revolution of the c_{10}-ring involves 10 discrete steps. This combination of 120° steps of the rotor and 36° steps of the c_{10}-ring results in multiple conformations of the ATP synthase during the reaction cycle. Furthermore, the ATP synthase can form homodimers (*2*–*4*), which further increases the number of possible conformations of the enzyme complex, making the analysis of the reaction mechanism on a molecular level challenging. Here we have used a genetic method to restrict the number of conformations, allowing us to study the monomeric form of the yeast ATP synthase. We reconstituted the monomeric enzyme complex into a lipid bilayer formed in nanodiscs to enable structural analysis under near native conditions.

To restrict the number of conformations, we genetically fused subunit F6 of the stator to the δ subunit of the rotor. The subunits were linked by T4 lysozyme, giving a final fusion of H_2N-F6–lysozyme-δ–CO_2H (fig. S1). The mitochondrial leader peptide from the β subunit (ATP2) was added to direct the import of the protein into the mitochondria, and the expression was controlled with the ATP2 transcriptional elements. The plasmid containing this fusion was integrated into the genome of a yeast strain that is devoid of the genes encoding F6 (ATP14) and the δ subunit (ATP16). The gene encoding ATP2 was also deleted in the strain, but this was complemented by integration of a vector into the genome that contains the β subunit with a His_6 tag on the amino terminus, allowing rapid purification of the enzyme.

We performed single-particle cryo–electron microscopy (cryo-EM) analysis on the nanodisc-reconstituted ATP synthase both with and without the inhibitor oligomycin. Three preparations of nanodiscs (*5*) were used, which differed in their lipid content (see methods). Overall, the cryo-EM density that gave rise to the model of the F_1F_o ATP synthase was more complete under the conditions with oligomycin than without, but the structures were similar. Thus, we will confine the discussion of the overall structure to the structure with bound oligomycin. To allow analysis of the proton translocation mechanism, the refinement was focused on F_o, which improved resolution of this region but also resulted in poorer resolution of the other parts of the enzyme. For the F_o regions, we compare the structures with and without bound oligomycin.

Overall structure of the ATP synthase

The cryo-EM structures of the yeast ATP synthase in nanodiscs were determined to overall resolutions of 3.6- and 3.8-Å for the entire enzyme complex in the absence or presence of oligomycin, respectively (see Fig. 2, Table 1, and figs. S1 to S5). The EM density for F_o is weaker and of lower resolution than that of F_1, likely owing to flexibility between these domains. Hence, F_o-focused three-dimensional (3D) classification and refinement improved the resolution and map quality. In the presence of oligomycin, the flexibility of the ATP synthase was reduced, resulting in better EM density for F_o and the stator and a greater number of residues in F_o with well-defined side-chain densities. The resolution varied between subunits and within subunits. Most residues in the F_1 subunits display excellent side-chain density, whereas the stator and F_o subunits showed varying resolutions. Many good side-chain densities could be seen for most of the components present in the cryo-EM structures, including the central stalk and c_{10}-ring. The secondary structural elements are also well resolved for the stator components. We were able to trace 27 chains in the density (Fig. 3A, Movie 2, and Table 2). The only chains that we did not see are those involved in dimerization of the ATP synthase (as this is the monomer form). The density for the T4 lysozyme molecule used to fuse F6

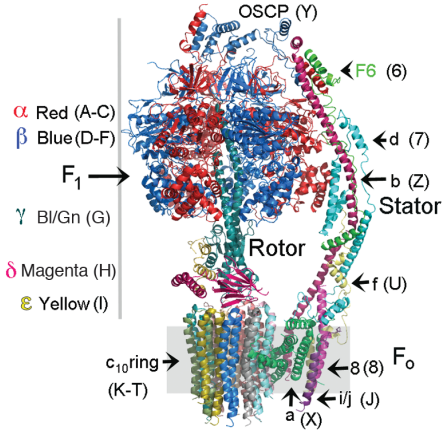

Fig. 1. Subunit composition and architecture of the monomeric yeast ATP synthase. The subunits are shown in a variety of colors to allow identification. The chain number or letter used in the PDB code is shown in parentheses. There are three α (red) and three β (blue) subunits that, with the γ (bl/gn, blue-green), δ (magenta), and ε (yellow) subunits, form F_1. The rotor is comprised of the γ, δ, and ε subunits of F_1. The core of F_o is comprised of the a subunit and the c_{10}-ring. The subunits of the stator are as shown.

[1]Department of Biological Chemistry and Molecular Biology, Chicago Medical School, Rosalind Franklin University, 3333 Green Bay Road, North Chicago, IL 60064, USA.
[2]Department of Cell Biology, Harvard Medical School, 250 Longwood Avenue, SGM 509, Boston, MA 02115, USA.
[3]Theoretical Molecular Biophysics Laboratory, National Heart, Lung, and Blood Institute, National Institutes of Health, 50 South Drive, Bethesda, MD 20892, USA.
*These authors contributed equally to this work.
†Corresponding author. Email: david.mueller@rosalindfranklin.edu (D.M.M.); maofu_liao@hms.harvard.edu (M.Li.)

with δ is seen in one of the cryo-EM maps from 3D classification (fig. S3C). Low-resolution density for the lipid nanodisc clearly delineates the membrane-embedded regions of F_o (Fig. 2).

There are three catalytic sites in F_1, each of which cycles between three states. In the first high-resolution crystal structure of the F_1 ATPase, the sites were occupied with adenosine diphosphate (ADP) or ATP and one site was empty, and thus they were named DP, TP, and E, respectively (Table 2) (*6*). The asymmetry of the catalytic sites is determined by the relative position of the γ subunit within F_1. In our cryo-EM structures, the rotor is in a single orientation, and the asymmetry of the catalytic sites is conserved. In this orientation, the stator bridges F_o with F_1 along the noncatalytic site formed by chains B (α_{TP}) and E (β_{DP}). There is contact between subunit d of the stator with α_{TP} (chain B).

The F_1 domain

The conformation of the yeast F_1 domain in the cryo-EM structures is nearly identical to that observed in the crystal structures of yeast F_1 (*7*) or yeast F_1-c_{10} (*8*, *9*), which also revealed the three distinct states of the catalytic sites DP, TP, and E. When we superimpose yeast F_1 onto the structure of yeast F_1F_o, we see that the rotor formed by the γ, δ, and ε subunits is twisted by about 9° in the direction of the rotation that leads to ATP synthesis (Fig. 3B). The twisting starts at about γ-Ile^{271}, which is in direct contact with the collar formed by the α and β subunits (*6*). At the bottom of the rotor, this twisting results in a displacement of about 5.6 Å in residues in the δ subunit. This displacement continues into the c_{10}-ring and causes a commensurate rotation of the c_{10}-ring relative to the a subunit in F_o (Fig. 3C). Although we believe that the constraint of the central stalk with the stator can mimic the twisting of the central stalk during the reaction cycle, this is a first approximation and has not been proven.

The stator domain

The stator (peripheral stalk) is composed of subunits OSCP (oligomycin sensitivity conferral protein), b, d, F6, f, i/j, and 8. Subunits OSCP, b, d, f, and F6 primarily serve as structural components of the stator. However, subunits b, d, f, i/j, and 8 are either embedded or attached to the membrane and are part of the complex purified as F_o; they may have a role in proton movement in addition to a structural role in forming the stator. Subunits b and d are similar to their homologs in the crystal structure of bovine subunits F6, b, and d [Protein Data Bank (PDB) 2CLY] (*10*); however, yeast F6 displays differences from bovine F6, including an additional helix (residues 76 to 91) at the C terminus, which adds additional interactions with the b and d subunits. Modeling of the domains of stator subunits that are part of F_o and embedded or bound to the membrane was aided by the high-resolution cryo-EM structure of yeast F_o (PDB 6B2Z) (*11*), and we did not see any major differences as compared to the reported structure.

The OSCP subunit anchors the stator at the top of F_1. As partially seen in the structure of the enzyme from the yeast *Pichia angusta* (*12*), the N terminus of the three α subunits interact to stabilize the binding of OSCP to the top of F_1 (fig. S7). The helix in α_{TP} (chain B) formed from BLys^4 to BAsn^{26} interacts with helices from F6 and the b subunit (fig. S7, region I). Furthermore, the three-helix bundle formed by residues B462 to B509 interact with two helices of the d subunit from residues 3 to 48, and a cluster of residues in OSCP ranging from 160 to 168 as well as residue 122 (region I). Residues in a random coil from α_{DP} (chain C, Gln^6 to Ser^{22}) run under and interact with OSCP (fig. S7, region III). The helix formed from residues Lys^4 to Lys^{19} in α_E (chain A) interacts with a helix and turn in OSCP formed by residues Thr^{46} to His^{78} (fig. S7, region IV). Thus, the N terminus of each α subunit makes specific contributions to the stabilization of the anchoring of OSCP to the top of F_1.

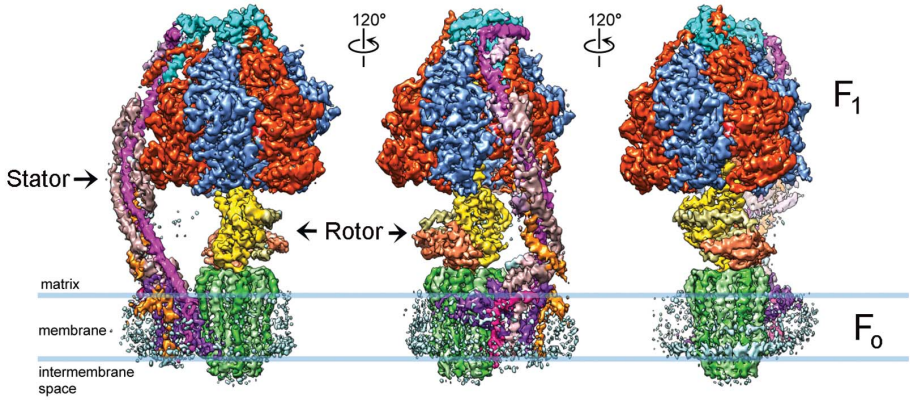

Fig. 2. Cryo-EM 3D reconstruction of nanodisc-embedded yeast ATP synthase bound with oligomycin. Three side views of the 3D reconstruction filtered to 3.8-Å resolution and rotated by 120° around the *y* axis. All subunits are differently colored. Blue lines indicate the membrane boundaries, as observed by the EM density of the lipid nanodisc.

Table 1. Statistics of the cryo-EM structures presented in this study.

Category	ATP synthase		ATP synthase with oligomycin	
Cryo-EM data collection and processing				
Electron microscope	Polara		Polara	
Voltage (kV)	300		300	
Electron dose (e^-/Å^2)	41		41	
Physical pixel (Å)	1.23		1.23	
Number of movies	5,935		2,896	
Number of particles	541,568		346,399	
	F_1F_o	F_o	F_1F_o	F_o
Number of particles for final map	160,937	109,206	104,280	104,280
Resolution (Å)	3.6	4.1	3.8	4.2
Map B-factor (Å^2)	−100	−180	−100	−200
Model refinement				
Number of protein residues	5,094	1,224	5,094	1,224
Number of side chains	5,061	1,198	5,061	1,199
Number of atoms	38,814	9,179	38,814	9,434
Geometric parameters (root mean square deviation)				
Bond length (Å)	0.007	0.008	0.009	0.003
Bond angle (°)	1.026	1.309	1.119	1.354
Ramachandran statistics				
Residues favored (%)	93.87	92.95	92.18	92.95
Residues allowed (%)	5.93	6.59	7.62	7.05
Residues disallowed (%)	0.20	0.46	0.20	0
Rotamer outliers (%)	0.15	3.23	0.36	0.21
MolProbity score	1.89	2.57	1.91	2.56
EMRinger score	1.61	0.94	1.55	0.91

The F_o domain

F_o is embedded in the inner membrane of the mitochondria. Our cryo-EM map showed clear density for the lipid bilayer in the nanodiscs (Figs. 1 and 4A). The cryo-EM density indicates that the bilayer spans about 37 Å, approximately from Pro^{49} to Phe^{74} on the outer helices of the c subunits. Phe^{74} is the last residue in helix 2 (residues 42 to 74) and is considerably shorter than helix 1 (residues 1 to 40).

The a subunit is adjacent to the c_{10}-ring and contributes to form the proton-conduction pathway from the cytosolic side of the mitochondria to protonation sites in the c_{10}-ring and from these sites to the matrix space (*13*–*15*). The protonation and deprotonation events at the interface between the a subunit and the c_{10}-ring couple the translocation of protons to the rotation of the c_{10}-ring and thus effect ATP synthesis. We obtained the near-atomic resolution F_o maps for the enzyme without bound oligomycin and with oligomycin, and the structural models from these maps are nearly identical. This suggests that oligomycin binding does not alter the overall structure of F_o.

The structure of the c_{10}-ring is nearly identical to that observed in a crystal structure of the isolated ring (*16*). (We have numbered the c subunits relative to the a subunit, with c^1Glu^{59} corresponding to the first c subunit that has interactions with the a subunit. The c subunits are numbered sequentially in the direction of rotation during ATP synthesis; refer to Fig. 3C.) Glu^{59} is the proton acceptor and donor that is responsible for net proton movement during the catalytic cycle. The side chain of Glu^{59} has been shown to be in one of two conformations: a "closed" conformation, which was suggested to represent the protonated form when in the membrane, and an "open" conformation, which was proposed to be present only at the a-c interface and to represent the state in which protonation and deprotonation occurs (*16*, *17*). We see four instances where Glu^{59} is in the open conformation in the membrane phase, suggesting that the closed conformation is not a necessary conformation of the protonated side chain in the membrane phase (fig. S8).

The structure of dimeric yeast F_o was solved by cryo-EM after stripping off F_1 by using NaBr (*11*). This structure likely represents the "ground state," as it is free from strain caused by assembly of the F_1F_o ATP synthase complex. We superimposed the F_o region from the ground state onto the F_o region from our native structures using the a and b subunits as the anchor (Fig. 3C). This analysis indicates that the c_{10}-ring of the native structure, relative to the a subunit, is rotated about 9° in the direction of ATP synthesis, as compared to the ground state. This is consistent with the rotation that we observed in the F_1 rotor, when comparing our structure to that of F_1 alone.

Arg^{176} of the a subunit is the only residue that is strictly conserved (*13*) (fig. S9). It has been proposed that Arg^{176} prevents the short-circuiting of protons in the proton pathway (*18*) as well as acting as a positive pole for attraction of the charged Glu^{59} (*14*). In the isolated F_o structure (*11*) (the ground state structure), atoms in the corresponding side chains of Arg^{176} and the closest Glu^{59} (c^2Glu^{59}) are separated by 5 to 7.5 Å, whereas in our structure, the side chains move closer, to within 3.8 Å (Fig. 3D). Extrapolation on the movement of the c_{10}-ring in the direction of ATP synthesis would predict an even closer configuration of Arg^{176} and Glu^{59}, thereby creating a potential contributing force for rotation of the c_{10}-ring. This attractive force will be much reduced once the ionized $cGlu^{59}$ is protonated.

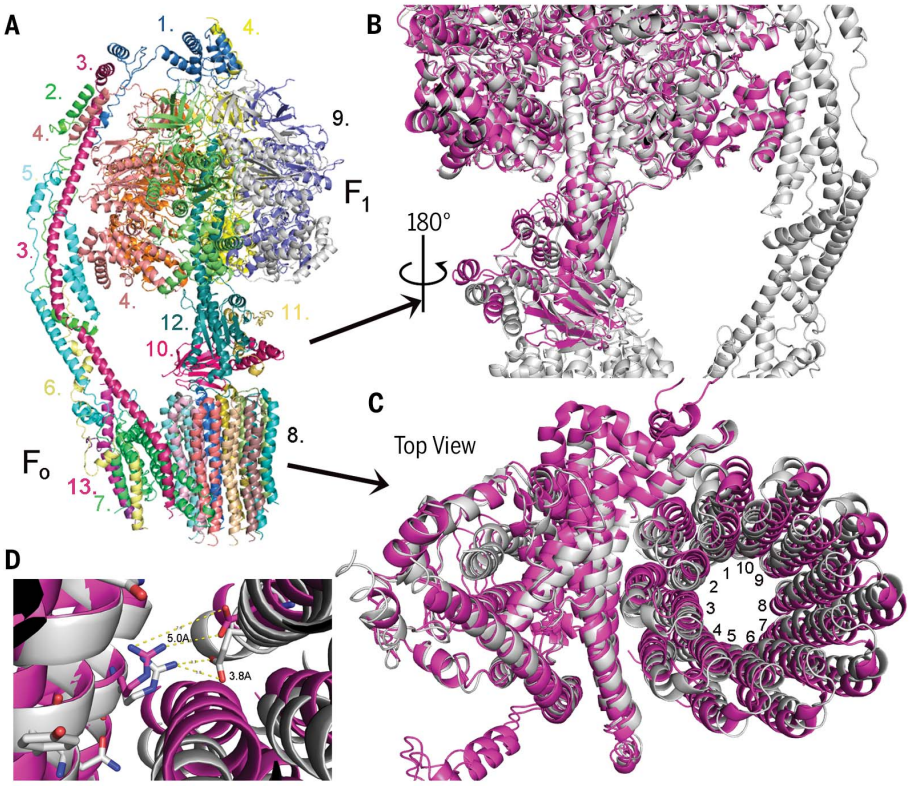

Fig. 3. Overall structure of the yeast ATP synthase. (**A**) Molecular model of the F_1F_o ATP synthase based on the cryo-EM density map. The subunits are color coded and labeled as follows: 1) OSCP, 2) F6, 3) b subunit, 4) α subunit, 5) d subunit, 6) f subunit, 7) a subunit, 8) c_{10}-subunit ring, 9) $\alpha_3\beta_3$ core, 10) δ subunit, 11) ε subunit, 12) γ subunit, and 13) i/j subunit. (**B**) Superimposition of the crystal structure of the yeast F_1 domain (magenta) onto the cryo-EM structure of yeast F_1F_o ATP synthase (gray). Three rotor subunits (γ, δ, and ε subunits) are displaced by a twisting in the counterclockwise direction. (**C**) Superimposition of the cryo-EM structure of yeast F_o (magenta, in the absence of F_1) onto the current structure of F_1F_o (gray). The c_{10}-ring is rotated by about 9° in the counterclockwise direction (the direction of ATP synthesis). The numbers indicate the c subunits numbered sequentially in the direction of rotation during ATP synthesis, relative to the a subunit. (**D**) Relative position of $aArg^{176}$ and the nearest $cGlu^{59}$ in the structure of yeast F_o (magenta) and F_1F_o (gray). The distance between the side chains of $aArg^{176}$ and $cGlu^{59}$ is reduced from about 5.0 to about 3.8 Å with the rotation of the c_{10}-ring by 9°.

The proton pathway

During ATP synthesis, protons transit from the cytosolic side of the mitochondrial membrane to protonate the c-subunit Glu^{59} closest to Arg^{176} (c^2Glu^{59}), thereby releasing this interaction. Protons must be released from c^1Glu^{59} into the matrix space (Fig. 4A), although not necessarily in concert with protonation, enabling this side chain to engage Arg^{176} following a 36° step. The hydrophilic spaces that provide pathways for protons from the cytosol and then to the matrix space, allowing protonation and later deprotonation of $cGlu^{59}$, are referred to as half-channels. Figure 4 and Movie 3 show the putative half-channels from the cytoplasm and to the matrix. Their location and identification is consistent with recent reports (*11*, *19*–*21*). The matrix-side half-channel is most obvious at the a-c interface, where the side chains of a number of residues appear to form a hydrophilic cavity that extends from c^1Glu^{59} to the surface of the membrane phase (Fig. 4, A, C, and D). $aGlu^{162}$ is an important, but not essential, residue in this pathway (*13*). The matrix half-channel extends up to the point that we have determined to be the edge of the membrane. By contrast, the cytoplasmic half-channel is formed by residues in the f, b, and a subunits. The proton-conduction pathway appears to include $aHis^{185}$ and $aGlu^{223}$ (Fig. 4, A and B). The proton-conduction pathway proceeds between helices 5 and 6 of the a subunit. $aHis^{185}$ and $aGlu^{223}$ are interchanged in the enzymes from other species but remain in comparable positions (fig. S9). The protonation of $cGlu^{59}$ likely

occurs in the transition from c^2Glu^{59} to c^3Glu^{59} and, in doing so, eliminates any charge interaction between $aArg^{176}$ and $cGlu^{59}$.

Possible role of $aGlu^{162}$ and $aGlu^{223}$

A requirement for a proton donor or acceptor in the reaction pathway is that the value of the pK_a (where K_a is the acid dissociation constant) of the donor and acceptor should be around the pH of the medium. The pH of the cytosol is around 7.0, whereas that of the matrix space during active ATP synthesis is around 8.0. Thus, the pK_a of the carboxyl of $cGlu^{59}$ should be around 7.0 at the a-subunit interface to be an effective proton carrier. If the pK_a of the carboxyl was the standard value in water, 5.0, then the carboxyl would rarely be in the protonated state, and rotation would be severely impeded during ATP synthesis. Although a low pK_a would allow the release of the proton to the matrix space during ATP synthesis, it would impede the reversal of the ATP synthase reaction—ATP hydrolysis—which is a fundamental feature of the enzyme. Thus, the pK_a of the $cGlu^{59}$ must be around 7.0 at both the sites for protonation and deprotonation to occur during ATP synthesis and hydrolysis. Although there is a report that the pK_a of the c-ring carboxylate is 7.0 (*22*), these measurements were not made under native conditions nor measured in the intact enzyme. On the basis of the structure, we suggest that $aGlu^{162}$ and $aGlu^{223}$ may play a role in shifting the pK_a of $cGlu^{59}$. Residue $aGlu^{162}$ is highly conserved across species. The corresponding residue in *Mycobacteria* is $aGln^{172}$, but just one turn away is a pair of glutamate residues, thus functionally conserving the role of $aGlu^{162}$ (fig. S9). The $cGlu^{59}$ carboxyl nearest to $aGlu^{162}$ (c^1Glu^{59}) (Fig. 4B) is thus likely to be the proton-releasing site. Rotation of the c_{10}-ring by about 9° places c^1Glu^{59} about 4 Å from $aGlu^{162}$ (fig. S10). On the cytosolic side, $aGlu^{223}$ is in a dyad interaction with $aHis^{185}$; this pair is nearly strictly conserved and likely to serve as an intermediate proton-binding site (fig. S9). Rotation of the c_{10}-ring by about 27°, facilitated by the deprotonation of c^1Glu^{59}, could bring c^2Glu^{59} close enough to interact with $aGlu^{223}$, with multiple bridging water molecules. These interactions of $aGlu^{162}$ and $aGlu^{223}$ with the side chain of $cGlu^{59}$ have the potential to shift the pK_a of the side-chain $cGlu^{59}$ up to around 7.0, where it needs to be to act as an effective proton-transfer group. There is precedence for glutamate-glutamate interactions and histidine-glutamate interactions altering the pK_a of carboxylates to around 7.0 (*23*–*26*). This hypothesis is consistent with biochemical data that show that replacements at these two positions alter the magnitude of the potential gradient that the enzyme can create with the hydrolysis of ATP (*13*, *27*, *28*). Of course, this is still hypothetical, and proof will require the structure determination of multiple intermediate states of the reaction cycle.

Inhibition by oligomycin

The crystal structure of the isolated yeast c_{10}-ring with bound oligomycin has been determined at 1.9 Å (PDB 4F4S) (*29*). Oligomycin was shown to bind to the c_{10}-ring with the inhibitor spanning the outer helices of two adjacent c subunits and centered over $cGlu^{59}$. It has been unclear whether oligomycin would bind to the c_{10}-ring in a lipid environment or to alternative sites in the ATP synthase. The cryo-EM analysis here shows densities at four sites on the c_{10}-ring where we modeled four oligomycin molecules (oligo1 to oligo4) (spanning c^5c^6, c^6c^7, c^7c^8, and c^8c^9); these densities are

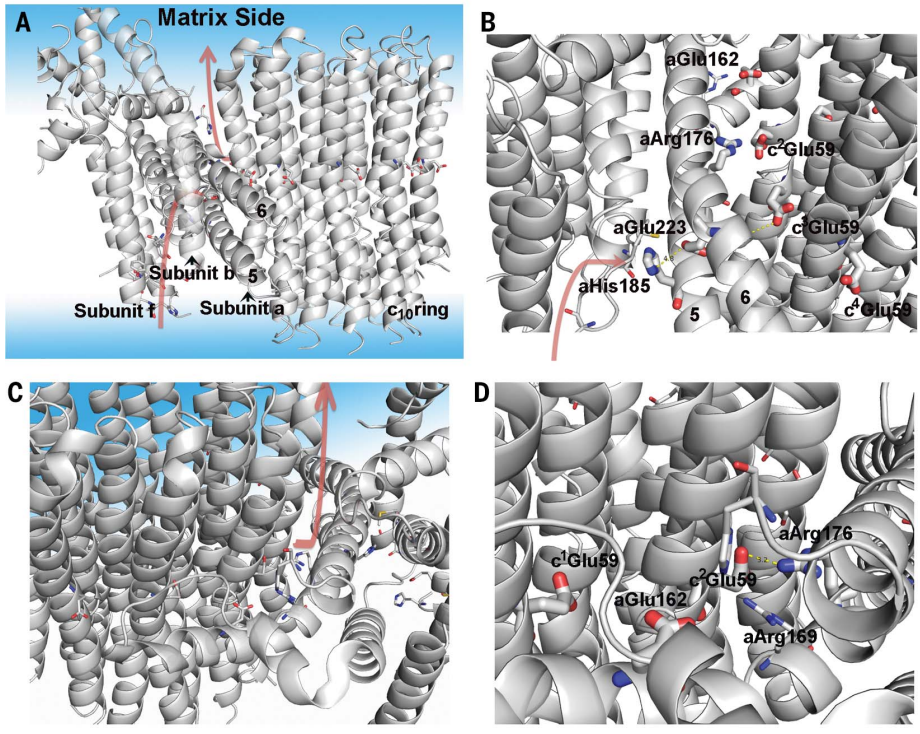

Fig. 4. Model of F_o and the proton pathways. (**A**) Overall model of F_o with subunits a, b, c, and f displayed. The aqueous phase is also displayed with a light blue coloring. The postulated proton pathways for the entry from the intermembrane space and exit to the matrix are shown with salmon-colored arrows. The protonation pathway during ATP synthesis is a path formed by subunits f, b, and a, with the final course formed by helices 5 and 6 (labeled) of the a subunit. (**B**) Side view of the entry pathway for protons during ATP synthesis, with key residues indicated (see text for discussion). (**C**) View from the top side of the proton pathway for proton exit to the matrix. (**D**) View of proton pathway from the exit site, showing helices 5 and 6 of the a subunit and the c_{10}-ring.

Table 2. Summary of subunit composition, chain names, and residues in this model. The DP, TP, and E sites in F_1 are composed of chains C and D, B and F, and A and E, respectively.

Subunit	Alias	Total number of residues	Molecular mass (kDa)	Role	Sector	Chain	Modeled residues
α		510	54.9	catalytic	F_1	A to C	4 (or 6) to 510
β		478	51.1	catalytic	F_1	D to F	6 (or 7) to 478
γ		278	30.6	catalytic	F_1	G	1 to 278
δ		138	14.6	catalytic	F_1	H	7 to 138
ε		61	6.1	catalytic	F_1	I	1 to 59
OSCP	5	195	20.9	structural	stator	Y	7 to 172
a	6	249	25.1	H^+ transfer	F_o	X	26 to 249
b	4	209	23.3	dual	F_o	Z	53 to 207
c	9	76	7.76	H^+ transfer	F_o	K to T	1 to 75 (or 76)
d	7	173	19.7	structural	stator	7	3 to 173
f		95	10.6	dual	F_o	U	1 to 85
i	j	59	6.7	H^+ transfer	F_o	J	1 to 37
F6		92	10.4	structural	stator	6	4 to 92
8	A6L	48	5.8	structural	stator	8	7 to 48

positioned in the membrane phase and at the same position where oligomycin was seen to bind in the crystal structure of the c_{10}-ring (*29*) (Fig. 5A). The density map for oligo1 to oligo4 suggests that there is some variation in the binding strength at each site. This may reflect slight differences in the conformation of the main and side chains at each binding site. There is also weak density at c^4c^5, which is at the edge of the a-c interface, but the best fit to the density with an oligomycin molecule (oligo5) places oligomycin in a much different binding mode as compared to those in the other sites (fig. S11). Furthermore, the conformation of oligo5, as modeled, is largely different from that observed previously. Likely, the weak density attributed to oligo5 is due in part to surrounding lipid molecules. Thus, we believe that this, at best, represents a minor binding mode.

To test the hypothesis that oligomycin can bind in a stable mode to the c_{10}-ring in a membrane environment, we evaluated the free energy of formation of this complex using all-atom molecular dynamics simulations (fig. S12). This binding free energy can be defined as $\Delta G_b = -k_BT \ln N + \Delta G_{int} + \Delta G_r + \Delta G_t$, where k_B is the Boltzmann constant, T is temperature, N is the number of available binding sites on the c_{10}-ring, ΔG_{int} is the free-energy difference between the associated and dissociated complex, and ΔG_r and ΔG_t are the free-energy penalties due to the loss of rotational and translational entropy of the inhibitor upon binding, respectively. The values calculated from the simulation data are (detailed in methods) $\Delta G_{int} = -6.6$ kcal/mol, $\Delta G_r = +1.6$ kcal/mol, and $\Delta G_t = +4.4$ kcal/mol, where the latter assumes that the mole fraction of oligomycin in the membrane is 0.01. For $N = 7$ (that is, the number of c subunits exposed to the membrane), the resulting value of the binding free energy, $\Delta G_b = -1.7$ kcal/mol, implies that oligomycin is about 20 times more likely to be bound to the c_{10}-ring than free in the lipid bilayer. (Note that ΔG_t would be reduced for higher oligomycin densities, and thus binding would be more favorable. For a mole fraction of 0.05, ΔG_t is +3.5 kcal/mol, and ΔG_b would range from −2.7 kcal/mol for $N = 7$ to −1.5 kcal/mol for $N = 1$, which translate into binding probabilities ranging from 90:1 to 10:1.) This energetic analysis hence supports the conclusion that oligomycin binds to the c_{10}-ring subunits exposed to the lipid bilayer. All available data therefore suggest that oligomycin inhibits the enzyme by first binding to the c_{10}-ring and thus impairs its rotation against subunit a. Likely, the c subunit with bound oligomycin is sterically prevented from entering the a-c interface, but, if it did, it would be unable to either release the bound proton or accept a proton during the catalytic cycle.

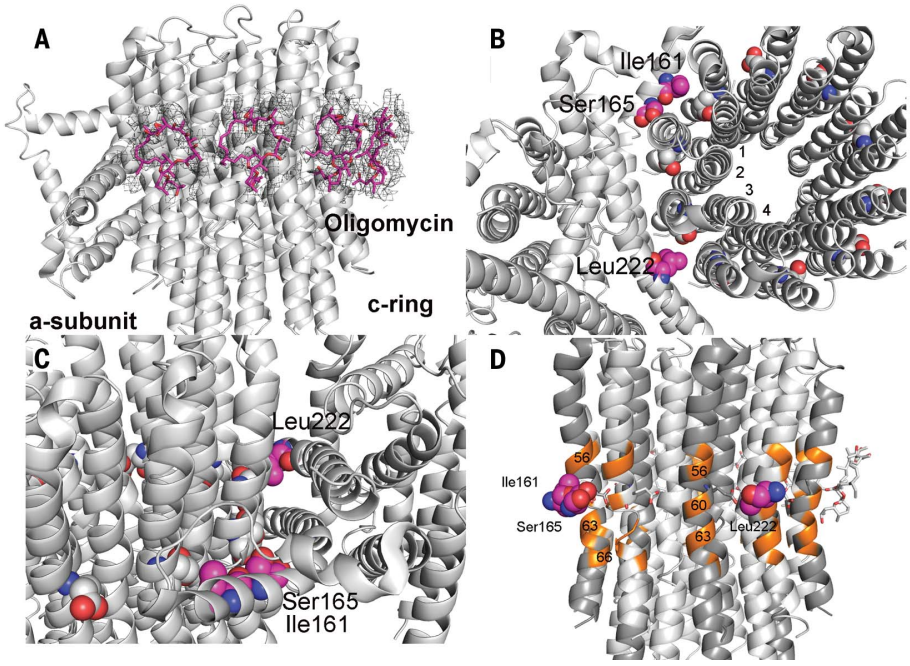

Fig. 5. Inhibition of the ATP synthase by oligomycin. (**A**) Model of oligomycin bound to the F_o. The electron density (shown at 4.5 σ) fitted with a model of an oligomycin molecule (magenta) at four superimposable positions on the c_{10}-ring. (**B**) Positions of residues in the a subunit at which replacements can confer resistance to oligomycin. The three residues Ile^{161}, Ser^{165}, and Leu^{222} in the a subunit are positioned at the interface between subunits c^1c^2 and c^3c^4 and directly in line with $cGlu^{59}$ (C) and (D). This position is precisely where oligomycin binds when the site is exposed to the membrane bilayer. (**C**) Side view of the residues in the a subunit. (**D**) Positions of residues in c subunits that interact with oligomycin. The c-subunit residues colored orange (Ala^{56}, Ala^{60}, Leu^{63}, Phe^{64}, and Leu^{66}) are a subset of residues that provide binding interactions with oligomycin (*29*). (Three of the c subunits are shaded darker gray.)

There are three sites reported in the a subunit where mutations cause yeast to be resistant to oligomycin. The mutations conferring resistance are Ile^{161}→Met; Ser^{165}→Thr, Cys, or Tyr; and Leu^{222}→Phe (*30*). The sites are mapped onto the model for F_o (Fig. 5, B to D). This poses a paradox, in that these mutations map to locations that are separated by as many as 61 residues along a single α helix and distant from the binding sites mapped on the c_{10}-ring. However, the resistance-forming residues all face the c_{10}-ring and are positioned almost at the center of the region where oligomycin is known to bind, though not at those specific sites. These bulky replacements in the a subunit will disrupt the c_{10}-ring at the point of their interaction but, in doing so, also disturb the interaction between the neighboring two c subunits. We propose that the disruption in the conformation of the c_{10}-ring, possibly just on the surface, is propagated through all c subunits, thereby allowing a stable c_{10}-ring and altering the conformation of all oligomycin binding sites. As such, the conformation of the wild-type c subunit (represented here as cO^S) is converted to a conformation that is resistant to oligomycin, cO^R. However, for a c_{10}-ring to form, each subunit must have identical contacts between the c_{10}-ring, and thus $c_1O^Rc_9O^S$ gets converted to $c_{10}O^R$ (where the subscript represents the number of c subunits) in the presence of the oligomycin-resistance mutation in the a subunit. This suggests that the conformation of the c_{10}-ring surface is plastic, in that it can assume new stable forms that allow it to function. This represents a mechanism that differs from allosteric interactions as they are normally thought of in relationship to enzyme regulation.

Materials and methods

Yeast strains and plasmids

Yeast wild type, USY006 (Matα, ade2-1, his3-11,15, leu2-1, trp1-1, ura3-52, atp2::LEU2, pRS304-ATP2H6::TRP1) and yeast with F6δ fusion, DMY741 (Mata, ade2-1, his3-11,15, trp1-1, ura3-52, $can1^R100$, atp2::loxP, atp7::loxP, atp1::KANR, F6δ::LEU2, ATP2-H6::TRP1, ATP1::URA3) were used throughout. pMSP1E3D1 (*31*) was a gift from Stephen Sligar (Addgene plasmid # 20066) and was transformed into BL21 (DE3) Gold (Agilent, Santa Clara, CA). Plasmid pRK792 (*32*) (to express TEV protease) was a gift from David Waugh (Addgene plasmid # 8830). The yeast was grown in a 60l fermentor in semisynthetic media with the glucose concentration controlled to about 0.2% (*33*). Bacteria were grown in LB media.

The parent strain for DMY741 was W303-1A (Rodney Rothstein via Alex Tzagoloff, Columbia University). Strain DMY741 was developed by sequentially deleting out the genes (*34*), ATP1, ATP2, ATP7, and ATP16 and then introducing the genes on plasmids containing ATP1, ATP2 with a His_6 tag, and the fusion construct contain subunit F6 (ATP7), T4-lysozyme, and the δ subunit (ATP16). The fusion construct was made by total synthesis of the DNA (Genscript, Piscataway, NJ). The DNA sequence that encoding T4 lysozyme was codon optimized for expression in yeast and was flanked

by two NarI sites that added Gly-Ala to the N and C termini of lysozyme. The assembled gene was used in a "gap repair" reaction to introduce it into the gene encoding the β subunit such that it was inserted just behind the codons encoding the mitochondrial leader peptide on the 5′ end and then at the stop codon on the 3′ end of the gene, as described (*35*). The fusion gene was subcloned into the integrating vector, pRS304 (*36*) and transformed (*37*) into the yeast strain.

Biochemistry

We chose to incorporate the yeast ATP synthase into nanodiscs as this is under near native conditions and the oligomycin binding site is at the surface of the c_{10}-ring in the membrane phase.

Yeast ATP synthase was purified essentially as described except a Co-affinity column was substituted for the Ni-affinity column (*33*). For reconstitution of the ATP synthase into nanodiscs, the enzyme was purified only through the Co-affinity column.

The membrane scaffolding protein (MSP), MSP1E3D1, was expressed in BL21-Gold (DE3) strain (Agilent, Santa Clara, CA) as described (*38*) with the following changes. After binding to the MSP to the Ni-column, the column was washed with five column volumes of WB (40 mM Tris-Cl, 0.3 M NaCl, 25 mM imidazole, 6 M guanidinium hydrochloride, 5 mM ε-amino caproic acid and 5 mM benzamidine HCl, 1 mM PMSF, pH 8.0) and then the MSP was eluted with 40 mM Tris-Cl, 0.3 M NaCl, 0.4 M imidazole, 6 M guanidinium hydrochloride, 5 mM ε-amino caproic acid and 5 mM benzamidine HCl, 1 mM PMSF, pH 8.0. The buffer was exchanged with a HiPrep 26/10 desalting column (GE Healthcare, Uppsala, Sweden) equilibrated with 25 mM Tris-Cl, 0.15 M NaCl, 1 mM EDTA, pH 8.0. The MSP was digested with TEV protease at 30°C for 6 hours [TEV/MSP ratio was 1/100 (mg/mg)]. The TEV digestion reaction mixture was passed through a HiPrep 26/10 desalting column (GE Healthcare, Uppsala, Sweden) equilibrated with WB containing 75 mM imidazole (WBI). The MSP was loaded onto Ni^{+2}-column equilibrated with WBI. The fractions containing protein that did not bind to the column were collected, pooled together, and dialyzed against storage buffer (25 mM Tris-Cl, 0.1 M NaCl, pH 8.0) at 4°C. The protein concentration of MSP1E3D1, was determined using the extinction coefficient of 26,930 M^{-1} cm^{-1} at 280 nm (*38*). MSP1E3D1 was lyophilized and stored at −20°C.

For reconstitution of F_1F_o into nanodiscs, we used three different lipid preparations. In the case of the structural analysis in the absence of oligomycin, we used nanodiscs prepared form total polar *E. coli* lipids spiked with ergosterol at a ratio of 3:1 on a molar basis, and we also used 1,2-dimyristoyl-*sn*-glycero-3-phosphocholine (DMPC). For the structure in the presence of oligomycin, we used 1-palmitoyl-2-oleoyl-*sn*-glycero-3-phosphocholine (POPC) mixed with cardiolipin (C:18) (CL), at a ratio of 3:1 by weight. The lipids were (obtained from Avanti Polar Lipids, Alabaster, Al) dissolved in chloroform, and stored under argon at −80°C.

The most improved method for reconstitution is reflected in the preparation using POPC:CL. In this procedure, the lipids were added to a glass test tube and the chloroform was removed with a gentle stream of nitrogen. The sample was placed under vacuum for overnight to remove the residual chloroform. The lipids were dissolved in 20 mM Tris-Cl, 0.15 M NaCl, pH 7.4 with 60 mM DDM with the aid of a water bath sonicator. Solubilized lipid was mixed with MSP1E3D1 and F_1F_o ATP synthase at a molar ratio of 120:15:2.5 (lipid:MSP:F_1F_o) and the mixture was incubated at 30°C for 1 hour with constant agitation. To initiate nanodisc assembly, Amberlite XAD-2 (Sigma Aldrich, Milwaukee, WI) beads (0.6 g/ml, final) were added and the mix was incubated at 30°C for 24 hours with constant agitation. Adsorbent beads were added in three batches; in first batch 8% of total beads were added and the reaction was incubated for 6 hours; in the second batch, additional 10% of total beads were added and the reaction mix was incubated for another 16 hours; in the final step of addition, the final 82% of total beads were added and the reaction was incubated for another 2 hours. For reconstitution using *E. coli* total polar lipids or DMPC, the adsorbent beads were added in four batches, 25% of the total beads per hour for a total of 4 hours. The beads were removed and the reaction mixture was purified on a Superose-6 (GE Healthcare, Uppsala, Sweden) size exclusion column equilibrated with 20 mM Tris-Cl, 50 mM sucrose, 4 mM $MgSO_4$, 1 mM EDTA, 0.25 mM ADP, 0.15 M NaCl, 5 mM ε-amino caproic acid and 5 mM benzamidine HCl, 1 mM PMSF, pH 8.0. The buffer was exchanged using a centrifugal column (*39*) (1 ml) using Bio-Gel P-6 (Bio-Rad, Hercules, CA) and buffer containing, 20 mM Tris-Cl, 4 mM $MgSO_4$, 1 mM EDTA, 0.25 mM ADP, 0.15 M NaCl, 5 mM ε-amino caproic acid and 5 mM benzamidine HCl, 1 mM PMSF, pH 8.0. The specific activity (u/mg) and percent oligomycin sensitive ATPase using wild-type enzyme was 10:42, 59:78, and 55:85% for reconstitution using *E. coli* polar lipids, DMPC an POPC/CL, respectively.

Cryo–electron microscopy data acquisition

Purified yeast F_1F_o reconstituted in nanodiscs at the concentration of 1 mg/ml (2.5 μl) was applied to a glow-discharged Quantifoil holey carbon grid (1.2/1.3, 400 mesh), and blotted for 3 s with ~91% humidity before plunge-freezing in liquid ethane using a Cryoplunge 3 System (CP3, Gatan). For cryo-EM of F_1F_o with oligomycin, 60 mM stock solution of oligomycin in dimethyl sulfoxide was added to a final concentration of 30 μM, and incubated on ice for 30 min. The mixture (2.5 μl) was applied to a grid, blotted and plunge-frozen. Cryo-EM data were recorded on a 300-kV Polara electron microscope (FEI) at Harvard Medical School. All cryo-EM movies were manually recorded with a K2 Summit direct electron detector (Gatan) in super-resolution counting mode using UCSF-Image4 (*40*). Details of the EM data collection parameters are listed in Table 1.

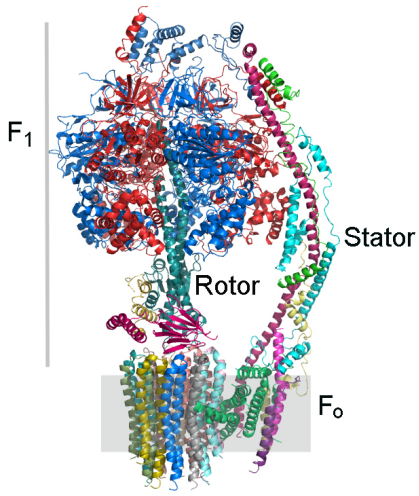

Movie 1. The architecture of the monomeric form of the yeast ATP synthase.

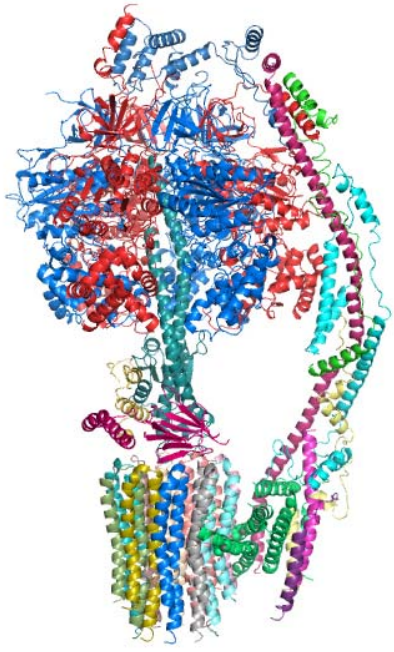

Movie 2. Rotation of ATP synthase around the *x* and *y* axes.

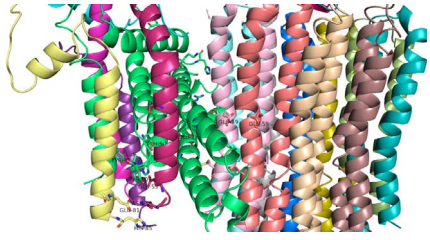

Movie 3. Views of the proton entry pathway and then the proton exit pathway.

EM image processing

EM data were processed as previously described (*41*). Dose-fractionated super-resolution movies collected using the K2 Summit direct electron detector were binned over 2 × 2 pixels, and subjected to motion correction using the program MotionCor2 (*42*). A sum of all frames of each image stack was calculated following a dose-weighting scheme, and used for all image-processing steps except for defocus determination. CTFFIND4 (*43*) was used to calculate defocus values of the summed images from all movie frames without dose weighting. Particle picking was performed using a semi-automated procedure with SAMUEL and SamViewer (*44*). Two- and three-dimensional (2D and 3D) classification and 3D refinement were carried out using "relion_refine_mpi" in RELION (*45*). Masked 3D classification focusing on F_o with residual signal subtraction was performed following a previously described procedure (*46*). All refinements followed the gold-standard procedure, in which two half data sets were refined independently. The overall resolutions were estimated based on the gold-standard criterion of Fourier shell correlation (FSC) = 0.143. Local resolution variations were estimated from two half data maps using ResMap. The amplitude information of the final maps were corrected by applying a negative B-factor using the program bfactor.exe.

Model refinement

The initial model was derived from the crystal structure of F_1 ATPase (PDB, 2WPD) and the c_{10}-ring from our previous crystal structure (PDB 3U2F). Models for subunits OSCP, b, F6, and subunit d were initiated as homology models based on bovine structures (PDB, 2CLY and 5FIK). Models for subunits a, A6L/subunit 8, f, j, and the N-terminal part of subunit b were derived from the cryo-EM structure (PDB 6B2Z). Initial models were rigid-body fitted to our cryo-EM maps, extensively rebuilt in Coot (*47*), and refined in Refmac (*48*) using the script *refine_local*, and subsequently, using real-space refinement in Phenix (*49*).

Final models were validated with statistics from Ramachandran plots, MolProbity scores, and EMRinger scores (Table 1). MolProbity and EMRinger scores were calculated as described (*50*, *51*).

Molecular dynamics simulations

All simulations were performed with NAMD2 (*52*), using CHARMM36 force-field for proteins and lipids (*53*, *54*), periodic boundary conditions, and constant temperature (298 K) and pressure (1 atm). Long-range electrostatic interactions were calculated using PME, with a real-space cut-off of 12 Å. Van der Waals interactions were computed with a Lennard-Jones potential, cut-off at 12 Å with a smooth switching function taking effect at 10 Å. Simulations were carried out for two systems: a complex of the yeast c_{10}-ring with four oligomycin molecules bound (PDB 4F4S), embedded in a hydrated, pre-equilibrated 1-palmitoyl-2-oleoyl-*sn*-glycero-3-phosphatidylcholine (POPC) lipid bilayer; and a system of the same components, with one oligomycin molecule dissociated from the c_{10}-ring and free in the lipid bilayer. Force-field parameters for oligomycin were derived using the GAAMP server (*55*). The c_{10}-ring complex was embedded in the POPC membrane using GRIFFIN (*56*), as previously described (*57*). Counter-ions were added to neutralize the charge of the simulation system. The simulation systems were equilibrated following a staged protocol whereby positional and conformational restraints acting of the protein-inhibitor complex are gradually weakened over 200 ns. The equilibrated systems were then used as the starting point for the analysis of the oligomycin binding free energy.

The inhibitor binding free-energy was calculated as $\Delta G_b = -k_BT \ln N + \Delta G_{int} + \Delta G_r + \Delta G_t$, where N is the number of available binding sites on the c_{10}-ring, ΔG_{int} is free-energy difference between the associated and dissociated complex, and ΔG_r and ΔG_t denote the free-energy penalties due to the loss of rotational and translational entropy of the ligand upon binding, respectively (k_B is the Boltzmann constant and T the temperature). ΔG_{int} was, in part, derived from calculations of the free-energy change associated with decoupling oligomycin from the rest of the molecular system, in both the bound and unbound states. Analogous calculations were carried out whereby oligomycin is recoupled to the system. These calculations used the Free-Energy Perturbation method, whereby the decoupling and recoupling process is induced through a parameter λ that scales the nonbonded interactions between the ligand and its environment. The parameter λ varied gradually and step-wise between 1 and 0, and vice versa, in 54 consecutive simulations. For each value of λ, in either direction, an incremental free-energy change was estimated from a simulation of 1 ns, after a 200-ps equilibration stage, in the case of bound oligomycin; for the dissociated ligand, the sampling and equilibration times per intermediate were 1.5 ns and 300 ps, respectively. The resulting values for this decoupling free-energy are 39.8 and 32.8 kcal/mol for the bound and unbound ligand, respectively. Intramolecular interactions thus result in a free-energy contribution that favors binding, i.e., $\Delta\Delta G_{FEP} = -7.0$ kcal/mol.

For computational efficiency, during the above-mentioned decoupling/recoupling simulations, the internal conformation of the oligomycin molecule considered was preserved using a harmonic RMSD restraint, defined relative to that in the equilibrated systems, with a force constant k = 9.6 kcal/mol Å^2. Hence, $\Delta G_{int} = \Delta\Delta G_{FEP} + \Delta\Delta G_{RMSD}$, where the latter term is the difference in the free-energy cost of imposing the conformational restraint on the bound versus the unbound ligand. This contribution was computed separately, through an additional set of simulations whereby k is scaled down gradually, using a parameter α that varies step-wise from 1 to 0, and vice versa. Specifically, 50 simulations of 1 ns each were carried out in each direction for the bound and unbound states. From each of these simulation series, the value of ΔG_{RMSD} can be derived using the expressions:

$$\Delta G_{RMSD} = -k_BT \sum_{w=1}^{W=50} \ln\left\langle \exp\left\{ -\frac{\Delta U_w(t)}{k_BT} \right\} \right\rangle$$

$$\Delta U_w(t) = \frac{1}{2} k(\alpha_{w+1} - \alpha_w)\mathrm{RMSD}(t)^2$$

where $\langle \ldots \rangle$ denotes a time-average. The calculated values of ΔG_{RMSD} are 0.5 and 0.9 kcal/mol for the bound and unbound ligand, respectively; that is, $\Delta\Delta G_{RMSD}$ = 0.4 kcal/mol, i.e., binding is only marginally disfavored due to loss of conformational dynamics of the inhibitor. The resulting value of ΔG_{int} is thus –6.6. kcal/mol.

When dissociated from the c_{10}-ring, oligomycin adopts primarily an upright orientation, i.e., its rotational freedom relative to the membrane plane is restricted; however, the molecule rotates freely around the membrane perpendicular. The free-energy cost associated with the loss of rotational entropy upon binding can be therefore estimated as $\Delta G_r = -k_BT \ln[\Delta\theta/2\pi]$, where Δθ is the rotational fluctuation of the bound ligand perpendicularly to the membrane; from our simulations we estimate that Δθ ~ 0.44 rad (or 25 degrees), and thus ΔG_r = 1.6 kcal/mol.

Similarly, to estimate the free-energy cost associated with the loss of translational entropy upon binding, we used the expression $\Delta G_t = -k_BT \ln[D^o \Delta A]$, where ΔA represents the translational freedom of the bound ligand on the membrane plane when bound to the protein, whereas D^o is the ligand area-density in the surrounding medium, akin to the standard concentration C^o used in the context of three-dimensional bi-molecular association. Although there is no analogous standard for D^o, the mole fraction of the inhibitor in the lipid membrane may be used to define a reference state. For example, an assumed mole fraction of 0.01, i.e., 1 inhibitor per 100 lipids, translates into D^o = 7,000 Å^2, for an area-per-lipid of ~70 Å^2. From our simulations we estimate that ΔA = 4 Å^2, and therefore an oligomycin mole fraction of 0.01 implies ΔG_t = 4.4 kcal/mol.

Primary sequence analysis

Primary sequence alignment was done using COBALT (*58*).

Figure images

Many of the images presented in the figures were made with the assistance of Pymol (*59*).

REFERENCES AND NOTES

1. T. Xu, V. Pagadala, D. M. Mueller, Understanding structure, function, and mutations in the mitochondrial ATP synthase. *Microb. Cell* **2**, 105–125 (2015). doi: 10.15698/mic2015.04.197; pmid: 25938092
2. I. Arnold, K. Pfeiffer, W. Neupert, R. A. Stuart, H. Schägger, Yeast mitochondrial F_1F_0-ATP synthase exists as a dimer: Identification of three dimer-specific subunits. *EMBO J.* **17**, 7170–7178 (1998). doi: 10.1093/emboj/17.24.7170; pmid: 9857174
3. B. Daum, D. Nicastro, J. Austin II, J. R. McIntosh, W. Kühlbrandt, Arrangement of photosystem II and ATP synthase in chloroplast membranes of spinach and pea. *Plant Cell* **22**, 1299–1312 (2010). doi: 10.1105/tpc.109.071431; pmid: 20388855

4. L. A. Baker, I. N. Watt, M. J. Runswick, J. E. Walker, J. L. Rubinstein, Arrangement of subunits in intact mammalian mitochondrial ATP synthase determined by cryo-EM. *Proc. Natl. Acad. Sci. U.S.A.* **109**, 11675–11680 (2012). doi: 10.1073/pnas.1204935109; pmid: 22753497
5. I. G. Denisov, Y. V. Grinkova, A. A. Lazarides, S. G. Sligar, Directed self-assembly of monodisperse phospholipid bilayer nanodiscs with controlled size. *J. Am. Chem. Soc.* **126**, 3477–3487 (2004). doi: 10.1021/ja0393574; pmid: 15025475
6. J. P. Abrahams, A. G. W. Leslie, R. Lutter, J. E. Walker, Structure at 2.8 Å resolution of F_1-ATPase from bovine heart mitochondria. *Nature* **370**, 621–628 (1994). doi: 10.1038/370621a0; pmid: 8065448
7. V. Kabaleeswaran, N. Puri, J. E. Walker, A. G. Leslie, D. M. Mueller, Novel features of the rotary catalytic mechanism revealed in the structure of yeast F_1 ATPase. *EMBO J.* **25**, 5433–5442 (2006). doi: 10.1038/sj.emboj.7601410; pmid: 17082766
8. A. Dautant, J. Velours, M. F. Giraud, Crystal structure of the Mg·ADP-inhibited state of the yeast F_1c_{10}-ATP synthase. *J. Biol. Chem.* **285**, 29502–29510 (2010). doi: 10.1074/jbc.M110.124529; pmid: 20610387
9. D. Stock, A. G. W. Leslie, J. E. Walker, Molecular architecture of the rotary motor in ATP synthase. *Science* **286**, 1700–1705 (1999). doi: 10.1126/science.286.5445.1700; pmid: 10576729
10. V. K. Dickson, J. A. Silvester, I. M. Fearnley, A. G. Leslie, J. E. Walker, On the structure of the stator of the mitochondrial ATP synthase. *EMBO J.* **25**, 2911–2918 (2006). doi: 10.1038/sj.emboj.7601177; pmid: 16791136
11. H. Guo, S. A. Bueler, J. L. Rubinstein, Atomic model for the dimeric F_o region of mitochondrial ATP synthase. *Science* **358**, 936–940 (2017). doi: 10.1126/science.aao4815; pmid: 29074581
12. K. R. Vinothkumar, M. G. Montgomery, S. Liu, J. E. Walker, Structure of the mitochondrial ATP synthase from *Pichia angusta* determined by electron cryo-microscopy. *Proc. Natl. Acad. Sci. U.S.A.* **113**, 12709–12714 (2016). doi: 10.1073/pnas.1615902113; pmid: 27791192
13. S. B. Vik, J. C. Long, T. Wada, D. Zhang, A model for the structure of subunit a of the *Escherichia coli* ATP synthase and its role in proton translocation. *Biochim. Biophys. Acta* **1458**, 457–466 (2000). doi: 10.1016/S0005-2728(00)00094-3; pmid: 10838058
14. S. B. Vik, B. J. Antonio, A mechanism of proton translocation by F_1F_0 ATP synthases suggested by double mutants of the *a* subunit. *J. Biol. Chem.* **269**, 30364–30369 (1994). pmid: 7982950
15. W. Junge, H. Lill, S. Engelbrecht, ATP synthase: An electrochemical transducer with rotatory mechanics. *Trends Biochem. Sci.* **22**, 420–423 (1997). doi: 10.1016/S0968-0004(97)01129-8; pmid: 9397682
16. J. Symersky *et al*., Structure of the c_{10} ring of the yeast mitochondrial ATP synthase in the open conformation. *Nat. Struct. Mol. Biol.* **19**, 485–491, S1 (2012). doi: 10.1038/nsmb.2284; pmid: 22504883
17. D. Pogoryelov, O. Yildiz, J. D. Faraldo-Gómez, T. Meier, High-resolution structure of the rotor ring of a proton-dependent ATP synthase. *Nat. Struct. Mol. Biol.* **16**, 1068–1073 (2009). doi: 10.1038/nsmb.1678; pmid: 19783985
18. N. Mitome *et al*., Essential arginine residue of the F_o-I subunit in F_oF_1-ATP synthase has a role to prevent the proton shortcut without c-ring rotation in the F_o proton channel. *Biochem. J.* **430**, 171–177 (2010). doi: 10.1042/BJ20100621; pmid: 20518749
19. N. Klusch, B. J. Murphy, D. J. Mills, Ö. Yildiz, W. Kühlbrandt, Structural basis of proton translocation and force generation in mitochondrial ATP synthase. *eLife* **6**, e33274 (2017). doi: 10.7554/eLife.33274; pmid: 29210357
20. M. Allegretti *et al*., Horizontal membrane-intrinsic α-helices in the stator *a*-subunit of an F-type ATP synthase. *Nature* **521**, 237–240 (2015). doi: 10.1038/nature14185; pmid: 25707805
21. V. Leone, J. D. Faraldo-Gómez, Structure and mechanism of the ATP synthase membrane motor inferred from quantitative integrative modeling. *J. Gen. Physiol.* **148**, 441–457 (2016). doi: 10.1085/jgp.201611679; pmid: 27821609
22. F. M. Assadi-Porter, R. H. Fillingame, Proton-translocating carboxyl of subunit *c* of F_1F_o H^+-ATP synthase: The unique environment suggested by the pK_a determined by ^{1}H NMR. *Biochemistry* **34**, 16186–16193 (1995). doi: 10.1021/bi00049a034; pmid: 8519776
23. M. J. Root, R. MacKinnon, Two identical noninteracting sites in an ion channel revealed by proton transfer. *Science* **265**, 1852–1856 (1994). doi: 10.1126/science.7522344; pmid: 7522344
24. J. A. Morrill, R. MacKinnon, Isolation of a single carboxyl-carboxylate proton binding site in the pore of a cyclic nucleotide-gated channel. *J. Gen. Physiol.* **114**, 71–84 (1999). doi: 10.1085/jgp.114.1.71; pmid: 10398693
25. T. K. Harris, G. J. Turner, Structural basis of perturbed pK_a values of catalytic groups in enzyme active sites. *IUBMB Life* **53**, 85–98 (2002). doi: 10.1080/15216540211468; pmid: 12049200
26. R. E. Koeppe II, R. M. Stroud, Mechanism of hydrolysis by serine proteases: Direct determination of the pK_a's of aspartyl-102 and aspartyl-194 in bovine trypsin using difference infrared spectroscopy. *Biochemistry* **15**, 3450–3458 (1976). doi: 10.1021/bi00661a009; pmid: 986162
27. F. I. Valiyaveetil, R. H. Fillingame, On the role of Arg-210 and Glu-219 of subunit a in proton translocation by the *Escherichia coli* F_oF_1-ATP synthase. *J. Biol. Chem.* **272**, 32635–32641 (1997). doi: 10.1074/jbc.272.51.32635; pmid: 9405480
28. F. I. Valiyaveetil, R. H. Fillingame, Transmembrane topography of subunit a in the *Escherichia coli* F_1F_0 ATP synthase. *J. Biol. Chem.* **273**, 16241–16247 (1998). doi: 10.1074/jbc.273.26.16241; pmid: 9632683
29. J. Symersky, D. Osowski, D. E. Walters, D. M. Mueller, Oligomycin frames a common drug-binding site in the ATP synthase. *Proc. Natl. Acad. Sci. U.S.A.* **109**, 13961–13965 (2012). doi: 10.1073/pnas.1207912109; pmid: 22869738
30. U. P. John, P. Nagley, Amino acid substitutions in mitochondrial ATPase subunit 6 of *Saccharomyces cerevisiae* leading to oligomycin resistance. *FEBS Lett.* **207**, 79–83 (1986). doi: 10.1016/0014-5793(86)80016-3; pmid: 2876917
31. I. G. Denisov, B. J. Baas, Y. V. Grinkova, S. G. Sligar, Cooperativity in cytochrome P450 3A4: Linkages in substrate binding, spin state, uncoupling, and product formation. *J. Biol. Chem.* **282**, 7066–7076 (2007). doi: 10.1074/jbc.M609589200; pmid: 17213193
32. R. B. Kapust *et al*., Tobacco etch virus protease: Mechanism of autolysis and rational design of stable mutants with wild-type catalytic proficiency. *Protein Eng.* **14**, 993–1000 (2001). doi: 10.1093/protein/14.12.993; pmid: 11809930
33. V. Pagadala, L. Vistain, J. Symersky, D. M. Mueller, Characterization of the mitochondrial ATP synthase from yeast *Saccharomyces cerevisae*. *J. Bioenerg. Biomembr.* **43**, 333–347 (2011). doi: 10.1007/s10863-011-9364-5; pmid: 21748405
34. U. Güldener, S. Heck, T. Fielder, J. Beinhauer, J. H. Hegemann, A new efficient gene disruption cassette for repeated use in budding yeast. *Nucleic Acids Res.* **24**, 2519–2524 (1996). doi: 10.1093/nar/24.13.2519; pmid: 8692690
35. N. Puri, J. Lai-Zhang, S. Meier, D. M. Mueller, Expression of bovine F_1-ATPase with functional complementation in yeast *Saccharomyces cerevisiae*. *J. Biol. Chem.* **280**, 22418–22424 (2005). doi: 10.1074/jbc.M411113200; pmid: 15817482
36. R. S. Sikorski, P. Hieter, A system of shuttle vectors and yeast host strains designed for efficient manipulation of DNA in *Saccharomyces cerevisiae*. *Genetics* **122**, 19–27 (1989). pmid: 2659436
37. R. D. Gietz, R. A. Woods, Transformation of yeast by lithium acetate/single-stranded carrier DNA/polyethylene glycol method. *Methods Enzymol.* **350**, 87–96 (2002). doi: 10.1016/S0076-6879(02)50957-5; pmid: 12073338
38. T. K. Ritchie *et al*., Chapter Eleven - Reconstitution of membrane proteins in phospholipid bilayer nanodiscs. *Methods Enzymol.* **464**, 211–231 (2009). doi: 10.1016/S0076-6879(09)64011-8; pmid: 19903557
39. H. S. Penefsky, A centrifuged-column procedure for the measurement of ligand binding by beef heart F_1. *Methods Enzymol.* **56**, 527–530 (1979). doi: 10.1016/0076-6879(79)56050-9; pmid: 156867
40. X. Li, S. Zheng, D. A. Agard, Y. Cheng, Asynchronous data acquisition and on-the-fly analysis of dose fractionated cryoEM images by UCSFImage. *J. Struct. Biol.* **192**, 174–178 (2015). doi: 10.1016/j.jsb.2015.09.003; pmid: 26370395
41. W. Mi *et al*., Structural basis of MsbA-mediated lipopolysaccharide transport. *Nature* **549**, 233–237 (2017). doi: 10.1038/nature23649; pmid: 28869968
42. S. Q. Zheng *et al*., MotionCor2: Anisotropic correction of beam-induced motion for improved cryo–electron microscopy. *Nat. Methods* **14**, 331–332 (2017). doi: 10.1038/nmeth.4193; pmid: 28250466
43. A. Rohou, N. Grigorieff, CTFFIND4: Fast and accurate defocus estimation from electron micrographs. *J. Struct. Biol.* **192**, 216–221 (2015). doi: 10.1016/j.jsb.2015.08.008; pmid: 26278980
44. H. Ru *et al*., Molecular mechanism of V(D)J recombination from synaptic RAG1-RAG2 complex structures. *Cell* **163**, 1138–1152 (2015). doi: 10.1016/j.cell.2015.10.055; pmid: 26548953
45. S. H. Scheres, RELION: Implementation of a Bayesian approach to cryo-EM structure determination. *J. Struct. Biol.* **180**, 519–530 (2012). doi: 10.1016/j.jsb.2012.09.006; pmid: 23000701
46. X. C. Bai, E. Rajendra, G. Yang, Y. Shi, S. H. Scheres, Sampling the conformational space of the catalytic subunit of human γ-secretase. *eLife* **4**, e11182 (2015). doi: 10.7554/eLife.11182; pmid: 26623517
47. P. Emsley, K. Cowtan, Coot: Model-building tools for molecular graphics. *Acta Crystallogr. D Biol. Crystallogr.* **60**, 2126–2132 (2004). doi: 10.1107/S0907444904019158; pmid: 15572765
48. G. N. Murshudov *et al*., REFMAC5 for the refinement of macromolecular crystal structures. *Acta Crystallogr. D Biol. Crystallogr.* **67**, 355–367 (2011). doi: 10.1107/S0907444911001314; pmid: 21460454
49. P. D. Adams *et al*., PHENIX: A comprehensive Python-based system for macromolecular structure solution. *Acta Crystallogr. D Biol. Crystallogr.* **66**, 213–221 (2010). doi: 10.1107/S0907444909052925; pmid: 20124702
50. B. A. Barad *et al*., EMRinger: Side chain-directed model and map validation for 3D cryo–electron microscopy. *Nat. Methods* **12**, 943–946 (2015). doi: 10.1038/nmeth.3541; pmid: 26280328
51. V. B. Chen *et al*., MolProbity: All-atom structure validation for macromolecular crystallography. *Acta Crystallogr. D Biol. Crystallogr.* **66**, 12–21 (2010). doi: 10.1107/S0907444909042073; pmid: 20057044
52. J. C. Phillips *et al*., Scalable molecular dynamics with NAMD. *J. Comput. Chem.* **26**, 1781–1802 (2005). doi: 10.1002/jcc.20289; pmid: 16222654
53. R. B. Best *et al*., Optimization of the additive CHARMM all-atom protein force field targeting improved sampling of the backbone φ, ψ and side-chain χ_1 and χ_2 dihedral angles. *J. Chem. Theory Comput.* **8**, 3257–3273 (2012). doi: 10.1021/ct300400x; pmid: 23341755
54. J. B. Klauda *et al*., Update of the CHARMM all-atom additive force field for lipids: Validation on six lipid types. *J. Phys. Chem. B* **114**, 7830–7843 (2010). doi: 10.1021/jp101759q; pmid: 20496934
55. L. Huang, B. Roux, Automated force field parameterization for non-polarizable and polarizable atomic models based on ab initio target data. *J. Chem. Theory Comput.* **9**, 3543–3556 (2013). doi: 10.1021/ct4003477; pmid: 24223528
56. R. Staritzbichler, C. Anselmi, L. R. Forrest, J. D. Faraldo-Gómez, GRIFFIN: A versatile methodology for optimization of protein-lipid interfaces for membrane protein simulations. *J. Chem. Theory Comput.* **7**, 1167–1176 (2011). doi: 10.1021/ct100576m; pmid: 24707227
57. W. Zhou, V. Leone, A. Krah, J. D. Faraldo-Gómez, Predicted structures of the proton-bound membrane-embedded rotor rings of the *Saccharomyces cerevisiae* and *Escherichia coli* ATP synthases. *J. Phys. Chem. B* **121**, 3297–3307 (2017). doi: 10.1021/acs.jpcb.6b08051; pmid: 27715045
58. J. S. Papadopoulos, R. Agarwala, COBALT: Constraint-based alignment tool for multiple protein sequences. *Bioinformatics* **23**, 1073–1079 (2007). doi: 10.1093/bioinformatics/btm076; pmid: 17332019
59. The PyMOL Molecular Graphics System, version 2.0, Schrödinger, LLC.

ACKNOWLEDGMENTS

Many thanks to J. Rubinstein for providing a copy of his manuscript and the model for yeast F_o before publication. **Funding:** The work was supported by a grant from NIH, R01GM066223, to D.M.M. W.Z. and J.D.F.-G. are funded by the Division of Intramural Research of the National Heart, Lung, and Blood Institute. **Author contributions:** A.P.S. designed and performed the biochemical experiments; M.Lu. performed EM data collection and image processing; W.Z. performed the molecular dynamics simulation studies; J.S. helped in the atomic model building and refinement; D.B. helped with the design and performed biochemical experiments; M.G.C. helped with the cryo-EM experiments; J.D.F.-G. designed and supervised the molecular dynamics simulation studies; and M.Li. supervised the EM studies. D.M.M. devised and supervised experiments and analyzed data. A.P.S., M.Lu., W.Z., J.S., D.B., J.D.F.-G., M.Li., and D.M.M. helped with writing the manuscript. **Competing interests:** None declared. **Data and materials availability:** Four 3D cryo-EM density maps of the yeast mitochondrial ATP synthase in nanodiscs have been deposited in the Electron Microscopy Data Bank under accession numbers EMD-7548 (F_1F_o), EMD-7549 (F_o), EMD-7546 (F_1F_o with oligomycin), and EMD-7547 (F_o with oligomycin). The corresponding atomic coordinates for the atomic models have been deposited in the Protein Data Bank under accession numbers 6CP6 (F_1F_o), 6CP7 (F_o), 6CP3 (F_1F_o with oligomycin), and 6CP5 (F_o with oligomycin). Correspondence and requests for materials should be addressed to the corresponding authors.

SUPPLEMENTARY MATERIALS

www.sciencemag.org/content/360/6389/eaas9699/suppl/DC1
Supplementary Text
Figs. S1 to S12
References

15 January 2018; accepted 30 March 2018
Published online 12 April 2018
10.1126/science.aas9699

RESEARCH ARTICLE SUMMARY

MOLECULAR MOTORS

Structure, mechanism, and regulation of the chloroplast ATP synthase

Alexander Hahn, Janet Vonck, Deryck J. Mills, Thomas Meier,* Werner Kühlbrandt*

INTRODUCTION: Green plant chloroplasts convert light into chemical energy, and adenosine triphosphate (ATP) generated by photosynthesis is the prime source of biologically useful energy on the planet. Plants produce ATP by the chloroplast F_1F_o ATP synthase (cF_1F_o), a macromolecular machine par excellence, driven by the electrochemical proton gradient across the photosynthetic membrane. It consists of 26 protein subunits, 17 of them wholly or partly membrane-embedded. ATP synthesis in the hydrophilic $\alpha_3\beta_3$ head (cF_1) is powered by the cF_o rotary motor in the membrane. cF_o contains a rotor ring of 14 *c* subunits, each with a conserved protonatable glutamate. Subunit *a* conducts the protons to and from the c-ring protonation sites. The central stalk of subunits γ and ε transmits the torque from the F_o motor to the catalytic cF_1 head, resulting in the synthesis of three ATP per revolution. The peripheral stalk subunits b, b′, and δ act as a stator to prevent unproductive rotation of cF_1 with cF_o.

All rotary ATP synthases are, in principle, fully reversible. To prevent wasteful ATP hydrolysis, cF_1F_o has a redox switch that inhibits adenosine triphosphatase (ATPase) activity in the dark.

RATIONALE: Understanding the molecular mechanisms of this elaborate nanomachine requires detailed structures of the whole complex, ideally at atomic resolution. Because of the dynamic nature of this membrane protein complex, crystallization has been difficult and no high-resolution structure of an entire, functional ATP synthase is available. We reconstituted cF_1F_o from spinach chloroplasts into lipid nanodiscs and determined its structure by cryo–electron microscopy (cryo-EM). Cryo-EM is the ideal technique for this study because it can deliver high-resolution structures of large, dynamic macromolecular assemblies that adopt a mixture of conformational states.

ON OUR WEBSITE

Read the full article at http://dx.doi.org/10.1126/science.aat4318

RESULTS: We present the cryo-EM structure of the intact cF_1F_o ATP synthase in lipid nanodiscs at a resolution of 2.9 Å (cF_1) to 3.4 Å (cF_o). In the cF_1 ATPase head, we observe nucleotides with their coordinating Mg ions and water molecules, allowing assignment to the three well-characterized functional states involved in rotary ATP synthesis. Subunit δ on top of the ATPase head binds to all three α subunits, ensuring that only one peripheral stalk can attach. The loosely entwined, long α helices of the peripheral stalk subunits b and b′ clamp the integral membrane subunit a in its position next to the c-ring rotor, thus connecting cF_1 to cF_o. Subunit γ has an L-shaped double hairpin with a redox sensor that can form a disulfide bond and a chock that blocks rotation to avoid wasteful ATP hydrolysis at night.

Protons are translocated through access routes in subunit a in all rotary ATPases. We observe a hydrophilic channel on the lumenal surface that connects to the glutamate residues on the c-ring rotor that carry protons for an almost full rotation before releasing them into the stroma through another hydrophilic channel. A strictly conserved arginine separates the access and exit channels, preventing leakage of protons through the membrane.

CONCLUSION: We observe three cF_1F_o conformations, each with the central rotor stalled in a different position. Ring rotation is unexpectedly divided into three unequal steps. The peripheral stalk may thus act like an elastic spring, evening out the different energy contributions of each step. The features of ATP synthase nanomachines are remarkably similar in chloroplasts and mitochondria, considering their evolutionary distance of a billion years or more. ■

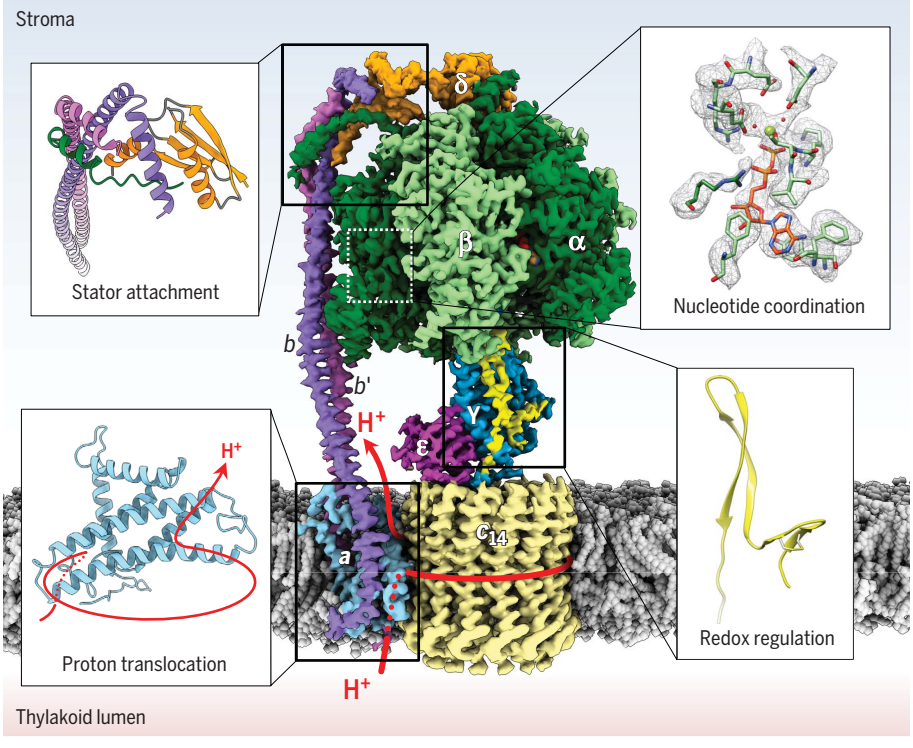

Cryo-EM structure of the chloroplast ATP synthase. Subunits α and β contain the nucleotide-binding sites with resolved nucleotides, Mg^{2+}, and water molecules. Subunit δ joins cF_1 to the membrane-embedded motor via the peripheral stalk (b, b′) that positions subunit a against the rotor ring. The electrochemical proton gradient drives ring rotation (arrow). The central stalk (γε) transmits torque to cF_1. The redox regulator blocks rotation in the dark.

Department of Structural Biology, Max Planck Institute of Biophysics, Max-von-Laue-Strasse 3, 60438 Frankfurt am Main, Germany.
*Corresponding author. Email: werner.kuehlbrandt@biophys.mpg.de (W.K.); t.meier@imperial.ac.uk (T.M.)
Cite this article as A. Hahn *et al.*, *Science* **360**, eaat4318 (2018). DOI: 10.1126/science.aat4318

RESEARCH ARTICLE

MOLECULAR MOTORS

Structure, mechanism, and regulation of the chloroplast ATP synthase

Alexander Hahn, Janet Vonck, Deryck J. Mills, Thomas Meier,*† Werner Kühlbrandt*

The chloroplast adenosine triphosphate (ATP) synthase uses the electrochemical proton gradient generated by photosynthesis to produce ATP, the energy currency of all cells. Protons conducted through the membrane-embedded F_o motor drive ATP synthesis in the F_1 head by rotary catalysis. We determined the high-resolution structure of the complete cF_1F_o complex by cryo–electron microscopy, resolving side chains of all 26 protein subunits, the five nucleotides in the F_1 head, and the proton pathway to and from the rotor ring. The flexible peripheral stalk redistributes differences in torsional energy across three unequal steps in the rotation cycle. Plant ATP synthase is autoinhibited by a β-hairpin redox switch in subunit γ that blocks rotation in the dark.

F-type adenosine triphosphate (ATP) synthases use the free energy of the membrane potential to synthesize ATP from adenosine diphosphate (ADP) and inorganic phosphate (*1*) by rotary catalysis (*2*, *3*). ATP is generated by the tightly coupled action of the catalytic F_1 head and the F_o motor in the membrane. F_1 consists of three asymmetric αβ heterodimers, which define the catalytic sites (*3*), and the central stalk of subunits γ and ε, which are attached to the c-ring (*4*, *5*). The F_o motor consists of the c-ring rotor, subunit a, and the peripheral stalk. Two aqueous channels in F_o, each spanning half of the membrane, were proposed to conduct protons to and from conserved glutamates in the c-ring to drive rotation (*6*, *7*) and were recently observed in mitochondrial ATP synthases (*8*–*10*). Rotation of the central stalk, driven by the proton motive force (pmf) across the membrane, causes sequential conformational changes in the αβ heterodimers, resulting in the synthesis of three molecules of ATP per revolution. The peripheral stalk acts as a stator to prevent unproductive rotation of F_1 with the F_o motor.

Green plants, algae, and cyanobacteria generate ATP and NADPH (reduced form of nicotinamide adenine dinucleotide phosphate) by photophosphorylation. The chloroplast ATP synthase (cF_1F_o) is located in the stroma lamellae and flat grana end membranes (*11*). It is spatially separated from the water-splitting photosystem II in the chloroplast grana. In contrast to mitochondrial ATP synthase dimers (*12*), cF_1F_o is monomeric and does not bend the membrane (*11*). In terms of overall structure and subunit composition, cF_1F_o closely resembles the ATP synthases of bacteria.

Department of Structural Biology, Max Planck Institute of Biophysics, Max-von-Laue-Strasse 3, 60438 Frankfurt am Main, Germany.
***Corresponding author. Email: werner.kuehlbrandt@biophys.mpg.de (W.K.); t.meier@imperial.ac.uk (T.M.)** †Present address: Department of Life Sciences, Imperial College London, Exhibition Road, London SW7 2AZ, UK.

ATP synthases are fully reversible and can catalyze ATP synthesis or hydrolysis. The catalytic direction depends on the pmf across the membrane and the concentration of ADP and ATP. Most organisms have developed inhibitory mechanisms that block wasteful ATP hydrolysis when the pmf is insufficient to drive ATP synthesis (*13*, *14*). The plant chloroplast ATP synthase has a ~40 amino acid insertion in the γ subunit that attenuates cF_1F_o activity in the dark through the formation of a disulfide bond (*15*, *16*), a process known as thiol modulation (*17*). Without an atomic model of this redox loop, the mechanism of thiol modulation was not understood.

So far, no high-resolution structure of a complete and functional ATP synthase has been available. We determined the structure of the intact spinach chloroplast ATP synthase by cryo–electron microscopy (cryo-EM), which enabled us to build atomic models of all its 26 subunits.

Overall structure and rotary conformations of cF_1F_o

We isolated native cF_1F_o from market spinach and reconstituted it into lipid nanodiscs (fig. S1A). The isolated complex contained all protein subunits and was highly pure and fully autoinhibited (fig. S1B). When detached from F_o by detergent, F_1 was hydrolytically active (fig. S1, B to D). Particles selected from cryo-EM images were sorted into three distinct conformations, each with the rotor arrested in a different rotary state (figs. S2 and S3). Conformation 1 was the most populated. A three-dimensional (3D) reconstruction of particles in this class had an overall resolution of 3.15 Å (Fig. 1A). After masking and local realignment, the F_1 head and the membrane-embedded F_o attained average resolutions of 3.0 and 3.4 Å, respectively (figs. S3, C and D, and S4). Three-dimensional maps of the less populated conformations 2 and 3 were reconstructed at ~4.5-Å resolution (fig. S3, A and B). The three maps differ in the orientation of the central rotor and represent different resting positions in rotary catalysis (Fig. 2A), similar to what has been observed at lower resolution in *Escherichia coli* (*18*) and mitochondrial ATP synthase (*19*, *20*). The three αβ assemblies show the open, loose, and tight conformations of the nucleotide-binding pockets (*21*). In conformation 2 and 3, the cF_1 head and peripheral stalk are tilted by ~10° with respect to conformation 1 (Fig. 2). Consequently, the cF_1 head and peripheral stalk together perform a precession movement around a central axis, as subunit γ pushes sequentially against each β subunit in the transition between the three rotary states (Movies 1 and 2). Simple mechanical models of ATP synthase assume that the 360° turn of the rotor is divided into three equal 120° steps that each result in the production of one ATP. The symmetry mismatch between the 14-fold F_o rotor and the near-threefold F_1 head means that the number of c subunits rotating past subunit a to generate one ATP is not an integer. cF_1F_o requires, on average, 4.67 c subunits, or protons, to produce one ATP. The nearest integral numbers of c subunits per step would be 4, 5, and 5, equivalent to rotation angles of 103°, 129°, and 129°. Surprisingly however, the three conformations are separated by rotations of 103°, 112°, and 145°, or 4, 4.4, and 5.6 c subunits (fig. S5C). This means that the position of the c subunits relative to subunit a in the three conformations differs.

The free enthalpy ΔG of ATP hydrolysis under physiological conditions in chloroplasts is about −51 kJ/mol (*22*). Given that ATP synthases operate reversibly close to thermodynamic equilibrium, each proton translocated by cF_1F_o contributes −51 × 3/14 or −10.9 kJ/mol to ATP synthesis. The three observed rotary states indicate energy contributions of −43.7, −48.1, and −61.2 kJ/mol per step. Single-molecule experiments with *E. coli* ATP synthase have been taken to indicate that energy differences due to symmetry mismatch are stored as a torsional force by the flexible subunit γ (*23*), whereas the peripheral stalk was thought to be too stiff (*24*). Our structures of the three rotary cF_1F_o states show that the peripheral stalk bends relative to the central axis (Fig. 2 and fig. S5) and thus couples F_1 elastically to F_o. The torsion of subunit γ would relax intermittently each time one molecule of ATP is produced. The bending energy stored in subunits b and b′ is released when the peripheral stalk reverts to its initial conformation after one full rotation and is thus distributed over all three steps. Acting like an elastic spring, the peripheral stalk evens out the energy minima between the three observed rotational states to optimize ATP synthesis by rotary catalysis.

Structure of the cF_1 head with bound nucleotides

Compared with mitochondrial ATP synthase, detailed information on the structure of the chloroplast complex is limited. In crystal structures of the catalytic subunits, the $\alpha_3\beta_3$ subcomplex is symmetrized and does not contain

nucleotides (*25*, *26*). In our structure, the cF_1 head is the best-resolved part of the map, with a local resolution of 2.9 Å (fig. S3C). Side chains, nucleotides, and some water molecules in the nucleotide-binding pockets are readily visible (Fig. 3C). The head is asymmetric with the three αβ pairs in different conformations (Fig. 3B). In crystal structures of mitochondrial F_1, one of the catalytic β subunits (β_{DP}) contains ADP, one (β_{TP}) a nonhydrolyzable ATP analog, and the third site (β_{empty}) is unoccupied (*3*). In our structure, both the β_{DP} and β_{TP} sites contain Mg-ADP (Fig. 3B). We isolated cF_1F_o without addition of nucleotides, nonhydrolysable substrates or inhibitors. cF_1 is most likely in the ADP-inhibited state (*27*) as a result of hydrolysis during isolation. This conclusion is supported by the absence of phosphate (P_i) density in the binding pockets. Mg-ATP is resolved in the nucleotide-binding sites of the three noncatalytic α subunits (Fig. 3B).

The F_1 nucleotide-binding sites are highly conserved throughout evolution; the α and β subunits of cF_1 respectively share 58 and 67% sequence identity with their mitochondrial counterparts, and the residues forming the nucleotide-binding sites are identical (*25*). A comparison of our cF_1 structure to F_1 from bovine mitochondria (PDB ID 1BMF) (*28*) reveals no differences in the nucleotide-binding sites (fig. S6), except the orientation of αArg^{366}, the catalytically essential "arginine finger" that is involved in coordinating the γ phosphate (*3*). In the bovine structure, this site (β_{TP}) contains the nonhydrolysable ATP analog adenylyl-imidodiphosphate (AMP-PNP).

Connection of F_1 head to the peripheral stalk

The peripheral stalk of cF_1F_o consists of subunits δ, b and b′. The δ subunit (called oligomycin sensitivity-conferring protein in mitochondria) connecting the peripheral stalk to the F_1 head consists of two domains. The structure of the α-helical N-terminal domain has been determined (*29*, *30*), but the C-terminal domain that binds the peripheral stalk has so far been seen only at low resolution and has not been modeled (*18*, *20*). The C-terminal domain consists of a four-stranded mixed β sheet and two α helices (Fig. 3D) and provides a binding platform for the kinked C terminus of the peripheral stalk subunit b. Remarkably, the fold of this domain is conserved in the peripheral stalk subunit of the A-type (*31*, *32*) (fig. S7). The N-terminal domain of δ is a bundle of six short α helices that sits in a central position on top of the F_1 crown (Fig. 3D). Each of three F_1 α subunits binds to δ in a different way. The N-terminal helix of αC (residues α10 to 20) forms an arc that interacts with δH1 and δH5 (Fig. 3E). By contrast, the N-terminal helix of αE (residues α10 to 25) sits vertically next to δH3 and δH4. The N terminus of αA extends to the far side of the δ-subunit C-terminal domain in a long loop that turns into a short helix (α6 to 18), which interacts with the C-terminal helix of peripheral stalk subunit b′ (Fig. 3E). The peripheral stalk is attached to the F_1 head mostly by hydrophobic helix-helix interactions of subunits α, δ, b, and b′. With its two-domain structure and central position on the F_1 head, subunit δ ensures that only one peripheral stalk can attach to the $\alpha_3\beta_3$ heterotrimer.

Subunits b and b′ are almost entirely α-helical and form a loose right-handed coiled coil (*33*) that ends just above the membrane surface (Fig. 4A). This arrangement is conserved in all rotary ATPases, including the b-subunit homodimer of the *E. coli* ATP synthase and the heterodimeric outer stalk of the A/V-type ATPase (*18*, *31*), which is very distantly related (fig. S7). Near the membrane surface, the helices separate and

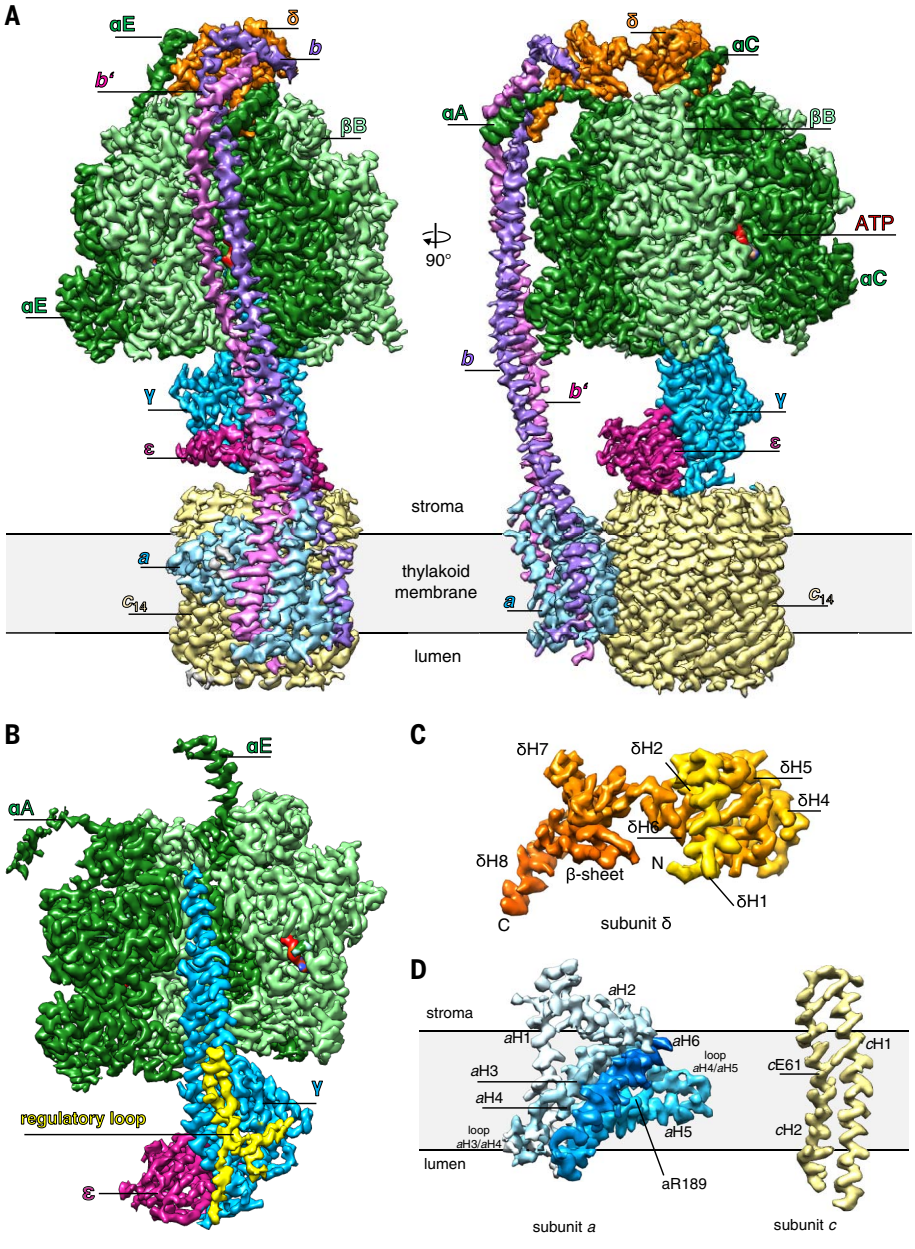

Fig. 1. High-resolution cryo-EM map of the spinach chloroplast cF_1F_o ATP synthase. (**A**) Surface representation of the overall structure. α subunits, dark green; β subunits, light green; γ, blue; δ, orange; ε, purple; a, light blue; b, violet, b′, pink; c_{14}, pale yellow; ATP, red. cF_o (abb′c_{14}) is embedded in the thylakoid membrane (gray), whereas cF_1 ($\alpha_3\beta_3\gamma\varepsilon\delta$) extends into the stroma. N-terminal helices of the αA, αC, and αE subunits are indicated. (**B**) Side view of segmented cF_1 subcomplex. Subunits βB, αC, and δ are omitted for clarity. The plant-specific L-shaped redox-loop of subunit γ is highlighted in yellow. (**C**) The map density of the two-domain subunit δ is colored from N terminus (yellow) to C terminus (orange). (**D**) Segmented maps of membrane-embedded subunits a and c. Subunit a density is colored from light to dark blue to show the N-terminal transmembrane helix H1, the amphipathic helix H2 on the stromal membrane surface, and the two-membrane-intrinsic helix hairpins H3/H4 and H5/H6. Residues $aArg^{189}$ and $cGlu^{61}$ that are essential for pmf-coupled ATP synthesis are indicated.

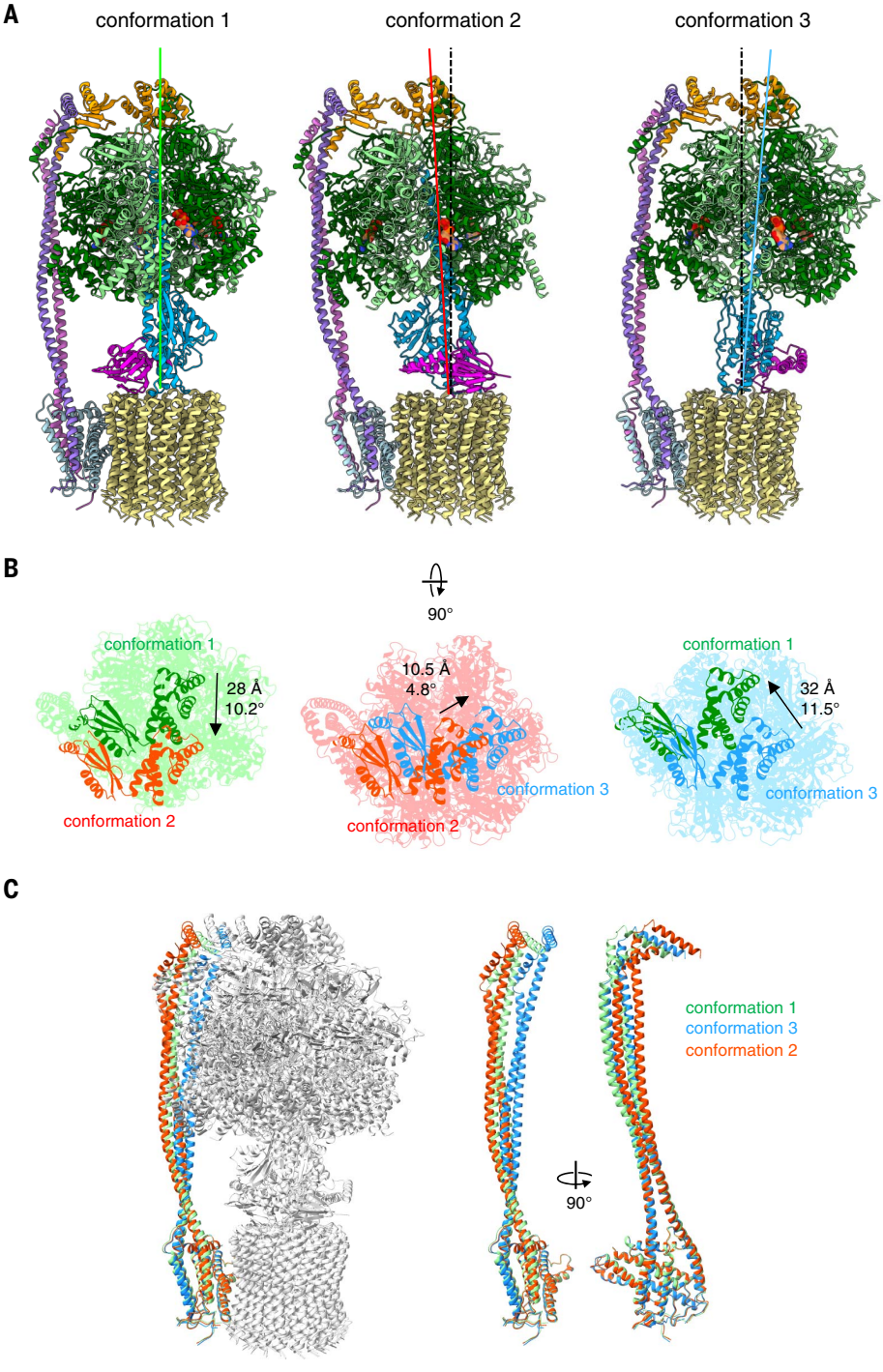

Fig. 2. Three rotary states of the chloroplast ATP synthase. (**A**) Three-dimensional classification of prealigned cF_1F_o particles indicates three different resting states, each with a distinct conformation. In conformation 2, subunits γ (blue) and ε (purple) of the central stalk are rotated by 112° in the ATP synthesis direction relative to conformation 1. In conformation 3, the central stalk is rotated further by 103°. The rotation angle from conformation 3 to conformation 1 is 145°. The dashed black line indicates the axis of c_{14}-ring and central stalk rotation. (**B**) Top view on the cF_1 head. Conformation 2 is tilted by 10.2° with respect to conformation 1, indicated by the shift of subunit δ (green to red). Conformation 3 is tilted by 4.8° with respect to conformation 2 (red to blue) and 11.5° with respect to conformation 1 (blue to green). This movement results in a precession of cF_1 relative to cF_o during rotary catalysis. (**C**) Conformation 1, 2, and 3 superimposed and aligned on subunit a. Subunits abb′ are colored by conformation (1, green; 2, red; 3, blue). The peripheral stalk of subunits bb′ is firmly attached to cF_1 by subunit δ and bends together with cF_1 in rotary conformation 2 and 3 relative to conformation 1.

enter the membrane, where they clamp the a subunit to the c-ring in the F_o subcomplex (Fig. 1A).

Proton translocation through cF_o

The proton translocation pathway is formed by the a subunit and its interface with the c-ring. All 14 subunits of the chloroplast c-ring rotor are equally well resolved (Fig. 1). The crystal structure of an isolated c_{14}-ring from pea chloroplasts (*34*) fits the density well. The membrane scaffold protein of the nanodisc is clearly visible as a horizontal belt of two α helices that wrap tightly around the most hydrophobic part of the F_o subcomplex (fig. S8). Subunit a contains six α helices, H1 to H6 (Fig. 4A and fig. S9). H1 spans the membrane. H2 is an amphipathic helix on the stromal membrane surface, located between b and b′. H3/H4 and H5/H6 form two long, membrane-intrinsic helix hairpins, as seen also in the mitochondrial and bacterial ATP synthases. The H5/H6 pair forms the interface with the c-ring and is the most conserved part of the subunit.

Two proton channels lead to and from a conserved glutamate in the c-ring (Fig. 4, B and C). The proton entrance channel from the thylakoid lumen is a deep cavity, lined by charged and polar residues of a-subunit helices H5 and H6 and the loop connecting H3 and H4 (fig. S10B). As in the mitochondrial ATP synthase (*9*, *10*), the lumenal channel passes through a narrow gap between the hairpin helices H5 and H6 and ends at the c-ring glutamate receiving the proton. Unlike the tight H5/H6 hairpin, the H3/H4 loop is long, flanked by the transmembrane helices of subunit a and b, and extends to the lumenal surface. The helix segments are highly hydrophobic, but the loop contains many polar residues that line the proton path. The H3/H4 hairpin is characterized by polar residues in all species (fig. S9), but its sequence is not highly conserved. The only residue in the hairpin conserved across all ATP synthases, aAsn^{109} on H3, is part of the channel wall (fig. S10C). The conserved aGln^{227} in H6 and aAsn^{193} near aArg^{189} in H5 contribute to the local hydrophilic environment at the a/c-ring interface. aAsn^{193} and aGln^{227} are within hydrogen bonding distance, apparently stabilizing the H5/H6 hairpin. Two charged residues, aGlu^{198} and aAsp^{197} on H5, channel protons through the gap between H5 and H6 to the c-ring Glu^{61} (fig. S10C). The arrangement of proton-translocating residues in the access channel is different in mitochondria, where a glutamate on H6 (*9*, *10*) appears to take on the role of aAsp^{197} in chloroplasts. The residue corresponding to aGlu^{198} in mitochondria is a histidine, which can accept or donate protons. In the *E. coli* sequence, the glutamate and histidine positions are reversed (fig. S9). A glutamate in one or the other position is essential for function (*35*). Taken together, the aqueous entrance channel is defined by charged and polar residues of H5, H6, and the H3/H4 loop that funnel protons from the low-pH thylakoid lumen toward the c-ring Glu^{61}. The uncharged, protonated glutamate can partition into the lipid phase. After an almost full rotation of the c-ring, it encounters

the proton exit channel and is deprotonated by the high pH of the chloroplast stroma (Fig. 4, B and C, and Movie 3). The iterative protonation and deprotonation of *c*Glu[61] under physiological conditions enforces the unidirectional rotation of the c-ring.

The exit channel forms a wedge-shaped cavity that extends from the stromal surface to a narrow pocket next to *a*Arg[189]. The cavity is lined by charged and polar side chains from H5, H6, and a proline-rich loop between H4 and H5 (fig. S11, B and C). H5 bends to follow the curvature of the c-ring, and polar residues in its amphipathic N-terminal half (fig. S9) face the c-ring or the stroma. The map density of the essential *a*Arg[189] is well-defined and faces the exit channel, as in mitochondrial ATP synthases (*9*, *10*). Overall, the high degree of conservation of this and other features is remarkable considering the long evolutionary distance between mitochondria and chloroplasts of a billion years or more (*36*). The ~4.5-Å spacing between the *a*Arg[189] side chain and the nearest c-ring glutamate suggests that it does not form a salt bridge, which would impede ring rotation and tend to arrest the c and a subunits in the same relative position. This conclusion is supported by the different positions of the c subunits relative to subunit a in the three conformations (fig. S5C).

The position of *a*Arg[189] between the two proton channels suggests that the positively charged guanidinium group is critical to prevent proton leakage, which would dissipate the pmf (*37*). Conserved hydrophobic residues in the vicinity of *a*Arg[189] (fig. S9) appear to have a structural role in maintaining the mutual orientation of H5 and H6. *a*Leu[186] and *a*Leu[190] on either side of *a*Arg[189] in adjacent helix turns of H5 pack closely against *a*Leu[234] and the conserved aromatic *a*Phe[231] on H6.

The central rotor

The central rotor consists of subunit γ, ε, and the c-ring. The γ subunit contains two long α helices in a tight, left-handed coiled coil that forms the rotor shaft (Fig. 1B), and their adjacent loops establish most of the close contacts to the c_{14}-ring. These contacts are mainly mediated by electrostatic interactions with the highly conserved c-subunit loop (Arg[41], Gln[42], and Pro[43]) (*38*). Our structure shows that 12 of the 14 c-ring subunits contribute to the firm attachment of the central stalk to the c-ring rotor; similar interactions exist in the ATP synthase of yeast mitochondria, which has a c_{10}-ring (*39*). The ε subunit, which consists of an N-terminal eight-stranded antiparallel β sandwich and a C-terminal α-helical domain, reinforces the close interaction with the c-ring with its conserved His[37] that intercalates between *c*Arg[41] and *c*Gln[42] of one c subunit. The β sheet of subunit ε is extended by a loop from the γ subunit. This loop contains the conserved γGlu[285] (fig. S13), which interacts with a *c*Arg[41]. Mutants of this conserved residue have reduced ATP synthesis capacity due to impaired rotor assembly (*40*, *41*).

In all three observed rotational states of cF_1F_o, the C-terminal domain of the ε subunit forms a horizontal α-helix hairpin next to subunit γ, similar to mitochondrial ATP synthase (*4*, *20*). By

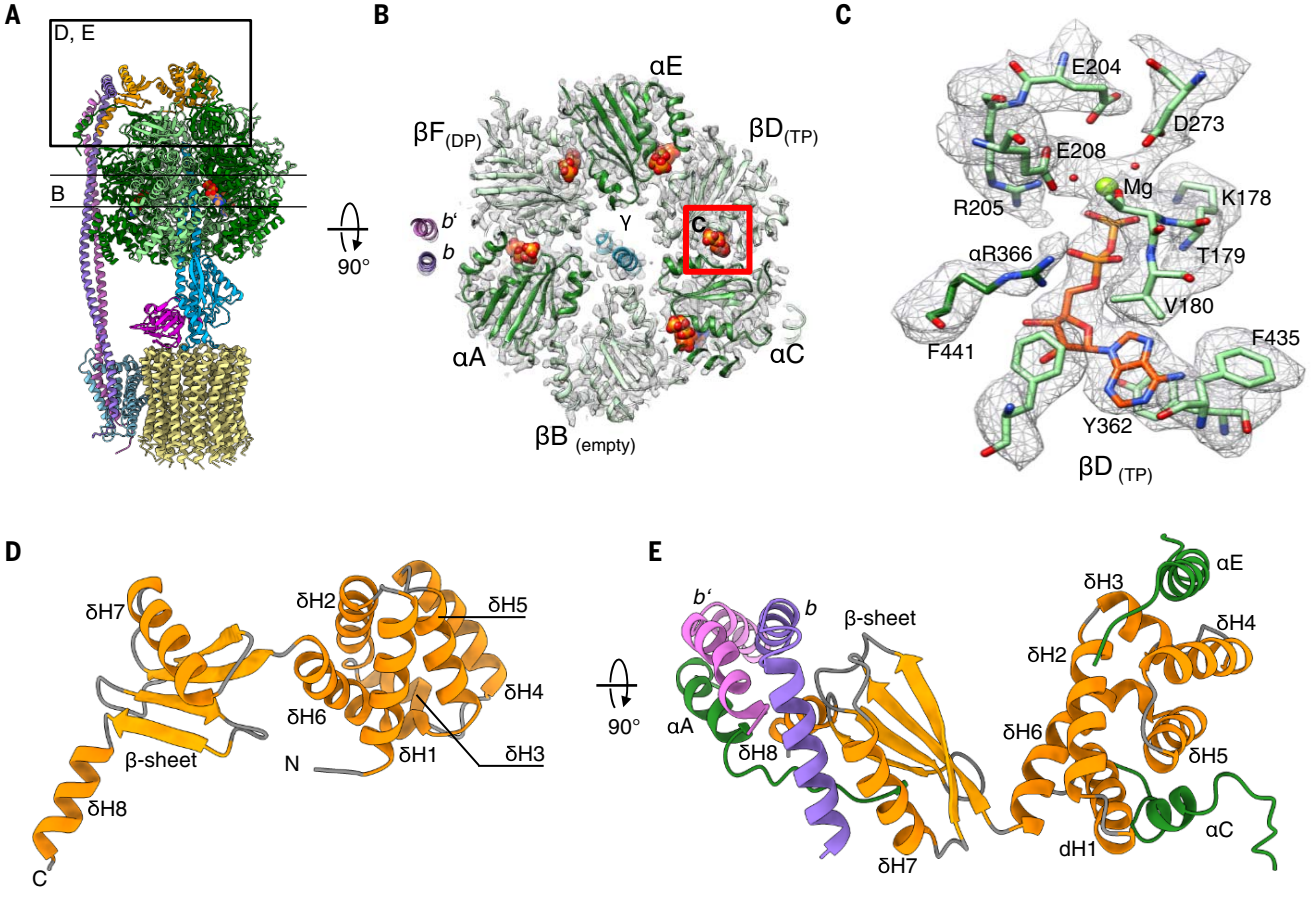

Fig. 3. Structure of the cF_1 head. (**A**) Overview of cF_1F_o, indicating the section through the nucleotide-binding domains (NBDs) in (B) and the position of subunit δ shown in (D) and (E). (**B**) Cross section through cF_1 as indicated in (A). Each αβ dimer (chains αAβB, αCβD, and αEβF) is stalled in a different conformation of the binding-change mechanism (*2*, *3*). Both NBDs of βD and βF (corresponding to β_{TP} and β_{DP}) are occupied by Mg-ADP. βB (corresponding to β_{empty}) is unoccupied. All noncatalytic α subunits bind ATP. (**C**) Details of the βD NBD with Mg-ADP bound. Mg ions, water molecules, and salt bridges involved in Mg coordination are resolved. (**D**) Two-domain structure of subunit δ. The δ N-terminal domain is a bundle of six α helices (δH1 to δH6). The δ C-terminal domain is a four-stranded mixed β sheet with two α helices (δH7 and δH8). (**E**) The δ subunit connects the peripheral stalk to the F_1 head. The N-terminal α-helix bundle interacts in different ways with the N termini of αC and αE. The N terminus of αA interacts with the peripheral stalk subunit b′ (pink). The C-terminal domain of δ binds to the kinked C terminus of b (purple).

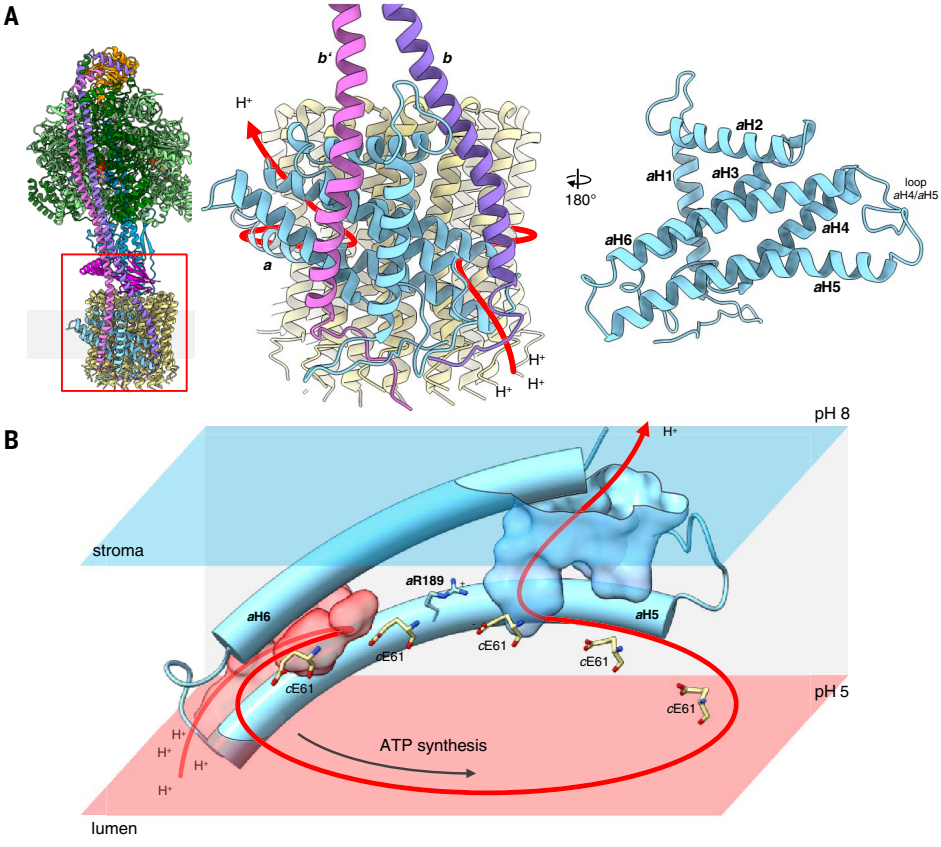

Fig. 4. Proton path through cF_o. (**A**) Subunits b (violet) and b′ (pink) form a right-handed coiled coil that is separated by the amphipathic H2 of subunit a at the point where b and b′ enter the membrane. (**B**) The long, membrane-intrinsic hairpin of subunit *a* helices H5 and H6 follows the curvature of the c_{14}-ring, forming the lumenal proton entry channel (transparent red) and stromal exit channel (transparent blue). The entry channel conducts protons from the acidic thylakoid lumen to the c-ring glutamate (cE61). After an almost full rotation of the c_{14}-ring, the glutamate encounters the large, hydrophilic exit channel that extends to the stromal membrane surface. Glutamates are deprotonated close to the essential *a*Arg^{189}, which separates the two channels, preventing proton leakage and counteracting the negative charge of the deprotonated glutamate at the subunit a/c_{14}-ring interface.

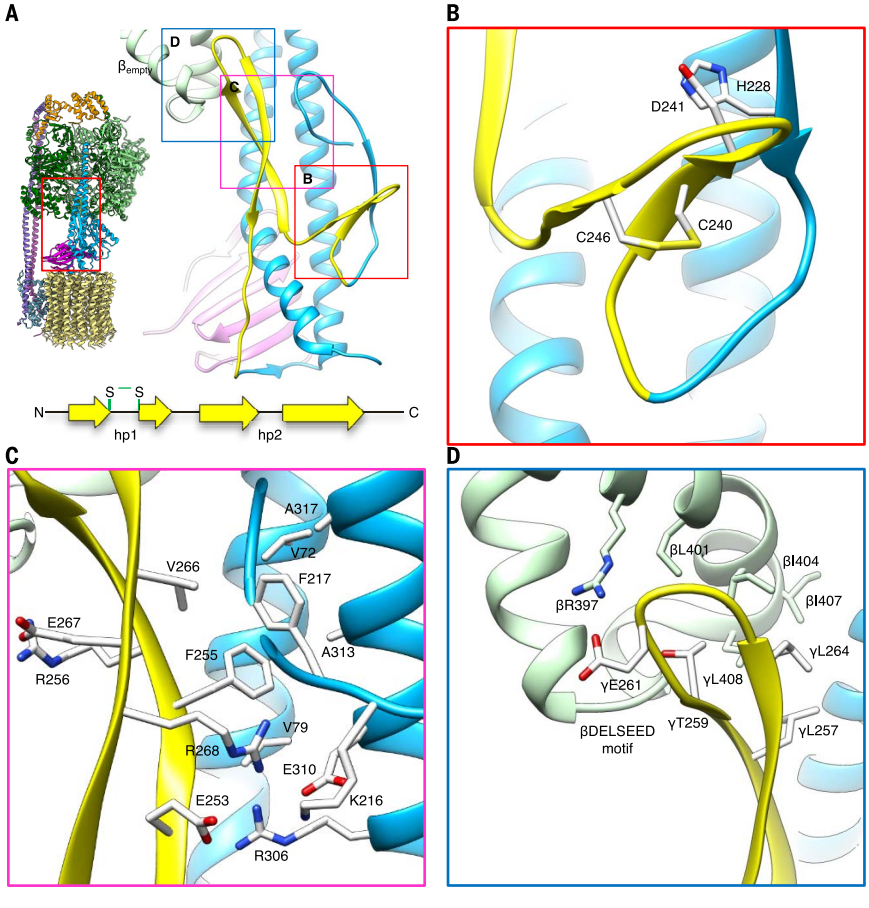

Fig. 5. Autoinhibition of cF_1F_o by thiol modulation. (**A**) Subunit γ of cF_1F_o contains a 40-residue insertion that includes two cysteines. The insertion forms two β hairpins in an L-shaped loop (yellow) that works as an autoinhibitor of rotation in response to the chloroplast redox potential. (**B**) The shorter, N-terminal hairpin (hp1) contains the cysteine motif (CDxNGxC) (fig. S11), which forms a disulfide bond under oxidizing conditions. (**C**) The conserved γF255 of the second hairpin (hp2) interacts with γF217 in a hydrophobic pocket of subunit γ. (**D**) γE261 in hp2 forms a salt bridge with an arginine in the β_{empty} subunit, blocking rotation. hp2 would clash with the βDELSEED motif if the rotor turns in the hydrolysis direction.

contrast, in the *E. coli* ATPase (*18*, *42*), this hairpin extends along the γ subunit into F_1 and interacts with a β subunit, blocking ATP hydrolysis by an effect known as ε inhibition (*14*) (fig. S12). ε inhibition has also been proposed for chloroplasts (*42*, *43*), but in our structure these helices do not interact with subunit β, suggesting that ε inhibition plays no role in cF_1F_o.

Redox regulation of cF_1F_o

The chloroplast γ subunit has a conserved ~40 amino acid insertion before the C-terminal α helix that is thought to work as a redox-controlled inhibitor of ATP hydrolysis (fig. S13). The insertion comprises two β hairpins arranged in an L shape between the nucleotide-free β subunit (β_{empty}) and the γ rotor (Fig. 5A). The short N-terminal hairpin hp1 halfway between the c_{14}-ring and the F_1 head is held in place by an electrostatic interaction between γAsp^{241} and γHis^{228}, residues conserved in plants. The hp1 arm contains two cysteine residues, γCys^{240} and γCys^{246}, positioned on opposite strands of the β hairpin. A disulfide bond is present in our structure between the strands (Fig. 5B), which locks the hairpin together. Previous work suggested a role for these cysteine residues as a redox sensor (*16*). Thioredoxins and NADPH-dependent thioredoxin reductase (NTRC) serve as electron donors to keep this motif reduced and cF_1F_o active under high and low light conditions (*44*). The redox potential drops during periods of prolonged darkness, when photosynthesis does not sustain the pmf across the thylakoid membrane (*45*). The formation of the disulfide bond has been proposed to trigger a conformational change that inhibits cF_1F_o at night to prevent ATP hydrolysis at low pmf (*46*). Our structure shows the oxidized, auto-inhibiting conformation of the redox loop.

The long, slightly twisted C-terminal hairpin hp2 of the redox loop runs vertically along the N-terminal α helix of subunit γ. It contains charged and polar residues with a conserved phenylalanine (γPhe^{255}) at its center (fig. S13). The γPhe^{255} side chain sits in a hydrophobic pocket formed by valine residues in the coiled coil of subunit γ, in an orthogonal π-π interaction with γPhe^{217} (Fig. 5C and Movie 4). This interaction, together with electrostatic interactions between γArg^{268}, γArg^{306}, γGlu^{310}, γGlu^{253}, and γLys^{216}, puts hp2 in close contact with the far side of the conserved DELSEED motif (*47*) of the β_{empty} subunit (Fig. 5D). Reduction of the disulfide bond would destabilize the redox loop and allow for hp2 to be pushed aside when the rotor turns in ATP synthesis direction. Under oxidizing conditions, the disulfide bond and the L shape of the redox loop reform. In this position, hp2 would clash with the DELSEED motif of the β_{empty} subunit and block rotation of the rotor in the ATP hydrolysis direction. In this way, the DELSEED loop functions as a catch for hp2 that blocks rotation in the dark. Although the inhibiting subunit is different, both redox regulation and ε inhibition act on the conserved DELSEED motif of subunit β (β_{empty} and β_{TP}, respectively) (fig. S12), which moves by more than 10 Å in the process of rotary catalysis (Movie 1).

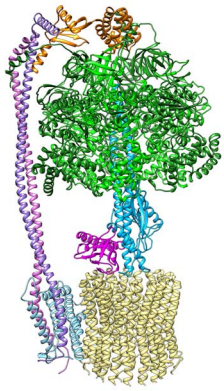

Movie 1. Interpolation between the three rotary conformations of cF_1F_o. Shown is a morph between the models fitted to the cryo-EM maps of conformation 1, 2, and 3, respectively. The a subunit (light blue) is kept stationary. The interpolation was created with Chimera (*67*).

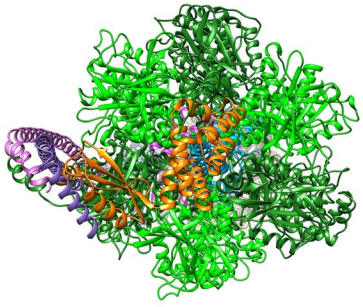

Movie 2. Top view of the interpolation between the three rotary conformations of cF_1F_o, as in Movie 1. The model was rotated 90° along the *x* axis with respect to Movie 1.

Concluding remarks

ATP synthases are central components of all membrane-based biological energy conversion systems and the only known macromolecular machines that convert an electrochemical transmembrane gradient directly into the chemical energy of a covalent bond. ATP generated by photosynthesis is the primary source of biologically useful energy on the planet. ATP synthases of chloroplasts, mitochondria, and bacteria all conform to essentially the same building plan and share the same key features, including the α and β subunits of the F_1 head, the proton or sodium ion-driven c-ring rotor, and subunit a with its two ion channels in the F_o motor, as well as the central and peripheral stalks that connect them. Exceptions are the regulatory mechanisms, such as the redox control switch in the central stalk of cF_1F_o, which is an adaptation to the day-night cycle of the chloroplasts redox potential. Considering the evolutionary distance between mitochondria and chloroplasts of around 1.5 billion years (*36*, *48*), these key properties are remarkably well conserved. Comparison of the cF_1F_o structure to x-ray structures (*3*) and recent partial cryo-EM structures of mitochondrial ATP synthases (*9*, *10*) reveals that many features are identical, down to the level of individual amino acid side chains. Evidently, maintaining the structural basis of ATP synthesis is critical to all living organisms; mutants that impair the optimized mechanism of rotary catalysis in any way are strongly selected against. Our high-resolution structure informs on all aspects of this mechanism for an intact, functional ATP synthase.

Materials and methods

Isolation of chloroplast ATP synthase from spinach leaves

Preparation of thylakoid membranes from young leaves of market spinach (*Spinacia oleracea*) and membrane protein solubilization were carried out as described (*49*). Briefly, cF_1F_o was enriched by fractionated ammonium sulfate precipitation. Fractions precipitated from 1.2 M to 1.8 M ammonium sulfate were recovered in 100 ml of Buffer A [30 mM HEPES pH 8.0, 2 mM $MgCl_2$, 0.5 mM Na_2 EDTA, 0.1% (w/v) *trans*-4-(*trans*-4'-propylcyclohexyl)cyclohexyl-α-*D*-maltoside (tPCC-α-M, Glycon, Luckenwalde, Germany]. Insoluble material was removed by ultracentrifugation (45,000 × g, 30 min, 4°C). The supernatant enriched in cF_1F_o was loaded on a POROS GoPure HQ 50 anion exchange column (Life Technologies, USA) equilibrated with Buffer B [30 mM HEPES pH 8, 50 mM NaCl, 2 mM $MgCl_2$, 0.04% (w/v) tPCC-α-M] and gradually eluted with Buffer C (Buffer B with 1 M NaCl) using an Äkta Explorer chromatography system (GE Healthcare, USA) at 4°C. Hydrolytic activity was assayed as described (*20*). Samples were analyzed by SDS polyacrylamide gel electrophoresis (SDS-PAGE); the protein concentration was determined by the bicinchoninic acid (BCA) assay (Thermo Fisher/Pierce, Germany).

Reconstitution of cF_1F_o into nanodiscs

Expression and purification of MSP2N2 nanodiscs (Addgene, USA) was carried out as described (*50*). Total membrane lipid was isolated from freshly prepared thylakoid membranes by chloroform/methanol extraction (*51*). The total lipid concentration was estimated by 2D thin-layer chromatography and iodine vapor staining (*52*, *53*) with phosphatidyl ethanolamine and phosphatidyl glycerol standards (Avanti Polar Lipids, US). MSP2N2, total thylakoid lipid extract and cF_1F_o were mixed at a molar lipid:MSP:protein ratio of 400:10:1. After 1 hour of incubation, detergent was removed with ~1% (w/w) Bio-Beads SM-2 (Bio-Rad Laboratories, USA) and overnight agitation at 4°C. The reconstitution mix was loaded on a 16/300 Superose-6 gel-filtration column equilibrated with Buffer D (Buffer A without detergent) at 4°C using an

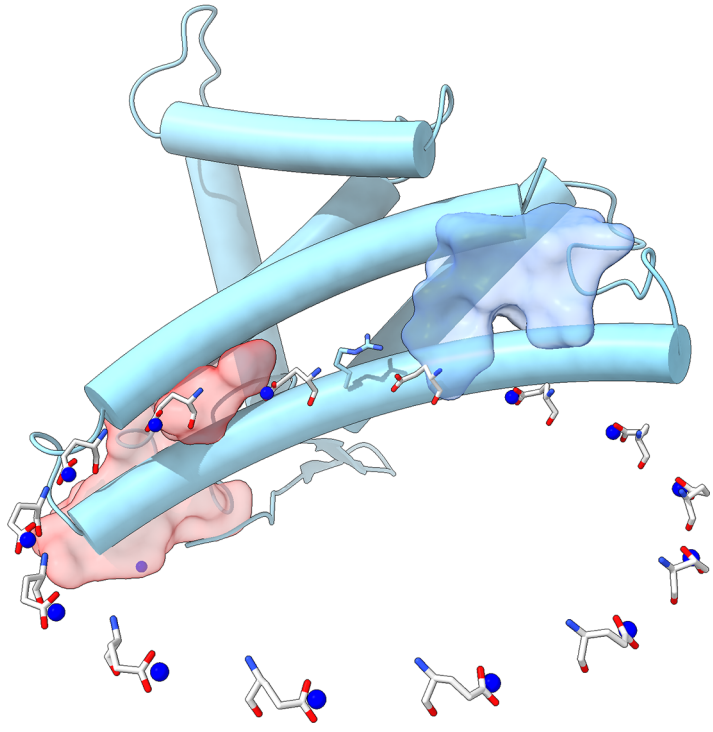

Movie 3. Illustration of the proton pathway through cF_o. The long, membrane-intrinsic hairpin of subunit a helices H5 and H6 follows the curvature of the c_{14}-ring, forming the luminal proton entry channel (transparent red) and stromal exit channel (transparent blue). The entry channel conducts protons from the acidic lumen to the c-ring glutamate (cE61). After an almost full rotation of the c_{14}-ring, the glutamate encounters the large, hydrophilic exit channel that extends to the stromal membrane surface. Glutamates are deprotonated close to the essential *a*Arg^{189}, which separates the two channels, preventing proton leakage and counteracting the negative charge of the deprotonated glutamate at the subunit a/c_{14}-ring interface.

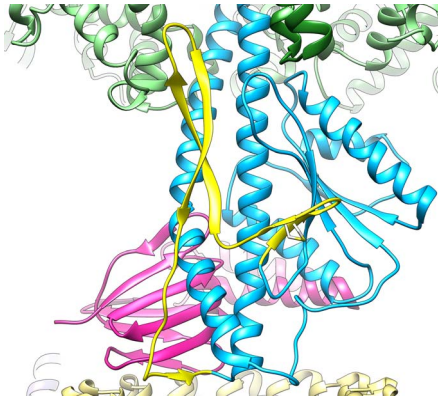

Movie 4. The redox loop of cF_1F_o. The redox loop (yellow) in the γ subunit of chloroplast ATP synthase (cyan) interacts with a β subunit (light green) to block ATP hydrolysis in the dark. Residues discussed in the text are indicated.

Äkta Explorer system). Nanodisc-reconstituted cF_1F_o elutes at a retention volume of ~12 ml as an almost symmetric peak with a small tailing shoulder of detached cF_1. The peak was collected in 0.25 ml fractions. The fraction with the highest protein concentration from the peak front was directly used for cryo-EM sample preparation.

Cryo-EM preparation and electron microscopy

3 μl of cF_1F_o at a concentration of 2 mg/ml was applied to freshly glow-discharged Quantifoil R1.2/1.3 grids and plunge-frozen in liquid ethane using a Vitrobot (Thermo Fisher/FEI). Images were recorded in a Titan Krios microscope operated at 300 kV (Thermo Fisher/FEI) on a Falcon III direct electron detector in electron counting mode at a nominal magnification of 75,000x, corresponding to a calibrated pixel size of 1.053 Å. Before data collection, a precise alignment of the pivot points, coma and rotation center was carried out at the electron flux (0.43 $e^- \times pixel^{-1} \times s^{-1}$) used to record data. 6254 dose fractionated movies were recorded using EPU (Thermo Fisher/FEI) over 62 s, corresponding to a total dose of ~25 e^-/A^2 in a defocus range of −1.5 to −2.5 μm.

Image processing

MotionCor2 was used to correct beam-induced motion and to generate dose-weighted images from movies for initial image processing (*54*). CTF parameters for each movie were determined with CTFFIND4 (*55*). A total of 670,614 particle images were automatically selected with RELION-2.1 (*56*) and extracted with a box size of 350 × 350 pixels. The data set was cleaned by 2D classification using ISAC (*57*). Particles were sorted into three classes by 3D classification in RELION-2.1 (*58*). Final maps were reconstructed in RELION-2.1 from 167,171 (conformation 1), 15,395 (conformation 2), and 14,409 (conformation 3) polished particles. To improve the reconstruction of the membrane region, the F_1-rotor ($\alpha_3\beta_3\gamma\varepsilon$) was subtracted from the extracted particle images (*59*), and a soft-edged mask around the aδbb'c_{14} subcomplex was applied before local realignment. Local resolution was assessed using the built-in routine of RELION-2.1 with an arbitrary B-factor of −150.

Model building and refinement

The structure was built into the EM maps in Coot (*60*), based on the following homologous structures: the 3.4 Å x-ray structure of a spinach chloroplast F_1-ATPase αβ dimer (PDB ID 1KMH) (*26*); the NMR solution structure of the *E. coli* F-ATPase δ subunit N-terminal domain in complex with the α subunit N-terminal 22 residues (PDB ID 2A7U) (*29*); the γ subunit from the 3.0 Å crystal structure of *Caldalkalibacillus thermarum* F_1-ATPase (PDB ID 5HKK) (*61*); the solution structure of an ε subunit chimera combining the N-terminal β-sandwich domain from *Thermosynechococcus elongatus* F_1 and the C-terminal α-helical domain from spinach chloroplast F_1 (PDB ID 2RQ7) (*62*); the 3.4 Å crystal structure of chloroplast ATP synthase c_{14}-ring from *Pisum sativum* (PDB ID 3V3C) (*34*). The a, b, and b′ subunits, the C-terminal domain of δ, the redox loop of γ and C and N-termini of the α and β subunits were built manually de novo. The structure was refined by Phenix real space refinement using Ramachandran restraints (*63*) followed by manual rebuilding in Coot. MolProbity (*64*) and EMRinger (*65*) were used for validation (table S1). Water-accessible regions of the membrane intrinsic F_o subcomplex were probed by mapping the interior surface using HOLLOW (*66*). Figures and movies were made with Chimera (*67*) or ChimeraX (*68*).

REFERENCES AND NOTES

1. P. Mitchell, Coupling of phosphorylation to electron and hydrogen transfer by a chemi-osmotic type of mechanism. *Nature* **191**, 144–148 (1961). doi: 10.1038/191144a0; pmid: 13771349
2. P. D. Boyer, The ATP synthase—a splendid molecular machine. *Annu. Rev. Biochem.* **66**, 717–749 (1997). doi: 10.1146/annurev.biochem.66.1.717; pmid: 9242922
3. J. P. Abrahams, A. G. Leslie, R. Lutter, J. E. Walker, Structure at 2.8 Å resolution of F_1-ATPase from bovine heart mitochondria. *Nature* **370**, 621–628 (1994). doi: 10.1038/370621a0; pmid: 8065448
4. D. Stock, A. G. Leslie, J. E. Walker, Molecular architecture of the rotary motor in ATP synthase. *Science* **286**, 1700–1705 (1999). doi: 10.1126/science.286.5445.1700; pmid: 10576729
5. T. Meier, P. Polzer, K. Diederichs, W. Welte, P. Dimroth, Structure of the rotor ring of F-type Na^+-ATPase from *Ilyobacter tartaricus*. *Science* **308**, 659–662 (2005). doi: 10.1126/science.1111199; pmid: 15860619
6. S. B. Vik, B. J. Antonio, A mechanism of proton translocation by F_1F_0 ATP synthases suggested by double mutants of the *a* subunit. *J. Biol. Chem.* **269**, 30364–30369 (1994). pmid: 7982950
7. W. Junge, H. Lill, S. Engelbrecht, ATP synthase: An electrochemical transducer with rotatory mechanics. *Trends Biochem. Sci.* **22**, 420–423 (1997). doi: 10.1016/S0968-0004(97)01129-8; pmid: 9397682

8. M. Allegretti *et al*., Horizontal membrane-intrinsic α-helices in the stator *a*-subunit of an F-type ATP synthase. *Nature* **521**, 237–240 (2015). doi: 10.1038/nature14185; pmid: 25707805
9. N. Klusch, B. J. Murphy, D. J. Mills, Ö. Yildiz, W. Kühlbrandt, Structural basis of proton translocation and force generation in mitochondrial ATP synthase. *eLife* **6**, e33274 (2017). doi: 10.7554/eLife.33274; pmid: 29210357
10. H. Guo, S. A. Bueler, J. L. Rubinstein, Atomic model for the dimeric F_O region of mitochondrial ATP synthase. *Science* **358**, 936–940 (2017). doi: 10.1126/science.aao4815; pmid: 29074581
11. B. Daum, D. Nicastro, J. Austin 2nd, J. R. McIntosh, W. Kühlbrandt, Arrangement of photosystem II and ATP synthase in chloroplast membranes of spinach and pea. *Plant Cell* **22**, 1299–1312 (2010). doi: 10.1105/tpc.109.071431; pmid: 20388855
12. K. M. Davies *et al*., Macromolecular organization of ATP synthase and complex I in whole mitochondria. *Proc. Natl. Acad. Sci. U.S.A.* **108**, 14121–14126 (2011). doi: 10.1073/pnas.1103621108; pmid: 21836051
13. P. J. Jackson, D. A. Harris, The mitochondrial ATP synthase inhibitor protein binds near the C-terminus of the F_1 beta-subunit. *FEBS Lett.* **229**, 224–228 (1988). doi: 10.1016/0014-5793(88)80832-9; pmid: 2894325
14. Y. Kato-Yamada *et al*., Epsilon subunit, an endogenous inhibitor of bacterial F_1-ATPase, also inhibits F_OF_1-ATPase. *J. Biol. Chem.* **274**, 33991–33994 (1999). doi: 10.1074/jbc.274.48.33991; pmid: 10567363
15. J. L. Arana, R. H. Vallejos, Involvement of sulfhydryl groups in the activation mechanism of the ATPase activity of chloroplast coupling factor 1. *J. Biol. Chem.* **257**, 1125–1127 (1982). pmid: 6460023
16. C. M. Nalin, R. E. McCarty, Role of a disulfide bond in the gamma subunit in activation of the ATPase of chloroplast coupling factor 1. *J. Biol. Chem.* **259**, 7275–7280 (1984). pmid: 6233280
17. U. Junesch, P. Gräber, Influence of the redox state and the activation of the chloroplast ATP synthase on proton-transport-coupled ATP synthesis/hydrolysis. *Biochim. Biophys. Acta* **893**, 275–288 (1987). doi: 10.1016/0005-2728(87)90049-1
18. M. Sobti *et al*., Cryo-EM structures of the autoinhibited *E. coli* ATP synthase in three rotational states. *eLife* **5**, e21598 (2016). doi: 10.7554/eLife.21598; pmid: 28001127
19. A. Zhou *et al*., Structure and conformational states of the bovine mitochondrial ATP synthase by cryo-EM. *eLife* **4**, e10180 (2015). pmid: 26439008
20. A. Hahn *et al*., Structure of a complete ATP synthase dimer reveals the molecular basis of mitochondrial membrane morphology. *Mol. Cell* **63**, 445–456 (2016). doi: 10.1016/j.molcel.2016.05.037; pmid: 27373333
21. P. D. Boyer, The binding change mechanism for ATP synthase—some probabilities and possibilities. *Biochim. Biophys. Acta* **1140**, 215–250 (1993). doi: 10.1016/0005-2728(93)90063-L; pmid: 8417777
22. D. Heineke *et al*., Redox transfer across the inner chloroplast envelope membrane. *Plant Physiol.* **95**, 1131–1137 (1991). doi: 10.1104/pp.95.4.1131; pmid: 16668101
23. K. Okazaki, G. Hummer, Elasticity, friction, and pathway of γ-subunit rotation in F_oF_1-ATP synthase. *Proc. Natl. Acad. Sci. U.S.A.* **112**, 10720–10725 (2015). doi: 10.1073/pnas.1500691112; pmid: 26261344
24. A. Wächter *et al*., Two rotary motors in F-ATP synthase are elastically coupled by a flexible rotor and a stiff stator stalk. *Proc. Natl. Acad. Sci. U.S.A.* **108**, 3924–3929 (2011). doi: 10.1073/pnas.1011581108; pmid: 21368147
25. G. Groth, E. Pohl, The structure of the chloroplast F_1-ATPase at 3.2 A resolution. *J. Biol. Chem.* **276**, 1345–1352 (2001). doi: 10.1074/jbc.M008015200; pmid: 11032839
26. G. Groth, Structure of spinach chloroplast F_1-ATPase complexed with the phytopathogenic inhibitor tentoxin. *Proc. Natl. Acad. Sci. U.S.A.* **99**, 3464–3468 (2002). doi: 10.1073/pnas.052546099; pmid: 11904410
27. C. Carmeli, Y. Lifshitz, Effects of P_1 and ADP on ATPase activity in chloroplasts. *Biochim. Biophys. Acta* **267**, 86–95 (1972). doi: 10.1016/0005-2728(72)90140-5; pmid: 4259760
28. J. P. Abrahams *et al*., The structure of bovine F_1-ATPase complexed with the peptide antibiotic efrapeptin. *Proc. Natl. Acad. Sci. U.S.A.* **93**, 9420–9424 (1996). doi: 10.1073/pnas.93.18.9420; pmid: 8790345
29. S. Wilkens, D. Borchardt, J. Weber, A. E. Senior, Structural characterization of the interaction of the δ and α subunits of the *Escherichia coli* F_1F_O-ATP synthase by NMR spectroscopy. *Biochemistry* **44**, 11786–11794 (2005). doi: 10.1021/bi0510678; pmid: 16128580
30. D. M. Rees, A. G. W. Leslie, J. E. Walker, The structure of the membrane extrinsic region of bovine ATP synthase. *Proc. Natl. Acad. Sci. U.S.A.* **106**, 21597–21601 (2009). doi: 10.1073/pnas.0910365106; pmid: 19995987
31. L. K. Lee, A. G. Stewart, M. Donohoe, R. A. Bernal, D. Stock, The structure of the peripheral stalk of *Thermus thermophilus* H^+-ATPase/synthase. *Nat. Struct. Mol. Biol.* **17**, 373–378 (2010). doi: 10.1038/nsmb.1761; pmid: 20173764
32. A. G. Stewart, L. K. Lee, M. Donohoe, J. J. Chaston, D. Stock, The dynamic stator stalk of rotary ATPases. *Nat. Commun.* **3**, 687 (2012). doi: 10.1038/ncomms1693; pmid: 22353718
33. P. A. Del Rizzo, Y. Bi, S. D. Dunn, ATP synthase *b* subunit dimerization domain: A right-handed coiled coil with offset helices. *J. Mol. Biol.* **364**, 735–746 (2006). doi: 10.1016/j.jmb.2006.09.028; pmid: 17028022
34. S. Saroussi, M. Schushan, N. Ben-Tal, W. Junge, N. Nelson, Structure and flexibility of the c-ring in the electromotor of rotary F_oF_1-ATPase of pea chloroplasts. *PLOS ONE* **7**, e43045 (2012). doi: 10.1371/journal.pone.0043045; pmid: 23049735
35. S. B. Vik, J. C. Long, T. Wada, D. Zhang, A model for the structure of subunit *a* of the *Escherichia coli* ATP synthase and its role in proton translocation. *Biochim. Biophys. Acta* **1458**, 457–466 (2000). doi: 10.1016/S0005-2728(00)00094-3; pmid: 10838058
36. M. F. Hohmann-Marriott, R. E. Blankenship, Evolution of photosynthesis. *Annu. Rev. Plant Biol.* **62**, 515–548 (2011). doi: 10.1146/annurev-arplant-042110-103811; pmid: 21438681
37. N. Mitome *et al*., Essential arginine residue of the F_o-*a* subunit in F_oF_1-ATP synthase has a role to prevent the proton shortcut without *c*-ring rotation in the F_o proton channel. *Biochem. J.* **430**, 171–177 (2010). doi: 10.1042/BJ20100621; pmid: 20518749
38. J. Vonck *et al*., Molecular architecture of the undecameric rotor of a bacterial Na^+-ATP synthase. *J. Mol. Biol.* **321**, 307–316 (2002). doi: 10.1016/S0022-2836(02)00597-1; pmid: 12144787
39. A. Dautant, J. Velours, M.-F. Giraud, Crystal structure of the Mg·ADP-inhibited state of the yeast F_1c_{10}-ATP synthase. *J. Biol. Chem.* **285**, 29502–29510 (2010). doi: 10.1074/jbc.M110.124529; pmid: 20610387
40. G. Wu, G. Ortiz-Flores, A. Ortiz-Lopez, D. R. Ort, A point mutation in *atpC1* raises the redox potential of the *Arabidopsis* chloroplast ATP synthase γ-subunit regulatory disulfide above the range of thioredoxin modulation. *J. Biol. Chem.* **282**, 36782–36789 (2007). doi: 10.1074/jbc.M707007200; pmid: 17959606
41. D. Pogoryelov *et al*., Probing the rotor subunit interface of the ATP synthase from *Ilyobacter tartaricus*. *FEBS J.* **275**, 4850–4862 (2008). doi: 10.1111/j.1742-4658.2008.06623.x; pmid: 18721138
42. G. Cingolani, T. M. Duncan, Structure of the ATP synthase catalytic complex (F_1) from *Escherichia coli* in an autoinhibited conformation. *Nat. Struct. Mol. Biol.* **18**, 701–707 (2011). doi: 10.1038/nsmb.2058; pmid: 21602818
43. M. L. Richter, Gamma–epsilon interactions regulate the chloroplast ATP synthase. *Photosynth. Res.* **79**, 319–329 (2004). doi: 10.1023/B:PRES.0000017157.08098.36; pmid: 16328798
44. L. R. Carrillo, J. E. Froehlich, J. A. Cruz, L. J. Savage, D. M. Kramer, Multi-level regulation of the chloroplast ATP synthase: The chloroplast NADPH thioredoxin reductase C (NTRC) is required for redox modulation specifically under low irradiance. *Plant J.* **87**, 654–663 (2016). doi: 10.1111/tpj.13226; pmid: 27233821
45. A. T. Jagendorf, Photophosphorylation and the chemiosmotic perspective. *Photosynth. Res.* **73**, 233–241 (2002). doi: 10.1023/A:1020415601058; pmid: 16245126
46. S. R. Ketcham, J. W. Davenport, K. Warncke, R. E. McCarty, Role of the gamma subunit of chloroplast coupling factor 1 in the light-dependent activation of photophosphorylation and ATPase activity by dithiothreitol. *J. Biol. Chem.* **259**, 7286–7293 (1984). pmid: 6233282
47. M. Tanigawara *et al*., Role of the DELSEED loop in torque transmission of F_1-ATPase. *Biophys. J.* **103**, 970–978 (2012). doi: 10.1016/j.bpj.2012.06.054; pmid: 23009846
48. D. M. Rand, R. A. Haney, A. J. Fry, Cytonuclear coevolution: The genomics of cooperation. *Trends Ecol. Evol.* **19**, 645–653 (2004). doi: 10.1016/j.tree.2004.10.003; pmid: 16701327
49. B. Varco-Merth, R. Fromme, M. Wang, P. Fromme, Crystallization of the c_{14}-rotor of the chloroplast ATP synthase reveals that it contains pigments. *Biochim. Biophys. Acta* **1777**, 605–612 (2008). doi: 10.1016/j.bbabio.2008.05.009; pmid: 18515064
50. T. K. Ritchie *et al*., Chapter 11 - Reconstitution of membrane proteins in phospholipid bilayer nanodiscs. *Methods Enzymol.* **464**, 211–231 (2009). doi: 10.1016/S0076-6879(09)64011-8 pmid: 19903557
51. E. G. Bligh, W. J. Dyer, A rapid method of total lipid extraction and purification. *Can. J. Biochem. Physiol.* **37**, 911–917 (1959). doi: 10.1139/y59-099; pmid: 13671378
52. N. Sato, M. Tsuzuki, in *Methods in Molecular Biology: Photosynthesis Research Protocols*, R. Carpentier, Ed. (2011), vol. 684, pp. 95–104.
53. G. Palumbo, F. Zullo, The use of iodine staining for the quantitative analysis of lipids separated by thin layer chromatography. *Lipids* **22**, 201–205 (1987). doi: 10.1007/BF02537303; pmid: 2437429
54. S. Q. Zheng *et al*., MotionCor2: Anisotropic correction of beam-induced motion for improved cryo-electron microscopy. *Nat. Methods* **14**, 331–332 (2017). doi: 10.1038/nmeth.4193; pmid: 28250466
55. A. Rohou, N. Grigorieff, CTFFIND4: Fast and accurate defocus estimation from electron micrographs. *J. Struct. Biol.* **192**, 216–221 (2015). doi: 10.1016/j.jsb.2015.08.008; pmid: 26278980
56. D. Kimanius, B. O. Forsberg, S. H. W. Scheres, E. Lindahl, Accelerated cryo-EM structure determination with parallelisation using GPUs in RELION-2. *eLife* **5**, e18722 (2016). doi: 10.7554/eLife.18722; pmid: 27845625
57. Z. Yang, J. Fang, J. Chittuluru, F. J. Asturias, P. A. Penczek, Iterative stable alignment and clustering of 2D transmission electron microscope images. *Structure* **20**, 237–247 (2012). doi: 10.1016/j.str.2011.12.007; pmid: 22325773
58. S. H. W. Scheres, RELION: Implementation of a Bayesian approach to cryo-EM structure determination. *J. Struct. Biol.* **180**, 519–530 (2012). doi: 10.1016/j.jsb.2012.09.006; pmid: 23000701
59. X. C. Bai, I. S. Fernandez, G. McMullan, S. H. W. Scheres, Ribosome structures to near-atomic resolution from thirty thousand cryo-EM particles. *eLife* **2**, e00461 (2013). doi: 10.7554/eLife.00461; pmid: 23427024
60. P. Emsley, K. Cowtan, Coot: Model-building tools for molecular graphics. *Acta Crystallogr. D Biol. Crystallogr.* **60**, 2126–2132 (2004). doi: 10.1107/S0907444904019158; pmid: 15572765
61. S. A. Ferguson, G. M. Cook, M. G. Montgomery, A. G. W. Leslie, J. E. Walker, Regulation of the thermoalkaliphilic F_1-ATPase from *Caldalkalibacillus thermarum*. *Proc. Natl. Acad. Sci. U.S.A.* **113**, 10860–10865 (2016). doi: 10.1073/pnas.1612035113; pmid: 27621435
62. H. Yagi *et al*., Structural and functional analysis of the intrinsic inhibitor subunit ε of F_1-ATPase from photosynthetic organisms. *Biochem. J.* **425**, 85–98 (2009). doi: 10.1042/BJ20091247; pmid: 19785575
63. P. D. Adams *et al*., PHENIX: A comprehensive Python-based system for macromolecular structure solution. *Acta Crystallogr. D Biol. Crystallogr.* **66**, 213–221 (2010). doi: 10.1107/S0907444909052925; pmid: 20124702
64. V. B. Chen *et al*., MolProbity: All-atom structure validation for macromolecular crystallography. *Acta Crystallogr. D Biol. Crystallogr.* **66**, 12–21 (2010). doi: 10.1107/S0907444909042073; pmid: 20057044
65. B. A. Barad *et al*., EMRinger: Side chain-directed model and map validation for 3D cryo-electron microscopy. *Nat. Methods* **12**, 943–946 (2015). doi: 10.1038/nmeth.3541; pmid: 26280328
66. B. K. Ho, F. Gruswitz, HOLLOW: Generating accurate representations of channel and interior surfaces in molecular structures. *BMC Struct. Biol.* **8**, 49 (2008). doi: 10.1186/1472-6807-8-49; pmid: 19014592
67. E. F. Pettersen *et al*., UCSF Chimera—a visualization system for exploratory research and analysis. *J. Comput. Chem.* **25**, 1605–1612 (2004). doi: 10.1002/jcc.20084; pmid: 15264254
68. T. D. Goddard *et al*., UCSF ChimeraX: Meeting modern challenges in visualization and analysis. *Protein Sci.* **27**, 14–25 (2018). doi: 10.1002/pro.3235; pmid: 28710774

ACKNOWLEDGMENTS

We thank M. Amrhein and T. Bausewein for their contributions during early stages of the project. We thank G. Hummer for discussions and N. Klusch and B. Murphy for reading the manuscript. **Funding:** This work was funded by the Max Planck Society, the Collaborative Research Center (CRC) 807 of the German Research Foundation (DFG), and the Wellcome Trust (WT110068/Z/15/Z). **Author contributions:** T.M. and W.K. directed the project; A.H. purified the protein; D.J.M. optimized the high-resolution EM alignment and the data collection procedure; A.H. and D.J.M. collected cryo-EM data; A.H. reconstructed the cryo-EM maps; A.H. and J.V. built and interpreted the model; A.H., J.V., T.M., and W.K. wrote the paper. **Competing interests:** Authors declare no competing interests. **Data and materials availability:** The cryo-EM maps have been deposited in the Electron Microscopy Data Bank with accession numbers EMD-4270, EMD-4271, and EMD-4272 for conformation 1, 2, and 3, respectively and EMD-4273 for the masked F_o of conformation 1. Atomic models have been deposited in the Protein Data Bank with accession numbers 6FKF, 6FKH, and 6FKI for conformation 1, 2, and 3, respectively.

SUPPLEMENTARY MATERIALS

www.sciencemag.org/content/360/6389/eaat4318/suppl/DC1
Figs. S1 to S13
Table S1
References (69–78)

26 February 2018; accepted 9 April 2018
10.1126/science.aat4318

RESEARCH ARTICLE

AMPHIBIAN DECLINE

Recent Asian origin of chytrid fungi causing global amphibian declines

Simon J. O'Hanlon,[1,2]* Adrien Rieux,[3] Rhys A. Farrer,[1] Gonçalo M. Rosa,[2,4,5] Bruce Waldman,[6] Arnaud Bataille,[6,7] Tiffany A. Kosch,[6,8] Kris A. Murray,[1] Balázs Brankovics,[9,10] Matteo Fumagalli,[11,12] Michael D. Martin,[13,14] Nathan Wales,[14] Mario Alvarado-Rybak,[15] Kieran A. Bates,[1,2] Lee Berger,[8] Susanne Böll,[16] Lola Brookes,[2] Frances Clare,[1,2] Elodie A. Courtois,[17] Andrew A. Cunningham,[2] Thomas M. Doherty-Bone,[18] Pria Ghosh,[1,19] David J. Gower,[20] William E. Hintz,[21] Jacob Höglund,[22] Thomas S. Jenkinson,[23] Chun-Fu Lin,[24] Anssi Laurila,[22] Adeline Loyau,[25,26] An Martel,[27] Sara Meurling,[22] Claude Miaud,[28] Pete Minting,[29] Frank Pasmans,[27] Dirk S. Schmeller,[25,26] Benedikt R. Schmidt,[30] Jennifer M. G. Shelton,[1] Lee F. Skerratt,[8] Freya Smith,[2,31] Claudio Soto-Azat,[15] Matteo Spagnoletti,[12] Giulia Tessa,[32] Luís Felipe Toledo,[33] Andrés Valenzuela-Sánchez,[15,34] Ruhan Verster,[19] Judit Vörös,[35] Rebecca J. Webb,[8] Claudia Wierzbicki,[1] Emma Wombwell,[2] Kelly R. Zamudio,[36] David M. Aanensen,[1,37] Timothy Y. James,[23] M. Thomas P. Gilbert,[13,14] Ché Weldon,[19] Jaime Bosch,[38] François Balloux,[12]† Trenton W. J. Garner,[2,19,32]† Matthew C. Fisher[1]*

Globalized infectious diseases are causing species declines worldwide, but their source often remains elusive. We used whole-genome sequencing to solve the spatiotemporal origins of the most devastating panzootic to date, caused by the fungus *Batrachochytrium dendrobatidis*, a proximate driver of global amphibian declines. We traced the source of *B. dendrobatidis* to the Korean peninsula, where one lineage, *Bd*ASIA-1, exhibits the genetic hallmarks of an ancestral population that seeded the panzootic. We date the emergence of this pathogen to the early 20th century, coinciding with the global expansion of commercial trade in amphibians, and we show that intercontinental transmission is ongoing. Our findings point to East Asia as a geographic hotspot for *B. dendrobatidis* biodiversity and the original source of these lineages that now parasitize amphibians worldwide.

The discovery of the amphibian-killing fungus *B. dendrobatidis* (*1*, *2*) was a turning point in understanding why amphibian species worldwide are in steep decline. Although amphibian declines and extinctions had been recorded by herpetologists as early as the 1970s, they were only recognized in 1990 as a global phenomenon that could not be explained by environmental changes and anthropogenic factors alone (*3*). The emergence of *B. dendrobatidis* and the disease that it causes, amphibian chytridiomycosis, as a causative agent of declines has been documented across six different regions: Australia (~1970s and 1990s) (*4*), Central America (~1970s) (*5*), South America (~1970s and 1980s) (*6*, *7*), the Caribbean islands (~2000s) (*8*), the North American Sierra Nevada (~1980s and 1990s) (*9*), and the Iberian Peninsula (~1990s) (*10*). The panzootic has been attributed to the emergence of a single *B. dendrobatidis* lineage, known as *Bd*GPL (Global Panzootic Lineage) (*11*). However, 20 years after identification of the disease, the timing of its worldwide expansion remains unknown and previous estimates for time to most recent common ancestor (TMRCA) for *Bd*GPL span two orders of magnitude, from 100 years before the present (*11*) to 26,000 years before the present (*12*). The geographic origin of the pathogen is similarly contested, with the source of the disease variously suggested to be Africa (*13*), North America (*14*), South America (*15*), Japan (*16*), and East Asia (*17*).

Global diversity of *B. dendrobatidis*

To resolve these inconsistencies, we isolated *B. dendrobatidis* from all the candidate source continents and sequenced the genomes of 177 isolates to high depth, then combined our data with published genomes from three prior studies (*11*, *12*, *18*) to generate a globally representative panel of 234 isolates (Fig. 1A and fig. S1). This data set covers all continents from which *B. dendrobatidis* has been detected to date, and spans infections of all three extant orders of Amphibia (fig. S1 and table S1). Mapped against the *B. dendrobatidis* reference genome JEL423, our sequencing recovered 586,005 segregating single-nucleotide polymorphisms (SNPs). Phylogenetic analysis recovered all previously detected divergent lineages (Fig. 1B and fig. S2). The previously accepted lineages *Bd*GPL (global), *Bd*CAPE (African), *Bd*CH (European), and *Bd*BRAZIL (Brazilian) were all detected (*19*), but our discovery of a new hyperdiverse lineage in amphibians native to the Korean peninsula (*Bd*ASIA-1) redefined these lineages and their relationships. The *Bd*CH lineage, which was previously thought to be enzootic to Switzerland (*11*), now groups with the *Bd*ASIA-1 lineage. A

[1]Department of Infectious Disease Epidemiology and MRC Centre for Global Infectious Disease Analysis, School of Public Health, Imperial College London, London W2 1PG, UK. [2]Institute of Zoology, Regent's Park, London NW1 4RY, UK. [3]CIRAD, UMR PVBMT, 97410 St. Pierre, Reunion, France. [4]Department of Biology, University of Nevada, Reno, NV 89557, USA. [5]Centre for Ecology, Evolution and Environmental Changes (CE3C), Faculdade de Ciências da Universidade de Lisboa, Lisboa, Portugal. [6]Laboratory of Behavioral and Population Ecology, School of Biological Sciences, Seoul National University, Seoul 08826, South Korea. [7]CIRAD, UMR ASTRE, F-34398 Montpellier, France. [8]One Health Research Group, College of Public Health, Medical and Veterinary Sciences, James Cook University, Townsville, Queensland 4811, Australia. [9]Westerdijk Fungal Biodiversity Institute, Uppsalalaan 8, 3584CT Utrecht, Netherlands. [10]Institute of Biodiversity and Ecosystem Dynamics, University of Amsterdam, Science Park 904, 1098 XH Amsterdam, Netherlands. [11]Department of Life Sciences, Silwood Park Campus, Imperial College London, Ascot, UK. [12]UCL Genetics Institute, University College London, London WC1E 6BT, UK. [13]Department of Natural History, NTNU University Museum, Norwegian University of Science and Technology (NTNU), Erling Skakkes gate 49, NO-7012 Trondheim, Norway. [14]Centre for GeoGenetics, Natural History Museum of Denmark, University of Copenhagen, Øster Voldgade 5-7, 1350 Copenhagen, Denmark. [15]Centro de Investigación para la Sustentabilidad, Facultad de Ecología y Recursos Naturales, Universidad Andres Bello, Republica 440, Santiago, Chile. [16]Agency for Population Ecology and Nature Conservancy, Gerbrunn, Germany. [17]Laboratoire Ecologie, Évolution, Interactions des Systèmes Amazoniens (LEEISA), Université de Guyane, CNRS, IFREMER, 97300 Cayenne, French Guiana. [18]Conservation Programmes, Royal Zoological Society of Scotland, Edinburgh, UK. [19]Unit for Environmental Sciences and Management, Private Bag x6001, North-West University, Potchefstroom 2520, South Africa. [20]Life Sciences, Natural History Museum, London SW7 5BD, UK. [21]Biology Department, University of Victoria, Victoria, BC V8W 3N5, Canada. [22]Department of Ecology and Genetics, EBC, Uppsala University, Norbyv. 18D, SE-75236, Uppsala, Sweden. [23]Department of Ecology and Evolutionary Biology, University of Michigan, Ann Arbor, MI 48109, USA. [24]Zoology Division, Endemic Species Research Institute, 1 Ming-shen East Road, Jiji, Nantou 552, Taiwan. [25]Department of Conservation Biology, Helmholtz Centre for Environmental Research–UFZ, 04318 Leipzig, Germany. [26]EcoLab, Université de Toulouse, CNRS, INPT, UPS, Toulouse, France. [27]Department of Pathology, Bacteriology and Avian Diseases, Faculty of Veterinary Medicine, Ghent University, B-9820 Merelbeke, Belgium. [28]PSL Research University, CEFE UMR 5175, CNRS, Université de Montpellier, Université Paul-Valéry Montpellier, EPHE, Montpellier, France. [29]Amphibian and Reptile Conservation (ARC) Trust, Boscombe, Bournemouth, Dorset BH1 4AP, UK. [30]Department of Evolutionary Biology and Environmental Studies, University of Zurich, 8057 Zurich, Switzerland, and Info Fauna Karch, UniMail-Bâtiment G, Bellevaux 51, 2000 Neuchâtel, Switzerland. [31]National Wildlife Management Centre, APHA, Woodchester Park, Gloucestershire GL10 3UJ, UK. [32]Non-profit Association Zirichiltaggi–Sardinia Wildlife Conservation, Strada Vicinale Filigheddu 62/C, I-07100 Sassari, Italy. [33]Laboratório de História Natural de Anfíbios Brasileiros (LaHNAB), Departamento de Biologia Animal, Instituto de Biologia, Unicamp, Campinas, Brazil. [34]ONG Ranita de Darwin, Nataniel Cox 152, Santiago, Chile. [35]Collection of Amphibians and Reptiles, Department of Zoology, Hungarian Natural History Museum, Budapest, Baross u. 13., 1088, Hungary. [36]Department of Ecology and Evolutionary Biology, Cornell University, Ithaca, NY 14853, USA. [37]Centre for Genomic Pathogen Surveillance, Wellcome Genome Campus, Cambridgeshire, UK. [38]Museo Nacional de Ciencias Naturales, CSIC c/ Jose Gutierrez Abascal 2, 28006 Madrid, Spain.

***Corresponding author. Email: simon.ohanlon@gmail.com (S.J.O.); matthew.fisher@imperial.ac.uk (M.C.F.)** †These authors contributed equally to this work.

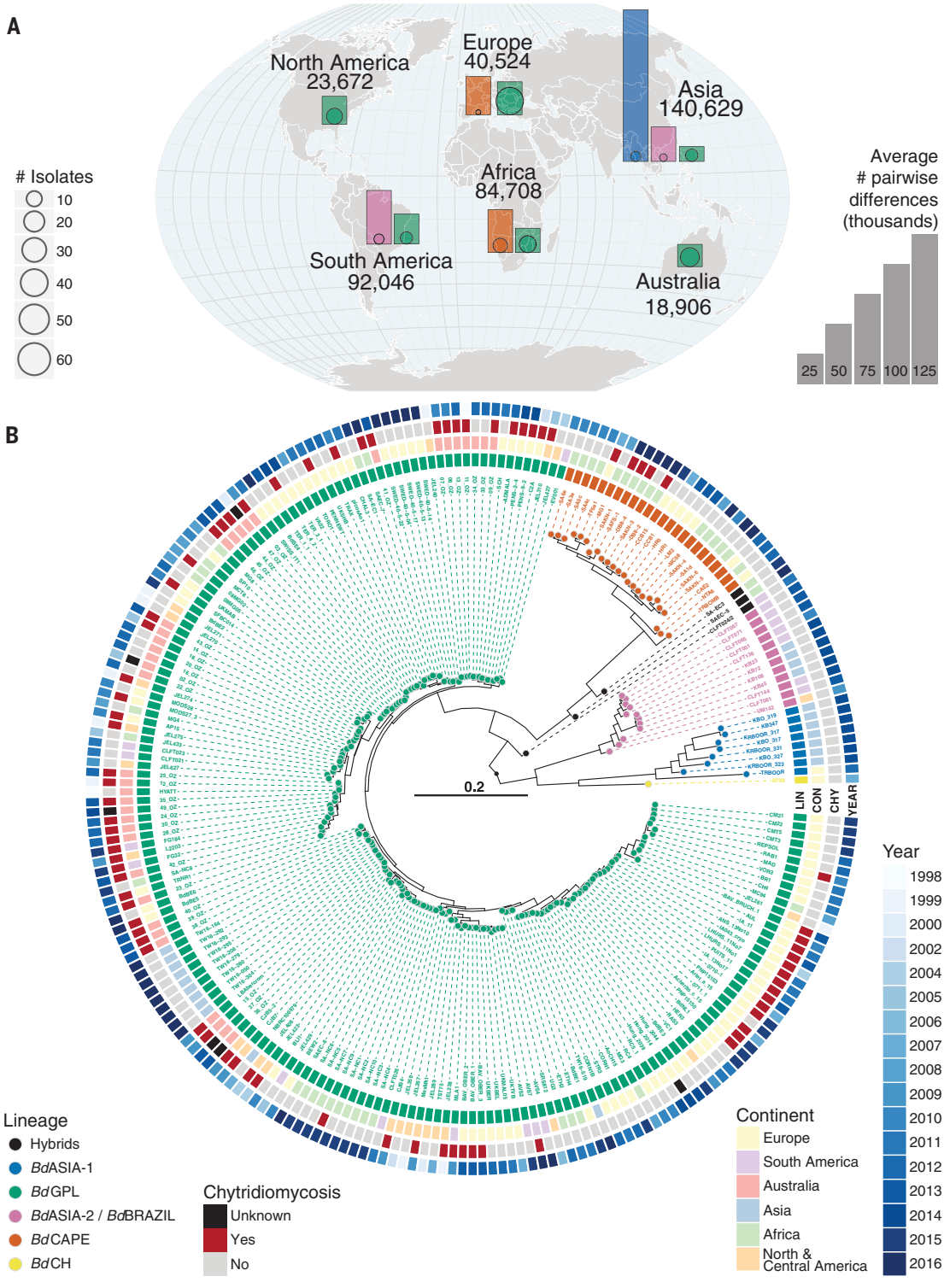

Fig. 1. Genetic diversity and phylogenetic tree of a global panel of 234 *B. dendrobatidis* isolates. (**A**) Map overlaid with bar charts showing the relative diversity of isolates found in each continent and by each major lineage (excluding isolates from traded animals). The bar heights represent the average numbers of segregating sites between all pairwise combinations of isolates of each lineage in each continent (therefore, only lineages with two or more isolates from a continent are shown). Outlined points at the base of each bar are scaled by the number of isolates for each lineage in that continent. The numbers around the outside of the globe are the average number of segregating sites between all pairwise combinations of isolates grouped by continent. Colors denote lineage as shown in (B). (**B**) Midpoint rooted radial phylogeny supports four deeply diverged lineages of *B. dendrobatidis*: *Bd*ASIA-1, *Bd*ASIA-2/*Bd*BRAZIL, *Bd*CAPE, and *Bd*GPL. All major splits within the phylogeny are supported by 100% of 500 bootstrap replicates. See fig. S2 for tree with full bootstrap support values on all internal branches.

second Asian-associated lineage (*Bd*ASIA-2) was recovered from invasive North American bullfrogs in Korea and is closely related to the lineage that is enzootic to the Brazilian Atlantic forest (*Bd*BRAZIL) (*20*). It was not possible to infer the direction of intercontinental spread between isolates within this lineage, so it was named *Bd*ASIA-2/*Bd*BRAZIL. Conditional on the midpoint rooting of the phylogeny in Fig. 1B, we now define the main diverged lineages as *Bd*GPL, *Bd*CAPE, *Bd*ASIA-1 (which includes the single *Bd*CH isolate), and *Bd*ASIA-2/*Bd*BRAZIL. Previous phylogenetic relationships developed using the widely used ribosomal intragenic spacer *ITS-1* region do not accurately distinguish *B. dendrobatidis* lineages (fig. S3), and this likely explains much of the place-of-origin conflict in the literature (*15*–*17*).

Pairwise comparisons among isolates within each lineage show that the average number of segregating sites is greater for *Bd*ASIA-1 than for any other lineage by a factor of 3 (Fig. 1A and Table 1) and that nucleotide diversity (π; fig. S4) is greater by a factor of 2 to 4. Seven of our eight *Bd*ASIA-1 isolates were recently cultured from wild South Korean frogs, and the other came from the pet trade in Belgium; all

Table 1. Comparison of common genetic diversity measures among *B. dendrobatidis* lineages. Total segregating sites for each lineage include all segregating sites where genotype calls were made in at least half of the isolates. Average pairwise-segregating sites are the average numbers of sites with different genotypes between all pairs of isolates within a lineage. Total homozygous segregating sites include all sites within a lineage where there is at least one homozygous difference between isolates. Average pairwise-homozygous segregating sites are the average numbers of sites with different homozygous genotypes between all pairs of isolates within a lineage. Nucleotide diversity (π) is the mean of the per-site nucleotide diversity. Tajima's *D* is reported as the mean over 1-kbp bins.

Lineage	Number of isolates	Total segregating sites	Average pairwise-segregating sites	Total homozygous segregating sites	Average pairwise-homozygous segregating sites	π	Tajima's *D*
*Bd*ASIA-1	8	327,996	142,437	108,353	21,716	0.0044	0.2540
*Bd*ASIA-2/*Bd*BRAZIL	12	148,021	51,069	48,722	6,216	0.0018	0.9825
*Bd*CAPE	24	146,466	38,881	53,884	4,977	0.0016	0.3143
*Bd*GPL	187	127,770	26,546	68,493	3,101	0.0009	0.9792

eight were aclinical infections. These isolates show that the Korean peninsula is a global center of *B. dendrobatidis* diversity and that East Asia may contain the ancestral population of *B. dendrobatidis*, as suggested by Bataille *et al.* (*17*).

We investigated this hypothesis further using Bayesian-based haplotype clustering (*21*) and found the greatest haplotype sharing among isolates within *Bd*ASIA-1 and between *Bd*ASIA-1 and all other lineages (fig. S5). This provides direct genetic evidence that *Bd*ASIA-1 shares more diversity with the global population of *B. dendrobatidis* than any other lineage. In an independent test of ancestry, we used OrthoMCL (*22*) to root a *B. dendrobatidis* phylogeny to its closest known relative, *B. salamandrivorans*, which currently threatens salamanders (*23*). This tree indicates that the Asian and Brazilian isolates of *B. dendrobatidis* lie outside a clade comprising all other isolates (fig. S6 and table S2). To identify the signature of demographic histories across lineages, we used Tajima's *D* (*24*). Genome scans of most lineages showed highly variable positive and negative values of *D* with maximum amplitude exhibited by *Bd*GPL (−2.6 to +6.2; Fig. 2F), indicating that these lineages (*Bd*ASIA-2/*Bd*BRAZIL, *Bd*CAPE, and *Bd*GPL) have undergone episodes of population fluctuation and/or strong natural selection that are consistent with a history of spatial and host radiations. In striking contrast, *Bd*ASIA-1 shows a flat profile for Tajima's *D* (Fig. 2F) indicating mutation-drift equilibrium likely reflective of pathogen endemism in this region.

Dating the emergence of *Bd*GPL

The broad range of previous estimates for the TMRCA of *Bd*GPL spanning 26,000 years (*11*, *12*) can be explained by two sources of inaccuracy: (i) unaccounted recombination and (ii) the application of unrealistic evolutionary rates. To address these, we first interrogated the 178,280-kbp mitochondrial genome (mtDNA), which has high copy number and low rates of recombination relative to the nuclear genome. To resolve the structure of the mtDNA genome, we resorted to long-read sequencing using a MinION device (Oxford Nanopore Technologies, Cambridge, UK), which allowed us to describe this molecule's unusual configuration; *B. dendrobatidis* carries three linear mitochondrial segments, each having inverted repeats at the termini with conserved mitochondrial genes spread over two of the segments (fig. S7). Additionally, we sought regions of the autosomal genome with low rates of recombination to obtain an independent estimate of the TMRCA of *Bd*GPL.

Detection of crossover events in the *B. dendrobatidis* autosomal genome (*18*) using a subset of the isolates in this study revealed a large (1.66 Mbp) region of Supercontig_1.2 in *Bd*GPL that exhibits several features that identified it as a recombination "coldspot": (i) a continuous region of reduced Tajima's *D* (Fig. 2F), (ii) sustained high values of population differentiation as measured by the fixation index (F_{ST}) when compared with all other lineages (Fig. 3A), (iii) a continuous region of reduced nucleotide diversity (π; fig. S4), and (iv) shared loss of heterozygosity (fig. S8). We expanded sampling to infer the temporal range of pathogen introductions using a broad panel of isolates with known date of isolation (n = 184, ranging from 1998 to 2016) and whole-genome RNA baiting to obtain reads from preserved amphibians that had died of chytridiomycosis. We then investigated whether our data set contained sufficient signal to perform tip-dating inferences by building phylogenetic trees using PhyML (*25*) (Fig. 2, A and C). We fitted root-to-tip distances to collection dates both at the whole-tree and within-lineage scales. We observed a positive and significant correlation within *Bd*GPL only, for both the mitochondrial and nuclear genomes, demonstrating sufficient temporal signal to perform thorough tip-dating inferences at this evolutionary scale (Fig. 2, B and D).

Tip-dating in BEAST was used to co-estimate ancestral divergence times and the rate at which mutations accumulate within the *Bd*GPL lineage. The mean mitochondrial substitution rate was 1.01×10^{-6} substitutions per site per year [95% highest posterior density (HPD), 4.29×10^{-7} to 1.62×10^{-6}]. The mean nuclear substitution rate was 7.29×10^{-7} substitutions per site per year (95% HPD, 3.41×10^{-7} to 1.14×10^{-6}), which is comparable to a recent report of an evolutionary rate of 2.4×10^{-6} to 2.6×10^{-6} substitutions per site per year for another unicellular yeast, *Saccharomyces cerevisiae* beer strains (*26*). These rate estimates are faster by a factor of >300 than the rate used in a previous study (*12*) to obtain a TMRCA of 26,400 years for *Bd*GPL. Accordingly, we estimate that the ancestor of the amphibian panzootic *Bd*GPL originated between 120 and 50 years ago (Fig. 2E), with HPD estimates of 1898 (95% HPD, 1809 to 1941) and 1962 (95% HPD, 1859 to 1988) for the nuclear and mitochondrial dating analyses, respectively (Fig. 2E).

We considered an additional calibration approach for the TMRCA of the mitochondrial genome where we included informative priors on nodes around the dates for the first historical descriptions of *Bd*GPL detection in Australia (1978), Central America (1972), Sierra de Guadarrama (Europe) (1997), and the Pyrenees (Europe) (2000). We did not include priors for nodes where observed declines have been reported but where the lineage responsible for those declines is unknown. This mixed dating method based on tip and node calibration yielded very similar estimates [TMRCA estimates of 1975 (95% HPD, 1939 to 1989) (fig. S9)], further strengthening our confidence in a recent date of emergence for *Bd*GPL. An expansion of *Bd*GPL in the 20th century coincides with the global expansion in amphibians traded for exotic pet, medical, and food purposes (*27*, *28*). Within our phylogeny, we found representatives from all lineages among traded animals (figs. S10 to S14) and identified 10 events where traded amphibians were infected with non-enzootic isolates (Fig. 4). This finding demonstrates the ongoing failure of international biosecurity despite the listing of *B. dendrobatidis* by the World Organisation for Animal Health (OIE) in 2008.

Hybridization between recontacting lineages of *B. dendrobatidis*

To determine the extent to which the four main lineages of *B. dendrobatidis* have undergone recent genetic exchange, we used the site-by-site–based approach implemented in STRUCTURE (*29*). Although most isolates could be assigned unambiguously to one of the four main lineages, we identified three hybrid genotypes (Fig. 3B), including one previously reported hybrid (isolate

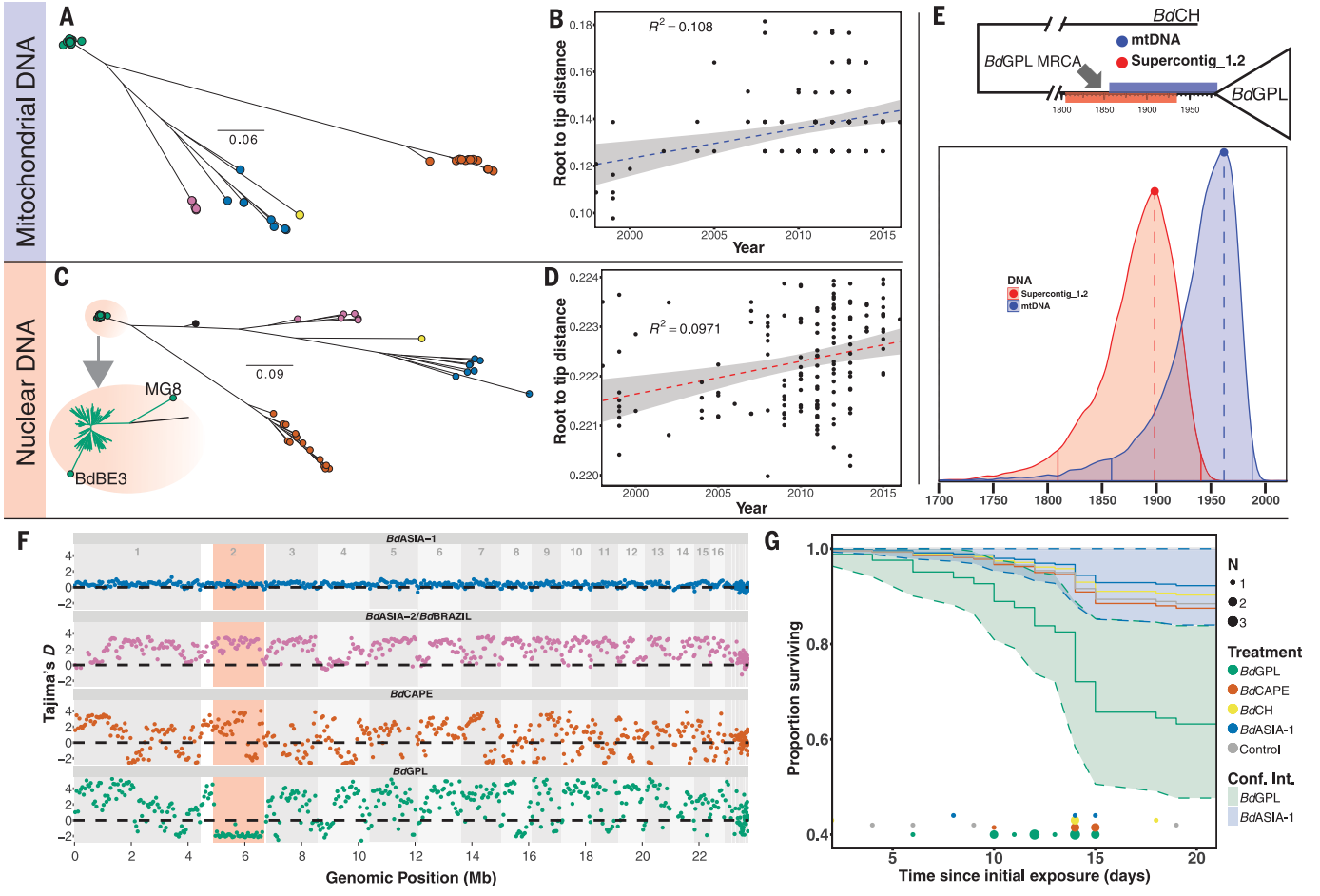

Fig. 2. Dating the emergence of *Bd*GPL. (**A**) Maximum likelihood (ML) tree constructed from 1150 high-quality SNPs found within the 178-kbp mitochondrial genome. (**B**) Linear regression of root-to-tip distance against year of isolation for *Bd*GPL isolates in mitochondrial DNA phylogeny in (A), showing a significant temporal trend ($F = 14.35$, $P = 0.00024$). (**C**) ML tree constructed from a 1.66-Mbp region of low recombination in Supercontig_1.2. Two *Bd*GPL isolates, BdBE3 and MG8, fall on long branches away from the rest of the *Bd*GPL isolates (see inset zoom) as a result of introgression from another lineage (*Bd*CAPE; see Fig. 3B) and were excluded from the dating analysis. (**D**) Linear regression of root-to-tip distance against year of isolation for *Bd*GPL isolates from phylogeny in (C), with a significant temporal trend ($F = 15.92$, $P = 0.0001$). (**E**) Top: *Bd*GPL and outgroup *Bd*CH, with the 95% HPD estimates for MRCA for *Bd*GPL from mtDNA dating (blue) and nuclear DNA dating (red). Bottom: Full posterior distributions from tip-dating models for mtDNA (blue) and partial nuclear DNA (red) genomes. Solid vertical lines are limits of the 95% HPD. Dashed vertical lines denote the maximal density of the posterior distributions. (**F**) Sliding 10-kb, nonoverlapping window estimates of Tajima's *D* for each of the main *B. dendrobatidis* lineages. The region highlighted in red is the low-recombination segment of Supercontig_1.2. (**G**) Survival curves for *Bufo bufo* metamorphs for different *B. dendrobatidis* treatment groups: *Bd*ASIA-1 (blue), *Bd*CAPE (orange), *Bd*CH (yellow), *Bd*GPL (green), and control (gray). Confidence intervals are shown for *Bd*GPL and *Bd*ASIA-1, showing no overlap by the end of the experiment. Instances of mortalities in each treatment group are plotted along the *x* axis, with points scaled by number of mortalities at each interval (day).

CLFT024/2) (*20*), and discovered two newly identified hybrids of *Bd*GPL and *Bd*CAPE in South Africa. Furthermore, *Bd*CH (isolate 0739) appears to be a chimera of multiple lineages that may represent unsampled genomic diversity residing in East Asia, rather than true hybridization. These hybrid genomes demonstrate that *B. dendrobatidis* is continuing to exchange haplotypes among lineages when they interact after continental invasions, generating novel genomic diversity. We analyzed isolate clustering using principal components analysis on a filtered subset of 3900 SNPs in linkage equilibrium, revealing an overall population structure that is consistent with our phylogenetic analyses (Fig. 3C). In addition, the putatively identified hybrid isolates of *B. dendrobatidis* were shown to fall between main lineage clusters (Fig. 3C), further strengthening our hypothesis of haplotype exchange occurring during secondary contact between lineages.

Associations among lineage, virulence, and declines

Genotypic diversification of pathogens is commonly associated with diversification of traits associated with host exploitation (*30*) and is most commonly measured as the ability to infect a host and to cause disease post-infection. We tested for variation of these two phenotypic traits across four *B. dendrobatidis* lineages by exposing larval and postmetamorphic common toads (*Bufo bufo*). Larvae are highly susceptible to infection but do not die before metamorphosis, in contrast to postmetamorphic juveniles, which are susceptible to infection and fatal chytridiomycosis (*31*). In tadpoles, both *Bd*GPL and *Bd*ASIA-1 were significantly more infectious than *Bd*CAPE and *Bd*CH (fig. S15 and tables S3 and S4). In metamorphs, *Bd*GPL was significantly more infectious than the other treatments, relative to the control group, and was significantly more lethal in experimental challenge than the geographically more restricted *Bd*CAPE, *Bd*ASIA-1, and *Bd*CH (Fig. 2G). We further tested for differences in virulence among lineages by using our global data set to examine whether chytridiomycosis was nonrandomly associated with *B. dendrobatidis* lineage. We detected a significant difference ($P < 0.001$) in the

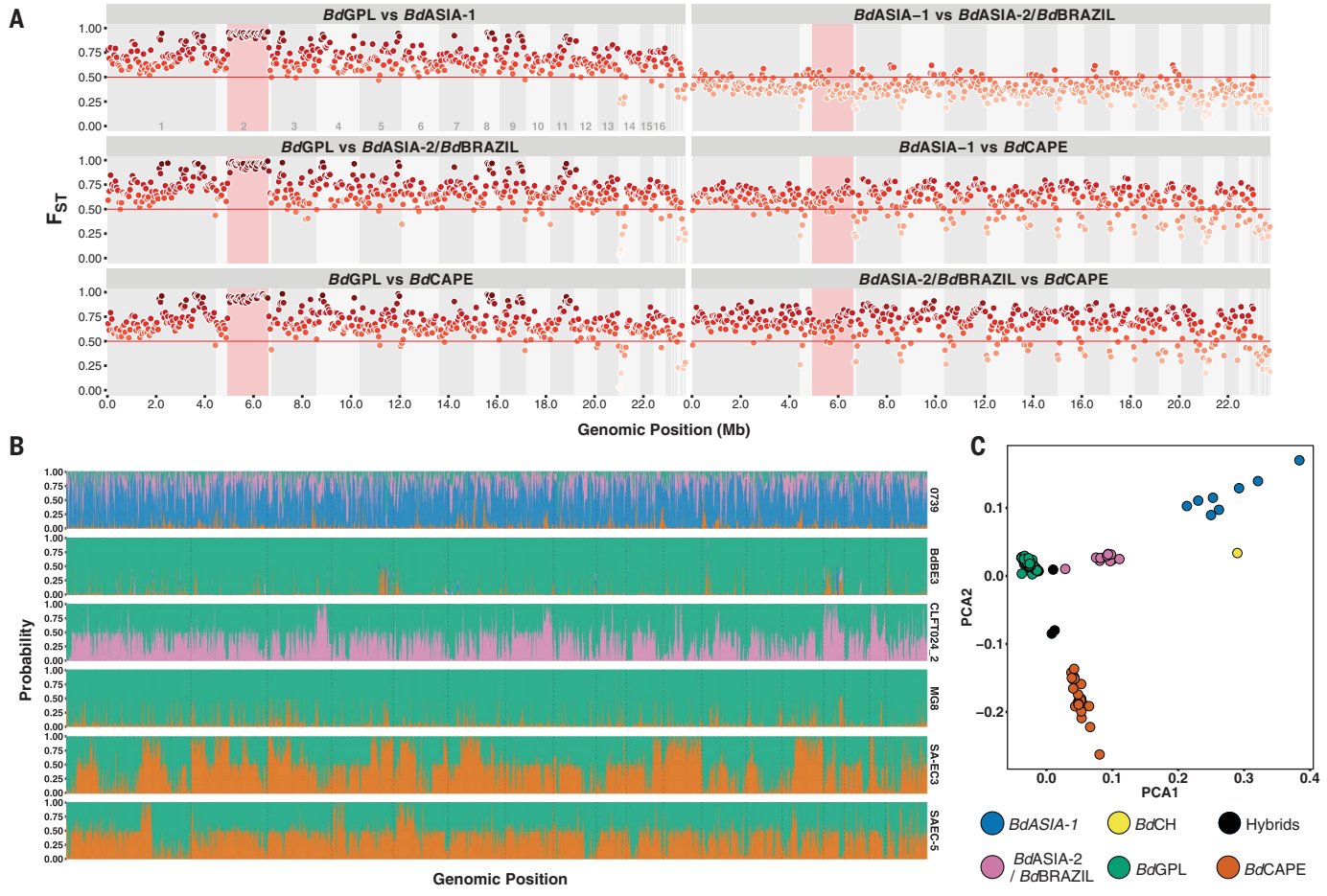

Fig. 3. F_{ST} and site-by-site STRUCTURE analysis. (**A**) Non-overlapping 10-kb sliding window of F_{ST} between lineages. The region highlighted in red is the Supercontig_1.2:500,000–2,160,000 low-recombination region. (**B**) Site-by-site analysis of population ancestry for a random selection of 9905 SNPs. Results show those isolates to be either hybrid (SA-EC3, SA-EC5, and CLFT024/2) or with significant introgression from nonparental lineages (isolates BdBE3 and MG8) or a chimera of unsampled diversity, likely originating from East Asia (0739, the *Bd*CH isolate). Each column represents a biallelic SNP position. The columns are colored according to the joint probability of either allele copy arising from one of four distinct populations. Colors represent assumed parental lineages as given in Fig. 3C. (**C**) Principal components analysis of 3900 SNPs in linkage equilibrium. Each point represents an isolate, colored by phylogenetic lineage. The isolates separate into clearly defined clusters. The axes plot the first and second principal components, PCA1 and PCA2.

proportion of isolates associated with chytridiomycosis among the three parental lineages (*Bd*ASIA-1 and *Bd*ASIA-2/*Bd*BRAZIL were grouped because of low sample sizes), and post hoc tests indicated significant excess in virulence in both *Bd*GPL and *Bd*CAPE lineages relative to the combined *Bd*ASIA-1 and *Bd*ASIA-2/*Bd*BRAZIL (all $P < 0.05$). However, we did not detect a significant difference between *Bd*GPL and *Bd*CAPE (fig. S16 and table S5). These data suggest that although *Bd*GPL is highly virulent, population-level outcomes are also context-dependent (*32*); under some conditions, other lineages can also be responsible for lethal amphibian disease and population declines (*33*).

Historical and contemporary implications of panzootic chytridiomycosis

Our results point to endemism of *B. dendrobatidis* in Asia, out of which multiple panzootic lineages have emerged. These emergent diasporas include the virulent and highly transmissible *Bd*GPL, which spread during the early 20th century via a yet unknown route to infect close to 700 amphibian species out of ~1300 thus far tested (*34*). With more than 7800 amphibian species currently described, the number of affected species is likely to rise. The international trade in amphibians has undoubtedly contributed directly to vectoring this pathogen worldwide (Fig. 4) (*35*, *36*), and within our phylogeny we identified many highly supported (≥90% bootstrap support) clades on short branches that linked isolates collected from wild amphibian populations across different continents (Fig. 4 and figs. S10 to S14). However, the role of globalized trade in passively contributing to the spread of this disease cannot be ruled out. It is likely no coincidence that our estimated dates for the emergence of *Bd*GPL span the globalization "big bang"—the rapid proliferation in intercontinental trade, capital, and technology that started in the 1820s (*37*). The recent invasion of Madagascar by Asian common toads hidden within mining equipment (*38*) demonstrates the capacity for amphibians to escape detection at borders and exemplifies how the unintended anthropogenic dispersal of amphibians has also likely contributed to the worldwide spread of pathogenic chytrids.

The hyperdiverse hotspot identified in Korea likely represents a fraction of the *Batrachochytrium* genetic diversity in Asia, and further sampling across this region is urgently needed because the substantial global trade in Asian amphibians (*39*) presents a risk of seeding future outbreak lineages. Unique ribosomal DNA haplotypes of *B. dendrobatidis* have been detected in native amphibian species in India (*40*, *41*), Japan (*16*), and China (*42*). Although caution should be observed when drawing conclusions about lineages based on short sequence alignments (fig. S3), other endemic lineages probably remain undetected within Asia. It is noteworthy that the northern European countryside is witnessing the emergence of *B. salamandrivorans*, which also has its origin in

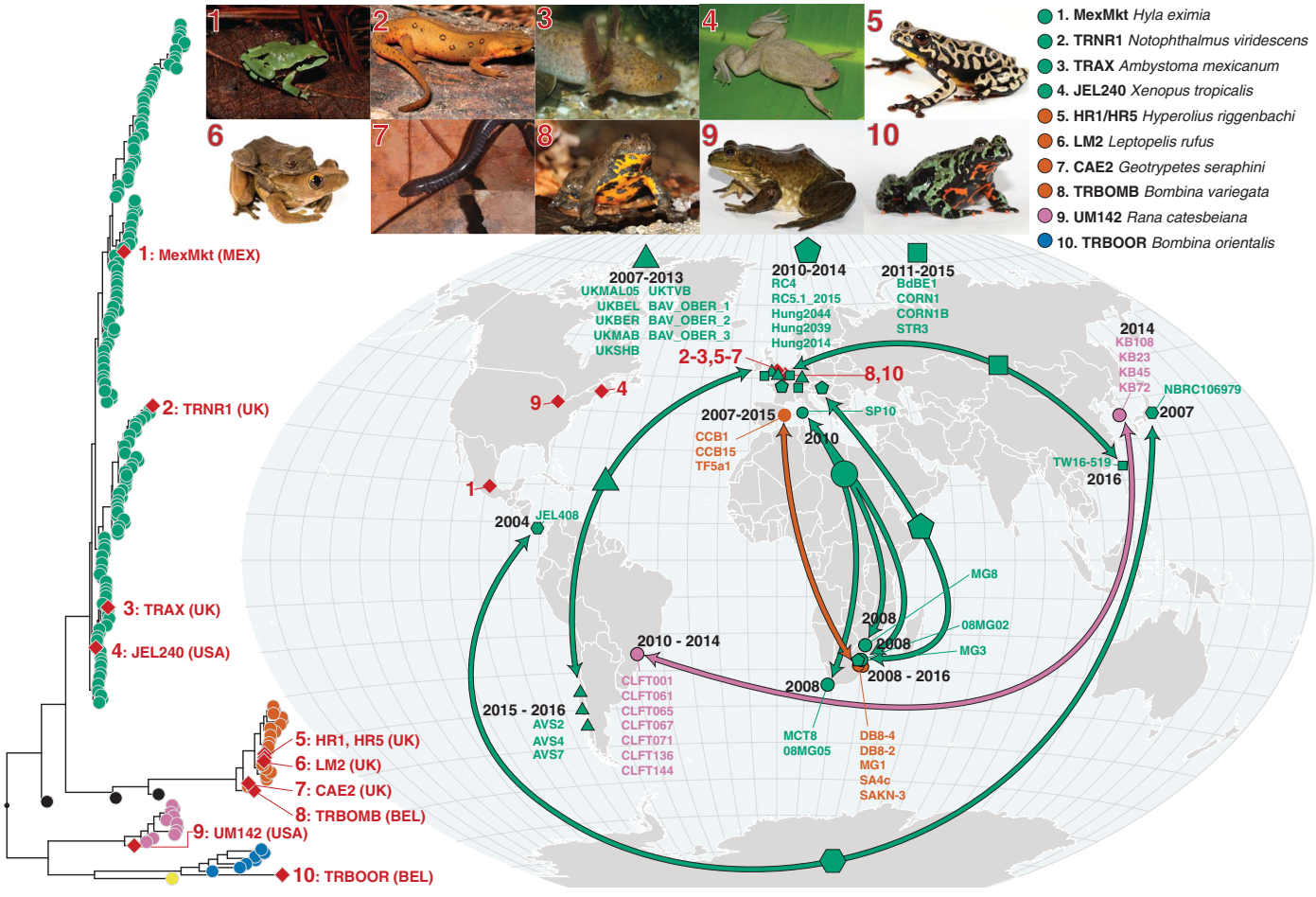

Fig. 4. Genotypes of *Bd* isolated from infected amphibians in the international trade and phylogenetically linked genotypes from segregated geographic localities. The red diamonds on the phylogeny indicate isolates recovered from traded animals. Their geographic location is displayed by the red diamonds on the map. The red numbers link each trade isolate to the relevant picture of the donor host species atop the figure and their placement in the phylogeny. The arrows on the map link geographically separated isolates that form closely related phylogenetic clades with high bootstrap support (≥90%). Each clade is denoted by a different-shaped point on the map; names of isolates within each clade are displayed on the map. The dates displayed indicate the sampling time frame for each clade. The phylogenetic position of each clade is displayed in figs. S10 to S14. The colors of points and arrows on the map indicate lineage according to Fig. 1. A browsable version of this phylogeny can be accessed at https://microreact.org/project/GlobalBd. [Photo credits: (1) *Hyla eximia*, Ricardo Chaparro; (2) *Notophthalmus viridescens*, Patrick Coin/CC-BY-SA 2.5; (3) *Ambystoma mexicanum*, Henk Wallays; (4) *Xenopus tropicalis*, Daniel Portik; (5) *Hyperolius riggenbachi* and (6) *Leptopelis rufus*, Brian Freiermuth; (7) *Geotrypetes seraphini*, Peter Janzen; (8) *Bombina variegata*, (9) *Rana catesbeiana*, and (10) *Bombina orientalis*, Frank Pasmans]

Asia. The emergence of *B. salamandrivorans* is linked to the amphibian pet trade (*43*), and the broad expansion of virulence factors that are found in the genomes of these two pathogens is testament to the evolutionary innovation that has occurred in these Asian *Batrachochytrium* fungi (*23*).

Our findings show that the global trade in amphibians continues to be associated with the translocation of chytrid lineages with panzootic potential. Ultimately, our work confirms that panzootics of emerging fungal diseases in amphibians are caused by ancient patterns of pathogen phylogeography being redrawn as largely unrestricted global trade moves pathogens into new regions, infecting new hosts and igniting disease outbreaks. Within this context, the continued strengthening of transcontinental biosecurity is critical to the survival of amphibian species in the wild (*44*).

REFERENCES AND NOTES

1. M. C. Fisher *et al.*, *Nature* **484**, 186–194 (2012).
2. L. Berger *et al.*, *Proc. Natl. Acad. Sci. U.S.A.* **95**, 9031–9036 (1998).
3. A. R. Blaustein, D. B. Wake, *Trends Ecol. Evol.* **5**, 203–204 (1990).
4. L. F. Skerratt *et al.*, *EcoHealth* **4**, 125–134 (2007).
5. T. L. Cheng, S. M. Rovito, D. B. Wake, V. T. Vredenburg, *Proc. Natl. Acad. Sci. U.S.A.* **108**, 9502–9507 (2011).
6. K. R. Lips, J. Diffendorfer, J. R. Mendelson, M. W. Sears, *PLOS Biol.* **6**, e72 (2008).
7. T. Carvalho, C. G. Becker, L. F. Toledo, *Proc. R. Soc. B* **284**, 20162254 (2017).
8. M. A. Hudson *et al.*, *Sci. Rep.* **6**, 30772 (2016).
9. L. J. Rachowicz *et al.*, *Ecology* **87**, 1671–1683 (2006).
10. J. Bosch, I. Martinez-Solano, M. Garcia-Paris, *Biol. Conserv.* **97**, 331–337 (2001).
11. R. A. Farrer *et al.*, *Proc. Natl. Acad. Sci. U.S.A.* **108**, 18732–18736 (2011).
12. E. B. Rosenblum *et al.*, *Proc. Natl. Acad. Sci. U.S.A.* **110**, 9385–9390 (2013).
13. C. Weldon, L. H. du Preez, A. D. Hyatt, R. Muller, R. Spears, *Emerg. Infect. Dis.* **10**, 2100–2105 (2004).
14. B. L. Talley, C. R. Muletz, V. T. Vredenburg, R. C. Fleischer, K. R. Lips, *Biol. Conserv.* **182**, 254–261 (2015).
15. D. Rodriguez, C. G. Becker, N. C. Pupin, C. F. B. Haddad, K. R. Zamudio, *Mol. Ecol.* **23**, 774–787 (2014).
16. K. Goka *et al.*, *Mol. Ecol.* **18**, 4757–4774 (2009).
17. A. Bataille *et al.*, *Mol. Ecol.* **22**, 4196–4209 (2013).
18. R. A. Farrer *et al.*, *PLOS Genet.* **9**, e1003703 (2013).
19. S. Argimón *et al.*, *Microb. Genomics* **2**, e000093 (2016).
20. L. M. Schloegel *et al.*, *Mol. Ecol.* **21**, 5162–5177 (2012).
21. D. J. Lawson, G. Hellenthal, S. Myers, D. Falush, *PLOS Genet.* **8**, e1002453 (2012).
22. L. Li, C. J. Stoeckert Jr., D. S. Roos, *Genome Res.* **13**, 2178–2189 (2003).
23. R. A. Farrer *et al.*, *Nat. Commun.* **8**, 14742 (2017).
24. F. Tajima, *Genetics* **123**, 585–595 (1989).
25. S. Guindon *et al.*, *Syst. Biol.* **59**, 307–321 (2010).

26. B. Gallone *et al*., *Cell* **166**, 1397–1410.e16 (2016).
27. M. C. Fisher, T. W. J. Garner, *Fungal Biol. Rev.* **21**, 2–9 (2007).
28. A. I. Carpenter, F. Andreone, R. D. Moore, R. A. Griffiths, *Oryx* **48**, 565–574 (2014).
29. J. K. Pritchard, M. Stephens, P. Donnelly, *Genetics* **155**, 945–959 (2000).
30. S. J. Price *et al*., *Curr. Biol.* **24**, 2586–2591 (2014).
31. T. W. J. Garner *et al*., *Oikos* **118**, 783–791 (2009).
32. K. A. Bates *et al*., *Nat. Commun.* **9**, 693 (2018).
33. B. J. Doddington *et al*., *Ecology* **94**, 1795–1804 (2013).
34. D. H. Olson, K. L. Ronnenberg, *FrogLog* **22**, 17–21 (2014).
35. S. F. Walker *et al*., *Curr. Biol.* **18**, R853–R854 (2008).
36. E. L. Wombwell *et al*., *EcoHealth* **13**, 456–466 (2016).
37. K. H. O'Rourke, J. G. Williamson, *Eur. Rev. Econ. Hist.* **6**, 23–50 (2002).
38. J. E. Kolby, *Nature* **509**, 563 (2014).
39. A. Herrel, A. van der Meijden, *Herpetol. J.* **24**, 103–110 (2014).
40. N. Dahanukar *et al*., *PLOS ONE* **8**, e77528 (2013).
41. S. Molur, K. Krutha, M. S. Paingankar, N. Dahanukar, *Dis. Aquat. Organ.* **112**, 251–255 (2015).
42. C. Bai, X. Liu, M. C. Fisher, W. J. T. Garner, Y. Li, *Divers. Distrib.* **18**, 307–318 (2012).
43. A. Martel *et al*., *Science* **346**, 630–631 (2014).
44. H. E. Roy *et al*., *Conserv. Lett.* **10**, 477–484 (2017).

ACKNOWLEDGMENTS

DNA sequencing was carried out in the NBAF GenePool genomics facility at the University of Edinburgh, and we thank the GenePool staff for their assistance. This work used the computing resources of the UK MEDical BIOinformatics partnership - aggregation, integration, visualization and analysis of large, complex data (UK MED-BIO) which is supported by the Medical Research Council (grant number MR/L01632X/1). We thank J. Rhodes for the provision of flow cells and reagents for MinION sequencing, the staff at Oxford Nanopore Technologies for admission to the MinION Early Access Programme, and three anonymous reviewers for constructive comments and suggestions. **Funding:** S.J.O., T.W.J.G., L.Br., A.Lo., A.A.C., D.S.S., E.A.C., C.M., J.B., D.M.A., F.C., and M.C.F. were supported through NERC (standard grant NE/K014455/1). S.J.O. acknowledges a Microsoft Azure for Research Sponsorship (subscription ID: ab7cd695-49cf-4a83-910a-ef71603e708b). T.W.J.G., A.Lo., A.A.C., D.S.S., E.A.C., C.M., J.B., D.M.A., F.C., and M.C.F. were also supported by the EU BiodivERsA scheme (RACE, funded through NERC directed grant NE/G002193/1 and ANR-08-Biodiversa-002-03) and NERC (standard grant NE/K012509/1). M.C.F., E.A.C., and C.M. acknowledge the Nouragues Travel Grant Program 2014. R.A.F. was supported by an MIT/Wellcome Trust Fellowship. T.W.J.G. was supported by the People's Trust for Endangered Species and the Morris Animal Foundation (D12ZO-002). J.M.G.S. and M.C.F. were supported by the Leverhulme Trust (RPG-2014-273) and the Morris Animal Foundation (D16ZO-022). F.B. was supported by the ERC (grant ERC 260801–Big_Idea). D.M.A. was funded by Wellcome Trust grant 099202. J.V. was supported by the Hungarian Scientific Research Fund (OTKA K77841) and Bolyai János Research Scholarship, Hungarian Academy of Sciences (BO/00579/14/8). D.J.G. was supported by the Conservation Leadership Programme (grant 0134010) with additional assistance from F. Gebresenbet, R. Kassahun, and S. P. Loader. C.S.-A. was supported by Fondecyt Nº11140902 and 1181758. T.M.D.-B. was supported by the Royal Geographical Society and the Royal Zoological Society of Scotland with assistance from M. Hirschfeld and the Budongo Conservation Field Station. B.W. was supported by the National Research Foundation of Korea (2015R1D1A1A01057282). L.F.T. was supported by FAPESP (#2016/25358-3) and CNPq (#300896/2016-6). L.Be., L.F.S., and R.J.W. were supported by the Australian Research Council (FT100100375, DP120100811). A.A.C. was supported by a Royal Society Wolfson Research Merit award. J.H., A.La., and S.M. were funded by the Swedish Research Council Formas (grant no. 2013-1389-26445-20). C.W. was funded by the National Research Foundation, South Africa. T.Y.J. and T.S.J. acknowledge NSF grant DEB-1601259. W.E.H. was funded by the NSERC Strategic and Discovery grant programs. **Author contributions:** All authors contributed ideas, data, and editorial advice. S.J.O., A.R., R.A.F., K.A.M., B.B., and M.C.F. conducted analyses. G.M.R., T.W.J.G., and L.Br. conducted disease experiments. S.J.O., F.B., T.W.J.G., and M.C.F. wrote the paper with input from all authors. **Competing interests:** K.A.M. sits on an expert panel at the European Food Safety Authority addressing the risks of importation and spread of the salamander chytrid *Batrachochytrium salamandrivorans*, a species of fungus that is the closest known relative to the pathogen addressed in this manuscript. **Data and materials availability:** Sequences have been deposited in the National Center for Biotechnology Information (NCBI) Sequence Read Archive (SRA). All sequences are available from NCBI BioProject accession PRJNA413876 (www.ncbi.nlm.nih.gov/bioproject/PRJNA413876). The supplementary materials contain additional data. Phylogenetic trees are available from TreeBASE, project accession URL http://purl.org/phylo/treebase/phylows/study/TB2:S22286. A browsable version of the phylogeny and metadata in Fig. 1B is accessible at https://microreact.org/project/GlobalBd.

SUPPLEMENTARY MATERIALS

www.sciencemag.org/content/360/6389/621/suppl/DC1
Materials and Methods
Figs. S1 to S16
Tables S1 to S5
Data S1 to S3
References (*45*–*90*)

14 October 2017; accepted 29 March 2018
10.1126/science.aar1965

NUCLEAR PHYSICS

Measurement of the neutron lifetime using a magneto-gravitational trap and in situ detection

R. W. Pattie Jr.,[1] N. B. Callahan,[2] C. Cude-Woods,[1,3] E. R. Adamek,[2] L. J. Broussard,[4] S. M. Clayton,[1] S. A. Currie,[1] E. B. Dees,[3] X. Ding,[5] E. M. Engel,[6] D. E. Fellers,[1] W. Fox,[2] P. Geltenbort,[7] K. P. Hickerson,[8] M. A. Hoffbauer,[1] A. T. Holley,[9] A. Komives,[10] C.-Y. Liu,[2] S. W. T. MacDonald,[1] M. Makela,[1] C. L. Morris,[1] J. D. Ortiz,[1] J. Ramsey,[1] D. J. Salvat,[11] A. Saunders,[1]* S. J. Seestrom,[1]† E. I. Sharapov,[12] S. K. Sjue,[1] Z. Tang,[1] J. Vanderwerp,[2] B. Vogelaar,[5] P. L. Walstrom,[1] Z. Wang,[1] W. Wei,[1] H. L. Weaver,[1] J. W. Wexler,[3] T. L. Womack,[1] A. R. Young,[3] B. A. Zeck[1,3]

The precise value of the mean neutron lifetime, τ_n, plays an important role in nuclear and particle physics and cosmology. It is used to predict the ratio of protons to helium atoms in the primordial universe and to search for physics beyond the Standard Model of particle physics. We eliminated loss mechanisms present in previous trap experiments by levitating polarized ultracold neutrons above the surface of an asymmetric storage trap using a repulsive magnetic field gradient so that the stored neutrons do not interact with material trap walls. As a result of this approach and the use of an in situ neutron detector, the lifetime reported here [877.7 ± 0.7 (stat) +0.4/−0.2 (sys) seconds] does not require corrections larger than the quoted uncertainties.

Measurement of free neutron decay to a proton, electron, and antineutrino, $n \rightarrow p + e^- + \bar{\nu}_e$, provides information about the fundamental parameters of the charged weak current of the nucleon and constrains many extensions to the Standard Model at and above the tera–electron volt scale. Knowledge of the mean neutron lifetime, τ_n, to an accuracy of better than 1 s is necessary to improve big-bang nucleosynthesis predictions of elemental abundances (*1*) and to search for physics beyond the Standard Model of nuclear and particle physics (*2*).

The neutron lifetime has recently been measured with two different techniques (*3*, *4*): counting the surviving ultracold neutrons after storage in material-walled traps, with a most precise result of 878.5 ± 0.8 s (*5*), and counting the number of decay products emerging from a passing beam of cold neutrons, with a result of 887.7 ± 2.2 s (*6*). The results of these techniques disagree by 9.2 s, or 3.9 standard deviations.

Our experiment was designed to reduce systematic uncertainties by using ultracold neutrons (UCNs) trapped in a storage volume closed by magnetic fields on the bottom and sides and by gravity on top, as previously demonstrated in (*7*, *8*). In this work, we have used an asymmetric trap to reduce the population of long-lived closed neutron orbits with kinetic energies over the storable energy threshold in the trap (*9*, *10*). We have also introduced in situ detection of the surviving neutrons to eliminate uncertainties associated with transporting the neutrons to an ex situ detector. Recent storage experiments used storage traps with variable volumes to extrapolate to infinite volume in an attempt to reduce uncertainties associated with losses of neutrons caused by interactions with the material walls (*5*, *11*–*15*). Our experiment had no detectable losses of neutrons caused by interactions with the magnetic and gravitational "walls" of the trap and thus required no extrapolation. In addition, we used a number of techniques to diagnose and eliminate effects of quasi-trapped neutrons. These neutrons have kinetic energies above the trapping potential but nevertheless can reside in the trap in quasi-stable orbits for hundreds of seconds, skewing the long storage time measurements.

Ultracold neutron delivery, storage, and measurement protocol

The experimental technique was described in detail in (*16*) and is summarized here. The experimental apparatus is shown in Fig. 1. UCNs were supplied by the west beam line of the Los Alamos Neutron Science Center UCN facility (*17*–*19*). The UCN flux was monitored by normalization detectors (*20*) that sampled the flux through small aperture holes in the beam guide. The neutrons were polarized with a 6-T solenoid magnet that transmitted only neutrons in the "high-field-seeking" spin state. An adiabatic fast passage spin flipper changed the spin state of the neutrons to low-field-seeking with ~90% efficiency by using an applied magnetic field of 14 mT and an oscillating radio-frequency field of 372 kHz. Another normalization detector mounted above the storage height of the neutron trap monitored the UCN flux just before the entrance to the trap. The neutrons reaching this detector height had too much kinetic energy to be confined by gravity in the magnetic trap. The flux at each detector was monitored throughout the filling period in order to determine the relative normalization of the number of neutrons entering the trap in each storage run. Neutrons filled the trap through a movable magnetic door located at the bottom of the apparatus.

The trap was constructed of a Halbach array of permanent magnets in which the magnetization of each row of permanent magnets was rotated 90° relative to its neighbors. Each NdFeB magnet was 2.54 cm by 5.08 cm by 1.27 cm, with a surface field of ~1.0 T. The magnets were installed along the surface of two intersecting tori, one with a major radius of 100 cm and a minor radius of 50 cm, the other with the radii interchanged and cut off at a height of 50 cm from the bottom of the trap, thus forming an asymmetric trap with a trapping potential of ~50 neV (corresponding to neutron temperature $\lesssim$0.58 mK) and a fiducial volume of 420 liters. An additional externally applied holding field of up to 10 mT, approximately perpendicular to the Halbach field, was used to maintain the neutron polarization during the storage period. The performance of the trap was described in (*10*).

At the end of the 150-s filling period, the 800-MeV proton beam that produced the UCN was turned off so as to reduce backgrounds, and the loading trap door and other valves in the UCN beam pipe were closed, preventing further neutrons from reaching the apparatus. A cleaning period followed, designed to eliminate any neutrons in the trap with kinetic energy sufficient to escape the trap. A horizontal sheet of polyethylene, called the "cleaner," removed neutrons with sufficient kinetic energy to reach its height via absorption or thermal upscattering. During the filling and cleaning periods, the cleaner was positioned 38 cm above the bottom of the trap, or 12 cm below the nominal open top of the trap. The cleaner covered approximately one half of the horizontal surface of the trap at its mounted height [~0.86 m^2, to be compared with the 0.23 m^2 horizontal cleaner used in the work of (*16*)], so that every neutron capable of reaching it did so quickly within a few tens of seconds after entering the trap. A second "active" cleaner, with 28% of the area of the primary cleaner, was mounted on the downstream side of the trap in the same plane as the primary cleaner. This second cleaner used ^{10}B-coated ZnS:Ag as the UCN absorber (*20*) and was

[1]Los Alamos National Laboratory, Los Alamos, NM 87545, USA. [2]Center for Exploration of Energy and Matter and Department of Physics, Indiana University, Bloomington, IN 47408, USA. [3]Triangle Universities Nuclear Laboratory and North Carolina State University, Raleigh, NC 27695, USA. [4]Oak Ridge National Laboratory, Oak Ridge, TN 37831, USA. [5]Department of Physics, Virginia Polytechnic Institute and State University, Blacksburg, VA 24061, USA. [6]West Point Military Academy, West Point, NY 10996, USA. [7]Institut Laue-Langevin, Grenoble, France. [8]Kellogg Radiation Laboratory, California Institute of Technology, Pasadena, CA 91125, USA. [9]Department of Physics, Tennessee Technological University, Cookeville, TN 38505, USA. [10]Department of Physics and Astronomy, DePauw University, Greencastle, IN 46135-0037, USA. [11]Department of Physics, University of Washington, Seattle, WA 98195-1560, USA. [12]Joint Institute for Nuclear Research, Dubna, Moscow region 141980, Russia.
*Corresponding author. Email: asaunders@lanl.gov
†Present address: Sandia National Laboratories, Albuquerque, NM 87185, USA.

observed with an array of photomultiplier tubes (PMTs), allowing the UCN density in the plane of the cleaners to be continuously monitored. At the conclusion of the cleaning period, 50 to 300 s for the data presented here, both cleaners were raised 5 cm in order to stop further interactions; at this point, the storage period began. The neutrons were stored for times typically ranging from 10 to 1400 s, chosen to optimize statistical reach in a given experimental running time while still permitting systematic studies.

At the end of the storage period, a UCN detector consisting of a vertical poly(methyl methacrylate) (PMMA) paddle coated on both sides with ZnS:Ag and ^{10}B, with a total active surface area of 750 cm^2 per side (~21% of the 3450 cm^2 area of the midplane of the trap), was lowered into the center of the trap. The detector could be lowered in multiple steps and, at its lowest position, reached to within 1 cm of the bottom of the trap. Because the detector could only access the fraction of UCNs that had sufficient energy to reach the height of each step, this permitted rate-dependent uncertainties to be studied by controlling the counting rate and also enabled the exploration of different neutron energy– and phase space–dependent systematic effects. The detector removed (or "unloaded") the surviving stored neutrons from the trap with a time constant of ~8 s. At the conclusion of the counting period (typically 100 to 300 s in length, or many 8-s mean draining times), the detector was left in the trap to count background rates with no neutrons in the trap for typically 150 s. The absolute efficiency of the detector, previously reported to be 96% (*16*), and those of the upstream monitor detectors cancel in the ratios used to extract the lifetime in this experiment.

Each neutron absorbed on the detector's boron layer generated a burst of scintillation photons in the ZnS:Ag scintillator that were converted and conducted from the transparent PMMA backing plate to a pair of photomultiplier tubes by an array of 2-mm-spaced wavelength shifting fibers. The photons in each PMT were individually counted with an 800-ps precision time stamp by an input channel of the same multichannel scaler (MCS) (*21*) that counted the output pulses from the normalization monitors.

In a typical measurement cycle, a pair of runs were performed, one with a nominal short storage time of 20 s and one with a nominal long storage time of 1020 s, each with ~2.5×10^4 neutrons in the trap at the beginning of the storage period. A total of 332 pairs of long and short runs were analyzed for the results in this paper, in five different running configurations. The different run conditions varied the cleaning time, the number of steps in which the detector was lowered into the trap, and the magnitude of the applied neutron polarization holding field. The five run conditions are listed in Table 1.

Shown in Fig. 2, A and B, are a "nine-step" and "three-step," respectively, unloading curve for a short and long storage time, summed over all the cycles in the respective run condition. An unloading curve is a plot of the instantaneous rate of neutron detection in the UCN detector, during the counting period after the UCN storage time. In each case, the first, highest detector step placed the bottom edge of the detector at the cleaning height so that no stored neutrons had sufficient energy to reach the 132 cm^2 of active area that extended below the position of the raised cleaners. No neutrons above background were detected in this step, putting constraints on systematic uncertainties caused by insufficient cleaning of high-energy neutrons and heating of neutrons by vibrations, to be described later: Only eight peaks are visible in the nine-step unloading curve and two in the three-step curve. The absolute start time of the

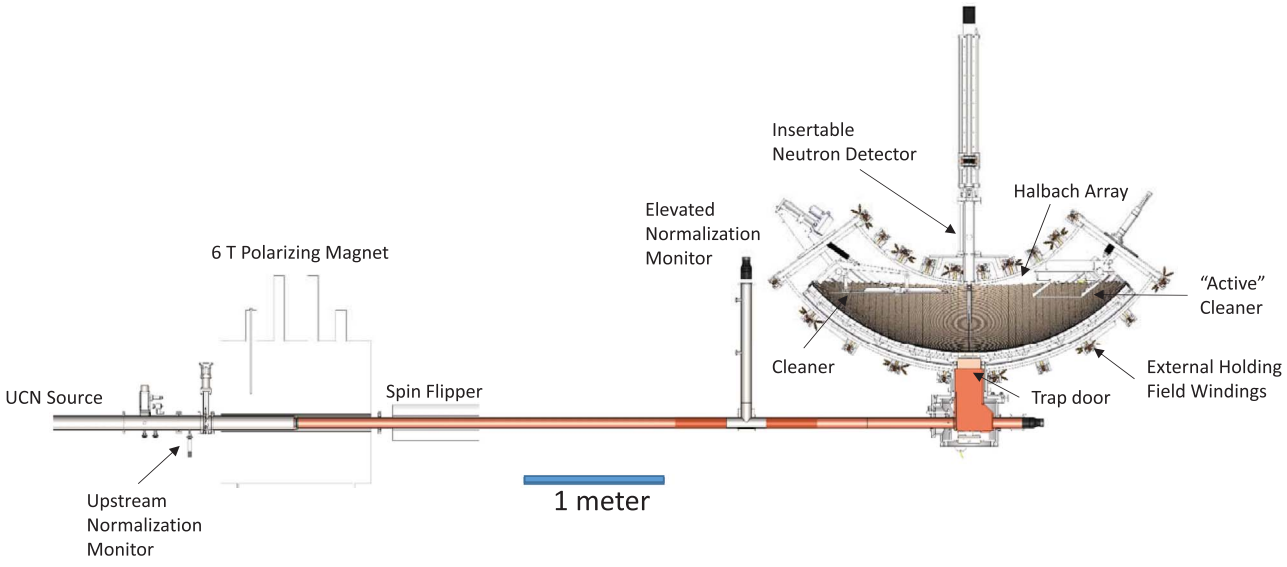

Fig. 1. Layout of the UCN beam line and trap used for these measurements.

Table 1. The five running conditions analyzed in this paper. "Detector steps" is the number of discrete counting positions as the neutron detector was lowered to the bottom of the trap; "Cleaning time" is the length of cleaning period from the closing of the neutron loading trap door to the raising of the cleaner; "Holding field" is the minimum strength of the externally applied polarization holding field in the trap; and "Run pairs" is the number of long-short run pairs acquired for this configuration, all with roughly equal numbers of initially loaded neutrons.

Run configuration	Detector steps	Cleaning time (s)	Holding field (mT)	Run pairs
A	1	200	6.8	79
B	9	200	6.8	66
C	9	300	6.8	70
D	3	50	6.8	60
E	3	50	3.4	57

long storage curve was adjusted in each plot by the difference between the nominal long and short storage times, to allow visual comparison of the curves.

The data were blinded by adjusting the nominal storage times (along with all the MCS time stamps in a blinded run) by a factor hidden from those analyzing the data, with the result that τ_n extracted from the blinded data differed from the actually measured value by a random offset of up to ±15 s.

Extracting the neutron lifetime

The expected number of surviving neutrons after storing an initial number N_0 of neutrons in the trap for a time t is $N_{surv} = N_0 e^{-t/\tau_{meas}}$, where τ_{meas} is the mean measured survival time of the trapped neutrons. The measured loss rate is the sum of the loss rate caused by neutron decay and all other sources of loss from the trap, such as losses caused by interactions with the walls, depolarization of neutrons during storage, thermal upscattering of neutrons from residual gas in the trap, or other sources of loss: $1/\tau_{meas} = 1/\tau_n + 1/\tau_{loss}$.

The number of surviving neutrons was estimated from the raw data, consisting of a string of time-stamped photon events from the two in situ detector PMTs, using two different techniques. The first method required a coincidence between photons from each of the two PMTs to identify a neutron. Coincidences were identified during a 50-ns window, followed by an above-threshold number of photons in a variable integration window of several microseconds. The threshold was determined by the number and arrival time of previously identified neutrons in the data stream. Identification of new neutrons was disabled during the integration window, creating a rate-dependent but calibrated software dead time for each counting bin. The integration window was extended in 1-μs steps as long as photon events continued to arrive, in order to maximize neutron identification efficiency while minimizing software dead time. The second method used individual photons, or "singles" data. Each individual photon was treated as an independent event, with no attempt made to identify the neutron responsible for each individual photon.

The normalized total signals of the surviving UCN populations, or yields, were calculated for each run by summing the counts measured in all detector positions, subtracting experimental backgrounds, and dividing by the relative number of neutrons loaded into the trap. The background at long holding times was on the order of 0.3% of signal for coincidence counting and 15% for singles counting. The raw numbers of neutrons (coincidence) or photons (singles) were corrected for dead time [(*22*), section 1]. The relative number of neutrons loaded into the trap was determined from the counts in the elevated normalization monitor [Fig. 1 and (*22*), section 2], exponentially weighted by the measured loading time constant of the trap (60 to 70 s). Spectral variations in the incident neutron flux were assessed by taking the ratio of the number of counts in the elevated normalization detector to the number in the upstream, beam-height normalization detector. The first-order correction to the normalization, as much as 10% over a period of 100 hours, was determined by minimizing the variance of neutron yields of short-storage runs only. Alternating long and short storage time runs reduced the effect of this correction on the lifetime uncertainty to negligible levels.

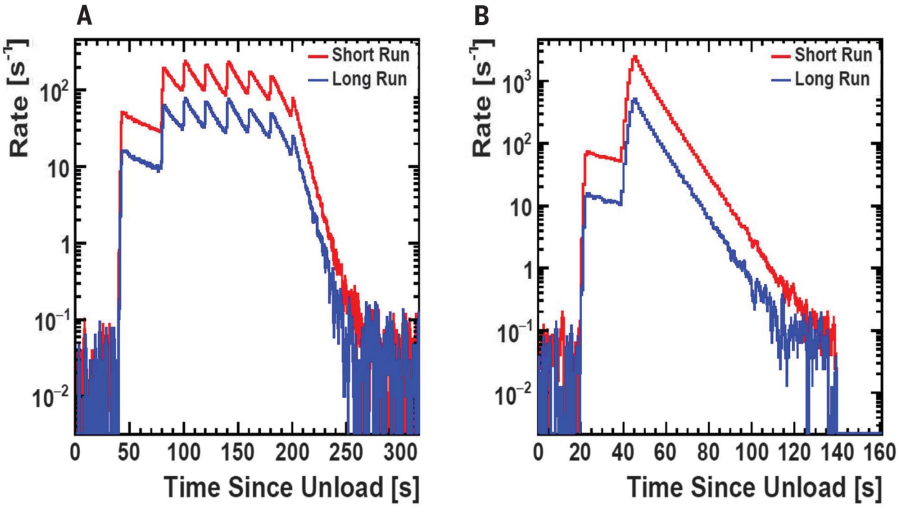

Fig. 2. Unloading time distributions. (**A** and **B**) The combined rates of the neutron signals and backgrounds for a (A) nine-step configuration and (B) three-step configuration. The times have been shifted to align the short storage time (red) and long storage time (blue) distributions.

The neutron lifetime and uncertainty were calculated from pairs of short and long storage time yields using

$$R_i \equiv \frac{Y_{is}}{Y_{il}} \quad (1)$$

$$\tau_{n,i} = \frac{(\bar{t}_l - \bar{t}_s)}{\ln(R_i)} \quad (2)$$

and

$$\Delta\tau_{n,i} = \frac{(\bar{t}_l - \bar{t}_s)}{\ln(R_i)^2}\frac{\Delta R_i}{R_i} \quad (3)$$

where the subscripts l and s denote long and short storage times, $\bar{t}$ is the mean neutron detection time during the counting period, Ys are the yields, τ_n is the lifetime, the Δs indicate uncertainties, and the subscript i denotes the individual run pairs. Uncertainties were calculated by using Poisson statistics for the UCN yields, including the statistics of the exponentially weighted elevated normalization monitor counts. The statistical uncertainty in the photon singles yields were obtained from the coincidence data and by analyzing the variance in the singles-extracted lifetimes, and both approaches produced consistent results.

Average lifetimes were calculated for each of the five run configurations in three ways. First, the average long and short yields across a run configuration were calculated and assigned uncertainties as the standard deviation of the individual yields divided by $\sqrt{N}$, where N is the number of individual run pair yields. The lifetimes and uncertainties were calculated from the average values by using Eqs. 1 to 3. The second method determined the lifetime from a weighted average of the lifetimes calculated from each individual run pair. In this case, the uncertainty was calculated from the weighted average of individual run pair uncertainties and multiplied by the square root of the reduced χ^2 to account for any remaining nonstatistical variation in the data set caused by smaller systematic effects such as higher-order time or spectral variations in the loaded neutrons. The third method was identical to the second, except that an unweighted average was used to compute the average lifetime.

Systematic uncertainties

The total systematic uncertainty in these results were estimated to be 0.28 s. The major sources of systematic uncertainties in these results are listed in Table 2.

The only correction applied to the central value of the lifetime was due to thermal upscattering of UCN from individual interactions of UCN, with residual gas particles in the trap during the storage period. Because the cross section for neutron scattering off of residual gas molecules is inversely proportional to the neutron velocity, the residual gas pressure, molecular make up, and interaction cross sections could be combined to extract a neutron loss lifetime, independent of neutron velocity, caused by this upscattering effect

$$1/\tau_{upscatter} = \sigma_{upscatter} v_n N_{gas} \quad (4)$$

$$\sigma_{\text{upscatter}} = \sigma_{\text{free}}\bar{v}_{\text{gas}} \Big/ v_n \quad (5)$$

$$1 \Big/ \tau_{\text{upscatter}} = \sigma_{\text{free}}\bar{v}_{\text{gas}}N_{\text{gas}} \quad (6)$$

where $\tau_{\text{upscatter}}$ is the loss lifetime because of this upscatter effect, $\sigma_{\text{upscatter}}$ is the cross section for upscattering of neutrons from residual gas molecules, σ_{free} is the velocity-independent neutron-gas interaction cross section, $\bar{v}_{\text{gas}}$ is the mean velocity of the gas molecules, and N_{gas} is the number density of gas molecules, proportional to the pressure. Equations 4 to 6 apply to a single gas species but could easily be summed over all gases in the storage volume. Two calibrated cold cathode gauges located above the midplane of the trap were used to measure the residual gas pressure (typically 6×10^{-7} torr), and a residual gas analyzer was used to measure the mass spectrum of the residual gas. From these measurements and the measured UCN cross sections from (*23*, *24*), we calculated the velocity-independent UCN lifetime ($\tau_{\text{upscatter}}$), which is caused by losses on the residual gas in the trap, using Eqs. 4 to 6. The loss rate from this lifetime was then subtracted from the measured neutron loss rate to yield the neutron decay loss rate, for a correction to the measured lifetime of 0.16 s with an uncertainty of 0.03 s [(*22*), section 3].

The systematic uncertainty caused by possible depolarization of neutrons during the storage period was assessed by measuring the neutron lifetime while varying the magnitude of the applied polarization holding field [(*22*), section 4]. High-precision lifetime measurements were made at holding field strengths of 6.8 and 3.4 mT, and lower-precision measurements at smaller fields down to 0 mT applied field. The resulting lifetimes were fitted by using a power law suggested in (*25*) from calculations of depolarization in the present trap geometry: $\frac{1}{\tau} = \frac{1}{\tau_n} + \frac{B_{\perp 0}^2}{B_\perp^2 \tau_{DP}}$, where $B_\perp$ is the holding field, $B_{\perp 0}$ is the full holding field, τ is the measured storage lifetime, τ_n is the neutron decay lifetime, and τ_{DP} is the loss lifetime due to depolarization. The result of the fit yielded a loss lifetime owing to depolarization of $\tau_{DP} = 1.1 \times 10^7$ s (with 1σ uncertainty bounds of 6.0×10^6 and 5.5×10^7 s) for an uncertainty on the measured neutron lifetime of 0.07 s. The 6.8 and 3.4 mT measurements showed no variation outside of statistics.

Neutrons can be heated by, for example, many small interactions with the vibrational motion of the UCN trap's magnetic field, slowly gaining enough energy to exceed the trap potential and escape from the trap during the long storage period. A limit on the uncertainty due to this effect was determined by looking for neutrons moving into the highest neutron detector position (38 cm above the bottom of the trap, or equal in height to the lowered cleaner), in run configurations B to E during the long storage time (Table 1).

The detector's ability to count these very low-energy UCNs (<5 neV kinetic energy at the top of their orbits in the trap) was verified by loading the trap with the cleaners and the neutron detector in their raised position. The counting curve from the active cleaner was observed to fall to its background rate in ~10 s and was constant thereafter, indicating that neutrons were efficiently cleaned to the height of the raised cleaners (43 cm above the bottom of the trap). The neutron detector was then lowered to the upper counting position and was observed to count UCN with sufficient energy to reach heights between 38 and 43 cm with a time constant of 260 s [(*22*), section 5]. Although only the lowest 5 cm of the detector was exposed below the raised cleaners during the first step of a nominal lifetime run, characterization of the neutron detector with a Gd-148 α particle source showed an approximately uniform optical response across the entire active area of the detector. In addition, heated UCN gain energy slowly and so have multiple opportunities to be captured by the detector before acquiring sufficient energy to reach the position of the raised cleaners. In estimating the cleaning and heating systematic uncertainties, a conservative factor of 20 was applied to account for neutrons that were not detected during the 20-s first-position counting time used for lifetime running.

The number of neutrons observed in the highest counting position was consistent with background in the long storage time runs. The systematic uncertainty due to heating was determined by the uncertainty of the yield calculated by using only the counts observed in the highest position. On the basis of this analysis, we put a 1σ limit on the lifetime uncertainty because of neutron heating of 0.23 s.

Similarly, insufficient cleaning of neutrons with energy above the trapping energy would result in an artificial excess of counts after the short storage time that could be lost over the long storage time. An analysis of excess neutrons in the highest counting position in the short storage time runs, which is also consistent with zero neutrons above background, allowed us to put a limit of 0.06 s on the uncertainty in the measured lifetime because of insufficient cleaning.

In the single-photon counting analysis method, a hardware dead time was caused by the 10-ns dead time of the discriminator used to detect the individual photons. The uncertainty due to correcting for this rate-dependent effect was set to 20% of the correction on each run, for a total uncertainty on the extracted lifetime of 0.04 s.

Phase space evolution can cause a possible change in effective detector efficiency between the short and long storage time runs caused by evolution of the neutron population in the trap between regions of phase space with different degrees of access to the detector location. Any effect of phase space evolution on the measured lifetime would cause a variation in the relative number of neutrons in the peaks corresponding to the different counting steps between the short

Table 2. Systematic uncertainties.

Effect	Upper bound (s)	Direction	Method of evaluation
Depolarization	0.07	+	Varied external holding field
Microphonic heating	0.24	+	Detector for heated neutrons
Insufficient cleaning	0.07	+	Detector for uncleaned neutrons
Dead time/pileup	0.04	±	Known hardware dead time
Phase space evolution	0.10	±	Measured neutron arrival time
Residual gas interactions	0.03	±	Measured gas cross sections and pressure
Background shifts	<0.01	±	Measured background as function of detector position
Total	0.28		(uncorrelated sum)

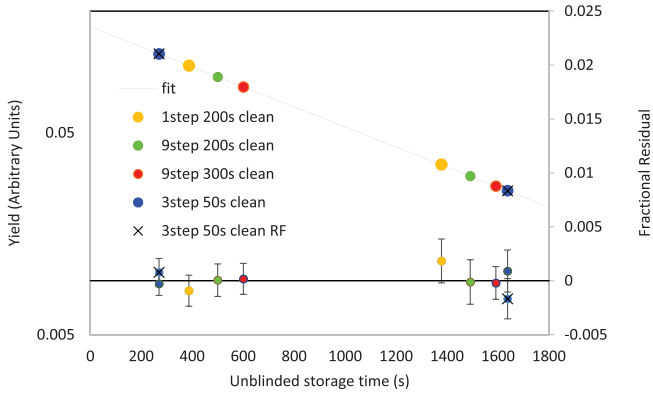

Fig. 3. Yields as a function of storage time. The yields are shown relative to the start of filling for each of the running conditions. The relative normalization of the data sets has been adjusted to account for the different running conditions. The dashed line shows an exponential fit to the yields. The fractional residuals, or differences between the yields and the fitted curve, are plotted against the right axis. RF denotes the use of a reduced polarization holding field strength of 3.4 mT instead of 6.8 mT.

and long storage time runs; therefore, a limit on this effect was estimated by calculating the statistical uncertainty of the centroid of the unloading curve for the nine-step measurements and was found to be 0.10 s [(*22*), section 6]. The effect was smaller for the one- and three-step measurements. A cross check was made for the presence of neutron population phase space evolution between the short and long storage periods by comparing the number of counts in each of the three or nine separate detector steps; the variation in these ratios was consistent with statistical fluctuations.

Results

As a final check for nonexponential behavior in the data, we performed a global fit to the yields of the long and short storage time measurements (Fig. 3). The unblinded measured neutron lifetime extracted from this fit was 877.6 ± 0.7 s, with a χ^2/df of 0.7. After correction for gas upscattering, the final unblinded measured mean neutron lifetime was 877.7 ± 0.7 (stat) +0.4/−0.2 (sys) s. The coincidence and the singles analysis methods described above yielded the same results. Three independent analyses were conducted and compared before unblinding. These analyses agreed to within 0.2 s. The central value of the result presented here is the average of the three results, the statistical uncertainty is the average of those from the three analyses, and the systematic uncertainty is that from Table 2 added in quadrature with an additional 0.2 s to account for the differences between the analysis techniques. Because the total uncertainty of this result is dominated by statistical uncertainty, and because the leading systematic uncertainties appear to be statistically driven and thus reducible with further study, we expect to ultimately reach a total uncertainty well below 0.5 s in future data runs using this apparatus.

The nonblinded data set presented in (*16*) was combined with a blinded systematics study data set, which had a statistical accuracy of $\Delta\tau_n$ = 1 s, to develop techniques to correct for incomplete cleaning of quasi-bound neutrons and to identify improvements to the trap-cleaning procedure. These improvements were implemented before acquiring the data discussed in this paper. The systematics study data were unblinded (based on two independent analyses) at the same time as the data presented here and produced a consistent result for τ_n. This data set was not included in the neutron lifetime result presented here.

The result presented here does not require corrections to the measured lifetime that are larger than the quoted uncertainties. This result agrees with the previous best measurement of the lifetime for neutron decay by using UCNs stored in a material trap and disagrees with the lifetime for neutron β-decay determined by using the beam technique.

REFERENCES AND NOTES

1. R. H. Cyburt, B. D. Fields, K. A. Olive, T.-H. Yeh, *Rev. Mod. Phys.* **88**, 015004 (2016).
2. W. J. Marciano, *Phys. Procedia* **51**, 19–24 (2014).
3. F. E. Wietfeldt, G. L. Greene, *Rev. Mod. Phys.* **83**, 1173–1192 (2011).
4. A. R. Young *et al.*, *J. Phys. G Nucl. Part. Phys.* **41**, 114007 (2014).
5. A. Serebrov *et al.*, *Phys. Rev. C Nucl. Phys.* **78**, 035505 (2008).
6. A. T. Yue *et al.*, *Phys. Rev. Lett.* **111**, 222501 (2013).
7. V. Ezhov *et al.*, *Nucl. Instrum. Methods Phys. Res. A* **611**, 167–170 (2009).
8. V. Ezhov *et al.*, arXiv:1412.7434 [nucl-ex] (23 December 2014).
9. P. Walstrom, J. D. Bowman, S. I. Penttila, C. Morris, A. Saunders, *Nucl. Instrum. Methods Phys. Res. A* **599**, 82–92 (2009).
10. D. J. Salvat *et al.*, *Phys. Rev. C Nucl. Phys.* **89**, 052501 (2014).
11. S. Arzumanov *et al.*, *Phys. Lett. B* **745**, 79–89 (2015).
12. A. Steyerl, J. M. Pendlebury, C. Kaufman, S. S. Malik, A. M. Desai, *Phys. Rev. C Nucl. Phys.* **85**, 065503 (2012).
13. A. Pichlmaier, V. Varlamov, K. Schreckenbach, P. Geltenbort, *Phys. Lett. B* **693**, 221–226 (2010).
14. J. Byrne *et al.*, *Europhys. Lett.* **33**, 187–192 (1996).
15. W. Mampe *et al.*, *JETP Lett.* **57**, 82 (1993).
16. C. L. Morris *et al.*, *Rev. Sci. Instrum.* **88**, 053508 (2017).
17. A. Saunders *et al.*, *Phys. Lett. B* **593**, 55–60 (2004).
18. A. Saunders *et al.*, *Rev. Sci. Instrum.* **84**, 013304 (2013).
19. T. M. Ito *et al.*, *Phys. Rev. C* **97**, 012501R (2018).
20. Z. Wang *et al.*, *Nucl. Instrum. Methods Phys. Res. A* **798**, 30–35 (2015).
21. FastCom, Model MCS6A, 64 Bit 5/(6) input 100 ps Multistop TDC, Multiscaler, Time-Of-Flight (2016); www.fastcomtec.com/fwww/datashee/photon/mcs6.pdf.
22. Supplementary text is provided as supplementary materials.
23. S. J. Seestrom *et al.*, *Phys. Rev. C Nucl. Phys.* **92**, 065501 (2015).
24. S. J. Seestrom *et al.*, *Phys. Rev. C Nucl. Phys.* **95**, 015501 (2017).
25. A. Steyerl, K. K. H. Leung, C. Kaufman, G. Müller, S. S. Malik, *Phys. Rev. C Nucl. Phys.* **95**, 035502 (2017).

ACKNOWLEDGMENTS

The authors thank the staff of LANSCE for their diligent efforts to develop the diagnostics and new techniques required to provide the proton beam for this experiment. **Funding:** This work was supported by the Los Alamos Laboratory Directed Research and Development (LDRD) office (no. 20140568DR), the LDRD Program of Oak Ridge National Laboratory, managed by UT-Battelle (no. 8215), the National Science Foundation (nos. 130692, 1307426, 161454, 1306997, and 1553861), NIST Precision Measurement Grant, IU Center for Space Time Symmetries (IUCSS), the LANSCE Rosen Scholarship program, and U.S. DOE Low Energy Nuclear Physics (nos. DE-FG02-97ER41042 and DE-AC05-00OR22725). **Competing interests:** None declared. **Author contributions:** Experiment design was performed by R.W.P., N.B.C., C.C.-W., E.R.A., S.M.C., W.F., P.G., K.P.H., A.T.H., A.K., C.-Y.L., M.M., C.L.M., J.R., D.J.S., A.S., S.J.S., E.I.S., S.K.S., J.V., P.L.W., and A.R.Y.; experiment construction was performed by R.W.P., N.B.C., C.C.-W., E.R.A., S.M.C., S.A.C., X.D., A.T.H., C.-Y.L., S.W.T.M., M.M., C.L.M., J.D.O., D.J.S., A.S., J.V., B.V., W.W., T.L.W., A.R.Y., and B.A.Z.; detector research and development was performed by R.W.P., C.C.-W., E.R.A., D.E.F., M.A.H., M.M., C.L.M., J.D.O., J.R., D.J.S., E.I.S., and Z.W.; data acquisition was performed by R.W.P., N.B.C., C.C.-W., E.R.A., L.J.B., S.M.C., E.B.D., E.M.E., D.E.F., P.G., K.P.H., A.T.H., A.K., C.-Y.L., M.M., C.L.M., J.D.O., D.J.S., A.S., S.J.S., S.K.S., Z.T., P.L.W., W.W., H.L.W., J.W.W., A.R.Y., and B.A.Z.; and data analysis was performed by R.W.P., N.B.C., C.C.-W., E.R.A., S.M.C., A.T.H., C.-Y.L., C.L.M., D.J.S., and S.J.S. **Data and materials availability:** The data shown in this paper are available as part of the supplementary materials. The raw data that underlie these results are curated at Los Alamos National Laboratory and are available upon request from the corresponding author.

SUPPLEMENTARY MATERIALS

www.sciencemag.org/content/360/6389/627/suppl/DC1
Supplementary Text
Figs. S1 to S9
Data File S1

2 June 2017; accepted 13 March 2018
Published online 6 May 2018
10.1126/science.aan8895

REPORT

METAMATERIALS

Handedness in shearing auxetics creates rigid and compliant structures

Jeffrey Ian Lipton,[1]* Robert MacCurdy,[1] Zachary Manchester,[2] Lillian Chin,[1] Daniel Cellucci,[3] Daniela Rus[1]*

In nature, repeated base units produce handed structures that selectively bond to make rigid or compliant materials. Auxetic tilings are scale-independent frameworks made from repeated unit cells that expand under tension. We discovered how to produce handedness in auxetic unit cells that shear as they expand by changing the symmetries and alignments of auxetic tilings. Using the symmetry and alignment rules that we developed, we made handed shearing auxetics that tile planes, cylinders, and spheres. By compositing the handed shearing auxetics in a manner inspired by keratin and collagen, we produce both compliant structures that expand while twisting and deployable structures that can rigidly lock. This work opens up new possibilities in designing chemical frameworks, medical devices like stents, robotic systems, and deployable engineering structures.

Many biological materials, such as DNA, keratin, and collagen, are composed of repeated patterns of simple monomers that form handed structures (*1*). Handed structures come in mirror-image pairs. The same underlying handed materials generate rigid, compliant, or flexible mechanical properties through variations in intermolecular bonding (*1*). Examples include collagens, which form rigid materials such as bone and teeth, as well as compliant structures like cartilage, tendon, and skin; and keratins, which form hair, horns, and hooves (*1*, *2*). These structures become stronger by increasing the amount of interlayer bonding; these are disulfide bonds and hydrogen bonds in the case of keratins (*3*) or collagen (*4*). Both collagen and keratin align and bond the termini of substructures to form larger structures. We used this same principle of coupling the termini with strong bonds, and using variable bonds along the length to rigidize composite handed auxetic tubes and spheres.

Similar to keratin and collagen, auxetic structures are composed of a repeated tiling of a basic unit cell (*5*). Their defining mechanical property is a negative Poisson's ratio, meaning that they expand perpendicular to the direction of tension when stretched (*6*). They can form planes (*7*–*9*), cylinders (*9*–*11*), spheres (*12*, *13*), and complex surfaces (*14*). The underlying geometric patterns that lead to auxetic behavior are scale and material independent (*5*). The patterns are naturally occurring at the nanometer scale in molecules and crystals (*15*–*17*), they exist at the millimeter scale in stents (*18*), and they occur at the meter scale in large structures (*19*). The material-agnostic nature of these patterns can potentially enable unconventional auxetic metamaterials to be designed (*20*).

Conventional auxetics are limited in a key way; the stiffness of an auxetic is predefined. It is derived primarily from the interplay between a fixed topology and the predefined energy required to deform the joints or struts of the structure (*7*, *8*, *21*). As a result, the same structure cannot switch between rigid and compliant states.

We used the biologically inspired technique of selectively bonding handed structures to form rigid or compliant structures from handed shearing auxetics (HSAs). We produced handedness in two-dimensional shearing auxetic material patterns that tile the surface of planes, cylinders, or spheres. We demonstrated a rigid deployable structure through concentric alignment of different HSA cylinders. We made compliant actuators via parallel arrangement of right- and left-handed cylinders. We can globally actuate the structures by applying a twist or linear stress. The ability to twist the auxetics allows us to actuate them with conventional motors.

The unit cell of an auxetic is a set of rigid links with variable relative angles (*5*), but with fixed connectivity. The cell's auxetic trajectory is controlled by a single number called the phase angle, which defines the continuous deformation of the unit cell (Fig. 1). Conventional auxetic structures are isotropic and expand uniformly under applied tension (*5*). Shearing auxetics, however, expand at different rates in different directions while shearing and therefore do not have a single Poison's ratio. The ratio varies as a function of direction and phase angle (*7*, *8*). For an auxetic pattern to shear and expand simultaneously, the unit cells must have C_2 or C_1 symmetry (*22*). In addition, no net shearing of the structure occurs if there are reflections or glide reflections continuously in the tiling pattern along the auxetic trajectory. This constrains shearing auxetics to 2 of the 17 wallpaper group tilings, 2222 and o in orbifold notation (*23*). In orbifold notation, * represents a reflection, and integers represent rotation centers of the integer's order. Integers before or without a * are not on a line of reflection, and those after a * are on a line of reflection. x represents a repeated mirror image without a line of reflection, and o represents only translations. In the notation, integers are listed next to each other, so 2222 represents four separate rotational centers of order 2 without reflections, and o represents a pattern with only translational symmetries.

Various auxetic structures behave differently along their auxetic trajectories (Fig. 1). All auxetics reach their maximum auxetic extension at a phase angle θ_{max}. Further deformation from this point causes them to either cease being auxetic or to contract. Because unit cells can change their shape throughout deformation, an auxetic tiling can transition from a 2222 or o symmetry to one that has reflections for a single point along the auxetic trajectory. The development of a line of reflection at a point along the auxetic trajectory allows a shearing auxetic that is shearing to the right to transition to shearing to the left. This produces a symmetric auxetic trajectory and thus an unhanded shearing auxetic. Such structures continuously shear from one direction to the other, which is equivalent to mirroring the entire structure (Fig. 1). Shearing auxetic trajectories that never develop a reflection at θ_{max} characterize the handed shearing auxetics. Therefore, preventing reflection symmetries at θ_{max} generates handedness. Handed auxetics come in right- and left-handed pairs. Because their mirror images are equally valid tilings of space, their left- and right-handed versions have distinct auxetic trajectories. The configuration of a left-handed auxetic cannot match that of a right-handed auxetic by choosing a different θ on the auxetic trajectory.

Handedness in a shearing auxetic structure can emerge at three different levels: in the joints, in the patterning itself, or in the placement of the pattern on an oriented surface. By limiting the joint angles to exclude θ_{max}, the symmetry of an unhanded shearing auxetic trajectory is broken. This prevents a shearing auxetic cell from transitioning between handedness. We removed the symmetries from the constituent elements of the unit cell (Fig. 1) to turn a shearing auxetic into a handed shearing auxetic. By turning one of the rectangles into a parallelogram, we prevented lines of reflection from developing. The components of the unit cell never align to form a global symmetry at θ_{max}. We performed similar modifications to make handed shearing auxetic patterns from rigid links and links with polygons (fig. S3) (*22*).

We constructed a handed cylinder made from an unhanded shearing auxetic pattern (Fig. 1 and movie S1). The circumferential and longitudinal

[1]MIT Computer Science and Artificial Intelligence Lab, Cambridge, MA 02139, USA. [2]School of Engineering and Applied Science, Harvard University, Cambridge, MA 02138, USA. [3]NASA Ames Research Center, Moffett Field, CA 94035, USA.
*Corresponding author. Email: jlipton@mit.edu (J.I.L.); rus@csail.mit.edu (D.R.)

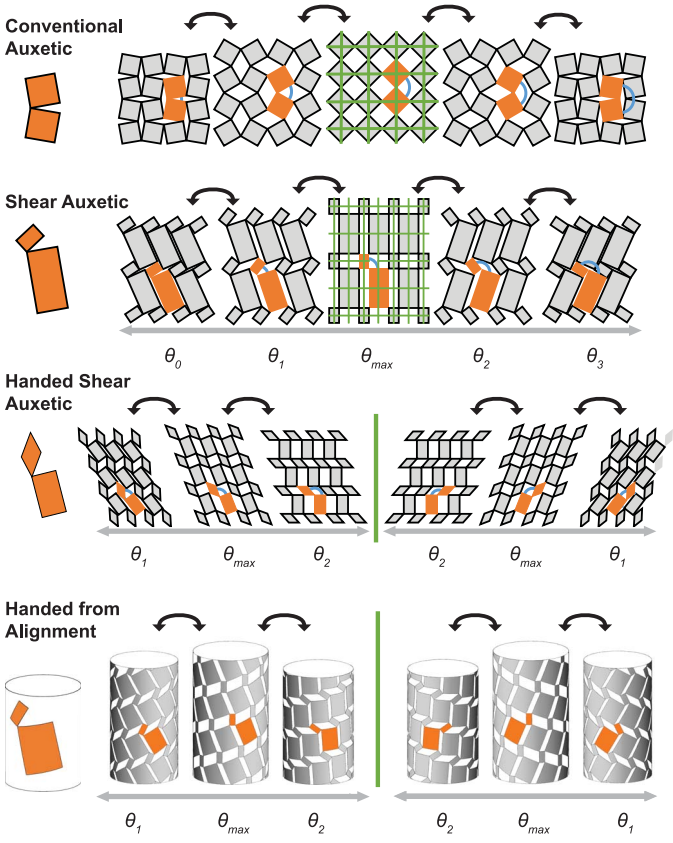

Fig. 1. Auxetic trajectories with and without mirrors. Shearing and handed shearing auxetics are made by changing the symmetries of the conventional auxetic patterns. The cells move along the auxetic trajectories by varying θ, marked in blue. At the point of maximum auxetic extension, θ_{max}, the trajectory is either symmetric or ceases to be auxetic. To be symmetric, θ_2 must be a reflection of θ_1. If an auxetic shears and it is not symmetric around θ_{max}, it is a handed shearing auxetic, and a vertical mirror switches between the handed patterns. Unhanded shearing auxetics tiled on a cylinder can produce a handed auxetic cylinder.

directions of a cylinder provided a natural coordinate system. A planar unhanded shearing auxetic pattern has a natural orientation along the direction of its emergent line of reflection. When the lines of reflection align with the circumferential or longitudinal directions, the cylinder has no net handedness. When the lines of reflection do not align with the circumferential or longitudinal direction, the cylinder has a net handedness, and the sign of the angle between the lines of reflection and the longitudinal axis determines handedness.

A shearing auxetic tiling on a cylinder or sphere couples the shape's radius, height, and orientation to a twist action around the shape's central axis (see movie S1). Tiling cylinders or spheres to make shearing auxetics requires changing the constraints on the structures. Planar and space filling auxetics have zero principal curvature and can be made of rigid links. However, the surface of a sphere or cylinder has directions of nonzero principal curvature. As the surface expands, the radius of curvature on its surface changes. This necessitates tiling the surface with flexible links that can bend and twist.

We fabricated handed auxetic cylinders and spheres using strips of 0.254-mm-thick spring steel (Fig. 2A). We constructed spheres with a 44 symmetry (fig. S6E). We made cylinders with a 224 pattern constructed from the planar pattern in Fig. 2B, which was based on the unit cell of the reentrant honeycomb auxetic tiling. We found that the cylinders expanded by 613% in length and 284% in width between their fully contracted and fully extended states. Prebending strips of spring steel can bias the structure to specific points on the auxetic trajectory (fig. S6). We made cylinders with 223 symmetry from tubes of polytetrafluoroethylene (PTFE) using a laser cutter (Fig. 3A), demonstrating that these structures can be fabricated automatically from continuous materials.

We created composite-handed auxetic structures by combining right- and left-handed cylinders or spheres. We aligned three concentric cylinders or spheres along a central axis. The middle structure turns counter to the inner and outer structures to produce left-right-left (LRL)–or right-left-right (RLR)–handed composites (Fig. 2F). We bonded the ends by constraining the poles or edges of the constituent structures to share the same position and orientation. This step ensures that if there is a twist, or compression, the ends of each layer move in unison.

Locking the poles or edges affects the entire composite structure. When the LRL or RLR composite structure is twisted or loaded, two antagonistic layers compress into each other (Fig. 2F). Either the innermost layer expands while the middle layer contracts, or the outermost layer contracts while the middle layer expands. Strong mechanical bonds form where the two antagonistic layers come into contact (Fig. 2D). As the structure is loaded, the forces between the antagonistic layers increase, fixing them relative to each other. Because of the mechanical bonds, the structure is unable to expand or contract under a load without buckling. This is analogous to the disulfide bonds of keratin or the hydrogen bonding on collagen that prevents the constituent elements from separating or sliding past each other.

When locked (the structure has been constrained to some particular θ), the primary resistance to deformation in the constituent layers is the energy needed to deform the links and hinges. In this state, other deformation modes, such as buckling of the links, must store the energy. Often the alignment of the different layers effectively shortens the links' length by introducing node points where two layers are in contact (Fig. 2, D and E). The LRL cylinders had 1.5 times the ultimate compressive strength of LLL and 6.8 times that of the single HSA cylinders (Fig. 2C). The LRL and LLL composite cylinders had the same effective stiffness, which was 6.2 times the stiffness of the individual cylinders and 2.7 times that of right-left (RL) composites. Unlike a bistable auxetic pattern (*24*), the rigid LRL composite state can exist at any point along the auxetic trajectory.

A simple RL composite cannot be rigid without torsional preloading because it may not form the mechanical bonds. Without preloading, the layers can separate when the outer layer expands and the inner layer contracts. This produces a notably more compliant structure under loading. Similarly, the left-left-left (LLL) or right-right-right (RRR) structures do not generate interlayer mechanical bonds, because there is little to no normal force on the contact points, allowing the structure to globally twist and collapse.

We made compliant structures by eliminating bonds along the lengths of differently handed cylinders while maintaining the end bonds. We composited cylinders of different handedness parallel to each other, but with mechanically coupled ends. The cylinders were hollow tubes of Teflon, 16 cm long, 25.4 mm in diameter, 1.59 mm thick, and cut with a 223 pattern. Each tube required a net torque or external force to maintain state. In Fig. 3C, we see the external loading relative to extension of a single tube. The two tubes required an equal and opposite torque because they were right- and left-handed, respectively. By connecting the ends to each other, the structure self-frustrated and remained opened. Because they were parallel and not concentric, they did not interfere with each other under flexural loading and therefore could flex substantially.

We created a linear actuator using the compliant parallel tube structure with one pair of cylinder ends connected to a rigid plate and the other to a set of gears (Fig. 3A). The ends with the gears could rotate counter to each other but maintained a fixed distance. When the gears rotated, the structure elongated. The two counter-rotating cylinders oppose each other, ensuring no net torque on the rigid plate. This actuator had a 30% elongation and can deflect under external forces (Fig. 3B). We arranged four cylinders in a two-by-two grid of alternating right- and left-handed cylinders (Fig. 3D and movie S2).

This configuration yields a 4-degree-of-freedom composite actuator. One end of each cylinder is connected to a rigid plate, and the other end is constrained to a plane and attached to a servo. This arrangement allows subsections of the actuator to activate, enabling control over linear extension, twist, and bending in two directions. The handed shearing auxetic structure converts the rotation into linear displacement without a screw and nut, rack and pinion, or linkage system typically found in a linear actuator. The actuator itself is hollow, allowing wiring or other structures to occupy the center of the actuator.

We can produce HSAs from a variety of materials to tile the plane, spheres, or cylinders. The

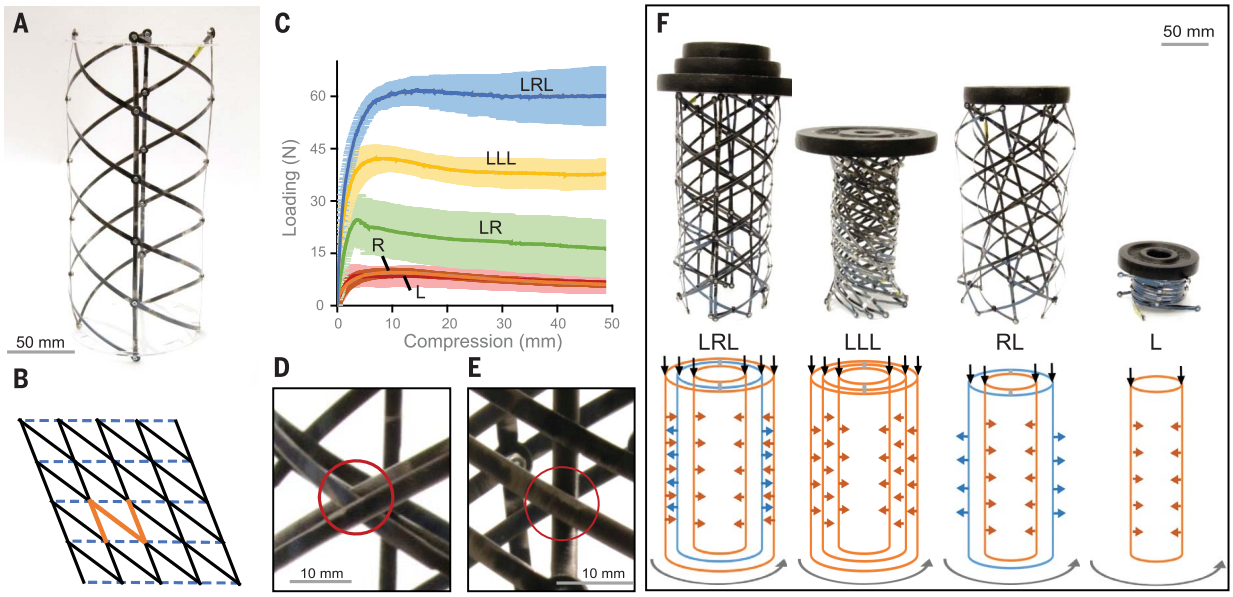

Fig. 2. Concentric handed shearing auxetics produce rigidity. Rigid and compliant structures made from handed shearing auxetic patterns. (**A** and **B**) A 2222 shearing auxetic tiling (B) can cover the plane and make HSA cylinders (A). (**C**) Composite HSA cylinders of different handedness have different strengths based on their structure. (**D**) LRL or RLR make mechanical bonds by self-interfering. (**E**)The LLL or RRR layers do not make mechanical bonds. (**F**) Under loading, the composite HSA performs quite differently. The LRL composite holds 4 kg without notable deformation. The LLL twists and collapses inward under 2.3 kg. The RL structure delaminates and can only hold 1.1 kg with deformation, and the single-layer HSA fully collapses under 0.57 kg of mass.

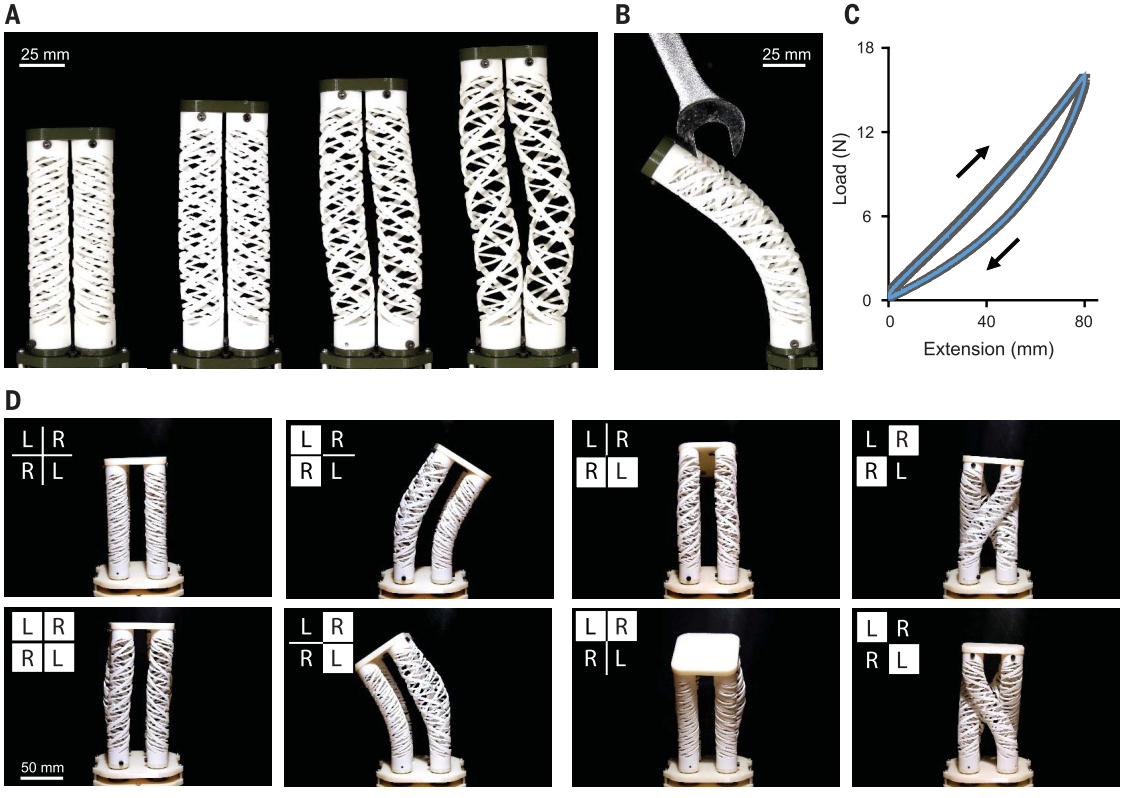

Fig. 3. Compliant handed shearing auxetic actuators. Actuators made from handed shearing auxetics. Right (R)– and left (L)–handed shearing auxetic (HSA) cylinders make compliant or rigid structures. (**A**) Counterrotating right and left HSA cylinders that are parallel to each other generate linear extension with no net torque. (**B**) While extended, these actuators remain compliant. (**C**) External loading of an HSA cylinder has hysteretic loss. (**D**) Four HSA cylinders combined to make a 4-degree-of-freedom actuator. Controlling the twist of each HSA allows the system to move up and down, side to side, and front to back and to twist left and right.

scale independence of this strategy could find application in engineered DNA structures, chemical microstructures, medical stents, or large engineered structures. We have shown that HSA spheres and cylinders can produce rigid structures that resist torsional and axial loading by exploiting global locking. Such deployable and rigidizing structures could be useful in biomedical, architectural, and space applications. Space structures made from HSAs may match the deployability of existing mast designs (*25*, *26*) with greater structural simplicity and reduced fabrication effort. If applied to stent and shunt design, smaller punctures could be used to implant rigid tubing. We have also harnessed the response of HSA cylinders to global twist to realize actuators that use conventional motors but are compliant like soft robotic actuators.

REFERENCES AND NOTES

1. E. Renuart, C. Viney, *Pergamon Materials Series* **4**, 223–267 (2000).
2. M. Feughelman, *Mechanical Properties and Structure of Alpha-Keratin Fibres: Wool, Human Hair and Related Fibres* (UNSW Press, 1997).
3. A. N. Parbhu, W. G. Bryson, R. Lal, *Biochemistry* **38**, 11755–11761 (1999).
4. M. D. Shoulders, R. T. Raines, *Annu. Rev. Biochem.* **78**, 929–958 (2009).
5. C. Borcea, I. Streinu, *Proc. Math. Phys. Eng. Sci.* **471**, 20150033 (2015).
6. R. Lakes, *Science* **235**, 1038–1040 (1987).
7. J. N. Grima *et al*., *Proc. Math. Phys. Eng. Sci.* **468**, 810–830 (2011).
8. J. N. Grima, E. Manicaro, D. Attard, *Proc. Math. Phys. Eng. Sci.* **467**, 439–458 (2010).
9. R. Gatt *et al*., *Sci. Rep.* **5**, 8395 (2015).
10. A. Lazarus, P. M. Reis, *Adv. Eng. Mater.* **17**, 815–820 (2015).
11. N. Karnessis, G. Burriesci, *Smart Mater. Struct.* **22**, 084008 (2013).
12. J. Shim, C. Perdigou, E. R. Chen, K. Bertoldi, P. M. Reis, *Proc. Natl. Acad. Sci. U.S.A.* **109**, 5978–5983 (2012).
13. W. J. Spenner Dolla, Rotational expansion auxetic structures. US Patent 8,652,602. (February 2014).
14. M. Konaković *et al*., *ACM Trans. Graph.* **35**, 89 (2016).
15. A. Yeganeh-Haeri, D. J. Weidner, J. B. Parise, *Science* **257**, 650–652 (1992).
16. A. Alderson, K. E. Evans, *Phys. Rev. Lett.* **89**, 225503 (2002).
17. K. Evans, B. Caddock, *J. Phys. D Appl. Phys.* **22**, 1883–1887 (1989).
18. M. N. Ali, J. J. Busfield, I. U. Rehman, *J. Mater. Sci. Mater. Med.* **25**, 527–553 (2014).
19. K. E. Evans, A. Alderson, *Adv. Mater.* **12**, 617–628 (2000).
20. T. Frenzel, M. Kadic, M. Wegener, *Science* **358**, 1072–1074 (2017).
21. J. Rossiter, K. Takashima, F. Scarpa, P. Walters, T. Mukai, *Smart Mater. Struct.* **23**, 045007 (2014).
22. Materials and methods are available as supplementary materials.
23. J. H. Conway, H. Burgiel, C. Goodman-Strauss, *The Symmetries of Things* (CRC Press, Boca Raton, 2016).
24. A. Rafsanjani, D. Pasini, *Extreme Mech. Lett.* **9**, 291–296 (2016).
25. M. E. McEachen, T. A. Trautt, D. M. Murphy, The ST8 SAILMAST validation experiment. *46th AIAA Structures, Structural Dynamics and Materials Conference* (2005).
26. N. Knight *et al*., 2012. FAST Mast structural response to axial loading: modeling and verification. *53rd AIAA/ASME/ASCE/AHS/ASC Structures, Structural Dynamics and Materials Conference 20th AIAA/ASME/AHS Adaptive Structures Conference 14th AIAA* (2012).

ACKNOWLEDGMENTS

Funding: This work was funded by NSF grants EFRI-1240383 and CCF-1138967 and in part by NASA Space Technology Research Grant NNX13AL38H. **Author contributions:** J.I.L. and D.C. developed the initial planar examples of handed shearing auxetics. J.I.L. extended the concept to nonplanar structures under the supervision of D.R. R.M. and L.C. developed the fabrication and testing processes and collected the data on the structures. J.I.L. and Z.M. developed the mathematical formalism. D.R. was responsible for the direction and funding of this research. All authors contributed to the writing of the paper. **Competing interests:** Two U.S. provisional patents (application numbers 62/630,739 and 62/491,089) have been filed related to this work. **Data and materials availability:** All data are available in the manuscript or the supplementary materials.

SUPPLEMENTARY MATERIALS

www.sciencemag.org/content/360/6389/632/suppl/DC1
Materials and Methods
Figs. S1 to S10
Tables S1 and S2
References (*27*–*35*)
Movies S1 to S3

9 November 2017; accepted 3 March 2018
10.1126/science.aar4586

INTERSTELLAR MEDIUM

Magnetic seismology of interstellar gas clouds: Unveiling a hidden dimension

Aris Tritsis[1,2,3]* and Konstantinos Tassis[1,3]*

Stars and planets are formed inside dense interstellar molecular clouds by processes imprinted on the three-dimensional (3D) morphology of the clouds. Determining the 3D structure of interstellar clouds remains challenging because of projection effects and difficulties measuring the extent of the clouds along the line of sight. We report the detection of normal vibrational modes in the isolated interstellar cloud Musca, allowing determination of the 3D physical dimensions of the cloud. We found that Musca is vibrating globally, with the characteristic modes of a sheet viewed edge on, not the characteristics of a filament as previously supposed. We reconstructed the physical properties of Musca through 3D magnetohydrodynamic simulations, reproducing the observed normal modes and confirming a sheetlike morphology.

Astronomical objects are seen in two-dimensional projection on the plane of the sky. This is particularly problematic for studies of the interstellar medium (ISM), because the three-dimensional (3D) structure of interstellar clouds encodes information regarding the physical processes (such as magnetic forces, turbulence, and gravity) that dominate the formation of stars and planets. We seek a solution to this problem by searching for resonant magnetohydrodynamic (MHD) vibrations in an isolated interstellar cloud and by analyzing its normal modes. Normal modes have been used extensively to describe and analyze various systems in the physical sciences, from quantum mechanics and helioseismology to geophysics and structural biology. Normal modes have been observed in the ISM in two small pulsating condensations (Bok globules) located inside two molecular clouds (interstellar clouds dense enough to allow the formation of molecular hydrogen) (*1*, *2*). Further applications have been limited because molecular clouds usually exhibit a complex morphology, including filamentary structures, as a result of turbulent mixing and shock interaction (*3*, *4*).

Recent wide-field radio observations of molecular clouds (*5*) have unveiled the presence of well-ordered, quasi-periodically spaced elongations, termed striations, on the outskirts of clouds. The thermal dust continuum emission survey of nearby molecular clouds by the Herschel Space Observatory has shown that striations are a common feature of clouds (*6*–*10*), often associated with denser filaments (*7*–*11*) inside which stars are formed. Complementary polarimetric studies have revealed that striations are always well aligned with the cloud's magnetic field projected onto the plane of the sky (*5*, *7*–*12*).

From a theoretical perspective, the only viable mechanism for the formation of striations involves the excitation of fast magnetosonic waves (longitudinal magnetic pressure waves) (*13*). Compressible fast magnetosonic waves can be excited by nonlinear coupling with Alfvén waves (incompressible transverse waves along magnetic field lines) and/or perturbations created by self-gravity in an inhomogeneous medium. These magnetosonic waves compress the gas and form ordered structures parallel to magnetic field lines, in agreement with observations of striations (*5*, *7*–*12*).

Once magnetosonic waves are excited, they can be reflected in regions of varying Alfvén speed (defined as $v_A = B/\sqrt{4\pi\rho}$, where B is the magnetic field and ρ is the density of the medium), setting up normal modes, just like vibrations in a resonating chamber. In regions where striations appear to be unassociated with denser structures (such as in H I clouds), this resonating chamber may be the result of external pressure confinement by a more diffuse, warmer medium. However, boundaries can also be naturally created, in the case of a contracting self-gravitating cloud, as a result of steep changes in density and magnetic field that in turn lead to sharp variations in the velocity of propagation of these waves (*14*). Any compressible fast magnetosonic waves excited during the formation of the cloud will then be trapped, thus resulting in striations in the vicinity of denser structures.

Fast magnetosonic waves traveling in both directions perpendicular to the magnetic field are coupled (*13*). By considering a rectangular box, we can express the spatial frequency k of each normal mode (n, m) as

$$k_{nm} = \sqrt{\left(\frac{\pi n}{L_x}\right)^2 + \left(\frac{\pi m}{L_y}\right)^2} \quad (1)$$

where the ordered component of the magnetic field is considered to be along the z axis and L_x and L_y are the lengths of the box along the x and y axes, respectively, with n and m being integers ranging from zero to infinity. By considering a rotation matrix, we can show that the spatial frequencies seen in the power spectra of cuts perpendicular to the long axis of striations are independent of the orientation of the cloud (*14*).

We analyzed these magnetohydrodynamic striations seen in Musca (designated G301.70-7.16), a molecular cloud located ~150 to 200 pc from Earth (*15*, *16*). Because of its elongated and ordered morphology and its low column density (the integrated volume density along the line of sight), Musca is considered to be the prototype of a filamentary (cylindrical) molecular cloud (*9*, *17*–*20*) and is used as a comparison by many theoretical models. Musca has been mapped by

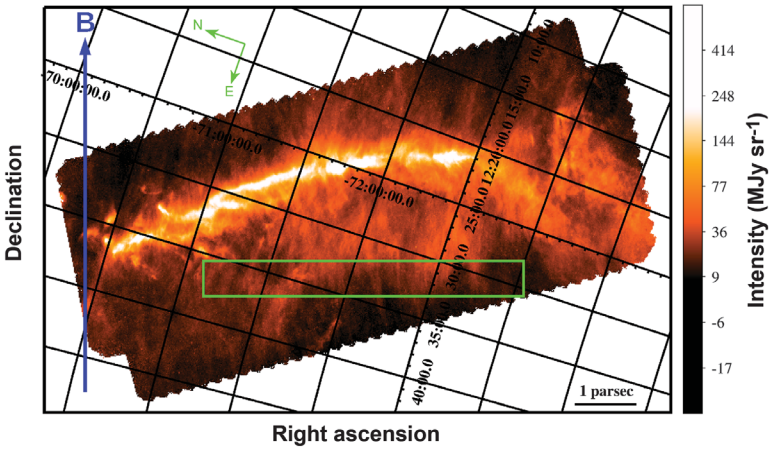

Fig. 1. The Musca molecular cloud. This Herschel 250-μm dust emission map of the Musca molecular cloud [with intensity expressed in megajanskies (MJy) per steradian] shows both striations and the dense elongated structure. The green rectangle marks the region where we have performed our normal-mode analysis, and the blue arrow shows the mean direction of the magnetic field projected onto the plane of the sky (*9*). Grid lines show equatorial coordinates.

[1]Department of Physics and Institute of Theoretical and Computational Physics, University of Crete, P.O. Box 2208, 71003 Heraklion, Crete, Greece. [2]Research School of Astronomy and Astrophysics, Australian National University, Canberra, ACT 2611, Australia. [3]Institute of Electronic Structure and Laser and Institute of Astrophysics, Foundation for Research and Technology–Hellas, P.O. Box 1527, 71110 Heraklion, Crete, Greece.
*Corresponding author. Email: tassis@physics.uoc.gr (K.T.); aris.tritsis@anu.edu.au (A.T.)

Herschel as part of the Gould Belt Survey (*9*) and exhibits clear striations oriented perpendicularly to the main body of the cloud. We have reanalyzed the archival data (*9*); Fig. 1 shows the Herschel Spectral and Photometric Imaging Receiver 250-μm dust emission map of Musca. We have considered cuts perpendicular to the long axis of striations inside the green rectangle in Fig. 1 in order to study their spatial power spectra. We have verified that our selection does not introduce biases by considering cuts perpendicular to the long axis of the striations and studying their spatial power spectra in other regions as well (*14*).

The normalized power spectra from each cut and the distribution of the identified peaks are shown in Fig. 2, A and B, respectively. From Eq. 1 and the assumption that L_x is the largest dimension of the cloud, the smallest possible wave number is obtained for (n, m) = (1, 0). Thus, the first peak in Fig. 2B has to correspond to (n, m) = (1, 0), yielding L_x = 8.2 ± 0.3 pc. This value is consistent with the observed size of the cloud on the plane of the sky, which is variously reported to be from 6.5 to 7.85 pc when scaled to our adopted cloud distance of 150 pc (*9*, *18*, *21*). The second peak could correspond to either (n, m) = (0, 1) or, in the case of a cylindrical cloud with $L_x \gg L_y$ (and thus $k_{0.1} \gg 1$), to (n, m) = (2, 0). However, with L_x ~ 8 pc, the (n, m) = (2, 0) peak is expected at k ~ 0.8 (pc)$^{-1}$, much higher than the actual location of the second peak. Thus, this second peak has to correspond to (n, m) = (0, 1). By inserting (n, m) = (0, 1) and the value of the second peak in Eq. 1, we deduce the hidden, line-of-sight dimension L_y to be 6.2 ± 0.2 pc, comparable to the largest dimension of the cloud. The other normal modes with their uncertainties determined through error propagation are predicted analytically by inserting these values for L_x and L_y into Eq. 1 and are overplotted in Fig. 2B. Therefore, Musca, previously considered to be a prototypical filamentary cloud, is instead a sheetlike structure seen edge on.

In Fig. 2B, we plot all the normal modes up to (n, m) = (2, 2). We find good agreement between the predicted wave numbers and observations up to the first few modes, with n or m = 4 corresponding to physical scales of ~1.6 pc (fig. S1). However, the shape of the cloud is more complicated than an idealized rectangle, exhibiting higher-order structure on smaller scales, so the normal modes may be better modeled by a rectangle with rounded edges or an ellipse. Thus, Eq. 1 is an approximation that applies only to the normal modes with small spatial frequencies (i.e., large physical scales). At spatial frequencies higher than ~2 (pc)$^{-1}$, the density of normal modes becomes so high that they cannot be identified in either the observations or the theoretical predictions (the uncertainties overlap for all predicted modes).

Through ideal (nondissipative) MHD simulations including self-gravity (*14*), we have constructed a 3D model of Musca, including the dense structure and striations in the low-density parts. In Fig. 3 we show the column density map from our simulation, which reproduces the observed dimensions of the cloud. A 3D representation of the volume density of the model of Musca is shown in Fig. 4. As intuitively expected from the normal-mode analysis of the observations, the shape of the cloud is that of a rectangle with rounded edges.

The maximum column density in the simulation, from an edge-on view, is 1.9 × 10^{22} cm^{-2}. For comparison, the maximum column density derived observationally from the dust emission maps (*9*) is ~1.6 × 10^{22} cm^{-2}. The maximum volume number density in the simulation is ~2 × 10^3 cm^{-3}, high enough for molecules to be collisionally excited and therefore observed via their rotational emission lines. Molecular line observations of the Musca molecular cloud are limited to CO, including several isotopologues, and NH_3 (*17*–*20*); the latter is observed only toward the densest core of Musca. The number densities required to excite CO and NH_3 lines are ~10^2 and 10^3 cm^{-3}, respectively (*22*), which are easily reached in our simulated model of the cloud. To reproduce the observed column density in any filamentlike geometry, in contrast to the sheetlike structure, the number density has to be ~5 × 10^4 cm^{-3} or higher (*18*). This value is well above the density threshold for star formation for clouds in the Gould Belt and a density threshold derived specifically for Musca (*23*). More evident star formation activity would be observed if Musca was a filament. Moreover, if the 3D shape of Musca was that of a filament, NH_3 would be easily excited and observed throughout the ridge of the dense structure.

We used a suite of simulations of clouds of different shapes to validate our analysis and verify that Eq. 1 can be used to extract the correct cloud dimensions (*14*). In each of our simulations, the known dimensions of the clouds were recovered by the simulated normal-mode analysis. In contrast to the distribution of peaks seen in Fig. 2B, in cylindrical clouds ($L_y \ll L_x$) the first few peaks at low spatial frequencies are all multiples of the first peak. The first few peaks for cylindrical clouds are due only to the largest dimension of the cloud, resulting in a sparser distribution of peaks than the sheet geometry (fig. S4). This is both quantitatively and qualitatively different from the distribution seen in the Musca data (Fig. 2), strengthening the case that the intrinsic shape of Musca is sheetlike. Sheetlike structures are common in turbulent clouds, as they may represent planarlike shocks from processes such as supernova explosions or expanding ionization regions or may result simply from accretion along magnetic field lines (*4*, *24*, *25*).

For decades, the determination of the 3D shapes of clouds has been pursued through statistical studies (*26*–*28*), which do not provide information

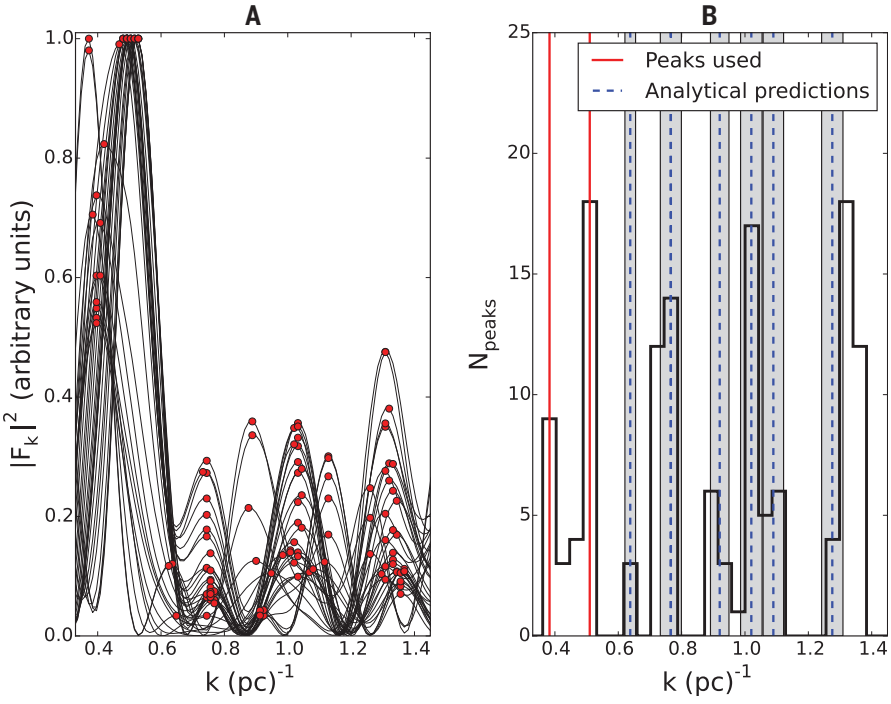

Fig. 2. Comparison of observed normal modes with the analytical solution. (**A**) Normalized power spectra (black lines) of cuts through the observations perpendicular to the striations. Peaks we identified are marked with red dots. F_k, normalized spectral power density. (**B**) Distribution of peaks at different spatial frequencies. The red lines depict the values used to derive the dimensions of the cloud. The blue dashed lines show the rest of the normal modes [up to (n, m) = (2, 0)], predicted analytically from Eq. 1 given the cloud dimensions derived from the first two peaks. Shaded regions indicate the 1σ regions of the analytical predictions due to uncertainties in the determination of the locations of the first two peaks, propagated through Eq. 1. The bin size is comparable to the standard deviations of the points constituting the first two peaks. N_{peaks}, number of peaks.

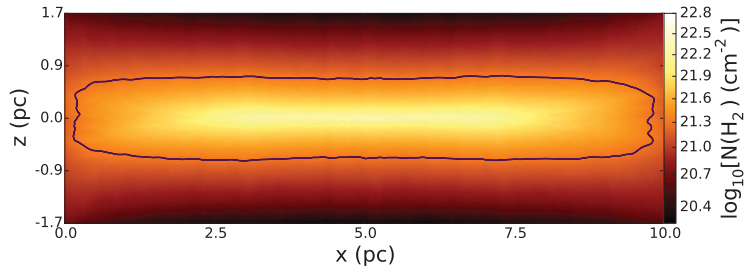

Fig. 3. Column density map of the model of the Musca molecular cloud. The map is an edge-on view of the molecular gas column density from our MHD simulation of a sheetlike structure. The color bar shows the logarithm of the column density. The purple contour marks the region with $N(H_2) > 2 \times 10^{21}$ cm^{-2}, used to identify Musca's main, dense filament (*9*). The magnetic field is along the *z* axis, and the time of the snapshot since the beginning of the simulation is ~2.7 million years.

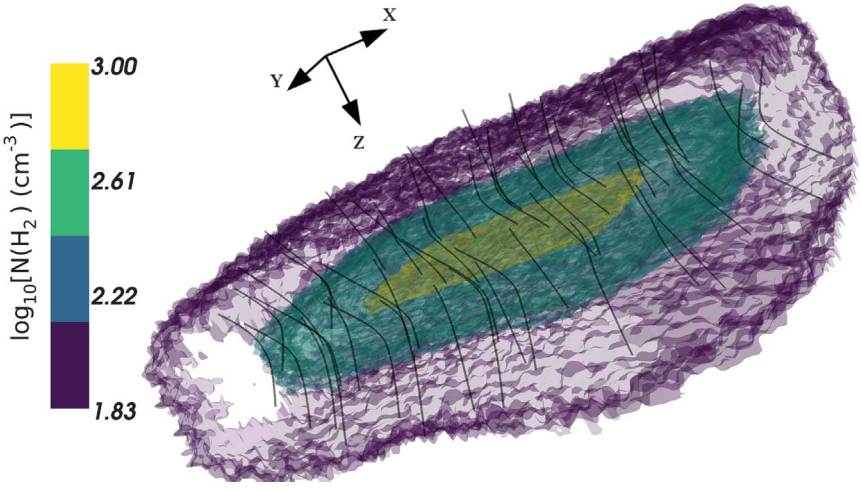

Fig. 4. 3D model of the Musca molecular cloud. The model shows the logarithmic 3D volume density in our MHD simulation of the Musca cloud. Density isosurfaces are set at 90, 75, 70, and 55% of the logarithm of the maximum number density. Black lines represent the magnetic field.

on a cloud-by-cloud basis. Other proposed methods (*29*, *30*) rely on complex chemical and/or radiative processes and thus depend on numerous assumptions. With its 3D geometry now determined, Musca can be used to test theoretical models of interstellar clouds.

REFERENCES AND NOTES

1. C. J. Lada, E. A. Bergin, J. F. Alves, T. L. Huard, *Astrophys. J.* **586**, 286–295 (2003).
2. E. D. Aguti, C. J. Lada, E. A. Bergin, J. F. Alves, M. Birkinshaw, *Astrophys. J.* **665**, 457–465 (2007).
3. P. André *et al.*, *Astron. Astrophys.* **518**, L102 (2010).
4. C. Federrath, *Mon. Not. R. Astron. Soc.* **457**, 375–388 (2016).
5. P. F. Goldsmith *et al.*, *Astrophys. J.* **680**, 428–445 (2008).
6. M.-A. Miville-Deschênes *et al.*, *Astron. Astrophys.* **518**, L104 (2010).
7. C. Alves de Oliveira *et al.*, *Astron. Astrophys.* **568**, A98 (2014).
8. P. Palmeirim *et al.*, *Astron. Astrophys.* **550**, A38 (2013).
9. N. L. J. Cox *et al.*, *Astron. Astrophys.* **590**, A110 (2016).
10. J. Malinen *et al.*, *Mon. Not. R. Astron. Soc.* **460**, 1934–1945 (2016).
11. N. Schneider *et al.*, *Astron. Astrophys.* **540**, L11 (2012).
12. G. V. Panopoulou, I. Psaradaki, K. Tassis, *Mon. Not. R. Astron. Soc.* **462**, 1517–1529 (2016).
13. A. Tritsis, K. Tassis, *Mon. Not. R. Astron. Soc.* **462**, 3602–3615 (2016).
14. Materials and methods are available as supplementary materials.
15. J. Knude, E. Høg, *Astron. Astrophys.* **338**, 897–904 (1998).
16. J. C. Gregorio Hetem, G. C. Sanzovo, J. R. D. Lepine, *Astron. Astrophys.* **76** (suppl.), 347–363 (1988).
17. E. M. Arnal, R. Morras, J. R. Rizzo, *Mon. Not. R. Astron. Soc.* **265**, 1–11 (1993).
18. J. Kainulainen *et al.*, *Astron. Astrophys.* **586**, A27 (2016).
19. A. Hacar, J. Kainulainen, M. Tafalla, H. Beuther, J. Alves, *Astron. Astrophys.* **587**, A97 (2016).
20. D. A. Machaieie *et al.*, *Astrophys. J.* **836**, 19 (2017).
21. Planck Collaboration, *Astron. Astrophys.* **586**, A136 (2016).
22. Y. L. Shirley, *Publ. Astron. Soc. Pac.* **127**, 299–310 (2015).
23. J. Kainulainen, C. Federrath, T. Henning, *Science* **344**, 183–185 (2014).
24. F. Nakamura, Z.-Y. Li, *Astrophys. J.* **687**, 354–375 (2008).
25. T. C. Mouschovias, *Astrophys. J.* **373**, 169–186 (1991).
26. P. C. Myers, G. A. Fuller, A. A. Goodman, P. J. Benson, *Astrophys. J.* **376**, 561–572 (1991).
27. C. E. Jones, S. Basu, J. Dubinski, *Astrophys. J.* **551**, 387–393 (2001).
28. K. Tassis, C. D. Dowell, R. H. Hildebrand, L. Kirby, J. E. Vaillancourt, *Mon. Not. R. Astron. Soc.* **399**, 1681–1693 (2009).
29. J. Steinacker, A. Bacmann, T. Henning, R. Klessen, M. Stickel, *Astron. Astrophys.* **434**, 167–180 (2005).
30. D. Li, P. F. Goldsmith, *Astrophys. J.* **756**, 12 (2012).

ACKNOWLEDGMENTS

We thank V. Pavlidou, G. Panopoulou, V. Charmandaris, N. Kylafis, A. Zezas, E. Economou, J. Andrews, S. Williams, P. Sell, D. Blinov, I. Liodakis, T. Mouschovias, and the three anonymous referees for comments that helped improve this paper. **Funding:** K.T. and A.T. acknowledge support by the Seventh Framework Programme through Marie Curie Career Integration grant PCIG-GA-2011-293531, "Onset of Star Formation: Connecting Theory and Observations." A.T. acknowledges funding from the European Research Council (ERC) under the European Union's Seventh Framework Programme (FP/2007-2013)/ERC grant agreement 617001. Usage of the Metropolis HPC Facility at the Crete Center for Quantum Complexity and Nanotechnology of the University of Crete, supported by the European Union Seventh Framework Programme (FP7-REGPOT-2012-2013-1) under grant agreement 316165, is acknowledged. **Author contributions:** A.T. performed the numerical simulations and the analysis of the observations and wrote the text. K.T. contributed to the interpretation of the results and the writing of the text. **Competing interests:** The authors declare no conflicts of interest. **Data and materials availability:** All observational data used in this research are from the Herschel Gould Belt Survey project and are publicly available at http://archives.esac.esa.int/hsa/whsa/#home (observation ID, 1342216012). All simulation outputs and setup files are available at https://doi.org/10.6084/m9.figshare.5950360. The FLASH software used in this work was developed in part by the Advanced Simulation and Computing Program of the National Nuclear Security Administration, U.S. Department of Energy, at the Flash Center for Computational Science at the University of Chicago and was obtained from http://flash.uchicago.edu/site/. The yt analysis toolkit is available at http://yt-project.org/#getyt, and Mayavi2 is available at https://github.com/enthought/mayavi.

SUPPLEMENTARY MATERIALS

www.sciencemag.org/content/360/6389/635/suppl/DC1
Materials and Methods
Figs. S1 to S4
References (*31*–*43*)

15 June 2017; accepted 14 March 2018
10.1126/science.aao1185

ORGANIC CHEMISTRY

Asymmetric nucleophilic fluorination under hydrogen bonding phase-transfer catalysis

Gabriele Pupo,[1]* Francesco Ibba,[1]* David M. H. Ascough,[1]* Anna Chiara Vicini,[1] Paolo Ricci,[1] Kirsten E. Christensen,[1] Lukas Pfeifer,[1] John Richard Morphy,[2] John M. Brown,[1] Robert S. Paton,[1] Véronique Gouverneur[1]†

Common anionic nucleophiles such as those derived from inorganic salts have not been used for enantioselective catalysis because of their insolubility. Here, we report that merging hydrogen bonding and phase-transfer catalysis provides an effective mode of activation for nucleophiles that are insoluble in organic solvents. This catalytic manifold relies on hydrogen bonding complexation to render nucleophiles soluble and reactive, while simultaneously inducing asymmetry in the ensuing transformation. We demonstrate the concept using a chiral bis-urea catalyst to form a tridentate hydrogen bonding complex with fluoride from its cesium salt, thereby enabling highly efficient enantioselective ring opening of episulfonium ion. This fluorination method is synthetically valuable considering the scarcity of alternative protocols and points the way to wider application of the catalytic approach with diverse anionic nucleophiles.

Phase-transfer catalysis (PTC) (*1*) has progressed enormously with the appearance of powerful asymmetric methods based on lipophilic chiral cationic (*2*) or anionic salts (*3*) as catalysts. Despite these advances, an outstanding challenge is asymmetric synthesis where the solid-phase reagent is a simple inorganic salt. Here, we propose a solution, based on anion recognition by hydrogen bonding, to enable asymmetric PTC in organic media with poorly soluble inorganic nucleophiles. For proof of concept, we focused on the activation of alkali-metal fluorides for the enantioselective installation of sp^3 C–F, a highly important functional group for applications in pharmaceutical sciences (*4*–*6*).

Catalytic enantioselective fluorination is dominated by methods employing electrophilic fluorinating reagents (*7*). Although alkali-metal fluorides are abundant and inexpensive, their low solubility and high Brønsted basicity have hindered their application to asymmetric nucleophilic fluorination (*8*–*12*). Both cationic (*13*) and anionic (*3*) PTC have been successfully applied to asymmetric electrophilic fluorinations (Fig. 1A). Phase-transfer agents enabling nucleophilic rather than electrophilic fluorination have been extensively investigated, and the most common approach to enhance metal fluorides' reactivity in organic solvents entails metal encapsulation with a crown ether (*14*, *15*). Despite these advances, enantioselective fluorination with metal fluorides under PTC remains an unsolved problem. This state of play prompted us to formulate a strategy that embraces the poor solubility of metal fluorides in organic solvents and the capacity of fluoride to engage in H-bonding interactions. Fluoride abstraction, and more generally anion abstraction, with a hydrogen bond donor (HBD) catalyst (*16*–*21*) has been explored to activate electrophiles via chiral ion pairs that react with an external nucleophile (Fig. 1B). Here, we introduce an alternative scenario in which the H-bonded fluoride complex itself is the nucleophile for fluorination. We envisioned that a chiral HBD could act as a solid-liquid phase-transfer catalyst enabling enantioselective nucleophilic fluorination with a metal fluoride insoluble in organic media. The in situ–formed H-bonded fluoride complex would become soluble and capable of mediating fluorination of an organic substrate with release of the HBD catalyst (Fig. 1C). Complexation of fluoride with HBDs is well documented but has not been explored to access enantioenriched alkyl fluorides (*22*–*24*). We reported that urea-fluoride complexes are suitable reagents for the nucleophilic substitution of alkyl bromides, the reactive species being a 1:1 urea-fluoride complex (*25*). We therefore selected ureas as catalysts capable of bringing insoluble alkali metal fluorides (e.g., KF or CsF) into nonpolar solution. For substrate choice, we sought inspiration from the fluorinase enzyme. The only known fluorination reaction in nature involves *S*-adenosyl-L-methionine with a sulfonium leaving group and proceeds via an S_N2 pathway, leading to a primary alkyl fluoride product (Fig. 1D). We focused on β-bromosulfides as model substrates because (i) they form highly electrophilic episulfonium ions that readily undergo diastereospecific bond-forming reactions with nucleophiles (*21*); (ii) the positively charged sulfur of the episulfonium ion can interact with the in situ–formed urea-fluoride complex in a manner reminiscent of the HB-fluoride-sulfonium prereaction complex characteristic of the enzyme (*26*–*29*); (iii) *meso*-episulfonium ions are suitable for enantioselective desymmetrization with a chiral urea catalyst; and (iv) the fluorination products contain both fluorine and sulfur, which are important elements in drug design, thus underlining the value of the products for medicinal chemistry (*4*–*6*, *30*).

Racemic β-bromosulfides were conveniently prepared from the corresponding *cis*-epoxides via a two-step sequence involving epoxide ring opening followed by bromination, or via a one-pot protocol from the corresponding *cis*-alkene (figs. S5 to S7). Preliminary experiments (fig. S1) revealed that **1a** performed particularly well under the designed catalytic conditions (Fig. 2A). No fluorination occurred at room temperature when **1a** was treated with 1.2 equivalents of CsF in toluene, acetonitrile, or dichloromethane (0.25 M); in contrast, C–F bond formation took place in the presence of 10 mol % of urea **2a** (*31*), affording the desired product **3a** in yields up to 80% in CH_2Cl_2. Retention of configuration occurred, an observation consistent with fluoride attack on an in situ–formed episulfonium ion. The reaction also proceeded with KF under urea catalysis, but this reagent required longer time (table S1). This solid-liquid phase-transfer manifold has advantages over the use of soluble fluoride sources such as AgF or n-$Bu_4NF{\cdot}3H_2O$, not least because it generates reactive fluoride at controllable low concentration and offers the possibility to induce asymmetry with a chiral nonracemic urea catalyst. Excision of the catalyst's HBD groups, or reduction of acidity through substituent effects, led to no reaction or a decrease in reactivity (table S1). No product was formed with the corresponding thiourea (fig. S3), prompting the use of urea catalysts for subsequent studies. These data gave insight into the parameters enabling catalysis and suggested that urea–fluoride HB is a key interaction to enable C–F bond formation.

Computational analysis of the reaction catalyzed by urea **2a** and the corresponding uncatalyzed pathway was undertaken to gain more insight (Fig. 2B). The thermodynamics of phase transfer were evaluated by combining experimental CsX formation free energies with density functional theory (DFT)–computed data in an anion-exchange process (fig. S9). The reaction is initiated by ionization of *rac*-**1k** to form the tight episulfonium-bromide ion pair **ii**, with a barrier to auto-ionization of 90 kJ/mol (**i**‡). Following ion-pair dissociation, uncatalyzed halide anion exchange (**iii** and **iv**) of free bromide for free fluoride in solution is unfavorable by 34 kJ/mol, the much higher lattice energy of CsF relative to CsBr playing a crucial role. Unfavorable ion transport is therefore responsible for the prohibitively high energetic span of the uncatalyzed pathway (122 kJ/mol). The key catalytic role of the urea is in promoting anion-exchange through preferential stabilization of fluoride in solution. With urea **2a**, anion exchange becomes favorable by

[1]University of Oxford, Chemistry Research Laboratory, 12 Mansfield Road, Oxford OX1 3TA, UK. [2]Medicinal Chemistry, Eli Lilly and Company Limited, Erl Wood Manor, Sunninghill Road, Windlesham GU20 6PH, UK.
*These authors contributed equally to this work.
†Corresponding author. Email: veronique.gouverneur@chem.ox.ac.uk

17 kJ/mol, owing to the stronger H-bonding of F^- over Br^- to the catalyst. The lower reactivity of fluoride sources such as KF arises from larger differences in lattice energies between the metal fluoride and bromide salts, which disfavors ion transport (table S9). Fluoride delivery [via transition structure (TS) **vi**‡] to form the product is irreversible, even in the presence of catalyst, with a barrier to the reverse reaction of 135 kJ/mol, indicating that the product is not susceptible to racemization and that this step is enantiodetermining with a chiral urea catalyst. In the fluoride delivery TS, the phenyl ring on the α-carbon stabilizes the TS by aligning its π system with the forming/breaking bonds (table S10).

Activation of otherwise insoluble fluoride by a urea ligand provides a platform for asymmetric catalysis (Fig. 2C). We considered axially chiral C_2-symmetric ureas derived from BINAM ([1,1'-binaphthalene]-2,2'-diamine) (*32*) because these systems can be readily tuned through structural modification. After initial optimization, **1a** underwent fluorination with (*S*)-**4a** (10 mol %) (*32*) in 1,2-difluorobenzene at room temperature, affording (+)-**3a** after 1.5 hours in >95% yield and an enantiomeric ratio (e.r.) of 86:14 (table S2). Catalysts (*S*)-**4b–e** modified at the binaphthyl core or presenting a phenyl instead of the 3,5-(trifluoromethyl)phenyl group were less effective (fig. S2). The presence of two urea motifs within catalyst **4a** prompted us to interrogate which H-bond interactions are necessary for reactivity and enantioselectivity, experimentally and computationally.

Molecular dynamics (MD) simulations of the solution-phase conformation of **4a** binding cesium fluoride indicated that isomerism of one urea proximal to the binaphthyl core from *anti-anti* to *anti-syn* was likely, and DFT calculations reinforced the energetic preference for the resulting tridentate H-bonding mode (tables S14 and S15). Experimentally, the fluorination of *rac*-**1a** was carried out with the corresponding mono- and dimethylated catalysts to probe the requirements for effective H-bonding (fig. S2). These catalysts were less effective or ineffective with the exception of **4f**, methylated at the N-H that is predicted computationally not to interact with fluoride. This catalyst is as active as **4a** and enhances enantiocontrol (>95% yield, 88:12 e.r.). The replacement of the *N*-methyl group with a larger alkyl group (**4g–h**), and further optimization (−30°C), afforded (+)-**3a** in 90% yield (95.5:4.5 e.r.).

On the basis of these data, we selected catalyst (*S*)-**4h** to study the scope of this process (Fig. 3A). Variation of the substituents on the carbon backbone of the electrophile revealed that aryl groups with meta- and para-positioned electron-donating and electron-withdrawing functionalities are compatible, affording the desired products (*S*,*S*)-**3a-l** in high yields and enantioselectivities. The sulfur substituent can also be modified with phenylethyl, affording the products with the highest enantioselectivity. By this route, a gram quantity of **1d** underwent fluorination affording (*S*,*S*)-**3d** in 51% overall yield as a single enantiomer (>99.9:0.1 e.r.) after one recrystallization. Despite recent interest in the preparation and properties of molecules containing the F–C–C–S(O)$_n$ (n = 0, 1 and 2) motif (*30*, *33*), no alternative method to access these scaffolds in enantiopure form has been developed to date.

The linear relationship between the enantiopurity of catalyst and product indicates that one chiral urea is involved in the enantiodetermining step (fig. S4). After extensive MD simulation of the reactive ion pair, more than

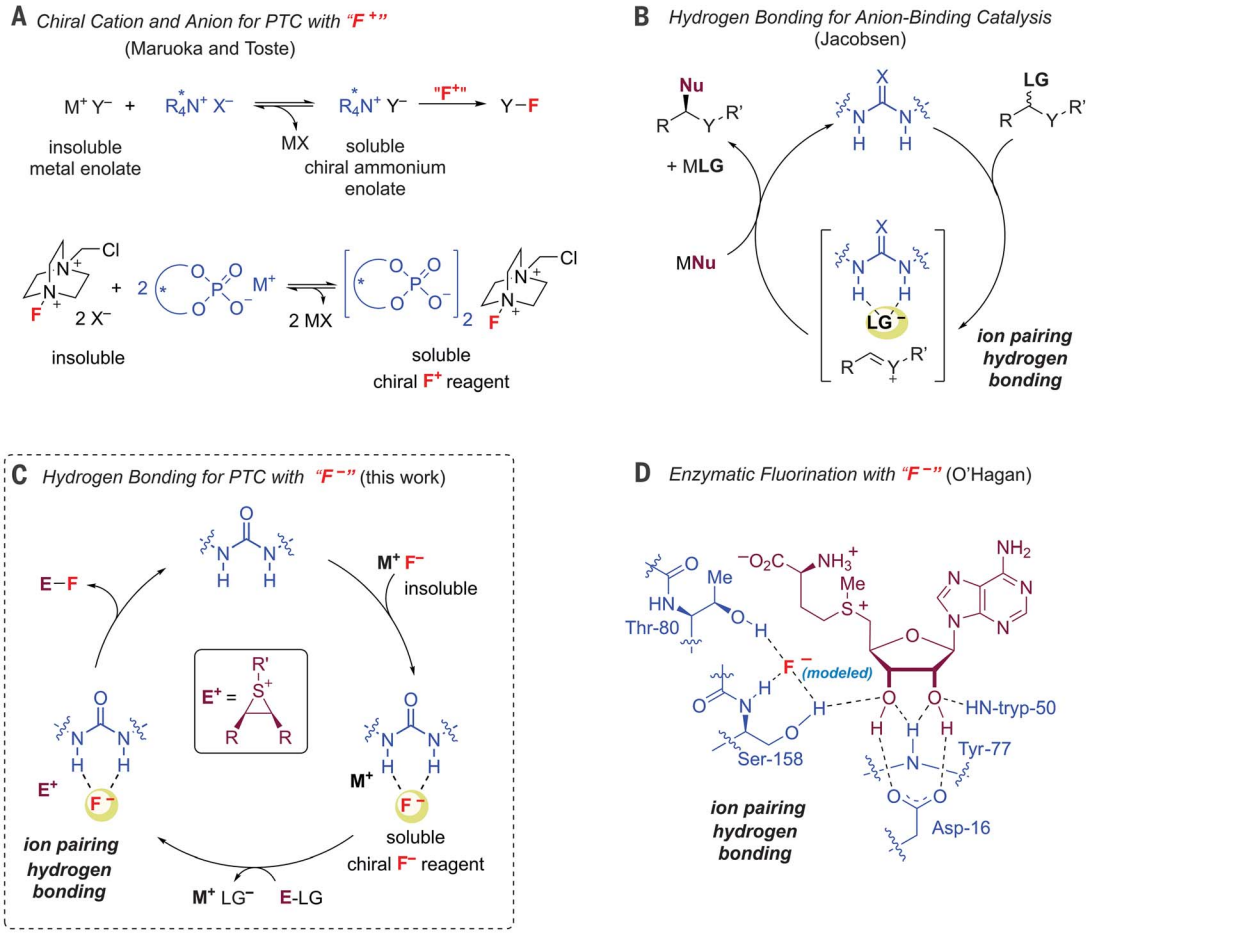

Fig. 1. Catalytic reaction design. (**A**) Enantioselective electrophilic fluorination under PTC. (**B**) Electrophile activation under hydrogen bonding catalysis. (**C**) Proposed enantioselective nucleophilic fluorination under hydrogen bonding PTC; urea-catalyzed fluorination of an episulfonium ion precursor with an alkali metal fluoride (M^+F^-). (**D**) Hydrogen-bonded fluoride complex for nucleophilic fluorination of *S*-adenosyl-L-methionine catalyzed by the fluorinase enzyme.

30 DFT-calculated TSs were optimized for catalysts (*S*)-**4f** and (*S*)-**4h** with substrate **1k** (figs. S24 and S27). A Boltzmann ensemble of competing (*S*)-**4h** TSs predicted (*S*,*S*)-product formation (supported by single-crystal x-ray diffraction) (fig. S33) in 96.5:3.5 e.r. (at 243.15 K), a result that aligns with the experimental value (91:9 e.r.). The alkylated urea adopts an *anti-syn* conformation in both the fluoride complex and the populated TSs, which were subsequently found to overlay well with the x-ray structure of tetrabutylammonium fluoride·**4h** (TBAF·**4h**) (fig. S32), in terms of catalyst conformation, fluoride binding mode, and position of the cation (Fig. 3B) (fig. S28). In the lowest-energy TSs (Fig. 3C), the catalyst interacts favorably with the substrate through cation-π and CH-π noncovalent interactions (fig. S30). Catalyst:substrate noncovalent interactions are similar in competing TSs; however, shorter distances in the major TS are consistent with preferential binding. Substrate conformation also contributes to the sense of selectivity. Phenyl ring rotation adjacent to the site of nucleophilic substitution is unfavorable, owing

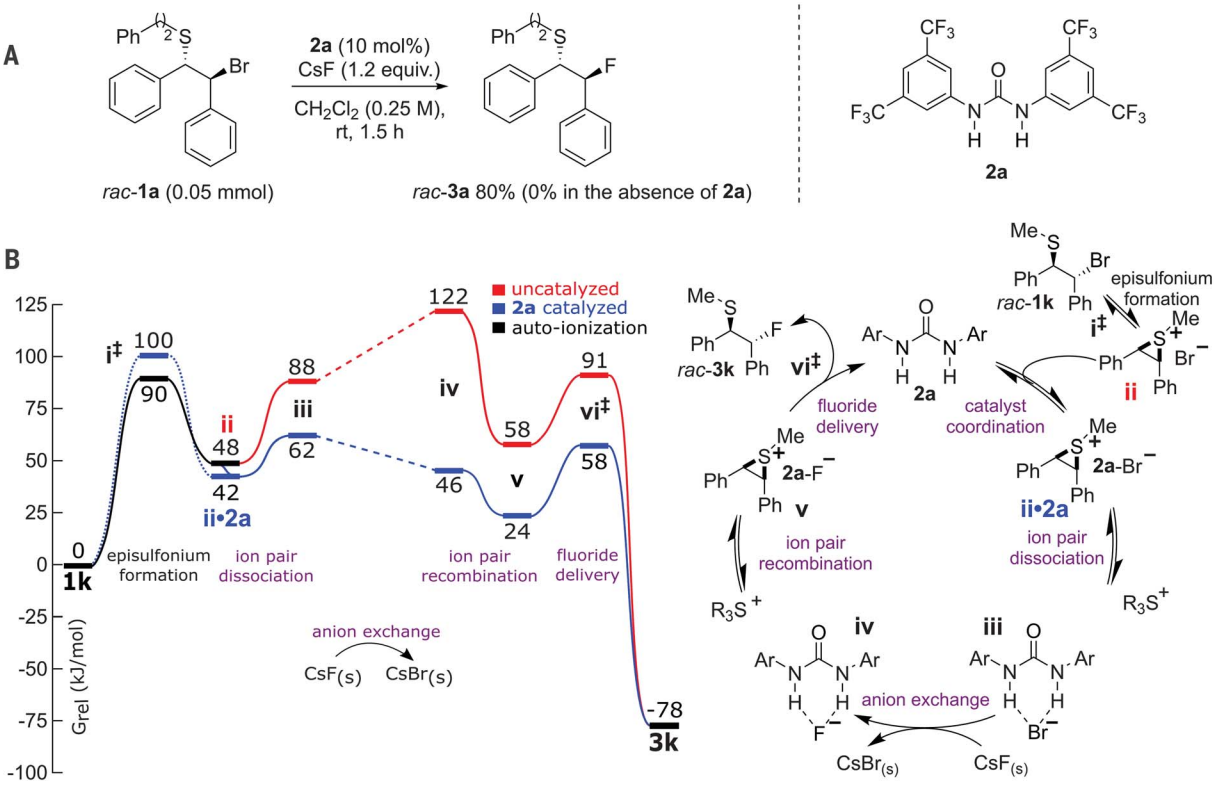

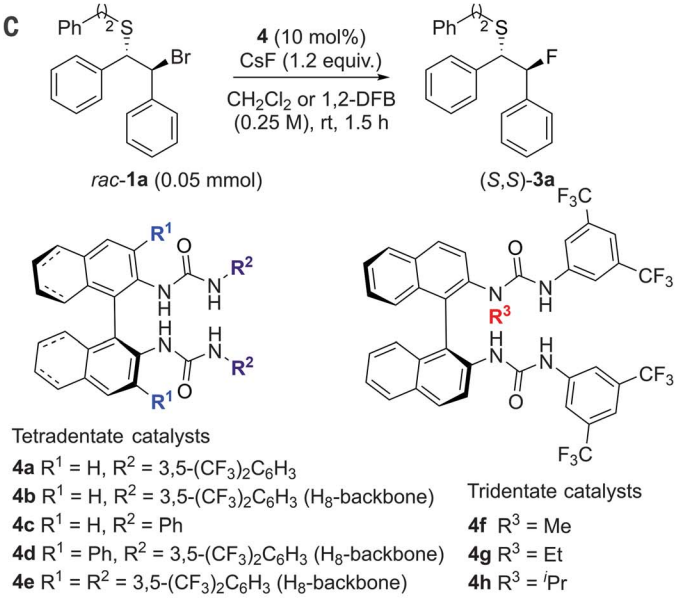

Entry	Catalyst	Solvent	Yield (%)*	e.r.†
1	**4a**	CH_2Cl_2	>95	82:18
2	**4a**	1,2-DFB‡	>95	86:14
3	**4b**	CH_2Cl_2	70	75:25
4	**4c**	CH_2Cl_2	45	68.5:31.5
5	**4d**	CH_2Cl_2	20	55:45
6	**4e**	CH_2Cl_2	65	55:45
7	**4f**	1,2-DFB	>95	88:12
8	**4g**	1,2-DFB	>95	91:9
9	**4g**	1,2-DFB (–30 °C, 72 h)§	>95	94:6
10	**4h**	1,2-DFB	>95	90:10
11	**4h**	1,2-DFB (–30 °C, 72 h)§	90	95.5:4.5

* Yields determined by ^{19}F-NMR using 4-fluoroanisole as internal standard, † e.r. is the enantiomeric ratio, ‡ DFB = difluorobenzene, § 2.0 equiv. of CsF.

Fig. 2. Reaction development. (**A**) Urea-catalyzed fluorination of *rac*-**1a**. (**B**) Computed Gibbs energy profile (ωB97X-D3/(ma)-def2-TZVPP/COSMO(CH_2Cl_2)//M06-2X/def2-SVP(TZVPPD)/ CPCM(CH_2Cl_2) at 298.15 K in kJ/mol) for urea-catalyzed (**2a**) fluorination of *rac*-**1k**, compared with the uncatalyzed reaction. (**C**) Enantioselective nucleophilic fluorination of *rac*-**1a** catalyzed by (*S*)-**4a–h**; rt, room temperature.

to loss of conjugation, and is more pronounced in the less favorable (i.e., minor) pathway contributing half of $\Delta\Delta G^{\ddagger}$ (fig. S29). Only in the major TS can the substrate dock into the catalyst, with a full complement of noncovalent interactions, while maintaining phenyl conjugation.

Because of the early TS position along the intrinsic reaction coordinate (IRC) pathway, all three H–F interactions remain bonded in the TS (<1.9 Å), but lengthen over the IRC pathway as a result of charge neutralization. This effect is strongest for H-bond 3, which lengthens at 1.8 to 3.5 times the rate of the other H-bonds, resulting in bidentate binding. In forming the major enantiomer, lengthening of H-bond 2 also occurs along the IRC pathway once the C–F bond is fully formed, resulting in one dominant H-bond with the product (fig. S31). The evolution of H-bonds closely mimics the fluorinase enzymatic mechanism, with the bidentate urea (H-bonds 1 and 2) mimicking Ser[158] and the alkylated urea (H-bond 3) mimicking the role of Thr[80] (*28*).

We have introduced hydrogen bonding phase-transfer catalysis (HB PTC) and have applied this approach to asymmetric nucleophilic fluorination with a metal fluoride. The protocol employs a safe fluoride source and a readily accessible urea catalyst, avoiding transition metals and the need to exclude air and moisture. Beyond fluorination, we anticipate that many inexpensive nucleophiles insoluble in organic solvents can be productively applied to enantioselective catalysis with this approach. More generally, this research opens new opportunities in the design of chiral catalysts for enantioselective catalysis.

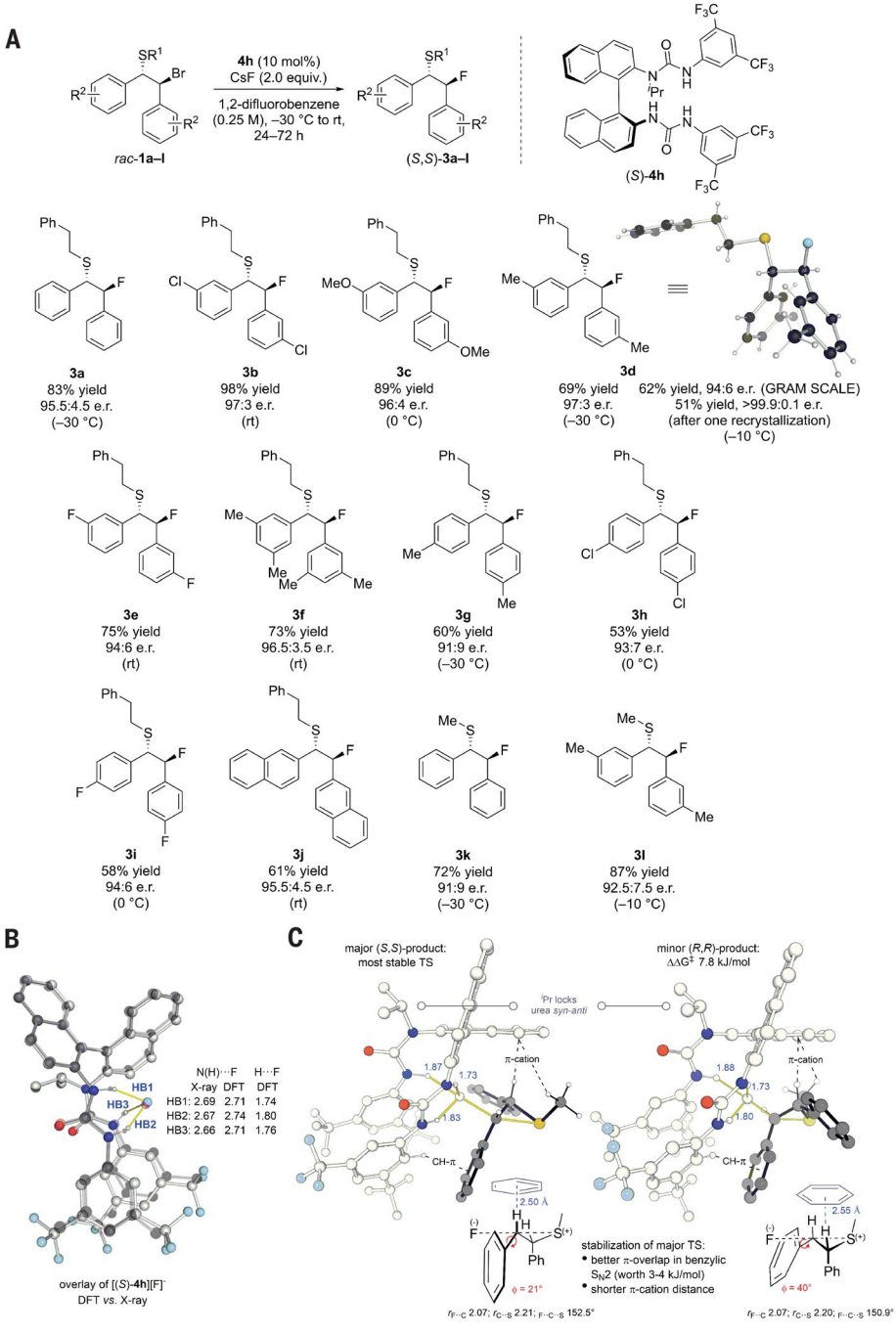

Fig. 3. Scope and mechanistic insights. (**A**) Substrate scope. Absolute configuration was assigned by x-ray diffraction analysis of **3d**. (**B**) Single-crystal structure of TBAF·**4h** overlaid with the DFT-predicted solvated structure of CsF·**4h** (excluding cations). (**C**) Competing major and minor transition states (DFT) leading to either enantiomer.

REFERENCES AND NOTES

1. K. Maruoka, Ed., *Asymmetric Phase Transfer Catalysis* (Wiley-VCH, Weinheim, Germany, 2008).
2. T. Ooi, K. Maruoka, *Angew. Chem. Int. Ed.* **46**, 4222–4266 (2007).
3. V. Rauniyar, A. D. Lackner, G. L. Hamilton, F. D. Toste, *Science* **334**, 1681–1684 (2011).
4. K. Müller, C. Faeh, F. Diederich, *Science* **317**, 1881–1886 (2007).
5. S. Purser, P. R. Moore, S. Swallow, V. Gouverneur, *Chem. Soc. Rev.* **37**, 320–330 (2008).
6. I. Ojima, Ed., *Fluorine in Medicinal Chemistry and Chemical Biology* (Wiley-Blackwell, Chichester, UK, 2009).
7. X. Yang, T. Wu, R. J. Phipps, F. D. Toste, *Chem. Rev.* **115**, 826–870 (2015).
8. J. A. Kalow, A. G. Doyle, *J. Am. Chem. Soc.* **132**, 3268–3269 (2010).
9. M. H. Katcher, A. G. Doyle, *J. Am. Chem. Soc.* **132**, 17402–17404 (2010).
10. J. A. Kalow, A. G. Doyle, *J. Am. Chem. Soc.* **133**, 16001–16012 (2011).
11. M. H. Katcher, A. Sha, A. G. Doyle, *J. Am. Chem. Soc.* **133**, 15902–15905 (2011).
12. S. Suzuki *et al.*, *Chem. Sci.* **5**, 2754–2760 (2014).
13. X. Wang, Q. Lan, S. Shirakawa, K. Maruoka, *Chem. Commun.* **46**, 321–323 (2010).
14. C. L. Liotta, H. P. Harris, *J. Am. Chem. Soc.* **96**, 2250–2252 (1974).
15. V. H. Jadhav, H. J. Jeong, W. Choi, D. W. Kim, *Chem. Eng. J.* **270**, 36–40 (2015).
16. J. A. Birrell, J. N. Desrosiers, E. N. Jacobsen, *J. Am. Chem. Soc.* **133**, 13872–13875 (2011).
17. A. G. Doyle, E. N. Jacobsen, *Chem. Rev.* **107**, 5713–5743 (2007).
18. K. Brak, E. N. Jacobsen, *Angew. Chem. Int. Ed.* **52**, 534–561 (2013).
19. S. M. Banik, A. Levina, A. M. Hyde, E. N. Jacobsen, *Science* **358**, 761–764 (2017).
20. R. J. Phipps, G. L. Hamilton, F. D. Toste, *Nat. Chem.* **4**, 603–614 (2012).
21. S. Lin, E. N. Jacobsen, *Nat. Chem.* **4**, 817–824 (2012).
22. J.-W. Lee *et al.*, *Chem. Soc. Rev.* **45**, 4638–4650 (2016).
23. S. Liang, G. B. Hammond, B. Xu, *Chem. Eur. J.* **23**, 17850–17861 (2017).
24. K. M. Engle *et al.*, *Chem. Sci.* **6**, 5293–5302 (2015).
25. L. Pfeifer *et al.*, *J. Am. Chem. Soc.* **138**, 13314–13325 (2016).
26. D. O'Hagan, C. Schaffrath, S. L. Cobb, J. T. G. Hamilton, C. D. Murphy, *Nature* **416**, 279 (2002).
27. C. Dong *et al.*, *Nature* **427**, 561–565 (2004).
28. X. Zhu, D. A. Robinson, A. R. McEwan, D. O'Hagan, J. H. Naismith, *J. Am. Chem. Soc.* **129**, 14597–14604 (2007).
29. D. O'Hagan, H. Deng, *Chem. Rev.* **115**, 634–649 (2015).
30. C. Thiehoff, M. C. Holland, C. Daniliuc, K. N. Houk, R. Gilmour, *Chem. Sci.* **6**, 3565–3571 (2015).
31. P. R. Schreiner, *Chem. Soc. Rev.* **32**, 289–296 (2003).
32. E. M. Fleming, T. McCabe, S. J. Connon, *Tetrahedron Lett.* **47**, 7037–7042 (2006).
33. Z. Yuan *et al.*, *J. Am. Chem. Soc.* **137**, 2468–2471 (2015).

ACKNOWLEDGMENTS

We thank R. Surgenor for selected experiments. **Funding:** This work was supported by the EU Horizon 2020 Research and Innovation Programme (Marie Skłodowska-Curie agreements 675071 and 316882), EPSRC (EP/R010064, SBM-CDT EP/L015838/1), and Lilly Research Award Program. We acknowledge the University of Oxford Advanced Research Computing facility (http://dx.doi.org/10.5281/zenodo.22558) and the Extreme Science and Engineering Discovery Environment (XSEDE) through allocation TG-CHE180006. **Author contributions:** G.P. and F.I. performed the experimental work in collaboration with A.C.V. Preliminary studies were performed by P.R. and L.P. The computational studies were performed by D.M.H.A. and R.S.P., and K.E.C. acquired the x-ray data. All authors contributed to the design of the experimental and computational work and to data analysis, discussed the results, and commented on the manuscript. R.S.P. and V.G. wrote the manuscript. V.G. conceived and supervised the project. **Competing interests:** All authors declare no conflicting interests. **Data and materials availability:** Crystallographic data are available free of charge from the Cambridge Crystallographic Data Centre under references CCDC 1812187 and CCDC 1812188. Additional optimization and mechanistic data are provided in the supplementary materials.

SUPPLEMENTARY MATERIALS

www.sciencemag.org/content/360/6389/638/suppl/DC1
Materials and Methods
Supplementary Text
Figs. S1 to S33
Tables S1 to S31
References (*34–103*)
Data File S1

19 December 2017; accepted 21 March 2018
10.1126/science.aar7941

FISHERIES

Fish reproductive-energy output increases disproportionately with body size

Diego R. Barneche,[1]*† D. Ross Robertson,[2] Craig R. White,[1] Dustin J. Marshall[1]

Body size determines total reproductive-energy output. Most theories assume reproductive output is a fixed proportion of size, with respect to mass, but formal macroecological tests are lacking. Management based on that assumption risks underestimating the contribution of larger mothers to replenishment, hindering sustainable harvesting. We test this assumption in marine fishes with a phylogenetically controlled meta-analysis of the intraspecific mass scaling of reproductive-energy output. We show that larger mothers reproduce disproportionately more than smaller mothers in not only fecundity but also total reproductive energy. Our results reset much of the theory on how reproduction scales with size and suggest that larger mothers contribute disproportionately to population replenishment. Global change and overharvesting cause fish sizes to decline; our results provide quantitative estimates of how these declines affect fisheries and ecosystem-level productivity.

How does reproductive output scale with body size? Despite the august history of this question (*1*, *2*), theoreticians, fisheries scientists, and field biologists still disagree about the answer (tables S1 and S2). Resolving this uncertainty is essential for understanding the forces driving the evolution of body size in general and for managing fish stocks sustainably. Most life-history models, mechanistic theories of growth, and fisheries models assume that reproductive output scales isometrically with female mass (table S1)—that is, for every increase in female somatic mass, there is a constant proportional increase in reproductive output (Fig. 1A, dashed line). Under such a model, the reproductive output of one 2-kg fish is equal to that of two 1-kg fish.

In contrast to most theoreticians and fisheries models, field biologists have repeatedly suggested that fish fecundity may increase disproportionately with body mass within species (that is, it scales hyperallometrically; table S2) (*3*, *4*). Thus, two 1-kg fish would have less reproductive output than a single 2-kg fish (Fig. 1). This discrepancy between theory and empiricism takes on particular importance because reproductive output drives the replenishment of fisheries (*3*). Energy investment into individual offspring may also change with female size, such that larger mothers produce larger offspring, which survive better (*4*, *5*). Many life-history models make explicit assumptions about the energy devoted to reproductive tissue (table S1). Therefore, understanding how reproductive output scales with female size requires not only fecundity estimates but also estimates of how egg size and egg energy scale with female size. Such an understanding would (i) improve the management of exploited populations and protected areas by better estimating the relationship between standing biomass and egg production (*3*, *4*, *6*) and (ii) allow direct tests of energy-budget models that characterize changes in reproductive allocation over ontogeny (*7*).

Here we perform a meta-analysis of intraspecific mass scaling of total reproductive-energy output (fecundity × egg volume × egg energy), with controls for phylogenetic nonindependence, for 342 species of marine fishes from 15 orders (*8*). We collected data on how egg energy content scales with egg volume within and among a subset of species (n = 1366 clutches from 126 species). We estimated scaling of both egg characteristics and fecundity because these traits could trade off against each other, resulting in no net relationship between maternal size and reproductive output. For example, if larger mothers produce more, but smaller, offspring, net reproductive output might not change with maternal size.

Fish fecundity varied from 11 to 57,600,000 eggs per clutch, spanning about seven orders of magnitude. Fish fecundity scaled hyperallometrically (a power-function relationship with an exponent greater than 1) with body mass (*8*) (Fig. 2A). In this analysis, 140 (79.1%) of the 177 species presented hyperallometric mass scaling of fecundity.

The volume of individual eggs varied from 0.01 to 344.8 mm^3 and increased hypoallometrically with female body mass. A 1.2-fold increase in egg volume would be expected with an increase in body mass from 0.3 to 1.3 kg (Fig. 2B), hence strengthening the effect of female mass on total reproductive output. Considering only the species for which we had both fecundity and egg-volume data (n = 45), we find a hyperallometric relationship between female mass and total reproductive volume (that is, fecundity × egg volume) [average scaling exponent = 1.21; 95% credible interval (CI) 1.07 to 1.37; table S6] (*8*).

Energy content of individual eggs varied from 0.07 to 299.41 J. Egg energy scaled hypoallometrically with egg volume (Fig. 2C). That is, larger eggs have slightly less energy content per unit volume than smaller eggs but still have a greater energy content in absolute terms. The combination of this relationship and the relationship between female mass and egg volume still yields a positive, hypoallometric relationship between female size and per-egg energy content (*8*).

By combining the posterior distributions of model parameters from the three models above (*8*), we were able to estimate how the average total reproductive-energy output changes with body size for marine fish. Total reproductive-energy output per spawning scales hyperallometrically with female body mass (mean scaling exponent = 1.29; 95% CI 1.20 to 1.38). An estimate of mass scaling of fecundity in the commercially important Atlantic cod (*Gadus morhua*) illustrates these scaling effects. If fecundity scaled isometrically with mass, then 15 2-kg female cod would produce the same number of eggs as 1 30-kg female. Instead, we find that a single 30-kg female produces more eggs than ~28 2-kg females (weighing a total of 56 kg). Further, because egg volume and egg energy content also increase with female size, a 30-kg female actually spawns a batch of eggs with a total energy content ~37 times as high as that of a batch of eggs from a single 2-kg female (Fig. 1B); assuming an isometric relationship would underestimate this difference by 147%.

Unsurprisingly, substantial variation in reproductive-energy output exists among species, and a small proportion of species (5.0%) show isometric or hypoallometric scaling (Fig. 3). Nevertheless, hyperallometric reproductive scaling holds for almost all species (95.0%) and is consistent for the subset of nine species for which we had data on all three relationships of interest (table S7) and for three studies in which all the data came from the same populations (table S8). Thus, larger females have disproportionately higher fecundity and produce offspring of greater size, content, and possibly quality. Assuming that larger mothers take part in at least as many reproductive bouts each reproductive season as smaller mothers [which seems likely (*4*)], these relationships may explain why larger fish are so important for the replenishment of marine fish populations (*6*, *9*).

Marine protected areas (MPAs) increase the size of fish by 28% on average (*7*). Because the per-capita reproductive output of fish increases with size, the potential for MPAs to replenish populations has been underestimated. For example, for the widow rockfish, *Sebastes entomelas*, an MPA could enhance population replenishment by 60 and 74% for fecundity and reproductive-energy output, respectively—no such increase would be predicted if reproductive output was assumed to be isometric (*8*).

[1]Centre for Geometric Biology, School of Biological Sciences, Monash University, Clayton, VIC 3800, Australia.
[2]Smithsonian Tropical Research Institute, Balboa, Panama.
*Present address: School of Life and Environmental Sciences, The University of Sydney, Sydney, NSW 2006, Australia.
†Corresponding author. Email: barnechedr@gmail.com

Our results also reveal the insidious costs of global change. Fish sizes are predicted to decrease in some instances as temperatures rise with global warming. For example, a 1.5°C increase in sea surface temperature will decrease fish lengths by ~15% in the Mediterranean (*10*). On the basis of our estimates, such a size decrease would incur a 50% per-capita reduction in fecundity for Atlantic mackerel, *Scomber scombrus* (*8*). Such effects would exacerbate the impacts of predicted decreases in total fish biomass associated with warming—warmer oceans will likely have fewer fish and much lower reproductive output (*11*).

Here we show that hyperallometry of reproductive-energy output is not the exception but rather the rule for marine fishes, a relationship that fisheries models now need to incorporate. For example, balanced harvesting approaches to fishing, which are the subject of intense debate (*12*, *13*), emphasize somatic productivity alone and assume isometric reproduction. Our results confirm the suspicion (*3*) that such assumptions severely underestimate the importance of larger females for population replenishment (*6*, *7*, *9*). Worryingly, many exploited species have declined in size as result of overharvesting, and our findings suggest that such declines will massively reduce reproductive output and recruitment (*14*).

Because our results formally establish a general hyperallometric body-mass scaling of reproductive output in marine fishes, they also have direct implications for fundamental theory. Most theories of growth and life history assume that reproductive output scales isometrically with size, hence underestimating the advantages of growing larger, although some branches of theory do anticipate our findings (table S1). However, even among studies that anticipate hyperallometric scaling, some assume that energy content of reproductive tissues stays constant with body size (table S1); our results contradict this core assumption for fishes, at least.

Future studies will establish whether our results are general across groups of organisms other than marine fishes, thus helping determine the generality of conclusions about the putative evolutionary advantages of large size to mothers. All

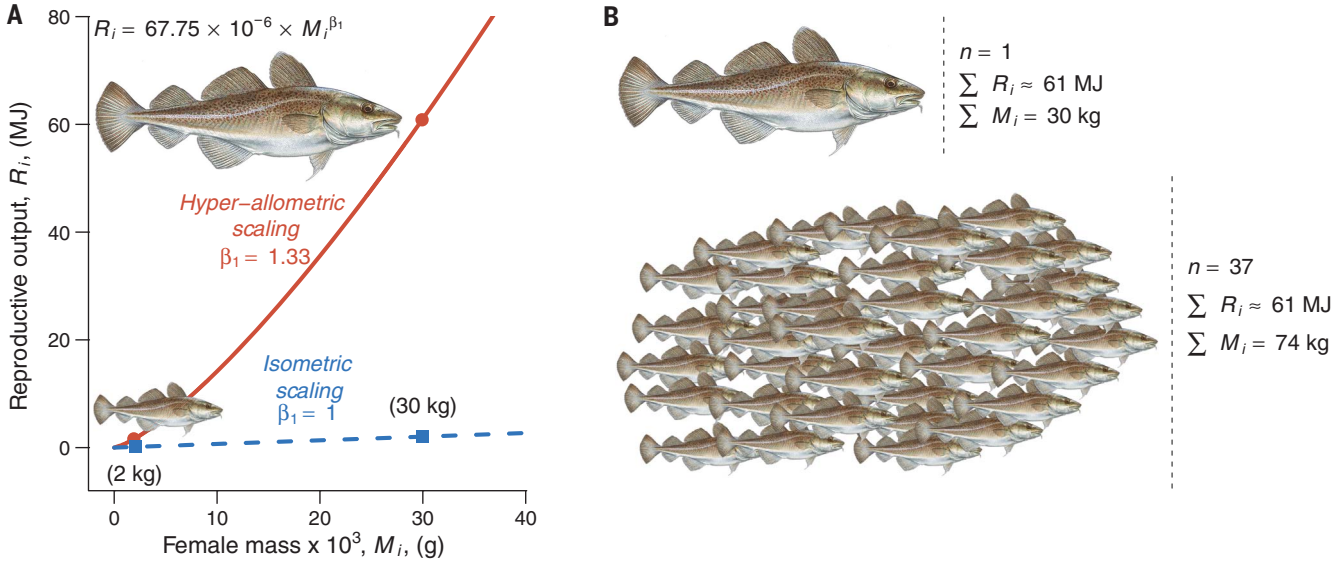

Fig. 1. Hyperallometric scaling of reproductive-energy output. (**A**) Hyperallometric ($\beta_1 = 1.33$, solid red curve; see table S7) and isometric mass scaling ($\beta_1 = 1$, dashed blue curve) relationships for the Atlantic cod, *G. morhua*. Fish sizes span more than one order of magnitude in mass (2 versus 30 kg). (**B**) Total population-level biomass ($\sum M_i$) required to produce the same reproductive output ($\sum R_i$, in megajoules) for two populations of fish with hyperallometric scaling that differ in the mass of the individual fish, where *i* is individuals: The standing-biomass ratio differs by ~2.5-fold (that is, 74 versus 30 kg) from the larger individual to the population with smaller individuals. [Illustration credit: Diane Rome Peebles]

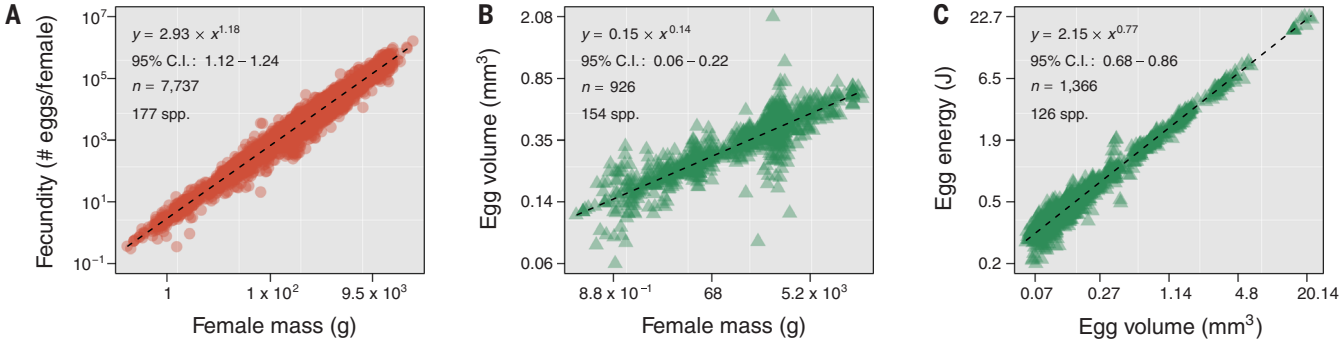

Fig. 2. Scaling relationships of fish reproductive traits. (**A**) Relationship between fecundity and female mass. Red circles represent individual clutches. (**B**) Mass scaling of egg volume. (**C**) Volume scaling of egg energy content. Green triangles represent independent observations [egg volume and egg energy content in (B) and (C), respectively]. The *y* axes were corrected for species-specific deviations on the intercept and scaling exponent, which were obtained using Bayesian phylogenetic hierarchical modeling. Equations in the top-left corners depict average fixed effects; 95% CI is Bayesian credible interval for the scaling exponent; *n* is the total number of observations. Dashed black lines depict average model fits. Species and family names and the data summary and contributions for the three models [shown in (A), (B), and (C)] (*8*) are provided in tables S3 to S5, respectively. Note both axes are logged.

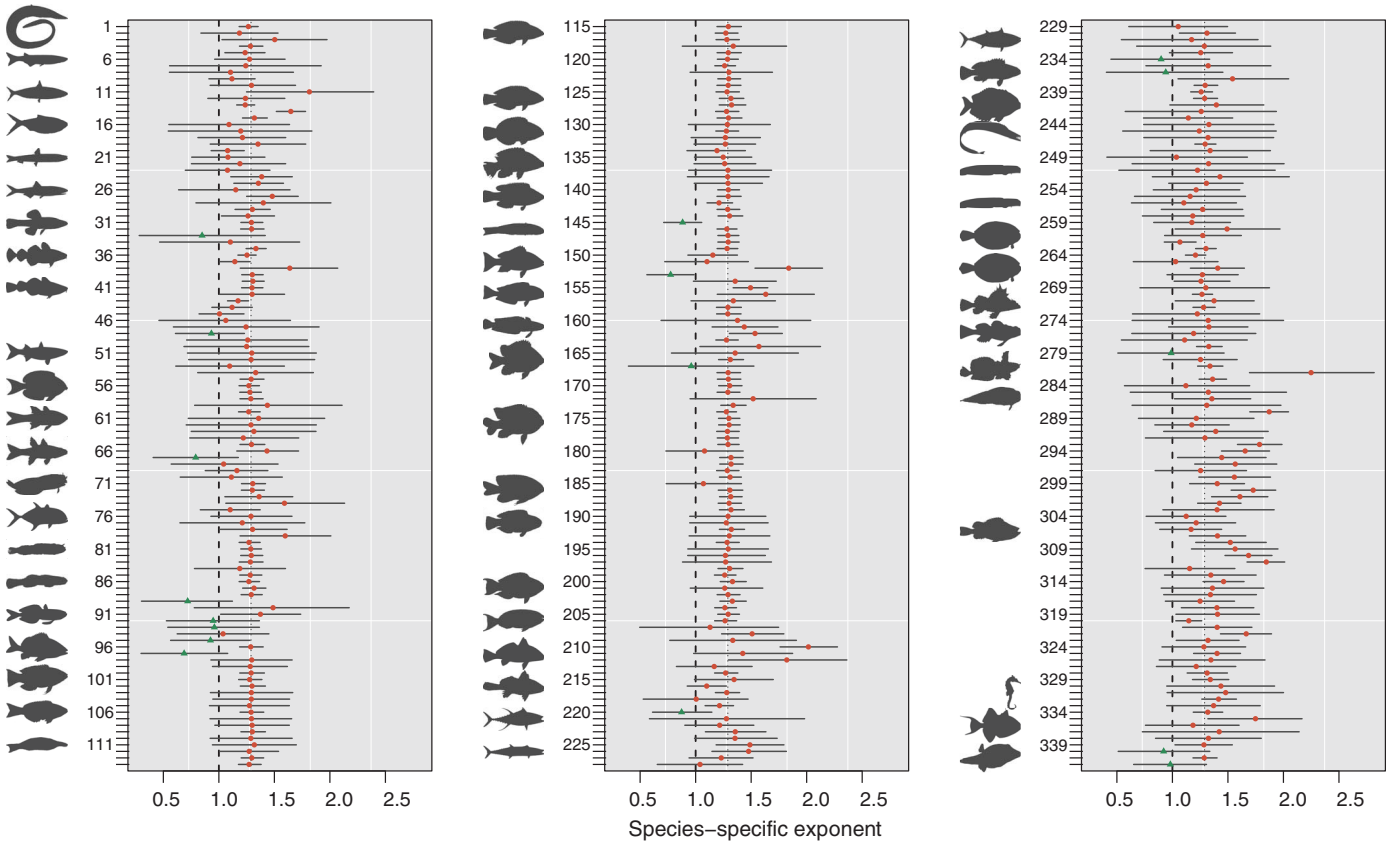

Fig. 3. Species-specific reproductive-energy mass-scaling exponents. Average exponents and 95% CIs (shown by horizontal bars) for 342 species were obtained by combining species-specific (when available) posterior estimates from models in Fig. 2, A to C (*8*). If a species was not present in a given data set, we used the population-level fixed-effect posterior estimates for the model in question. The dashed line represents the reproductive isometry reference point; the dotted line represents the average fixed-effect exponent value. Red circles and green triangles represent species whose scaling exponents are greater than and less than 1, respectively. Fish silhouettes depict the major clades represented in this figure. See table S7 for species and family names and estimates of reproductive energy–output slopes.

else being equal, size declines reduce the capacity of marine fish populations to replenish, particularly if increased egg size increases recruitment success [but see (*15*)]. Our findings prove particularly relevant in light of body-size declines of major fishery species owing to overharvesting and climate change (*10*, *16*, *17*) and suggest that the reproductive consequences of these size declines will be dramatic.

REFERENCES AND NOTES

1. R. E. Earll, in *National Oceanic and Atmospheric Administration Report of the United States Commissioner of Fisheries*, S. F. Baird, Ed. (Government Printing Office, San Diego, 1881), pp. 395–426.
2. R. J. H. Beverton, S. J. Holt, *On the Dynamics of Exploited Fish Populations* (Fishery Investigations Series II, Her Majesty's Stationery Office, London, 1957), vol. 19.
3. C. T. Marshall, C. L. Needle, A. Thorsen, O. S. Kjesbu, N. A. Yaragina, *Can. J. Fish. Aquat. Sci.* **63**, 980–994 (2006).
4. M. A. Hixon, D. W. Johnson, S. M. Sogard, *ICES J. Mar. Sci.* **71**, 2171–2185 (2014).
5. J. N. Lim, A. M. Senior, S. Nakagawa, *Evolution* **68**, 2306–2318 (2014).
6. C. Birkeland, P. K. Dayton, *Trends Ecol. Evol.* **20**, 356–358 (2005).
7. S. E. Lester *et al.*, *Mar. Ecol. Prog. Ser.* **384**, 33–46 (2009).
8. Materials and methods are available as supplementary materials.
9. R. Beldade *et al.*, *Proc. R. Soc. Lond. B Biol. Sci.* **279**, 2116–2121 (2012).
10. I. van Rijn, Y. Buba, J. DeLong, M. Kiflawi, J. Belmaker, *Glob. Chang. Biol.* **23**, 3667–3674 (2017).
11. D. R. Barneche *et al.*, *Ecol. Lett.* **17**, 1067–1076 (2014).
12. K. H. Andersen *et al.*, *ICES J. Mar. Sci.* **73**, 1651–1655 (2016).
13. R. Froese *et al.*, *ICES J. Mar. Sci.* **73**, 1640–1650 (2016).
14. M. Heino *et al.*, *ICES J. Mar. Sci.* **70**, 707–721 (2013).
15. D. J. Marshall, S. S. Heppell, S. B. Munch, R. R. Warner, *Ecology* **91**, 2862–2873 (2010).
16. C. J. Harvey, N. Tolimieri, P. S. Levin, *Ecol. Appl.* **16**, 1502–1515 (2006).
17. M. J. Genner *et al.*, *Glob. Change Biol.* **16**, 517–527 (2010).

ACKNOWLEDGMENTS

We would like to thank M. Elgar for kindly sharing his life-history database with us. We thank L. Chapman, B. Comerford, and the Interlibrary Loan Team at Monash University for helping D.R.B. and D.J.M. compile the data sets. Many people expended a substantial amount of effort by providing eggs to D.R.R. for calorimetric measurements. These included V. Scholey, A. Oliver, E. Schultz, H. Munehara, P. Sikkel, L. McKelvey, D. Hoesey, and J. Elliott. Numerous people assisted with laboratory analyses of egg content, including A. Cedeno, E. Pena, and C. Guerra. People assisting with field collections included U. Schober, A. Cedeno, S. Swearer, L. Gutierrez, E. Paredes, and C. Guerra. We also thank O. J. Luiz for comments on previous versions of the manuscript. **Funding:** This study was funded by the Centre for Geometric Biology, Monash University. **Author contributions:** D.R.B., C.R.W., and D.J.M. conceived the study; D.R.B. and D.J.M. compiled data; D.R.R. collected the egg size and energy-content data; D.J.M. compiled data on egg dry weight; and D.R.B. compiled, standardized, and analyzed the data and wrote the first draft of the manuscript. All authors contributed substantially to revisions. **Competing interests:** None declared. **Data and materials availability:** All data, metadata, and R code can be downloaded and cited as "D. R. Barneche, D. R. Robertson, C. R. White, D. J. Marshall, Data and code from: Fish reproductive-energy output increases disproportionately with body size. Zenodo (available at https://github.com/dbarneche/fishFecundity), doi:10.5281/zenodo.1213118."

SUPPLEMENTARY MATERIALS

www.sciencemag.org/content/360/6389/642/suppl/DC1
Materials and Methods
Fig. S1
Tables S1 to S8
References (*18*–*244*)

29 October 2017; accepted 23 March 2018
10.1126/science.aao6868

SEX DETERMINATION

The histone demethylase KDM6B regulates temperature-dependent sex determination in a turtle species

Chutian Ge,[1]*† Jian Ye,[2]* Ceri Weber,[3] Wei Sun,[1] Haiyan Zhang,[1] Yingjie Zhou,[1] Cheng Cai,[1] Guoying Qian,[1]† Blanche Capel[3]†

Temperature-dependent sex determination is a notable model of phenotypic plasticity. In many reptiles, including the red-eared slider turtle *Trachemys scripta elegans* (*T. scripta*), the individual's sex is determined by the ambient temperature during egg incubation. In this study, we show that the histone H3 lysine 27 (H3K27) demethylase KDM6B exhibits temperature-dependent sexually dimorphic expression in early *T. scripta* embryos before the gonad is distinct. Knockdown of *Kdm6b* at 26°C (a temperature at which all offspring develop into males) triggers male-to-female sex reversal in >80% of surviving embryos. KDM6B directly promotes the transcription of the male sex-determining gene *Dmrt1* by eliminating the trimethylation of H3K27 near its promoter. Additionally, overexpression of *Dmrt1* is sufficient to rescue the sex reversal induced by disruption of *Kdm6b*. This study establishes causality and a direct genetic link between epigenetic mechanisms and temperature-dependent sex determination in a turtle species.

In many reptiles, including the red-eared slider turtle *Trachemys scripta elegans* (*T. scripta*), gonadal sex is determined by the environmental temperature experienced during embryogenesis (*1*–*4*). However, the molecular mechanisms underlying this phenotypic plasticity have remained elusive. Recently, epigenetic marks, such as DNA methylation and histone modifications of known regulators of gonadal differentiation, have been shown to differ between temperatures in species with temperature-dependent sex determination (*5*–*11*). However, all available reports are correlative, and whether the differential epigenetic status is a cause or consequence of sexual development in species for which sex is determined by temperature has not been elucidated. Here we provide molecular and genetic evidence that the epigenetic regulator *Kdm6b* plays a causal role in male sex determination by demethylating H3K27me3 (trimethylated histone H3 lysine 27) at the promoter of *Dmrt1*.

Trimethylation of H3K27 contributes to transcriptional repression in many organisms (*12*). KDM6B (also called JMJD3) is a histone demethylase that specifically demethylates H3K27me3 and is involved in transcriptional activation during normal development (*13*–*16*). We previously sequenced the *T. scripta* gonadal transcriptome during developmental stages 15 to 21 at male-producing (26°C) and female-producing (32°C) temperatures and found that *Kdm6b* was upregulated at 26°C (*17*). A reverse transcription quantitative real-time fluorescence polymerase chain reaction (qRT-PCR) analysis revealed that the 26°C-specific expression of *Kdm6b* began in *T. scripta* gonad-mesonephros complexes as early as stage 13, before the gonad was distinct (Fig. 1A and fig. S1). This sexually dimorphic expression profile was maintained in gonads throughout the temperature-sensitive period (stages 15 to 20) (Fig. 1B). Immunofluorescence and in situ hybridization showed that mRNA and protein of *Kdm6b* were detected in gonadal somatic cells of seminiferous cords but not germ cells (Fig. 1C and fig. S2), implying that KDM6B functions in somatic cells to regulate the sexual development of *T. scripta*. We next examined the responses of *Kdm6b* expression to temperature shifts and sex hormone–induced sex reversal during the temperature-sensitive window. In gonads shifted from either 26° to 32°C or 32° to 26°C at stage 16, significant changes in *Kdm6b* expression were evident by stage 17, preceding gonadal sex differentiation (Fig. 1D). In addition, *Kdm6b* responded quickly to estrogen treatment at 26°C by stage 17 and to treatment at 32°C with the aromatase inhibitor by stage 18 (fig. S3). These expression profiles suggest that *Kdm6b* is an early responder to temperature or hormone treatments, with the potential to act as a master regulator of somatic gene expression at 26°C.

[1]Zhejiang Provincial Top Key Discipline of Biological Engineering, Zhejiang Wanli University, Ningbo, 315100, China. [2]Hangzhou Aquacultural Technique Extending Centre, Hangzhou, 310001, China. [3]Department of Cell Biology, Duke University Medical Center, Durham, NC 27710, USA.
*These authors contributed equally to this work.
†Corresponding author. Email: cge@zwu.edu.cn (C.G.); qiangy@zwu.edu.cn (G.Q.); blanche.capel@duke.edu (B.C.)

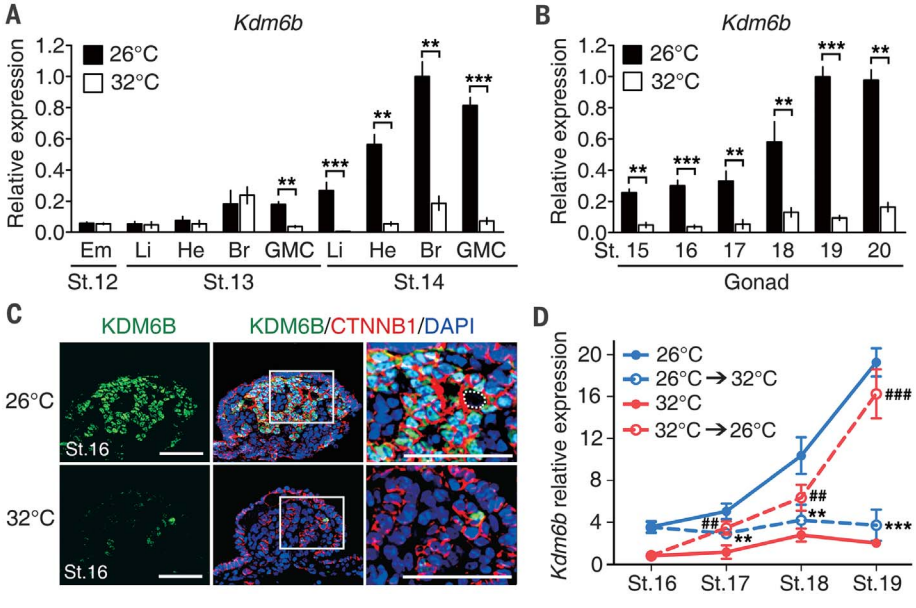

Fig. 1. *Kdm6b* exhibits a temperature-dependent sexually dimorphic expression pattern in early gonads of *T. scripta*. (**A** and **B**) Results from qRT-PCR analysis of *Kdm6b* in (A) whole embryos at stage 12 and different embryonic tissues at stages 13 and 14 and (B) embryonic gonads at stages 15 to 20. Analyses were conducted at both 26° and 32°C. Expression was normalized to *Gapdh*. The relative expression levels, both measured at 26°C, in the brain at stage 14 and the gonad at stage 19 were defined as 1.0 in (A) and (B), respectively. St, stage; Em, embryo; Li, liver; He, heart; Br, Brain; GMC, gonad-mesonephros complex. (**C**) Coimmunofluorescence of KDM6B (green) and CTNNB1 (β-catenin, red) in gonadal sections of stage 16 embryos at 26° and 32°C. The panels at right are higher-magnification views of the boxed areas in the middle panels. The dotted circle outlines a germ cell. DAPI, 4′,6-diamidino-2-phenylindole. Scale bars, 50 μm. (**D**) Time course response of *Kdm6b* expression to temperature shifts in vivo at each stage from 16 to 19. Gonads were dissected for qRT-PCR analysis. Results were normalized to *Gapdh*, and the expression level in stage 16 gonads at female-producing temperature (32°C) was defined as 1. Data in (A), (B), and (D) are means ± SD, $n = 3$ biological replicates. ** $^{\#\#}P < 0.01$; *** $^{\#\#\#}P < 0.001$.

We previously established a method of introducing short hairpin RNAs (shRNAs) in ovo during early stages of *T. scripta* embryonic development that results in 30 to 50% viability (*18*). To investigate the functional role of *Kdm6b* in sex determination of *T. scripta*, we used RNA interference (RNAi) to generate loss-of-function mutants by injecting lentivirus carrying an shRNA specific to *Kdm6b* into 26°C embryos at stage 13 (fig. S4). Approximately 20 to 50% of injected embryos survived to stage 21. Lentiviral treatment of two different shRNAs led to a 73 to 82% reduction of *Kdm6b* transcripts in 26°C gonads from early stage 15 onward (fig. S4), as compared with treatment with nonsilencing scrambled virus. Control 26°C embryos treated with the scrambled virus exhibited typical cylindrically shaped testes, and control 32°C embryos displayed typical long and flat ovaries (Fig. 2A). *Kdm6b*-deficient 26°C gonads became elongated and exhibited varying degrees of female-like morphology (Fig. 2A), characterized by a thickened outer cortex containing a number of primordial germ cells and degenerated medullary cords (fig. S5). Overall, two independent experiments with different shRNAs showed that 39 of 45 (86.7%) and 45 of 56 (80.4%) *Kdm6b*-knockdown embryos displayed a complete male-to-female shift in sexual trajectory at 26°C (Fig. 2B).

To confirm the activation of the female pathway in 26°C embryos with *Kdm6b* knocked down, we analyzed the expression of the testicular Sertoli cell markers *Amh* and *Sox9* and the ovarian regulators *Cyp19a1* and *Foxl2* in gonads after sex determination at stages 19, 21, and 25. qRT-PCR analysis showed that expression of *Amh* and *Sox9* sharply decreased, whereas expression of *Cyp19a1* and *Foxl2* significantly increased in *Kdm6b*-deficient 26°C gonads relative to controls (fig. S6). SOX9 protein was expressed specifically in the nuclei of precursor Sertoli cells in control 26°C gonads, whereas it was sharply reduced or absent in *Kdm6b*-deficient 26°C gonads (Fig. 2C and fig. S7), where ectopic activation of aromatase was detected in the gonadal medulla (fig. S8). Immunofluorescence showed that VASA-positive germ cells, some of which were labeled with the meiotic marker SCP3, exhibited a female-like distribution pattern in the developed outer cortex of *Kdm6b*-knockdown 26°C gonads (Fig. 2D and figs. S9 and S10). These data provide functional evidence that disruption of *Kdm6b* leads to female development at 26°C, indicating that high transcript levels of *Kdm6b* are critical to activate the male pathway in this temperature-dependent sex determination system.

To address the molecular basis of this sex-reversal phenotype induced by knockdown of *Kdm6b*, we aimed to identify the target genes responsible for regulation of temperature-dependent sex determination by *Kdm6b*. Of the six earliest male-biased genes previously reported (*17*), only *Dmrt1* and *Rbm20* displayed >50% reduction of mRNA expression in response to *Kdm6b* knockdown at stage 15 (fig. S11). *Dmrt1* was of particular interest because the early male-specific expression pattern is detected at stage 14 (*18*), just after dimorphic expression of *Kdm6b* is detected at stage 13 (Fig. 1A). In addition, we previously demonstrated that the loss of *Dmrt1* redirected gonads incubating at 26°C toward female fate, whereas the gain of *Dmrt1* redirected gonads incubating at 32°C toward male fate (*18*). *Dmrt1* mRNA levels were reduced to ~13% in *Kdm6b*-deficient 26°C gonads from stage 15 onward (Fig. 3A), and DMRT1 protein was also reduced or absent (Fig. 3B). This observation indicates that *Dmrt1*

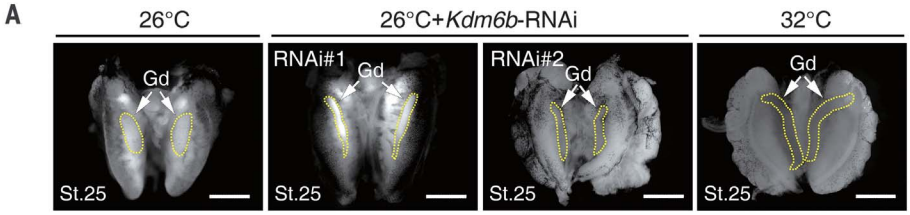

B

Viral treatment	Injected eggs	Viable embryos	GFP+ embryos	Testes	Ovaries	Sex ratio (% ovaries)
Control-RNAi	100	55	31	31	0	**0/31(0%)**
Kdm6b-RNAi#1	318	74	45	6	39	**39/45(86.7%)**
Kdm6b-RNAi#2	386	119	56	11	45	**45/56(80.4%)**

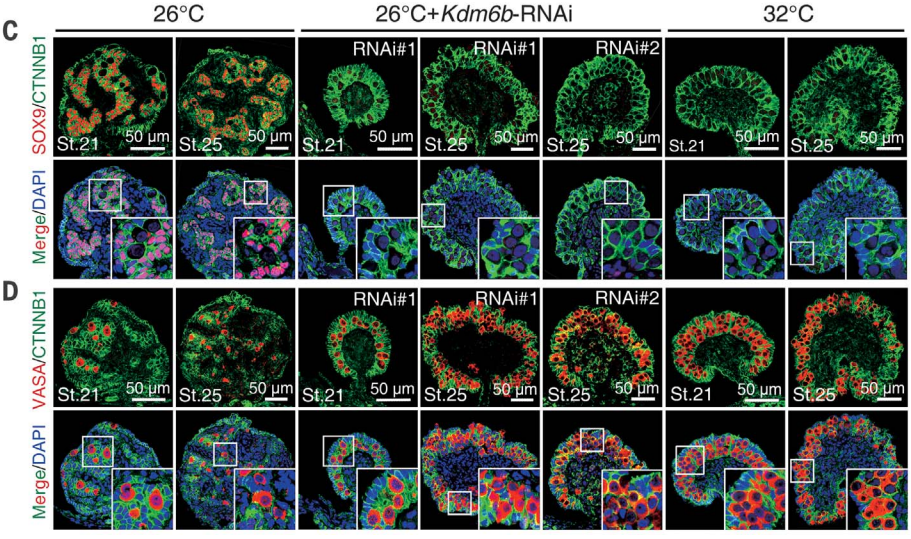

Fig. 2. Knockdown of *Kdm6b* at 26°C leads to male-to-female sex reversal in *T. scripta*. (**A**) Representative images of the gonad-mesonephros complexes from 26°C control, 26°C loss-of-function mutants (*Kdm6b*-RNAi#1 and *Kdm6b*-RNAi#2), and 32°C control embryos at stage 25. Gd, gonad (outlined by yellow dotted lines). Scale bars, 1 mm. (**B**) Sex reversal ratio (percentage of ovaries) of gonads with *Kdm6b*-RNAi#1 and *Kdm6b*-RNAi#2 at 26°C. Gonadal sex was determined by morphological analysis of gonads and the SOX9 stain. GFP, green fluorescent protein. (**C**) Coimmunofluorescence of SOX9 and CTNNB1 (β-catenin) in gonadal sections of 26°C control embryos, three examples of embryos at 26°C after *Kdm6b* knockdown, and 32°C control embryos at stages 21 and 25. (**D**) VASA and CTNNB1 delineate the distribution pattern of germ cells in *Kdm6b*-deficient gonads at stages 21 and 25.

responds rapidly and strongly to *Kdm6b* knockdown at the very beginning of the temperature-sensitive period. Together, these results suggest that *Dmrt1* could be a critical target of KDM6B. As a test of this idea, we knocked down *Kdm6b* and experimentally overexpressed *Dmrt1* in a group of *T. scripta* embryos (fig. S12). Overexpression of *Dmrt1* rescued the male pathway of 16 of 18 (88.9%) *Kdm6b*-deficient 26°C gonads, with both morphology and expression patterns similar to those of control 26°C gonads (Fig. 3C and table S1). SOX9 protein was robustly activated in the primary sex cords of *Kdm6b*-deficient 26°C gonads overexpressing *Dmrt1* (Fig. 3D), and the *Kdm6b* knockdown–induced reduction of *Amh*

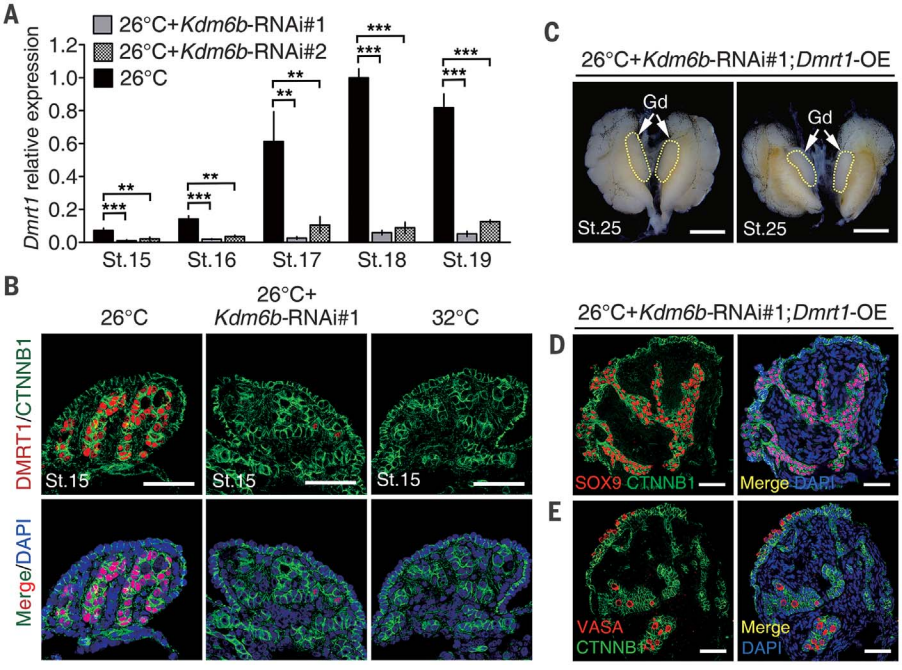

Fig. 3. Knockdown of *Kdm6b* abolishes the expression of *Dmrt1*, but the male pathway can be rescued by overexpression of *Dmrt1*. (**A**) Results of qRT-PCR analysis of *Dmrt1* in gonads from 26°C control embryos, 26°C *Kdm6b*-RNAi#1 embryos, and 26°C *Kdm6b*-RNAi#2 embryos at stages 15 to 19. After normalization to *Gapdh*, the relative expression level in stage 18 gonads at 26°C was defined as 1.0. Data are means ± SD, $n = 3$ biological replicates. $^{**}P < 0.01$; $^{***}P < 0.001$. (**B**) Immunofluorescence of DMRT1 with CTNNB1 in stage 15 gonadal sections from 26°C control, 26°C *Kdm6b*-RNAi#1, and 32°C control embryos. Scale bars, 50 μm. (**C**) Two representative light microscopy images of 26°C *Kdm6b*-RNAi#1 gonads overexpressing *Dmrt1* (*Dmrt1*-OE) at stage 25. Scale bars, 1 mm. (**D** and **E**) Immunofluorescence analysis for SOX9 (D) and VASA (E) with CTNNB1 in stage 25 *Kdm6b*-RNAi#1 gonads at 26°C after forced ectopic expression of *Dmrt1*. Scale bars, 50 μm.

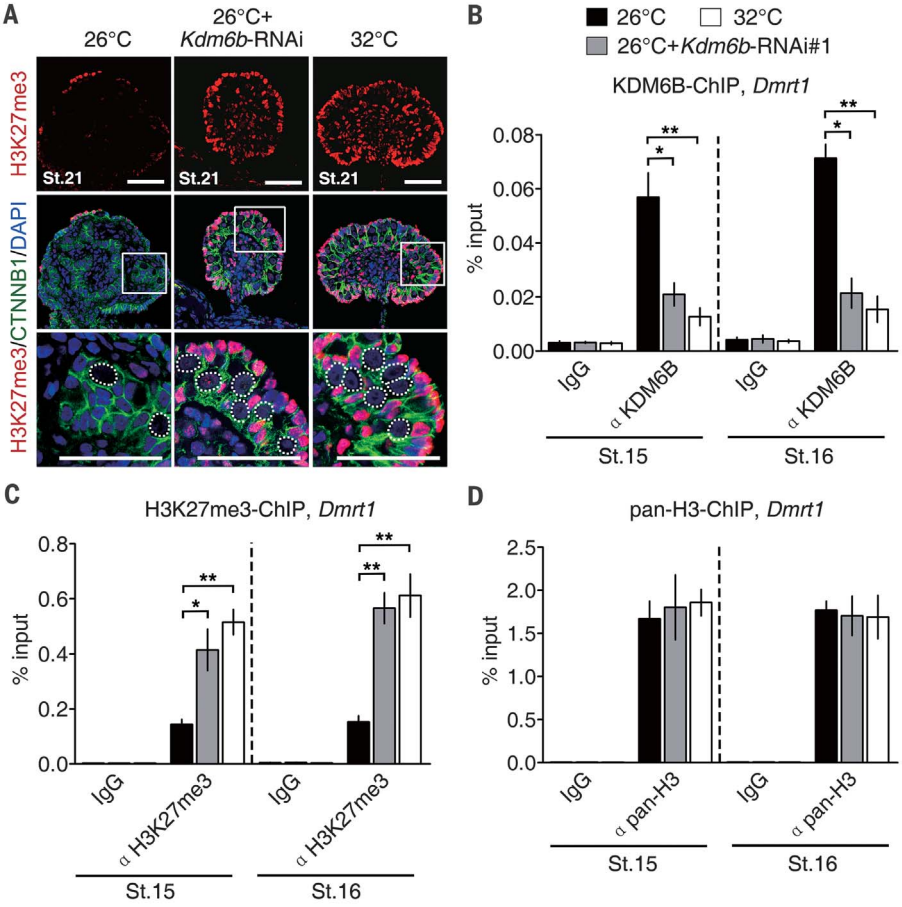

Fig. 4. *Kdm6b* directly regulates H3K27 demethylation at the *Dmrt1* locus. (**A**) Immunofluorescence of H3K27me3 with CTNNB1 in gonadal sections of 26°C control, 26°C *Kdm6b*-RNAi#1, and 32°C control embryos at stage 21. The dotted circles indicate germ cells. Scale bars, 50 μm. (**B**) Quantitative enrichment of KDM6B at the promoter region of *Dmrt1* in 26°C control, 32°C control, and 26°C *Kdm6b*-deficient gonads at stages 15 and 16, as determined by ChIP-qPCR analysis. Signals are shown as a percentage of the input. IgG, immunoglobulin G. (**C** and **D**) Results of ChIP-qPCR assays with antibodies specific for H3K27me3 (C) and pan-H3 (D) at the promoter of *Dmrt1* in 26°C control, 32°C control, and 26°C *Kdm6b*-deficient gonads at stages 15 and 16. Data in (B) to (D) are means ± SD, $n = 3$ biological replicates. $^{*}P < 0.05$; $^{**}P < 0.01$.

and the up-regulation of the female markers *Cyp19a1* and *Foxl2* were all reversed (fig. S13). Male-specific medullar distribution of germ cells was observed in the rescued gonads, although some germ cells remained in the cortex (Fig. 3E). These results indicate that *Dmrt1* functions downstream of *Kdm6b* to initiate the male pathway in *T. scripta*.

We next investigated the molecular mechanism by which *Kdm6b* regulates *Dmrt1* expression. *Kdm6b* was the most highly expressed H3K27 demethylase gene in early male gonads (fig. S14). Immunofluorescence analysis revealed that H3K27me3 was more highly enriched in gonadal cells at 32°C than at 26°C. Knockdown of *Kdm6b* increased the total level of H3K27me3 in gonadal cells at 26°C (Fig. 4A and figs. S15 to S17), consistent with a dominant role for KDM6B in catalyzing demethylation of the repressive mark H3K27me3 and activating target genes.

To investigate a direct link between *Kdm6b* function and *Dmrt1* expression, we next examined KDM6B and H3K27me3 levels at the promoter of *Dmrt1* in *T. scripta* gonads at stages 15 and 16 by performing chromatin immunoprecipitation (ChIP) followed by quantitative PCR (qPCR) analyses. Our results show that KDM6B is strongly recruited to the promoter region of *Dmrt1*, with higher enrichment at 26°C than at 32°C (Fig. 4B). Knockdown of *Kdm6b* reduced KDM6B binding to the promoter of *Dmrt1* in gonadal cells (Fig. 4B). Consistently, the enrichment of H3K27me3 in the promoter region of *Dmrt1* was significantly higher at 32°C than at 26°C (Fig. 4C). Knockdown of *Kdm6b* at 26°C led to a significant increase in H3K27me3 levels within the *Dmrt1* locus, without altering histone H3 occupancy (Fig. 4, C and D). In contrast to the ChIP signal at the *Dmrt1* locus, no occupancy of KDM6B or H3K27me3 was found in other early sex-biased genes *Amh*, *Cyp19a1*, *Fdxr*, *Pcsk6*, *Nov*, and *Vwa2* (fig. S18). These results strongly implicate KDM6B as the upstream regulator of the male pathway via catalysis of H3K27 demethylation near the promoter of *Dmrt1*.

This study in *T. scripta* supports a critical role for the chromatin modifier KDM6B in eliminating a repressive mark from *Dmrt1*, a key gene responsible for male sex determination (*18*). An independent RNA sequencing analysis in gonads of the American alligator (*Alligator mississippiensis*) also identified rapid changes in *Kdm6b* expression after shifting eggs from female-producing temperature to male-producing temperature (*19*). Another recent report showed differential intron retention in two members of the jumonji family, *Kdm6b* and *Jarid2*, in adult female dragon lizards that experienced in ovo sex reversal driven by high temperatures (*20*). Sexually dimorphic intron retention of these two genes also was detected in the embryonic transcriptomes of alligators and turtles with temperature-dependent sex determination, but no sex correlation was observed across these species (*20*). Although these findings suggest a reptile-wide role of *Kdm6b* in regulating temperature-dependent sex determination, they also suggest that both evolutionary recruitment to the pathway and the molecular mechanism of action differ across species. Further interspecies comparative experiments considering the broader jumonji family of proteins will be required to unravel this puzzle. Future experiments will also be necessary to determine whether overexpression of *Kdm6b* is sufficient to drive male development at a female-producing temperature.

Another important question is how expression of *Kdm6b* is linked to temperature in *T. scripta*. The gene is not inherently responsive to temperature, as its male-specific expression was initiated at stage 13 in the gonad-mesonephros complexes but not in other embryonic tissues (Fig. 1A). One possibility is an upstream regulator of *Kdm6b* that acts as a gonad-mesonephros complex–specific temperature sensor. This entity could be a gene whose expression is inherently responsive to temperature or a protein whose activity responds to temperature (*17*). Identification of the link between temperature and differential expression of an epigenetic regulator may finally solve the puzzle of how the incubation temperature of the egg can exert its effect on sex determination, a problem that has defied explanation for the 50 years since its initial discovery in reptiles.

REFERENCES AND NOTES

1. M. Charnier, *C. R. Seances Soc. Biol. Fil.* **160**, 620–622 (1966).
2. J. J. Bull, R. C. Vogt, *Science* **206**, 1186–1188 (1979).
3. M. W. Ferguson, T. Joanen, *Nature* **296**, 850–853 (1982).
4. C. Pieau, M. Dorizzi, N. Richard-Mercier, *Cell. Mol. Life Sci.* **55**, 887–900 (1999).
5. Y. Matsumoto, A. Buemio, R. Chu, M. Vafaee, D. Crews, *PLOS ONE* **8**, e63599 (2013).
6. L. Navarro-Martín *et al.*, *PLOS Genet.* **7**, e1002447 (2011).
7. B. B. Parrott, S. Kohno, J. A. Cloy-McCoy, L. J. Guillette Jr., *Biol. Reprod.* **90**, 2 (2014).
8. F. Piferrer, *Dev. Dyn.* **242**, 360–370 (2013).
9. Y. Matsumoto, B. Hannigan, D. Crews, *PLOS ONE* **11**, e0167362 (2016).
10. S. Radhakrishnan, R. Literman, B. Mizoguchi, N. Valenzuela, *Epigenetics Chromatin* **10**, 28 (2017).
11. C. Shao *et al.*, *Genome Res.* **24**, 604–615 (2014).
12. E. T. Wiles, E. U. Selker, *Curr. Opin. Genet. Dev.* **43**, 31–37 (2017).
13. K. Agger *et al.*, *Nature* **449**, 731–734 (2007).
14. F. Lan *et al.*, *Nature* **449**, 689–694 (2007).
15. S. Hong *et al.*, *Proc. Natl. Acad. Sci. U.S.A.* **104**, 18439–18444 (2007).
16. J. S. Burchfield, Q. Li, H. Y. Wang, R. F. Wang, *Int. J. Biochem. Cell Biol.* **67**, 148–157 (2015).
17. M. Czerwinski, A. Natarajan, L. Barske, L. L. Looger, B. Capel, *Dev. Biol.* **420**, 166–177 (2016).
18. C. Ge *et al.*, *Development* **144**, 2222–2233 (2017).
19. R. Yatsu *et al.*, *BMC Genomics* **17**, 77 (2016).
20. I. W. Deveson *et al.*, *Sci. Adv.* **3**, e1700731 (2017).

ACKNOWLEDGMENTS

We thank B. L. M. Hogan for advice on the manuscript and members of the Capel laboratory for support. **Funding:** This work was supported by a grant to B.C. from the NSF (IOS-1256675), grants to C.G. from the National Natural Science Foundation of China (31101884) and the Natural Science Foundation of Zhejiang Province (LY14C190008), and grants to G.Q. from the Major Agricultural Project of Ningbo (2017C110012) and the Zhejiang Provincial Project of Selective Breeding of Aquatic New Varieties (2016C02055-4). **Author contributions:** C.G., G.Q., and B.C. designed the study; C.G., J.Y., C.W., W.S., H.Z., Y.Z., and C.C. performed experiments and analyzed data; and C.G., G.Q., and B.C. wrote the manuscript. **Competing interests:** The authors declare no competing interests. **Data and materials availability:** All data needed to evaluate the conclusions in the paper are present in the main text or the supplementary materials. The nucleotide sequence data used in this study have been submitted to the National Center for Biotechnology Information under accession numbers SRP079664, MG760437, and KY945220.

SUPPLEMENTARY MATERIALS

www.sciencemag.org/content/360/6389/645/suppl/DC1
Materials and Methods
Figs. S1 to S18
Tables S1 and S2
References (*21*–*23*)

31 August 2017; accepted 13 March 2018
10.1126/science.aap8328

SNOWBALL EARTH

Rapid sea level rise in the aftermath of a Neoproterozoic snowball Earth

P. M. Myrow,[1]* M. P. Lamb,[2] R. C. Ewing[3]

Earth's most severe climate changes occurred during global-scale "snowball Earth" glaciations, which profoundly altered the planet's atmosphere, oceans, and biosphere. Extreme rates of glacioeustatic sea level rise are predicted by the snowball Earth hypothesis, but supporting geologic evidence has been lacking. We use paleohydraulic analysis of wave ripples and tidal laminae in the Elatina Formation, Australia—deposited after the Marinoan glaciation ~635 million years ago—to show that water depths of 9 to 16 meters remained nearly constant for ~100 years throughout 27 meters of sediment accumulation. This accumulation rate was too great to have been accommodated by subsidence and instead indicates an extraordinarily rapid rate of sea level rise (0.2 to 0.27 meters per year). Our results substantiate a fundamental prediction of snowball Earth models of rapid deglaciation during the early transition to a supergreenhouse climate.

Close monitoring of the Antarctic ice sheet indicates rapid and considerable collapse (*1*) due in part to anthropogenically induced climate change. Present rates of ice sheet collapse are constrained by observations, but little is known about rates during ancient deglaciations. The Late Neoproterozoic snowball Earth events represent an extreme climate change scenario, in which the collapse of global ice sheets during deglaciation is thought to have caused extremely large and rapid sea level rise (*2*–*4*). Complete deglaciation occurring over only 2000 to 10,000 years and rapid sea level rise are inferred from estimates of ice volume and greenhouse conditions (*5*), with CO_2 concentrations of ~400 to 660 times present-day atmospheric levels and surface temperatures of ~50°C (*2*). However, paleomagnetic reversals within cap carbonate beds, which mantle glaciogenic deposits and are part of the glacioeustatic sea level rise succession (Fig. 1A), indicate slow deposition over $>10^4$ to 10^6 years (*6*, *7*), presenting a major challenge to the snowball Earth hypothesis. Such slow rise rates may be tied to late-stage thermal expansion of the oceans. However, early-stage rapid sea level rise from ice melt (*4*) is predicted, and geologic evidence for this has been lacking. Here we show that a siltstone unit that rests below a cap carbonate records the extremely rapid initial sea level rise predicted by the snowball Earth hypothesis.

The Elatina Formation in South Australia contains a distinctive record of the Marinoan snowball Earth (~635 million years ago) that includes evidence for ice advance and subsequent deglaciation, including the early postglacial interval, given that it is directly overlain by the Nuccaleena cap carbonate (*8*) (Fig. 1A). Paleomagnetic data constrain deposition of the formation to <15°N (*9*), supporting a low-latitude glaciation consistent with a snowball Earth. Within the deglaciation succession, a ~30-m-thick tidal-rhythmite siltstone unit records a complete daily record of sedimentation driven by tidal currents and wave action (*10*). We use a suite of sedimentary structures in these deposits to test a fundamental prediction of the snowball Earth model—namely, rapid glacioeustatic sea level rise during deglaciation.

Siltstone of the upper Elatina Formation crops out across ~4500 km^2 of the Adelaide Rift Complex and Stuart Shelf of South Australia. It consists of centimeter-scale packages of ~12 pairs of millimeter-thick silt and muddy silt laminae [average grain sizes are 61 and 37 μm, respectively (*11*)] that vertically thicken and thin. These lamina pairs were initially considered to be varves formed in a periglacial lake (*12*) and later to be tidal delta deposits formed by spring-neap cycles (*13*). The rhythmites are preserved within bedforms (ripples) that aggrade vertically with few erosional surfaces, and individual bedforms can be continuously tracked vertically across meters of strata (*8*). Within this facies, several hierarchies of bedforms are preserved.

The first-order bedforms (i.e., the largest class) are straight-crested, relatively symmetrical ripples (Fig. 1, B and C) with average heights of h = 1.8 ± 0.6 cm and average crest-to-crest spacings of λ = 33 ± 11 cm (±1σ) (table S1). Locally, cross-lamination is convex-up (Fig. 2A), typical of combined-flow ripples (*14*), and shows gradual vertical shifts, including reversals, in migration direction (Fig. 2C). Several new observations provide independent evidence that the large ripples were deposited under reversing tidal currents. First, the large ripple strata locally contain reactivation surfaces, which indicate a current reversal that eroded the bedform flank. Second, ripple–cross-laminated beds contain isolated, fully preserved ripples, less than 5 mm in height, that rest just below, or on, the larger ripple crests (Fig. 2B). These small ripples are oriented

[1]Department of Geology, Colorado College, Colorado Springs, CO 80903, USA. [2]Division of Geological and Planetary Sciences, California Institute of Technology, Pasadena, CA 91124, USA. [3]Department of Geology and Geophysics, Texas A&M University, College Station, TX 77843, USA.
*Corresponding author. Email: pmyrow@coloradocollege.edu

Fig. 1. Elatina Formation. (**A**) Generalized stratigraphic succession of Marinoan glacial and postglacial deposits [modified from (*2*)] and study location (star) with paleolatitude lines (*26*) in South Australia. TST, transgressive systems tract; MF, maximum flooding surface; HST, highstand systems tract. Black triangles indicate large clasts in diamictite. (**B**) Planview (bedding plane) outcrop showing larger first-order ripples oriented perpendicular to smaller second-order ripples with locally developed bifurcations. (**C**) Vertically climbing secondary ripples in cross section. Millimeter-scale tidal laminae are present. Laminae bundle boundaries are highlighted by centimeter-scale–spaced darker laminae. The pencil is 14 cm long.

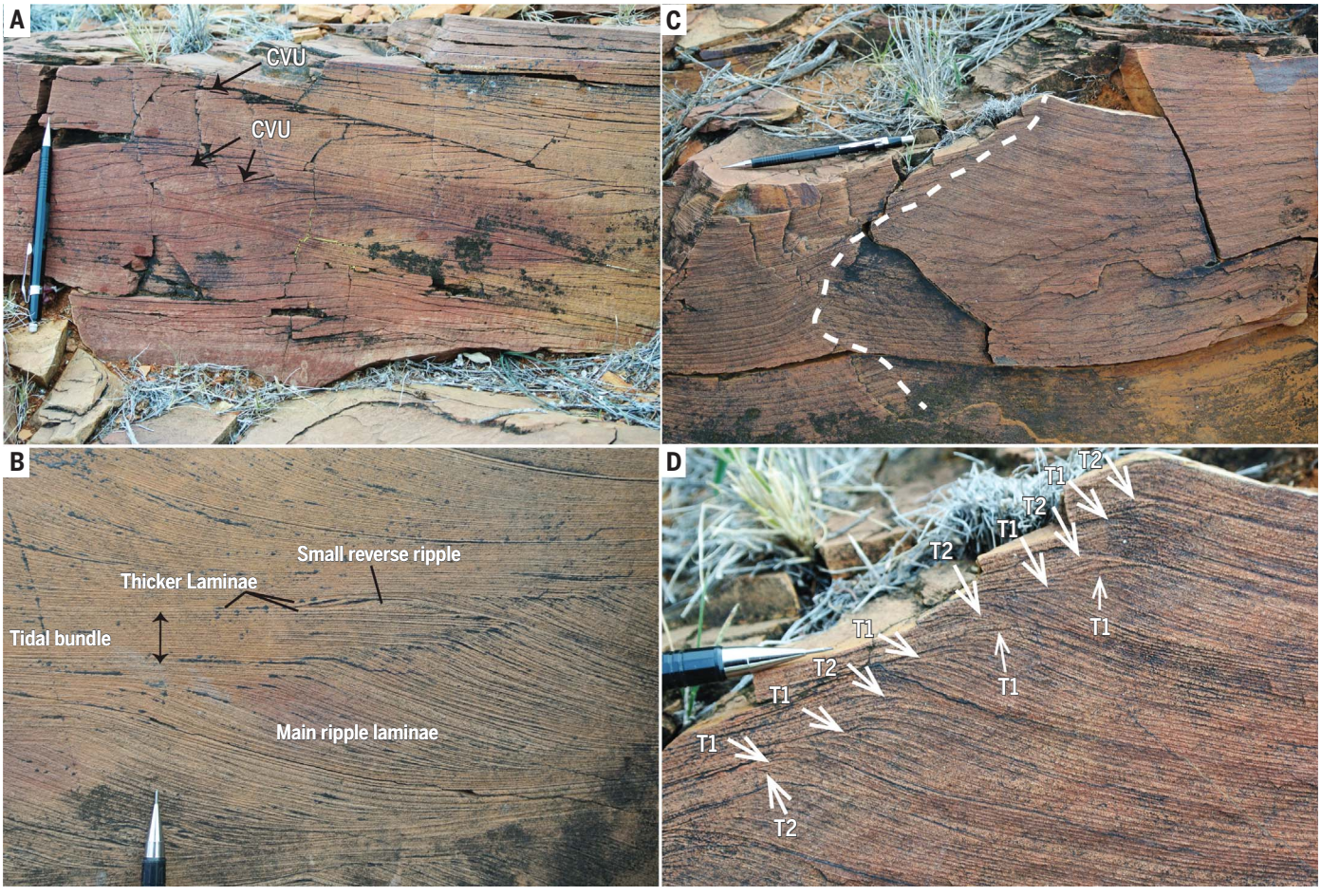

Fig. 2. Sedimentary structures of first-order ripples. (**A**) Stoss-erosional to nearly stoss-preservational first-order ripple cross-stratification with convex-up (CVU) lamination typical of combined-flow ripples. (**B**) Migrating ripple lamination with bundled tidal laminae. A small ripple with cross-stratification that dips opposite to the main ripple laminae is indicated. (**C**) Climbing first-order ripple cross-stratification, with the lower part recording bedform climb to the left and the upper part reversing to the right (the dashed line marks the position of the crestline over time), similar to cap carbonate strata (*27*). (**D**) Close-up of the upper part of (C). Surfaces that are moderately inclined to the left (T1) truncate the main cross-lamination of the ripple. Truncation surfaces that are flat to slightly inclined to the right (T2) become conformable downdip with laminae defining the cross-lamination of the ripple. These surfaces truncate laminae on the stoss side of the ripple that are dipping to the left. The two truncation-surface types generally alternate along the trace of the ripple crest. The pencil is 14 cm long.

opposite to the dominant ripple cross-lamination and are bounded by the thickest laminae of the tidal bundles, indicating that the strongest reversing currents (i.e., spring tides) produced traction transport against the dominant tide. Last, in cases, the first-order ripple cross-lamination contains two alternating types of erosional surfaces, half of which dip antithetical to the main cross-lamination and truncate the ripple foresets, whereas the other half dip in the dip direction of the large ripples, but at a lower angle (Fig. 2D). The two truncation-surface types alternate upward along the trace of the preserved climbing ripple crests, and the surfaces are contiguous with millimeter-thick white laminae that define rhythmite bundle boundaries, which again links the erosion surfaces to spring tides and cyclic lamination to reversing tidal currents.

The troughs of the first-order ripples preserve vertically aggraded second-order bedforms (i.e., smaller bedforms superimposed on the larger ones) that align perpendicular to the first-order ripple crests (Fig. 1B). The second-order bedforms consist of symmetrical to moderately asymmetrical two-dimensional ripples with h = 0.4 ± 0.2 cm and λ = 6.0 ± 2.1 cm (table S1). Second-order bedforms show locally developed bifurcations typical of straight-crested wave ripples. Their aspect ratio is h/λ = 0.06 ± 0.02, and their ripple symmetry index, which is the ratio of the width of the stoss side to that of the lee side, is 1.9 ± 1.6 (table S2), making them consistent with postvortex anorbital wave ripples (*15*). Aspect ratios of these bedforms are smaller than those of wave ripples produced experimentally in sand but are consistent with ripples formed in silty sand beds in the presence of substantial suspension of mud (*16*).

The sedimentological characteristics indicate deposition during both wave and current activity in an ice-free body of water, consistent with the latest to post–snowball Earth climate. Whereas there is some spatial and stratigraphic variation, the most complete succession shows no systematic vertical changes in the heights and spacings of first- and second-order ripples throughout at least 16 m of the rhythmite unit (*8*). The small ripples are oriented north-northeast–south-southwest (fig. S1 and table S3), orthogonal to the first-order tidally influenced ripples, and thus the wave action that generated the second-order ripples was normal to the tidal currents, consistent with expected equatorial easterlies and northwest-oriented wind fields inferred from eolian dunes (*17*).

Wave ripples in sand and silt, whether orbital or anorbital, show a consistent relation between their aspect ratio, h/λ, and the formative wave orbital diameter, d_o (Fig. 3A), which can be used to reconstruct the paleo–water depth. For the Elatina wave ripples, we estimate d_o = 0.95 ± 0.15 m (*11*). Wave generation constraints (*11*) dictate that for a given average wind speed and

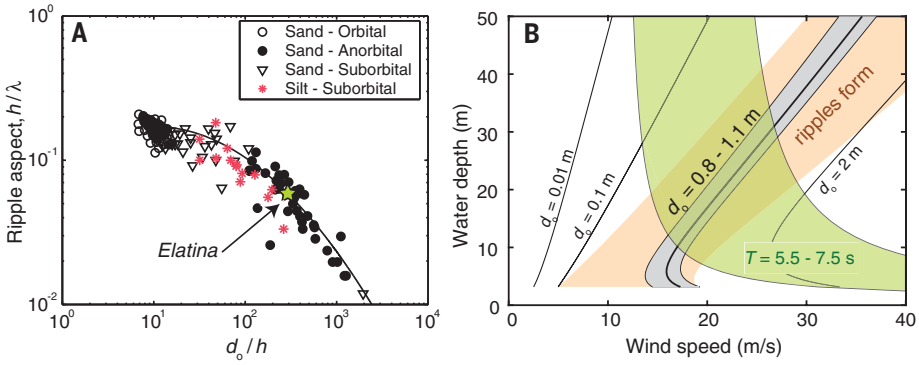

Fig. 3. Paleohydraulic reconstructions. (**A**) Wave ripple geometry (*h*, ripple height; λ, ripple crest-to-crest spacing) as a function of normalized orbital diameter, d_o. Sand-bed field data (*28*) include orbital, suborbital, and anorbital ripples. Silt-bed experiments (*16*) produced ripples with geometries and grain sizes similar to those of Elatina ripples. The solid line represents eq. S1 (*11*). (**B**) Combinations of average wind speed and water depth capable of producing d_o = 0.95 ± 0.15 m (gray shading) according to a wave generation model (*11*). The orange-shaded region marks where wave ripples are stable (*29*) for 50-μm silt (*11*), and the green-shaded region corresponds to wave periods (*T*) of 5.5 to 7.5 s, conditions in which ripples similar to those of the Elatina formed in experiments (*16*). The reconstruction is based on a 75-km fetch inferred from paleogeographic reconstructions (*10*); varying fetch within a factor of 2 (38 to 150 km) has a negligible effect on the water depth.

d_o = 0.95 ± 0.15 m, water depths varied by less than ~7 m (Fig. 3B). A near-uniform average daily wind speed is expected owing to trade winds, possibly modulated by diurnal katabatic winds (*8*). A larger change in water depth during deposition requires an unlikely systematic covariation between depth and wind speed (Fig. 3B), and therefore relative sea level must have risen nearly commensurately with sediment accumulation.

Constraints on absolute water depth require an estimate of the wave period or average wind speed during ripple formation. Oscillatory duct experiments (*16*) with d_o = 0.8 to 1.0 m in silty sand produced ripples of equivalent dimensions to those in the Elatina Formation, with wave periods of *T* = 5.5 to 7.5 s. The wave generation model (*11*) indicates that this combination of wave parameters (*T* = 5.5 to 7.5 s and d_o = 0.8 to 1.1 m) limits absolute water depths to 9 to 30 m (Fig. 3B and fig. S2). The deeper end-member (30 m) requires the unlikely case of reoccurring whole gale–force winds (25 m/s), whereas the lower bound (9 to 16 m) indicates reasonable average wind speeds of ~16 m/s, equivalent to speeds previously proposed (*8*). Burial of the Elatina Formation would have been to ~5 to 6 km depth (*18*) with ~40% compaction (*19*). Thus, the original (decompacted) deposit thickness of ~27 m (*11*) exceeds our estimated maximum change in water depth (~7 m), in addition to the likely absolute water depth (9 to 16 m; Fig. 3B); these two independent constraints establish that the rate of relative sea level rise must have closely matched the accumulation rate.

The preservation of tidal laminae in the Elatina Formation provides a means to explain how two scales of superimposed bedforms accreted over 27 m with little change in ripple dimensions and inferred water depth. Williams (*13*) identified 1580 neap-spring tidal cycles in a 9.39-m-thick core of the Elatina Formation that was devoid of truncation surfaces, which he used to constrain depositional time, but he did not consider implications for sea level rise. Alternating thick and thin packages of laminae throughout the core, with each package containing ~12 pairs of silt and mud laminae, represent the neap-spring cycles within half a lunar month. Spectral analysis of these packages yielded the number of lunar months per year (13.1 ± 0.1) and a duration of 60.3 ± 0.5 years for the deposition of the 9.39-m-thick core (*13*). We use the resulting accumulation rate to estimate that the original thickness of ~27 m determined for our rippled section was deposited over ~100 years with an accumulation rate of ~27 cm/year (*11*), or 20 cm/year if water depth shallowed during deposition by the maximum amount allowed (7 m). This accumulation rate is higher than any previously estimated for a large marine basin over century time scales or longer (*20*) and is consistent with high suspended-sediment concentrations during rapid deglaciation of a snowball Earth episode. Given that subsidence over ~100 years would be negligible (*21*), the inferred ~27 m of accumulation could only be accomplished through a rapid rise in sea level, specifically at 20 to 27 cm/year.

The rhythmite unit represents a fraction of the total deglaciation deposit, and duration estimates for complete deglaciation, based on ice volumes and greenhouse conditions, are typically 2000 to 10,000 years (6000 years on average) (*5*). The total sea level rise due to melting of Marinoan glaciers has been estimated at ~1000 to 1500 m (*2*, *22*), which likely varied spatially owing to gravitational effects (*23*). A glacioeustatic rise of 1.5 km over 2000 to 10,000 years corresponds to a long-term rise rate of 15 to 75 cm/year, or 25 cm/year for a 6000-year deglaciation, which is consistent with our independent short-term geologic constraint of 20 to 27 cm/year. This rate of sea level rise is 100 times as high as present-day rates (*24*) and five times as high as the highest rates during Pleistocene deglaciations (*25*). Sea level rise of this magnitude is a strong confirmation of a major tenet of the snowball Earth hypothesis—namely, rapid deglaciation during the early transition from icehouse to hypergreenhouse conditions.

REFERENCES AND NOTES

1. H. D. Pritchard *et al.*, *Nature* **484**, 502–505 (2012).
2. P. F. Hoffman *et al.*, *Sci. Adv.* **3**, e1600983 (2017).
3. J. L. Kirschvink, in *The Proterozoic Biosphere*, J. W. Schopf and C. Klein, Eds. (Cambridge Univ. Press, 1992), pp. 51–52.
4. J. Yang, M. F. Jansen, F. A. Macdonald, D. S. Abbot, *Geology* **45**, 615–618 (2017).
5. P. F. Hoffman, A. J. Kaufman, G. P. Halverson, D. P. Schrag, *Science* **281**, 1342–1346 (1998).
6. R. I. F. Trindade, E. Font, M. S. D'Agrella-Filho, A. C. R. Nogueira, C. Riccomini, *Terra Nova* **15**, 441–446 (2003).
7. B. Kilner, C. Mac Niocaill, M. Brasier, *Geology* **33**, 413–416 (2005).
8. C. V. Rose *et al.*, *Geosci. Can.* **40**, 256–293 (2013).
9. D. A. D. Evans, T. D. Raub, *Geol. Soc. London Memoirs* **36**, 93–112 (2011).
10. W. V. Preiss, in *The Adelaide Geosyncline: Late Proterozoic Stratigraphy, Sedimentation, Palaeontology and Tectonics*, W. V. Preiss, Ed. (Bulletin 53, Geological Survey of South Australia, 1987), pp. 29–34.
11. Materials and methods are available as supplementary materials.
12. G. E. Williams, *Nature* **291**, 624–628 (1981).
13. G. E. Williams, *J. Geol. Soc. London* **146**, 97–111 (1989).
14. P. M. Myrow, W. Fischer, J. W. Goodge, *J. Sediment. Res.* **72**, 641–656 (2002).
15. H. E. Clifton, J. R. Dingler, in *Wave-Dominated Coastal Environments*, B. Greenwood, R. A. Davis Jr., Eds. (Elsevier, 1984), pp. 165–198.
16. M. P. Lamb, J. D. Parsons, *J. Sediment. Res.* **75**, 386–397 (2005).
17. G. E. Williams, *Aust. J. Earth Sci.* **45**, 733–741 (1998).
18. P. W. Schmidt, G. E. Williams, *Earth Planet. Sci. Lett.* **134**, 107–124 (1995).
19. J. P. Grotzinger *et al.*, *Science* **350**, aac7575 (2015).
20. C. A. Partin, P. M. Sadler, *Geology* **44**, 1019–1022 (2016).
21. E. Carminati, G. Martinelli, *Eng. Geol.* **66**, 241–255 (2002).
22. P. F. Hoffman, *Sedimentology* **58**, 57–119 (2011).
23. J. R. Creveling, J. X. Mitrovica, *Earth Planet. Sci. Lett.* **399**, 74–85 (2014).
24. T. M. Cronin, *Quat. Sci. Rev.* **56**, 11–30 (2012).
25. T. Hanebuth, K. Stattegger, P. M. Grootes, *Science* **288**, 1033–1035 (2000).
26. R. C. Ewing *et al.*, *Earth Planet. Sci. Lett.* **406**, 110–122 (2014).
27. P. A. Allen, P. F. Hoffman, *Nature* **433**, 123–127 (2005).
28. P. L. Wiberg, C. K. Harris, *J. Geophys. Res. Oceans* **99**, 775–789 (1994).
29. Z. J. You, B. Yin, *Sedimentology* **53**, 1181–1190 (2006).

ACKNOWLEDGMENTS

We thank the reviewers of this manuscript for their helpful and insightful reviews. We thank C. Rose, W. Fischer, and J. C. Creveling for discussions concerning the results of our work. **Funding:** This study was supported by the U.S. National Science Foundation through award EAR-1225879 to P.M.M. and award EAR-PF-0846233 to R.C.E. **Author contributions:** All authors contributed equally to the study concept, data collection and analysis, and manuscript writing. **Competing interests:** The authors have no competing interests. **Data and materials availability:** All data are available in the manuscript or the supplementary materials.

SUPPLEMENTARY MATERIALS

www.sciencemag.org/content/360/6389/649/suppl/DC1
Materials and Methods
Figs. S1 and S2
Tables S1 to S3
References (*30*–*34*)

3 September 2017; accepted 5 April 2018
Published online 19 April 2018
10.1126/science.aap8612

COGNITIVE PSYCHOLOGY

Efficient coding explains the universal law of generalization in human perception

Chris R. Sims*

Perceptual generalization and discrimination are fundamental cognitive abilities. For example, if a bird eats a poisonous butterfly, it will learn to avoid preying on that species again by generalizing its past experience to new perceptual stimuli. In cognitive science, the "universal law of generalization" seeks to explain this ability and states that generalization between stimuli will follow an exponential function of their distance in "psychological space." Here, I challenge existing theoretical explanations for the universal law and offer an alternative account based on the principle of efficient coding. I show that the universal law emerges inevitably from any information processing system (whether biological or artificial) that minimizes the cost of perceptual error subject to constraints on the ability to process or transmit information.

If a bird eats a poisonous or unpalatable species of butterfly, it will quickly learn to avoid preying on that species again in the future, by avoiding butterflies that look visually similar (*1*). This requires perceptual generalization, as no two butterflies look exactly alike. If generalization is too narrow—it learns to avoid one specific butterfly, but not others of the same species—the bird will continue to mistakenly consume toxic butterflies. However, if generalization is too broad—it avoids all butterflies—it will unnecessarily exclude edible food sources and consequently limit its fitness. A closely related ability is perceptual discrimination: If an edible species of butterfly closely resembles a different, toxic species (Batesian mimicry), the failure to perceptually discriminate between the two will also lead to negative consequences.

These examples demonstrate that adaptive behavior requires perceptual generalization and discrimination abilities that are finely calibrated to the costs of perceptual error. This is true not just for predator–prey relationships, but is equally important for expert-level human performance in domains such as medicine (*2*). Not surprisingly, the theoretical study of generalization is also central to progress in artificial intelligence and machine learning (*3*–*5*).

Just over 30 years ago, cognitive scientist Roger Shepard suggested that perceptual generalization was a suitable candidate for the first "universal law" in psychological science (*6*). Shepard's universal law of generalization states that the generalization between two stimuli (essentially, the probability of confusion) decreases as an exponential function of their distance within an appropriate metric "psychological space." This exponential generalization pattern has indeed proved to be near-universal, and the success of the empirical law has been impressive, accounting for data spanning a wide range of domains, sensory modalities, and across multiple species (*6*–*8*).

Shepard's explanation for this phenomenon revolves around the concept of a "consequential region" within psychological space that corresponds to a concept. For example, the concept of poisonous butterflies encompasses some set of stimuli in psychological space. Given one stimulus known to be an element of this set, the task facing the organism is to infer whether a novel stimulus will also fall in the same region; this task can be framed as one of probabilistic inference. Subsequent work (*9*, *10*) expanded on the idea of generalization as probabilistic inference, to include extrapolating from multiple exemplars and exploring alternative measures of perceptual distance or dissimilarity.

Here, I offer a qualitatively different explanation for the origins of the universal law in human perception, based on the principle of efficient coding (*11*), or the idea that biological information processing should seek to maximize performance

Department of Cognitive Science, Rensselaer Polytechnic Institute, Troy, NY 12180, USA.
***Corresponding author. Email: simsc3@rpi.edu**

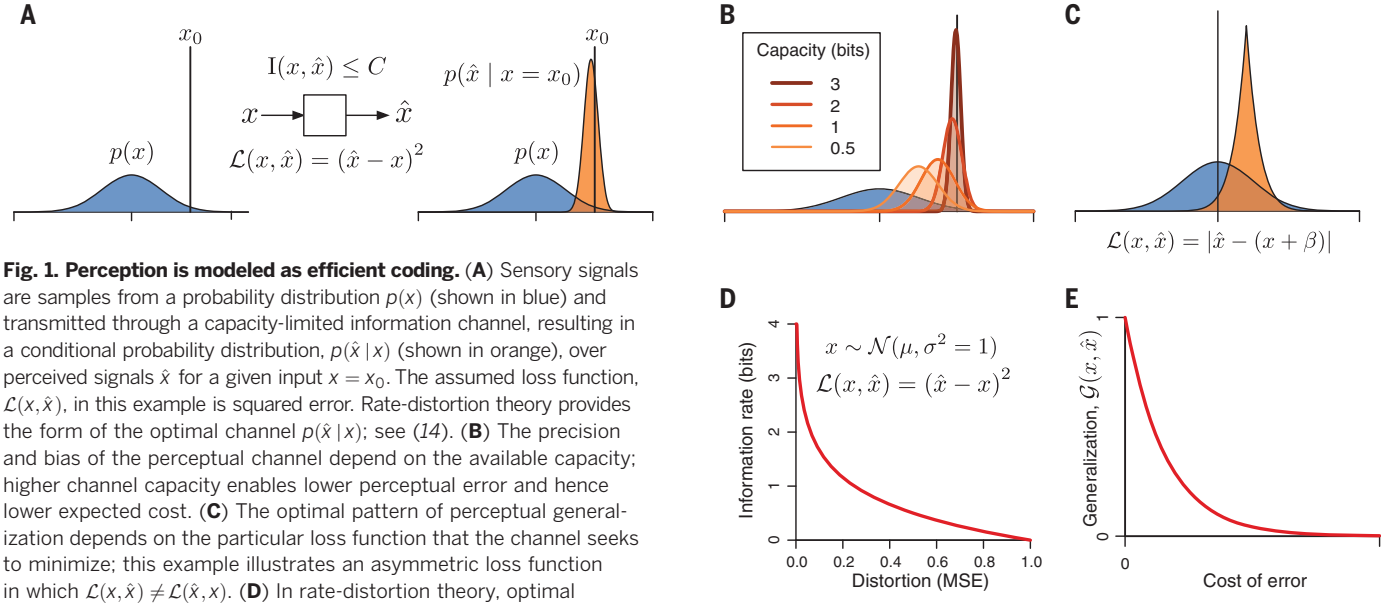

Fig. 1. Perception is modeled as efficient coding. (**A**) Sensory signals are samples from a probability distribution $p(x)$ (shown in blue) and transmitted through a capacity-limited information channel, resulting in a conditional probability distribution, $p(\hat{x}\,|\,x)$ (shown in orange), over perceived signals $\hat{x}$ for a given input $x = x_0$. The assumed loss function, $\mathcal{L}(x,\hat{x})$, in this example is squared error. Rate-distortion theory provides the form of the optimal channel $p(\hat{x}\,|\,x)$; see (*14*). (**B**) The precision and bias of the perceptual channel depend on the available capacity; higher channel capacity enables lower perceptual error and hence lower expected cost. (**C**) The optimal pattern of perceptual generalization depends on the particular loss function that the channel seeks to minimize; this example illustrates an asymmetric loss function in which $\mathcal{L}(x,\hat{x}) \neq \mathcal{L}(\hat{x},x)$. (**D**) In rate-distortion theory, optimal achievable performance is dictated by a "rate-distortion curve," which plots the minimum information rate (bits per transmission) necessary to achieve a given level of expected cost. The slope at any point along this curve is mathematically related to the steepness of the generalization gradient. This example illustrates the rate-distortion curve for a Gaussian information source with squared error cost function. (**E**) Without further assumptions, rate-distortion theory directly predicts an exponential generalization gradient as a function of the cost of perceptual error.

subject to constraints on information processing capacity.

Critically, the proposed approach also generates unique predictions that distinguish it from competing explanations for the universal law. These include predictions that relate the slope of the generalization gradient to information-theoretic quantities, asymmetric generalization gradients in situations where there are asymmetric costs for perceptual error, and the finding that artificial systems (such as the JPEG image compression algorithm) can also produce an exponential generalization gradient. The result is a revised universal law of perceptual generalization, which subsumes Shepard's statement of the law as a special case.

The approach uses results from the field of rate-distortion theory, a subdiscipline within information theory concerned with the design and analysis of optimal, but capacity-limited, information channels (*12*–*14*). Previous work has shown that rate-distortion theory offers a compelling account of human visual working memory limitations (*15*, *16*).

The current results can be concisely stated as follows: Perceptual generalization in any efficient communication system will necessarily follow an exponential function of the cost of perceptual error. In this framework, the emergence of the universal law is the signature of an organism that seeks to perceive the world as best as possible, according to some utility measure, subject to available resource limitations.

Figure 1 shows the theoretical framework and its properties. Perception is modeled as a capacity-limited information channel in which afferent sensory signals (x) are distributed according to the distribution $p(x)$. The perceived signal ($\hat{x}$) is related to its veridical value by a conditional probability distribution $p(\hat{x} \mid x)$. Capacity limits in the channel prevent transmitting sensory signals with perfect fidelity, and hence in general, $\hat{x} \neq x$. Instead, the goal of the channel is to minimize a given loss function, specified by $\mathcal{L}(x, \hat{x})$, subject to the constraint that the amount of information transmitted by the channel, measured by the mutual information $I(x, \hat{x})$, is at or below a capacity limit C. Rate-distortion theory provides analytical and numerical tools for solving such constrained optimization problems (*12*–*14*).

Notably, several of the properties illustrated in Fig. 1 (such as a "bias to the mean effect," Fig. 1A) are also predicted by Bayesian models of perception. As both are rational or optimal models of cognition, this is not surprising. Whereas Bayesian models of perception often make atheoretic assumptions about the nature of "internal noise" within a perceptual channel [e.g., (*17*)], rate-distortion theory instead gives sensory processing limitations a strong theoretical interpretation in terms of constructs from information theory. Hence, rate-distortion theory can be viewed as a special case of the more general class of Bayesian models of perception. As will be shown presently, this also allows the framework to generate unique predictions.

To connect rate-distortion theory to perceptual generalization, one needs a measure of the strength of generalization from one stimulus to another. Shepard (*6*) defined the following measure:

$$\mathcal{G}_{x\hat{x}} \triangleq \left(\frac{p_{x\hat{x}} \cdot p_{\hat{x}x}}{p_{\hat{x}\hat{x}} \cdot p_{xx}} \right)^{\frac{1}{2}} \quad (1)$$

where $p_{x\hat{x}}$ indicates the probability that a response associated with stimulus $\hat{x}$ is made to stimulus x. According to Shepard's universal law, generalization will follow an exponential function of the distance between x and $\hat{x}$ in an appropriate psychological space, where the distance is assumed to obey the basic metric axioms. Rate-distortion theory suggests a more general formulation for this law. Using Shepard's measure of generalization, rate-distortion theory directly predicts that generalization should follow

$$\mathcal{G}_{x\hat{x}} = \exp\left[s \frac{1}{2} \Big(\mathcal{L}(x, \hat{x}) + \mathcal{L}(\hat{x}, x) - \mathcal{L}(x, x) - \mathcal{L}(\hat{x}, \hat{x}) \Big) \right] \quad (2)$$

where the constant parameter $s < 0$ is monotonically related to the capacity of the channel. Note that this includes Shepard's original universal law as a special case. If the loss function satisfies two of the axioms of distance metrics, namely symmetry $[\mathcal{L}(x, \hat{x}) = \mathcal{L}(\hat{x}, x)]$ and identity $[\mathcal{L}(x, x) = \mathcal{L}(\hat{x}, \hat{x}) = 0]$, then one can easily verify that the generalization function reduces to

$$\mathcal{G}_{x\hat{x}} = \exp[s\ \mathcal{L}(x, \hat{x})] \quad (3)$$

Consequently, when the loss function is taken to be distance in a psychological space, Shepard's original universal law emerges from rate-distortion theory exactly. However, the result in Eq. 2 holds true under very general conditions, even when the psychological representation does not correspond to a metric space. As one example, if the mental representation of complex stimuli consists of a taxonomy of nested categories (*18*), the loss function may be defined in terms of tree distance between exemplars.

Rate-distortion theory was applied to the results of several published perceptual identification

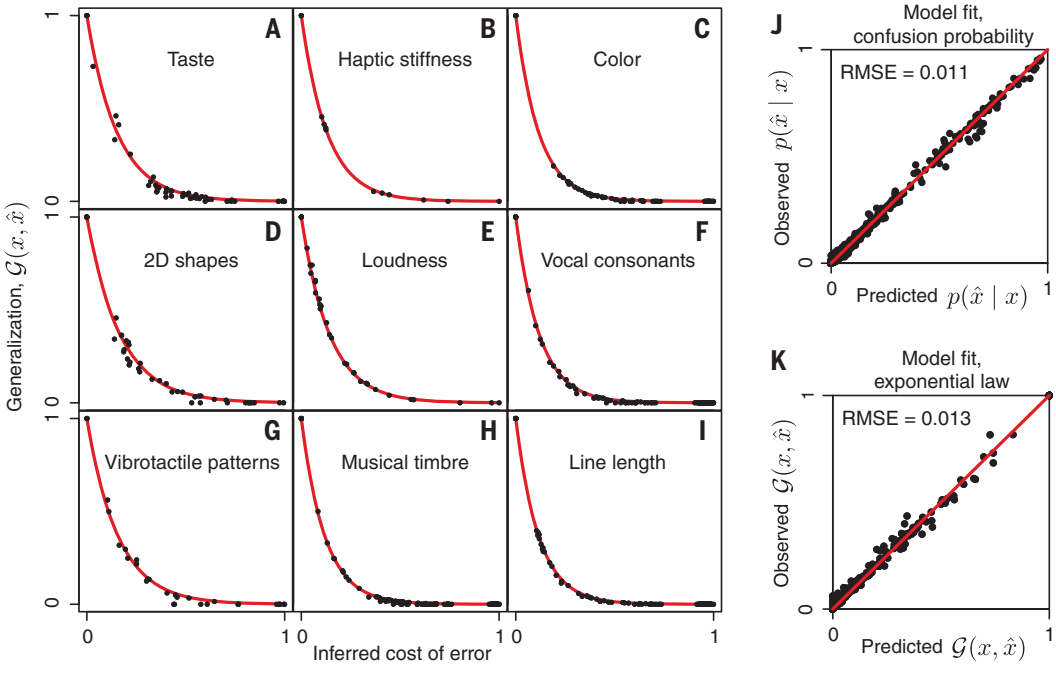

Fig. 2. Rate-distortion theory applied to a range of perceptual identification experiments. (**A** to **I**) Each panel plots the strength of generalization against the inferred cost of perceptual error. Cost functions were estimated by using Bayesian inference. Sources of empirical data are as follows: (A) (*27*); (B) (*28*) veterinarian data; (C) (*29*) data from block 3; (D) (*30*) experiment 1; (E) (*23*) unbiased condition; (F) (*21*) signal-to-noise = 0 dB condition; (G) (*31*) combined data from finger and forearm; (H) (*32*); (I) (*33*) subject MP, set size = 13 condition. (**J**) Goodness of fit to the empirical confusion matrices across all experiments, in terms of root mean squared error (RMSE). (**K**) Deviation between empirical generalization and the exponential generalization gradient predicted by rate-distortion theory across all experiments.

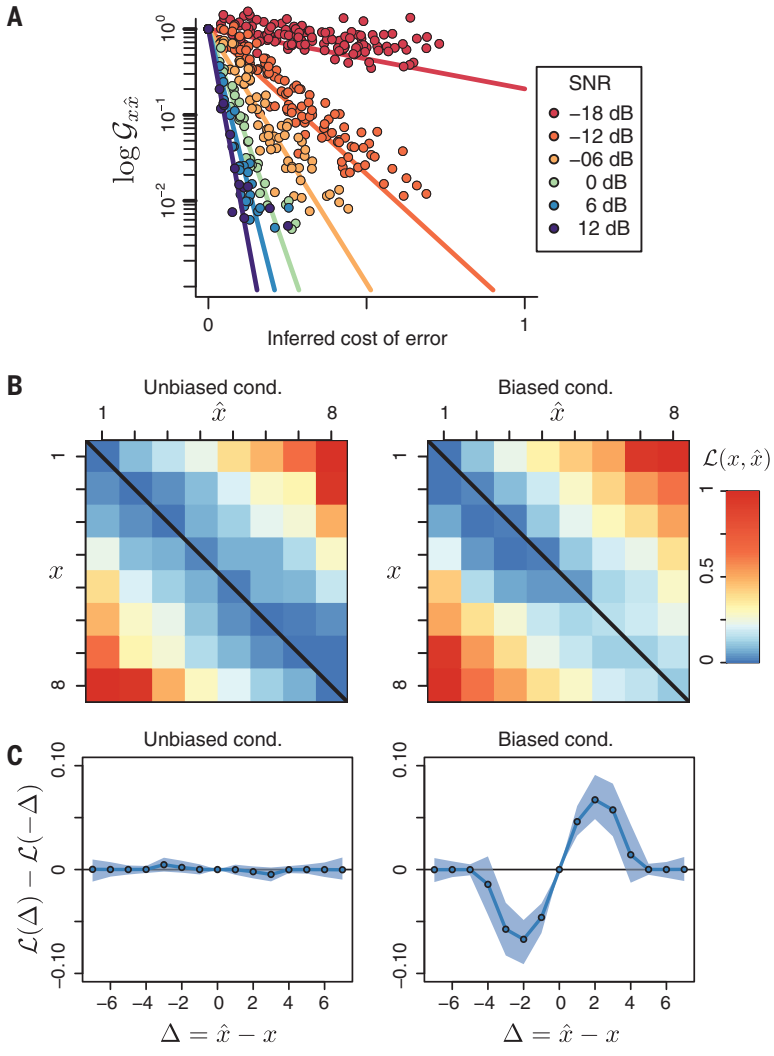

Fig. 3. Unique predictions of rate-distortion theory. (**A**) Rate-distortion theory predicts that the slope of the generalization gradient depends on the information rate of the perceptual channel. In this experiment (*21*), observers must identify vocal consonants embedded in varying levels of white noise. When plotted on a logarithmic axis, an exponential generalization gradient appears as a straight line. Rate-distortion theory is used to predict the slope of the generalization gradient for each condition. (**B**) Left and right panels show the inferred loss functions for the unbiased payoff condition, and biased payoff condition of the experiment reported in (*23*). (**C**) Asymmetry in the loss function is revealed by plotting the average cost for an overestimation error relative to the cost for an underestimation error of the same magnitude. The solid line indicates the maximum a posteriori estimate. The shaded region indicates the estimated 95% highest-density Bayesian credible interval. The figure demonstrates that asymmetry in the cost function appears only when there are task-defined asymmetries in the cost of perceptual error.

experiments (Fig. 2) that use a range of perceptual modalities (visual, haptic, auditory, gustatory). Archives of these data, along with model code, are provided online (*19*). On each trial of an identification experiment, a stimulus is randomly selected from a set, and the observer must identify it with a unique response. The resulting data consist of a perceptual confusion matrix, which gives the empirical frequency that stimulus x produced response $\hat{x}$. The perceptual loss function, $\mathcal{L}(x,\hat{x})$, is estimated from this confusion matrix by means of Bayesian inference.

As shown in Fig. 2, the observed relationship between the inferred cost of perceptual error (the estimated loss function $\mathcal{L}$) and the empirical generalization strength ($\mathcal{G}_{x\hat{x}}$, given by Eq. 1) follows an exponential gradient nearly exactly. Notably, this is not a consequence of a model that fits the data poorly but forces an exponential gradient. Rather, as shown in Fig. 2, J and K, rate-distortion theory simultaneously produces a precise model of the full probability distribution over perceptual confusion, as well as accurately predicts the exponential form of the generalization gradient. The supplementary materials also include a comparison of rate-distortion theory to an alternative existing model of perceptual identification, known as the Luce–Shepard choice model (*20*).

The key test, however, is whether rate-distortion theory generates predictions that distinguish it from competing explanations. The remainder of the paper focuses on three such predictions. The first is that the steepness of the generalization gradient should be monotonically related to the information rate of the perceptual channel. Specifically, when plotted on a logarithmic axis, exponential curves such as those shown in Fig. 2 will appear as straight lines with slope s. Whereas prior work has treated the slope of generalization as a free parameter, rate-distortion theory uniquely provides a strong theoretical interpretation for this quantity. In particular, for an optimal communication channel, the slope satisfies

$$s = \frac{\mathrm{d}R}{\mathrm{d}D} \qquad (4)$$

where the term on the right-hand side of this equation is the slope of the rate-distortion curve for the channel (*12*), as illustrated in Fig. 1D. Consequently, experimental manipulations designed to influence the information rate of the perceptual channel (the numerator of this equation) should have a direct and predictable impact on the slope of the generalization gradient.

A test of this prediction is provided by the classic experiments reported in (*21*). In these experiments, subjects were asked to identify vocal consonants embedded in six different levels of white noise (signal-to-noise ratio ranging from 12 to −18 dB). Intuitively, increasing the amount of noise will decrease the amount of information about the signal that the observer can process. Under the assumption that the stimulus noise influences the information rate of the channel (the numerator of Eq. 4), but not the cost function for perceptual error (the denominator), it is possible to predict the slope of the generalization gradient in a parameter-free manner. The results are shown in Fig. 3A. In this plot, the generalization curves are shown on a logarithmic

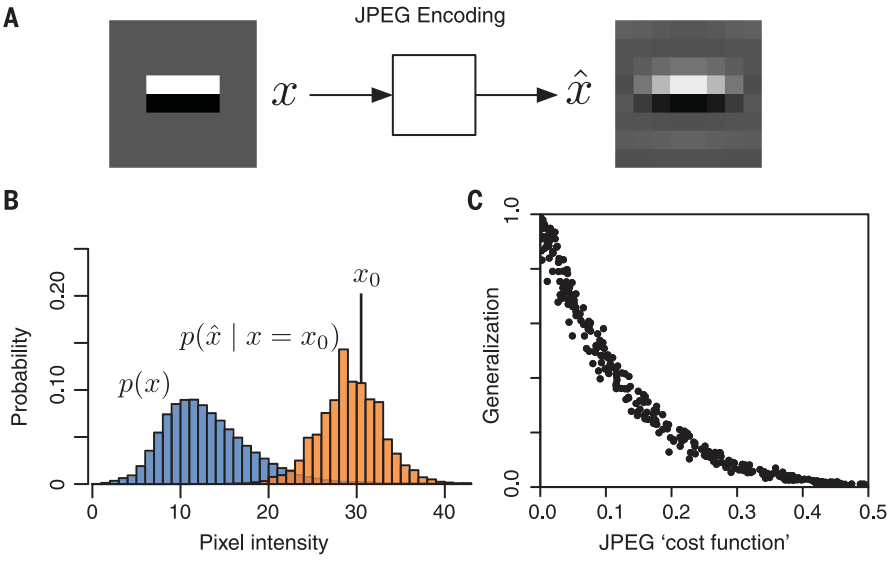

Fig. 4. Investigating perceptual generalization in the JPEG image compression algorithm. (**A**) An image patch encoded by JPEG will typically introduce pixel-level deviations. In particular, JPEG optimizes the transmission of low–spatial frequency components at the expense of introducing larger errors in coding higher spatial frequencies. Squared error within this scaled frequency domain closely approximates the "cost function" for JPEG image coding. (**B**) Conditional probability distribution over JPEG encoding of a particular pixel intensity, averaged over a large number of image patches drawn from a natural scene image. The behavior of the channel closely mirrors the predictions of rate-distortion theory (compare to Fig. 1A). (**C**) Deviations between an input and JPEG-encoded grayscale image of a natural scene conform to the universal law of generalization.

axis to illustrate the change in slope across stimulus noise conditions. The empirical slope of the generalization gradient closely follows the predictions of rate-distortion theory.

A second prediction of rate-distortion stems from the fact that unlike in Shepard's theoretical account, there is no requirement that perceptual generalization must be symmetric. Empirical asymmetries in generalization have previously been raised as an argument against a metric representation of perceptual similarity (*22*). In the present case, a different theoretical origin for asymmetry is predicted in terms of asymmetric costs of perceptual error. An empirical test of this prediction is found in an experiment reported in (*23*). In this experiment, subjects were tasked with identifying pure tones of varying loudness. Subjects were motivated to perform accurately by awarding points for correct responses and deducting points for errors; points were exchanged for a monetary bonus at the end of the experiment. Each subject completed two experimental conditions. In the neutral condition, payoffs were symmetric for all types of errors, whereas in the biased condition, overestimate errors were more costly than underestimate errors.

The inferred loss functions are illustrated in Fig. 3B for both the neutral and biased condition. Inferred costs for perceptual error are symmetric in the unbiased penalty condition, but substantially asymmetric in the biased penalty condition. Formal model comparisons (reported in the supplementary materials) reveal that the data are better explained by rate-distortion theory with an asymmetric cost function, compared to an alternative model that assumes symmetric perceptual distance.

Lastly, rate-distortion theory predicts that exponential generalization gradients should not be limited to biological information processing, but rather should be exhibited by any communication system that operates efficiently in the rate-distortion sense, whether natural or artificial. Figure 4 illustrates an identification "experiment" conducted on the JPEG image compression algorithm. The experiment was performed by taking grayscale photographs from a natural scene database (*24*) and encoding them using the JPEG algorithm. As JPEG is a form of lossy compression, the encoded images will almost certainly introduce perceptual "confusions"—an input pixel replaced by a somewhat different pixel at the output stage (Fig. 4A). A confusion matrix is obtained by collecting the joint statistics of input and JPEG-encoded pixels. Compared to human participants, JPEG has the useful feature that the objective for perceptual coding is obtainable by inspection of its algorithm. In brief, JPEG performs a discrete cosine transform (DCT) on an input image and scales the coefficients by a weight matrix that emphasizes coding accuracy for low spatial frequencies. This weighted DCT representation is essentially the "psychological space" for JPEG encoding. Figure 4C plots the strength of generalization between pixel values against the average squared error distance in quantized DCT space. The results illustrate that JPEG image coding also conforms to the universal law of generalization. Although this finding is consistent with rate-distortion theory, it is difficult to reconcile with alternative explanations for the universal law.

The current work is only part of a growing body of literature showing the broad applicability of efficient coding as a means of understanding biological information processing (*25*, *26*). As a theoretical framework, efficient coding is not an alternative to the popular Bayesian perception framework, but rather is an extension in which sensory limitations are attributed to information processing capacity limitations. As perception exists to maximize the utility of behavior, it is a compelling idea that evolution drives perceptual systems toward the regime of rate-distortion efficiency: optimizing performance subject to information processing constraints.

REFERENCES AND NOTES

1. J. V. Z. Brower, *Evolution* **12**, 32–47 (1958).
2. M. Myles-Worsley, W. A. Johnston, M. A. Simons, *J. Exp. Psychol. Learn. Mem. Cogn.* **14**, 553–557 (1988).
3. T. M. Mitchell, *Artif. Intell.* **18**, 203–226 (1982).
4. B. M. Lake, R. Salakhutdinov, J. B. Tenenbaum, *Science* **350**, 1332–1338 (2015).
5. A. Esteva *et al.*, *Nature* **542**, 115–118 (2017).
6. R. N. Shepard, *Science* **237**, 1317–1323 (1987).
7. K. Cheng, *Psychol. Sci.* **11**, 403–408 (2000).
8. S. Ghirlanda, M. Enquist, *Anim. Behav.* **66**, 15–36 (2003).
9. J. B. Tenenbaum, T. L. Griffiths, *Behav. Brain Sci.* **24**, 629–640 (2001).
10. N. Chater, N. P. M. Vitányi, *J. Math. Psychol.* **47**, 346–369 (2003).
11. H. Barlow, in *Sensory Communication* (MIT Press, Cambridge, MA, 1961), pp. 217–234.
12. T. Berger, *Rate Distortion Theory: A Mathematical Basis for Data Compression* (Prentice Hall, Englewood Cliffs, NJ, 1971).
13. R. Blahut, *IEEE Trans. Inf. Theory* **18**, 460–473 (1972).
14. C. R. Sims, *Cognition* **152**, 181–198 (2016).
15. C. R. Sims, R. A. Jacobs, D. C. Knill, *Psychol. Rev.* **119**, 807–830 (2012).
16. C. R. Sims, *J. Vis.* **15**, 2 (2015).
17. A. A. Stocker, E. P. Simoncelli, *Nat. Neurosci.* **9**, 578–585 (2006).
18. J. B. Tenenbaum, C. Kemp, T. L. Griffiths, N. D. Goodman, *Science* **331**, 1279–1285 (2011).
19. For an online archive of data sets and model code, see https://osf.io/x5ckn. Additional details of the model and parameter estimation are provided in the supplementary materials.
20. R. N. Shepard, *Psychometrika* **22**, 325–345 (1957).
21. G. A. Miller, P. E. Nicely, *J. Acoust. Soc. Am.* **27**, 338–352 (1955).
22. A. Tversky, *Psychol. Rev.* **84**, 327–352 (1977).
23. D. E. Kornbrot, *Atten. Percept. Psychophys.* **24**, 193–208 (1978).
24. W. S. Geisler, J. S. Perry, *J. Vis.* **11**, 14 (2011).
25. X. X. Wei, A. A. Stocker, *Proc. Natl. Acad. Sci. U.S.A.* **114**, 10244–10249 (2017).
26. S. E. Marzen, S. DeDeo, *J. R. Soc. Interface* **14**, 20170166 (2017).
27. T. P. Hettinger, J. F. Gent, L. E. Marks, M. E. Frank, *Percept. Psychophys.* **61**, 1510–1521 (1999).
28. N. Forrest, S. Baillie, H. Z. Tan, in *EuroHaptics 2009*, IEEE, pp. 646–651 (2009).
29. R. M. Nosofsky, *J. Exp. Psychol. Learn. Mem. Cogn.* **13**, 87–108 (1987).

30. F. G. Ashby, W. W. Lee, *J. Exp. Psychol. Gen.* **120**, 150–172 (1991).
31. M. Azadi, L. Jones, in *World Haptics Conference (WHC)*, IEEE, pp. 347–352 (2013).
32. J. M. Grey, *J. Acoust. Soc. Am.* **61**, 1270–1277 (1977).
33. J. N. Rouder, R. D. Morey, N. Cowan, M. Pfaltz, *Psychon. Bull. Rev.* **11**, 938–944 (2004).

ACKNOWLEDGMENTS

Funding: This research was supported by NSF grant DRL-1560829. **Author contributions:** C.R.S. conducted the research and wrote the manuscript. **Competing interests:** None declared. **Data and materials availability:** Online data archives associated with this paper are provided via the Open Science Framework, at https://osf.io/x5ckn/.

SUPPLEMENTARY MATERIALS

www.sciencemag.org/content/360/6389/652/suppl/DC1
Materials and Methods
Fig. S1

2 October 2017; accepted 3 April 2018
10.1126/science.aaq1118

EVOLUTIONARY GENOMICS

Natural selection interacts with recombination to shape the evolution of hybrid genomes

Molly Schumer,[1,2,3,4]* Chenling Xu,[5] Daniel L. Powell,[4,6] Arun Durvasula,[7] Laurits Skov,[8] Chris Holland,[4,6] John C. Blazier,[6,9] Sriram Sankararaman,[7,10] Peter Andolfatto,[11]† Gil G. Rosenthal,[4,6]† Molly Przeworski[3,12]*

To investigate the consequences of hybridization between species, we studied three replicate hybrid populations that formed naturally between two swordtail fish species, estimating their fine-scale genetic map and inferring ancestry along the genomes of 690 individuals. In all three populations, ancestry from the "minor" parental species is more common in regions of high recombination and where there is linkage to fewer putative targets of selection. The same patterns are apparent in a reanalysis of human and archaic admixture. These results support models in which ancestry from the minor parental species is more likely to persist when rapidly uncoupled from alleles that are deleterious in hybrids. Our analyses further indicate that selection on swordtail hybrids stems predominantly from deleterious combinations of epistatically interacting alleles.

Understanding speciation is central to understanding evolution, but so much about the process still puzzles us. Foundational work in evolutionary biology envisioned speciation as an ordered process in which reproductive barriers, once established, prevent gene flow between species (*1*). We now realize, however, that speciation is much more dynamic, with evidence of historical and ongoing hybridization visible in the genomes of myriad species (*2*–*5*). The ubiquity of hybridization raises the question of how species that interbreed remain distinct.

At least part of the answer lies in widespread selection on hybrid genomes (*1*). Analyses of hominin and swordtail fish hybrids indicate that ancestry from the "minor" parent species (the parent that contributed less to the gene pool of hybrids) is decreased near functionally important elements (*4*, *6*, *7*), presumably because such regions are enriched for harmful alleles. Aside from these observations, however, little is known about how hybrid genomes evolve. Decades of experimental work have demonstrated that Bateson-Dobzhansky-Muller incompatibilities (BDMIs) are a central mechanism underlying reproductive isolation once species are formed (*8*–*10*), but the importance of BDMIs in the evolution of hybrid genomes remains unknown, as does the role of other modes of selection. When there is introgression from a species with a smaller effective population size, hybrids may suffer from increased genetic load ("hybridization load") due to the introduction of weakly deleterious alleles (*6*, *11*, *12*). Depending on the environment in which hybrids find themselves, alleles that underlie ecological adaptations in the parental species may also be deleterious (*13*, *14*). Complicating matters further, the sources of selection on hybrids will likely vary from system to system, depending on the extent of genetic and ecological differentiation between the parental species as well as the differences in their effective population sizes.

Regardless of the source of selection, however, one feature is expected to play a central role in mediating its effects: variation in recombination rates along the genome (*6*, *11*, *15*–*17*). In models of BDMIs, neutral ancestry from the minor parent is more likely to persist in regions of higher recombination, where it is more rapidly uncoupled from mutations deleterious in the prevalent (major parent) genetic background (Fig. 1, A and B) (*17*). Similarly, in models of hybridization load, all else being equal, shorter linkage blocks tend to carry fewer weakly deleterious mutations and thus be less rapidly purged by selection (fig. S1) (*6*, *11*). Previous studies have reported patterns consistent with these expectations (*18*–*20*) but without investigating ancestry patterns and their relationship to local recombination rates, distinguishing among selection in the parental or hybrid lineages, or determining the major sources of selection in hybrid populations.

To address these issues, we took advantage of naturally occurring hybrid populations between sister species of swordtail fish, *Xiphophorus birchmanni* and *X. malinche* (Fig. 1, C to E) (*21*). The species are ~0.5% divergent at the nucleotide level, and because of the small effective population size of *X. malinche*, incomplete lineage sorting between the two is relatively rare (Fig. 1F) (*21*). We focused on three hybrid populations that formed independently between the two species fewer than 100 generations ago (*22*). Previous analyses of hybrids between these species suggested that there are ~100 unlinked BDMI pairs segregating, with estimated selection coefficients of ~0.02 to 0.05, in addition to which there could also be linked BDMIs (*22*, *23*).

To infer local ancestry patterns, we generated ~1× coverage whole-genome data for 690 hybrids sampled from the three hybrid populations and then estimated local ancestry patterns by applying a hidden Markov model to ~1 million sites genome-wide (*21*, *24*). Two of the hybrid populations derive on average 75 to 80% of their genomes from *X. birchmanni*, whereas individuals in the third population derive on average 72% of their genomes from *X. malinche* (Fig. 1E) (*21*), with median homozygous tract lengths for the minor parent ranging from 84 to 225 kb across the three populations (*21*).

Our previous work (*25*) indicated that local recombination rates should be conserved between *X. birchmanni* and *X. malinche* (*21*). To consider the relationship between local ancestry and recombination rate, we inferred a fine-scale genetic map for *X. birchmanni* from patterns of linkage disequilibrium (table S1) (*21*). We also generated a crossover map from ancestry switch points in hybrids, which was concordant with the one obtained for *X. birchmanni* (fig. S2) (*21*).

In all three hybrid populations, the probability of carrying ancestry from the minor parent increases with the local recombination rate (Fig. 2 and table S2). The relationship remains, irrespective of the choice of scale (fig. S3) and after thinning of the single-nucleotide polymorphism and ancestry data so as to control for possible differences in the reliability of estimated recombination rates or the power to call ancestry across windows (*21*). This pattern is not expected under neutrality (fig. S1) but can readily be generated under several models of selection, including selection against BDMIs or hybridization load or widespread ecological selection against loci from the minor parent (Fig. 1B and fig. S1). Thus, our finding supports models in which minor parent ancestry persists where it was more likely to have been rapidly uncoupled from the deleterious alleles with which it was originally linked (*21*).

In principle, the chance of minor parent ancestry persisting should be a function of the exact number of deleterious alleles to which it was linked since hybridization occurred. Local recombination rates are one proxy for this (unknown) parameter, as is the number of coding or conserved base

[1]Howard Hughes Medical Institute (HHMI), Boston, MA, USA. [2]Harvard Society of Fellows, Harvard University, Cambridge, MA, USA. [3]Department of Biological Sciences, Columbia University, New York, NY, USA. [4]Centro de Investigaciones Científicas de las Huastecas "Aguazarca," Calnali, Hidalgo, Mexico. [5]Center for Computational Biology, University of California at Berkeley, Berkeley, CA, USA. [6]Department of Biology, Texas A&M University, College Station, TX, USA. [7]Department of Human Genetics, David Geffen School of Medicine, University of California, Los Angeles, Los Angeles, CA, USA. [8]Bioinformatics Research Centre, Aarhus University, Aarhus, Denmark. [9]Texas A&M Institute for Genome Sciences and Society, College Station, TX, USA. [10]Department of Computer Science, University of California, Los Angeles, Los Angeles, CA, USA. [11]Department of Ecology and Evolutionary Biology and Lewis-Sigler Institute for Integrative Genomics, Princeton University, Princeton, NJ, USA. [12]Department of Systems Biology, Columbia University, New York, NY, USA.
***Corresponding author. Email: schumer@fas.harvard.edu (M.S.); mp3284@columbia.edu (M.P.)** †These authors contributed equally to this work.

pairs nearby. Both features predict average minor parent ancestry (figs. S4 and S5) (*21*), but in our data, recombination is the stronger predictor and remains similarly strong after controlling for the number of coding (or conserved) base pairs (tables S2 and S3).

To investigate the mode of selection on hybrids, we considered correlations in local ancestry between pairs of hybrid populations: Though weaker between populations with different major parent ancestries, the correlation was in all cases significantly positive (with the recombination rate controlled for) (Fig. 3, A and B). These correlation patterns should not arise from ecological selection but are expected from selection against hybridization load as well as, less intuitively, from selection on the same BDMIs (fig. S6) (*21*).

Further evidence about the mode of selection comes from an analysis of genome sequences from *X. malinche* (*3*, *22*) and *X. birchmanni*, which indicates that *X. malinche* has had a smaller long-term effective population size over the last ~20,000 generations (Fig. 1F) (*21*), as reflected in its four times lower heterozygosity (0.03% versus 0.12% per base pair). Accordingly, the *X. malinche* genome carries significantly more derived putatively deleterious alleles (a 2.5% excess) than that of *X. birchmanni* (*21*, *26*). As a result of this difference, the three hybrid populations of swordtail fish provide an informative contrast: Whereas BDMIs should lead to selection against minor parent ancestry in all three populations, hybridization load should favor the major parent in the first two populations (Totonicapa and Aguazarca) and the minor parent in the third (Tlatemaco) (Figs. 1E and 3C). That minor parent ancestry also increases with recombination in the Tlatemaco population (Fig. 2) then indicates that hybrid

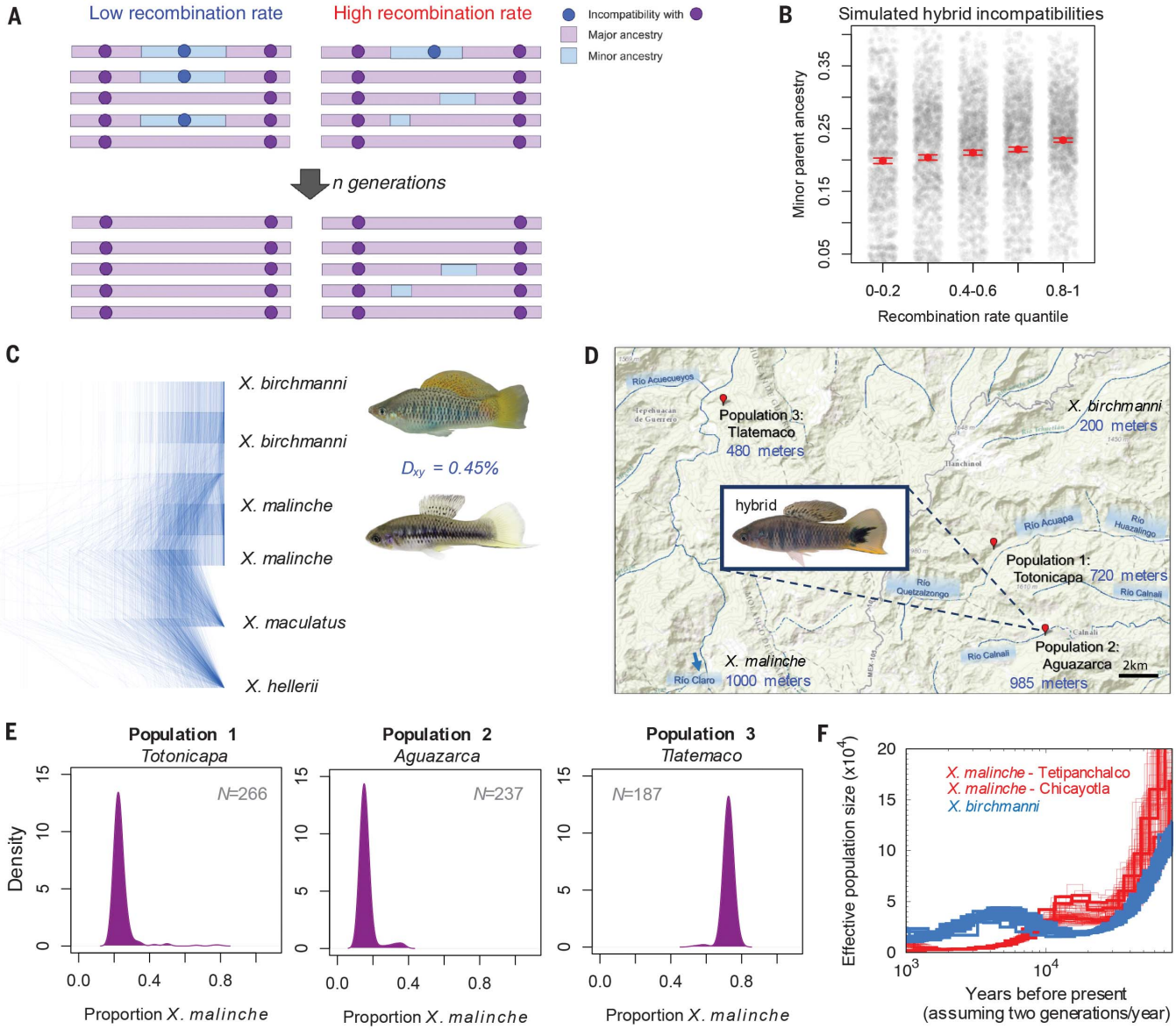

Fig. 1. Predicted relationships between minor parent ancestry and recombination rates and properties of focal swordtail populations. (**A**) In the presence of hybrid incompatibilities, minor parent ancestry is more likely to persist in regions of high recombination. (**B**) One randomly chosen replicate of simulations under plausible parameters for swordtail species (*21*). Red points indicate the means, and whiskers indicate 2 SEM; gray points are raw data. (**C**) Maximum likelihood trees from RAxML for 1000 alignments of randomly selected 10-kb regions in swordtail species. D_{xy} refers to the average nucleotide divergence between *X. birchmanni* and *X. malinche*. (**D**) Locations of hybrid populations in river systems in Hidalgo, Mexico. Elevations of the hybrid populations and typical elevations for parental populations are listed in blue. (**E**) Inferred ancestry proportions for individuals (*n*) sampled from each population. (**F**) Effective population sizes inferred from three *X. malinche* genomes (sampled from two populations) and 20 *X. birchmanni* genomes. Fifty bootstraps are shown for one individual from each *X. malinche* population (*21*).

incompatibilities are the dominant source of selection, rather than hybridization load (Fig. 3C and fig. S7) (*21*). In principle, ecological selection favoring the major parent could also produce a positive correlation between recombination and minor parent ancestry (but not positive correlations in ancestry between populations) (Fig. 3, A and B). However, this explanation would require two of the hybrid populations to occur in more *X. birchmanni*–like environments and one in a more *X. malinche*–like environment, when available evidence suggests otherwise (Fig. 1D) (*21*).

Furthermore, in all populations, minor parent ancestry is unusually low near previously mapped putative BDMIs (*22*, *23*). Lower minor parent ancestry does not result from the approach used to identify BDMIs (*21*, *22*) but is expected from selection on epistatically interacting alleles (Fig. 3D)

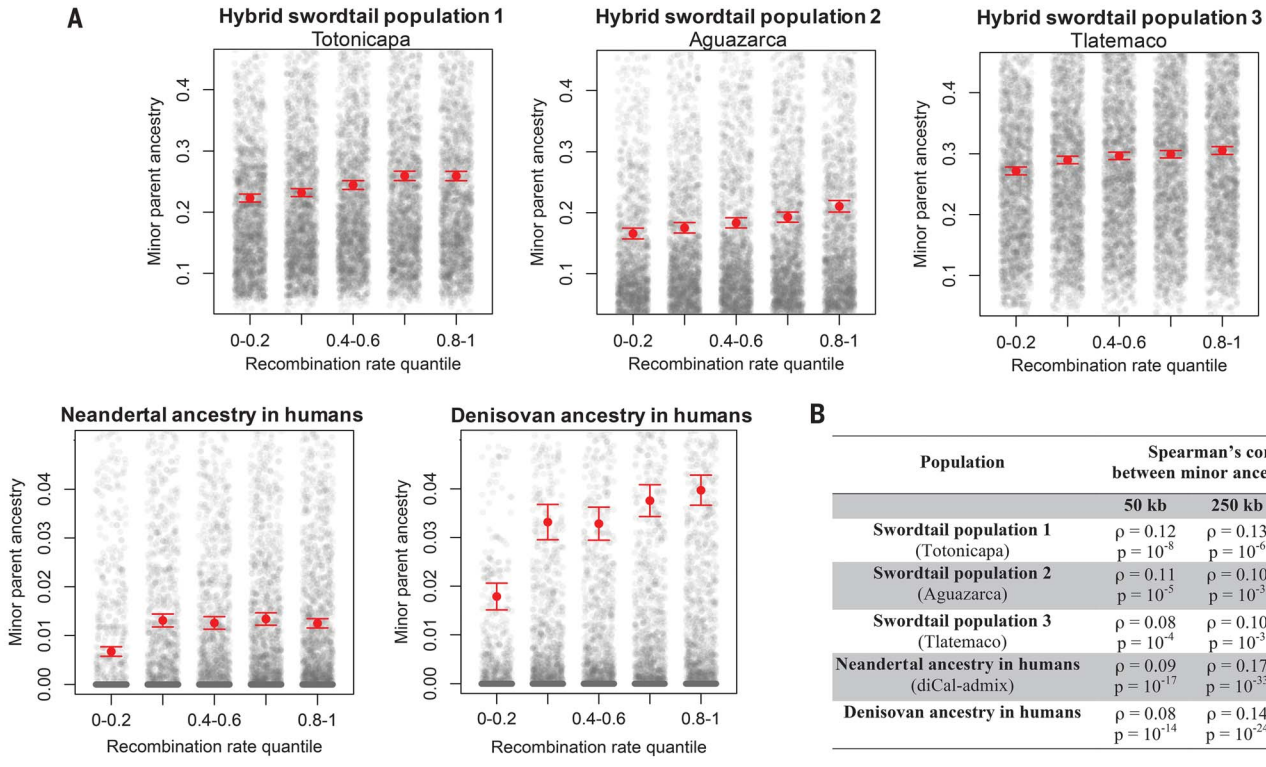

B

Population	Spearman's correlation between minor ancestry and rate		
	50 kb	250 kb	500 kb
Swordtail population 1 (Totonicapa)	$\rho = 0.12$ $p = 10^{-8}$	$\rho = 0.13$ $p = 10^{-6}$	$\rho = 0.18$ $p = 10^{-9}$
Swordtail population 2 (Aguazarca)	$\rho = 0.11$ $p = 10^{-5}$	$\rho = 0.10$ $p = 10^{-3}$	$\rho = 0.09$ $p = 10^{-3}$
Swordtail population 3 (Tlatemaco)	$\rho = 0.08$ $p = 10^{-4}$	$\rho = 0.10$ $p = 10^{-3}$	$\rho = 0.11$ $p = 10^{-4}$
Neandertal ancestry in humans (diCal-admix)	$\rho = 0.09$ $p = 10^{-17}$	$\rho = 0.17$ $p = 10^{-33}$	$\rho = 0.19$ $p = 10^{-42}$
Denisovan ancestry in humans	$\rho = 0.08$ $p = 10^{-14}$	$\rho = 0.14$ $p = 10^{-24}$	$\rho = 0.15$ $p = 10^{-29}$

Fig. 2. Relationships between minor parent ancestry and recombination rate in swordtails and hominins. (**A**) Relationship between minor parent ancestry and recombination rate in swordtails and in humans, summarized in 50-kb windows for swordtail analyses and 250-kb windows for humans (fig. S8), so that the numbers of windows are similar. (**B**) Spearman's correlations between average minor parent ancestry and recombination rate at several scales [complete results are provided in table S2, and details of the Denisovan analysis are provided in (*21*)]. In (A), red points and whiskers indicate the means with 2 SEM determined by bootstrapping; gray points show raw data. Quantile binning is for visualization; statistical tests were performed on the unbinned data.

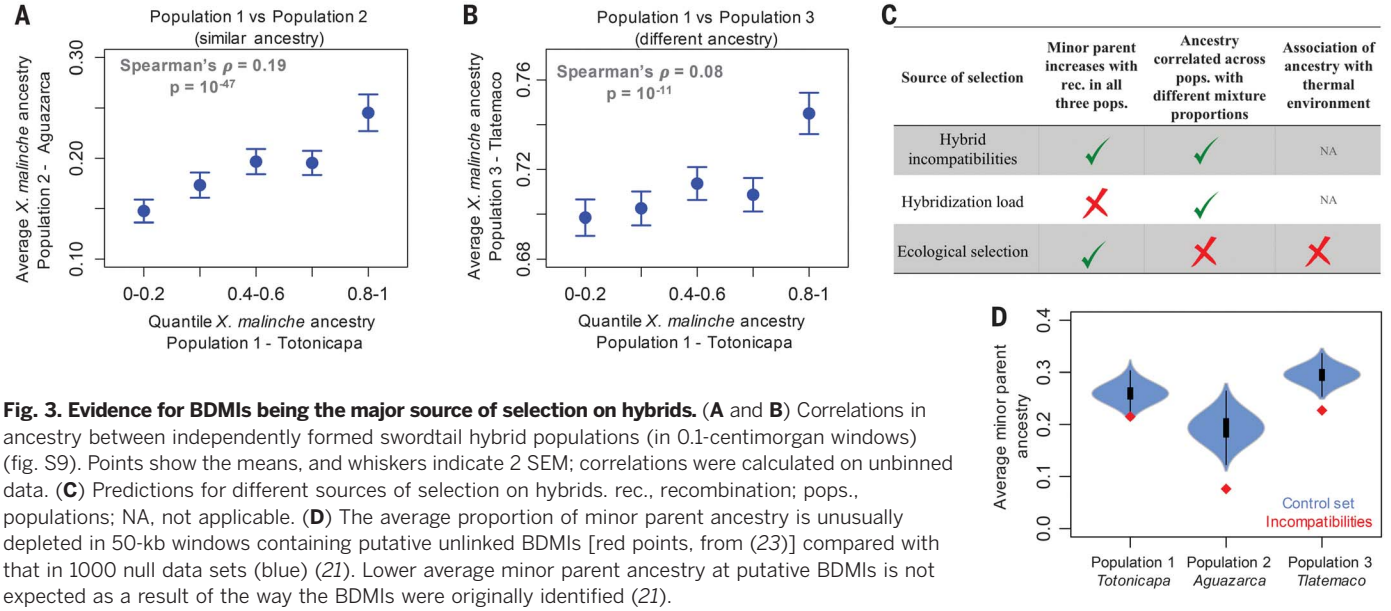

Fig. 3. Evidence for BDMIs being the major source of selection on hybrids. (**A** and **B**) Correlations in ancestry between independently formed swordtail hybrid populations (in 0.1-centimorgan windows) (fig. S9). Points show the means, and whiskers indicate 2 SEM; correlations were calculated on unbinned data. (**C**) Predictions for different sources of selection on hybrids. rec., recombination; pops., populations; NA, not applicable. (**D**) The average proportion of minor parent ancestry is unusually depleted in 50-kb windows containing putative unlinked BDMIs [red points, from (*23*)] compared with that in 1000 null data sets (blue) (*21*). Lower average minor parent ancestry at putative BDMIs is not expected as a result of the way the BDMIs were originally identified (*21*).

(*21*). Together, these lines of evidence indicate that BDMIs are the predominant—though not necessarily sole—source of selection filtering minor parent ancestry in these three swordtail hybrid populations (Fig. 3C).

To explore the generality of these relationships, we considered admixture between humans and archaic hominins. Several studies have reported that Neandertal ancestry tends to decrease with the number of linked coding base pairs and with a measure of purifying selection at linked sites (*4*, *6*, *11*), patterns for which both BDMIs and hybridization load—in part because of the smaller effective population size of Neandertals (*27*)—have been proposed as explanations (*4*, *6*, *11*). Reanalyzing the data, we found that the proportion of Neandertal ancestry decreases in regions of the human genome with lower recombination rates (Fig. 2 and tables S2 and S4). This relationship is seen by using three different approaches to infer Neandertal ancestry (table S2) and is not explained by variation in power to identify introgression or the number of coding base pairs nearby (table S2) (*21*). Repeating these analyses for Denisovan ancestry, we obtained the same pattern (Fig. 2 and table S2) (*21*).

As with the persistence of minor parent ancestry in swordtails, the persistence of archaic hominin ancestry in regions of higher recombination is not expected under neutrality (fig. S1). However, our conclusion about the source of selection reached for swordtails need not hold for hominins—a priori, because modern humans were less diverged from Neandertals and Denisovans when they interbred (*28*), and because plausible models of hybridization load have been shown to provide a good fit to the distribution of Neandertal ancestry in the human genome (*6*).

Thus, minor parent ancestry is predicted by the local recombination rate across three replicate admixture events in swordtails, as well as in two cases of admixture in hominins. Together with earlier indications in other species (*18*–*20*), our findings show the distribution of minor parent ancestry to be at least in part predictable from genomic features. Knowledge of local recombination should therefore provide a guide to where in the genome minor parent ancestry is expected to be highest. In hominins, meiotic recombination is directed to the genome by binding of the *PRDM9* gene; in swordtails, meiotic recombination is not and tends to occur near promoter-like features (*21*, *25*). Accordingly, minor parent ancestry is higher around promoter-like features in swordtails but not in humans (Fig. 4) (*21*). Thus, the mechanism by which recombination is directed to the genome affects the distribution of minor parent ancestry.

One implication is that the reliance on PRDM9 to direct recombination may affect reproductive isolation between species not only directly [as in mice (*29*)] but also indirectly. For example, if epistatic interactions often occur between regulatory and coding regions, hybrids with recombination concentrated in promoter-like regions may experience greater negative selection due to BDMIs but more opportunities for adaptive introgression. As genomic data accumulate for hybridizing species across the tree of life, the consequences of recombination mechanisms for the fate of hybrids can be evaluated systematically.

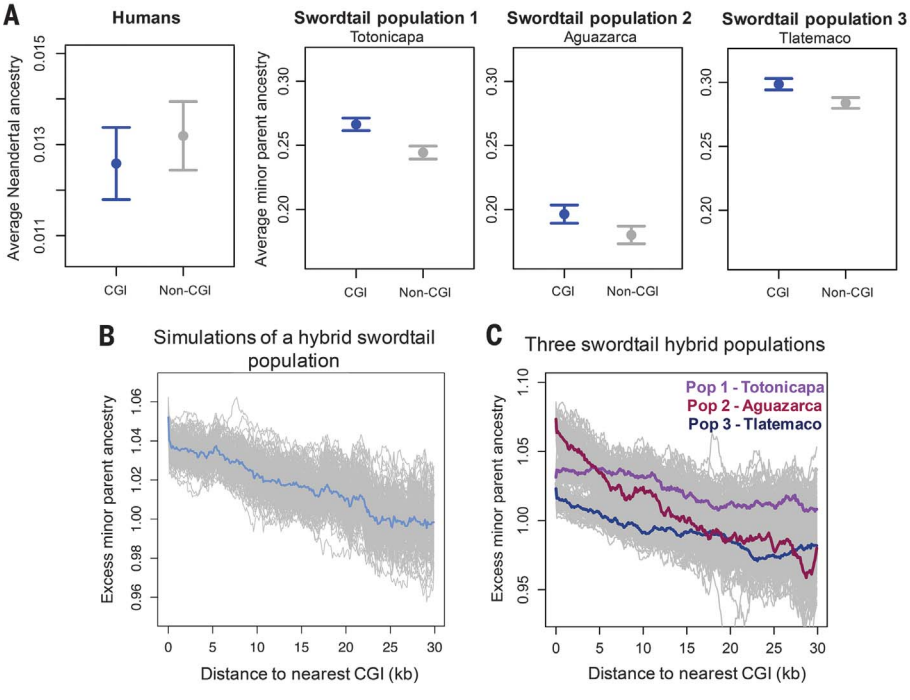

Fig. 4. The recombination mechanism shapes the distribution of minor parent ancestry. (**A**) Neandertal ancestry is not elevated in 50-kb windows that overlap with CpG islands (CGIs) compared with windows that do not but have similar GC content. The fold difference λ is 0.95 ($P = 0.91$) (*21*). The same analysis for swordtail hybrids reveals that the proportion of minor parent ancestry is higher in windows that overlap CGIs (population 1, $\lambda = 1.09$, $P < 0.005$; population 2, $\lambda = 1.09$, $P < 0.005$; population 3, $\lambda = 1.02$, $P < 0.005$). Points show the means, and whiskers indicate 2 SEM obtained from 1000 joint bootstraps. (**B**) Simulations of incompatibility selection in swordtails predict an enrichment of minor parent ancestry near CGIs. (**C**) This prediction is met for all hybrid populations. In (B) and (C), gray lines show results of 500 replicate simulations bootstrapping 5-kb windows; colored lines indicate the means for all replicates in sliding 5-kb windows.

REFERENCES AND NOTES

1. J. A. Coyne, H. A. Orr, *Speciation* (Sinauer Associates, 2004).
2. L. H. Rieseberg, J. Whitton, K. Gardner, *Genetics* **152**, 713–727 (1999).
3. R. Cui *et al.*, *Evolution* **67**, 2166–2179 (2013).
4. S. Sankararaman *et al.*, *Nature* **507**, 354–357 (2014).
5. F. Jacobsen, K. E. Omland, *Mol. Ecol.* **20**, 2236–2239 (2011).
6. I. Juric, S. Aeschbacher, G. Coop, *PLOS Genet.* **12**, e1006340 (2016).
7. M. Schumer, R. Cui, D. L. Powell, G. G. Rosenthal, P. Andolfatto, *Mol. Ecol.* **25**, 2661–2679 (2016).
8. J. P. Masly, D. C. Presgraves, *PLOS Biol.* **5**, e243 (2007).
9. K. Bomblies *et al.*, *PLOS Biol.* **5**, e236 (2007).
10. H.-Y. Lee *et al.*, *Cell* **135**, 1065–1073 (2008).
11. K. Harris, R. Nielsen, *Genetics* **203**, 881–891 (2016).
12. N. Bierne, T. Lenormand, F. Bonhomme, P. David, *Genet. Res.* **80**, 197–204 (2002).
13. L. H. Rieseberg *et al.*, *Science* **301**, 1211–1216 (2003).
14. M. E. Arnegard *et al.*, *Nature* **511**, 307–311 (2014).
15. C. I. Wu, *J. Evol. Biol.* **14**, 851–865 (2001).
16. M. A. F. Noor, K. L. Grams, L. A. Bertucci, J. Reiland, *Proc. Natl. Acad. Sci. U.S.A.* **98**, 12084–12088 (2001).
17. M. W. Nachman, B. A. Payseur, *Philos. Trans. R. Soc. London Ser. B* **367**, 409–421 (2012).
18. Y. Brandvain, A. M. Kenney, L. Flagel, G. Coop, A. L. Sweigart, *PLOS Genet.* **10**, e1004410 (2014).
19. M. Carneiro, N. Ferrand, M. W. Nachman, *Genetics* **181**, 593–606 (2009).
20. A. Geraldes, P. Basset, K. L. Smith, M. W. Nachman, *Mol. Ecol.* **20**, 4722–4736 (2011).
21. Materials and methods are available as supplementary materials.
22. M. Schumer *et al.*, *eLife* **3**, e02535 (2014).
23. M. Schumer, Y. Brandvain, *Mol. Ecol.* **25**, 2577–2591 (2016).
24. P. Andolfatto *et al.*, *Genome Res.* **21**, 610–617 (2011).
25. Z. Baker *et al.*, *eLife* **6**, e24133 (2017).
26. R. Do *et al.*, *Nat. Genet.* **47**, 126–131 (2015).
27. K. Prüfer *et al.*, *Nature* **505**, 43–49 (2014).
28. H. A. Orr, M. Turelli, *Evolution* **55**, 1085–1094 (2001).
29. B. Davies *et al.*, *Nature* **530**, 171–176 (2016).

ACKNOWLEDGMENTS

We thank Y. Brandvain, E. Calfee, G. Coop, J. Pickrell, J. Pritchard, D. Reich, G. Sella, S. Singhal, M. Steinrücken, and members of the Przeworski and Sella laboratories for helpful discussions and/or comments. We thank the federal government of Mexico for permission to collect fish. **Funding:** This project was supported by grant R01 GM83098 to M.P.; NSF grant DEB-1405232, an HHMI Hanna H. Gray fellowship, and a Milton grant to M.S.; and a grant from the Cancer Prevention Research Institute of Texas to G.G.R. **Author contributions:** M.S. and M.P. designed the project and wrote the manuscript; M.S., D.L.P., C.H., L.S., and J.C.B. collected data; M.S., C.X., A.D., and S.S. performed analyses; and P.A. and G.G.R. provided expertise and technical support. **Competing interests:** The authors declare no competing interests. **Data and materials availability:** Data and scripts are available through Dryad (doi: 10.5061/dryad.rd28k4r), and raw data are available through NCBI (Sequence Read Archive accession nos. SRP130891 and SRP018918).

SUPPLEMENTARY MATERIALS

www.sciencemag.org/content/360/6389/656/suppl/DC1
Materials and Methods
Figs. S1 to S31
Tables S1 to S8
References (*30*–*89*)

31 October 2017; accepted 23 March 2018
Published online 19 April 2018
10.1126/science.aar3684

CANCER

An anatomic transcriptional atlas of human glioblastoma

Ralph B. Puchalski,[1,2*†] Nameeta Shah,[2,3*†] Jeremy Miller,[1] Rachel Dalley,[1] Steve R. Nomura,[2] Jae-Guen Yoon,[2] Kimberly A. Smith,[1] Michael Lankerovich,[2] Darren Bertagnolli,[1] Kris Bickley,[1] Andrew F. Boe,[1] Krissy Brouner,[1] Stephanie Butler,[1] Shiella Caldejon,[1] Mike Chapin,[1] Suvro Datta,[1] Nick Dee,[1] Tsega Desta,[1] Tim Dolbeare,[1] Nadezhda Dotson,[1] Amanda Ebbert,[1] David Feng,[1] Xu Feng,[4] Michael Fisher,[1] Garrett Gee,[1] Jeff Goldy,[1] Lindsey Gourley,[1] Benjamin W. Gregor,[1] Guangyu Gu,[1] Nika Hejazinia,[1] John Hohmann,[1] Parvinder Hothi,[2] Robert Howard,[1] Kevin Joines,[1] Ali Kriedberg,[1] Leonard Kuan,[1] Chris Lau,[1] Felix Lee,[1] Hwahyung Lee,[2] Tracy Lemon,[1] Fuhui Long,[1] Naveed Mastan,[1] Erika Mott,[1] Chantal Murthy,[2] Kiet Ngo,[1] Eric Olson,[1] Melissa Reding,[1] Zack Riley,[1] David Rosen,[1] David Sandman,[1] Nadiya Shapovalova,[1] Clifford R. Slaughterbeck,[1] Andrew Sodt,[1] Graham Stockdale,[1] Aaron Szafer,[1] Wayne Wakeman,[1] Paul E. Wohnoutka,[1] Steven J. White,[5] Don Marsh,[5] Robert C. Rostomily,[6,7] Lydia Ng,[1] Chinh Dang,[1] Allan Jones,[1] Bart Keogh,[4] Haley R. Gittleman,[8] Jill S. Barnholtz-Sloan,[8] Patrick J. Cimino,[9] Megha S. Uppin,[10] C. Dirk Keene,[9] Farrokh R. Farrokhi,[11] Justin D. Lathia,[12] Michael E. Berens,[13] Antonio Iavarone,[14,15,16] Amy Bernard,[1] Ed Lein,[1] John W. Phillips,[1] Steven W. Rostad,[17] Charles Cobbs,[2] Michael J. Hawrylycz,[1]† Greg D. Foltz[2]‡

Glioblastoma is an aggressive brain tumor that carries a poor prognosis. The tumor's molecular and cellular landscapes are complex, and their relationships to histologic features routinely used for diagnosis are unclear. We present the Ivy Glioblastoma Atlas, an anatomically based transcriptional atlas of human glioblastoma that aligns individual histologic features with genomic alterations and gene expression patterns, thus assigning molecular information to the most important morphologic hallmarks of the tumor. The atlas and its clinical and genomic database are freely accessible online data resources that will serve as a valuable platform for future investigations of glioblastoma pathogenesis, diagnosis, and treatment.

Glioblastoma is the most common and the most lethal malignant brain tumor (*1*). Even for patients receiving aggressive treatment, the median survival is 12 to 15 months (*2*). The tumors evolve rapidly as they acquire new mutations; the resultant increase in intratumor genomic heterogeneity leads to the development of drug resistance, which limits the long-term efficacy of therapies (*3*, *4*). Two large-scale efforts aimed at characterizing the genomic alterations in human glioblastoma are The Cancer Genome Atlas (TCGA), which is a catalog of multi-omics data, including genomics, transcriptomics, DNA methylomics, proteomics, etc. (*5*, *6*), and REMBRANDT (Repository for Molecular Brain Neoplasia Data), which also includes multiple data domains (*7*). These efforts helped to clarify the role of genomic alterations in the pathogenesis of glioblastoma but were not designed to address intratumor heterogeneity. Subsequent studies addressed heterogeneity spatially within bulk tumor or at the single-cell level (*4*, *8*–*12*). Nonetheless, we still lack a systematic understanding of the tumor's molecular heterogeneity as it relates to anatomical heterogeneity. By "anatomical heterogeneity," we mean the variable combination of the classical histological features of glioblastoma, such as tumor infiltration, endothelial cell proliferation, and necrosis. Here, we describe the Ivy Glioblastoma Atlas (http://glioblastoma.alleninstitute.org/), a comprehensive molecular pathology map of glioblastoma in which we have assigned key genomic alterations and gene expression profiles to the tumor's anatomic features. The atlas will facilitate accurate deconvolution of anatomic features in new samples of glioblastoma, providing unique information for the comprehensive diagnostic characterization of the tumor's heterogeneity.

To create the atlas, we surveyed the tumor's anatomic features by in situ hybridization (ISH), analyzed these features' transcriptomes by laser microdissection (LMD) and RNA sequencing (RNA-seq), and validated the feature-specific gene expression enrichment of newly identified markers by ISH (Fig. 1). We created a clinical and genomic database (http://ivygap.org/) for the 41-patient cohort (table S1) whose tumors (n = 42) were evaluated to create the atlas. We describe gene sets whose expression is enriched in the anatomic features, measurements of intra- and intertumor heterogeneity, and a molecular subtype classification of transcriptomic samples from our atlas and from TCGA. Together, these two online resources constitute the Ivy Glioblastoma Atlas Project (Ivy GAP).

To identify gene sets with enriched expression in each anatomic feature (fig. S1), we used LMD to isolate RNA from the leading edge (LE), infiltrating tumor (IT), cellular tumor (CT), pseudopalisading cells around necrosis (PAN), and microvascular proliferation (MVP). In total, we isolated 122 samples from three different blocks per tumor in 8 to 10 tumors. In consultation with a neuropathologist, we manually drew outlines (LMD guidelines) for each of the anatomic features on images of histologically stained tissue sections. Three additional neuropathologists independently validated the LMD guidelines, and the results showed excellent concordance (table S2). Differential gene expression analysis revealed a total of 3627 genes that had enriched expression in LE, CT, PAN, and MVP samples (Fig. 2A and table S3). Multidimensional scaling demonstrated that samples from these four features were largely distinct, whereas IT appeared to fall on a continuum between LE and CT (Fig. 2B). Gene Ontology enrichment analysis of gene sets with enriched expression in anatomic features (Fig. 2C) confirmed and extended previous reports (*13*, *14*). In general, samples from the same anatomic feature, whether derived from the same or different tumors, were more similar to each other than to samples from other anatomic features of the same tumor (Fig. 2D). Within a given anatomic feature, intertumor heterogeneity exceeded intratumor heterogeneity (fig. S2).

We selected 31 genes with enriched expression in anatomic features for further analysis by ISH, and found that 27 showed at least partial agreement and 22 showed good agreement between

[1]Allen Institute for Brain Science, Seattle, WA 98109, USA. [2]Ben and Catherine Ivy Center for Advanced Brain Tumor Treatment, Swedish Neuroscience Institute, Seattle, WA 98122, USA. [3]Mazumdar Shaw Center for Translational Research, Bangalore 560099, India. [4]Radia Inc., Lynnwood, WA 98036, USA. [5]White Marsh Forests, Seattle, WA 98119, USA. [6]Department of Neurosurgery, Institute for Stem Cell and Regenerative Medicine, University of Washington School of Medicine, Seattle, WA 98195, USA. [7]Department of Neurological Surgery, Houston Methodist Hospital and Research Institute, Houston, TX 77030, USA. [8]Case Comprehensive Cancer Center, Case Western Reserve University School of Medicine, Cleveland, OH 44106, USA. [9]Department of Pathology, Division of Neuropathology, University of Washington School of Medicine, Seattle, WA 98104, USA. [10]Nizam's Institute of Medical Sciences, Punjagutta, Hyderabad 500082, India. [11]Virginia Mason Medical Center, Seattle, WA 98101, USA. [12]Department of Cellular and Molecular Medicine, Cleveland Clinic, Cleveland, OH 44195, USA. [13]TGen, Translational Genomics Research Institute, Phoenix, AZ 85004, USA. [14]Institute for Cancer Genetics, Columbia University, New York, NY 10032, USA. [15]Department of Neurology, Columbia University, New York, NY 10032, USA. [16]Department of Pathology, Columbia University, New York, NY 10032, USA. [17]CellNetix, Seattle, WA 98122, USA.
*These authors contributed equally to this work.
†Corresponding author. Email: mikeh@alleninstitute.org (M.J.H.); rbpuchalski@gmail.com (R.B.P.); nameeta.shah@gmail.com (N.S.)
‡Deceased.

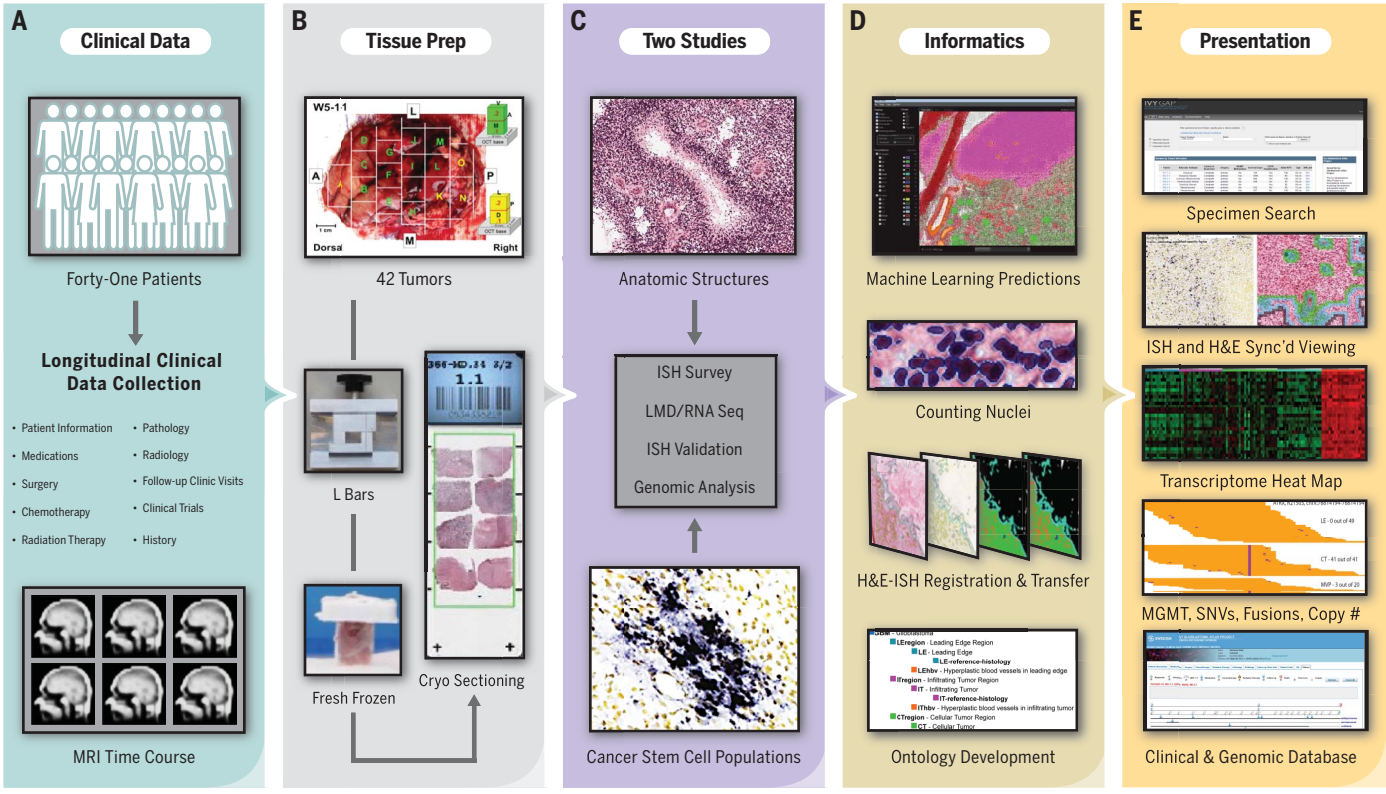

Fig. 1. Data generation, analysis, and presentation pipeline for the Ivy Glioblastoma Atlas Project. (**A**) Clinical data were collected for the Ivy cohort of 41 patients. (**B**) Tissue preparation required en bloc resection and formation of tissue blocks with custom-made L bars. (**C**) Two studies, anatomic feature–based profiling and cancer stem cell marker–based profiling, provided a framework for the ISH surveys, LMD and RNA-seq experiments, and ISH validations. (**D**) Informatics included image registration, ontology development, and anatomic feature prediction based on a novel machine learning (ML) analysis of histological data. Search tools enable queries of the data set by tumor, tumor block, and gene expression filtered by anatomic feature, molecular subtype, and clinical information. Searchable manual labels delineating the laser microdissections for 270 RNA-seq samples from the two studies overlay the histology images. The atlas is equipped with image viewers that resolve the histology at 0.5 μm per pixel, a transcriptome browser, an application programming interface, and help documentation. The database has detailed longitudinal clinical information and MRI time courses (table S1). (**E**) This free resource is made available as part of the Ivy Glioblastoma Atlas Project (Ivy GAP). (http://glioblastoma.alleninstitute.org/) via the Allen Institute data portal (www.brain-map.org), the Ivy GAP Clinical and Genomic Database (http://ivygap.org/) via the Swedish Neuroscience Institute (www.swedish.org/services/neuroscience-institute), and the Cancer Imaging Archive (https://wiki.cancerimagingarchive.net).

RNA-seq and ISH assessments of enrichment in PAN, CT, or MVP (Fig. 2, E to I, and table S4). Assessing enrichment of gene expression by ISH required that we calculate the overlap between the expression pattern and our machine learning (ML) annotations for each anatomic feature, which we validated using (i) ML-determined rates of accuracy and precision (table S5); (ii) an inter-neuropathologist test to establish agreement on definitions of anatomic features (fig. S1 and tables S6 and S7); and (iii) neuropathology concordance analyses (tables S8 to S11).

To characterize intratumor genetic heterogeneity across anatomic features, we assessed RNA-seq–derived copy number changes in the features and compared them to the DNA-level copy number variations (CNVs) (*12*) from the corresponding bulk tumor (fig. S3 and table S12). The CT and PAN samples consistently showed gene expression changes corresponding to the CNVs, whereas LE samples did not, as LE samples by definition consist largely of non-neoplastic cells and hence would not harbor the CNVs. On the other hand, MVP samples showed some gene expression changes corresponding to the CNVs, indicating a mixture of tumor and non-neoplastic cells. To evaluate the distribution of somatic mutations targeting key glioblastoma genes within the different anatomic features of this tumor, we used RNA-seq to call single-nucleotide variants (SNVs) in eight genes (*TP53*, *PTEN*, *EGFR*, *ATRX*, *IDH1*, *NF1*, *PIK3R1*, *PIK3CA*) known to harbor recurrent and functionally important mutations in glioblastoma across anatomic features for tumors where there was at least one sample available from each of the LE, CT, PAN, and MVP features (fig. S4 and table S13). We detected somatically mutated alleles in RNA from CT, PAN, and MVP samples, whereas we found only the wild-type variants in LE samples (fig. S4A). The ratio of mutant to wild-type expression was least for MVP relative to CT and PAN samples (fig. S4B). Some of the SNVs occurring across anatomic features were corroborated by ISH data (table S1). Together, the copy number and mutation analyses indicated that LE samples largely consist of non-neoplastic cells, CT and PAN samples largely consist of tumor cells, and MVP samples contain a mixture of tumor and non-neoplastic cells. The observed intratumor heterogeneity in copy number and mutation profiles is consistent with previous studies (*8*, *9*). Only three tumors from our 41-patient cohort harbored the $Arg^{132} \rightarrow His$ mutation in isocitrate dehydrogenase 1 (*IDH1*) (table S1); thus, there was insufficient statistical power for analysis of this mutation by anatomic feature. We did not identify any mutation associated with a particular anatomic feature that predicted overall survival better than the promoter methylation status of the *MGMT* gene in the bulk tumor (fig. S5, A and B) (*15*).

Finally, we developed an admixture model using a 293–gene signature matrix (table S14) for computational decomposition of bulk tumor samples into four anatomic features (LE, CT,

PAN, and MVP) and classified the 122 anatomic feature RNA-seq samples on the basis of histology, admixture (table S14), molecular subtype (*6*), and cell type gene expression signature (table S15) enrichment (fig. S6, A to D, and table S16). Several genes exhibited differential expression across known molecular subtypes of glioblastoma within each anatomic feature (fig. S7, A to C). Enrichment of the cell type gene expression signatures in the anatomic features was consistent with Gene Ontology enrichment analyses (Fig. 2C). The correlation between the anatomic feature gene sets and molecular subtypes (table S16) is broadly consistent with results of previous studies (*8*, *9*). When we applied our admixture model to 167 RNA-seq samples of the TCGA data, we observed similar patterns (fig. S8, A to C, and table S16).

This atlas and the associated database for clinical and genomic data will serve as a useful platform for developing and testing new hypotheses

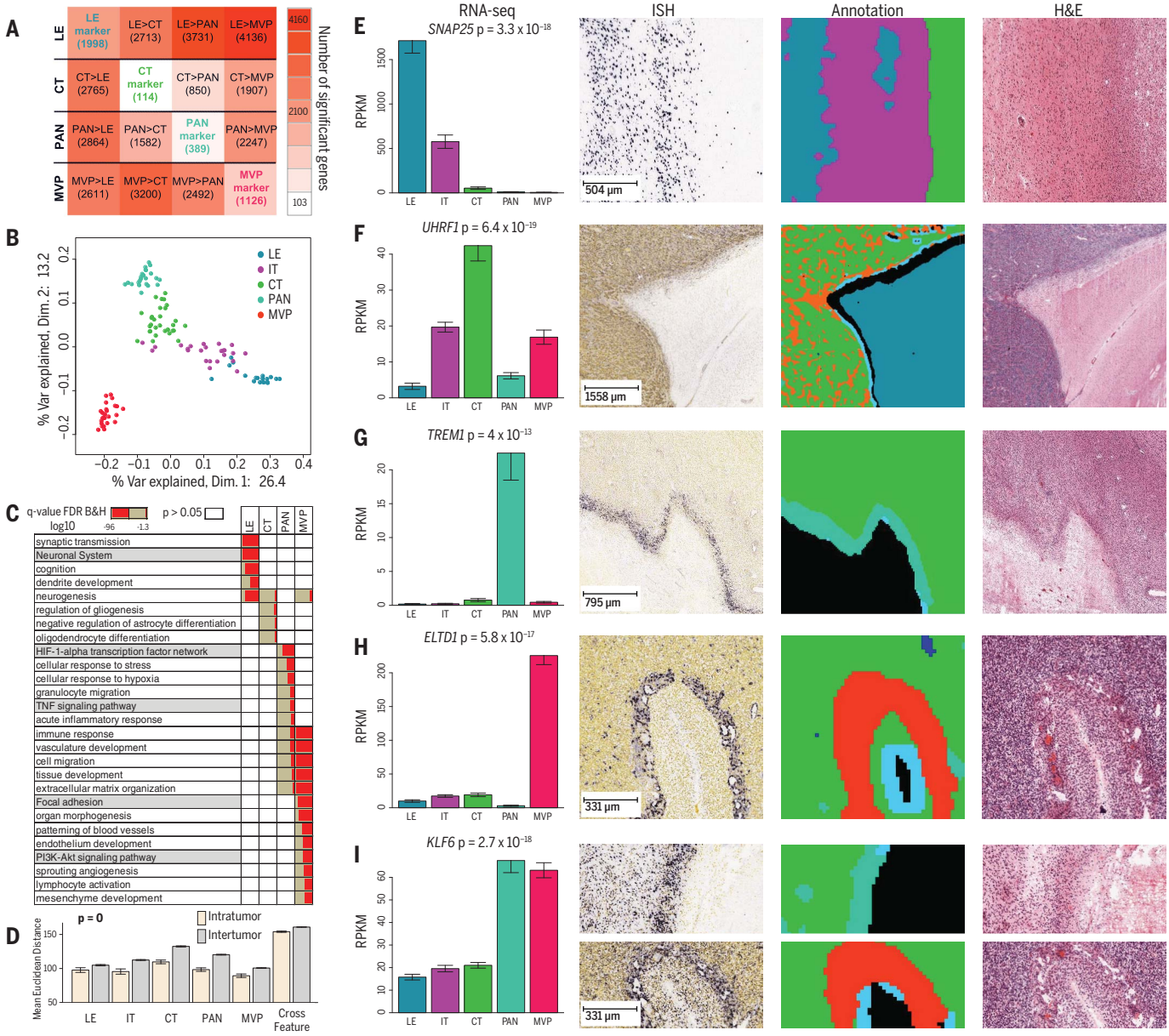

Fig. 2. Gene expression in anatomic features. (**A**) Differential expression matrix based on genes identified in the 122 anatomic feature RNA-seq samples isolated in triplicate from 8 to 10 tumors. Values are numbers of genes whose expression is enriched in the row feature relative to the column feature [false discovery rate < 0.01, relative (fold) change >2; $P < 0.1$, Benjamini-Hochberg corrected]. Values on the diagonal are numbers of genes with higher expression in one feature versus all other features (i.e., top marker genes). (**B**) Multidimensional scaling of all genes reflects anatomic specificity. (**C**) Gene Ontology enrichment analysis. LE and CT were enriched for Gene Ontology terms related to neuronal systems and glial cell differentiation, respectively, whereas PAN was associated with stress, hypoxia, and immune responses, and MVP was related to angiogenesis, immune regulation, and response to wounding. (**D**) Mean Euclidean distance within and between tumors based on hierarchical clustering of all genes in all 122 anatomic feature RNA-seq samples grouped by anatomic feature (figs. S1 and S2). Cross Feature measures variance between anatomic features. (**E** to **I**) Representative marker genes showing RNA-seq expression levels (in RPKM, reads per kilobase of transcript per million mapped reads) for features isolated by LMD, representative ISH, ML annotations for ISH and H&E (hematoxylin and eosin stain), and H&E adjacent to ISH. Color code: blue, LE; purple, IT; green, CT; light blue, PNZ; turquoise, PAN; orange, HBV; red/magenta, MVP; black, necrosis.

related to the pathogenesis, diagnosis, and treatment of glioblastoma. We note that investigators are already leveraging this resource (*16*–*33*). In one preclinical study, Miller *et al.* (*22*) used the atlas to prioritize potential druggable targets based on relationships to tumor microenvironment signatures. In another preclinical study, Yu *et al.* (*31*) used the Ivy GAP data set to identify anatomic regions of glioblastoma that are enriched in tumor-initiating cells. On the basis of this information, they delivered an experimental drug to these tumor regions as a way to maximize its therapeutic effect.

REFERENCES AND NOTES

1. Q. T. Ostrom *et al.*, *Neuro-Oncol.* **19** (suppl. 5), v1–v88 (2017).
2. R. Stupp *et al.*, *N. Engl. J. Med.* **352**, 987–996 (2005).
3. V. Frattini *et al.*, *Nat. Genet.* **45**, 1141–1149 (2013).
4. M. Meyer *et al.*, *Proc. Natl. Acad. Sci. U.S.A.* **112**, 851–856 (2015).
5. Cancer Genome Atlas Research Network, *Nature* **455**, 1061–1068 (2008).
6. R. G. Verhaak *et al.*, *Cancer Cell* **17**, 98–110 (2010).
7. S. Madhavan *et al.*, *Mol. Cancer Res.* **7**, 157–167 (2009).
8. A. Sottoriva *et al.*, *Proc. Natl. Acad. Sci. U.S.A.* **110**, 4009–4014 (2013).
9. A. Kumar *et al.*, *Genome Biol.* **15**, 530 (2014).
10. T. Mazor *et al.*, *Cancer Cell* **28**, 307–317 (2015).
11. J. K. Lee *et al.*, *Nat. Genet.* **49**, 594–599 (2017).
12. A. P. Patel *et al.*, *Science* **344**, 1396–1401 (2014).
13. A. Pen, M. J. Moreno, J. Martin, D. B. Stanimirovic, *Glia* **55**, 559–572 (2007).
14. S. Dong *et al.*, *J. Neuropathol. Exp. Neurol.* **64**, 948–955 (2005).
15. M. E. Hegi *et al.*, *N. Engl. J. Med.* **352**, 997–1003 (2005).
16. S. Müller *et al.*, *Mol. Syst. Biol.* **12**, 889 (2016).
17. M. Mineo *et al.*, *Cell Rep.* **15**, 2500–2509 (2016).
18. M. Cheerathodi *et al.*, *Mol. Cancer Res.* **14**, 1277–1287 (2016).
19. D. Ghosh *et al.*, *Stem Cells* **34**, 2276–2289 (2016).
20. J. Pollak *et al.*, *PLOS ONE* **12**, e0172884 (2017).
21. X. Jin *et al.*, *Nat. Med.* **23**, 1352–1361 (2017).
22. T. E. Miller *et al.*, *Nature* **547**, 355–359 (2017).
23. J. Godlewski *et al.*, *Stem Cell Rep.* **8**, 1497–1505 (2017).
24. Q. Wang *et al.*, *Cancer Cell* **32**, 42–56.e6 (2017).
25. S. Müller *et al.*, *Genome Biol.* **18**, 234 (2017).
26. I. G. Cantanhede, J. R. M. de Oliveira, *Sci. Rep.* **7**, 15271 (2017).
27. Y. Otani *et al.*, *Oncogene* **37**, 777–786 (2018).
28. B. N. Mills, G. P. Albert, M. W. Halterman, *Cancer Microenviron.* **10**, 57–68 (2017).
29. S. Y. Lee, J. K. Kim, H. Y. Jeon, S. W. Ham, H. Kim, *Mol. Cells* **40**, 515–522 (2017).
30. E. Johansson *et al.*, *Cell Rep.* **20**, 1641–1653 (2017).
31. D. Yu *et al.*, *Proc. Natl. Acad. Sci. U.S.A.* **114**, E6147–E6156 (2017).
32. S. C. Kwiatkowski *et al.*, *PLOS ONE* **12**, e0185065 (2017).
33. S. Khagi, C. R. Miller, *Neuro-Oncol.* **19**, 1570–1571 (2017).

ACKNOWLEDGMENTS

We thank the Allen Institute founders, P. G. Allen and J. Allen, for their vision, encouragement, and support. We thank B. Aronow, B. Bernard, D. Ghosh, L. Hood, C. Hubert, J. Lathia, B. Lin, J. Olson, N. Sanai, I. Shmulevich, Q. Tian, and I. Ulasov for providing lists of genes for putative cancer stem cell markers; J. Rich for critical review of the manuscript and helpful comments; N. Hansen from Swedish Research Institute for help with patient consent and clinical data collection; T. Crossley for help with the ivygap.org website; P. Sonpatki for help with neuropathology evaluation forms; and B. Facer and N. Stewart for artistic and administrative assistance, respectively. **Funding:** Supported by The Ben and Catherine Ivy Foundation. R.C.R. was supported by NINDS R01 NS091251 and NCI R01 CA136808 grants (to R.C.R.), and A.I. was supported by NCI grants R01CA178546, U54CA193313, R01CA179044, R01CA190891, and R01NS061776 and The Chemotherapy Foundation (to A.I.). **Author contributions:** G.D.F. and R.B.P. conceived of and secured funding for the creation of the resource. R.B.P., G.D.F., and N.S. designed and (with M.H. and C.C.) supervised the creation of the resource. R.B.P., N.S., J.M., and M.J.H. wrote the manuscript. N.S., J.M., M.L., and C.M. conducted computational data analysis. N.S. and M.L. developed ivygap.org. J.Y., G.D.F., S.W.R., and R.B.P. developed methods for tissue block generation. R.B.P., S.W.R., and R.D. identified anatomic features in tissue blocks. J.Y. and H.L. did genomic studies. P.H. generated cell lines. R.B.P., P.H., and N.S. prepared cancer stem cell marker gene list. R.B.P. compared several platforms for semi-automated annotation of images. X.F. and B.K. were responsible for MRI data collection and processing. C.D. and L.N. managed overall online product design. S.R.N., with assistance from S.W.R., R.D., N.S., and R.B.P., was responsible for semi-automated annotation of H&E images. N.S. used the Definiens platform to count nuclei in images of H&E-stained sections. S.J.W. and D.M. created the ML application for the semi-automated annotation of H&E images. C.R.S. and S.D. provided engineering support. S.W.R. was responsible for neuropathology throughout the creation of the atlas. R.B.P. and N.S. designed and supervised the neuropathology concordance analyses with input from the neuropathologists, C.D.K., P.J.C, M.U., who performed the study, and the biostatisticians, J.S.B.-S., N.S., and H.R.G., as well as R.B.P. who analyzed the data. G.D.F., C.C., and F.R.F. performed surgeries. A.J., P.E.W., J.W.P., A.B., E.L., M.J.H., L.N., J.H., K.S., A.E., and J.H. provided valuable insight and oversight of their teams' contributions to project at the Allen Institute. R.C.R., J.L., E.L., and M.E.B. critically read the manuscript. A.I. critically read and revised the manuscript. J.L. and R.C.R. provided valuable insight regarding cancer stem cell markers. M.E.B. gave input on glioblastoma biology and invasion markers. R.B.P., N.D., and Z.R. were responsible for methods development. R.D., M.F., K.J., D.R., D.S., T.D., and J.H. were responsible for image quality control. J.G. and K.A.S. were responsible for probe design and development. M.C., T.D., D.F., G.G., L.K., C.L., F.L., N.H., F.L., A.So., A.Sz., and W.W. contributed to design, development, and testing of image visualization tools. D.B., T.L., E.M., K.N., E.O., M.R., A.F.B., S.B., N.D., N.M., K.B., N.D., K.B., S.C., A.E., L.G., G.G., J.G., B.W.G., R.H., A.K., N.S., K.A.S., and G.S. contributed to reagent preparation and tissue sample processing through sectioning, histology, ISH, laser microdissection, and imaging. **Competing interests:** The authors declare no competing interests. **Data and materials availability:** A materials transfer agreement was executed on 20 May 2010 between the Allen Institute for Brain Science and Swedish Health Services to govern the transfer of human tissue between the two institutions, consistent with the approved IRB protocol and consent form. Requests for tissue should be addressed to R.B.P. Tissue accrued in the study will be shared with the scientific community depending on the availability, requested amount, and proposed study plan. Requests for tissue sent to Swedish Health Services will be reviewed for merit, IRB consent, and scientific value on a case-by-case basis. The RNA-seq and copy number data are publically available at Gene Expression Omnibus through GEO series accession number GSE107560. The MRIs are available at the Cancer Imaging Archive (https://wiki.cancerimagingarchive.net/display/Public/Ivy+GAP). The atlas image and RNA-seq FPKM data are available as part of the Ivy Glioblastoma Atlas Project (http://glioblastoma.alleninstitute.org/) via the Allen Institute data portal (www.brain-map.org). The detailed clinical data are available through the Ivy GAP Clinical and Genomic Database (http://ivygap.org/) via the Swedish Neuroscience Institute (www.swedish.org/services/neuroscience-institute). **Dedication:** This project is dedicated to G.D.F., a dedicated and talented neurosurgeon as well as a visionary in glioblastoma research, who passed away during the course of the study.

SUPPLEMENTARY MATERIALS

www.sciencemag.org/content/360/6389/660/suppl/DC1
Materials and Methods
Tables S1 to S16
Figs. S1 to S8
References (*34*–*65*)

15 January 2016; accepted 30 March 2018
10.1126/science.aaf2666

STRUCTURAL BIOLOGY

Structural basis for recognition of frizzled proteins by *Clostridium difficile* toxin B

Peng Chen,[1]* Liang Tao,[2]* Tianyu Wang,[1] Jie Zhang,[2] Aina He,[2,3] Kwok-ho Lam,[1] Zheng Liu,[1] Xi He,[4] Kay Perry,[5] Min Dong,[2]† Rongsheng Jin[1]†

Clostridium difficile **infection is the most common cause of antibiotic-associated diarrhea in developed countries. The major virulence factor, *C. difficile* toxin B (TcdB), targets colonic epithelia by binding to the frizzled (FZD) family of Wnt receptors, but how TcdB recognizes FZDs is unclear. Here, we present the crystal structure of a TcdB fragment in complex with the cysteine-rich domain of human FZD2 at 2.5-angstrom resolution, which reveals an endogenous FZD-bound fatty acid acting as a co-receptor for TcdB binding. This lipid occupies the binding site for Wnt-adducted palmitoleic acid in FZDs. TcdB binding locks the lipid in place, preventing Wnt from engaging FZDs and signaling. Our findings establish a central role of fatty acids in FZD-mediated TcdB pathogenesis and suggest strategies to modulate Wnt signaling.**

Clostridium difficile is an opportunistic pathogen that colonizes the colon in humans when the normal gut microbiome is disrupted. The infection leads to disruption of the colonic epithelial barrier, resulting in diarrhea and pseudomembranous colitis and ~30,000 deaths annually in the United States alone (*1*–*5*). The diseases associated with *C. difficile* infection (CDI) are caused by two *C. difficile* exotoxins, toxin A (TcdA) and toxin B (TcdB), which act as glucosyltransferases to inactivate small guanosine triphosphatases, leading to actin cytoskeleton disruption and cell death (*3*, *6*–*8*). Of the two toxins, TcdB alone is capable of causing the full spectrum of diseases in humans because $TcdA^-TcdB^+$ strains have been clinically isolated (*9*–*12*). Chondroitin sulfate proteoglycan 4 (CSPG4), poliovirus receptor-like 3 (PVRL3), and frizzled proteins (FZDs) have been recently identified as TcdB receptors (*13*–*16*), with FZDs thought to be the major receptors in the colonic epithelium (*13*, *17*). FZDs are a family of transmembrane receptors for lipid-modified Wnt morphogens (*18*, *19*). Binding of TcdB to FZDs—especially FZD1, -2, and -7—not only mediates toxin entry but also inhibits Wnt signaling, which regulates self-renewal of colonic stem cells and differentiation of the colonic epithelium (*13*, *20*, *21*). The mechanism by which TcdB specifically recognizes FZDs and inhibits Wnt signaling is unknown.

TcdB is a large multidomain protein (~270 kDa) (Fig. 1A). We first screened and characterized a series of TcdB truncations and narrowed down a short TcdB fragment (residues 1285 to 1804), referred to as the FZD-binding domain (TcdB-FBD) (table S1), which robustly binds to the cysteine-rich domain of FZD2 [residues 24 to 156, referred to as cysteine-rich domain 2 (CRD2)]. Biolayer interferometry (BLI) analysis confirmed that TcdB-FBD binds to CRD2 with an affinity [dissociation constant (K_d) ~ 13 nM] similar to that of full-length TcdB (K_d ~ 19 nM) (fig. S1, A and F) (*13*). We determined the cocrystal structure of TcdB-FBD in complex with human CRD2 at 2.5-Å resolution using TcdB-FBD produced in *Escherichia coli* and CRD2 produced as a secreted protein from human embryonic kidney (HEK) cells (table S2). The structure reveals one TcdB-FBD-CRD2 complex in an asymmetric unit, with a total buried interface of ~1488 $Å^2$ (Fig. 1B). CRD2 adopts the conserved CRD fold with four α helices and two β strands stabilized by five disulfide bridges. The comparison between CRD2 and FZD7-CRD [Protein Data Bank (PDB) 5URV] and FZD8-CRD (PDB 4F0A) yielded root-mean-square deviations of ~0.62 and ~1.13 Å, respectively (*22*, *23*). TcdB-FBD adopts an L shape with its vertex bound by CRD2, and the overall structure of TcdB-FBD is similar to the homologous region in TcdA (Fig. 1B and fig. S2, A and B) (*24*).

A 16-Å-long cylinder-like electron density was observed in a hydrophobic groove in CRD2, which is completely buried between TcdB-FBD and CRD2 (Fig. 1C). The homologous groove in CRD8 binds a palmitoleic acid (PAM) lipid modification of Wnt8, a conserved posttranslational modification crucial for Wnt signaling (*23*, *25*, *26*). The PAM molecule seen in the structure of the CRD8-Wnt8 complex matches the electron density pattern in the hydrophobic pocket between TcdB-FBD and CRD2 (Fig. 1C) (*23*). We assume that this PAM was copurified with CRD2 from HEK cells, although we could not unambiguously determine whether it is PAM or palmitic acid.

This PAM is bound by both CRD2 and TcdB-FBD (Fig. 2A). CRD2 binds to PAM mainly through hydrophobic interactions: residues Q75, F76, M125, and F130 stabilize PAM from the side of its carboxylic group, and residues P78, L79, V82, L124, and F128 stabilize the middle of PAM's hydrocarbon chain (Fig. 2B). This binding mode is similar to how Wnt PAM is stabilized in CRD8 (*23*). The tail of the PAM acyl chain and some hydrophobic PAM-binding residues in CRD8 are exposed to solvent. In the CRD2 complex, these hydrophobic patches, which are energetically suboptimal in an aqueous environment, are fully shielded by TcdB-FBD. Specifically, F1597 of TcdB stabilizes the middle part of PAM, whereas residues L1433, M1437, S1486, L1493, and S1495 (together with V82 and L124 of CRD2) form a hydrophobic pocket to cap the PAM tail protruding from the CRD2 groove (Fig. 2, B and C). This PAM is therefore completely buried, involving ~580 and ~320 $Å^2$ of surface areas with CRD2 and TcdB-FBD, respectively. Besides PAM-mediated interactions, TcdB-FBD engages CRD2 directly through an extensive network of hydrogen bonds and hydrophobic interactions surrounding the lipid-binding groove, which likely provides the major driving force for assembling the complex (Fig. 2, D and E, and table S3). Many of these residues involved in protein-protein interactions also participate in PAM binding, suggesting that binding between TcdB-FBD and CRD is synergistically mediated by both proteins and PAM (Fig. 2F).

To further probe the TcdB-FBD-lipid-FZD binding specificity, we examined binding of selected site-specific mutants of TcdB-FBD to FZDs. We first examined binding of TcdB-FBD variants to immobilized His- or Fc-tagged CRD2 using pull-down assays (fig. S3A) or BLI assays (fig. S1). No exogenous PAM was added in either assays. TcdB-FBD variants carrying mutations that disrupt binding to both PAM and CRD2 (such as F1597G, F1597D, M1437D/L1493A, and L1433D/M1437D/L1493A) did not yield detectable binding in either pull-down or BLI assays (K_d > 10 μM). Mutations at the protein-protein interface (such as D1501A, Y1509A/N1511A, and Y1509A/Q1599A) drastically weakened the TcdB-FBD-CRD2 binding affinity by ~43 to 138 times compared with that of wild-type (WT) TcdB-FBD (fig. S1F). A single point mutation (L1433D) disrupting a hydrophobic pocket in TcdB that accommodates the distal acyl tail of PAM also decreased the binding to CRD2 by ~37 times. None of these TcdB-FBD variants interfere with protein folding, as verified with a thermal shift assay (fig. S4). We then examined binding of TcdB-FBD variants to HeLa cells transiently transfected with full-length FZD2 (Fig. 3A) or stably expressed glycosylphosphatidylinositol (GPI)–anchored FZD7-CRD (fig. S3, B and C). TcdB-FBD variants did not show detectable binding to FZD2 or FZD7-CRD-GPI at the concentration tested (50 nM), whereas

[1]Department of Physiology and Biophysics, University of California, Irvine, Irvine, CA, USA. [2]Department of Urology, Boston Children's Hospital, Department of Microbiology and Immunobiology and Department of Surgery, Harvard Medical School, Boston, MA, USA. [3]Department of Oncology, Affiliated Sixth People's Hospital, Shanghai Jiaotong University, No. 600, Yishan Road, 200233 Shanghai, PRC. [4]F. M. Kirby Neurobiology Center, Boston Children's Hospital, Department of Neurology, Harvard Medical School, Boston, MA, USA. [5]NE-CAT and Department of Chemistry and Chemical Biology, Cornell University, Argonne National Laboratory, Argonne, IL, USA.
*These authors contributed equally to this work.
†Corresponding author. Email: r.jin@uci.edu (R.J.); min.dong@childrens.harvard.edu (M.D.)

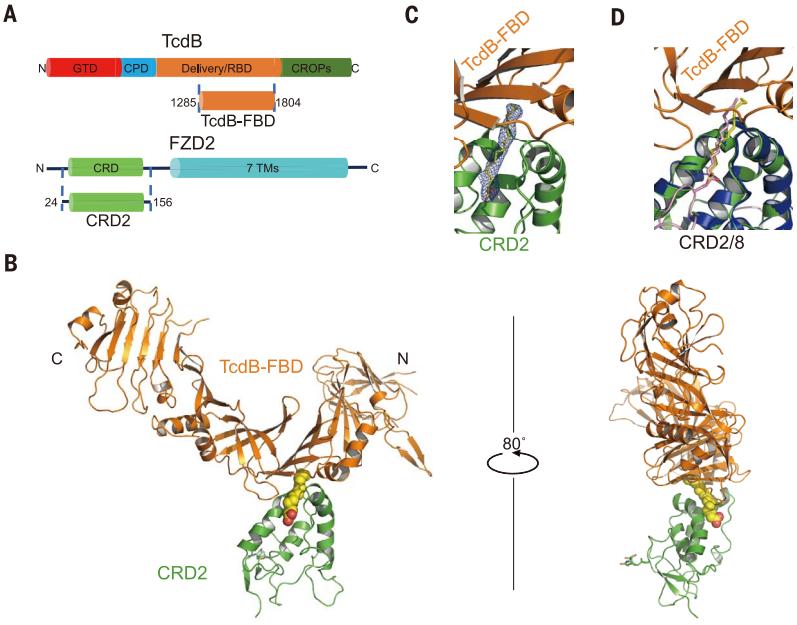

Fig. 1. Overall structure of TcdB-FBD in complex with CRD2. (**A**) Schematic diagrams showing the domain structures of TcdB and FZD2, as well as the two interacting fragments used in this study. GTD, glucosyltransferase domain; CPD, cysteine protease domain; Delivery/RBD, delivery and receptor-binding domain; CROPs, combined repetitive oligopeptides domain; CRD, cysteine-rich domain; 7TMs, 7 transmembrane helices. (**B**) Illustrated representation of the complex, with TcdB-FBD in orange, CRD2 in green, and PAM in a yellow sphere model. An *N*-acetyl glucosamine (NAG) due to N-linked glycosylation on CRD2-N53 is shown as sticks. (**C**) Electron density of the PAM bound between TcdB-FBD and CRD2. An omit electron density map contoured at 2.5σ was overlaid with the final refined model. (**D**) The PAM molecules bound in the TcdB-FBD-CRD2 and the Wnt8-CRD8 (Wnt8 and CRD8 are colored purple and blue, respectively) complexes are shown as yellow and purple sticks, respectively, when the two complexes are superimposed based on CRD2 and CRD8.

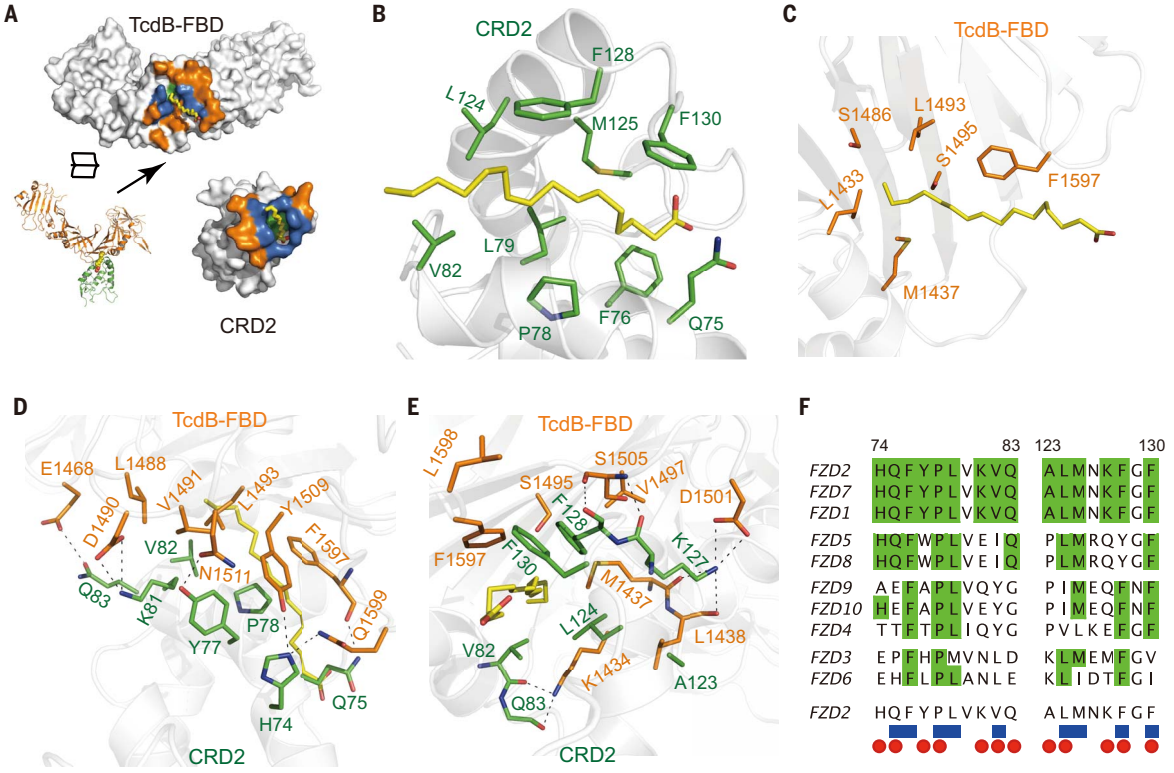

Fig. 2. TcdB-FBD recognizes CRD2 through combined fatty acid– and protein-mediated interactions. (**A**) An open-book view of the TcdB-FBD-CRD2 interface. Residues that participate in protein-protein, protein-lipid, or both are colored orange, green, and blue, respectively. (**B** and **C**) A PAM molecule simultaneously interacts with CRD2 (B) and TcdB-FBD (C). Key PAM-binding residues and PAM are shown as stick models. (Single-letter abbreviations for the amino acid residues are as follows: A, Ala; C, Cys; D, Asp; E, Glu; F, Phe; G, Gly; H, His; I, Ile; K, Lys; L, Leu; M, Met; N, Asn; P, Pro; Q, Gln; R, Arg; S, Ser; T, Thr; V, Val; W, Trp; and Y, Tyr. In the mutants, other amino acids were substituted at certain locations; for example, F1597G indicates that phenylalanine at position 1597 was replaced by glycine.) (**D** and **E**) Two neighboring protein-mediated interfaces between TcdB-FBD and CRD2, which surround the lipid-binding groove in CRD2. (**F**) Amino acid sequence alignment among the 10 human FZDs within the TcdB-FBD–interacting region. Invariable residues are colored green. CRD2 residues that bind to PAM and TcdB-FBD are labeled as blue cubes and red ovals, respectively.

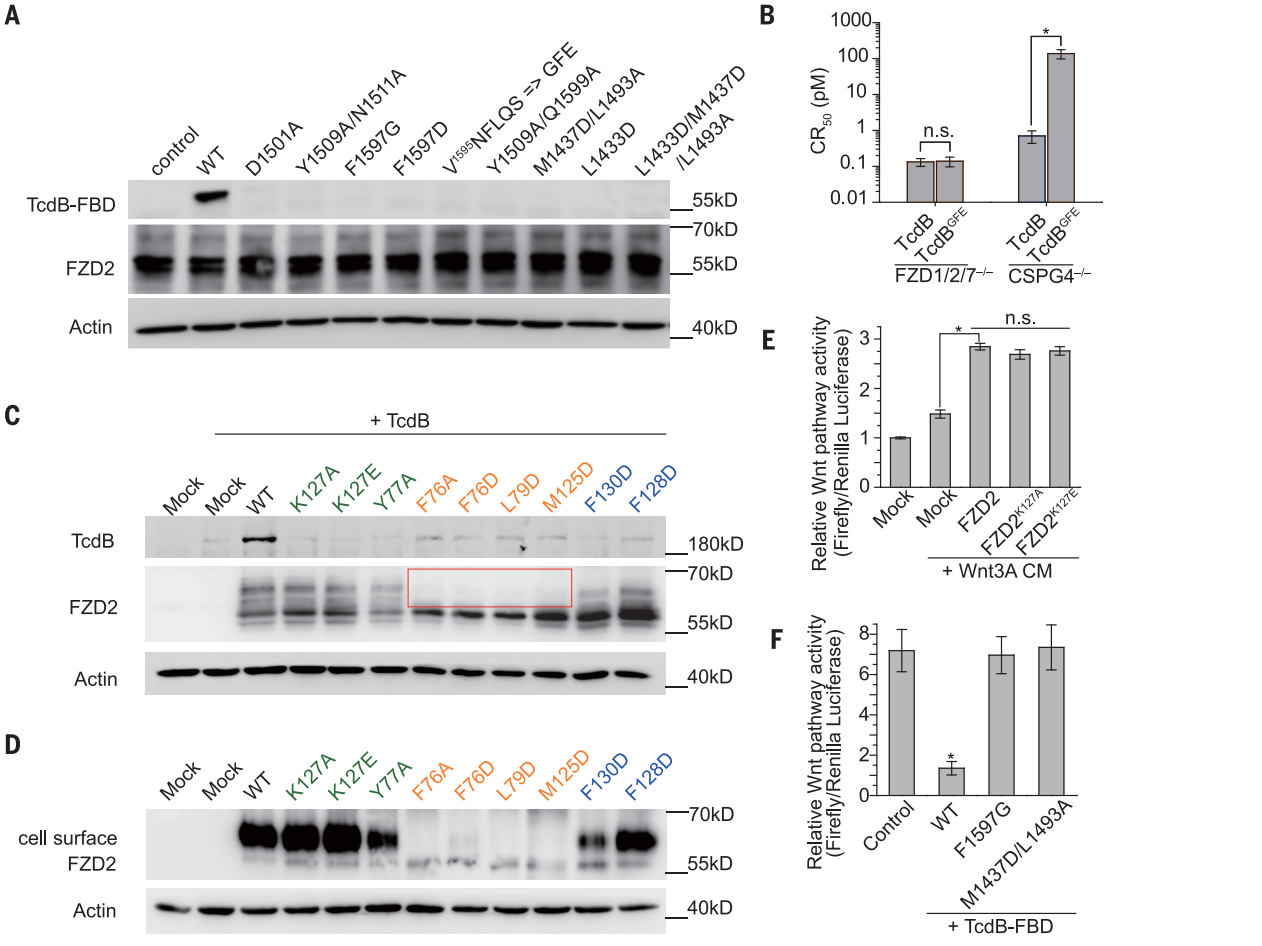

Fig. 3. Structure-based mutagenesis analyses of the interactions between TcdB and FZD2. (**A**) Mutations in TcdB-FBD that disrupt its interactions with PAM and/or CRD2 impaired TcdB-FBD (50 nM) binding to HeLa cells overexpressing FZD2. (**B**) The sensitivity of FZD1/2/7 triple-KO HeLa cells and CSPG4 KO HeLa cells to full-length WT TcdB and TcdB^{GFE} was determined with cell-rounding assays. CR_{50} is defined as the toxin concentration that induces 50% of cells to become round in 24 hours. (**C**) When expressed in HeLa cells, WT FZD2 but not the mutated variants mediated robust binding of full-length TcdB (10 nM) on cell surfaces. Mutations in CRD2 that are located in the protein-protein interface with TcdB, in the core lipid-binding groove, or at the edge of the lipid-binding groove are marked in green, orange, and blue, respectively. Four FZD2 variants lacking detectable levels of glycosylation are highlighted in a box. (**D**) These four FZD2 variants failed to reach cell surfaces as examined by detecting biotinylated FZD2 on cell surfaces. (**E**) FZD2-K127A/E were capable of mediating Wnt signaling to a level similar to that of WT FZD2. (**F**) WT TcdB-FBD but not the mutated variants (F1597G and M1437D/L1493A) inhibited signaling by Wnt3A CM in HEK293T cells as measured with the TOPFLASH reporter assay. Data are mean ± SD, $n = 6$ biologically independent samples, *$P < 0.01$, Mann-Whitney test [(B) and (F)] or Kruskal-Wallis analysis of variance (E).

WT TcdB-FBD bound robustly to these cells. The pull-down (fig. S3A) and the BLI (fig. S1) assays were more sensitive than the cell-based assays (Fig. 3A and fig. S3C) in detecting weak interactions between CRD2 and TcdB-FBD variants, likely as a result of relatively low concentrations of FZD2/7 expressed on the cell surface. The mutagenesis studies thus verify the structural findings and suggest that TcdB exploits a free fatty acid as the co-receptor to engage FZDs.

The CRD2- or PAM-interacting residues in TcdB are not conserved in TcdA (fig. S2C), explaining the unresponsiveness of FZDs to TcdA (*13*). In particular, we found that TcdA and TcdB are distinct in a small area that contains three residues (F1597, L1598, and Q1599) that bind to PAM and CRD2 (fig. S2C). When we replaced this region in TcdB-FBD (^{1595}VNFLQS) with the corresponding residues in TcdA (^{1596}GFE), the mutated TcdB-FBD could no longer bind FZD2, confirming the importance of this region in TcdB for FZD binding (Fig. 3A and figs. S1F and S3A). We then generated a full-length TcdB carrying the same mutations that abolish FZD binding (termed TcdB^{GFE}) and used it as a molecular tool to determine the physiological relevance of FZDs and lipids to the toxicity of TcdB. We first validated the activity of TcdB^{GFE} using a cell-rounding assay (CR_{50}) on FZD1/2/7 knockout (KO) HeLa cells, which still express a high level of CSPG4 that could mediate toxin entry (*13*). As shown in Fig. 3B, TcdB^{GFE} and WT TcdB displayed a similar toxicity on FZD1/2/7 KO HeLa cells, indicating that TcdB^{GFE} was properly folded. To separate the contribution of CSPG4 and FZDs to toxin cell entry, we further tested the activity of TcdB^{GFE} and WT TcdB on CSPG4 KO HeLa cells. Indeed, FZD-binding–deficient TcdB^{GFE} displayed a ~190 times reduced toxicity compared with that of the WT toxin, demonstrating the functional role of FZDs in mediating TcdB binding and entry into cells (Fig. 3B).

The binding site for the lipid co-receptor in FZDs also accommodates the Wnt PAM or exogenous lipids in vitro (*22*, *27*). Do FZDs bind free fatty acids endogenously, and if so, what are their functions? To answer these questions, we designed mutations to selectively disrupt the core of the lipid-binding groove in CRD2 (such as F76A, F76D, L79D, and M125D) and expressed

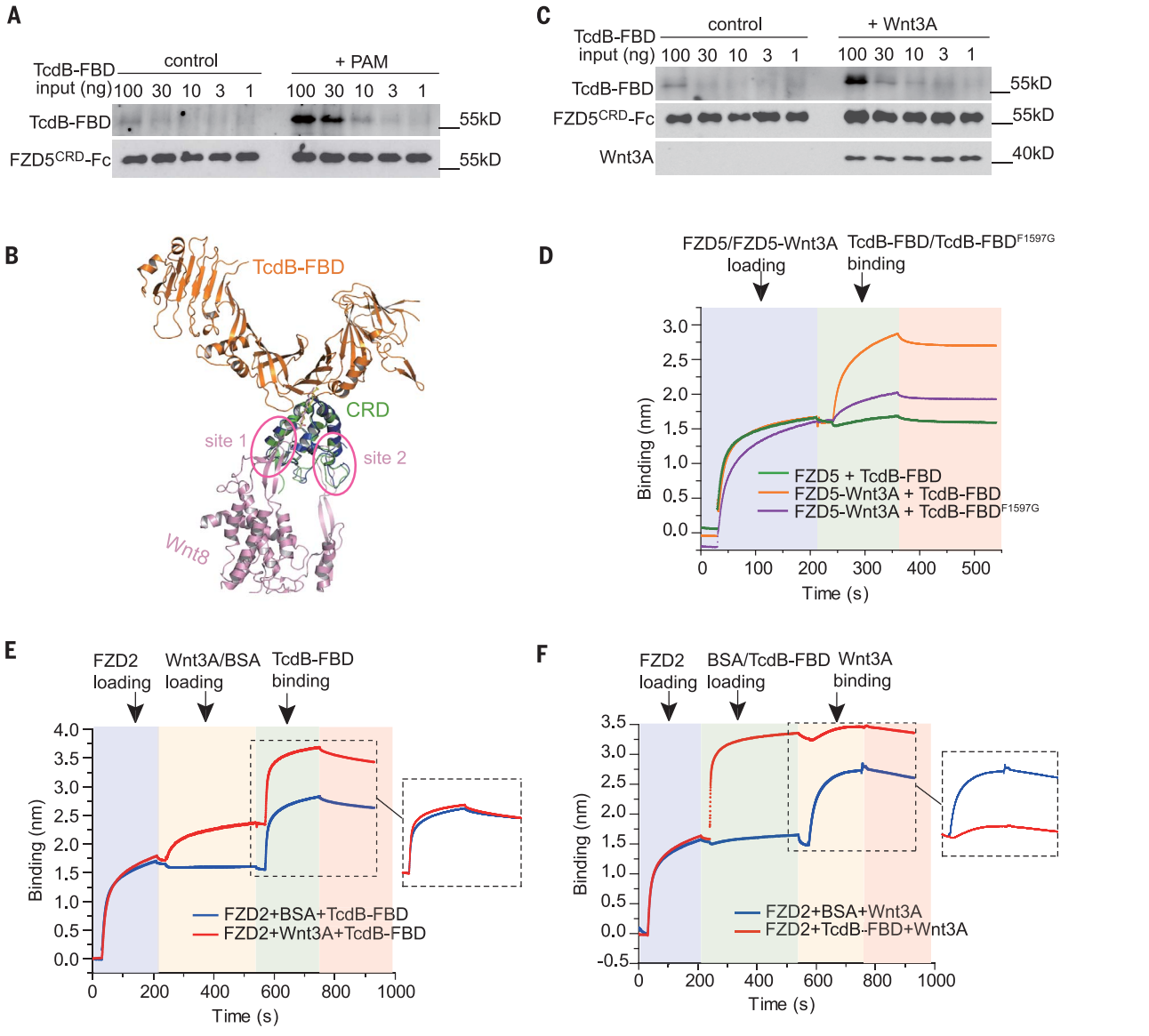

Fig. 4. A free fatty acid facilitates binding of TcdB to FZD-CRDs, which in turn prevents docking of the Wnt PAM. (**A**) Preloading FZD5-CRD with PAM enhanced its binding to TcdB-FBD according to pull-down assays. (**B**) Superimposed structures of the TcdB-FBD-CRD2 and the Wnt8-CRD8 complexes. The two distinct interfaces between Wnt8 (purple) and CRD8 (blue) are highlighted in circles (site 1 and 2). (**C** and **D**) Preloading Wnt3A to FZD5-CRD enhanced its binding to TcdB-FBD according to (C) pull-down assays and (D) BLI assays. The enhancement was minimal for TcdB-FBD-F1597G. Sequential loading of different proteins to the biosensor and binding dissociation are indicated with different background colors. (**E**) Preloading Wnt3A to CRD2 did not interfere with subsequent binding of TcdB-FBD. (**F**) Preloading CRD2 with TcdB-FBD impeded subsequent binding of Wnt3A.

the corresponding full-length mouse FZD2 in CSPG4 KO HeLa cells (residue numbering is based on human FZD2 sequence). The use of CSPG4 KO HeLa cells also allows us to examine the interactions between these lipid-binding–deficient FZD2 variants and TcdB. Although all four FZD2 variants were expressed in cells, they lacked detectable levels of glycosylation (Fig. 3C). Surface biotinylation assays confirmed that these four variants failed to reach the cell surface (Fig. 3D). In comparison, mutating CRD2 residues in the protein-protein interface with TcdB-FBD (such as K127A, K127E, and Y77A) or residues at the edge of the lipid-binding groove (such as F128D and F130D) did not notably alter FZD2 glycosylation and surface expression. We also confirmed that FZD2-K127A/E mediated similar levels of Wnt signaling as WT FZD2 did in cells, demonstrating that they were correctly folded (Fig. 3E, and fig. S5, A and B). These results thus suggest that binding of an endogenous free fatty acid in CRD2 is crucial for proper folding, glycosylation, and/or trafficking of FZD2, providing evidence for the existence and importance of free lipid-FZD interaction in a physiological context. Furthermore, none of these FZD2 variants mediated binding of full-length TcdB when expressed in CSPG4 KO HeLa cells (Fig. 3C), further illustrating the role of FZDs as TcdB receptors.

Besides FZD1, -2, and -7, which are high-affinity receptors for TcdB (*13*), other FZDs likely also bind endogenous fatty acids because the hydrophobic lipid-binding groove in CRD2 is largely conserved across all 10 members of FZDs (Fig. 2F). But subtle amino acid differences in

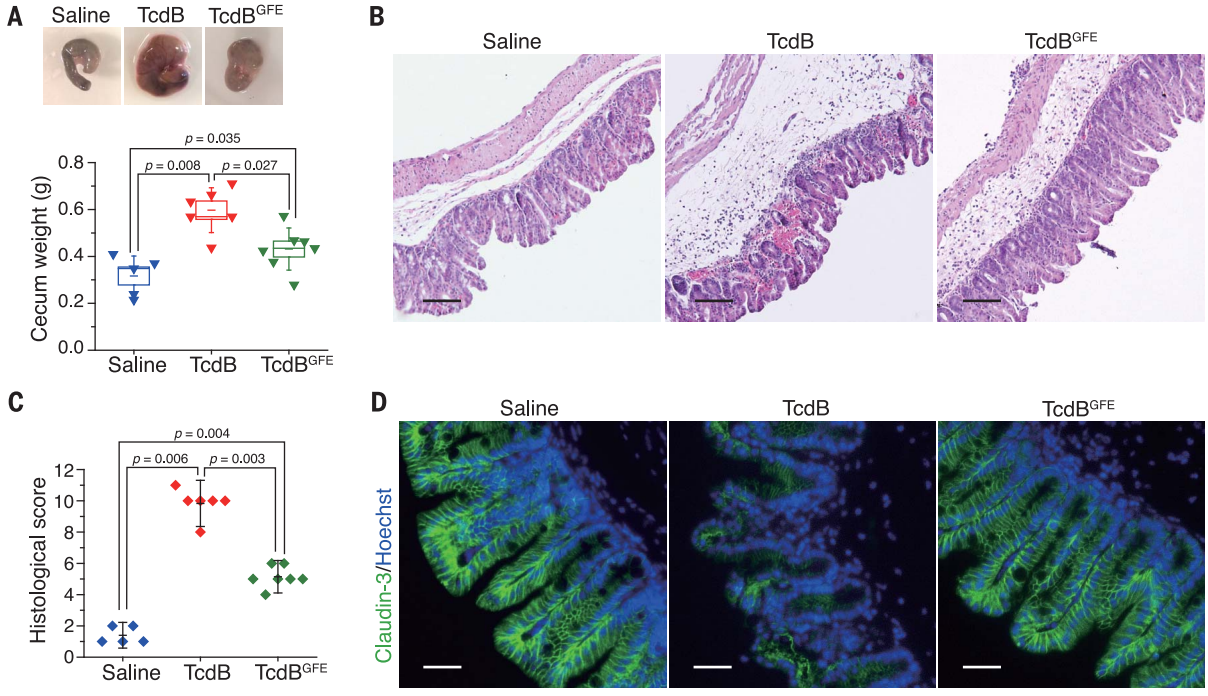

Fig. 5. FZDs and the FZD-bound fatty acids are the major pathologically relevant receptors for TcdB in the colonic tissues. (**A**) WT TcdB (15 μg), TcdB^{GFE} (15 μg), or the saline control was injected into the cecum of WT mice in vivo. The cecum tissues were harvested 12 hours later. The representative cecum tissues were shown, and the weight of each cecum was measured and plotted. Boxes represent mean ± SEM, and the bars represent SD; Mann-Whitney test. (**B** and **C**) Cecum tissue sections were subjected to hematoxylin and eosin staining. The representative images are shown in (B). The histological scores (C) were assessed on the basis of disruption of the epithelia, hemorrhagic congestion, mucosal edema, and inflammatory cell infiltration. Data are mean ± SD; Mann-Whitney test. Scale bar, 100 μm. (**D**) Immunofluorescent staining of epithelial cell junction marker Claudin-3 (green) in ceca from mice injected with saline, TcdB, or TcdB^{GFE} (blue indicates cell nuclei). Scale bar, 50 μm.

this groove or the neighboring region may influence how tightly a fatty acid binds to a CRD. For example, recombinant CRD5 does not contain a free fatty acid, which may have dissociated during CRD5 purification, but it could bind exogenous PAM provided in solution (*22*). We confirmed that CRD5 by itself only weakly pulled down TcdB-FBD, but preincubation of CRD5 with PAM clearly increased its binding to TcdB-FBD (Fig. 4A). This "gain of function" for CRD5 to bind TcdB-FBD aided by the free PAM further supports the notion that a CRD-bound fatty acid is a critical co-receptor for TcdB. Our data suggest that the affinity and specificity of different FZDs toward TcdB are likely determined by a combination of their interactions with free fatty acids, as well as their specific protein-protein contacts with TcdB. For instance, residues Y77, K81, V82, A123, and K127 of CRD2 that contact TcdB are only conserved in FZD1, -2, and -7 (Fig. 2F). Disrupting such protein-protein interactions in FZD2 (such as Y77A and K127A/E) greatly decreased binding by full-length TcdB when expressed in CSPG4 KO HeLa cells (Fig. 3C).

It is well established that Wnt binds to FZD-CRD via the Wnt PAM as a major driving force (*18*, *21*, *23*). The Wnt PAM occupies the same hydrophobic groove in CRD as the free lipid (Fig. 1D). We found that TcdB-FBD can bind to the Wnt-FZD complex using the Wnt PAM as a co-receptor because TcdB-FBD engages CRD2 from the opposite side of the Wnt-binding interface without direct steric competition with Wnt (Fig. 4B). The ability to recognize Wnt-bound FZDs is perhaps particularly advantageous for TcdB to recognize certain FZDs that may have weaker affinities for free lipids. Indeed, we found that preincubation of Wnt3A with CRD5 enhanced binding of TcdB-FBD to CRD5 in pull-down and BLI assays, whereas the enhancement was dramatically reduced for TcdB-FBD-F1597G (Fig. 4, C and D). Similar Wnt-mediated enhancement was also observed for three other CRDs (human FZD4, FZD8, and FZD9) (fig. S6, A to C) and was further confirmed by using full-length TcdB and CRD5 (fig. S6D). Thus, TcdB can use the Wnt PAM, a conserved Wnt posttranslational modification, as a co-receptor to recognize a broad range of FZDs despite their sequence variations.

CRD2 and the preformed CRD2-Wnt3A complex were recognized equally well by TcdB-FBD or full-length TcdB (Fig. 4E and fig. S7A). This suggests that either the free lipid or the Wnt PAM supports TcdB binding to CRD2. By contrast, upon binding to TcdB-FBD or full-length TcdB, CRD2 could no longer bind Wnt3A (Fig. 4F and fig. S7B). This is likely because the Wnt PAM cannot displace the free fatty acid once it is locked in place by TcdB. This is consistent with the observation that TcdB-FBD blocked Wnt3A-induced signaling in cells, whereas the CRD-binding–deficient TcdB-FBD variants did not (Fig. 3F and fig. S5, C and D). Recent studies suggested that Wnt PAM may contribute to CRD dimerization, although the contribution of such FZD dimerization to activate Wnt signaling remains to be fully established (*22*, *27*). Two different CRD dimer configurations have been reported (fig. S8A) (*22*, *27*). Binding of TcdB, or TcdB-FBD, would prevent CRD dimerization in either configuration because of steric competitions, which may also contribute to Wnt signaling inhibition (fig. S8B).

Given our extensive in vitro and ex vivo data demonstrating the role of FZDs and the FZD-bound fatty acids as TcdB receptors, we sought to determine the physiological relevance of TcdB-lipid-FZD interactions to the toxicity of TcdB in vivo. Colonic tissues are the pathological relevant target tissue for TcdB. It has been shown that FZDs are major receptors in the colonic epithelium, whereas CSPG4 is expressed in the subepithelial myofibroblasts but not colonic epithelium (*13*). We therefore used a mouse cecum injection model, which has been previously used to assess TcdB-induced damage to colonic tissues (*28*, *29*). Briefly, a full-length FZD-binding–deficient TcdB variant, TcdB^{GFE} (Fig. 3B); the WT TcdB; or the control saline

solution was injected into cecum of WT mice. Mice were allowed to recover, and cecum tissues were harvested 12 hours later for analysis. WT TcdB induced severe bloody fluid accumulation and vesicular congestion in the cecum, resulting in drastic swelling as expected. By contrast, $TcdB^{GFE}$ induced much less fluid accumulation and no obvious vesicular congestion (Fig. 5A). To further examine the damage to tissues, we carried out histological analysis with paraffin-embedded cecum tissue sections. These tissues were scored according to four histological criteria—including disruption of the epithelium, hemorrhagic congestion, mucosal edema, and inflammatory cell infiltration—on a scale of 0 to 3 (normal, mild, moderate, or severe). WT TcdB induced extensive disruption of the epithelium and inflammatory cell infiltration, as well as severe hemorrhagic congestion and mucosal edema, whereas $TcdB^{GFE}$ induced much less damage on all four criteria (Fig. 5, B and C). We further assessed the integrity of epithelial tight junction by means of immunofluorescent staining for tight junction marker Claudin-3. WT TcdB induced extensive loss of Claudin-3 in the epithelium, whereas the overall morphology of the epithelial tight junction was not changed after treatment with $TcdB^{GFE}$ (Fig. 5D). Taken together, these data further prove that FZDs are the major pathologically relevant receptors for TcdB in the colonic tissues.

Wnt signaling is critical for development, tissue homeostasis, stem cell biology, and many other processes, and its malfunction is implicated in diseases, including a variety of human cancers and degenerative diseases (*21*, *30*). The FZD-antagonizing mechanism exploited by TcdB turns a toxin into a potential pharmacological tool for research and therapeutic applications. The unexpected fatty acid–dependent binding of TcdB to FZDs also exposes a vulnerability of TcdB, which could be exploited to develop antitoxins that block toxin-receptor recognition.

REFERENCES AND NOTES

1. M. Rupnik, M. H. Wilcox, D. N. Gerding, *Nat. Rev. Microbiol.* **7**, 526–536 (2009).
2. L. Heinlen, J. D. Ballard, *Am. J. Med. Sci.* **340**, 247–252 (2010).
3. D. E. Voth, J. D. Ballard, *Clin. Microbiol. Rev.* **18**, 247–263 (2005).
4. J. J. Hunt, J. D. Ballard, *Microbiol. Mol. Biol. Rev.* **77**, 567–581 (2013).
5. W. K. Smits, D. Lyras, D. B. Lacy, M. H. Wilcox, E. J. Kuijper, *Nat. Rev. Dis. Primers* **2**, 16020 (2016).
6. T. Jank, K. Aktories, *Trends Microbiol.* **16**, 222–229 (2008).
7. X. Sun, T. Savidge, H. Feng, *Toxins (Basel)* **2**, 1848–1880 (2010).
8. R. N. Pruitt, D. B. Lacy, *Front. Cell. Infect. Microbiol.* **2**, 28 (2012).
9. D. Drudy, S. Fanning, L. Kyne, *Int. J. Infect. Dis.* **11**, 5–10 (2007).
10. D. Lyras *et al.*, *Nature* **458**, 1176–1179 (2009).
11. S. A. Kuehne *et al.*, *Nature* **467**, 711–713 (2010).
12. G. P. Carter *et al.*, *mBio* **6**, e00551 (2015).
13. L. Tao *et al.*, *Nature* **538**, 350–355 (2016).
14. P. Yuan *et al.*, *Cell Res.* **25**, 157–168 (2015).
15. M. E. LaFrance *et al.*, *Proc. Natl. Acad. Sci. U.S.A.* **112**, 7073–7078 (2015).
16. P. Gupta *et al.*, *J. Biol. Chem.* **292**, 17290–17301 (2017).
17. N. Terada *et al.*, *Histochem. Cell Biol.* **126**, 483–490 (2006).
18. B. T. MacDonald, X. He, *Cold Spring Harb. Perspect. Biol.* **4**, a007880 (2012).
19. Y. Wang, H. Chang, A. Rattner, J. Nathans, *Curr. Top. Dev. Biol.* **117**, 113–139 (2016).
20. A. Gregorieff, H. Clevers, *Genes Dev.* **19**, 877–890 (2005).
21. R. Nusse, H. Clevers, *Cell* **169**, 985–999 (2017).
22. A. H. Nile, S. Mukund, K. Stanger, W. Wang, R. N. Hannoush, *Proc. Natl. Acad. Sci. U.S.A.* **114**, 4147–4152 (2017).
23. C. Y. Janda, D. Waghray, A. M. Levin, C. Thomas, K. C. Garcia, *Science* **337**, 59–64 (2012).
24. N. M. Chumbler *et al.*, *Nat. Microbiol.* **1**, 15002 (2016).
25. R. Takada *et al.*, *Dev. Cell* **11**, 791–801 (2006).
26. K. Willert *et al.*, *Nature* **423**, 448–452 (2003).
27. Z. J. DeBruine *et al.*, *Genes Dev.* **31**, 916–926 (2017).
28. Y. Zhang *et al.*, *Anaerobe* **48**, 249–256 (2017).
29. K. M. D'Auria *et al.*, *Infect. Immun.* **81**, 3814–3824 (2013).
30. Z. Steinhart *et al.*, *Nat. Med.* **23**, 60–68 (2017).

ACKNOWLEDGMENTS

Funding: This work was partly supported by National Institute of Health (NIH) grants R01AI091823, R01 AI125704, and R21AI123920 to R.J.; R01 NS080833 and R01 AI132387 to M.D; and R01GM057603 and R01GM126120 to X.H. M.D. and X.H. also acknowledge support by the Harvard Digestive Disease Center (NIH P30DK034854) and Boston Children's Hospital Intellectual and Developmental Disabilities Research Center (NIH P30HD18655). M.D. holds the Investigator in the Pathogenesis of Infectious Disease award from the Burroughs Wellcome Fund. X.H. is an American Cancer Society Research Professor. NE-CAT at the Advanced Photon Source (APS) is supported by a grant from the National Institute of General Medical Sciences (P41 GM103403). The Pilatus 6M detector on 24-ID-C beam line is funded by a NIH-ORIP HEI grant (S10 RR029205). Use of the APS, an Office of Science User Facility operated for the U.S. Department of Energy (DOE) Office of Science by Argonne National Laboratory, was supported by the U.S. DOE under contract DE-AC02-06CH11357. **Author contributions:** M.D. and R.J. conceived the project. P.C., T.W., K.-h.L., Z.L., and R.J. carried out the protein expression, purification, characterization, structure determination and analysis, and structure-based mutagenesis. L.T., A.H., J.Z., and M.D. performed structure-based mutagenesis, all the functional characterization, and BLI binding studies. K.P. collected the x-ray diffraction data. X.H. helped with Wnt signaling assays and provided advice. P.C., L.T., M.D., and R.J. wrote the manuscript with input from other authors. **Competing interests:** A provisional patent application on using TcdB-FBD to modulate Wnt signaling has been filed jointly by Boston Children's Hospital and University of California, Irvine. **Data and materials availability:** Coordinates and structure factors of the TcdB-FBD-CRD2 complex have been deposited in PDB under accession code 6C0B. All other data are available in the manuscript or the supplementary materials.

SUPPLEMENTARY MATERIALS

www.sciencemag.org/content/360/6389/664/suppl/DC1
Materials and Methods
Figs. S1 to S11
Tables S1 to S3
References (*31*–*36*)

12 October 2017; accepted 4 April 2018
10.1126/science.aar1999

gairdner
LES PRIX CANADA GAIRDNER AWARDS

Do you know a DESERVING biomedical or global health researcher?

Gairdner invites the scientific community to **nominate qualified scientists** for the 2019 Canada Gairdner Awards

Consider nominating researchers for the following three awards:

THE CANADA GAIRDNER INTERNATIONAL AWARD recognizes outstanding biomedical scientists who have made original contributions to medicine with the goal of contributing through research to increased understanding of human biology and disease.

THE JOHN DIRKS CANADA GAIRDNER GLOBAL HEALTH AWARD recognizes the world's top scientists who have made outstanding achievements in global health research. Nominees should be individuals who have made major scientific advances with a significant impact on health outcomes in the developing world.

THE CANADA GAIRDNER WIGHTMAN AWARD recognizes exceptional leadership in Canadian medical science. Nominees should also have a high-level sustained research career in a biomedical discipline.

Deadline is October 1, 2018. Learn more at www.gairdner.org

@gairdnerawards **gairdner.org**

CELEBRATING EXCELLENCE CONVENING LEADERS INSPIRING THE NEXT GENERATION

want new technologies?

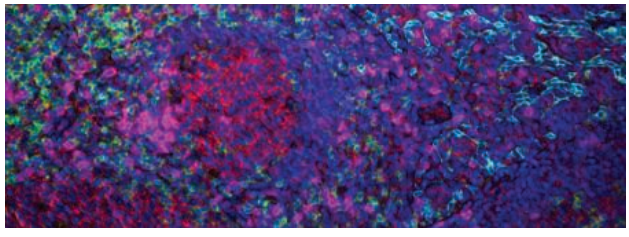

antibodies
apoptosis
biomarkers
cancer
cytometry
data
diseases
DNA
epigenetics
genomics
immunotherapies
medicine
microbiomics
microfluidics
microscopy
neuroscience
proteomics
sequencing
toxicology
transcriptomics

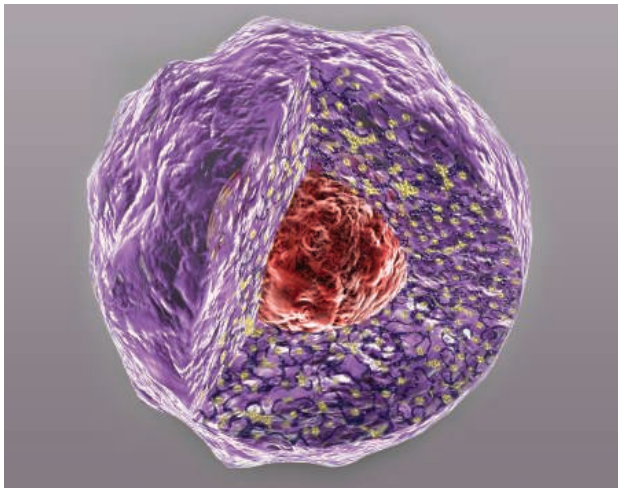

watch our webinars

Learn about the latest break-throughs, new technologies, and ground-breaking research in a variety of fields. Our expert speakers explain their quality research to you and answer questions submitted by live viewers.

VIEW NOW!
webinar.sciencemag.org

Science
AAAS

Brought to you by the *Science*/AAAS Custom Publishing Office

@SciMagWebinars

Restore vision with software.

Not only THINGS but even the BRAIN and CELLS connect to the Internet. For example, it is no longer a dream for blind people to regain their vision through software control. The NEW.VISION project is now on track to make it a reality. Check out our website for details.

SOFTWARE-BASED VISION RESTORATION PROJECT

NEW.VISION

HTTPS://WWW.NEWVISION-PRJ.COM/EN

JIG-SAW INC. (TSE Mothers Stock Code: 3914)
Otemachi Financial City Grand Cube 18th Floor, 1-9-2 Otemachi, Chiyoda-Ku, Tokyo
https://www.jig-saw.com/en

JIG-SAW

PCR: Thirty-five years and counting

In the 35 years since its invention, polymerase chain reaction (PCR) has become a standard technique in laboratory biology, but scientists continue to find groundbreaking—and even life-saving—applications for it. **By Alan Dove**

In May 1983, Kary Mullis, then a scientist at the Cetus Corporation in Emeryville, California, synthesized some oligonucleotides, mixed them with a small amount of template DNA, and added a polymerase enzyme and a few other reagents. After a series of incubations, the polymerase had copied the template many times over in a chain reaction, just as Mullis had hoped.

Mullis eventually moved away from the scientific mainstream, and Cetus was swallowed by a series of other companies, but PCR persisted. Like the DNA templates it targets, PCR has been replicated, amplified, and extended into laboratories worldwide. Dedicated thermal cyclers and related tools flood the market, vendors sell a wide selection of thermostable polymerases, and undergraduates worldwide learn the technique in introductory biology courses.

Now marking its 35th anniversary, PCR has become a ubiquitous laboratory tool. Nonetheless, researchers, engineers, and physicians are still finding ways to propel it into new territories. A sampling of a few of these efforts shows just how far PCR's reach has grown: from dairies to clinics, and from classrooms to outer space.

The launch sequence

The primary hardware component of PCR is the thermal cycler, a machine capable of heating and cooling sample tubes rapidly, and maintaining them at precise temperatures for specific periods of time. Though three decades of development and competition have improved these machines immensely, they are still relatively heavy, power-hungry, and expensive. As a result, one of the defining techniques of modern molecular biology has remained stubbornly inaccessible to educators and unusable in many remote locations.

"PCR is one of the most important [research] technologies, and yet it is one of the most limiting when you're outside of the lab because of the size and cost" of the equipment, says Zeke Alvarez-Saavedra, geneticist and cofounder of **MiniPCR** in Cambridge, Massachusetts. Frustrated by PCR's persistent immobility, Alvarez-Saavedra teamed with molecular neurobiologist Sebastian Kraves in 2013 to build a portable thermal cycler.

Most thermal cyclers control their temperatures using Peltier junctions, thermoelectric devices that can switch rapidly between heating and cooling. Unfortunately, Peltier junctions are inefficient, and the components required to operate them keep PCR machines heavy and greedy for electricity.

Alvarez-Saavedra and Kraves took a different approach, heating the samples with a thin-film resistive heater similar to the window defrosters found in cars. For cooling, the team uses a simple fan. A microcontroller drives the heating, cooling, and incubation cycles. The simpler design made the machine much smaller and lighter than ordinary thermal cyclers, and brought other benefits too. "When you make something smaller, it has less parts and the power supply is smaller ... so that helps reduce the cost," says Alvarez-Saavedra.

As they had hoped, the low-cost MiniPCR system immediately appealed to schools. "Going through high school without being able to get close to biotechnology was kind of a pain point for us [when we were] becoming scientists, so we wanted to do away with those barriers," says Kraves. The company has also developed a small, simple agarose gel electrophoresis system as a companion product. A complete kit with the MiniPCR thermal cycler, gel system, and accessories sells for less than USD 1,000, putting it well within the budgets of many school systems.

Upcoming features
Proteomics: Big Data Sharing—June 15 ■ Genomics: Pharmacogenomics—September 28 ■ Animal Models: Better Mouse Models—October 12

Like the DNA templates it targets, PCR has been replicated, amplified, and extended into laboratories worldwide.

Though schools have become a major market for MiniPCR, others have been quick to adopt the platform as well. Kraves says field scientists, animal breeders, and food companies have all put the system to use, often finding it cheaper and faster to do their own PCR-based assays on the spot rather than send samples to a remote lab.

The most surprising call, though, came from engineers working on the International Space Station. "We never really designed the technology to be space-friendly, so we were surprised when the space agencies ... told us it was very well designed for space flight," says Kraves. The MiniPCR system is now the core component of the ongoing Genes in Space competition, where secondary school students propose PCR-based experiments that are then carried out in microgravity by astronauts on the space station.

Smartphone PCR

MiniPCR was the first company to get PCR into space, but they are not the only one trying to make the technique cheaper and more portable. **Ahram Biosystems** in Seoul, South Korea, sells the Palm PCR miniaturized thermal cycler, which is similar to the MiniPCR device. Meanwhile, **Biomeme** in Philadelphia, Pennsylvania, is taking the portable PCR idea to a new level, extending it to include real-time PCR.

In real-time or quantitative PCR (qPCR), experimenters use fluorescent markers to monitor the progress of PCR amplification continuously. By measuring the rate at which new DNA copies appear, researchers can calculate how many template molecules must have been in the starting sample. They can also read results directly from the PCR reaction tubes without having to run agarose gels. All that monitoring and calculating, however, requires substantial computing power and additional equipment, making qPCR even more complicated and expensive than standard PCR.

At Biomeme, cofounders Marc DeJohn, Jesse van Westrienen, and Max Perelman thought that an unrelated trend might help bring qPCR out of the lab. "We thought, 'hey, everybody's got a smartphone in their pocket,' [and] we didn't really see anybody using them for molecular diagnostics," says van Westrienen. While addressing the same engineering problems MiniPCR faced with its thermal cycler, Biomeme also tackled the difficulties of adding optical sensors via a smartphone application that can both control and monitor qPCR reactions, and shelf-stable reagent kits for sample preparation.

For field use, "sample prep is arguably the most difficult thing ... and one of our focuses from day one has been to develop a very simple product that doesn't require any expertise or special lab equipment," says van Westrienen. The result is a catalog of kits designed for different applications, each with freeze-dried reagents and primers premeasured in sample tubes.

Perelman says that by using one of the company's kits, a minimally trained experimenter can turn a crude sample into a set of qPCR reactions ready for the thermal cycler in a few minutes. The machine itself has a dock compatible with standard smartphone connectors. Biomeme's web-based data portal can store the resulting raw data, which researchers can analyze online or download to their own computers.

At about USD 4,000, the current Biomeme device is considerably more expensive than MiniPCR's system, but Perelman argues that it offers additional utility: "You can complete everything in under an hour... just left swipe or right swipe in the app and [you're] able to see the amplification in real time." Perelman adds that the company is now working with defense and law enforcement users as well as field scientists and food companies.

The quick and the dead

While portable PCR is expanding the technique's reach dramatically, researchers worldwide continue to push its capabilities forward in countless incremental ways as well. The problem of distinguishing live from dead bacteria provides a good example.

PCR is exquisitely sensitive and specific for detecting nucleic acid sequences, but simply knowing that a particular DNA or RNA sequence is present doesn't prove it's associated with a live organism. That's a major problem in the food industry, where both pasteurized and unpasteurized foods will test positive for pathogenic bacteria by PCR, even though the bacteria are safely dead in the former and dangerously alive in the latter. As a result, food labs have long relied on relatively slow, cumbersome culture assays for definitive testing.

DNA crosslinking reagents that can only penetrate dead bacteria provided the first major advance in this field. Crosslinking prevents the dead bacteria's DNA from amplifying in the subsequent PCR reaction. The first generation of these reagents was hard to work with, requiring a darkroom and careful cold storage. More recently, Takashi Soejima and colleagues at **Morinaga Milk Industry** in Kanagawa, Japan, have developed stable, light-tolerant compounds that similarly target dead bacteria. The team's most recent work involved cont.>

Featured participants

Ahram Biosystems
ahrambio.com

Biodesix
www.biodesix.com

Biomeme
biomeme.com

Bio-Rad
www.bio-rad.com

East Carolina University
www.ecu.edu

LaCAR MDx Technologies
www.lacar-mdx.com

MiniPCR
www.minipcr.com

Morinaga Milk Industry
www.morinagamilk.co.jp/english

palladium-based reagents that selectively interfered with PCR amplification of DNA from dead, but not live bacteria. Combining the palladium reagents with qPCR yielded a test that could replace the older, more expensive techniques, streamlining production in dairies and other food facilities (*1*).

Getting the drop on cancer

Researchers and equipment makers have also made more radical modifications to PCR by borrowing technologies from other fields. One such effort yielded droplet digital PCR (ddPCR), which combines aspects of fluorescence-activated cell sorting with conventional PCR. Though the protocol for ddPCR is somewhat complicated, it's also become highly automated. Indeed, **Bio-Rad** in Hercules, California, now sells complete ddPCR machines that can run the entire procedure automatically. In these systems, a sprayer separates a prepared PCR reaction into thousands of nanoliter-size droplets, then keeps the droplets separate during the thermal cycling steps. Each droplet hosts its own series of amplifications, which the machine then sorts with fluorescent markers to detect target sequences.

ddPCR has proven particularly useful for detecting scarce targets in samples with very high background levels of nontarget DNA, such as DNA tumor markers circulating in patient blood samples. The technique has become robust enough that at least one company, **Biodesix** in Boulder, Colorado, now offers clinical tests called "liquid biopsies," based on ddPCR. Using a small blood sample, the Biodesix test can quickly identify the precise mutations in a lung cancer patient's tumor, allowing doctors to pick the most effective drugs for that tumor type.

"Once we know the exact mutations, there are targeted therapies that can make a difference in their outcome, and that's ... shifting the entire paradigm of how we treat patients," says Mark Bowling, Paul R. and Kathryn M. Hettinger Walker Distinguished Professor of Clinical Oncology at **East Carolina University** in Greenville, North Carolina, and an early adopter of the new test. While conventional biopsy analysis and sequencing can yield the same information, the Biodesix test is much faster. "We can get test results back within three days," says Bowling. Standard biopsy testing can take over two weeks. Bowling says the difference can literally be life or death for patients whose tumors will respond to targeted therapies.

Because it's based on PCR, the Biodesix test has room to expand, as drug makers release more genetically targeted treatments. However, Bowling says that even with the limited selection of current targeted chemotherapy drugs, knowing a patient's exact tumor type already changes his team's treatment strategy about one third of the time.

Building a better cycle

Clinical tests have always been a major focus for PCR developers, but sometimes the technique's requirements have held it back. The first proof-of-principle publication describing Mullis' PCR technique demonstrated how it could be used to identify the hemoglobin mutation responsible for the sickle-cell trait (*2*). Unfortunately, PCR remains too expensive for many clinical labs in sub-Saharan Africa, where sickle-cell anemia is endemic.

Even as PCR continues to expand into new areas, these and other limitations have inspired numerous researchers to develop alternative nucleic acid amplification techniques. Many of these methods operate with similar principles but offer different sets of benefits. Multiple displacement amplification, which uses a highly processive polymerase, has become a standard technique in genomic sequencing, while rolling-circle amplification, which can copy a target sequence repeatedly onto a single strand of DNA, has found wide use in biochemistry.

Meanwhile, loop-mediated isothermal amplification (LAMP) has become a popular choice for researchers who want to get DNA-based tests into rural settings. As its name implies, LAMP uses an enzyme that can open and repeatedly copy a DNA molecule at a constant temperature, eliminating the need for expensive thermal cyclers.

That's appealing for companies like **LaCAR MDx Technologies** in Liège, Belgium, which is trying to develop clinical tests for use in less-developed countries. "We were just looking for a way to make molecular genetic testing easier. You could use some cartridge or [PCR device], but then you need to have expensive materials and complicated technology," says Arnaud Allaer, LaCAR's CEO.

Instead, the company began working with LAMP, and quickly discovered that it was extremely robust. Besides operating without a thermal cycler, the company's LAMP-based assays can identify point mutations in a gene from fresh or frozen blood samples, or even dried blood spots on blotter paper, without requiring a DNA extraction step. Finally fulfilling the promise of the original PCR paper, LaCAR has now developed an inexpensive, robust test for the sickle-cell trait based on their findings. "We have done one clinical trial at the University of Liège, [and] we'll do one also in the Congo," says Allaer (*3*).

Whether they're making portable thermal cyclers, using cutting-edge PCR tests for rapid cancer diagnosis, or exploring other techniques to break free of PCR's limitations, experts in the field are optimistic about the next 35 years of DNA amplification. "It's an exciting time," says Bowling.

References

1. T. Soejima, K. Iwatsuki, *Appl. Environ. Microbiol.* **82**, 6930–6941 (2016).
2. R. K. Saiki *et al.*, *Science* **230**, 1350–1354 (1985).
3. L. Detemmerman, S. Olivier, V. Bours, F. Boemer, *Hematology* **23**, 181–186 (2018).

Alan Dove is a science writer and editor based in Massachusetts.

Real-Time PCR Thermal Cyclers

The qTOWER^3 product family assures accurate, real-time PCR results that benefit from precise temperature control in the sample block, regardless of the number of samples used. A patented, fiberoptic shuttle system with its unique light source, composed of four high-performance LEDs, guarantees the ideal excitation of known fluorescent dyes up to the deep-red range. In the process, the detection module can accept up to six different color filter modules. The silver-block technology of the quantitative PCR cyclers offers fine control of ±0.1°C over the entire 96-well block in a 0.2-mL format. Thanks to the gradient function, the device can be optimally adapted to new assays. Cyclers are available either as standalone devices with integrated touchscreen operation (10 in.) or as computer-aided systems. The software includes a broad spectrum of optimized analysis algorithms, including absolute and relative quantification, delta-delta cycle threshold (ddCt) method, PCR efficiency, allelic discrimination, endpoint detection, and melting curve and protein analysis.

Analytik Jena
For info: +49-(0)-3641-77-7444
www.analytik-jena.de/en

Taq DNA Polymerase

BioReady Taq Polymerase is a great choice for your everyday PCR needs. This recombinant DNA polymerase is optimized for improved efficiency, and can amplify between 50 base pairs (bp) and 5,000 bp. When used with any of our thermal cyclers, protocols can be completed in less than 1 hour. BioReady Taq is manufactured under stringent GMP control, and though we don't recommend it, this ultrapure enzyme extract is still fully active after days at 37°C. It is also a great enzyme to consider for dramatically reducing the cost of your quantitative PCR experiments.

Bulldog Bio
For info: 603-570-4248
www.bulldog-bio.com/bioreadyrtaq.html

PCR Machine

Eppendorf's new Mastercycler X50 accommodates PCR with outstanding speed and optimization capabilities. With heating rates averaging 10°C/s, Eppendorf provides a rapid 96-well cycler compatible with standard-format consumables. PCR optimization reaches a new magnitude with the innovative 2D-Gradient, which brings totally new expectations for PCR yields and specificity. Additionally, the intuitive touchscreen interface helps users program the PCR cycler even faster, and connectivity to Eppendorf's VisioNize software offers a broad range of monitoring functions.

Eppendorf
For info: 800-645-3050
www.eppendorf.com

SNP Genotyping System

Integrated DNA Technologies' rhAmp SNP Genotyping System enables researchers to make accurate, confident, single-nucleotide polymorphism (SNP) calls both quickly and cost-effectively. rhAmp technology uses a unique ribonuclease H2/DNA polymerase two-enzyme system coupled with RNA–DNA hybrid primers, to eliminate nonspecific amplification and primer-dimer formation, which are challenges for other genotyping chemistries. The rhAmp SNP chemistry matches the current market leader for accuracy (greater than 99.5% call accuracy in over 90% of assays), and also provides simple, fast, and affordable results, with assays shipped in less than seven business days. Saving time and simplifying workflow, rhAmp SNP features a simple, single-tube assay setup that is easily automated and designed to work on all leading commercially available quantitative PCR platforms. Custom assay design is also available for proprietary and nonhuman SNP designs. The rhAmp Genotyping Design Tool can deliver designs in difficult sequence regions, accommodating very short amplicons (as small as 40 base pairs).

Integrated DNA Technologies
For info: 800-328-2661
www.idtdna.com

PCR Beads

PuReTaq Ready-To-Go PCR Beads are premixed, predispensed, single-dose reactions optimized for performing standard PCR amplifications. The use of recombinant PuReTaq DNA polymerase and other high-purity reagents guarantees reliable, robust performance in both endpoint and real-time fluorescence-based PCR amplifications, and ensures the lowest possible levels of contaminating prokaryotic and eukaryotic nucleic acids. These beads are preformulated to provide greater reproducibility between reactions, minimize pipetting steps, and reduce the potential for pipetting errors and contamination. The only additional reagents required are water, primers, and template DNA. The beads come predispensed into either 0.2-mL or 0.5-mL PCR tubes. The 0.2-mL tubes are also supplied in a 96-well (8 × 12) plate format, allowing individual strips of eight tubes to be easily removed. This flexibility enables use of the entire plate, strips of eight, or individual 0.2-mL tubes.

GE Healthcare Life Sciences
For info: 800-526-3593
www.gelifesciences.com

PCR Plates

FrameStar plates feature thin-walled polypropylene tubes for optimum PCR results, combined with a rigid polycarbonate frame to increase the plate's thermal stability during PCR. Unlike a standard polypropylene plate, the FrameStar plate will not warp and expand with rapid heating and cooling, so the integrity of the seals will remain consistent and less of your sample will evaporate. With FrameStar, you can spend less on expensive reagents because you will retain more during PCR. Each plate variety comes in a range of colors, including white wells for real-time PCR and quantitative PCR.

4titude
For info: +44-(0)-1306-884-885
www.4ti.co.uk/pcr/framestar-pcr-qpcr-plates/about-framestar

Electronically submit your new product description or product literature information! Go to www.sciencemag.org/about/new-products-section for more information.

Newly offered instrumentation, apparatus, and laboratory materials of interest to researchers in all disciplines in academic, industrial, and governmental organizations are featured in this space. Emphasis is given to purpose, chief characteristics, and availability of products and materials. Endorsement by *Science* or AAAS of any products or materials mentioned is not implied. Additional information may be obtained from the manufacturer or supplier.

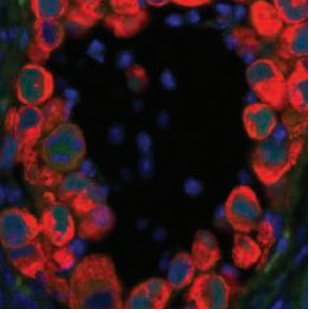
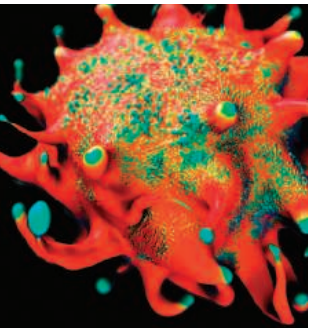

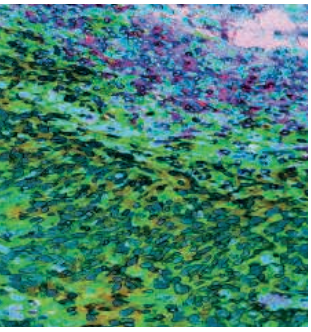

2018 SCIENTIFIC CONFERENCES

Presenting the most significant research on cancer etiology, prevention, diagnosis, and treatment

Cancer Dormancy and Residual Disease
Conference Cochairs: Julio A. Aguirre-Ghiso, Ann F. Chambers, Cyrus M. Ghajar, Christoph A. Klein, and Dorothy A. Sipkins
June 19-22, 2018 | Montreal, QC, Canada

Inaugural AACR International Meeting on Advances in Malignant Lymphoma: Maximizing the Basic-Translational Interface for Clinical Application
Scientific Committee Chair: Ari M. Melnick
June 22-26, 2018 | Boston, MA

Sixth JCA-AACR Special Joint Conference on the Latest Advances in Lung Cancer Research: From Basic Science to Therapeutics
Organizing Committee: Hiroyuki Mano, Seiji Yano, Hiroyoshi Nishikawa, Alice T. Shaw, Roy S. Herbst, and Charles M. Rudin
July 10-12, 2018 | Kyoto, Japan

Pancreatic Cancer: Advances in Science and Clinical Care
Conference Cochairs: Ronald M. Evans, Manuel Hidalgo, Steven D. Leach, Gloria M. Petersen, and Brian M. Wolpin
September 21-24, 2018 | Boston, MA

Second AACR International Conference on Translational Cancer Medicine
Conference Cochairs: Carlos L. Arteaga, Carlos Gil M. Ferreira, and Gabriel A. Rabinovich
September 27-29, 2018 | São Paulo, Brazil

Intestinal Stem Cells and Colon Cancer: Biology to Therapy
Conference Cochairs: Anil K. Rustgi, Johanna Bendell, Hans Clevers, Christina Curtis, and Owen Sansom
September 27-30, 2018 | Washington, DC

Metabolism and Cancer
Conference Cochairs: Ralph J. Deberardinis, Tak W. Mak, Joshua D. Rabinowitz, and M. Celeste Simon
September 28-October 1, 2018 | New York, NY

Fourth CRI-CIMT-EATI-AACR International Cancer Immunotherapy Conference: Translating Science into Survival
September 30-October 3, 2018 | New York, NY

EACR-AACR-ISCR Conference: The Cutting Edge of Contemporary Cancer Research
Conference Cochairs: Richard M. Marais, Eli Pikarsky, and Robert A. Weinberg
October 9-11, 2018 | Jerusalem, Israel

30th Anniversary AACR Special Conference Convergence: Systems Biology and Physical Sciences in Oncology
Conference Cochairs: Phillip A. Sharp and William C. Hahn
October 14-17, 2018 | Newport, RI

11th AACR Conference on The Science of Cancer Health Disparities in Racial/Ethnic Minorities and the Medically Underserved
Conference Cochairs: Laura Fejerman, Scarlett Lin Gomez, Augusto C. Ochoa, Brian M. Rivers, and Ivis Sampayo
November 2-5, 2018 | New Orleans, LA

EORTC-NCI-AACR Molecular Targets and Cancer Therapeutics Symposium
Scientific Committee Cochairs: Charles Swanton, James L. Gulley, and Antoni Ribas
November 13-16, 2018 | Dublin, Ireland

AACR-KCA Joint Conference on Precision Medicine in Solid Tumors
Program Committee Cochairs: Tae-You Kim and Charles L. Sawyers
November 15-17, 2018 | Seoul, South Korea

Tumor Immunology and Immunotherapy
Conference Cochairs: James P. Allison, Lisa M. Coussens, Ira Mellman, and Drew M. Pardoll
November 27-30, 2018 | Miami Beach, FL

Learn more and register at
AACR.org/Calendar

AACR American Association for Cancer Research®
FINDING CURES TOGETHER®

Institute of Physics (CAS)
Celebrates 90 Years of Innovations

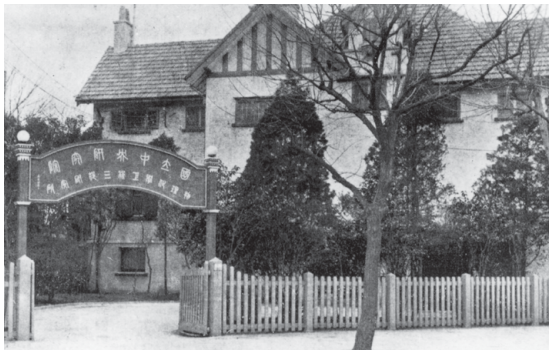

The Institute of Physics (IOP) at the Chinese Academy of Sciences (CAS) is the flagship physics research institute in China. IOP is also designated as the National Research Center for Condensed Matter Physics, one of six centers recently named by the country's Ministry of Science and Technology. The collection of articles in this supplement represent selected major achievements in condensed matter physics research over IOP's 90-year history, as well as the innovations in technology and industry that have resulted. IOP's latest development is also discussed—a group of multiple infrastructures and R&D facilities in Huairou Science City, a planned science center with a 100-km^2 area, located in the northeast suburbs of Beijing.

Read about the institute's distinguished past and promising future in this latest supplement to *Science*, available at scim.ag/cas_iop.

ARTICLES

Sponsored by

中国科学院物理研究所九十周年
90TH ANNIVERSARY OF INSTITUTE OF PHYSICS CAS

Produced by the *Science*/AAAS Custom Publishing Office

Science
AAAS

Science Careers

SCIENCE CAREERS ADVERTISING

For full advertising details, go to ScienceCareers.org and click For Employers, or call one of our representatives.

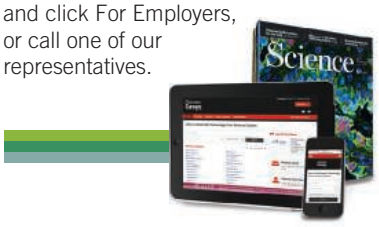

AMERICAS

+1 202 326-6577
+1 202 326-6578
advertise@sciencecareers.org

EUROPE, INDIA, AUSTRALIA, NEW ZEALAND, REST OF WORLD

+44 (0) 1223 326527
advertise@sciencecareers.org

CHINA, KOREA, SINGAPORE, TAIWAN, THAILAND

+86 131 4114 0012
advertise@sciencecareers.org

JAPAN

+81 3-6459-4174
advertise@sciencecareers.org

CUSTOMER SERVICE

AMERICAS

+1 202 326-6577

REST OF WORLD

+44 (0) 1223 326528

advertise@sciencecareers.org

All ads submitted for publication must comply with applicable U.S. and non-U.S. laws. *Science* reserves the right to refuse any advertisement at its sole discretion for any reason, including without limitation for offensive language or inappropriate content, and all advertising is subject to publisher approval. *Science* encourages our readers to alert us to any ads that they feel may be discriminatory or offensive.

ScienceCareers
FROM THE JOURNAL SCIENCE AAAS

ScienceCareers.org

SANOFI - INSTITUT PASTEUR
2018 AWARDS
€ 350 000
FOR BIOMEDICAL RESEARCH

INSPIRED BY INSTITUT PASTEUR
SUPPORTED BY SANOFI

CALL FOR NOMINATIONS

SPECIAL FOCUS FOR GLOBAL HEALTH

1 – IMMUNOLOGY
2 - MICROBIOLOGY & INFECTION

2 AWARDS

1 International award - € 200 000
1 International Mid-Career award - € 150 000

DEADLINE FOR APPLICATION : JUNE, 25th
Awards Ceremony : Thursday, 15th November, 2018

CONTACT :
2018awards@pasteur.fr

MORE INFORMATION ON :
www.sanofi-institutpasteur-awards.com

A distinguished international Jury will choose the Awardees:
Dr. Elizabeth H. Blackburn, Prof. Pascale Cossart, Prof. Catherine Dulac, Dr. Yasmine Belkaïd, Prof. Alain Fischer, Prof. Jörg H. Hacker, Prof. Jules A. Hoffmann, Prof. Antonio Lanzavecchia, Dr Gary J. Nabel, Prof. Staffan Normark, Prof. Michel C. Nussenzweig, Prof. Anne O'Garra, Prof. Jeffrey V. Ravetch, Prof. Philippe Sansonetti.

Scientific Coordinator of Awards: Prof. Pascale Cossart

SANOFI

Institut Pasteur

10 ways that *Science* Careers can help advance your career

1. Register for a free online account on **ScienceCareers.org**.
2. Search thousands of job postings and find your perfect job.
3. Sign up to receive e-mail alerts about job postings that match your criteria.
4. Upload your resume into our database and connect with employers.
5. Watch one of our many webinars on different career topics such as job searching, networking, and more.
6. Download our career booklets, including Career Basics, Careers Beyond the Bench, and Developing Your Skills.
7. Complete an interactive, personalized career plan at "my IDP."
8. Visit our Career Forum and get advice from career experts and your peers.
9. Research graduate program information and find a program right for you.
10. Read relevant career advice articles from our library of thousands.

Visit **ScienceCareers.org** today — all resources are free

ScienceCareers
FROM THE JOURNAL SCIENCE AAAS

SCIENCECAREERS.ORG

Associate Research Scientist position in the Giraldez laboratory

Department of Genetics,
Yale University School of Medicine

The Giraldez laboratory at Yale University is seeking to recruit a highly qualified Associate Research Scientist as a long-term scientist in the laboratory (www.giraldezlab.org). Prerequisites for appointment on the research scientist track include a doctoral degree and relevant postdoctoral experience. This is a non-tenured track faculty appointment under the principal investigator. (https://medicine.yale.edu/facultyaffairs/appts/ap_procedures/nonladder.aspx)

The qualifications for this position are post-doctoral experience with an extensive publication record in high quality journals, track record of leadership skills, and outstanding commitment to research. Expertise in molecular biology, chromatin biology, developmental biology, genomics, and/or imaging will be highly regarded in evaluating the candidates.

The goals of this long-term scientist position are to mentor and manage day to day operations in the laboratory, in addition to drive a successful scientific project aligned with the major interests of the laboratory. This scientist will work closely with Dr. Giraldez and individual scientists in the laboratory to provide mentoring and guidance in the day to day operations. This appointment can be renewed indefinitely as long as the need for the position continues, the funding for the position is available, and the expectations for performance are met.

To apply to this position please submit: (1) One page cover letter describing motivation for the position, research experience, mentoring/managerial experience, (2) biosketch or CV, (3) three letters of references and (4) the PDF of three publications using the Interfolio Link: **https://apply.interfolio.com/50482**. For inquiries please contact hiba.codore@yale.edu. Please include "Associate Research Scientist" in the subject of the email.

Yale University is an Affirmative Action/Equal Opportunity Employer. Yale values diversity among its students, staff, and faculty and strongly welcomes applications from women, persons with disabilities, protected veterans, and underrepresented minorities.

Department of Health and Human Services
National Institutes of Health
National Cancer Institute
Center for Cancer Research
Lymphoid Malignancies Branch
Staff Clinician

The Waldmann Laboratory and Clinical Trials Team of the Lymphoid Malignancies Branch (LMB), National Cancer Institute (NCI), wish to recruit an outstanding clinician scientist as a Staff Clinician. Applicants with an M.D. degree, board certified in internal medicine, board eligible/certified in hematology and medical oncology, and who have a track record of accomplishments in basic oncology research and its translation into immunotherapeutic clinical trials utilizing cytokines for patients with cancer, are encouraged to apply.

The candidate will be a member of the Thomas A. Waldmann, M.D. Laboratory and the Clinical Trials Team and will coordinate with the staff to design and execute clinic trials using IL-15 co-discovered by Dr. Waldmann in drug combination therapy of cancer. IL-15 will be used with agents to relieve checkpoints on the immune system, with cancer directed monoclonal antibodies to augment their antibody-dependent, cell-mediated cytotoxicity (ADCC) and with an agonistic anti-CD40 antibody used to generate antigen-specific CD8 cytotoxic T cells. Other trials used are kinase inhibitors to translate insights defining the molecular abnormalities of the JAK/STAT system in T-cell malignancies. Examples of these approaches have been published recently in *Cancer Immunology Research* 2015, 5(3): 219-227 and the *Journal of Clinical Oncology* 2015, 33(1): 74-U123.

The candidate must have strong communication skills in oral and written (English) and be able to interact effectively with patients and physicians to achieve clinical trial goals. Salary is commensurate with research experience and accomplishments. Please send your curriculum vitae, a description of relevant experience, contact information for 3 references to: **Dr. Thomas A. Waldmann c/o Sildiz Ali, Program Specialist, Lymphoid Malignancies Branch, National Cancer Institute** at Email: **alis@mail.nih.gov**. Applications must be submitted **between June 1st to June 30th, 2018**.

DHHS, NIH, and NCI are Equal Opportunity Employers.

NIH NATIONAL CANCER INSTITUTE

Professor and Chair, Department of MEDICAL ANATOMICAL SCIENCES

The College of Osteopathic Medicine of the Pacific (COMP) at Western University of Health Sciences invites applications for the tenure-track position of Chair in the Department of Medical Anatomical Sciences. Western University seeks applicants (PhD/DO/MD) at the Associate or Full Professor level with distinguished academic and administrative accomplishments. The successful applicant will be expected to:

(1) Perform effective administrative duties: Good interpersonal skills and a commitment to mentoring are essential to promote professional growth and development of department faculty, as well as establish collaboration with other basic and clinical science departments. The Chair is a vital member of the College's leadership who will participate in setting COMP goals and assessment of departmental and college outcomes.

(2) Maintain an active research program: Competitive salary, start-up support, laboratory space, and access to core facilities will be offered. Preferred applicants will have an established research program supported by extramural funding.

(3) Participate in health professions education: Limited teaching in Gross Anatomy, Histology, Embryology, and/or Neuroanatomy to first- and second-year medical students. Applicants must have several years of experience in anatomical sciences teaching and curriculum development.

The review of applications will begin immediately and continue until the position is filled. Applicants should submit a (1) cover letter, (2) research statement, (3) teaching philosophy statement, and (4) curriculum vitae with contact information for three references to posting A00270 on **http://apptrkr.com/1205815**

Inquiries can be addressed to the Search Committee Chair: Dr. Mathew Wedel, tel #: 909-469-6842, e-mail: mwedel@westernu.edu.

By **Shuai Li**

Pitch imperfect

Holding the $10,000 check felt unreal. It represented almost half of my annual stipend as a graduate student, and I had earned it in just 3 days by pitching my startup idea at the first Idaho Entrepreneur Challenge. Standing at center stage on the top floor of the tallest building in the state capital, facing an audience of prominent businesspeople, politicians, and other young entrepreneurs, I felt like a celebrity. My success was all the more rewarding because, as a nonnative English speaker, I had spent the previous 8 years struggling with a lack of confidence in my ability to communicate.

When I came to the United States from China in my early 20s to further my education, I knew that my language skills would need a lot of work. Although I had learned some technical English as part of my software engineering degree, I certainly couldn't hold a conversation. But I felt that the United States was the best place for me to grow, so I made the leap.

My accent and poor grammar made for tough going at first. While working at the college tutoring center, the most common question I would receive was not about a particular class subject, but rather a simple, "Can you say that again?" When a student ordered a quesadilla from me as I worked in the school cafeteria, I thought to myself, "I have no idea what kind of burger that is." It was frustrating, embarrassing, and stressful. I felt I was letting others down and wasting their time, and I started to doubt my abilities. At times, I wondered whether coming to the United States had been the right decision after all.

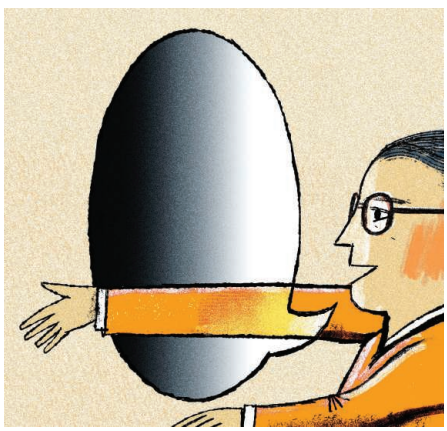

"The only way forward was to confront my discomfort with English by practicing."

But during those first dreadful months, I realized that the only way forward was to confront my discomfort with English by practicing at every opportunity. I forced myself to initiate conversations, including at home with my host family, at my part-time jobs, and while volunteering at a local museum. Talking to random strangers with my imperfect English was intimidating at first, but more often than not I received a friendly response, a nod or a faint smile, which made me feel that my effort was worth it. Every day I spent hours with a recorder, capturing and reviewing my pronunciation, looking forward to the day when people would understand me loud and clear.

During the entrepreneurship event, I realized that my practice had finally paid off. In the months that followed, I went on a pitching spree and managed to gather enough seed money to fund my startup. I forced myself to speak confidently in front of business mentors, my startup co-founders, and our new hires. I was even invited to speak at my university's first ever TEDx event about what inspired me to become an entrepreneur. Buoyed in part by my recent successes, I accepted the rare invitation. Even so, I was nervous about speaking at such a high-profile event. When I walked into the beaming stage light, I took my glasses off so that I wouldn't make eye contact with the hundreds of people in the audience. I prayed to all the deities I knew to calm me so that my tongue wouldn't move faster than my thoughts. All I wanted was to deliver a crystal-clear talk. When it was over, I was exhausted but relieved—and the audience's applause indicated that I had done a good job. Perhaps most important, I had proved to myself that I could confidently deliver a complex speech to a large crowd—in English.

My startup didn't take off, and I'm now back on a more traditional research path. These days, I put my ever-improving communication skills to use in mentoring students in the lab. Outside of academia, I'm more confident during social gatherings. A slight accent may betray my origin, but I know I can still grab my listeners' attention. And I greatly appreciate the people who have helped me reach this point by patiently listening to me over the years.

I've found that many international scholars tend to withdraw or build community mainly with people from their home country, and I understand why. But if English is not your first language, allow me to pitch you an idea: Talk to someone new every day. Get comfortable with discomfort and start using English to tell your story. ■

Shuai Li is a postdoctoral fellow at Washington State University in Pullman and will move to the Mayo Clinic in Rochester, Minnesota, this month.

ILLUSTRATION: ROBERT NEUBECKER